

<b>REPORT DOCUMENTATION PAGE</b>			Form Approved OMB No. 0704-0188	
Public reporting burden for this collection of information is estimated to average 1 hour per response, including the time for reviewing instructions, searching existing data sources, gathering and maintaining the data needed, and completing and reviewing the collection of information. Send comments regarding this burden estimate or any other aspect of this collection of information, including suggestions for reducing this burden, to Washington Headquarters Services, Directorate for Information Operations and Reports, 1215 Jefferson Davis Highway, Suite 1204, Arlington, VA 22202-4302, and to the Office of Management and Budget, Paperwork Reduction Project (0704-0188), Washington, DC 20503.				
1. AGENCY USE ONLY (Leave blank)		2. REPORT DATE May 15, 2004		3. REPORT TYPE AND DATES COVERED Technical 08/01/01 to 05/15/04
4. TITLE AND SUBTITLE Measurements of the Tip-Gap Turbulent Flow Structure in a Low-speed Compressor Cascade			5. FUNDING NUMBERS N00014-99-1-0302 N00014-04-1-0291	
6. AUTHORS Genglin Tang and Roger L. Simpson				
7. PERFORMING ORGANIZATION NAME(S) AND ADDRESS(ES) Department of Aerospace and Ocean Engineering Virginia Polytechnic Institute and State University Blacksburg, Virginia 24061-0203			8. PERFORMING ORGANIZATION REPORT NUMBER  VPI-AOE-288	
9. SPONSORING/MONITORING AGENCY NAME(S) AND ADDRESS(ES) Office of Naval Research, 800 N. Quincy Street Arlington, Virginia 22217			10. SPONSORING/MONITORING AGENCY REPORT NUMBER	
11. SUPPLEMENTARY NOTES <b>DISTRIBUTION STATEMENT A</b> Approved for Public Release Distribution Unlimited				
12a. DISTRIBUTION/AVAILABILITY STATEMENT Unlimited			12b. DISTRIBUTION CODE	
13. ABSTRACT (Maximum 200 words) Experimental results are presented from a study of the tip-gap turbulent flow structure in a low-speed linear compressor cascade wind tunnel at Virginia Tech that includes a moving belt system to simulate the relative motion between the tip and the casing. Endwall pressure measurements and surface oil flow visualizations were made on a stationary endwall to obtain some global flow features. A custom-made miniature 3-orthogonal-velocity-component fiber-optic laser-Doppler velocimeter (LDV) with a 50 micron spherical measurement volume was used to measure all three components of instantaneous velocity within the gap between the endwall and the blade tip, mainly for the stationary wall with 1.65% and 3.30% of chord tip gaps, as well as some initial experiments with the moving wall. The surface skin friction velocity was obtained by using viscous sublayer velocity profiles, which verified the presence of an intense lateral shear layer that was observed from surface oil flow visualizations. All second- and third-order turbulence quantities are presented. Tip gap flows are complex, pressure-driven, unsteady highly skewed three-dimensional turbulent flows. The crossflow velocity normal to the blade chord is nearly uniform in the mid tip-gap and changes substantially from the pressure to suction side due to the local tip pressure loading, which is different from the mid-span pressure loading because of tip leakage vortex influence. Normalized circulation within the tip gap is independent of the gap size. The tip gap flow interacts with the primary flow, separates from the endwall, and rolls up on the suction side to form the tip leakage vortex, which is unsteady as observed from the TKE transport vector and oil flow visualizations. Other than the nearest endwall and blade tip regions, the TKE does not vary much in tip gap. The tip leakage vortex produces high turbulence intensities. The tip gap flow correlations of streamwise and wall normal velocity fluctuations decrease significantly from the leading edge to the trailing edge of the blade due to flow skewing. The tip gap flow is a strongly anisotropic turbulent flow. Rapid distortion ideas do not apply. A turbulence model based on stress transport equations is necessary to reflect the tip gap flow physics. For the moving endwall, relative motion skews the inner region flow which is decorrelated with the outer layer flow. Hence, the TKE and correlations of streamwise and wall normal velocity fluctuations are lower.				
14. SUBJECT TERMS Three-dimensional Flow, Turbulent Boundary Layers, compressor flows, tip gap flows			15. NUMBER OF PAGES 384	
			16. PRICE CODE	
17. SECURITY CLASSIFICATION OF REPORT UNCLASSIFIED	18. SECURITY CLASSIFICATION OF THIS PAGE UNCLASSIFIED	19. SECURITY CLASSIFICATION OF ABSTRACT UNCLASSIFIED	20. LIMITATION OF ABSTRACT UNLIMITED	

# Contents

<b>Acknowledgements</b>	<b>iv</b>
<b>Table of Contents</b>	<b>vi</b>
<b>List of Figures</b>	<b>xii</b>
<b>List of Tables</b>	<b>xxiii</b>
<b>Nomenclature</b>	<b>xxiv</b>
<b>1 Introduction</b>	<b>1</b>
1.1 Brief Review of Tip Gap Flow . . . . .	2
1.1.1 Previous Research in a Tip Gap . . . . .	5
1.1.2 Relative Motion Effect . . . . .	8
1.2 Dissertation Study . . . . .	10
<b>2 Apparatus and Instrumentation</b>	<b>13</b>
2.1 Cascade Wind Tunnel . . . . .	14
2.1.1 Evolution of the Test Section Set-up . . . . .	14
2.1.2 Teflon-covered Tunnel Floor . . . . .	16
2.1.3 Measurement Windows . . . . .	17

2.1.4	Tunnel-enclosed Environmental Tent . . . . .	18
2.1.5	Flow Temperature Control . . . . .	18
2.1.6	Test Condition Monitor . . . . .	19
2.2	Moving Belt System . . . . .	19
2.2.1	Operational Fundamentals . . . . .	20
2.2.2	Sure Tracker Belt Controller . . . . .	21
2.2.3	Belt Speed Variation and Control . . . . .	22
2.2.4	Striped Bed . . . . .	23
2.2.5	Active Blowing . . . . .	24
2.2.6	Cleaning Devices . . . . .	24
2.2.7	Control Booth . . . . .	25
2.3	Miniature LDV . . . . .	25
2.3.1	LDV head . . . . .	26
2.3.2	Optical Table for LDV . . . . .	28
2.3.3	LDV Signal Processing . . . . .	28
2.3.4	LDV Seeding . . . . .	29
2.3.5	Positioning Plate for LDV . . . . .	30
2.3.6	LDV Probe Volume Position Determination . . . . .	31
2.3.7	LDV Monitoring . . . . .	31
2.3.8	Dust-free Housing for LDV Head . . . . .	31
2.4	Optical Sensors . . . . .	32
2.4.1	Fiber Optic Belt Displacement Sensor . . . . .	32
2.4.2	Belt-Joint Detector . . . . .	33
2.5	Integrated Data Acquisition System . . . . .	33

2.5.1	IDAS Hardware Platform . . . . .	34
2.5.2	IDAS Software Framework . . . . .	35
2.6	Data Post-Processing . . . . .	36
2.6.1	LDV Data Post-Processing . . . . .	36
2.6.2	Analog Data Post-Processing . . . . .	37
2.7	System Improvements . . . . .	38
2.7.1	Previous Efforts . . . . .	38
2.7.2	New Efforts to Solve Problems . . . . .	38
2.8	Equipment Improvements and Future Recommendations . . . . .	40
<b>3</b>	<b>Measurements on a Stationary Wall</b>	<b>55</b>
3.1	Coordinate Systems . . . . .	56
3.2	Calibration . . . . .	57
3.2.1	Tunnel Calibration . . . . .	57
3.2.2	LDV Calibration . . . . .	59
3.3	Measurement Uncertainty . . . . .	60
3.3.1	Position Measurements . . . . .	60
3.3.2	LDV Measurements . . . . .	60
3.4	Surface Oil Flow Visualizations . . . . .	61
3.4.1	Endwall . . . . .	61
3.4.2	Blade Surfaces . . . . .	63
3.5	Surface Pressure Measurements . . . . .	64
3.5.1	Blade Pressure Loading . . . . .	64
3.5.2	Endwall Static Pressure Distribution . . . . .	65
3.6	LDV Measurements . . . . .	66



3.6.1	Test Matrix . . . . .	68
3.6.2	Skin Friction Velocity . . . . .	69
3.6.3	Mean Velocity Vector . . . . .	71
3.6.4	Reynolds Stress Tensor . . . . .	75
3.6.5	Triple Product Tensor . . . . .	82
3.6.6	Circulation, Vorticity, and Helicity . . . . .	84
3.6.7	Turbulence-modelling Related Parameters . . . . .	88
3.6.8	TKE-based Quantities . . . . .	96
3.6.9	Application of Rapid Distortion Ideas . . . . .	98
3.6.10	Spectral Estimation . . . . .	99
3.7	Flow Structure Discussion . . . . .	101
3.7.1	Disturbed Inflow . . . . .	102
3.7.2	Tip Gap Mean Flow . . . . .	103
3.7.3	Tip Gap Flow Turbulence . . . . .	107
3.7.4	Tip Gap Size Effects . . . . .	110
<b>4</b>	<b>Measurements on a Moving Wall</b>	<b>192</b>
4.1	Calibration and Uncertainty . . . . .	193
4.1.1	Tunnel and LDV Calibration . . . . .	193
4.1.2	LDV Uncertainty . . . . .	193
4.2	Blade Surface Oil Flow Visualization . . . . .	194
4.3	LDV Measurements . . . . .	194
4.3.1	Mean Velocity . . . . .	195
4.3.2	Turbulence . . . . .	198
4.4	Flow Structure Discussion . . . . .	200

<b>5</b>	<b>Conclusions</b>	<b>220</b>
5.1	Stationary End-Wall . . . . .	220
5.2	Moving End-Wall . . . . .	224
5.3	Future Work . . . . .	225
	<b>References</b>	<b>227</b>
<b>A</b>	<b>Operation and Maintenance of a High quality LDV</b>	<b>237</b>
A.1	Beam Intensity . . . . .	237
A.2	Beam Polarization . . . . .	238
A.3	Beam Frequency . . . . .	238
A.4	Beam Path . . . . .	239
A.5	Beam Mode . . . . .	239
A.6	Alignment of Measurement Volume . . . . .	239
A.7	Receiving Adjustment . . . . .	239
A.8	Photomultiplier Tube . . . . .	240
A.9	Signal conditioning and Processing . . . . .	240
A.10	Radio Frequency . . . . .	240
A.11	Data Transfer . . . . .	241
A.12	Seeding . . . . .	241
A.13	Test Flow . . . . .	241
A.14	Daily Maintenance . . . . .	241
A.15	Troubleshooting . . . . .	242
<b>B</b>	<b>Uncertainty Analysis of LDV</b>	<b>243</b>
B.1	Uncertainty Sources . . . . .	243

B.1.1	Beam Quality . . . . .	244
B.1.2	Fringe Pattern . . . . .	244
B.1.3	Signal and Data Processing . . . . .	245
B.1.4	Seeding Particles . . . . .	246
B.2	Uncertainty Estimation . . . . .	246
B.3	Skin-friction Velocity Uncertainty . . . . .	247
B.4	Wall Location Uncertainty . . . . .	247
<b>C</b>	<b>Skin Friction Velocity and Wall Location Refinement</b>	<b>249</b>
C.1	Skin Friction Velocity . . . . .	249
C.2	Wall Location Refinement . . . . .	250
<b>D</b>	<b>Least Square Fitting of Experimental Data</b>	<b>252</b>
D.1	Parabolic Fit . . . . .	252
D.2	Quadric Fit . . . . .	253
D.3	Least Square Error . . . . .	254
D.4	Pseudo-Inverse . . . . .	255
<b>E</b>	<b>Mean Velocities for a Stationary Endwall</b>	<b>256</b>
<b>F</b>	<b>Reynolds Stresses for a Stationary Endwall</b>	<b>266</b>
<b>G</b>	<b>Triple Products for a Stationary Endwall</b>	<b>285</b>
<b>H</b>	<b>Comprehensive Parameters for a Stationary Endwall</b>	<b>316</b>
<b>Vita</b>		<b>361</b>

# List of Figures

1.1	Flow features in the blade tip region . . . . .	12
2.1	Top view of experimental test section setup in the Cascade Wind Tunnel	41
2.2	Side view of experimental test section setup in the Cascade Wind Tunnel	42
2.3	The working tunnel with laser beams . . . . .	43
2.4	Two anti-static brushes facing the moving belt . . . . .	44
2.5	Upstream end of bed with 12" PVC pipe attached . . . . .	44
2.6	Sure Tracker . . . . .	45
2.7	Tunnel with moving belt and instrumentation setup for moving wall experiments . . . . .	46
2.8	Part of the bed with high temperature tape strips for the moving belt system	47
2.9	Two face to face brushes used for a moving belt . . . . .	47
2.10	Miniature 3D fiber-optic LDV head . . . . .	48
2.11	Schematic of 3-orthogonal-velocity-component fiber-optic LDV head . . .	48
2.12	Assembly of LDV head and displacement sensor along with a traverse . .	49
2.13	Assembly of LDV head and displacement sensor on the positioning plate and under the tunnel . . . . .	49
2.14	Schematic of LDV signal conditioning for the Cascade Wind Tunnel . . .	50

2.15 DOP generator with an impactor can under the contraction of the Cascade Wind Tunnel . . . . .	50
2.16 Seeding pipe downstream of flow conditioning screens in the contraction of the Cascade Wind Tunnel . . . . .	51
2.17 Monitor for LDV beams out of the optical glass window inside the tunnel	51
2.18 Calibration curve for the displacement sensor . . . . .	52
2.19 Output of both displacement sensor and joint detector for moving wall experiments . . . . .	53
2.20 Schematic of integrated data acquisition system . . . . .	54
3.1 Setup of Compressor Cascade Wind Tunnel . . . . .	121
3.2 Coordinate systems and multiple window locations in the test section . .	122
3.3 Velocities at tunnel half height upstream ( $x/c_a = -0.705$ ) and downstream ( $x/c_a = 2.95$ ) of blade row for stationary wall experiments in bed coordinates . . . . .	123
3.4 Test matrices for 1.65% and 3.30% . . . . .	124
3.5 Validation with direct numerical simulation for the LDV measurement . .	125
3.6 Endwall oil flow visualizations for 1.65% and 3.30% . . . . .	126
3.7 Blade surface oil flow visualizations for 1.65% . . . . .	127
3.8 Blade surface oil flow visualizations for 3.30% . . . . .	128
3.9 Mid-span pressure blade loading for 1.65% and 3.30% . . . . .	129
3.10 Endwall static pressure distributions for 1.65% and 3.30% . . . . .	130
3.11 Static pressure $C_p$ distribution of blade projection onto endwall in chord coordinate system . . . . .	131
3.12 Static pressure difference $\Delta C_p$ of mid-span and projection onto endwall in chord coordinate system . . . . .	132

3.13 Pressure and pressure gradient along $x/c_a = 0.18$ for 1.65% and $x/c_a = 0.42$ for 3.30% in the bed coordinate system . . . . .	133
3.14 Skin friction velocity on endwall for 1.65% and 3.30% . . . . .	134
3.15 Mean $U$ , $V$ , $W$ and $U^+$ , $V^+$ , $W^+$ at $x/c_a = 0.42$ for 3.30% in chord coordinate system . . . . .	135
3.16 Mean $U/U_{ref}$ for both 1.65% and 3.30% in chord coordinate system . . .	136
3.17 Mean $V/U_{ref}$ for both 1.65% and 3.30% in chord coordinate system . . .	137
3.18 Mean $W/U_{ref}$ for both 1.65% and 3.30% in chord coordinate system . . .	138
3.19 Normal stress $\overline{u^2}/U_{ref}^2$ for both 1.65% and 3.30% in chord coordinate system	139
3.20 Normal stress $\overline{v^2}/U_{ref}^2$ for both 1.65% and 3.30% in chord coordinate system	140
3.21 Normal stress $\overline{w^2}/U_{ref}^2$ for both 1.65% and 3.30% in chord coordinate system	141
3.22 Shear stress $\overline{uv}/U_{ref}^2$ for both 1.65% and 3.30% in chord coordinate system	142
3.23 Shear stress $\overline{vw}/U_{ref}^2$ for both 1.65% and 3.30% in chord coordinate system	143
3.24 Shear stress $\overline{uw}/U_{ref}^2$ for both 1.65% and 3.30% in chord coordinate system	144
3.25 Triple product $\overline{uvw^2}/U_{ref}^3$ for both 1.65% and 3.30% in chord coordinate system . . . . .	145
3.26 Triple product $\overline{v^3}/U_{ref}^3$ for both 1.65% and 3.30% in chord coordinate system	146
3.27 Triple product $\overline{v^2w}/U_{ref}^3$ for both 1.65% and 3.30% in chord coordinate system . . . . .	147
3.28 Circulation $\Gamma_x$ for both 1.65% and 3.30% . . . . .	148
3.29 Vorticity at $x/c_a = 0.27$ for both 1.65% and 3.30% in bed coordinate system	149
3.30 Helicity at $x/c_a = 0.27$ for both 1.65% and 3.30% in bed coordinate system	150
3.31 Flow angle for both 1.65% and 3.30% in chord coordinate system . . . .	151
3.32 Flow gradient angle for both 1.65% and 3.30% in chord coordinate system	152
3.33 Shear stress angle for both 1.65% and 3.30% in chord coordinate system .	153

3.34	Anisotropy factor $N$ for both 1.65% and 3.30% in chord coordinate system	154
3.35	Turbulent kinetic energy $TKE/U_{ref}^2$ for both 1.65% and 3.30%	155
3.36	Townsend structure al for both 1.65% and 3.30% in chord coordinate system	156
3.37	$1/S$ for both 1.65% and 3.30%	157
3.38	$B$ for both 1.65% and 3.30% in chord coordinate system	158
3.39	$B2$ for both 1.65% and 3.30% in chord coordinate system	159
3.40	TKE Transport vector for 1.65% and 3.30% in chord coordinate system	162
3.41	TKE production at $x/c_a = 0.27$ for both 1.65% and 3.30% in bed coordinate system	163
3.42	$\overline{u^2}U/U_{ref}^3$ , $\overline{w^2}W/U_{ref}^3$ , $(\overline{u^2} + \overline{v^2})Q/U_{ref}^3$ at $x/c_a = 0.18$ for both 1.65% and 3.30% in chord coordinate system	164
3.43	$\overline{u^2}U^{0.5}/U_{ref}^3$ , $\overline{w^2}W^{0.5}/U_{ref}^3$ , $(\overline{u^2} + \overline{v^2})Q^{0.5}/U_{ref}^3$ at $x/c_a = 0.18$ for both 1.65% and 3.30% in chord coordinate system	165
3.44	$\sqrt{U^2 + V^2 + W^2}/U_{ref}$ , $\sqrt{\overline{u^2} + \overline{v^2} + \overline{w^2}}/U_{ref}$ at $x/c_a = 0.18$ and $x/c_a = 0.42$ for both 1.65% and 3.30% in chord coordinate system	166
3.45	Spectra estimation of velocity component $u$ for profile $uu$ and $1d$ in free-stream chord coordinate system	167
3.46	Spectra estimation of velocities for tip leakage vortex with 1.65% and 3.30% tip gaps	168
3.47	Inflow $U$ , $V$ , and $W$ profiles at $x/c_a$ for both 1.65% and 3.30% in free-stream coordinate system	169
3.48	Inflow TKE, Reynolds stress, $FA$ , $A1$ , and $1/S$ for both 1.65% and 3.30% in free-stream coordinate system	170
3.49	$U/U_{ref}$ , $V/U_{ref}$ , $W/U_{ref}$ at $x/c_a = 0.18$ for both 1.65% and 3.30% in chord coordinate system	171
3.50	$VW$ vector plots at $x/c_a = 0.18$ for both 1.65% and 3.30% in chord coordinate system	172

3.51	Maximum $W$ for 1.65% and 3.30% in the chord coordinate system . . . . .	173
3.52	VW vector plots at $x/c_a = 0.18$ with 1.65% and $x/c_a = 0.42$ with 3.30% in the separation-line coordinate system . . . . .	174
3.53	Mean velocity vector $UW$ for 1.65% and 3.30% . . . . .	175
3.54	Mean Velocity vector $VW$ for 1.65% and 3.30% in chord coordinate system	178
3.55	$W/U_{ref}$ on the suction side for 1.65% and 3.30% in chord coordinate system	179
3.56	VW vector plot in local camber coordinate system for 1.65% . . . . .	180
3.57	VW vector plot in local camber coordinate system for 3.30% . . . . .	181
3.58	Gap Model - Mean Flow . . . . .	182
3.59	$U/U_\tau$ , $W/U_\tau$ , and $R_{uw}$ at $x/c_a = 0.18$ for both 1.65% and 3.30% in wall shear coordinate system . . . . .	183
3.60	FA, FGA, and SSA at $x/c_a = 0.18$ for both 1.65% and 3.30% in chord coordinate system . . . . .	184
3.61	FA, FGA, and SSA at local upstream for both 1.65% and 3.30% in chord coordinate system . . . . .	185
3.62	$\overline{u^2}/U_{ref}^2$ , $\overline{v^2}/U_{ref}^2$ , and $\overline{w^2}/U_{ref}^2$ at $x/c_a = 0.18$ for 1.65% and at $x/c_a = 0.42$ for 3.30% in chord coordinate system . . . . .	186
3.63	$TKE/U_{ref}^2$ at the origin of tip leakage vortex for both 1.65% and 3.30% .	187
3.64	VW vector and TKE contour plots at $x/c_a = 0.18$ with 1.65% and $x/c_a =$ $0.42$ with 3.30% in the chord coordinate system . . . . .	188
3.65	Comparison between $V\vec{W}$ and $V\vec{W} + \vec{V}_q$ for 1.65% and 3.30% in separation- line coordinate system . . . . .	189
3.66	Gap Model - Turbulence . . . . .	190
3.67	Correlation coefficients of $\overline{uw}$ at suction side for both 1.65% and 3.30% in chord coordinate system . . . . .	191
4.1	Location of data taken for moving wall . . . . .	206



4.2	Velocities at tunnel half height upstream ( $x/c_a = -0.705$ ) and downstream ( $x/c_a = 2.95$ ) of blade row in bed co-ordinates . . . . .	206
4.3	Blade suction surface oil flow visualizations for 1.65% and 3.30% with moving wall . . . . .	207
4.4	Mean velocity U, V, W at $x/c_a = -0.33$ with 3.30% tip gap . . . . .	208
4.5	Mean velocity U, V, W and flow angle at $x/c_a = -0.33$ with 3.30% tip gap in the bed coordinate system . . . . .	209
4.6	Flow angle at $x/c_a = -0.33$ with 3.30% tip gap in the moving coordinate system . . . . .	210
4.7	UW Vector plots of profile uu at $x/c_a = -0.33$ with 3.30% tip gap in stationary bed and moving wall coordinate systems . . . . .	211
4.8	Mean velocity U, V, and W of profiles 5p, 5s, and e3 at $x/c_a = 0.18$ with 1.65% tip gap in the bed and chord coordinate systems . . . . .	212
4.9	Velocity vector plots of profiles 5p, 5s, and e3 at $x/c_a = 0.18$ with 1.65% tip gap in the stationary bed coordinate system . . . . .	213
4.10	Flow angles of profiles 5p, 5s, and e3 at $x/c_a = 0.18$ with 1.65% tip gap in the stationary bed and moving wall coordinate systems . . . . .	214
4.11	Velocity vector Plots of profiles 5p, 5s, and e3 at $x/c_a = 0.18$ with 1.65% tip gap in the moving coordinate systems . . . . .	215
4.12	Reynolds stress profile uu at $x/c_a = -0.33$ with 3.30% tip gap for both free stream and bed coordinate system . . . . .	216
4.13	Normalized TKE and 1/S of profile uu at $x/c_a = -0.33$ with 3.30% tip gap	217
4.14	Reynolds stress of profiles 5p, 5s, and e3 at $x/c_a = 0.18$ with 1.65% tip gap in bed coordinate system . . . . .	218
4.15	Normalized TKE and 1/S of profiles 5p, 5s, and e3 at $x/c_a = 0.18$ with 1.65% tip gap . . . . .	219
E.1	Mean $U/U_{ref}$ , $V/U_{ref}$ , and $W/U_{ref}$ at $x/c_a = 0.00$ for both 1.65% and 3.30% in chord coordinate system . . . . .	257

E.2	Mean $U/U_{ref}$ , $V/U_{ref}$ , and $W/U_{ref}$ at $x/c_a = 0.04$ for both 1.65% and 3.30% in chord coordinate system . . . . .	258
E.3	Mean $U/U_{ref}$ , $V/U_{ref}$ , and $W/U_{ref}$ at $x/c_a = 0.09$ for both 1.65% and 3.30% in chord coordinate system . . . . .	259
E.4	Mean $U/U_{ref}$ , $V/U_{ref}$ , and $W/U_{ref}$ at $x/c_a = 0.12$ for both 1.65% and 3.30% in chord coordinate system . . . . .	260
E.5	Mean $U/U_{ref}$ , $V/U_{ref}$ , and $W/U_{ref}$ at $x/c_a = 0.12$ for both 1.65% and 3.30% in chord coordinate system . . . . .	261
E.6	Mean $U/U_{ref}$ , $V/U_{ref}$ , and $W/U_{ref}$ at $x/c_a = 0.27$ for both 1.65% and 3.30% in chord coordinate system . . . . .	262
E.7	Mean $U/U_{ref}$ , $V/U_{ref}$ , and $W/U_{ref}$ at $x/c_a = 0.42$ for both 1.65% and 3.30% in chord coordinate system . . . . .	263
E.8	Mean $U/U_{ref}$ , $V/U_{ref}$ , and $W/U_{ref}$ at $x/c_a = 0.65$ for both 1.65% and 3.30% in chord coordinate system . . . . .	264
E.9	Mean $U/U_{ref}$ , $V/U_{ref}$ , and $W/U_{ref}$ at $x/c_a = 1.00$ for both 1.65% and 3.30% in chord coordinate system . . . . .	265
F.1	Reynolds normal stresses $\overline{u^2}/U_{ref}^2$ , $\overline{v^2}/U_{ref}^2$ , and $\overline{w^2}/U_{ref}^2$ at $x/c_a = 0.00$ for both 1.65% and 3.30% in chord coordinate system . . . . .	267
F.2	Reynolds normal stresses $\overline{u^2}/U_{ref}^2$ , $\overline{v^2}/U_{ref}^2$ , and $\overline{w^2}/U_{ref}^2$ at $x/c_a = 0.04$ for both 1.65% and 3.30% in chord coordinate system . . . . .	268
F.3	Reynolds normal stresses $\overline{u^2}/U_{ref}^2$ , $\overline{v^2}/U_{ref}^2$ , and $\overline{w^2}/U_{ref}^2$ at $x/c_a = 0.09$ for both 1.65% and 3.30% in chord coordinate system . . . . .	269
F.4	Reynolds normal stresses $\overline{u^2}/U_{ref}^2$ , $\overline{v^2}/U_{ref}^2$ , and $\overline{w^2}/U_{ref}^2$ at $x/c_a = 0.12$ for both 1.65% and 3.30% in chord coordinate system . . . . .	270
F.5	Reynolds normal stresses $\overline{u^2}/U_{ref}^2$ , $\overline{v^2}/U_{ref}^2$ , and $\overline{w^2}/U_{ref}^2$ at $x/c_a = 0.18$ for both 1.65% and 3.30% in chord coordinate system . . . . .	271
F.6	Reynolds normal stresses $\overline{u^2}/U_{ref}^2$ , $\overline{v^2}/U_{ref}^2$ , and $\overline{w^2}/U_{ref}^2$ at $x/c_a = 0.27$ for both 1.65% and 3.30% in chord coordinate system . . . . .	272

F.7	Reynolds normal stresses $\overline{u^2}/U_{ref}^2$ , $\overline{v^2}/U_{ref}^2$ , and $\overline{w^2}/U_{ref}^2$ at $x/c_a = 0.42$ for both 1.65% and 3.30% in chord coordinate system . . . . .	273
F.8	Reynolds normal stresses $\overline{u^2}/U_{ref}^2$ , $\overline{v^2}/U_{ref}^2$ , and $\overline{w^2}/U_{ref}^2$ at $x/c_a = 0.65$ for both 1.65% and 3.30% in chord coordinate system . . . . .	274
F.9	Reynolds normal stresses $\overline{u^2}/U_{ref}^2$ , $\overline{v^2}/U_{ref}^2$ , and $\overline{w^2}/U_{ref}^2$ at $x/c_a = 1.00$ for both 1.65% and 3.30% in chord coordinate system . . . . .	275
F.10	Reynolds shear stresses $-\overline{uv}/U_{ref}^2$ , $-\overline{vw}/U_{ref}^2$ , and $-\overline{uw}/U_{ref}^2$ at $x/c_a =$ 0.00 for both 1.65% and 3.30% in chord coordinate system . . . . .	276
F.11	Reynolds shear stresses $-\overline{uv}/U_{ref}^2$ , $-\overline{vw}/U_{ref}^2$ , and $-\overline{uw}/U_{ref}^2$ at $x/c_a =$ 0.04 for both 1.65% and 3.30% in chord coordinate system . . . . .	277
F.12	Reynolds shear stresses $-\overline{uv}/U_{ref}^2$ , $-\overline{vw}/U_{ref}^2$ , and $-\overline{uw}/U_{ref}^2$ at $x/c_a =$ 0.09 for both 1.65% and 3.30% in chord coordinate system . . . . .	278
F.13	Reynolds shear stresses $-\overline{uv}/U_{ref}^2$ , $-\overline{vw}/U_{ref}^2$ , and $-\overline{uw}/U_{ref}^2$ at $x/c_a =$ 0.12 for both 1.65% and 3.30% in chord coordinate system . . . . .	279
F.14	Reynolds shear stresses $-\overline{uv}/U_{ref}^2$ , $-\overline{vw}/U_{ref}^2$ , and $-\overline{uw}/U_{ref}^2$ at $x/c_a =$ 0.18 for both 1.65% and 3.30% in chord coordinate system . . . . .	280
F.15	Reynolds shear stresses $-\overline{uv}/U_{ref}^2$ , $-\overline{vw}/U_{ref}^2$ , and $-\overline{uw}/U_{ref}^2$ at $x/c_a =$ 0.27 for both 1.65% and 3.30% in chord coordinate system . . . . .	281
F.16	Reynolds shear stresses $-\overline{uv}/U_{ref}^2$ , $-\overline{vw}/U_{ref}^2$ , and $-\overline{uw}/U_{ref}^2$ at $x/c_a =$ 0.42 for both 1.65% and 3.30% in chord coordinate system . . . . .	282
F.17	Reynolds shear stresses $-\overline{uv}/U_{ref}^2$ , $-\overline{vw}/U_{ref}^2$ , and $-\overline{uw}/U_{ref}^2$ at $x/c_a =$ 0.65 for both 1.65% and 3.30% in chord coordinate system . . . . .	283
F.18	Reynolds shear stresses $-\overline{uv}/U_{ref}^2$ , $-\overline{vw}/U_{ref}^2$ , and $-\overline{uw}/U_{ref}^2$ at $x/c_a =$ 1.00 for both 1.65% and 3.30% in chord coordinate system . . . . .	284
G.1	Triple products $\overline{uv^2}/U_{ref}$ , $\overline{v^3}/U_{ref}$ , and $\overline{v^2w}/U_{ref}$ at $x/c_a = 0.00$ for both 1.65% and 3.30% in chord coordinate system . . . . .	286
G.2	Triple products $\overline{uv^2}/U_{ref}^3$ , $\overline{v^3}/U_{ref}^3$ , and $\overline{v^2w}/U_{ref}^3$ at $x/c_a = 0.04$ for both 1.65% and 3.30% in chord coordinate system . . . . .	287

G.3	Triple products $\overline{uv^2}/U_{ref}^3$ , $\overline{v^3}/U_{ref}^3$ , and $\overline{v^2w}/U_{ref}^3$ at $x/c_a = 0.09$ for both 1.65% and 3.30% in chord coordinate system . . . . .	288
G.4	Triple products $\overline{uv^2}/U_{ref}^3$ , $\overline{v^3}/U_{ref}^3$ , and $\overline{v^2w}/U_{ref}^3$ at $x/c_a = 0.12$ for both 1.65% and 3.30% in chord coordinate system . . . . .	289
G.5	Triple products $\overline{uv^2}/U_{ref}^3$ , $\overline{v^3}/U_{ref}^3$ , and $\overline{v^2w}/U_{ref}^3$ at $x/c_a = 0.18$ for both 1.65% and 3.30% in chord coordinate system . . . . .	290
G.6	Triple products $\overline{uv^2}/U_{ref}^3$ , $\overline{v^3}/U_{ref}^3$ , and $\overline{v^2w}/U_{ref}^3$ at $x/c_a = 0.27$ for both 1.65% and 3.30% in chord coordinate system . . . . .	291
G.7	Triple products $\overline{uv^2}/U_{ref}^3$ , $\overline{v^3}/U_{ref}^3$ , and $\overline{v^2w}/U_{ref}^3$ at $x/c_a = 0.42$ for both 1.65% and 3.30% in chord coordinate system . . . . .	292
G.8	Triple products $\overline{uv^2}/U_{ref}^3$ , $\overline{v^3}/U_{ref}^3$ , and $\overline{v^2w}/U_{ref}^3$ at $x/c_a = 0.65$ for both 1.65% and 3.30% in chord coordinate system . . . . .	293
G.9	Triple products $\overline{uv^2}/U_{ref}^3$ , $\overline{v^3}/U_{ref}^3$ , and $\overline{v^2w}/U_{ref}^3$ at $x/c_a = 1.00$ for both 1.65% and 3.30% in chord coordinate system . . . . .	294
G.10	Triple products $\overline{u^3}/U_{ref}^3$ , $\overline{u^2v}/U_{ref}^3$ , and $\overline{u^2w}/U_{ref}^3$ at $x/c_a = 0.00$ for both 1.65% and 3.30% in chord coordinate system . . . . .	295
G.11	Triple products $\overline{u^3}/U_{ref}^3$ , $\overline{u^2v}/U_{ref}^3$ , and $\overline{u^2w}/U_{ref}^3$ at $x/c_a = 0.04$ for both 1.65% and 3.30% in chord coordinate system . . . . .	296
G.12	Triple products $\overline{u^3}/U_{ref}^3$ , $\overline{u^2v}/U_{ref}^3$ , and $\overline{u^2w}/U_{ref}^3$ at $x/c_a = 0.09$ for both 1.65% and 3.30% in chord coordinate system . . . . .	297
G.13	Triple products $\overline{u^3}/U_{ref}^3$ , $\overline{u^2v}/U_{ref}^3$ , and $\overline{u^2w}/U_{ref}^3$ at $x/c_a = 0.12$ for both 1.65% and 3.30% in chord coordinate system . . . . .	298
G.14	Triple products $\overline{u^3}/U_{ref}^3$ , $\overline{u^2v}/U_{ref}^3$ , and $\overline{u^2w}/U_{ref}^3$ at $x/c_a = 0.18$ for both 1.65% and 3.30% in chord coordinate system . . . . .	299
G.15	Triple products $\overline{u^3}/U_{ref}^3$ , $\overline{u^2v}/U_{ref}^3$ , and $\overline{u^2w}/U_{ref}^3$ at $x/c_a = 0.27$ for both 1.65% and 3.30% in chord coordinate system . . . . .	300
G.16	Triple products $\overline{u^3}/U_{ref}^3$ , $\overline{u^2v}/U_{ref}^3$ , and $\overline{u^2w}/U_{ref}^3$ at $x/c_a = 0.42$ for both 1.65% and 3.30% in chord coordinate system . . . . .	301

G.17 Triple products $\overline{u^3}/U_{ref}^3$ , $\overline{u^2v}/U_{ref}^3$ , and $\overline{u^2w}/U_{ref}^3$ at $x/c_a = 0.65$ for both 1.65% and 3.30% in chord coordinate system . . . . .	302
G.18 Triple products $\overline{u^3}/U_{ref}^3$ , $\overline{u^2v}/U_{ref}^3$ , and $\overline{u^2w}/U_{ref}^3$ at $x/c_a = 1.00$ for both 1.65% and 3.30% in chord coordinate system . . . . .	303
G.19 Triple products $\overline{uw^2}/U_{ref}^3$ , $\overline{vw^2}/U_{ref}^3$ , and $\overline{w^3}/U_{ref}^3$ at $x/c_a = 0.00$ for both 1.65% and 3.30% in chord coordinate system . . . . .	304
G.20 Triple products $\overline{uw^2}/U_{ref}^3$ , $\overline{vw^2}/U_{ref}^3$ , and $\overline{w^3}/U_{ref}^3$ at $x/c_a = 0.04$ for both 1.65% and 3.30% in chord coordinate system . . . . .	305
G.21 Triple products $\overline{uw^2}/U_{ref}^3$ , $\overline{vw^2}/U_{ref}^3$ , and $\overline{w^3}/U_{ref}^3$ at $x/c_a = 0.09$ for both 1.65% and 3.30% in chord coordinate system . . . . .	306
G.22 Triple products $\overline{uw^2}/U_{ref}^3$ , $\overline{vw^2}/U_{ref}^3$ , and $\overline{w^3}/U_{ref}^3$ at $x/c_a = 0.12$ for both 1.65% and 3.30% in chord coordinate system . . . . .	307
G.23 Triple products $\overline{uw^2}/U_{ref}^3$ , $\overline{vw^2}/U_{ref}^3$ , and $\overline{w^3}/U_{ref}^3$ at $x/c_a = 0.18$ for both 1.65% and 3.30% in chord coordinate system . . . . .	308
G.24 Triple products $\overline{uw^2}/U_{ref}^3$ , $\overline{vw^2}/U_{ref}^3$ , and $\overline{w^3}/U_{ref}^3$ at $x/c_a = 0.27$ for both 1.65% and 3.30% in chord coordinate system . . . . .	309
G.25 Triple products $\overline{uw^2}/U_{ref}^3$ , $\overline{vw^2}/U_{ref}^3$ , and $\overline{w^3}/U_{ref}^3$ at $x/c_a = 0.42$ for both 1.65% and 3.30% in chord coordinate system . . . . .	310
G.26 Triple products $\overline{uw^2}/U_{ref}^3$ , $\overline{vw^2}/U_{ref}^3$ , and $\overline{w^3}/U_{ref}^3$ at $x/c_a = 0.65$ for both 1.65% and 3.30% in chord coordinate system . . . . .	311
G.27 Triple products $\overline{uw^2}/U_{ref}^3$ , $\overline{vw^2}/U_{ref}^3$ , and $\overline{w^3}/U_{ref}^3$ at $x/c_a = 1.00$ for both 1.65% and 3.30% in chord coordinate system . . . . .	312
G.28 $\overline{uvw}/U_{ref}^3$ for both 1.65% and 3.30% in chord coordinate system . . . . .	315
H.1 Flow angle (FA) for both 1.65% and 3.30% in chord coordinate system . . . . .	319
H.2 Flow gradient angle (FGA) for both 1.65% and 3.30% in chord coordinate system . . . . .	322
H.3 Shear stress angle (SSA) for both 1.65% and 3.30% in chord coordinate system . . . . .	325

H.4	FA, FGA, and SSA away from pressure side for both 1.65% and 3.30% in chord coordinate system . . . . .	326
H.5	FA, FGA, and SSA on suction side for both 1.65% and 3.30% in chord coordinate system . . . . .	327
H.6	Anisotropy factor N for both 1.65% and 3.30% in chord coordinate system	330
H.7	$TKE/U_{ref}^2$ for both 1.65% and 3.30% . . . . .	333
H.8	$TKE/U_{ref}^2$ of local gap inflow for both 1.65% and 3.30% . . . . .	334
H.9	$TKE/U_{ref}^2$ underneath quarter line of the blade from the pressure side for both 1.65% and 3.30% . . . . .	335
H.10	$TKE/U_{ref}^2$ underneath the camber line for both 1.65% and 3.30% . . . .	336
H.11	$TKE/U_{ref}^2$ on the suction side for both 1.65% and 3.30% . . . . .	337
H.12	A1 for both 1.65% and 3.30% in chord coordinate system . . . . .	340
H.13	1/S for both 1.65% and 3.30% . . . . .	343
H.14	B for both 1.65% and 3.30% in chord coordinate system . . . . .	346
H.15	B2 for both 1.65% and 3.30% in chord coordinate system . . . . .	349
H.16	Correlation coefficients of $\overline{uv}$ for both 1.65% and 3.30% in chord coordinate system . . . . .	352
H.17	Correlation coefficients of $\overline{vw}$ for both 1.65% and 3.30% in chord coordinate system . . . . .	355
H.18	Correlation coefficients of $\overline{vw}$ for both 1.65% and 3.30% in chord coordinate system . . . . .	358
H.19	Correlation coefficients of $\overline{uv}$ , $\overline{uw}$ , $\overline{vw}$ on pressure side for both 1.65% and 3.30% in chord coordinate system . . . . .	359
H.20	Correlation coefficients of $\overline{uv}$ , $\overline{uw}$ , $\overline{vw}$ on suction side for both 1.65% and 3.30% in chord coordinate system . . . . .	360

# List of Tables

1	Nomenclature . . . . .	xxv
3.1	Rotation angles of local camber coordinate systems for both 1.65% and 3.30% tip gaps . . . . .	112
3.2	Rotation angles of local wall-shear coordinate systems for both 1.65% and 3.30% tip gaps . . . . .	113
3.3	Uncertainties for the stationary wall in the Cascade Wind Tunnel . . . . .	114
3.4	Test matrix with stationary endwall (1.65%) . . . . .	115
3.5	Test matrix with stationary endwall (3.30%) . . . . .	116
3.6	Pressure and its gradient with stationary endwall (1.65%) . . . . .	117
3.7	Pressure and its gradient with stationary endwall (3.30%) . . . . .	118
3.8	$U_\tau$ and $y_{shift}$ for stationary endwall (1.65%) . . . . .	119
3.9	$U_\tau$ and $y_{shift}$ for stationary endwall (3.30%) . . . . .	120
4.1	Uncertainties for the moving wall in the Cascade Wind Tunnel . . . . .	205
4.2	Test matrix for moving endwall . . . . .	205

# Nomenclature



Table 1: Nomenclature

$1/S$	Reynolds stresses ratio defined as Equation 3.20
$b$	Location between the pressure side and the camber line under the blade
$B$	Triple products ratio defined as Equation 3.21
$B2$	Triple products ratio defined as Equation 3.22
$c$	Chord length: 25.4 cm or location under the camber line of the blade
$c_a$	Axial chord length $c_a = c \cos(56.9^\circ)$
$CC$	standard correlation coefficient between velocity magnitude fluctuation and data rate fluctuation defined as Equation B.1
$C_p$	Pressure coefficient $\frac{P - P_{ref}}{2\rho U_{ref}^2}$
$C_1, C_2$	Coefficients for curve fit of skin friction velocity
$f$	frequency
$FA$	Mean flow angle defined as Equation 3.14
$FGA$	Flow gradient angle defined as Equation 3.15
$\bar{h}$	Normalized helicity defined as Equation 3.13
$\hat{h}$	Helicity density defined as Equation 3.12
$n$	Number of LDV data samples for a given profile
$l$	Mark length of belt joint
$N$	Anisotropy Factor,
$N_k$	Number of points in one slot for spectral analysis
$N_S$	Number of slots for spectral analysis
$P$	Mean Pressure
$P_{atm} and T_{atm}$	Ambient pressure and temperature
$p$	Instantaneous static pressure or location under the pressure side of the blade
$p, q, \text{ and } k$	Integer
$Q$	Coordinate system independent velocity $\sqrt{U^2 + W^2}$
$\tau_i$	Data rate: $1/(t_i - t_{i-1})$
$R$	Correlation coefficient of determination defined as Equation C.7
$\hat{R}(\tau_k)$	Estimated correlation of velocity at the slot $\tau_k$
$Re_\theta$	Momentum thickness Reynolds number $U_\infty \theta / \nu$
$Re_x$	Reynolds number $U_\infty x / \nu$
$R_{uw}, R_{vw}, \text{ and } R_{vw}$	Correlation coefficients of shear stresses
$s$	Blade spacing 23.6 cm or location under the suction side of the blade
$\hat{S}(f)$	Estimated spectrum of velocity

---

SSA	Shear stress angle defined as Equation 3.16
$t$	Gap height and time period
$t_i$	Absolute time of the $i^{th}$ velocity measured by the LDV
TKE	Turbulent Kinetic Energy defined as Equation 3.18
$u$	location at local gap inflow
$U, V, W$	Reynolds-averaged mean velocities components
$u_i, v_i, w_i$	The $i^{th}$ Instantaneous velocity components measured by LDV
$u', v', \text{ and } w'$	Velocity fluctuations
$\frac{-\overline{u_i u_j} U_{i,j}}{\overline{u^2}, \overline{v^2}, \overline{w^2}}$	TKE Production defined as Equation 3.24
$U^+, V^+, W^+$	Reynolds-averaged normal stresses
$U/U_\tau, V/U_\tau, W/U_\tau$	Reynolds-averaged shear stresses
$\overline{u_i u_j}$	Second-order moments
$-\overline{uv}, -\overline{uw}, -\overline{vw}$	Reynolds-averaged shear stresses
$\overline{u_i u_j u_k}$	Third-order moments
$\overline{u^2 v}, \overline{v w^2}, \overline{v^3}$	Reynolds-averaged triple products used in stress transport equations 3.30, 3.31, and 3.32
$U_{ref}$	Free-stream velocity of inflow
$U_\tau$	Skin friction velocity $\sqrt{\tau_w/\rho}$
$\vec{V}$	Velocity vector
$ V $	Mean velocity magnitude
$V_{belt}$	Velocity of the belt motion
$ v_i $	The $i^{th}$ instantaneous velocity magnitude measured by the LDV
$\sqrt{u_i^2 + v_i^2 + w_i^2}$	
$\vec{V}_q$	TKE transport vector defined as Equation 3.23
$W_m$	Velocity component in z direction in the moving-wall coordinate system
$W_s$	Velocity component in z direction in the bed coordinate system
$x, y, z$	Tunnel co-ordinate system shown in Figure 3.2
$y_{shift}$	Wall location refinement
$y_{measured}$	Location of LDV profile
$y^+$	$y U_\tau / \nu$

---

---

$\delta$	Boundary layer thickness
$\Delta H$	Water column difference for free-stream velocity
$\Delta C_p$	Pressure difference between the pressure and suction sides
$\vec{\nabla} P$	Pressure gradient vector
$\partial C_p / \partial x, \partial C_p / \partial z$	Pressure gradient components
$\Gamma_x$	Circulation (in the y-z plane) defined as Equation 3.5
$\epsilon_x$	x eddy viscosity
$\epsilon_z$	z eddy viscosity
$\theta$	Boundary layer momentum thickness
$\theta_y$	rotation angle about y
$\sigma_r$	Standard deviation data rate used in Equation B.1
$\sigma_v$	Standard deviation of velocity magnitude used in Equation B.1
$\rho$	Mass density of flow
$\nu$	Kinematic viscosity
$\tau$	Shear stress
$\tau_m$	Maximum lag time
$\Delta \tau$	Slot width
$\tau_w$	Wall shear stress
$\psi$	Volumetric mass flow rate per unit span defined as Equation 3.25
$\vec{\Omega}$	Vorticity curl $\vec{V}$
$\Omega_x$	X-component vorticity defined as Equation 3.7
$\Omega_y$	Y-component vorticity defined as Equation 3.8
$\Omega_z$	Z-component vorticity defined as Equation 3.9

---

# Chapter 1

## Introduction

The tip gap between blade tips and the casing inevitably exists for an axial turbomachine. When flow passes it, the tip gap flow travels under the blade tip because of the pressure difference between the pressure side and the suction side of the blade. The tip gap flow develops a progressively stronger cross flow as the lateral pressure gradient changes, depending on the blade loading, from the leading edge to the trailing edge of the blade. It also features a tip leakage vortex that detaches from the suction side of the first half of the blade and separates from the endwall in the passage.

The tip leakage vortex occurs because the gap flow intersects with the primary flow of the suction side and rolls up into the vortex because of the momentum of the primary flow. The tip gap flow appears to be a blockage flow for the primary flow in the passage. The intersection of the gap flow and primary flow results in strong interaction and mixing, especially near the endwall where the two flow directions are almost perpendicular. The tip gap flow modifies the flow structure of the primary flow which passes through the gap region. It also affects the efficiency and stability of the machine.

The understanding of the tip gap flow structure including its turbulence structure is very important for improving turbulence modelling. Numerous studies have been reported in the open literature since the review of Rains (1954).

## 1.1 Brief Review of Tip Gap Flow

Tip gap flow research is a broad field that can be divided into different categories by different configurations, such as a real turbomachine or an ideal cascade; compressor, pump, and turbine; and stationary wall or moving wall; even a single rotor or a single stage or multiple stages. Even though tip gap flow structures depend on a specific configuration of interest, the fundamental physics does not change. The tip gap flow can also be divided into different zones: inlet, downstream, passage, and gap. Tip gap flows have been extensively studied analytically, computationally, and experimentally.

Correlations of tip gap flow effects were analytically derived to model the pressure loss and trajectory of the tip leakage vortex in turbomachine design, which was reviewed by Sjolander (1997). The correlations are simple and practically useful to engineers. As an advancement of turbomachine information, the flow structure need to be described not just qualitatively but also quantitatively in detail. Computational fluid dynamics (CFD) has been used for the gap flow field, but it has not been a reliable tool because the flow physics is not well described. Lee et al. (1997) established a three-dimensional Reynolds-averaged Navier-Stokes (RANS) solver to characterize the formation and development of the tip leakage vortex in a linear compressor cascade and a one-stage shrouded pump rotor. CFD is also a parallel tool for the present experimental study. Shin (2001) developed a three-dimensional RANS-based model to calculate the tip gap flow of a stationary compressor cascade with 1.65% gap. You et al. (2003) used a large-eddy

simulation (LES) to simulate the similar flow with a moving endwall.

Experimental studies of tip gap flows in the literature have investigated various configurations to reveal flow structures of different stators, rotors, stator-rotor interactions, and rotor-stator interactions. Tip gap flows are highly complex in nature and require full three-dimensional measurements of the flow field. Data on these flow fields can be obtained either intrusively or nonintrusively. The two major intrusive methods of hot wires/films [e.g., Inoue and Kuroumaru (1988)] and Pitot probes [e.g., by Storer and Cumpsty (1991)] are able to measure three-dimensional flows but generate some flow field interference that becomes more significant as the probe nears solid surfaces.

However, laser measurements are nonintrusive and obtain data near the wall. Laser Doppler Velocimetry (LDV) was used to measure tip gap flows by a few researchers. Murthy and Lakshminarayana (1986) used a two-component LDV to measure the tip leakage flow disturbance in the tip region flow field within and aft of an axial compressor rotor blade passage. Later, Lakshminarayana and Murthy (1988) examined the correlation of the velocity and pressure field of the tip leakage vortex using the measurements of both LDV and pressure in an annulus wall boundary layer of the same compressor rotor as Murthy and Lakshminarayana (1986). Stauter (1993) investigated the character of the tip leakage vortex in the flow field between the compressor blade rows and within the rotating blade passages of a two-stage axial compressor model using a two-color five-beams LDV. Hobson and Dober (1997) mapped the location and velocity distribution of the downstream wake and tip leakage vortex system in the endwall region of a linear compressor cascade using a TSI three-component fiber-optic LDV with three-color six beams. Wernet et al. (2002) even acquired the trajectory and unsteady behavior of the tip leakage vortex at the peak efficiency and near stall operating conditions in a low speed compressor rotor using a 3D digital particle image velocimeter (PIV).

Denton (1993) pointed out that the tip leakage flow over compressor blades is not different in principle from that in turbines. The smaller blade thickness of compressor blades results in that tip gap flow is less likely to reattach to the blade tip. The relative motion increases the tip gap flow in a compressor and decreases it in a turbine.

The extensive research of the flow in the passage and immediate downstream of compressor, linear cascade, and axial pump has been summarized by Muthanna and Devenport (2004). These studies all revealed that tip leakage vortices originate from the suction side of the first half of the blade and develop in the passage downstream. A low momentum and high turbulence flow zone along the trajectory of the tip leakage vortices is associated with the interaction between the tip gap flow and primary flow. However, the structure of the tip gap flow observed in cascades and rotors is significantly different. The tip gap flow rolled up into a discrete vortex in a compressor cascade. For a compressor rotor, the tip leakage flow formed a well-organized vortex in the experiment of Inoue and Kuroumaru (1988), but only produced an intense shear layer and separated flow on the suction side rather than a concentrated vortex as in the test of Lakshminarayana et al. (1995). Lakshminarayana et al. (1995) explained that the difference between their data and the data of Inoue and Kuroumaru (1988) was due to the difference of flow turning, blade loading, and inlet flow turbulence in the two experiments. They further inferred that the formation of a tip leakage vortex depends on various parameters, such as configuration, inflow condition, and blade loading. Sjolander (1997) totally reviewed all aspects of the turbine gap flow research, consisting of physics and modelling of tip gap flow in axial turbines.

From the description above, most previous research examined the mean flow structures in the blade passage and downstream. However, turbulent structures in the passage and downstream as well as flow structures near the endwall or casing and in the gap are

not well understood. The subject of this dissertation is to measure the turbulent structure of the tip gap flow. A few relevant experiments in the gap and about the effect of relative motion of the endwall are summarized below.

### 1.1.1 Previous Research in a Tip Gap

The tip gap is usually small so that it is very difficult to measure the three-dimensional flow in a gap. Figure 1.1 illustrates some typical features around the tip gap region. Some researchers have conducted a few in-gap experiments to make oil flow visualizations of the endwall and blade surfaces, to take pressure measurements of the endwall and blade tip, and to measure the flow velocity at the tip exit for a compressor cascade. Storer and Cumpsty (1991) as well as Kang and Kirsh (1993) measured the exit flow velocity using a small Pitot probe and found that the gap flow leaves the gap exit like a jet flow.

Storer and Cumpsty (1991) measured the velocity magnitude and direction of flow at the exit of tip gaps of both 2% and 4% of chord in a five 45.55° circular-arc-camber blade compressor cascade by a flattened five-hole Pitot probe. The chord, pitch, and span of the blade was 30.0 cm, 18.0cm, and 43.5cm, respectively. The stagger and inlet flow angle from the axial direction was 22.2° and 45.0°. The Reynolds number based on the chord was 500,000 and the displacement thickness of the inlet endwall boundary layer 140% chord upstream was 2.9 mm. Detailed velocity profiles were acquired with 25 points across the gap at ten chordwise locations. The data displayed similar patterns of leakage flow velocity at the tip gap for two different gap sizes. The exit velocity results showed the relationship between the tip leakage flow and the total pressure loss. A core of very low loss fluid bounded by the endwall and a free shear layer at about 75% of the gap height occurred from near the minimum pressure location and all the downstream measurement



location. Accordingly, the flow velocity and direction remained nearly invariant in the core. However, the flow direction varied  $50^\circ$  across the shear layer bounded on the surface of the blade tip end.

Storer and Barton (1991) further measured the total pressure and turbulence intensity inside the 4% gap at the 65% chord plane in the same facility with the same Pitot probe above. For the measurement of turbulence intensity from the near endwall to the blade tip using a single subminiature hot-wire probe with the prongs bent forward to be inserted through the endwall, it was assumed that turbulence in the gap is isotropic so that the probe stayed in the same direction to measure the fluctuating component of velocity normal to the probe. The acquired data demonstrated that the pressure loss and turbulence intensity were negligible around the mid gap while they were huge in the two shear layers bounded on the endwall and the blade tip surface. Static pressure on the blade tip end was measured with 1.0% to 4.0% gaps and provided the signature of flow attachment on the blade tip.

Kang and Kirsh (1993) conducted oil flow visualizations of the endwall and blade tip surfaces in a linear compressor cascade with seven NACA 65-1810 blades. The inlet and outlet flow angles are  $40^\circ$  and  $-4.02^\circ$  relative to the axial, respectively. The test Reynolds number based on the chord was 290,000. The endwall flow pattern showed limiting streamlines with a reattachment line on the pressure side and a separation line on the suction side. The blade tip surface flow pattern suggested that three vortices originated from the gap flow, consisting of a well-known tip leakage vortex, a tip separation vortex in the pressure side corner, and a secondary vortex with opposite rotation in the suction side corner. The tip separation vortex takes place in the similar location to the separation bubble or vena contracta discovered by Rains (1954), but it was an aligned vortex along the tip rather than a separation bubble. They concluded that the flow inside the gap

is strongly three dimensional flow because the limiting streamlines on the endwall and blade tip are not perpendicular to the camber line as suggested by Rains (1954).

Kang and Kirsh (1994) later reported the endwall static pressure, the tip blade loading, and the exit velocity of the gap flow in the same facility as Kang and Kirsh (1993). The endwall pressure distribution exhibited the different features between the smaller and higher gap when tip leakage flow accelerated from the gap entrance to the inside gap and then decelerated till the separation. The tip blade loading demonstrated different characteristic leading part and trailing part of the tip gap. The exit velocity profiles showed a good symmetry in the exit of the first quarter gap and a wake-like distribution in the rest exit of the gap.

Yaras et al. (1989) measured the flow field in a 2.9%-chord gap along the blade camber line at a large number of chordwise planes. The mean flow velocity vectors showed that the tip gap mass flow rate mainly came from the lower gap part, which was a nearly loss-free core confirmed by the total pressure measurements of the upstream gap. The flow direction near the blade tip indicated that the separated flow around the pressure side corner is well organized and forms a chordwise vortex.

Sjolander and Cao (1995) measured the flow velocity vectors at several pitchwise stations in the gap where the gap height-to-blade thickness ratio is 66%. The velocity vectors suggested a thin shear layer near the endwall and separation vortical structure on the blade tip, which is similar to the observations of the smaller gap used by Yaras et al. (1989). From the oil flow visualization of the blade tip, a three-dimensional separation line was observed on the tip surface only at the chord ratio where the gap height-to-blade thickness ratio is 66%. Sjolander (1997) concluded that the tip gap flow of turbines seems to form a extremely thin endwall shear layer and a tip separation bubble with multiple well-organized chordwise vortices. The bulk of the tip gap mass flow rate passes through

the core with nearly loss-free fluid near the endwall.

Inoue and Kuroumaru (1988) studied the structure of tip gap flows of two different isolated compressor rotors with the gap height from 0.5mm to 5mm using periodic multi-sampling techniques with a single hot-wire of  $5\mu\text{m}$  diameter in the gap and with a high response pressure sensor on the casing wall. The two rotors had a NACA 65 blade profile with a chord length of 22.45cm at the tip. The test speed of rotors was 1300rpm and the displacement thickness of the inlet boundary layer was about 0.7mm. To obtain the three-component velocity vector, the probe was rotated on its axis about 20 different positions at each survey plane. Ensemble-average and phase-locked measurements were used to get the flow pattern in the tip gap. A scraping vortex, which means the blade pressure surface scrapes up fluid entrained on the moving wall and thus imparts a rolling motion to the air in the vicinity of the pressure surface, is recognized at the pressure side near the trailing edge only for the smaller tip gap. The radial flow due to centrifugal force becomes noticeable near the trailing edge of the suction side only for larger tip gap.

### 1.1.2 Relative Motion Effect

The experiments mentioned above show significantly different tip gap flow structures between a compressor cascade and a compressor rotor. The different tip gap flow behavior in cascades and rotors suggests that the cascade experiments do not simulate all features of a real turbomachine. The major difference is the relative motion between the blade tips and the end wall. The relative motion modifies the trajectory of tip leakage vortex and turbulence structure in the interference zone of endwall boundary and tip leakage flow.

To investigate the relative motion effect, some researchers have simulated the wall

motion using a moving belt in a linear cascade setup. Wang (2000) showed the substantial effects of wall motion in a linear low-speed compressor cascade. Generally speaking, the moving endwall reduced the strength of the tip leakage vortex. The vortex region with the moving wall swept farther along the moving direction than that with the stationary wall. The shape of the vortex was stretched by the moving endwall and the structure of the vortex was disturbed by the moving wall.

Yaras and Sjolander (1992) and Yaras et al. (1992) simulated the relative wall motion influence on the tip gap and downstream flow field for a gap of 3.8% of chord in a planar cascade of turbine blades. The velocities for three different wall speeds were measured across the gap along the camber line at various locations as well as at the 48% of axial chord downstream. Flow velocity vectors in the gap change across the gap. The flow rate decreases as the wall speed increases because the wall motion direction is reversed relatively to the tip gap flow in a turbine. At the test conditions matching the flow coefficient of the actual turbine, the reduction was about 50 percent. This tip-gap flow rate reduction is due to a general reduction in the pressure difference driving the fluid into the gap. This explanation is supported by the pressure measurements around the blade tip by Morphis and Bindon (1988). From their structure research of the downstream flow field, it was found that the strength of tip vortex was reduced considerably with the introduction of wall motion. The passage vortex adjacent to the tip-leakage vortex was enhanced by the scraping effect of the blades on the end-wall boundary layer. Another phenomenon observed was the dragging of the two vortices toward the suction side of the passage, partly blocking the tip-gap. This blockage seems to raise the pressure at the gap outlet, thereby reducing the pressure difference for the leakage flow. It was also confirmed by the blade pressure measurement.

From experiments in a compressor cascade and a turbine cascade, the relative motion

was confirmed to play an important role. The tip leakage vortex was intensified and shifted toward the pressure side of the passage in the experiment of Wang (2000). The flow rate dropped as the wall speed increased in the turbine cascade test by Yaras and Sjolander (1992). To understand the tip gap flow completely, the relative motion is necessary to be included in the research.

## 1.2 Dissertation Study

The purpose of this dissertation is to investigate the tip-gap flow turbulent structure inside the gap between the blade tip and endwall in a low-speed linear compressor cascade wind tunnel at Virginia Tech, in which Devenport and coworkers [Muthanna (1998), Wenger (1999), Wang (2000), de la Riva (2001), Muthanna (2002), Mish (2003), and Ma (2003)] have studied extensively from the inflow to the far downstream, with and without upstream vortex generators, on both a stationary and a moving wall with different gap sizes. Ma (2003) summarized the main results from their previous studies in his dissertation: the tip leakage vortex originates from the tip gap pressure driven flow and detaches from the suction side around the 25% chord, separates from the endwall, and moves toward the pressure side of the next blade from the upstream to downstream; the structures of tip leakage flow were affected by the relative motion, free-stream turbulence, and unsteady inflow generated by vortical generators; the tip leakage vortex is unsteady with low frequency meandering and is highly anisotropic turbulent flow associated with a streamwise velocity deficit.

Because Devenport and his workers used the hot-wire, they could not measure the flow near the endwall and inside the gap. However, these data near the endwall and inside the gap are very important to understand tip gap flow. Kuhl (2001) proved that data can

be taken through the glass window on the endwall using a fiber-optic three dimensional LDV system accommodated to the same tunnel. This current study continues to be complementary research to Devenport and coworkers. The data will be also provided for the parallel LES efforts of You et al. (2003).

This study will mainly examine tip gap flows in tip gaps of 1.65% and 3.30% of chord with a stationary endwall using oil flow visualization, pressure measurement, and LDV measurement. Much effort has been done to improve the moving wall experiments. Surface oil flow visualization of the blade suction side has been made for two the tip gaps and some LDV data have been taken at both inlet and exit of tip gap in the gap 3.30% of chord.

The dissertation consists of five major chapters. Chapter 1 has reviewed the literature of tip gap flows, summarized the previous or parallel experiments investigated in the tunnel, and introduced the motivation and subjects of my dissertation study. Chapter 2 presents the modification of the facility and the instrumentation used in the study after Kuhl (2001). Chapter 3 describes the results and analysis of the stationary endwall flow experiments. Chapter 4 presents the results and analysis of the moving endwall flow experiments. Chapter 5 draws conclusions from this dissertation study and suggests the future work to extend more search of the tip gap flow.

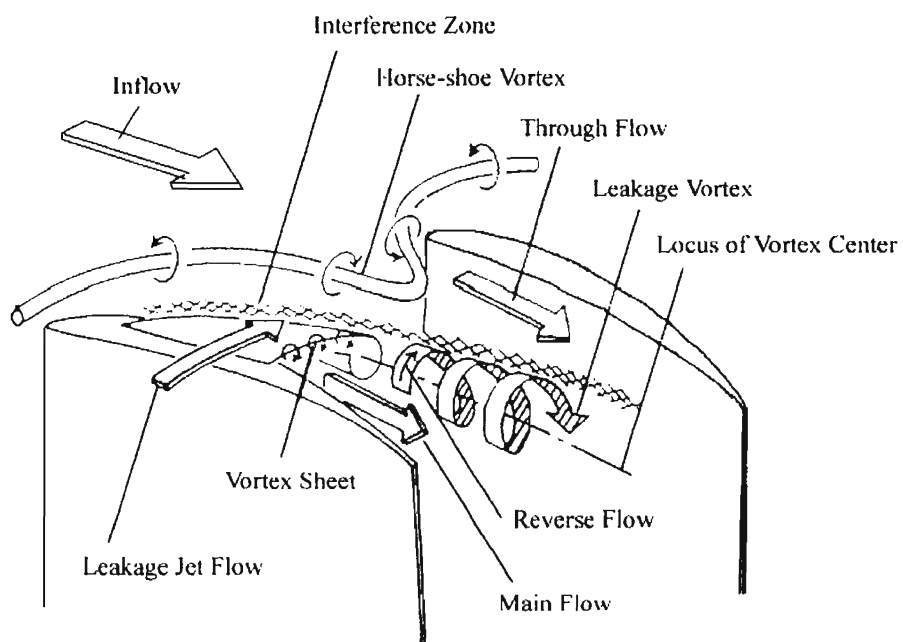


Figure 1.1: Flow features in the blade tip region from Inoue and Kuroumaru (1988)

# Chapter 2

## Apparatus and Instrumentation

This chapter describes the apparatus and instrumentation used in this dissertation to measure the tip gap turbulent structures in a linear low speed compressor cascade wind tunnel (Cascade Wind Tunnel) at Virginia Tech using a miniature three-orthogonal-velocity-component fiber-optic laser-Doppler velocimeter (LDV). The cascade wind tunnel includes a moving belt system to simulate the relative motion between blade tips and casing. Two optical sensors are used to detect the fluctuating vertical displacement and joint location of the moving belt relative to probe volume of the LDV, respectively. An integrated data acquisition system collects LDV data and the two optical signals. A data post processing system analyzes all acquired data for characterization of the tip gap flow.

Sections 2.1 and 2.2 of this chapter describe the cascade tunnel set-up and moving belt system. Sections 2.3 and 2.4 detail the LDV measurement system and optical sensors. The data acquisition and post-processing systems are presented in Sections 2.5 and 2.6. Sections 2.7 and 2.8 discuss the system improvements and future recommendation. Chapter 3 will describe the stationary wall experiments and Chapter 4 will present the moving wall experiments based on the data collected from the experimental apparatus



as introduced in this chapter.

## 2.1 Cascade Wind Tunnel

The cascade wind tunnel has an overall length of 11m. The blower section of the tunnel consists of a centrifugal fan powered by a 15 HP motor with an impeller diameter of 1.12m. Then a diffuser and settling chamber connect with the blower in a length of 4.26m. Conditioning screens are placed at the two ends of the settling chamber to reduce turbulence levels in the flow and to serve as air filters as well. Between the two screens, paper tubes are stacked to straighten the flow. The flow is contracted at a 6.43:1 ratio before entering the 30"x12" rectangular section which guides the flow onto the compressor cascade.

The tunnel became dirty over time so that the free-stream velocity decreased. The flow velocity of the tunnel decreased from 27 m/s with the initial setup three downstream tunnel exit back pressure screens by Muthanna (1998) to 24.2 m/s with two tunnel exit screens for the stationary wall experiments in this study. For the moving wall experiments in this study, the blower blades, ten upstream conditioning screens, and the tunnel walls were cleaned and two condition screens were replaced so that the flow velocity reached the same level of the experiments of Muthanna (1998). In order to keep the same flow velocity, a cardboard baffle plate partly blocked the inlet flow of the blower.

### 2.1.1 Evolution of the Test Section Set-up

The initial configuration of the low-speed linear compressor cascade wind tunnel at Virginia Tech is fully described by Muthanna (1998). As shown in Figure 2.1, the cascade

consists of 8 cantilevered GE rotor B section blades mounted with a tip gap of 1.65% or 3.30% chord. The blades have a chord of 10" and an effective span of just under 10". The cascade configuration has a rectangular cross section of 65"x10". The blade spacing is 9.29". The stagger angle of the cascade is 56.93°. The inlet angle of the cascade is 65.1°. The turning angle is 11.8°. Three back pressure screens are placed at the exit of the test section. The approach free-stream velocity is approximately 25 m/s. At 18.8 cm upstream of the leading edge of the cascade are two, three-quarter inch high, suction slots on the upper and lower end-walls removing the boundary layers from the inlet (see Figure 2.2). The flow is tripped by a single square bar with 0.24 cm in height mounted on the 0.6 cm downstream of the lower suction slot also shown in Figure 2.2. Figure 2.3 shows this setup including LDV laser beams.

Wang et al. (1999) built a moving belt system to model the relative motion influence between the blade tips and endwall. A 175"X31" rectangle plywood bed was made as a tunnel floor to accommodate the test section with eight GE rotor B blades. Accordingly, a 184"X36" rectangle frame was used to support the plywood bed and two rollers. The frame was braced from the ground at different cross sections. Ten legs of the frame were bolted on the ground to be adjusted for the bed level. Two 8 inch diameter and 30 inch wide rollers from Timesavers Inc. were mounted on either end of the frame. A Dodge CP400 belt roller tension adjustment mechanism was installed for manual belt tracking.

Ma et al. (2000) utilized hot-wire anemometry to measure the wake of Blade 4 and 5 with the moving end-wall and vortex generators. He shifted the blades row 218 mm downstream to accommodate the location of the vortex generators row.

The modifications to the tunnel by Kuhl (2001) were made to accommodate a LDV measurement setup under Blade 5. Two square bars were welded to strengthen the tunnel structure and to attach the positioning plate for the LDV. An entire sheet Teflon-covered

bed was made with a plexiglas insert. An environmental tent was erected to contain the LDV seed material. The rest of the tunnel is kept in the same configuration as Ma et al. (2000).

The experiment for the stationary wall in the study was done in the same tunnel setup as Kuhl (2001). A Sure Tracker (in Section 2.2.2) belt position controller was installed and a special bed (in Section 2.2.4) for the moving wall belt was built.

### 2.1.2 Teflon-covered Tunnel Floor

The floor in the test section of the cascade wind tunnel was a plywood bed mounted underneath the cascade of compressor blades, over which the Teflon sheet was covered for the moving Mylar belt in the moving wall setup. The bed (0.8 m x 3.2 m x 1.9 cm in dimensions) starts 5.2 cm downstream from the leading edge of the lower suction slot.

The Mylar belt does not slide across the bare plywood and plexiglas since this would create too much friction and melt the belt. Both the plywood and plexiglas are each covered with a single sheet of 1/16 inch thick Teflon to avoid surface discontinuities. Any bump causes more friction between the Mylar belt and the Teflon covered bed and a potential melting point for the Mylar.

Changes in temperature cause the joints between the plexiglas insert and the plywood as well as between the glass insert and the plexiglas to form small steps in the floor. Any edge detectable by hand will cause the belt to melt. To avoid scratching from these steps, such steps must be eliminated or small rearward-facing steps (less than 1/16 inch) are tolerable for each joint.

### 2.1.3 Measurement Windows

Because the tip gap region and near endwall are the regions of interest as shown in Figure 2.1, the miniature LDV system presented in Section 2.3 makes measurements through the transparent tunnel floor. The optical glass window for measurement under the blade tip is 203.2 mm (8 inches) in diameter and 6 mm thick with an anti-reflective coating to improve LDV measurements close to the floor. However, the area being measured is much larger than the optical glass window. In order to probe all regions of interest, multiple positions of the optical glass window are necessary. For convenience, the optical glass window is embedded in different Plexiglas inserts. The open hole through the tunnel floor is used to install these different inserts.

A Plexiglas insert is mounted beneath blades 4, 5 and 6 on the plywood bed. The Plexiglas insert is approximately 16 inches wide and 20 inches long (on a side) and the edges make a  $45^\circ$  angle with the suction slot (see Figure 2.1). Three inserts with different hole locations for the optical glass were used in this study. The center of the optical glass for these are (0.75, -0.65), (1.2, -1.0), and (1.33, -1.05) from the leading edge of blade 5 (in inches, using the coordinate system labelled in Figure 2.1).

The glass window location in the newly modified striped bed for moving wall experiments was shifted toward the drive pulley for the measurement of endwall static pressure distribution. The test blade was blade 5, the same as the stationary wall. Four adjustable feet attached to the Plexiglas hold the optical glass from underneath. High temperature tape (3M 5413 Polyimide Film Tape) is applied around the glass window, attaching it to the Plexiglas from the top side. The tape is 2.7 mils thick and the adhesive resists melting up to  $260^\circ\text{C}$ . The tape keeps the glass from spinning when the belt is running. This bed/insert/window configuration design made it easier to probe different locations

under optimum time and money efforts.

There is an 8 inch x 0.5 inch hole cut in the plexiglas parallel to the suction slot 0.65 inches downstream of the optical glass window. Through this hole the displacement sensor is traversable in the y and x directions in order to measure the displacement of the belt in the y direction when the belt is running (see Figure 2.1).

#### 2.1.4 Tunnel-enclosed Environmental Tent

To prevent the LDV seeding from spreading over the laboratory, a parallelepiped tent which was 20 ft long, 10 ft wide, and 10 ft high was constructed to contain the entire tunnel. The tent is supported by a steel frame and covered with Dura-Therm Clear HVA Greenhouse, 8 mils thick Film manufactured by AT Plastics Inc. Weights and duct tape are used on the bottom edge of the tent to seal it to the concrete floor. To make sure the tent was not interfering with the flow, the tent was secured away from the inlet of the tunnel fan.

#### 2.1.5 Flow Temperature Control

For the LDV measurements the temperature of the air in the tunnel should be  $25 \pm 1^\circ\text{C}$  to keep a nearly constant velocity of the test flow. Because the tent completely contains the tunnel, over time the air temperature in the tent rises due to the tunnel fan power. Near the inlet to the tunnel, a 29000 Btu/hr air conditioner is used to control the air temperature in the tent. The air conditioner blows cool air into the tent and exhausts warm air into the surrounding room outside the tent. A two way, digital thermometer with resolution of  $0.1^\circ$  is used to monitor the air temperature inside and outside the tent. To keep a stable flow temperature, the cool air rate is tuned as necessary.

### 2.1.6 Test Condition Monitor

After the tunnel setup was finalized by calibration, the configuration could change if the flow blocking duct tape comes off the downstream back pressure screen or misalignment of the side walls occurs. Two manometers, one in the free-stream of the tunnel entrance and the other in the downstream of the compressor blades row, are used to monitor the test condition.

## 2.2 Moving Belt System

The tip gap flow is set up at the Virginia Tech cascade wind tunnel (Section 2.1) that utilizes a moving belt system to simulate the relative motion between the tip and the casing used by Wang et al. (1999), Ma et al. (2000), and Kuhl (2001).

The moving belt extends more than two-chord lengths axially downstream of the trailing edge plane of the blades as well as a short distance upstream. The belt moves at around 23 m/s which matches the tangential velocity of the free-stream of 25m/s. The Dupont Mylar D film belt material is 0.01" thick, 27" wide, and 27 ft long. The belt is joined into a continuous loop by spot-melting a Mylar belt joint using a soldering iron at several hundred points at a 45° angle (see Figure 2.1). The joint region is approximately 1.5" wide and takes up around 0.5% of the whole belt length. A 0.25 mm thick Mylar belt is looped around two parallel 20 cm diameter cylindrical rollers approximately 4.2 m apart, set at either end of the 3.2 m long plywood bed. The rollers are mounted approximately 0.5 m from the bed edge on either end. The belt is driven by a 15HP AC synchronous motor. The Mylar belt rolls over a Teflon covered bed. A laser pointer and a photodiode are utilized to detect the position of the belt joint which is marked on the

surface to block the laser pointer beam from the photodiode.

### 2.2.1 Operational Fundamentals

A belt leading edge cover illustrated in Figure 2.1 and Figure 2.2 lays flat against the moving belt, so that there is no gap between the cover and the moving belt. This arrangement prevents the tunnel flow from going under the belt and lifting it up and to provide a uniform backward facing step along the belt to produce the same surface vorticity flux along the belt length. It is taped to the suction slot and overlaps the moving Mylar by 1/2 inch. It is made of the same Mylar film as the belt with 0.25 mm thick Dupont Mylar D.

When the Mylar belt is moving around the two rollers, the system acts like a van de Graaff generator. To neutralize the charge, two anti-static brushes are wired together and mounted one on top and the other underneath the belt. Figure 2.4 shows a picture of the two brushes which are mounted next to the drive roller (see Figure 2.1). Figure 2.5 shows the curved leading edge of the bed used to reduce belt scratching. The anti-static carbon brushes are Meech Passive Induction Bars Model 974, one 28 inches long the other 45 inches long. The anti-static brushes consist of an aluminum rod with thousands of tiny carbon fibers around 1.6 cm in length coming out of it. The rods sit above and below the belt not touching the belt.

To prevent scratches on the belt from blocking passage of the LDV beams, a piece of 8.3 mils thick 3M 5453 PTFE Glass Cloth tape is attached longitudinally to the underside of the belt next to the measurement volume. The tape extends the entire length of the belt and lifts the area next to it just enough to lift it off the floor and prevent scratches from forming (see Figure 2.1). The tape is a high temperature tape that resists melting

caused from the friction between the tape and the Teflon. The adhesive on the tape resists melting up to 204°C. The width of the optically clear region kept clean by the tape, at operating velocity, is roughly 0.35 inches wide.

The free roller controls the axial position of the belt. The screws mounted on either end of the drum twist the free roller axis relative to the drive roller axis creating a difference in tension axially across the belt. The differential in tension drives the belt back and forth across the rollers. The tolerance of controlling the axial position of the belt at full speed is approximately  $\pm 0.25$  inch. The level of control is dependent upon the jointing quality of the belt and running time. While starting and stopping the belt, much adjustment is required to prevent it from slipping axially along the roller. As the belt increases in speed, the adjustments become more fine to control the belt position. As the belt becomes older, more adjustment is necessary.

### 2.2.2 Sure Tracker Belt Controller

A Sure Tracker in Figure 2.6a provided by the Regional Supply Inc. of Marietta, Georgia was used to control the belt tracking automatically. The Sure Tracker is a one roller system specified to track the belt within 1/16 inch spanwise variation. Drag along the roller axis on the belt provides the spanwise adjusting force to the belt. It has stainless steel side plates, utilize Schrader bellows air cylinders and has external bearings for longer life.

The tracker was installed as square as possible to the side frame of the belt bed structure in Figure 2.6b. The active side of the tracker moves in the nylon side. The air cylinder extends when the optical Sure Tracker sensor detects the moving belt and the changing roller angle to the belt moves the belt away from the eye. The pneumatic arm



will re-track and the process repeats itself. Adjustment screws are used to restrict the travel of the tracking roller and control its response. The tracker is continually adjusting the belt.

The belt should contact the tracker roller snugly and make positive contact. The Sure Tracker was installed 1/4 to 1/2" vertically lower than the horizontal position of the moving belt without the Sure Tracker. The air pressure of 40 psi enough to move the tracker when the belt is detected by the photo eye shown in Figure 2.6c. Figure 2.7a shows the Sure Tracker equipment with labelled components. Additional benefits brought up by the Sure Tracker were to discharge the statics generated by the moving belt.

### 2.2.3 Belt Speed Variation and Control

The uncertainty in the belt speed while running was 0.24% r.m.s. or  $V_{belt} \pm 0.03m/s$  (Ma et al., 2000). The standard deviation of the belt velocity between runs was 1.52%, which was calculated from the moving end-wall data taken before each run (Kuhl, 2001). The fine tuning of the belt speed is necessary. The speed of the drive roller is adjusted with a variable speed controller while the free roller spins freely. An oscilloscope and an optical sensor are used to monitor the belt speed as reported by Ma et al. (2000). A strip of black electric tape of a certain length is attached on the belt joint. The sensor picks up the black mark at a regular period. The time period between successive mark signals is displayed on the oscilloscope.

The belt speed should cancel out the tangential velocity component of the inflow and should be monitored and adjusted to match up with the free-stream velocity. The belt was driven by a motor-powered pulley so that ideally the belt speed was the tangential speed of the driven pulley. In reality, belt wander and possible slippage between the

belt and pulley occurred inevitably. However, the belt speed stability could worsen if the belt was run over 20 hours. Using the oscilloscope to monitor the belt speed, a fine adjustment of the motor controller was necessary if the belt speed deviated  $\pm 0.1 m/s$  from the nominal speed.

Meanwhile, the tunnel velocity was slightly different from day to day. After the tunnel was running, the atmospheric pressure and tunnel temperature were used to calculate the flow speed  $U_{ref}$  of the free-stream, and the corresponding speed of the belt  $V_{belt}$  was derived. If the time between successive belt black mark signals was different than the expected, a fine adjustment was necessary to change the belt motor rpm. The following equations were used:

$$U_{ref} = \sqrt{1430.914(T_{atm} + 273.15) \times \Delta H / P_{atm}} \quad (2.1)$$

$$V_{belt} = U_{ref} \cos(24.9^\circ) \quad (2.2)$$

$$t = \frac{l}{V_{belt}} \quad (2.3)$$

Here  $T_{atm}$  and  $P_{atm}$  are the room atmospheric temperature and pressure, respectively,  $\Delta H$  is the reading from the manometer, and  $l$  is the length of the electric tape over the joint. The  $U_{ref}$  is free-stream velocity of inflow,  $V_{belt}$  is speed of moving belt, and the angle between the flow and the belt moving direction is  $24.9^\circ$ .

### 2.2.4 Striped Bed

As described in Sections 2.1.2 and 2.2.1, the Teflon-covered bed was the best choice for the moving belt system because of its low static and dynamic friction coefficient. However, the moving Mylar belt scratches the Teflon bed producing fine dust of Teflon particles.

Kuhl (2001) documented that the Teflon particles could block the laser beam after the belt ran 30 minutes. In order to reduce the flying particles, a striped bed (Figure 2.8) was covered using the half inch wide 3M 5453 high temperature tape at half inch intervals producing 25 bands. This meant that the total contact area between the supporting bed and the moving belt would decrease substantially. Accordingly the amount of Teflon dust particles became less and less. A new insert hole was cut 2 inch more in the test section toward the drive roller to cover the shift of a tip leakage vortex for a moving endwall.

### 2.2.5 Active Blowing

When the belt is moving across the floor a lot of particles are generated from the belt and bed. After the striped bed was used, the particles became fewer and finer. Of course, they could not be eliminated. The buildup of the powder on the optical glass window can affect the beam transmission over the time. An active blowing was used to remove the buildup of the powder. The blowing air was introduced by a tube under a strip of the high temperature tape next to the velocity profile measurement location. The air pressure is 40 psi and the inner diameter of the tube is 0.25 mm. The blowing mass flow rate is 1 kg/s.

### 2.2.6 Cleaning Devices

As described in section 2.2.1, static electricity was generated by the moving belt. Some powder film can be formed on the optical glass window over time even with the active air blowing. An extra fine fiber brush was mounted on the moving belt to mop the dust film off the optical glass window.

The worn particles attached on the inside and outside of the moving belt can cut

off the beam transmission through the Mylar belt. Two bristle brushes installed on the tunnel frame structure face against face were used to dust the moving belt in Figure 2.9. After the cleaning devices for the moving belt system were developed, the available data acquisition time period increased significantly.

### 2.2.7 Control Booth

The moving belt system is the part of the cascade wind tunnel which is covered by the tunnel-contained environment tent. The belt operator had to control the belt wander inside the tent while the belt was running. The seeding for LDV measurement was within the tent so that the operator used a respiratory mask. A control booth was set up to keep the belt operator away from the heavy seeding inside the tent. The control booth was made of black plastic film, one foot square and as high as the tent.

## 2.3 Miniature LDV

The miniature fiber-optic 3D LDV was used to measure the total velocity vector and all Reynolds stress tensor terms in the cascade wind tunnel described in Section 2.1. The LDV system in this study was modified after the measurements of Kuhl (2001). Here the highlights of the system and modifications are presented.

The LDV system consists of a LDV head, an optical table, a signal-conditioning board, three digital signal processors, and a seeding generator. The seeding particles pass through the measurement probe formed by the five modulated laser beams from the Coherent argon-ion laser in the optical table. The off-axis scattered light of the particles is collected by the two PM tubes. The signals from the PM tubes are necessarily amplified

and filtered through a signal conditioning board. The RF generated signals are mixed to remove the carrier frequency generated by the Bragg cell Oscillator from the three Doppler-burst-based signals. The Doppler frequency of the LDV signals were analyzed using three Macrodyne model FDP3100 frequency domain signal processors operating in profile coincidence mode. The uncertainties of all the calculated velocities are shown in Table 3.3 in Section 3.3.

### 2.3.1 LDV head

The LDV head shown in Figures 2.10 and 2.11 was developed by Chesnakas (1995) , which transmits 3 green (514.5 nm) and 2 blue (488 nm) argon-ion laser beams and receives the off-axis backscatter signal through an optical glass window presented in Section 2.1.3. In this manner the flow is undisturbed by the presence of the LDV head under the tunnel floor.

The crossing of these beams created a nearly spherical control volume of around  $50\mu m$  diameter, which was calculated using the beam waist equation found in Durst et al. (1995). The fringe spacing for each pair of laser beams was calculated to be approximately  $5\mu m$  using equations found in Durst et al. (1981).

The LDV head (Figure 2.11) is composed of two transmitting beams assemblies at right angles each other and a receiving assembly vertically assembled in an aluminum chassis base. The transmitting and receiving assemblies are adjustable. The LDV head is mounted to a two-dimensional traverse system with an range of 22.86 cm (9 inches) along z and 2.54 cm along y (Made by Parker Positioning System Daedal Division), which is screwed into a positioning plate (Section 2.3.5) made of aluminum attached to the underside of the tunnel floor. The traverse for the LDV head was automatically

operated with a National Aperture controller MC-4B, which can be manual or computer controlled. The computer-based controller saved the transition time from one point to the next for the LDV system.

For the moving wall setup, the LDV head and a displacement sensor are integrated so that they slide back and forth together along the 9.5 inch tangential traverse. Also mounted to this traverse with an extended arm is the displacement position sensor which sticks up through a hole next to the optical glass window in the Plexiglas insert. The traverse for the displacement sensor was manually adjusted. The sensor is lined up with the measurement probe of the LDV head in the  $z$  direction. Figure 2.12 shows the traverse for the LDV head and displacement position sensor outside of the tunnel. Figure 2.13 shows the LDV head, sensor and traverse mounted to the table under the tunnel floor.

The adjustments needed to produce coincident measurement volume are critical for the LDV system to achieve a high 3-velocity-component data rate. A fast and reliable approach was developed in this study. Two 0.25 inches thick aluminum blocks are placed 0.5 cm apart on the optical glass window. The five laser beams came out of the glass between the two blocks and can be adjusted up and down about 1 cm along the space. A thin polishing film is put over and between the two blocks. The focal volume of the five beams cross approximately on the film for a coarse alignment. A white paper is glued over the tunnel ceiling. An objective lens mounted on a vertical traverse is installed above the crossing point of the film to help visualize a fine alignment. The five beam focal volumes are projected by the lens onto the white paper with about 1 inch diameter images. Adjusting the three axes make all five beams cross at the exact point. A trial and error method is necessary for the precise crossing.

### 2.3.2 Optical Table for LDV

The LDV optical table used in this study was modified substantially after the previous LDV study of Kuhl (2001) because some optical parts were returned to their owner in 2001. Besides the laser and the beam launchers, other necessary parts were replaced. Compared to the old system, a beam polarizer and two beam splitters were eliminated. The beam system was simplified and more efficient. The single beam out of the laser is color separated by a prism. A mirror is used to extend the beam path so that all five color beams expand wider. Then another mirror redirects the two selective color beams. The blue beam is split into two equal power beams by a Bragg cell. The green beam is divided into two branches by a beamsplitter. The beam intensity distribution is controlled by a rotational polarizer. The parallel beam is further split with a Bragg cell. Three Bragg cell drivers were used to shift the beam frequency at 40 MHz for the blue and -27 MHz and 50 MHz for the green beams. All five beams go into the fiber optic couplers. The optical fiber is protected by a rubber hose between the optical table and the LDV head. The receiving assembly is on the table. The photo-multiplier tubes were Electron Tubes Limited models 9125B and 9124B, which are optimized for green and blue light, respectively. They were driven with high voltage power sources. An He-Ne laser on the table was used as a receiving beam to check the beam crossing.

### 2.3.3 LDV Signal Processing

The LDV output signals are the digital signals from the three Macrodyne model FDP3100 frequency domain signal processors. The Macrodyne units process analog signals with input from the two photomultiplier tubes through the signal conditioning board. The photomultiplier tubes receive the signals through a multimode receiving optical fiber,

shown as a black dot in Figure 2.1, from the LDV head.

Figure 2.14 shows a schematic of the signal conditioning system. The left hand side of the figure shows the received signal beam coming in from the LDV head. The beam is split with a dichroic mirror into a blue and a green beams. The two beams are converted into an electrical signal in their corresponding PM tubes. The analog signal out of the green-featured PM tube is further equally divided into two channels: -27 MHz and 50 MHz. All three signals are amplified and then mixed with their respective RF signal generated by a variable RF generator to demodulate into three different Doppler signals. Finally each electrical analog Doppler frequency goes into an FDP3100 Macrodyne.

The Macrodyne basically determines if the signal is valid and digitizes the validated burst with a FFT algorithm. Data were acquired by the IDAS computer over 3, 25-pin cables only if all signals are coincident within 10  $\mu$ s from the three Macrodyne processors. The detail functions and operations of the Macrodyne is well documented in the Macrodyne Manual (1992).

### 2.3.4 LDV Seeding

An aerosol generator for LDV seeding designed by Echols and Young (1963) was used in the cascade tunnel, shown in Figure 2.15. The seed is piped into the inlet of the tunnel contraction through a 0.5 inch diameter pipe. The pipe is located at the upstream of the tunnel contraction in the tunnel as shown in Figure 2.16. The last plenum screen is just upstream of the pipe. The pipe exit position is adjusted by rotating the pipe left and right as well as moving up and down until the smoke is injected into the LDV probe volume. The fluid in the generator is dioctyl phthalate (DOP) with a mean particle size slightly less than  $2\mu m$  (Kuhl, 2001).



Several traverses with the pitot probe approximately 100 cm upstream of the suction slot show no measurable influence or effect of the pipe on the downstream flow (Kuhl, 2001). The maximum mean velocity difference was within 0.2% with and without the pipe.

### 2.3.5 Positioning Plate for LDV

The positioning plate, on which the miniature LDV head with a traverse system rests and is positioned, was mounted underneath Blade 5, the Mylar belt, and the optical glass so that the LDV head shoots laser beams into the tunnel and collects the scatter of light off of the particles in the flow. The plate is a 1/4 inch thick sheet of aluminum screwed into the bed frame, shown in Figure 2.2 and Figure 2.13. Three things were done in the modified arrangement after experience with the arrangement used by Kuhl (2001). The plate was stiffened against gravitational sag, the positioning holes for the measurement matrix were drilled precisely by a digital control milling machine, and the positioning pinhole was punched on the steel square and the plate. The belt returns one half inch below the positioning plate. The plate is slightly larger than the plexiglas insert so that the LDV head can be mounted on different axial locations to measure flow upstream and downstream of the blade row. A hole is open for adjusting the receiving lens whenever the crossing alignment is necessary. Using four clamps, the plate can be easily attached onto and detached from the tunnel floor without disrupting the head alignment whenever the measurement window is moved.

### 2.3.6 LDV Probe Volume Position Determination

A spectrum analyzer was used to find the exact probe volume position relative to the wall at the beginning of any velocity profile traverse. It is very critical to know the precise LDV measurement volume location in the viscous sublayer. At the beginning of taking every profile, one of the LDV signal channels is plugged into the spectrum analyzer. A large burst signal peak is captured as the measurement volume of the LDV crosses the interface of the window glass and fluid, thus identifying the actual wall location.

### 2.3.7 LDV Monitoring

Two x10 spy cameras are used to monitor the laser beam and data rate, respectively. After the tunnel-contained environmental tent (Section 2.1.4) was built, the laser beams out of the LDV head under the tunnel floor can be barely seen from outside the tent. The beam intensity monitoring is necessary to optimize the beam whenever the data rate drops. This monitoring camera is also used to observe whether the measurement probe is blocked by the belt for the moving wall setup in Figure 2.17. The other monitoring camera is used to maximize the data rate for the moving wall by fine-tuning the belt location. Two independent monitors are used in the monitoring system, a 19 color TV and 9 inch black and white TV.

### 2.3.8 Dust-free Housing for LDV Head

The volume surrounding the LDV head, the traverse, and the Belt-hite sensor was enclosed by a plastic film, which kept the LDV head away from the flying particles while the belt is running.

## 2.4 Optical Sensors

Two analog signals were added into the LDV system for the stationary wall. The first optical sensor detects the belt fluctuation signal, which measures the belt displacement in the y direction. The second optical sensor detects the passage of the belt joint. After the sensor is connected to the signal processor, a negative pulse is generated whenever the sensor is blocked by the mark on the belt joint.

### 2.4.1 Fiber Optic Belt Displacement Sensor

In order to monitor the vertical belt fluctuation associated with the profile location of the LDV measurement, a Philtec, Inc Fiber Optic Displacement Sensor mount was integrated into the LDV head (Section 2.3.1), shown in Figure 2.13 and viewed the belt through a hole. The tip of the displacement sensor sits 0.5 mm away from the moving Mylar belt. The displacement sensor then is traversed up into the hole on a 2 inch traverse in the y direction. Kuhl (2001) documented the calibration for the Mylar belt shown in Figure 2.18. From the plot the middle range is linear. To make sure the real time fluctuation of the moving belt was within the linear range, the position of the sensor head under the moving belt had to be adjusted after the belt achieved its full speed.

The moving wall was flattened on the supporting bed due to belt tension and suction produced by removal of air between the belt and the bed. Due to the unevenness of the Teflon-covered bed and belt wandering, the belt fluctuated slightly while in motion at full speed. To check the belt fluctuation, a pretest vertical displacement was acquired at clear belt conditions for the moving wall experiments, as shown in Figure 2.19a. The large jump in signal is when the belt joint passes over the probe. When the belt joint passes over the sensor, the signal jumps. The jump displacement is measured to be greater

than  $100\text{ }\mu\text{m}$ . The signal was taken at 30 KHz (a resolution of 0.8 mm longitudinal movement of the belt). Figure 2.19b shows the results at particle loaded belt conditions. The uncertainty of wall vertical fluctuation was  $\pm 8.3\mu\text{m}$  under clear particle-free belt conditions including the belt joint, and  $\pm 7.4\mu\text{m}$  after the belt had run for some time not including the belt joint after the joint was covered by electrical tape. The rms belt fluctuation was  $7\text{ }\mu\text{m}$ .

### 2.4.2 Belt-Joint Detector

The Mylar belt joint in Figure 2.1 is not flat since the belt is overlapped, melted, and taped. Therefore, the data from the joint region can be removed by blocking the laser beams parallel to the position of the joint. The same sensing system as used for determining the vortex generator locations was used. A photodiode sensor is screwed into the plexiglass insert in at the position shown in Figure 2.1. The sensor goes up into the floor as shown in Figure 2.2. A laser pointer is mounted to the top of the tunnel and shoots a beam into the photodiode. The electrical tape marks shown in Figure 2.1 block the sensor as they go by. Figure 2.19b is the typical output of the photodiode processor when the belt is running at full speed. It is also used for belt speed monitoring because the mark length was known in order to calculate the real time belt speed.

## 2.5 Integrated Data Acquisition System

An integrated data acquisition system (IDAS) had to be used for the two setups of the study to take 30,000 samples of the five input signals at each point. Three signals are the simultaneous digital output of the velocity components from the LDV system.

These digital signals contain the frequencies created by the particles passing through the measurement volume. The two analog signals are from the two analog sensors.

A data acquisition system was originally designed by Kevin Shimpagh and Christopher Chesnakas and documented in Chesnakas (1995) for the pressure-velocity measurement of a prolate spheroid, which had one analog signal and three digital signals capability. That system was set-up to synchronize one analog signal with each LDV signal output by the processors. For this study, the IDAS needed the capability of handling two analog signals for the moving wall. For the moving end-wall, the three digital signals and the two analog signals were acquired simultaneously, so that they are all synchronized. For the stationary end-wall, the three digital signals, but no analog signals, were acquired.

### 2.5.1 IDAS Hardware Platform

Since time variation of signals is an important consideration in the LDV experiments, much care was taken to synchronize the three LDV signals with the two analog signals. Two A/D boards and copies of the analog cable wiring were connected with a two-input terminal box. The three digital signals from the LDV signal processors are input to a connector box through 25 pin connectors. The output of the connector box is input to the digital I/O board of the computer with 2 48 pin connectors. Signals are acquired when a trigger signal from the master Macrodyne processor is received in the connector box. A digital I/O, two A/D boards, a timer board were inserted into the expansion slots of the computer motherboard. In Figure 2.20 the schematic of the IDAS used in the study is illustrated .

The computer used to collect the data and run the IDAS software is a 166MHz IBM

350 P90 (6586-47H) with a 8 GB hard drive (4 partitions) and 64 MB of RAM. DOS 6.2 operating system is installed on the computer. The computer uses a Iomega 100 zip drive to transport the raw data to the processing computer.

### 2.5.2 IDAS Software Framework

The original DAS software was written by Chesnakas in Microsoft QuickC 2.0 for pressure-velocity measurements, including the user interface, data acquisition board driver, configuration files, and data files management. As stated in Section 2.5.1, the DAS needed the capability to add one more analog signal. While the software framework remained the same, many revisions were made to input new parameters, streamline the profile names, increase the data storage, and improve the data transfer rate. The old software was limited to 16384 samples. New memory management was used to acquire as much data as required, such as 128,000 samples for the moving wall with vortex generators.

In the original software, the IDAS data rate was more than three times slower than the Macrodyne data rate out. It was discovered that two coincidence time windows were used simultaneously in the IDAS. One is the 10  $\mu$ s coincidence time window set up by the three Macrodynes. The other was a “soft” coincidence window made by the software in the PC. Once the “soft” window was eliminated, since it was unnecessary, the IDAS data rate increased to around 80% of the Macrodyne data rate. The loss of the LDV data rate is acceptable and reasonable because of the additional processing time of two analog signals.

## 2.6 Data Post-Processing

The software was recoded in Visual Basic by Kuhl (2001) from the same noise removal scheme as Ölçmen and Simpson (1995a). The post-processing code was basically modified to accept the new IDAS format with two analog inputs and three digital inputs. The output of the initial post-processing procedures was the time-averaged mean velocities, Reynolds stresses, and triple products.

The data are split into two different categories for post-processing: stationary end-wall data and moving end-wall data. With the stationary end-wall the Mylar belt is not used and therefore the two extra analog signals are not used. For the moving end-wall experiments, the black tape covers the belt joint. Thus, no LDV data are acquired when the belt joint passes by the LDV probe. The LDV post-processing is the same as for the stationary end-wall data.

The computer used to post-process the data is a PII 300 MHz computer with a 9.1 GB hard drive (3 partitions) and 64 MB of RAM and operating Windows XP. Along with an Iomega 100 zip drive the computer also has a Writable CD-ROM (8x4x32) to burn the raw and processed data to compact disks. The computer has all SCSI components to increase file transfer speed between large storage devices. The computer is hooked up to the network for file sharing capabilities.

### 2.6.1 LDV Data Post-Processing

There are two major steps for the post-processing of the data, the first being preparation of the acquired data and the second being calculation of the desired quantities. The preparation of the data was conducted with the three problem issues of LDV data in

mind: noise, signal biasing and broadening effects, and co-ordinate and wall location adjustments. Mean velocities, turbulent stresses and the triple products were calculated after the following procedure to get clean samples.

With LDV systems, like any electronic measurement system, there is always a certain amount of extraneous noise present during data collection. The method used to remove noise from the data was that used by Ölçmen and Simpson (1995a). A parabola was fit to each side of the logarithm of the velocity component histogram ordinate in the range between 1 % to 80 % of the peak histogram value. The data lying outside of the intersection of the parabolas with the ordinate value were discarded. If one of the velocity components was deemed unusable, all three were discarded. The clean velocity information for all three velocity components was transformed into tunnel co-ordinates and saved. Once more a parabola was fit to each side of the logarithm of the histogram, this time to the transformed data, and the noise was removed. The number of samples taken at each point ranged from 15,000 to 30,000.

### 2.6.2 Analog Data Post-Processing

Two analog data sets were taken for the moving wall. About 8% of the time period data were discarded because of the belt joint. A threshold value of the joint-finding signal was set from the monitoring multimeter before the IDAS acquired data. The value was used to filter the data associated with the joint while doing the data post processing.



## 2.7 System Improvements

Many problem issues for the LDV experiments in the cascade tunnel were encountered. Many were documented in the study of Kuhl (2001). Some new improvements were made in the current study. Other suggestions are made for future studies.

### 2.7.1 Previous Efforts

Kuhl (2001) described the problem experimental issues that were resolved in the previous study. The miniature LDV worked well with two new PM tubes. A regular check of the incident laser beams polarization was necessary. The LDV head was modified for easier beams crossing. The data acquisition system worked well, even though there was the occasional failure of computer memory chips. The data transfer rate was normal after the critical error was corrected. The most important concern was the function of the moving belt system. Even though the system was proven to work, there was much effort to solve the four main continuing issues: belt friction and dust particles, belt reflection, belt wandering, and belt life.

### 2.7.2 New Efforts to Solve Problems

The difficulty of obtaining proper LDV laser beam alignment required improvements to the LDV head adjustment mechanism for the two color laser beam transmitting units (Figure 2.11). Due to the original design, the two axes adjustment for the green unit were not independent. It became worse over time due to the failure of the springs and wear of the structure. A replacement standard two-dimensional traverse was preferred but would require a substantial change of the LDV head chassis. However, due to the limited

time a quick practical modification was used for short term benefits. The adjustment ranges for the two units expanded 0.5 cm each. A practical solution was to add two more springs to each of three axes, respectively. The tunnel test showed the effectiveness of this modification.

The optical table for LDV system had to be rebuilt because the optical parts based on the TSI two dimensional system were returned to the owner after the previous study of Kuhl (2001). As described before, the new optical table arrangement improved the laser power efficiency, which contributed partially to the higher data rate.

The LDV head positioning plate was used as in the previous study of Kuhl (2001). However, an obvious discrepancy was found for the mean velocity at the same location of the stationary wall between the previous data and the current data with the same LDV system. Troubleshooting suggested that the positioning plate made of the aluminum sheet should be strengthened with the braced bars to avoid any gravitational sag. It was also determined that accurately machined holes for installing the LDV head should replace the holes that were drilled manually. Furthermore, two positioning pins were used to keep the positioning plate at the exactly same location for all experiments.

A bed with strips of tape to lift the belt away from the bed was an intuitive solution to reduce the scratching problem for the moving belt system. The experiments verified that the striped bed worked well and the belt life was no longer a problem because the direct wear became less.

## 2.8 Equipment Improvements and Future Recommendations

The modification has been done to improve the maximum data rate and the data rate over the time in the low-speed linear compressor cascade wind tunnel at Virginia Tech for LDV measurements in the tip gap of blade 5. The improvements includes: 1) the tunnel, 2) the data acquisition system, 3) moving belt system, and 4) LDV system.

The maximum data rates of over 1700 samples/sec show that the LDV measurements work very well for the stationary end-wall data. With a moving end-wall a reasonable LDV data rate of over 700 samples/sec was setup for the region in the passage and upstream away from the blade. However, it was not very successful to take LDV data in the gap region because of the strong refraction and flaring between the Mylar belt and blade tip, shown in Figure 2.7b.

Throughout the work many problems were encountered, some of which remain to be addressed. A new design, like a blowing device, is needed for the displacement sensor to work all the time while taking moving end-wall data. One or both of the two following suggestions can help increase the data rate to an acceptable level for a moving end-wall. First, a better belt material may be found to replace the Mylar film. Second, a transparent test blade with anti-reflection coating can be shaped. Maybe the practical way is to redirect the measurement tool. A new fine spatial resolution LDV with a long optical distance could sense the flow from the side wall instead of the endwall with the miniature LDV.

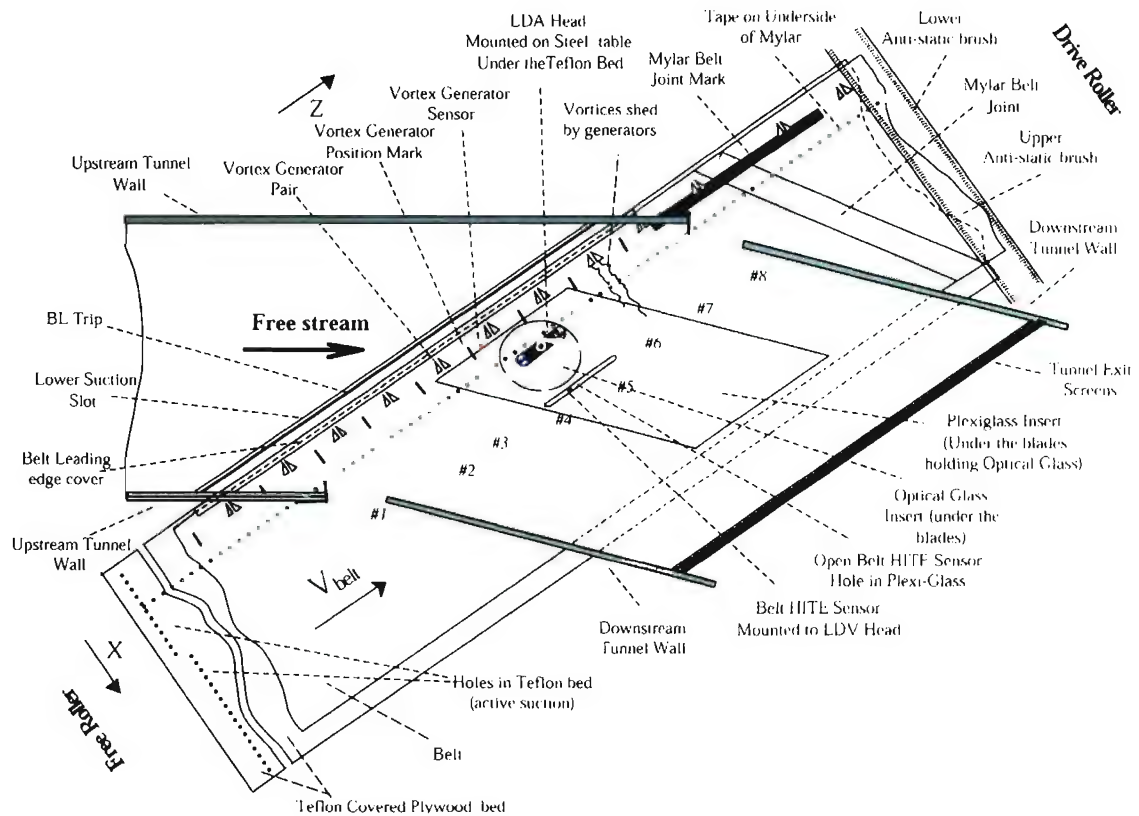


Figure 2.1: Top view of experimental test section setup in the Cascade Wind Tunnel from Kuhl (2001)

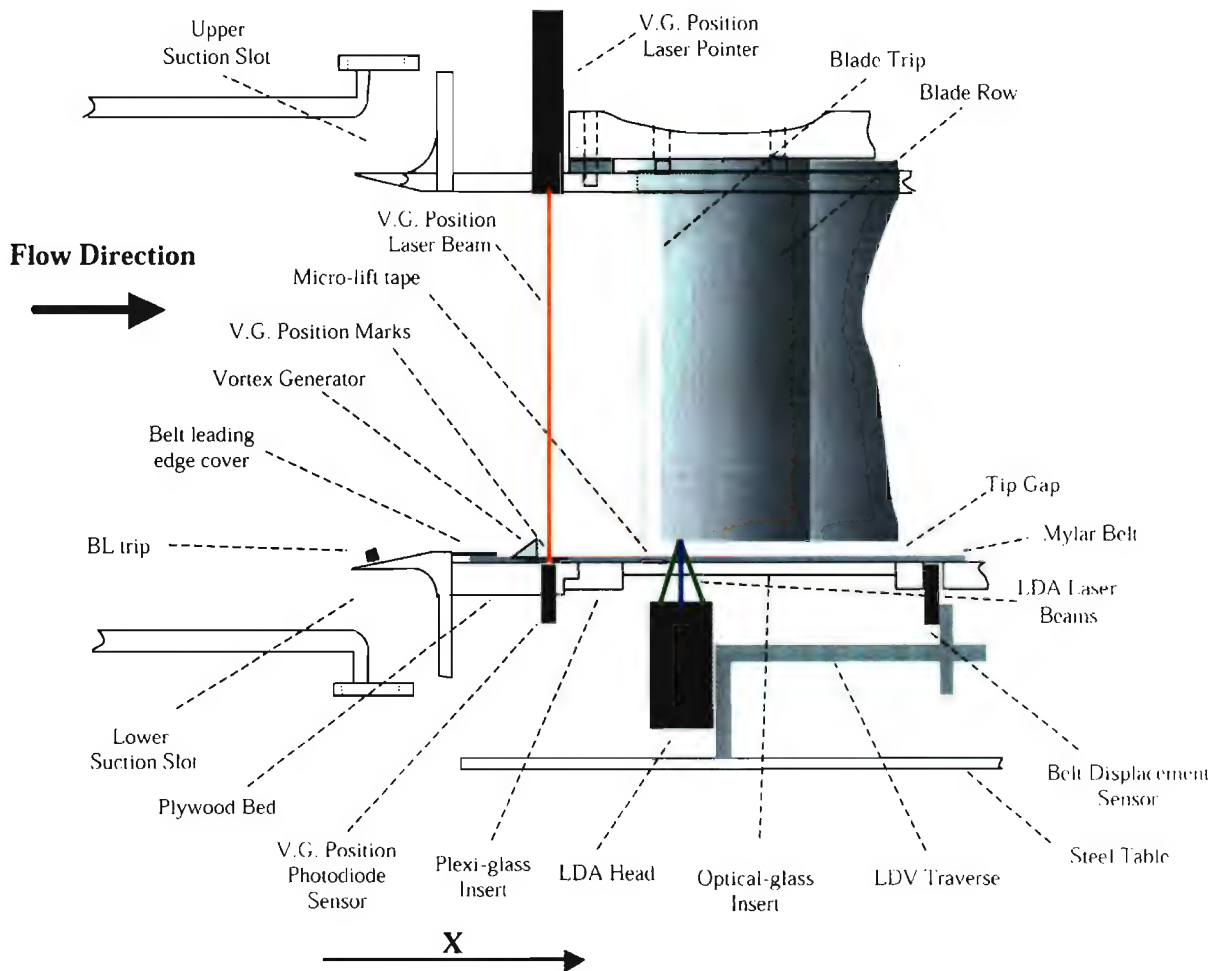


Figure 2.2: Side view of experimental test section setup in the Cascade Wind Tunnel from Kuhl (2001)

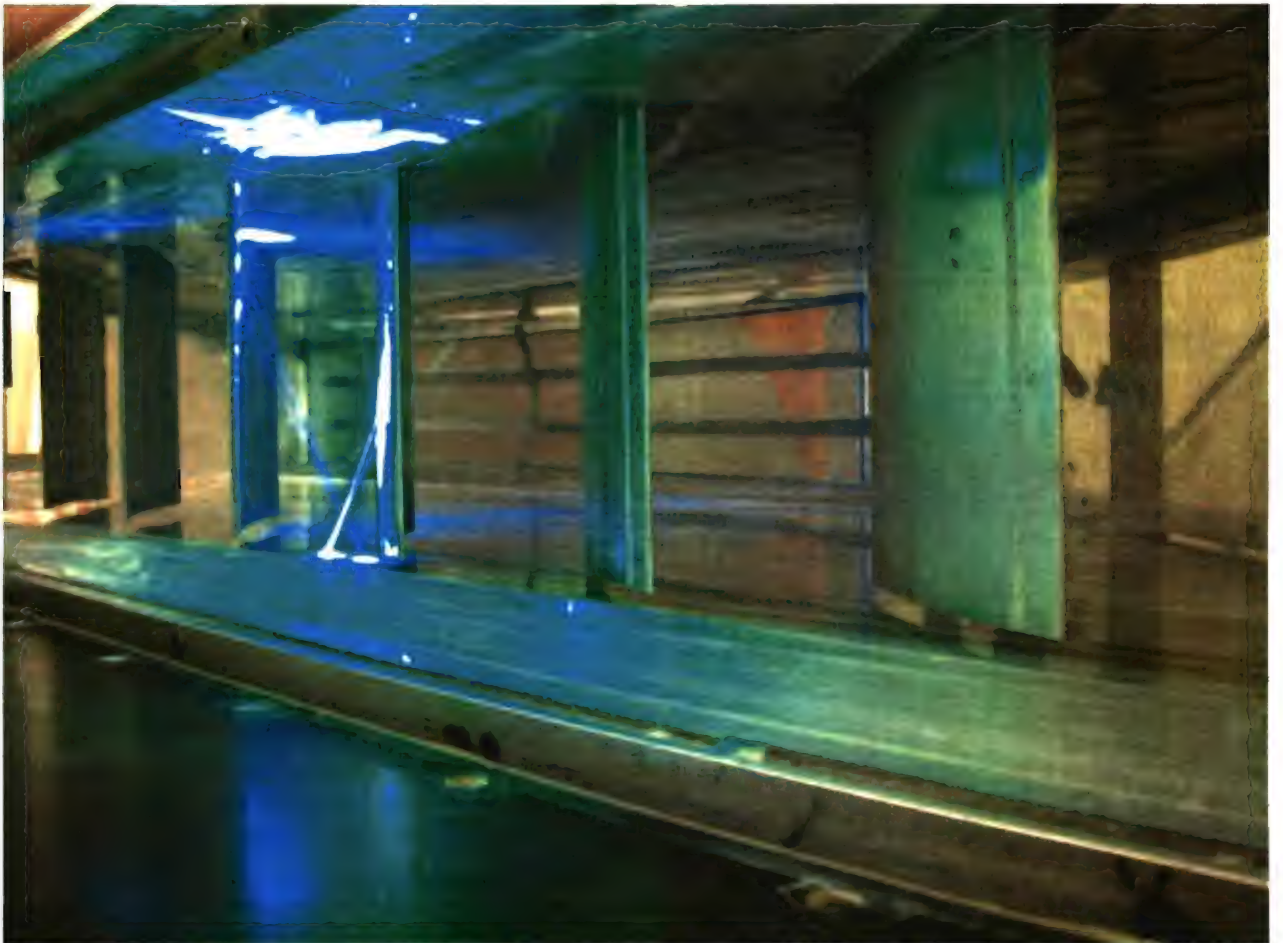


Figure 2.3: The working tunnel with laser beams

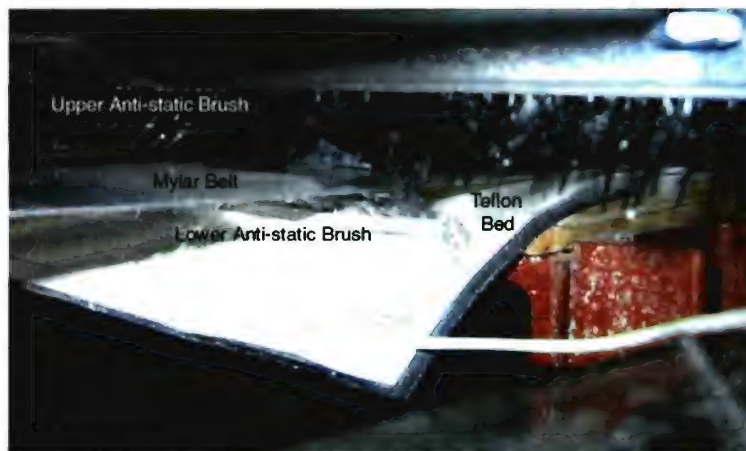


Figure 2.4: Two anti-static brushes facing the moving belt

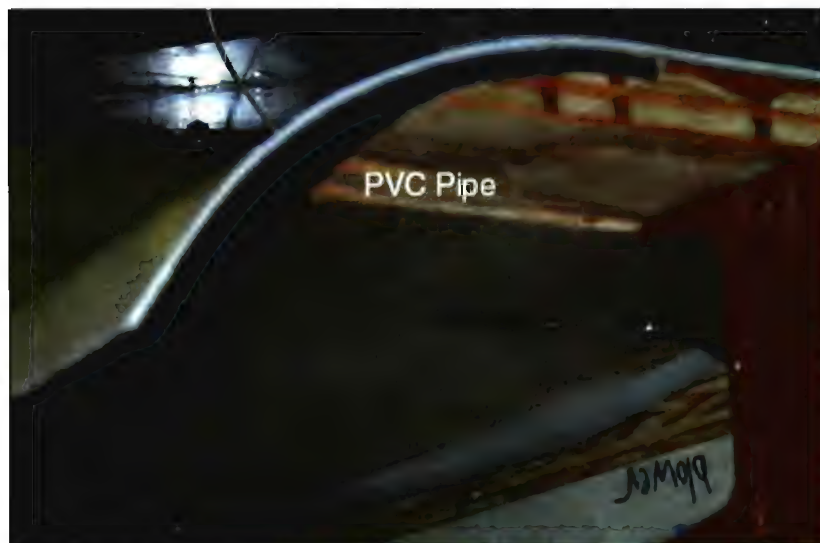
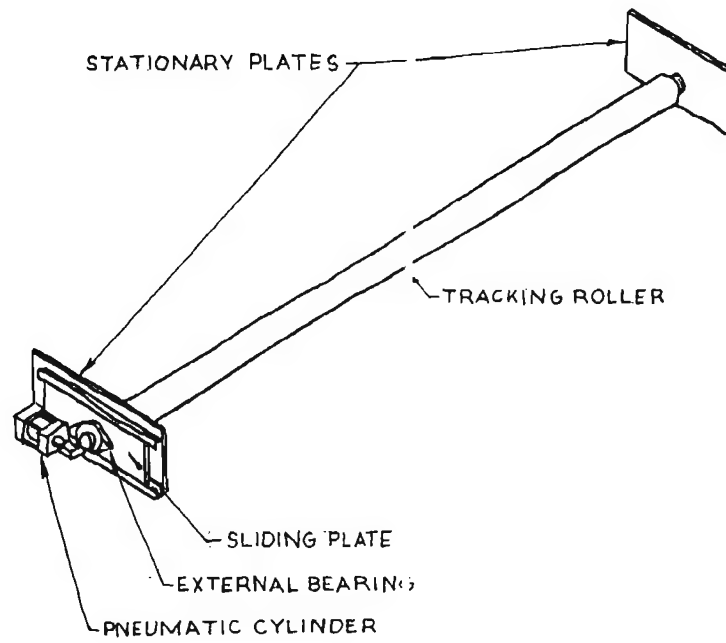
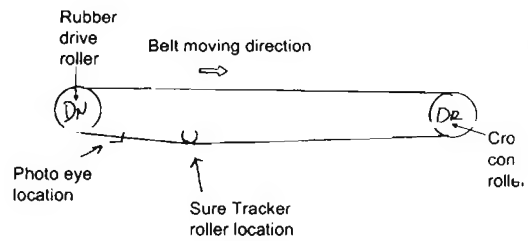


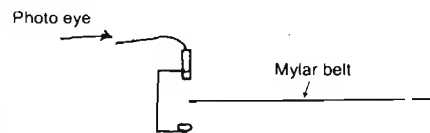
Figure 2.5: Upstream end of bed with 12" PVC pipe attached



(a) Single Roller



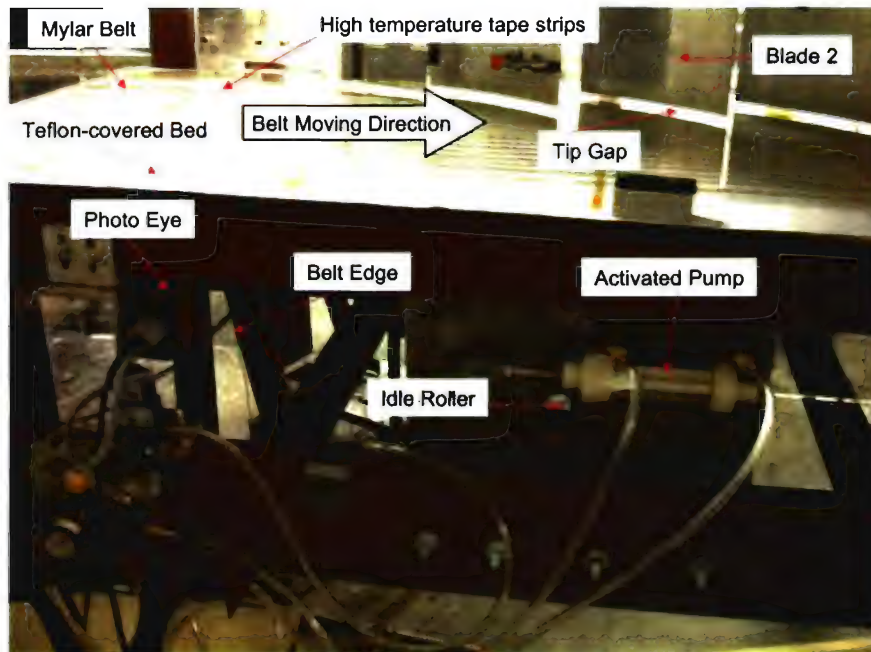
(b) Location of Roller



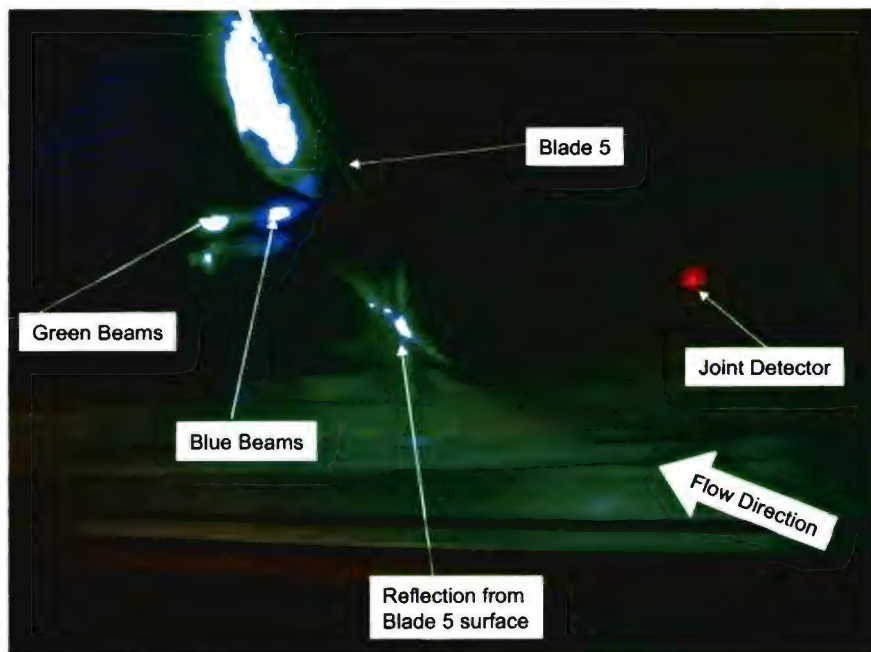
(c) Photo eye next to belt edge

Figure 2.6: Sure Tracker





(a) Side view of striped Bed and Sure Tracker



(b) Top view of LDV and Joint detector

Figure 2.7: Tunnel with moving belt and instrumentation setup for moving wall experiments

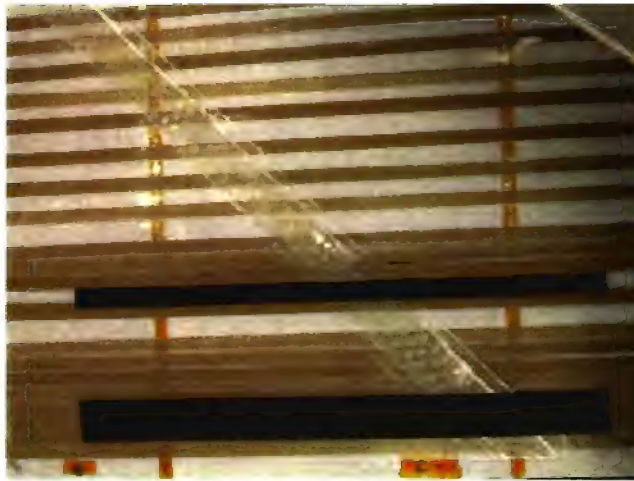


Figure 2.8: Part of the bed with high temperature tape strips for the moving belt system



Figure 2.9: Two face to face brushes used for a moving belt



Figure 2.10: Miniature 3D fiber-optic LDV head

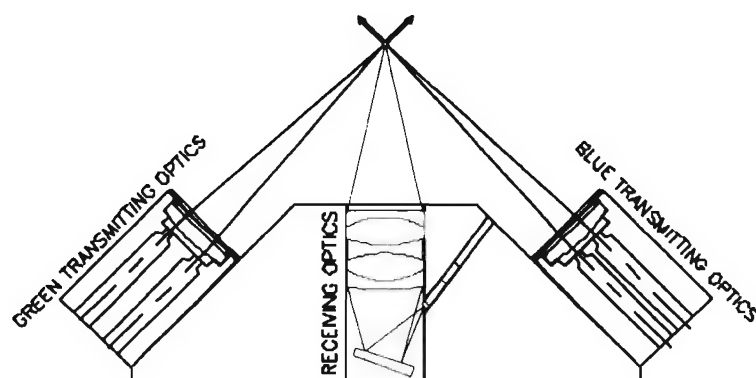


Figure 2.11: Schematic of 3-orthogonal-velocity-component fiber-optic LDV head

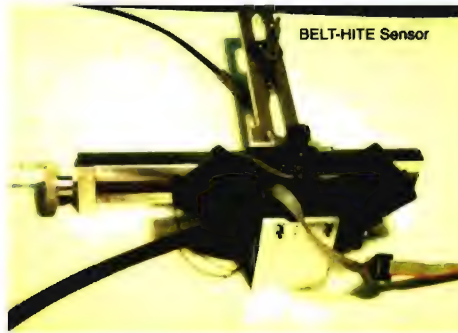


Figure 2.12: Assembly of LDV head and displacement sensor along with a traverse



Figure 2.13: Assembly of LDV head and displacement sensor on the positioning plate and under the tunnel

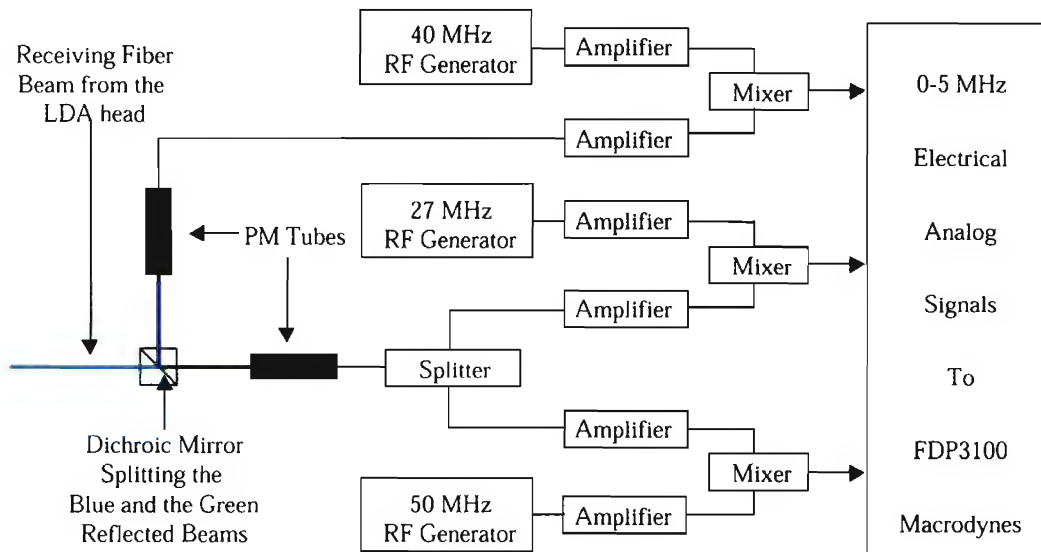


Figure 2.14: Schematic of LDV signal conditioning for the Cascade Wind Tunnel



Figure 2.15: DOP generator with an impactor can under the contraction of the Cascade Wind Tunnel





Figure 2.16: Seeding pipe downstream of flow conditioning screens in the contraction of the Cascade Wind Tunnel



Figure 2.17: Monitor for LDV beams out of the optical glass window inside the tunnel

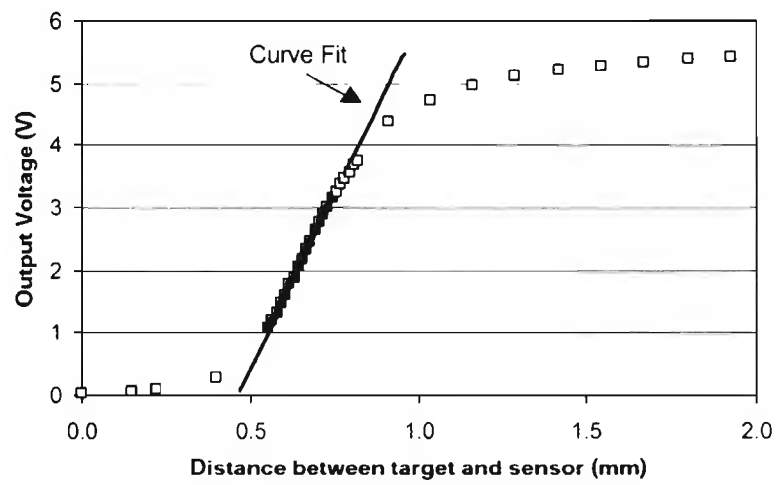
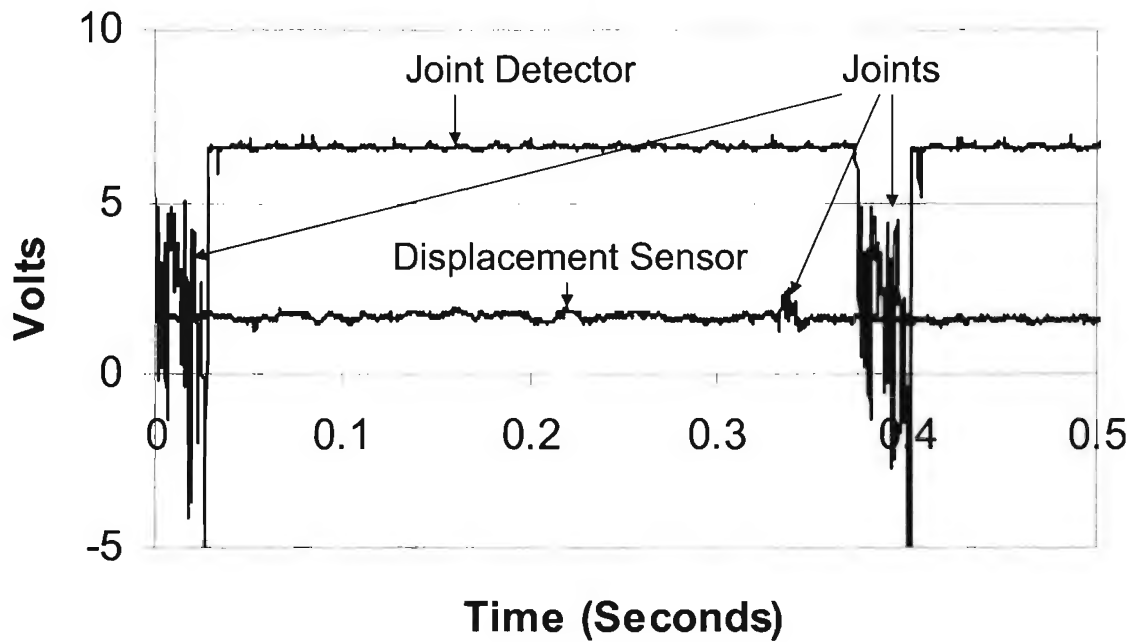
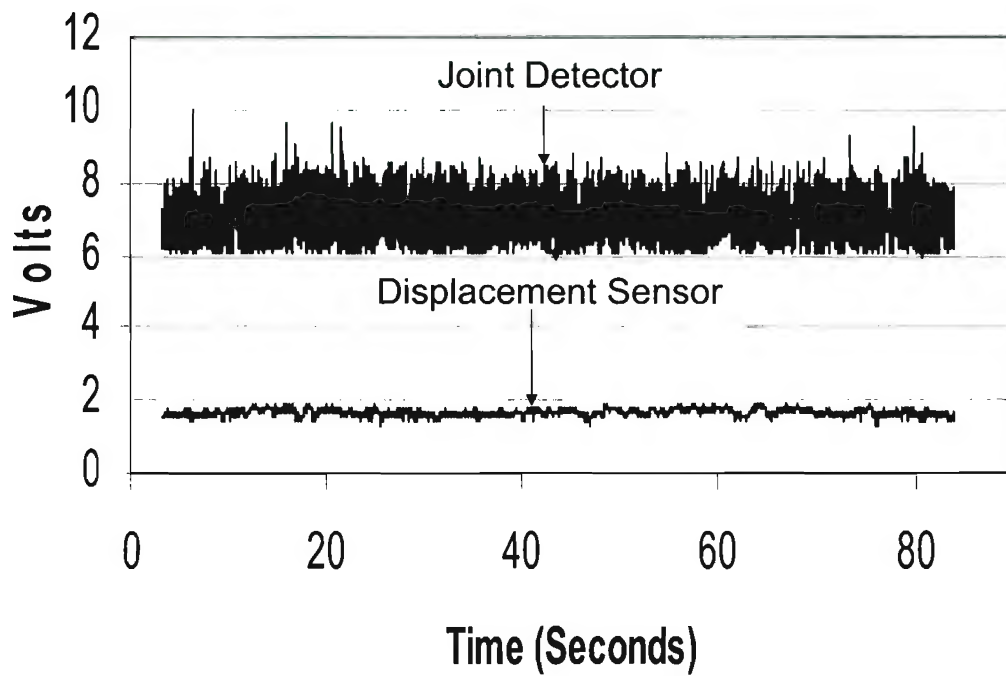


Figure 2.18: Calibration curve for the displacement sensor



(a) Clean belt condition



(b) Particle loaded belt condition

Figure 2.19: Output of both displacement sensor and joint detector for moving wall experiments



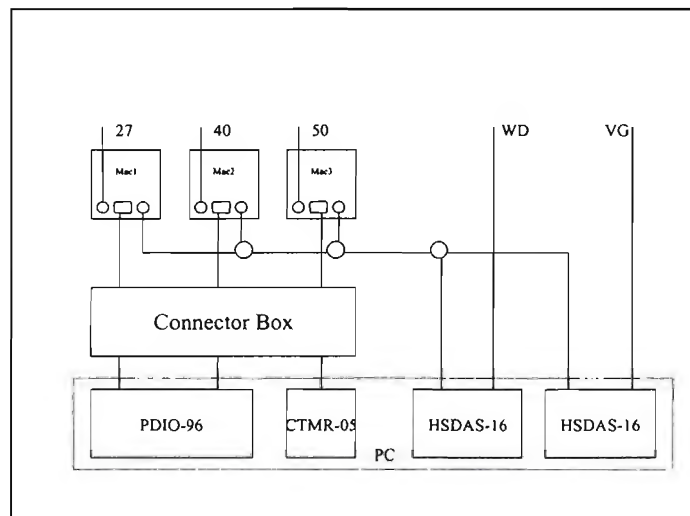


Figure 2.20: Schematic of integrated data acquisition system, where Mac1, Mac2, and Mac3 are signal processors from MacroDynes; WD is an analog signal of wall displacement; VG is an analog signal of the position of belt joint PDIO is a digital input/output board; CTMR-05 is a timer; HSDAS is a data acquisition of analog signals.

## Chapter 3

# Measurements on a Stationary Wall

The core part of this dissertation reports the tip-gap flow results with a stationary endwall in a low speed compressor cascade tunnel at Virginia Tech. It is much easier to make measurements for the tip-gap flow without a moving endwall. Important flow structures can be discovered with a stationary wall setup, such as tip leakage vortices and other vortices around the tip gap region. Chapter 4 describes data with a moving wall that adds relative motion imposed on the stationary wall flow. A thorough study has been done including surface oil flow visualizations, surface pressure measurements, and LDV measurements. The tunnel setup is the same as in Chapter 2. The flow turning angle downstream of the cascade is  $11.8^\circ$  as shown in Figure 3.1.

In order to examine the effect of tip gap size, two gaps of 1.65% and 3.30% of the blade chord have been examined. For each tip gap, surface oil flow visualizations on endwall and blade surfaces were made to reveal the flow characteristics near the physical boundaries. The static pressure distributions on the endwall and mid-span of the blade were measured as well. About 50 velocity profiles of LDV data for each gap size were taken around the tip gap region in 10 planes at different chord ratios from the upstream

to the downstream along Blade 5.

The first three sections of this chapter present coordinate systems, calibrations, and measurement uncertainty, respectively, for stationary wall experiments. The results of surface oil flow visualizations, surface pressure measurements, and LDV measurements are described in Sections 3.4, 3.5, and 3.6, separately. The final section characterizes the tip gap turbulent flow structure for a stationary wall.

## 3.1 Coordinate Systems

For convenience, some coordinate systems in Figure 3.2 have been used throughout the dissertation such as a bed coordinate system, a chord coordinate system, a free-stream velocity coordinate system, a separation-line coordinate system of the tip leakage vortex, local camber coordinate systems, and local wall shear stress coordinate systems. For all coordinate systems organized by the right hand rule, the origin and axis  $y$  are the same. The origin is the midpoint between Blade 4 and Blade 5 along with the leading edge of the blade row on the tunnel floor. The axis  $y$  is perpendicular to the tunnel floor.

The bed coordinate system, with axis  $z$  along the leading edge of the blade row and parallel to the edge of suction slot and  $x$  axis perpendicular to the edge of suction slot, is used to mark the test matrix and to project the beam angles of the LDV probe in the tunnel. As long as data are referenced to the bed coordinate system, they can be easily transformed to any other coordinate system through the coordinate rotation of the bed coordinate system at a rotation angle  $\theta_y$ . The chord coordinate system, with  $x$  along the chord of the blade, is set up by the rotation of  $\theta_y = 56.9^\circ$  and is used to characterize flow in the gap. The free-stream velocity system, with  $x$  along the flow direction entering the test section and  $\theta_y = 65.1^\circ$ , is used to describe the collateral flow upstream of the blade

row. The rotation angle  $\theta_y$  is  $72.819^\circ$  and  $75.352^\circ$  for 1.65% and 3.30% in the separation-line coordinate systems of the tip leakage vortex, respectively. The local camber and wall shear-stress coordinate systems are used to describe flow features at each profile of LDV measurements with a specifically different coordinate system. For the latter two types of systems, rotation  $\theta_y$  relative to the bed coordinate system are reported in Table 3.1 and Table 3.2. For the local wall shear-stress coordinate system at a specific profile, the x-axis is defined as the direction of vector of mean velocity component U and W so that  $\theta_y$  is the nearest endwall flow angle in the bed coordinate system. For the local camber coordinate system at a given chord ratio, x-axis is defined as the tangential direction at each chord ratio of the blade so that  $\theta_y$  is the tangential angle of the blade camber line presented in the bed coordinate system.

## 3.2 Calibration

In order to acquire accurate measurements of flows of interest, the cascade free-stream flow was adjusted and monitored to ensure that the flow is as expected and the LDV was calibrated to measure the instantaneous flow velocity precisely.

### 3.2.1 Tunnel Calibration

The flows of interest are produced by a blower-based wind tunnel. The freestream of the tunnel after the contraction segment enters the cascade test section, passes through the compressor blades, turns  $11.8^\circ$ , and moves downstream of the cascade. Three cross-sections of the flow path that are critical were measured, the freestream after the boundary layer removal at the entrance of the tunnel, 9.78 cm upstream of the blade row, and

41.02 cm downstream of the blade row in the test section. Measurements must be made to verify expected flow velocity distribution.

In order to set up the tunnel as expected, tip gap size is aligned carefully first. Since the blades are portable and need to be adjusted independently, care has to be taken to ensure that the blades are perpendicular to the tunnel floor and parallel to each other. A precise gauge block is used to check gap size and a level is used to check tilt of the blades. The gap size has to be uniform and consistent because three separate measurement windows mentioned in Section 2.1.3 were used for this study.

After the blade tip size was set up, a long straight edge ruler was used to check the lineup of the leading edges of all eight blades. A cross check is the surface oil flow visualization. Figures 3.6a and 3.6b show a spatially periodic flow in the test section. Since the tunnel floor is not perfectly level and flat, a tradeoff is made between the gap size and the line-up of the blade leading edge. The maximum tip gap height variation along the chord was 4.2% for the 1.65% and 2.7% for the 3.30%, respectively. The uncertainties of the gap size and blade row will be described in Section 3.3.1.

Major control parameters were used to adjust the flow, such as suction slots, side panels, back pressure screens, while taking the measurements of velocity distribution across the three cross-sections in the mid-height of the tunnel. The free-stream velocity is uniform after the boundary removal at the entrance of the tunnel. As shown in Figure 3.3a, flow at the upstream of the blade row is nearly uniform but is disturbed by the blade row because the velocity distribution has a periodically minor ripple around 1. In the downstream of the blade row, the dips show the periodic velocity deficit in the wake of the blades. The velocity calibration upstream and downstream of the blade row was made at the same locations as Kuhl (2001) and the velocity distribution were repeatable.

After the tunnel was calibrated, the same flow conditions should be maintained for all LDV measurements. Two manometers are used to monitor velocities in Section 2.1.6. One was set to measure the free-stream velocity after the boundary layer removal at the entrance of the tunnel and the other was placed at the downstream flow of the blade row in the test section.

### 3.2.2 LDV Calibration

For the LDV, uncertainty exists in the measurement of beam angles in the bed coordinate system. The only way to correct for the effect of uncertainty is to measure a known flow, such as a two-dimensional boundary layer flow or use a calibration wheel. Through the coordinate rotation the LDV measurements can match the known flow. If fine corrections are very small, they prove that measurements of beam angles are approximately correct. Otherwise, it could be a poor measurement and it is necessary to measure the beam angles again. For this cascade flow, there is no two-dimensional flow condition that can be measured as a benchmark. A spinning wheel is used to generate the known velocity for calibration. It is assumed that the wheel cover tangential velocity is aligned with the  $x$  direction so that velocity component  $u$  equals to linear velocity of the wheel and the other two components  $v$  and  $w$  are zero in the bed coordinate system. The wheel is 3.57 inches in diameter and is driven by a motor set to 1000 rpm. The motor is mounted in an aluminum block so that the motor shaft has been precisely aligned with the aluminum base. After the base was placed on the floor, the wheel centerline is aligned with the LDV probe. Again due to the uncertainty of measurements of beam angles and misalignment of the LDV probe relative to the floor, there is a small discrepancy between measured velocity and theoretical velocity so that a fine rotation of data is necessary to get known conditions. The rotation angles of pitch, yaw, and roll are  $1.795^\circ$ ,  $0.601^\circ$ , and  $-0.012^\circ$ ,

respectively.

### 3.3 Measurement Uncertainty

Uncertainties come from measurements of different physical quantities: distance, velocity, and static pressure. The uncertainty of surface pressure measurements was documented by Tian (2003).

#### 3.3.1 Position Measurements

For profile locations measured with the LDV, a ruler with 1/64 inch scale division was used so that the x and z coordinates uncertainties are  $\pm 0.008$  inches. The y uncertainties are  $\pm 0.01mm$  for the LDV with a traverse. Uncertainties of the tip gap size are  $\pm 0.001$  inch.

#### 3.3.2 LDV Measurements

To assess whether there are velocity biases in the experimental data, a standard correlation coefficient between velocity magnitude fluctuation and data rate fluctuation was calculated for each location in the same way as Kuhl (2001). With two sets of data taken in two different days, the measured correlation coefficient was 0.02 so that no velocity bias existed for the flow of interest.

Figure 3.5 shows the comparison between profiles at location uu in Figure 3.4 and the DNS results of Spalart (1988) over a flat plate at three different  $Re_\theta$  values. The differences between the DNS and the current experimental data are mostly due to unre-

laxed flow structure and differences in  $Re_\theta$ . The unrelaxed flow structure was discussed by Kuhl (2001). The effects of  $Re_\theta$  were described in AGARD (1996). Nearest the wall there is a very good agreement. Uncertainty in  $U_\tau$  could cause differences between the DNS data and the experimental data. The  $U_\tau$  uncertainties were calculated by Tian (2003). Table 3.3 shows the uncertainties for all mean and turbulent quantities. The uncertainty analysis procedure is described in Appendix B.

## 3.4 Surface Oil Flow Visualizations

Flow visualization is a simple but powerful tool to quickly observe a surface flow pattern, which is considered as the perception of the boundary conditions of the test flow. In this study, surface oil flow visualizations are used to map out flow features on the endwall and blade surfaces, which provide qualitative information that is not acquired quantitatively by the LDV from a broad area, like the endwall and blade surfaces. They are also used to guide the locations of the most interesting flow features.

### 3.4.1 Endwall

For the endwall, due to the limited space the oil flow contact film can not be placed underneath the blade first and then brushed with the oil mixture. A film painted with kerosene, titanium oxide, and oleic acid at ratio 40:15:1 has to be prepared first and moved into the tip gap very quickly. Fine limited streamlines can be obtained for digitizing the oil visualization using less oleic acid. The digitizing of endwall surface oil flow visualizations was done by Tian (2003). Because of motion, static electricity is generated. In order to keep static-free, grounding is necessary. Figure 3.6a and Figure 3.6b show the finished



film sheet.

The 1.65% tip gap flow visualization in Figure 3.6a was made by Muthanna (2002), who described the flow features captured by the oil flow. For both Figure 3.6a and Figure 3.6b, there are similar flow patterns on the endwall except a different origin of tip leakage vortices for 1.65% and 3.30% tip gaps. Obviously, the tip leakage vortex separation zone forms for each blade and shows spatially periodic flow. For the 3.30% case in Figure 3.6b, the film covers three complete blades, four tip separation zones, upstream three and half inches and downstream three inches and shows flow structures of the inflow and wake flow. Streamline patterns for each passage and blade show spatially periodic features. When the incoming flow approaches the blade, the flow is disturbed by the blade about two inches ahead of the blade row, and divides into two branches near the leading edge, one accelerates on the suction side and the other decelerates on the pressure side. Due to the tip gap, the near wall flow is not divided by the blade. Thus, the flow on the pressure side tends to be sucked into the suction side of the blade. The streamlines underneath the blade show that the crossflow near the wall is about perpendicular to the streamline of the primary flow. The dark region under the blade shows the strong shear flow. White powder accumulation shows low momentum fluid piled up around the separation and low velocity zone.

On the pressure side in Figure 3.6b, a reattachment line shows the flow moves inward the endwall and divides into two branches: one turns 90 degrees progressively and goes below the tip gap from the pressure side to the suction side and the other moves toward the separation zone in the passage. From the onset of the reattachment line in the pressure side, a shear layer forms over the tip gap on the endwall till the separation line in the suction side. Around the trailing edge of the blade, surface streamline directions appear divergent, implying that the tip leakage vortex spirals and interacts with the wake

of the blade. The band of the separation and the breakup of streaks show the unsteady tip separation vortex because of the interaction between the primary flow and the tip leakage vortex development throughout the passage as well as the interaction of the tip leakage vortex and the wake of blades in the downstream.

### 3.4.2 Blade Surfaces

For the blade surface, a similar technique can be used but contact film can be attached on the blade surface first. Due to gravitational effects on an oil mixture, a relative dry mixture of ratio 35:15:1 was used to obtain Figure 3.7 for the 1.65% and Figure 3.8 for the 3.30% tip gaps.

On the pressure side, most of the streamlines are parallel to the blade tip except the trailing edge, which bend down due to the gravitational effects. Near the blade tip within 2% of the blade span, the streamlines change their directions and sharply turn into the tip end. The region is affected by the tip leakage flow.

On the suction side, oil flow visualization is very complex and hard to explain. Again, most of the blade shows a two-dimensional boundary layer and some gravity effect. Since the flow is separated near the trailing edge, the gravitational effect is stronger than on pressure side. The influenced area is bigger than on the pressure side because of the tip leakage vortex and confluence of tip leakage flow and primary flow. Curved streamlines around mid chord of the blade show the attachment of the tip leakage vortex. White powder accumulates on the suction side above the blade tip, showing low momentum fluid. There is a dark line inclined to the blade tip end about  $2^\circ \sim 4^\circ$ , which is a big difference from the inclined angle of  $12^\circ$  by the reattachment of tip leakage vortex observed by Lakshminarayana and Horlock (1967). This may be scoured by the second

tip separation vortex around the suction side corner of the blade tip end. Flow around the blade tip corner near the suction side is very complex, such as the boundary layer on the suction side, a dominated tip leakage vortex, and possible small multiple discrete vortices. The full understanding needs further measurements of surface pressure and velocity profiles in this region.

## 3.5 Surface Pressure Measurements

The tip gap flow of interest is basically a pressure-driven flow so pressure loading of the blade is a very important factor to determine the performance of a compressor cascade. The endwall static pressure distribution is very useful information to understand the tip gap flow. A Scanivalve with pressure transducers is used to measure the  $C_p$  coefficient of static pressure.

### 3.5.1 Blade Pressure Loading

The pressure taps were inserted at midspan of the pressure side and suction side in two different blades. The midspan pressure distributions represent the generic flow condition because the flow is spatially periodic. The specific locations were measured by Muthanna (2002). For both tip gaps, the midspan distributions are presented in Figure 3.11. It is also a cross-check of the tunnel calibration discussed in Section 3.2.1. Figure 3.9 shows results of both 1.65% and 3.30% tip gaps. The blade loading or pressure difference between the pressure side and the suction side is illustrated in Figure 3.12.

All experiments done in the low-speed linear cascade wind tunnel at Virginia Tech by Ma (2003), Muthanna (2002), Kuhl (2001), and Wang (2000) show very good agreement

so that the flow is very repeatable. From the plots, the mid-span pressure distribution is like an airfoil. The  $C_p$  spikes near the leading edge on both pressure side and suction side show the effect of two trips on the pressure side and suction side, respectively.

### 3.5.2 Endwall Static Pressure Distribution

Pressure gradients near the wall are very important because they produce a strong shear layer. The pressure measurements utilized the endwall window opening for the LDV access. A pressure plate with 247 tubes was used to obtain the full endwall pressure distribution in the two different window locations. The consistency of pressure data measured twice proved that the variations of the tip gap height along the blade chord were within the tolerance of the repeatable flow conditions. The specific procedure is described by Tian (2003). Figure 3.10a and Figure 3.10b present the contour plot of static pressure distribution with tip gap 1.65% and 3.30%, respectively.

For both tip gaps, the pressure distribution patterns are similar as shown in Figure 3.10. A low pressure trough on the suction side is associated with the tip leakage vortex. The contour lines were distorted after the trough. A peak line to the left of the trough denotes the separation line of the tip leakage vortex and a valley reflects the center of the tip leakage vortex. The distorted contour lines of isobar means less compression of the flow around the tip gap than its counterpart of the midspan blade. The trough that extended into the gap indicates that the head of tip leakage vortex starts from the tip gap. For 1.65%, onset of the dip begins at chord ratio 0.12 and ends at 0.42. The trough shape is fork-like. Minimum  $C_p$  is -0.5 and maximum one is 0.45. For 3.30%, the  $C_p$  at the onset of trough is 0.40 and ends up with 0.65 at the tail of the trough. The trough shape for 3.30% is elliptic-like and different with the case of 1.65%. The minimum  $C_p$  is

-0.45 and the maximum one is 0.5.

By analogy to the midspan, the line distributions of pressure on the pressure and suction sides are extracted in Figure 3.11 from the projecting of blade configuration locations on the endwall. Obviously, the distributions onto the endwall are totally different from the midspan for both 1.65% and 3.30% tip gaps. On the pressure side, the pressure is negative at some mid chord for the 3.30% tip gap. The minimum pressure on the suction side occurs at  $x/c = 0.3$  for the 1.65% and at  $x/c = 0.5$  for the 3.30% because of influence from different origins of the tip leakage vortex. Figure 3.12 shows the pressure difference on the endwall between the pressure side and the suction side along the projected locations of blade configuration. The maximum pressure difference occurs at  $x/c = 0.38$  for the 1.65% and at  $x/c = 0.54$  for the 3.30%.

The pressure gradients are strong under the tip gap and the directions are almost perpendicular to the camber line. The pressure gradients can be extracted from the static pressure distribution. Since the data have irregular locations, a quadric surface method was used for this purpose. The detailed method is given in Appendix D.

In Figure 3.13, pressure gradients ( $\partial C_p/\partial x$ ,  $\partial C_p/\partial z$ ) are strong in the gap and almost zero in the mid passage along  $x/c_a = 0.18$  for 1.65% tip gap and  $x/c_a = 0.42$  for 3.30% tip gap in the bed coordinate system. The effect of pressure gradients on  $U_\tau$  was used for corrected values described in Section 3.6.2.

## 3.6 LDV Measurements

An LDV measurement is an instantaneous velocity vector at a point. To obtain good statistical turbulent properties of the measured flow, 30,000 samples are taken at a specific

point. Multiple points are chosen to form a velocity profile in a preset test matrix. Post data processing software is used to remove the noise and to compute 19 statistical quantities: three mean velocity components ( $U$ ,  $V$ , and  $W$ ), six Reynolds stresses (normal stress  $\overline{u^2}$ ,  $\overline{v^2}$ , and  $\overline{w^2}$  and shear stress  $-\overline{uv}$ ,  $-\overline{vw}$ , and  $-\overline{uw}$ ), and ten triple products ( $\overline{u^3}$ ,  $\overline{v^3}$ ,  $\overline{w^3}$ ,  $\overline{u^2v}$ ,  $\overline{uv^2}$ ,  $\overline{u^2w}$ ,  $\overline{uw^2}$ ,  $\overline{v^2w}$ ,  $\overline{vw^2}$ , and  $\overline{uvw}$ ), which are valuable in the discussion of the flow structures described later in Section 3.7. Although many adjustments and corrections require much time to obtain LDV data, it is a validate tool used to get data near the boundary. Even in this case, a careful plan is necessary to efficiently obtain enough data for capturing the flow features of interest.

As discussed in Section 3.1, different coordinate systems are used in this study for either convenient descriptions or physical meaning. The locations of the test matrix are addressed in the bed coordinate system. The beam angles of the LDV measurement volume were measured in the bed coordinate system. Measurements were directly taken in the bed coordinate system. Since the LDV calibration revealed the misalignment between the known flow velocity and the measured velocity in Section 3.2.2, a coordinate transformation is necessary to correct this discrepancy. The rotation angles from the LDV calibration are applied to all LDV profiles of the stationary wall case in this study. After the coordinate transformation, update LDV data are ultimately tabulated in the bed coordinate system. Because the tip gap flow is a pressure-driven flow crossing the gap in a normal direction to the blade chord line, the LDV data are used to understand the flow mechanism mainly in the chord coordinate system.

### 3.6.1 Test Matrix

Due to the difficulty and inefficiency of LDV measurements, only limited data can be taken for the flow of interest in the compressor cascade wind tunnel. Most of the critical flow features are around the leading region of a compressor blade row, as observed from the oil flow visualization, so that the selected axial logarithmic spacing of measurements was based on an intuitive guess. The results proved it to be a good choice.

In the bed coordinate system as shown in Figure 3.4, data were taken in ten cross section planes of the chord ratio,  $x/c_a$ : -0.33, 0, 0.04, 0.09, 0.12, 0.18, 1.27, 0.42, 0.65, and 1.00. Here  $x$  is the x-coordinate and  $c_a$  is the axial chord length of the blade. For each chord ratio, multiple profiles were measured under the blade tip in the gap along the  $z$  axis. Among them, “p”, “c”, and “s” represent the pressure side, camber line, and suction side. From the data of Kuhl (2001), the flow turning angle changes substantially from the pressure side to the camber line so that one extra profile is necessarily taken to understand the flow completely. Since the flow passes through the gap from the pressure side, profile “u” is taken as a baseline to evaluate the flow development since the local upstream is close to the pressure side. In the leading edge and trailing edge of the blade, the thickness of the blade is small so that one extra profile d is taken to get more information. Profile c1 is at the same location as the hot wire measurements of Muthanna (2002).

Table 3.4 and Table 3.5 give the detailed coordinates in the bed coordinate system for the 1.65% and 3.30% tip gaps. Figure 3.4a and Figure 3.4b show locations in the test section. For 1.65% and 3.30%, three profiles uu, ub, and ud were obtained at  $x/c_a = -0.33$  as inflow to the compressor cascade. Three profiles c1, 1u, 1b, and 1d were obtained at  $x/c_a = 0.00$ ; At  $x/c_a = 0.04$  four profiles 2u, 2p, 2c, and 2s were also

acquired; Five profiles u, p, b, c, and s were taken for  $x/c_a=0.09, 0.12, 0.18, 0.27, 0.42$ , and  $0.65$ . At the last  $x/c_a = 1.00$ , five profiles were obtaining 9u, 9p, 9c, 9s, and 9d. Besides, more profiles were taken for the separation region in the passage. For 1.65%, three profiles e1, e2, e3 were measured at  $x/c_a = 0.18$ ; For 3.30%, five profiles x1, x2, x3, x4, x5 were taken at  $x/c_a = 0.42$ . To compare with 1.65%, two profiles e1 and e2 were measured for 3.30% at the same location as that of 1.65%.

For all profiles along the normal wall distance y, there are 20 to 26 points upward from the endwall. These points are logarithmically spaced, starting from  $30\ \mu\text{m}$  off the endwall. The ending point is about at the gap height in the gap and range 1 cm to 3 cm depending on access constraints of the LDV head. Due to the wall uncertainty, a  $y_{shift}$  correction was calculated (see Appendix C) to finalize all LDV data profiles in the following section.

### 3.6.2 Skin Friction Velocity

In order to get accurate measurement profiles, the wall position and  $U_\tau$  must be calculated from viscous sublayer data to complete the profile data. For this flow, flow angles are about the same in the viscous sublayer so that it is a collateral flow in the viscous sublayer. The velocity equation for the viscous sublayer is derived by analogy to the two-dimensional turbulent boundary layer in Appendix C. The least square curve-fitting necessary to do this is described in Appendix D. In order to do so, at least five points or more are available in the viscous sublayer. The viscous sublayer is in the region  $y^+ < 10$ . From Figure 3.20,  $\overline{v^2}$  does not change so that in the viscous sublayer, it is proper to assume that the spanwise pressure gradient is zero from Equation 3.1. Also, the pitchwise pressure gradient is very big so that pressure gradient correction is necessary to calculate



$U_\tau$ . The pressure gradients at the locations of all LDV profiles were calculated using a quadric surface fitting in Appendix D and are listed in Table 3.6 and Table 3.7.

$$\frac{\partial P}{\partial y} = -\rho \frac{\partial \bar{v}^2}{\partial y} \quad (3.1)$$

The following velocity of the collateral or constant flow angle direction flow in the viscous sublayer was derived in Appendix C.

$$Q = C_1 y + \frac{\vec{\nabla} P \cdot \vec{t}}{2\mu} y^2 + C_2 y^4 \quad (3.2)$$

where  $Q = \sqrt{U^2 + W^2}$ ,  $y = y_{shift} + y_{measured}$ ,  $\vec{\nabla} P$  is the endwall pressure gradient in Section 3.5.2, and  $\vec{t}$  is a unit vector of  $Q$ . Then  $C_1$  and  $C_2$  are obtained using the iteratively optimized procedure introduced in Appendix C. Then  $C_1$  was determined for  $U_\tau$ . By definition,

$$U_\tau^2 = \nu \frac{\partial U}{\partial y} \Big|_{wall} \quad (3.3)$$

The derivative of Equation 3.2 evaluated at the wall produces

$$U_\tau = \sqrt{\frac{C_1}{\nu}} \quad (3.4)$$

So that the actual  $y$  location must include a  $y$  shift because the wall location can not be accurately found by the wall finding procedure in Section 2.3.6. The magnitudes of  $U_\tau$  are in Table 3.8 and Table 3.9 but its vectors are in the Figure 3.14a and Figure 3.14b.

### 3.6.3 Mean Velocity Vector

Three components  $U$ ,  $V$ , and  $W$  of the mean velocity vector in the bed coordinate system were obtained from the ensemble data sampled at the same point of interest. As described in Section 3.6.2, the nearest wall data were first used to evaluate  $U_\tau$  and  $y_{shift}$ . They also were used to calculate the flow angle and circulation. Their gradients were used to compute flow gradient angle, vorticity, and turbulence production. The measured and derived mean quantities can be used to explain the mean flow structures along with the oil flow visualization and pressure data.

Figure 3.15 describe typical three mean velocity components ( $U$ ,  $V$ , and  $W$ ) as a function of corrected wall distance  $y$  and three non-dimensional velocity components ( $U/U_\tau$ ,  $V/U_\tau$ , and  $W/U_\tau$ ) as a function of  $y^+$  at the same chord ratio  $x/c_a = 0.42$  for tip gaps 3.30% in the chord coordinate system. By comparison of Figure 3.15a and 3.15b, Figures 3.15c and 3.15d, and Figure 3.15e and 3.15f, normalized quantities are different with original ones because of different  $U_\tau$  at different profiles so that the original data were scaled by different factors. The dimensionless data do not collapse so that the flow is neither simply a two-dimensional flow nor an equilibrium flow. Thus, in order to observe how the mean velocity varies at different locations, a free-stream velocity  $U_{ref}$  is used to non-dimensionalized the mean velocity components, while  $y^+$  on a log scale is not affected much by the  $U_\tau$  variation.

Figures 3.16, 3.17, and 3.18 are plots of mean velocity  $U/U_{ref}$ ,  $V/U_{ref}$ , and  $W/U_{ref}$  respectively, for both 1.65% and 3.30% in the chord coordinate system at locations shown in Figure 3.4. In each plot, results at  $x/c_a = 0.18$ , their local gap inflow, and suction side were presented. The following explains key features of the results in the above plots. The velocity plots of all profiles are available in Appendix E.

### Mean U

Generally speaking in Figures 3.16a and 3.16b, the chordwise  $U/U_{ref}$  of any profile increases monotonically with  $y^+$  for both tip gaps. For 1.65%, the mean  $U/U_{ref}$  profiles in Figure 3.16a collapse for  $10 < y^+ < 60$  for profiles 5u, 5p, 5b, 5c, and 5s from the pressure side to the suction side. Profiles at locations e1, e2, and e3 are above the five profiles. No apparent semi-log regions exists for the mean  $U/U_{ref}$  in all eight profiles. The  $U/U_{ref}$  increases slowly near the blade tip around  $y^+ = 250$ , where the magnitude of  $V/U_{ref}$  for e1 and e2 become large but the magnitude of mean  $W/U_{ref}$  decreases. This implies that profiles e1 and e3 are in the spiral vortex region. For the 3.30% case, the mean  $U/U_{ref}$  in Figure 3.16b has two subgroups, five profiles in the gap and two profiles in the suction side of the passage. Five profiles (5u to 5s) have a collapsed semi-log region with  $25 < y^+ < 200$ , but the  $U/U_{ref}$  are quite different near the endwall and blade tip. The two profiles e1 and e2 on the suction side are quite different and have a smaller slope near the endwall at  $y^+ < 160$  and a larger slope near the blade tip at  $y^+ > 200$  than the five profiles in the passage.

The  $U/U_{ref}$  of profile uu upstream of the blade (Figure 3.16c) demonstrates the characteristics of a two-dimensional boundary layer: a viscous sublayer, a semi-log region, and an outer layer are clearly recognized. The  $U/U_{ref}$  of the other profiles have some similarity with a recognizable semi-log region and a local free-stream region in the potential core of passage flow, but with different ranges of  $y^+$  and slopes. For the 1.65% case in Figure 3.16c, the  $U/U_{ref}$  on the pressure side decreases from profile uu to profile 6u and increases back from profile 6u to profile 9u because the minimum endwall pressure in Figure 3.11 occurs at  $x/c = 0.3$  along the pressure side in the chord coordinate system. The linear slopes of the semi-log region ( $18 < y^+ < 100$ ) are very close for all profiles. For the 3.30%, there are obvious semi-log regions in all profiles except profile 7u

in Figure 3.16d. The  $U/U_{ref}$  decreases from profile uu to profile 7u and increases back from profile 7u to profile 9u because the minimum endwall pressure shown in Figure 3.11 occurs at  $x/c = 0.45$  along the pressure side in the chord coordinate system. The linear slope of all profiles but profiles 7u, 8u, and 9u in their semi-log region ( $30 < y^+ < 170$ ) are nearly the same.

On the suction side, the  $U/U_{ref}$  changes from the leading edge to the trailing edge are similar to the local pressure side discussed above. However,  $U/U_{ref}$  for most profiles has a peak for both 1.65% and 3.30% cases; the peak location appears to decrease from upstream to downstream. In Figure 3.16e for 1.65%, there is barely a semi-log region for any profile. On the other hand, there is a short semi-log region ( $35 < y^+ < 107$ ) only for 2s, 3s, and 4s in Figure 3.16f for 3.30%.

### Mean V

For profiles inside the blade tip gap shown in Figures 3.17a and b, the magnitude of  $V$  at profiles 5b, 5c, and 5s increases slowly from the endwall to the mid gap but then changes significantly and reaches a peak near the blade tip. From profile 5u to 5s, the sign of  $V$  changes from negative to positive in general because the flow moves down and then up relative to the endwall from the pressure side to the suction side of the blade. The peaks imply the presence of vortical flow zone between profile 5p and 5s. The maximum peak value of  $V/U_{ref}$  is nearly 0.4 so that the flow can not be simplified as a boundary layer around this region. For the 1.65% case in Figure 3.17a, the sign of  $V/U_{ref}$  becomes positive in profile 5b just under the blade tip. For 3.30%, the sign of  $V/U_{ref}$  in Figure 3.17b becomes positive in profile 5c. These data suggest that the location of the tip separation vortex shifts with different tip gaps. The maximum absolute  $V/U_{ref}$  at profile 5u is smaller at 3.30% than at 1.65%. On the other hand, the maximum absolute

$V/U_{ref}$  of profile 5c and 5s are bigger at 3.30% than at 1.65%, indicating a significant effect of tip gap, which will be discussed later.

For the local gap inflow, the distribution of  $V/U_{ref}$  along  $y$  is similar for all profiles of the two tip gaps. The negative peak of  $V/U_{ref}$  changes along the chord and the peak location is proportional to the absolute  $V/U_{ref}$ . For 1.65% in Figure 3.17c, the maximum peak  $V/U_{ref}$  takes place at profile 6u. For 3.30%, the maximum peak  $V/U_{ref}$  takes place at profile 7u in Figure 3.17d.

On the suction side, the  $V/U_{ref}$  in Figure 3.17e and Figure 3.17f is similar for the two tip gaps. However, the maximum magnitude of  $V/U_{ref}$  is smaller for 1.65% than for 3.30%. The  $V/U_{ref}$  is positive compared to the pressure side because the flow is more upward after leaving the tip gap. The global maximum magnitude of  $V/U_{ref}$  occurs at profile 5s for 1.65% and profile 7s for 3.30%. The oscillatory shape of  $V/U_{ref}$  versus  $y$  from profile 6s to 8s indicates the vortical flow zone near the blade tip.

### Mean W

For any given profile, the shape of  $W/U_{ref}$  in the chord coordinate system is bell-like with a flat top corresponding to the mid gap. The  $W/U_{ref}$  has a smooth corner from the endwall to the mid gap but a sharp corner from the mid gap to the blade tip, even with a spike at some profiles in the tip separation vortex. For 1.65%, the corresponding mean  $W/U_{ref}$  in Figure 3.18a reaches a plateau between  $20 < y^+ < 350$  whose width becomes slightly smaller from the pressure side to the suction side. For 3.30%, there are lower magnitudes of the  $W/U_{ref}$  plateau between  $30 < y^+ < 500$  at the same locations corresponding with the 1.65% case, as shown by profiles in Figure 3.18b. A peak exists for profiles 5b and 5c.

For the local gap inflow, Figure 3.18c and d show the cross-flow velocity distribution in the chord coordinate system. From the upstream to the downstream, the maximum magnitude of the peak plateau of  $W/U_{ref}$  happens at profile 6u for 1.65% and profile 7u for 3.30% associated with the different locations of the minimum endwall pressure for both 1.65% and 3.30% tip gaps as shown in Figure 3.11. The minimum endwall pressure occurred at the immediate downstream of the beginning of the tip leakage vortex. The  $W/U_{ref}$  of profile 9u near the trailing edge is positive for 1.65% but negative for 3.30%. For 3.30%, the magnitude of  $W/U_{ref}$  in Figure 3.18d is also smaller than that of 1.65% for corresponding locations.

On the suction side, the  $W/U_{ref}$  is similar to the pressure side with a peak next to the blade tip for 3.30% in Figure 3.18f. However, the absolute  $W/U_{ref}$  is much bigger than on the pressure side. The plateau width of 3.30% is wider than that of the 1.65% case.

### 3.6.4 Reynolds Stress Tensor

The Reynolds stress tensor  $\overline{u_i u_j}$  is a second order tensor, consisting of 9 quantities. Due to symmetry of cross-product quantities, the number of members in  $\overline{u_i u_j}$  reduces to six quantities, normal stresses  $\overline{u^2}$ ,  $\overline{v^2}$ , and  $\overline{w^2}$  and shear stress  $-\overline{uv}$ ,  $-\overline{vw}$ , and  $-\overline{uw}$ , which are second moments extracted from the measured instantaneous velocity vector using an ensemble-averaged method. Reynolds stresses can be used to validate turbulence models for any CFD effort. Three normal stresses, representing the velocity fluctuations, are used to compute an important quantity, the turbulent kinetic energy (TKE), which is often modelled for a turbulent flow.

The three shear stresses appearing in the momentum equations need to be modelled

for closure. They also are used to examine the flow structures through an octant analysis detailed in Madden and Simpson (1997), which separates the measurements into octants of the three-fluctuation-velocity-component velocity space. This technique separates the flow events into ejections, sweeps and interactions depending upon the signs of the velocities in that particular octant. The results of the octant analysis for these tip gap flows were presented by in Tian (2003).

A typical method of checking the LDV calibration is by measuring a known two-dimensional flow. After properly aligning the beam crossing of the measurement volume, there is reasonably time coincident data (within  $10 \mu S$ ) for each of the three velocity components. The correlation coefficient of  $\overline{uv}$ ,  $\overline{uv}/u'v'$ , is an important parameter used to check the measurement of beam angles and the coincidence of data from the same particle. If the measured correlation coefficient of  $\overline{uv}/u'v'$  is larger than 0.4, the measured beam angles represent the actual orientation of coincident measurement volumes of a LDV. At lower correlation coefficients, the measurement of beam angles may not be accurate and measurement volumes may not be coincident, so that it leads to the inaccurate LDV measurements.

Figures 3.19 through 3.24, and 3.23 are plots of Reynolds-averaged stresses  $\overline{u^2}/U_{ref}^2$ ,  $\overline{v^2}/U_{ref}^2$ ,  $\overline{w^2}/U_{ref}^2$ ,  $-\overline{uv}/U_{ref}^2$ ,  $-\overline{vw}/U_{ref}^2$ , and  $-\overline{uw}/U_{ref}^2$  respectively, for both 1.65% and 3.30% in the chord coordinate system. For each quantity, results at  $x/c_a = 0.18$ , the local gap inflow, and the suction side are presented. The following paragraphs explain the key features of the results in these plots. The Reynolds stresses plots of all profiles are available in Appendix F.

$\overline{u^2}$

Figures 3.19a and 3.19b describe the normal stress  $\overline{u^2}/U_{ref}^2$  at  $x/c_a = 0.18$  for both 1.65% and 3.30% tip gap cases in the chord coordinate system. For the profiles outside the tip gap, Reynolds normal stresses have a peak in the inner layer like a regular two-dimensional boundary layer. However, two peaks can be visibly identified near the endwall and the blade tip inside the tip gap. After the first peak,  $\overline{u^2}/U_{ref}^2$  drops with increasing  $y^+$  because of the potential core; after reaching a local minimum, it jumps up suddenly near the tip because of the tip separation vortex. The magnitudes of  $\overline{u^2}/U_{ref}^2$  near the endwall increase from the pressure side to the suction side due to the interaction with the primary flow. Near the blade tip, the magnitude of  $\overline{u^2}/U_{ref}^2$  is 5 times higher than that the maximum of  $\overline{u^2}/U_{ref}^2$  in the inner region due to the presence of mixing in the tip separation vortex and possible vibration of the blade. The peak positions near the blade tip are different in the plots because of different  $U_\tau$  values at different profiles. The  $\overline{u^2}/U_{ref}^2$  of the 3.30% case is slightly less than that for the 1.65% case because the tip leakage flow is weaker for the larger gap.

In Figure 3.19a for 1.65%, the peak value of  $\overline{u^2}$  is less than that of inflow profile  $uu$  and its location shifts from  $y^+ = 15$  to  $y^+ = 30$  for profiles 5u to 5s and further to about 40 for profiles e1 to e3 in the passage. The peak near the blade tip ( $y^+ = 300 \sim 500$ ) is about 4 times that of the near endwall in the gap. In Figure 3.19b for 3.30%, the peak of  $\overline{u^2}$  is less than that of inflow  $uu$  and its location shifts from  $y^+ = 15$  to  $y^+ = 22$  for profiles 5u to 5s and further up to  $y^+ = 35$  at profile e1 and  $y^+ = 50$  at profile e2 because the boundary layer thickness near the endwall increases from the pressure side to the suction side. The peak near the blade tip (300  $\mu m$  away from the tip surface) is less than that of 1.65%. The second peak for profiles e1 and e2 is much smaller than the peak near the endwall because the tip leakage flow lines up with the primary flow.



For the local gap inflow in Figure 3.19c and 3.19d, most profiles tend to have just one peak near the endwall because of no blade tip constraints. However, The  $\overline{u^2}/U_{ref}^2$  tends to be nearly constant between  $20 < y^+ < 200$  from profiles c1 to 6u at the 1.65% tip gap and  $50 < y^+ < 150$  for all profiles at the 3.30% tip gap. The peak and its location changes as flow travels from the upstream to the downstream. The maximum of  $\overline{u^2}/U_{ref}^2$  is 0.014 at profile 8u for 1.65% and 0.015 at profile 9u for 3.30%. At profile c1, the two peaks exist for the 1.65% but just one for 3.30% tip gap. The second peak away from the endwall may be caused by the passage vortex for the 1.65% case.

In Figures 3.19e and 3.19f, the  $\overline{u^2}/U_{ref}^2$  has two peaks for all profiles on the suction side because the profiles are located at the exit of the gap and have two wall shear layers of near the endwall and blade tip. The peak value near the endwall decreases from the leading edge to profile 4s at  $x/c_a = 0.12$  and then increases from profile 4s to the trailing edge of the blade.

$\overline{v^2}$

Figures 3.20a and 3.20b describe  $\overline{v^2}/U_{ref}^2$  at  $x/c_a = 0.18$  for both 1.65% and 3.30% in the chord coordinate system. Near the endwall,  $\overline{v^2}/U_{ref}^2$  in the gap remains unchanged except close to the blade tip. Near the blade tip, the maximum peak  $\overline{v^2}/U_{ref}^2$  is much larger. For profiles e1, e2, and e3 at 1.65% in Figure 3.20a,  $\overline{v^2}$  increases continuously from the endwall and reaches a peak at  $y^+ > 230$ , where there is likely to be a vortex. A peak occurs at profile e1 and e2 for 3.30% in Figure 3.20b. Profiles e1 and e2 are outside of the gap on the suction side of the blade.

For the local gap inflow in Figures 3.20c and 3.20d,  $\overline{v^2}/U_{ref}^2$  is quite small relative to  $\overline{u^2}/U_{ref}^2$  in the same profile. The peak  $\overline{v^2}/U_{ref}^2$  of profile uu is smallest for 1.65%. The

maximum peak  $\overline{v^2}/U_{ref}^2$  occurs at profile 7u or 8u for 1.65% and at profile 9u for 3.30%. The peak location is  $y^+ = 103 \pm 10$  for 1.65% and  $y^+ = 200 \pm 100$  for 3.30%.

For the suction side in Figures 3.20e and 3.20f, the maximum  $\overline{v^2}/U_{ref}^2$  is near the blade tip and increases dramatically from profile 5s to profile 9s. The highest peak at profile 8s is 8 times higher for 1.65% and 11 times higher for 3.30% than that of the inflow at profile uu.

$\overline{w^2}$

Figures 3.21a and 3.21b describe  $\overline{w^2}/U_{ref}^2$  at  $x/c_a = 0.18$  for both 1.65% and 3.30% in the chord coordinate system. For  $\overline{w^2}/U_{ref}^2$  in the gap, the 1.65% and 3.30% results are similar. However, outside the gap in the passage,  $\overline{w^2}/U_{ref}^2$  of the 1.65% case is two and half times of the 3.30% case near the endwall. The peak of  $\overline{w^2}/U_{ref}^2$  near the endwall increases from the pressure side to the suction side; and the peak location increases as well. Near the blade tip, the maximum peak  $\overline{w^2}/U_{ref}^2$  is bigger than the first peak near the endwall. However, the ratio of the two peak values is smaller than that for  $\overline{u^2}/U_{ref}^2$ . For profiles away from the suction side, the second to first peak value ratio is less than one.

For the local gap inflow in Figures 3.21c and 3.21d,  $\overline{w^2}/U_{ref}^2$  profiles are clustered except profile c1 for 1.65% and profile 9u for 3.30%. The peak value is  $\pm 0.0008$  around profile uu. The peak location is  $y^+ = 9$  to 40 for 1.65% and  $y^+ = 10$  to 30 for 3.30%. The peak position decreases from upstream to downstream locations.

For the suction side in Figures 3.21e and 3.21f,  $\overline{w^2}/U_{ref}^2$  has two peaks: a weak one near the endwall and strong one near the blade tip. The peak magnitude ratio is 2 for 1.65% and 5 for 3.30%.

$-\overline{uv}$

Figures 3.22a and 3.22b describe typical shear stresses  $-\overline{uv}/U_{ref}^2$  at  $x/c_a = 0.18$  for both 1.65% and 3.30% in the chord coordinate system. In the gap, the shear stress profiles show similar shapes. However, outside the gap, features are different for the two gaps. For 1.65%, the magnitude of  $\overline{uv}/U_{ref}^2$  at profiles e1, e2, and e3 change dramatically in Figure 3.22a. The magnitude in Figure 3.22b stays the same as in the gap. The sign changes near the blade tip.

On the local gap inflow shown in Figures 3.22c and 3.22d, the peak  $-\overline{uv}/U_{ref}^2$  occurs at  $y^+ \sim 100$  for 1.65% and at  $y^+ \sim 200$  for 3.30%. Profile uu is the lower bound of  $\overline{uv}/U_{ref}^2$  at  $y^+ < 50$  for both 1.65% and 3.30% tip gaps. For the suction side in Figures 3.22e and 3.22f, profile uu is the lower bound for all profiles except 7s and 8s near the blade tip for 3.30%. The sign changes near the blade tip because of the boundary layer there.

$-\overline{vw}$

Figures 3.23a and 3.23b describe shear stress  $-\overline{vw}/U_{ref}^2$  profile at  $x/c_a = 0.18$  for both 1.65% and 3.30% in the chord coordinate system. In the gap, the shear stress profiles appear to be similar. But outside the gap, the features are different for the two gaps. For 1.65%, the magnitudes of  $\overline{vw}/U_{ref}^2$  at profiles e1, e2, and e3 change dramatically in Figure 3.23a. The magnitudes in Figure 3.23b are about the same as in the gap.

On the local gap inflow with Figures 3.23c and 3.23d, the magnitude of  $\overline{vw}/U_{ref}^2$  is very small except near the blade tip. It is nearly zero at profile uu. This is because flow at these locations has not been influenced much by the gap.

For the suction side in Figures 3.23e and 3.23f,  $-\overline{vw}/U_{ref}^2$  changes sharply downstream

from profile 4s at  $x/c_a = 0.12$  to profile 9s at  $x/c_a = 1.00$  for the 1.65% and from profile 6s at  $x/c_a = 0.27$  to profile 9s at  $x/c_a = 1.00$  for the 3.30%. The sharp change is probably due to the formation of the tip leakage vortex at  $x/c_a = 0.16$  for the 1.65% and  $x/c_a = 0.36$  for the 3.30%.

$-\overline{uw}$

Figures 3.24a and 3.24b describe shear stress  $-\overline{uw}/U_{ref}^2$  at  $x/c_a = 0.18$  for both 1.65% and 3.30% cases in the chord coordinate system, which are typical of other planes. Considerable variations occur between the near endwall and blade tip. In the gap, shear stress profiles are similar. But outside the gap, features are different for the two gaps. For 1.65%, the magnitude of  $\overline{uw}/U_{ref}^2$  at profiles e1, e2, and e3 changes dramatically while for 3.30% is about the same as in the gap. The  $\overline{uw}$  changes sign and its magnitude is huge near the endwall in Figure 3.24b. The shear stresses  $\overline{uv}$ ,  $\overline{vw}$ , and  $\overline{uw}$  are the same order of magnitude at a given profile of 1.65% and 3.30% tip gaps. Thus, the flow is not a two-dimensional flow because  $\overline{uw}$  is not negligible.

On the local gap inflow with Figures 3.24c and 3.24d,  $\overline{uw}/U_{ref}^2$  above  $y^+ > 40$  for 3.30% is more clustered than for 1.65%. Near the endwall,  $\overline{uw}$  basically decreases from profile uu at  $x/c_a = -0.33$  to profile 9u at  $x/c_a = 1.0$ .

For the suction side in Figures 3.24e and 3.24f,  $\overline{uw}/U_{ref}^2$  near the endwall and the blade tip data show more variation than upstream. The magnitude at the edge of the viscous sublayer is much bigger than that of  $\overline{uv}/U_{ref}^2$  and  $\overline{vw}/U_{ref}^2$ .

### 3.6.5 Triple Product Tensor

Triple products tensor  $\overline{u_i u_j u_k}$  is a third order tensor, in which total members are 27, consisting of ten quantities based on the symmetry of cross-product items:  $\overline{u^3}$ ,  $\overline{v^3}$ ,  $\overline{w^3}$ ,  $\overline{u^2 v}$ ,  $\overline{uv^2}$ ,  $\overline{u^2 w}$ ,  $\overline{uw^2}$ ,  $\overline{v^2 w}$ ,  $\overline{vw^2}$ , and  $\overline{uvw}$ , which are the third moments calculated from the LDV measurements. The tensor can be used to help validate the second order turbulence models for CFD effort. Among ten triple products,  $\overline{uv^2}$ ,  $\overline{v^3}$ , and  $\overline{v^2 w}$  are in the Reynolds stresses transport equations of three dimensional turbulent boundary layer. The triple products plots of all profiles are available in Appendix G.

Again, similar to the discussion of mean velocities and Reynolds stresses, Figures 3.25, 3.26, and 3.27 are plots of Reynolds averaged  $\overline{uv^2}/U_{ref}^3$ ,  $\overline{v^3}/U_{ref}^3$ , and  $\overline{v^2 w}/U_{ref}^3$  respectively, for both 1.65% and 3.30% in the chord coordinate system. In each plot, results at  $x/c_a = 0.18$ , the local gap inflow, and the suction side were presented. The key features of the results in the plots are interpreted as follows.

$$\overline{uv^2}$$

Figures 3.25a and 3.25b describe  $\overline{uv^2}/U_{ref}^3$  at  $x/c_a = 0.18$  for both 1.65% and 3.30% in the chord coordinate system, which are typical results for all different chord ratios. For profiles 5u to 5s, it is small from near the wall up to  $y^+ < 200$  for 1.65% and  $y^+ < 400$  for 3.30%. In the mid gap region,  $\overline{uv^2}/U_{ref}^3$  is negative, indicating dominance of the negative fluctuating velocity  $u'$ . But  $\overline{uv^2}/U_{ref}^3$  of a few points near the blade tip at profile 5b, 5c, and 5s is big and looks like outliers.

On the local gap inflow with Figures 3.25c and 3.25d, the magnitude of  $\overline{uv^2}/U_{ref}^3$  is very small except near the blade tip. The sign changes twice for 1.65% but just once for 3.30%. The  $\overline{uv^2}/U_{ref}^3$  tends to become more negative for all profiles with increasing wall

distance  $y$ .

For the suction side in Figures 3.25e and 3.25f, near wall  $\overline{uv^2}/U_{ref}^3$  is small for all profiles. The signs change near the blade tip but it seems to be more on the positive side.

$\overline{v^3}$

Figures 3.26a and 3.26b show  $\overline{v^3}/U_{ref}^3$  profiles at  $x/c_a = 0.18$  for both 1.65% and 3.30% in the chord coordinate system. The magnitudes near the blade tip at 1.65% are 50% bigger than those of 3.30% because of the stronger vortex separation for smaller tip gap. The magnitudes near the endwall are small for  $0 < y^+ < 200$ .

On the local gap inflow with Figures 3.26c and 3.26d for 1.65% and 3.30% tip gaps, the magnitudes of  $\overline{v^3}/U_{ref}^3$  are nearly zero when  $y^+ < 30$  because of the suppression of the endwall. From  $y^+ = 30$  to the end of profiles,  $\overline{v^3}/U_{ref}^3$  has oscillatory distributions. The sign of  $\overline{v^3}$  changes about  $y^+ = 200$  for 1.65% and  $y^+ = 130$  for 3.30%. The  $\overline{v^3}/U_{ref}^3$  is much bigger at profile 9u than the other profiles 1u - 8u because of the blade wake.

For the suction side in Figures 3.26e and 3.26f,  $\overline{v^3}/U_{ref}^3$  is nearly zero when  $y^+ < 20$  for all profiles of the two tip gaps. As flow travels from upstream to downstream, the absolute  $\overline{v^3}/U_{ref}^3$  increases significantly. So the instantaneous velocity  $v$  does not have a symmetric histogram and appears to be more skewed as the flow develops.

$\overline{v^2w}$

Figures 3.27a and 3.27b describe  $\overline{v^2w}/U_{ref}^3$  profiles at  $x/c_a = 0.18$  for both 1.65% and 3.30% in the chord coordinate system, which are typical for these flows. Their magnitude at 1.65% is 50% bigger than those of 3.30%. They are small from near the wall up to  $y^+ < 200$ . The  $\overline{v^2w}/U_{ref}^3$  near the blade tip has more variations than  $\overline{v^3}/U_{ref}^3$  in the

3.30% gap.

On the local gap inflow with Figures 3.27c and 3.27d, the magnitude of  $\overline{v^2 w}/U_{ref}^3$  is very small for all profiles at two tip gaps except profile 9u of 3.30%. For downstream profiles 5u to 9u,  $\overline{v^2 w}/U_{ref}^3$  changes its sign around  $y^+ = 100$  and looks antisymmetric about this point in this log plot.

For the suction side in Figures 3.27e and 3.27f,  $\overline{v^2 w}/U_{ref}^3$  of the near endwall changes sharply only from profile 6s to 9s. It increases at a lower position as flow moves from upstream to downstream.

### 3.6.6 Circulation, Vorticity, and Helicity

The tip gap flow is a pressure gradient driven flow. To characterize the formation and development of the tip leakage vortices, circulation and vorticity are very important parameters connected with the vortical flow structure. Helicity is a parameter to relate the vortical structure to the turbulent flow.

#### Circulation

A simple closed circuit was chosen for this purpose so that just two profiles were involved in the calculation in the bed coordinate system: one is the profile "p" on the pressure side; the other "s" is on the suction side. Making use of the physical boundaries of the endwall and blade tip surfaces to complete the circuit. According to the non-slip condition, the two solid surfaces do not contribute to the circulation contained in the gap. Circulation in the y-z plane was calculated for eight different chord ratios from  $x/c_a=0.04$  to  $x/c_a=1.00$  of the two tip gaps using a numerical integration around the

outer edge of the flow field,

$$\Gamma_x = \oint V ds = \int_p V dy - \int_s V dy \quad (3.5)$$

Since the tip leakage vortex is in a more streamwise direction and the circulation was calculated in the y-z plane in the bed coordinate system, the circulation does not relate to the tip leakage vortex directly. The tip leakage vortex is a result of the tip gap flow and streamwise flow impinging on one another. So circulation at each chord ratio reflects the vorticity contribution from different chord ratios. The circulation was normalized on the average free-stream velocity over all of the profiles and with the height of the tip gap ( $t=0.42\text{cm}$  for 1.65% or  $t=0.83\text{cm}$  for 3.30%). The normalized circulation ( $\Gamma_x/tU_{ref}$ ) values are shown in Figure 3.28. The plot shows that the normalized circulation is independent of the tip gap sizes. It suggests that the tip gap flow depends on the blade loading for smaller gap sizes. The mass flow rate may be proportion to the gap size.

Furthermore, two points in Figure 3.28 show the circulation of the tip leakage vortex in the y-z plane of the bed coordinate system, respectively, for 1.65% and 3.30% tip gaps. For 1.65%, the circuit includes the profiles e1 and e3, the endwall and the  $y=4\text{mm}$  plane. For 3.30%, the circuit consists of the profiles x1 and x5, the endwall and the  $y=8\text{mm}$  plane. The normalized circulation of tip leakage vortex is about two times the circulation at the same chord ratio in the gap.

### Vorticity

Vorticity is defined as the curl of the velocity vector,

$$\vec{\Omega} = \nabla \times \vec{V} \quad (3.6)$$



$$\Omega_x = \frac{\partial W}{\partial y} - \frac{\partial V}{\partial z} \approx \frac{\partial W}{\partial y} \quad (3.7)$$

$$\Omega_y = \frac{\partial U}{\partial z} - \frac{\partial W}{\partial x} \approx 0 \quad (3.8)$$

$$\Omega_z = \frac{\partial V}{\partial x} - \frac{\partial U}{\partial y} \approx -\frac{\partial U}{\partial y} \quad (3.9)$$

To estimate the vorticity, velocity gradients are relatively convenient to be calculated using the acquired data in the bed coordinate system. The y derivatives,  $\partial U/\partial y$  and  $\partial W/\partial y$ , are easily computed using a five point parabolic curve fit (see Appendix D). The z derivatives,  $\partial U/\partial z$  and  $\partial V/\partial z$ , were computed using a two-point finite difference method based on an interpolated points of a neighboring profile. For data available in this study, it is difficult to evaluate all x derivatives,  $\partial V/\partial x$  and  $\partial W/\partial x$ , for all profiles. Actually, only at  $x/c_a = 0.27$  can the x derivatives be roughly estimated because the neighboring data of  $x/c_a = 0.18$  can be used in calculating the x derivatives. Hence, the vorticity vector can be approximated from all derivatives necessary just at  $x/c_a = 0.27$  for both 1.65% and 3.30%. Since the y derivatives are much larger than the x and z derivatives, especially near the endwall, vorticity in the y direction is small relative to x and z vorticity and x and z vorticity is slightly different using all and just y derivatives. To estimate the vorticity in other planes, the approximations shown in equations 3.7, 3.8, and 3.9 are used.

From the normalized vorticity  $\Omega_x/tU_{ref}$ ,  $\Omega_z/tU_{ref}$ , and  $\Omega/tU_{ref}$  plots in different chord ratio of the bed coordinate system, a large region of positive vorticity is generated near the blade tip as the flow enters the gap. A thin zone of negative vorticity is bound to the endwall. The thickness of the two layers contains the vorticity generated in the leakage flow. A close comparison of two layers in Figure 3.29 shows that the thickness of the bounded vorticity layer increases from the pressure side to the suction side, indicating vorticity production. However, there is no vortex center found along the pressure side

corner of the blade. So there is no evidence of a recirculation zone in Figure 3.29. Vorticity contour plots show the positive vorticity in most parts of the gap and negative vorticity near the endwall and blade tip.

### Helicity Density

Helicity  $= \int \vec{V} \cdot \vec{\Omega} d(Vol)$  is an important feature of turbulent flow topology, which is constant if the helicity density  $h = \vec{V} \cdot \vec{\Omega}$  is integrated over the global domain of an inviscid Euler flow. However, the  $h$  mainly has large spatial variations if turbulent flow is far from equilibrium. Hussain (1986) stated that the  $h$  is connected with the dissipation for a vortical flow. From the trigonometric identity

$$\frac{|\vec{V} \cdot \vec{\Omega}|^2}{|\vec{V}|^2 |\vec{\Omega}|^2} + \frac{|\vec{V} \times \vec{\Omega}|^2}{|\vec{V}|^2 |\vec{\Omega}|^2} = 1 \quad (3.10)$$

and the Naiver-Stokes equation

$$\frac{\partial \vec{V}}{\partial t} + \vec{V} \times \vec{\Omega} = -\nabla \left( \frac{P}{\rho} + \frac{V^2}{2} \right) + \nu \nabla^2 \vec{V} \quad (3.11)$$

Normalized density  $\hat{h}$  and  $\bar{h}$  are defined as follows

$$\hat{h} = \frac{\vec{V} \cdot \vec{\Omega}}{|\vec{V}| |\vec{\Omega}|} \quad (3.12)$$

$$\bar{h} = \frac{\vec{V} \cdot \vec{\Omega}}{U_{ref}/t} \quad (3.13)$$

Wherever  $\hat{h}$  is large, the  $\vec{V} \times \vec{\Omega}$  is small based on equation 3.10. The  $\vec{V} \times \vec{\Omega}$  is associated with vortex stretching to cause decay of the larger eddies to the smaller eddies. If the  $\vec{V} \times \vec{\Omega}$  is small, the production of fine eddies becomes weaker and hence the dissipation

becomes less. The normalized helicity ( $U * \Omega_x / tU^2_{ref}$ ) is plotted in Figure 3.30. Helicity density  $\hat{h}$  and  $\bar{h}$  signs change near the endwall because mean  $U$  is negative in the bed chord coordinate system. From the plots, vorticity was stretched in the endwall boundary layer because the flow direction is perpendicular to the vorticity direction. But near the blade tip, the vorticity direction is more aligned with the chord direction.

### 3.6.7 Turbulence-modelling Related Parameters

Some derived parameters can be calculated and compared to those for two-dimensional and three-dimensional flows, for which Ciochetto (1997) examined a broad range of flows. Because the tip gap flow is highly three dimensional, these derived parameters show that the two-dimensional flow features do not apply to the tip gap flow.

In the following discussion, several parameters are discussed separately. Among them are flow angle, flow gradient angle, shear stress angle, anisotropy factor, turbulent kinetic energy, Townsend structure parameter  $a1$ ,  $1/S$ ,  $B$ , and  $B2$ . Comprehensive parameters for all profiles are available in Appendix H. Once again, similar to the above discussion of the mean velocity, Reynolds stress, and triple products, results for each parameter mentioned above are only presented at  $x/c_a = 0.18$ , for the local gap inflow, and the suction side.

#### Mean Flow Angle

The mean flow angle (FA) denotes the degree of cross flow by three-dimensional effects. If the FA in a coordinate system is bigger than  $45^\circ$  at a specific point, the cross flow is

locally stronger than streamwise flow.

$$FA = \tan^{-1}\left(\frac{W}{U}\right) \quad (3.14)$$

The range of FA across the measured profile reflects the extent of three dimensionality of the flow. The flow angles show highly skewed three-dimensional flow in the gap region. Also, the tip leakage flow direction through the gap is dependent on the spanwise location. Near the tip, the leakage flow follows closer in direction to the blade's camber line. Near the endwall, the flow direction is perpendicular to the camber line and is nearly a collateral flow in the viscous sublayer ( $y^+ < 10$ ), in which LDV data are used to determine the skin friction velocity. Especially in the mid part of the blade, the flow angle changes more than  $90^\circ$ .

The typical flow angles are presented in Figure 3.31 for both 1.65% and 3.30% in the chord coordinate system. For these flows, mean  $U$  is always positive in the chord coordinate system. For negative FA, flow travels toward the suction side; otherwise, the flow goes to the pressure side. Two types of FA variations are observed: a monotonic distribution as the increase of  $y$  for profile "u" outside the gap or a monotonic distribution from the endwall to the mid gap, but with a locally small zigzag segment near the blade tip for the profiles "p", "b", "c", and "s" within the gap because of the shear layer bound to the blade tip. In Figure 3.31a with the  $x/c_a = 0.18$  for 1.65%, absolute flow angles increase slightly from  $70^\circ$  at profile 5u to  $75^\circ$  at profile 5c and then decrease dramatically from  $60^\circ$  to  $35^\circ$  corresponding from profile 5s to e3. For one of profiles 5u, 5p, 5c, and 5s, flow angle monotonically changes from the high negative angle to the positive angle as the increase of  $y$  from the endwall to the blade tip. Around  $y^+ = 200$ , the flow angle changes sign for profiles 5u, 5c, e1, e2, and e3.

In Figure 3.31c and Figure 3.31d, flow angles increase monotonically with the normal distance  $y$  from the wall for all profiles from the leading edge to the trailing edge at the local upstream away from the pressure side. Flow angles appears to converge to  $-15^\circ$  at  $y^+$  around 600 for 1.65% and 1000 for 3.30% away from the wall. In Figure 3.31c for 1.65%, flow angles near the wall increase negatively from  $-15^\circ$  at chord ratio  $x/c_a = -0.33$  to  $-72^\circ$  at chord ratio  $x/c_a = 0.27$  and turn back from here to  $4^\circ$  at chord ratio  $x/c_a = 1.00$ . Profiles from 3u to 8u are similar. In Figure 3.31d for 3.30%, the FA near the wall is  $70^\circ$  at chord ratio  $x/c_a = 0.42$ .

For FAs at the suction side in Figure 3.31e and Figure 3.31f, the changes with  $y$  are not monotonic but in a zigzag shape because of the interference from the primary flow on the suction side. For FAs that change sign, this implies the occurrence of a vortex. It seems that the nearly collateral near wall region is thicker for the suction side than on the pressure side.

### Flow Gradient Angle

The flow gradient angle (FGA) is defined as the ratio of two  $y$  derivatives, which is used to reflect flow strain change associated with the flow.

$$FGA = \tan^{-1}\left(\frac{\partial W/\partial y}{\partial U/\partial y}\right) \quad (3.15)$$

If the  $y$  derivatives in the streamwise and spanwise vorticity are dominant, the FGA represents the vorticity direction. If the absolute angle is bigger than  $45^\circ$ , the cross flow changes faster than chordwise flow.

Typical flow gradient angles are in Figure 3.32a for 1.65% and 3.30% in the chord coordinate system. Most profiles have zero FGA around mid gap ( $50 < y^+ < 200$ ),

indicating that  $|\Omega_z| \gg |\Omega_x|$  in the chord coordinate system. Since the absolute flow gradient angles are bigger than  $45^\circ$  near the wall and near the blade tip, the vorticity along  $x$  is bigger than the  $z$  direction.

In Figure 3.32c and Figure 3.32d for the pressure side, the range of FGA is about  $150^\circ$  for a profile from 3u to 8u because the  $\partial W/\partial y$  changes sign around  $y^+ = 60 - 100$ . The features of the two gaps are similar except for profiles 4u and 5u. Similar observations can be made from Figure 3.32e and Figure 3.32f for the suction side.

### Shear Stress Angle

The shear stress angle (SSA) is defined as the arctan of the ratio of two shear stresses in the  $x$ - $z$  plane, which is used to describe the direction of the effective turbulent stress in the flow.

$$SSA = \tan^{-1}\left(\frac{-\overline{vw}}{-\overline{uv}}\right) \quad (3.16)$$

Figures 3.33a and 3.33b show that the SSA is equal to the FA near the wall because of the collateral flow in the viscous sublayer. The SSAs are more scattered near the blade tip, indicating a vortical shear flow in the tip region.

In Figure 3.33c and Figure 3.33d for the pressure side, the range of SSA is about  $120^\circ$  for a profile from 3u to 8u at 1.65% tip gap and about  $150^\circ$  for a profile from 3u to 8u at 3.30% tip gap. Like the FGA, SSA changes signs. More scatter near the blade tip can be observed from Figure 3.33e and Figure 3.33f for the suction side. However, there is no sign change until the tip region. This indicates that there is some lag of the shearing stress angles relative to the FGA.

### Anisotropy Factor

N is the ratio of eddy viscosity in the z-direction over the eddy viscosity in the x-direction.

$$N = \frac{\epsilon_z}{\epsilon_x} = \frac{-\overline{vw}/\partial W/\partial y}{-\overline{uv}/\partial U/\partial y} = \frac{\tan(SSA)}{\tan(FGA)} \quad (3.17)$$

The N parameter is dependent on the coordinate system chosen. For isotropic flow, N should be one. Departure from one indicates that the flow is anisotropic. Plots of N in Figure 3.34 show that N is scattered away from one in the chord coordinate system. Thus, the flow is strongly three-dimensional in the gap and passage. N is mainly larger than 1 because the z direction eddy viscosity is bigger than that of x-direction eddy viscosity, indicating the stronger interaction perpendicular to the chord than along the chord. Some N values are negative because of the local decorrelation between the shear stress  $-\overline{uv}$  and  $-\overline{vw}$ . Since the SSA lags the FGA, the development of the shearing stress lags the streamwise vorticity development, so no constant eddy viscosity ratio is possible.

### Turbulent Kinetic Energy (TKE)

The TKE is normalized by  $U_{ref}^2$  as follows

$$\frac{TKE}{U_{ref}^2} = \frac{\overline{u^2} + \overline{v^2} + \overline{w^2}}{2U_{ref}^2} \quad (3.18)$$

Plots of  $TKE/U_{ref}^2$  are presented in Figure 3.35 for tip gaps of 1.65% and 3.30%. Profiles 5p to 5s in the gap show double peaks near the endwall and tip end, respectively; the second peak value over the first peak value is about 4 because there is larger TKE production in the tip separation vortex bound to the blade tip. Profiles e1 to e3 in the

tip leakage vortex region have a peak near the endwall and one through the tip separation vortex region with comparable magnitudes. In the mid gap, the TKE profiles tend to collapse. When the flow is driven from the pressure side to the suction side at a specific chord ratio, the endwall peak increases significantly. In Figure 3.35a for 1.65%, the near wall peak TKE increases and the corresponding  $y^+$  decreases from profile 5u to 5c because tip gap flow accelerates and increases from profile 5c to e3 because of the intersection with the primary flow in the passage. The increase of TKE near the endwall results from the rise of  $\overline{w^2}$  due to large  $\overline{v^2}\partial W/\partial y$  production. The TKE is almost constant between  $y^+ = 40$  and  $y^+ = 200$  for Profiles 5u to 5s. In Figure 3.35b for 3.30%, the near endwall peak TKE largely increases the with a  $y^+$  increase from pressure side to the suction side. The TKE almost decreases linearly between the near wall peak and the dip. Profiles 5u to 5c have similar distributions except near the blade tip peak.

For the pressure side in Figures 3.35c and 3.35d, TKE has just one peak near the endwall and monotonically approaches zero after the peak TKE. For 1.65%, the position for  $y^+$  for each profile decreases slightly from profile 1u to profile 5u and decreases significantly in the downstream after  $x/c_a = 0.18$  because of the origin of the tip leakage vortex. For 3.30%, the position  $y^+$  of the peak TKE for each profile increases slightly from profile 1u to profile 5u because of the endwall favorable pressure gradients and the endwall shear and then increases significantly in the downstream direction after  $x/c_a = 0.18$  because of the endwall adverse pressure gradients.

For the suction side in Figures 3.35e and 3.35f, TKE has two peaks with the peak near the blade tip is about 4 times stronger than the peak near the endwall. The peak in profiles 1d to 4s is smaller than profile uu and the peak of profiles 5s to 9s is bigger than that of profile uu.



### a1 Parameter

The a1 is a ratio of the shear stress in a horizontal plane to the summation of the three normal stresses or twice the turbulent kinetic energy (TKE).

$$a1 = \frac{\sqrt{(-\overline{uv})^2 + (-\overline{vw})^2}}{\overline{u^2} + \overline{v^2} + \overline{w^2}} = \frac{|\tau/\rho|}{2TKE} \quad (3.19)$$

It is always positive and independent of the rotation of coordinate systems. The a1 proposed by Townsend (1956) is 0.15 for two-dimensional flow in the outer layer. It can be used as an algebraic model to relate the Reynolds shear stress with TKE for simplification. In Figures 3.36a and 3.36b, a1 has a peak for all measured profiles with an almost linear increase near the endwall for planes from  $x/c_a = -0.33$  to 0.12 for 1.65% and from  $x/c_a = -0.33$  to 0.42 for 3.30%.

In Figures 3.36c and 3.36d, the a1 peak values increase slightly and the location shifts to a higher  $y^+$  from the leading edge to the trailing edge. The a1 is more scattered on the suction side than the pressure side because the shear stress and the TKE have large changes across the gap. The a1 is not constant and does not correlate profiles of the data well, so that the tip gap flow has a strong three-dimensional effect on turbulence.

### 1/S Parameter

The 1/S is a ratio of shear stress to normal stress  $\overline{v^2}$ , defined by Simpson (1996).

$$1/S = \frac{\sqrt{(-\overline{uv})^2 + (-\overline{vw})^2}}{\overline{v^2}} = \frac{|\tau/\rho|}{\overline{v^2}} \quad (3.20)$$

The 1/S highlights the effect of fluctuating velocity  $v'$  and reaches a constant 0.6 for a typical 2D flow. It can be used to simplify turbulence models in such a flow. However,

near the wall ( $y^+ < 30$ ) and blade tip, the  $1/S$  has double peaks in the typical plots of Figures 3.37a and 3.37b and Appendix H.

The parameter is plotted in Figures 3.37c and 3.37d. This parameter is less than typical value of 2D when  $20 < y^+ < 200$ . The  $1/S$  decreases from the leading edge to the trailing edge for both pressure and suction sides, implying a flow decorrelation because the near wall and upper turbulent flows come from different directions and have different histories.

### B Parameter

Since  $v$  is a characterizing fluctuation, triple products  $\overline{u^2v}$ ,  $\overline{v^3}$ , and  $\overline{w^2v}$  for the transport of TKE in the  $y$  direction should scale on the  $\overline{v^3}$ .

$$B = \frac{\overline{v^3}}{\overline{u^2v} + \overline{v^3} + \overline{w^2v}} \quad (3.21)$$

The B parameter is plotted in Figure 3.38 for both 1.65% and 3.30%. Figures 3.38a and 3.38b show the B at  $x/c_a = 0.18$ . The log region is the best collapse for this parameter. Near the wall and blade tip some deviation occurs because of higher LDV measurement uncertainty near the physical boundaries and possible blade vibration. The B parameter shows that the turbulent transport of TKE is closely related to the  $v$  transport of  $v^2$ . This could simplify mid-gap region modelling.

In Figures 3.38c and 3.38d for the entry flow profiles 1u - 9u of the blade, the sign change reflects the sign of  $\overline{v^3}$ . They are antisymmetric about the mid gap. Due to the wall suppression, the average B is zero. The complete set of plots are in Appendix H.

### B2 Parameter

The B2 is used to correlate the third moment of  $v'$  and the shear stress diffusion terms  $\overline{uv^2}$  and  $\overline{v^2w}$ . The  $\overline{uv^2}$ ,  $\overline{v^3}$ , and  $\overline{v^2w}$  occur in higher order three-dimensional turbulent boundary layer stress transport equation and B2 is also invariant to rotation about the y axis.

$$B2 = \frac{\overline{v^3}}{\sqrt{(\overline{uv^2})^2 + (\overline{v^2w})^2}} \quad (3.22)$$

This parameter relates the turbulent transport of instantaneous stresses  $-\overline{v^2}$ ,  $-\overline{uv}$  and  $-\overline{vw}$  in the y direction. In Figures 3.39c and 3.39d for profiles 1u - 9u of gap inflow, only a small region of  $y^+ < 200$  has a good collapse of the data for this parameter. The scatter of B2 parameter is due to uncertainty of triple product data using the LDV for a complex flow.

### 3.6.8 TKE-based Quantities

TKE is a very important parameter to describe a turbulent flow. TKE transport and production are key terms in the TKE balance equation. TKE transport vector and TKE production rate are calculated as follows.

#### TKE Transport Vector

The TKE transport vectors are defined as follows

$$\vec{V}_q = \frac{\overline{u^2v} + \overline{v^3} + \overline{vw^2}}{TKE * U_e} \vec{j} + \frac{\overline{u^2w} + \overline{v^2w} + \overline{w^3}}{TKE * U_e} \vec{k} \quad (3.23)$$

In Figure 3.40, the TKE transport vectors show the amount of jitter, or small occasional jumpy movements, in the region of a structure such as a vortex, implying that the meandering of the tip leakage vortex may exist tangentially and vertically. The  $\vec{V}_q$  is the direction of infrequent large-scale motions since the triple products are skewed in that direction. The larger the vectors, the higher the jitter. The vectors also show the directions of jitter. Obviously, the most jitter occurs just around the surrounding of the mean vortex center, near the endwall and next to the blade tip of the flow. The jitter for the tip leakage vortex shows that the vortex occasionally moves outward and away upward more strongly than downward and into the center of the tip leakage vortex.

### TKE Production Rate

TKE Production Rate,  $-\overline{u_i u_j} U_{i,j}$ , is expanded as follows

$$\begin{aligned}
 TKEProductionRate = & -\overline{u^2} \frac{\partial U}{\partial x} - \overline{uv} \frac{\partial U}{\partial y} - \overline{uw} \frac{\partial U}{\partial z} \\
 & -\overline{uv} \frac{\partial V}{\partial x} - \overline{v^2} \frac{\partial V}{\partial y} - \overline{vw} \frac{\partial V}{\partial z} - \overline{uw} \frac{\partial W}{\partial x} - \overline{vw} \frac{\partial W}{\partial y} - \overline{w^2} \frac{\partial W}{\partial z}
 \end{aligned} \tag{3.24}$$

For the LDV profiles at all chord ratios except  $x/c_a \neq 0.27$ ,  $\partial/\partial x$  can not be estimated. From the results of  $x/c_a = 0.27$ ,  $\partial/\partial x$  is one order smaller than  $\partial/\partial y$ . So the production of TKE associated with  $\partial/\partial x$  is relatively small. Figure 3.41 shows that more TKE is produced near the blade tip and the endwall as well as in the interaction zone between the tip leakage flow and the primary flow. The  $\overline{v^2} \partial W / \partial y$  and  $\overline{w^2} \partial W / \partial z$  are dominant production terms, accounting for about 70% of the total TKE production rate. While in the mid gap where velocity gradients are very small, turbulence production is negligible. It is reasonable that almost potential core exists in the mid gap.

### 3.6.9 Application of Rapid Distortion Ideas

Rapid distortion ideas can explain rapid change of a turbulent flow distorted by velocity gradients (Batchelor, 1953). Assume that the turbulence of a turbulent flow decreases if the turbulent flow accelerates and vice versa. If some quantities connected with the mean velocity and turbulence can be used to correlate data from different regions of the flow, the rapid distortion theory can be used to explain the flow physics. Generally speaking, a formula  $U^p \overline{u^{2^q}} = \text{constant}$  that correlated profiles of data reflects the ideas that rapid distortion of the flow is producing the observed changes.

Volumetric mass flow rate per unit span is defined as

$$\psi = \int \sqrt{U^2 + V^2 + W^2} dy \quad (3.25)$$

$\psi$  is independent of coordinate system. Some quantities such as  $\overline{u^2}U^k/U_{ref}^{2+k}$ ,  $\overline{w^2}W^k/U_{ref}^{2+k}$ ,  $(\overline{u^2} + \overline{v^2})Q^k/U_{ref}^{2+k}$  were calculated at the same  $\psi$  for different profiles in the same region of flow with  $k=1$  and  $0.5$ . For a given  $\psi$ , if inviscid rotational flow (rapid distortion) is dominant, then the turbulent structure should follow rapid distortion along the streamline, i.e., in vector direction of flow on the stream surface.

The  $\overline{u^2}U^k/U_{ref}^{2+k}$ ,  $\overline{w^2}W^k/U_{ref}^{2+k}$ ,  $(\overline{u^2} + \overline{v^2})Q^k/U_{ref}^{2+k}$  are functions of  $y^+$  in Figures 3.42 and 3.43.  $\sqrt{U^2 + V^2 + W^2}/U_{ref}$ ,  $\sqrt{\overline{u^2} + \overline{v^2} + \overline{w^2}}/U_{ref}$  are functions of  $\psi/tU_{ref}$  in Figure 3.44. For all plots, no possible combination collapses data from different profiles in the tip gap. Thus, the tip gap flow is not governed by the rapid distortion theory idea, even in the mid gap region. Due to a favorable pressure gradient, the mean cross flow velocity increases apparently from the pressure side to the suction side under the gap but the corresponding TKE does not decrease.

### 3.6.10 Spectral Estimation

A spectral analysis was done on the velocity fluctuations of some LDV data. The spectral analysis was done to see if there was low frequency meandering of the positions of the vortices. Spectra are also used to represent the energy distribution of different sizes of eddies from the largest scales all the way down to the Kolmogoroff scale where energy is dissipated. Perry et al. (1986) defined three types of scaling: inner, outer, and dissipating eddy for the power spectrum in an attached turbulent boundary layer based on dimensional analysis. These types of scaling were expanded to a detached and near-detached flow under adverse pressure gradient by Simpson et al. (1990).

In Figure 3.40, the jitter phenomena indicate unsteady behavior of the tip gap flow because asymmetric distribution of histogram of instantaneous velocity. Thus, some significant fluctuation occurs occasionally. In this study, the scaling velocity is the free-stream velocity and the length scale is the tip gap height.

For LDV measurements, the particle arrival times are totally irregular. Hence, the standard method of regularly sampling signals is not applicable. A correlation-based slotting technique was proposed by Robert (1986). This approach first estimates the correlation between a pair of data samples that are accumulated in time delay "slots" in the correlation plane. Then the spectrum is estimated using a Fourier transformation.

Assume that the error of quantization at the original sample time  $t_i$  is ignored. Another sample occurs at time  $t_j$ . The following quantization procedure is carried out for a pair of data samples with the lag time  $t_j - t_i$ . Suppose that the maximum lag time among all pairs of data samples is  $\tau_m$ . Then  $N_s$  slots are divided evenly along the maximum lag time  $\tau_m$ . The origin of the lag time axis,  $\tau = 0$ , is the mid point of the first slot.

The slot width is

$$\Delta\tau = \tau_m/N_s$$

thus there are a number of points in this slot width  $\Delta\tau$ . the  $N_k$  is the number of data points in the slot  $\tau_k$ , where  $(k - 1/2)\Delta\tau < \tau_k < (k + 1/2)\Delta\tau$ .

The correlation is estimated as follows. At  $\tau = 0$ , an estimate of  $R(0)$  is

$$\hat{R}(0) = \sum_{i>j} x(t_i)x(t_j) \quad (3.26)$$

where  $-\frac{\Delta\tau}{2} < (t_j - t_i) < \frac{\Delta\tau}{2}$ ;  $x(t_i)$  and  $x(t_j)$  are the sampled instantaneous velocity at instant time  $t_i$  and  $t_j$ , respectively.

$$\hat{R}(\tau_k) = \frac{\sum x(t_i)(t_j)}{N_k} \quad (3.27)$$

where  $N_k$  is the number of cross-products in the k-th slot.  $\tau_k - \frac{\Delta\tau}{2} < (t_j - t_i) < \tau_k + \frac{\Delta\tau}{2}$ .

A Hanning window is used as a time-lag window

$$D(\tau_k) = \begin{cases} 0.5[1 + \cos(\pi \frac{\tau_k}{\tau_m})] & \tau_k < \tau_m \\ 0 & \tau_k > \tau_m \end{cases}$$

Then  $\hat{f}(\tau_k)$  is defined as follows,

$$\hat{f}(\tau_k) = \hat{R}(\tau_k) \cos(2\pi f \tau_k) D(\tau_k) \quad (3.28)$$

Thus, the spectral estimate is

$$\hat{S}(f) = 4\Delta\tau \{0.5\hat{f}(0) + \hat{f}(\tau_1) + \hat{f}(\tau_2) + \cdots + \hat{f}(\tau_{N_s})\} \quad (3.29)$$

Based on the above procedure, the velocity spectra were evaluated at different locations. Profile uu at  $x/c_a = -0.33$  is a nearly two-dimensional flow in the free-stream coordinate system. The flow of profile ld at  $x/c_a = 0.00$  for 3.30% is a three-dimensional flow in the free-stream coordinate system. One point for profile uu and ld at the maximum  $\overline{u^2}$  was used to analyze the spectra of the u instantaneous velocity. The tip leakage vortex was separated at profile e3 for 1.65% tip gap and Profile x3 for 3.30% tip gap. One point at the maximum  $\overline{w^2}$  was used to analyze the spectra of the w instantaneous velocity in the separation line coordinate system. The results of spectral analysis are shown in Figure 3.45 and 3.46. From Figure 3.45, the u spectra are like a typical distribution of a two-dimensional flow. The spectrum of u at profile ld of 3.30% tip gap has two regions with the power of -1 and -5/3 related to the inner layer and the inertial subrange, respectively. However, the spectrum with the power of -1 and -5/3 of u at profile ld of 3.30% tip gap can not be observed because the LDV data rate was not high enough. From Figure 3.46, the w spectra for 1.65% and 3.30% do not have large scale unsteady motion of tip leakage vortex but weak unsteadiness. The spectral distributions vs. frequency are like typical turbulent flow. Spectra for 1.65% and 3.30% are similar so that the meandering behavior of a tip leakage vortex is independent of the gap sizes. In addition, the spectral magnitude of w in the tip separation vortex is higher than in the leading edge of the blade, indicating that the turbulence in the tip leakage vortex increases from the leading edge to the tip leakage vortex in the passage.

### 3.7 Flow Structure Discussion

A two-dimensional inflow develops into a highly three dimensional and non-equilibrium turbulent flow from upstream of the compressor cascade to its downstream and then



relaxes back toward a mean two-dimensional flow far downstream. In the gap, due to the pressure gradient between the pressure and suction sides, a cross flow is generated relative to the primary flow. The behavior of the tip gap flow without the turbulent-non-turbulent interface is different from many half-constrained 3D turbulent boundary layer flows. Two distinct strong shear layers occur near the endwall and the blade tip. Multiple discrete vortices are generated around the square corners of the blade tip due to the flow turning in the gap and in the passage due to the gap flow interaction with the primary flow.

### 3.7.1 Disturbed Inflow

For the tunnel calibration at  $x/c_a = -0.705$  in Figure 3.3 in the bed coordinate system, the velocity ripple curve shows that the inflow flow is disturbed by the blade row. Muthanna (2002) observed a similar blade influence at  $x/c_a = -0.23$  and no blade influence at  $x/c_a = -0.80$  using his hot wire measurements. Thus, the influence of blade row probably extends forward to the half chord length from the leading edge of the blade row.

Three inflow LDV profiles for each gap inflow were measured at  $x/c_a = -0.33$  and show in Figure 3.47 that their velocity profiles are not totally identical for a given gap size nor totally similar for different gap sizes. There must be some effect of the blade row on the inflow. Moreover in Figure 3.48, the flow angle FA is small; a1 has a peak value of 0.11 for  $y=2$  mm and  $1/S$  is about 0.6 at that point. The change of the near wall flow angle versus the increase of  $y^+$  for a given profile suggests the effect of the turbulent boundary layer trip on the endwall. The poorly collapsed  $U^+$  suggest that the near wall flow is not fully relaxed after the proceeding trip. The mean W is not close to the zero,

indicating that the flow disturbed by the existence of both the tip gap and the turbulent boundary layer trip. Thus, the inflow is not exactly a two-dimensional flow.

### 3.7.2 Tip Gap Mean Flow

The tip gap flow is mainly determined by the pressure loading and gap sizes. The strong lateral pressure gradient produces crossflow from the pressure side to suction side. The tip gap flow is totally different from the almost two-dimensional mean flow in the mid-span passage. Since the flow direction in the gap is different than the primary flow, interactions take place between the tip gap flow and the primary flow in the passage, including some spanwise flow above the edge of the blade suction side. As the tip gap flow develops from the leading edge to trailing edge, the crossflow is bounded by two shear layers in the gap: one is near the endwall and the other is near the blade tip.

The midspan pressure loading used to represent the strength of the crossflow across the gap along the blade. A comparison of the  $C_p$  between the midspan and endwall shows its similarity and difference in Figure 3.11 and Figure 3.12. Obviously, there is a peak  $\Delta C_p$  between the pressure side and the suction side. The peak  $\Delta C_p = 0.64, 0.49$ , and  $0.55$  is located at  $x/c = 0.44$  for the mid-span, at  $x/c = 0.38$  for the 1.65% tip gap, and at  $x/c = 0.54$  for the 3.30% tip gap, respectively.

The crossflow within the gap is driven by a pressure gradient  $\partial p / \partial z$  in the chord coordinate system. The magnitude of mean  $W$  at the mid gap increases more than 100% but the mean  $U$  does not change as much from profile 5u to 5c at  $x/c_a = 0.18$  as shown in Figures 3.49e and f for both 1.65% and 3.30% tip gaps. The  $W$  profile is nearly flat throughout 70-80% of the gap height for a given profile, so that the flow is jet-like (Storer and Cumpsty, 1991) relative to the chord line. Velocity profiles do not collapse

in Figure 3.15, so that the flow is not at equilibrium.

The dramatic change of mean  $V$  and  $W$  next to the blade tip indicates a tip separation vortex bound to the blade tip, which is easily recognized in the  $VW$  vector plots of Figures 3.50a and b at  $x/c_a = 0.18$  for 1.65% and 3.30%, respectively. The tip separation vortex forms right after the blade tip corner on the pressure side because the flow sharply turns around the pressure side. The tip separation vortex tends to reattach on the blade tip between profile 5b and 5c for 1.65% shown in Figures 3.50a as well as between profile 5c and 5s for 3.30% tip gap shown in Figures 3.50b. From the featured maximum cross-flow velocity in Figure 3.51a and Figure 3.51b, the maximum cross flow velocity at  $x/c_a = 0.18$  occurs between the profile b and c for 1.65% and profile c and s for 3.30%. However, the maximum  $W$  magnitude is not located at the mid gap but toward the blade tip. The maximum mean  $W$  and its locations indicate that the vena-contract crossflow area for some analytical flow results is actually between the tip separation vortex and the endwall. From the surface oil flow visualization on the suction side shown in Figures 3.7b and 3.8b, a second tip separation vortex must be located at the corner of the suction side due to the flow turning and continuity conditions.

Near the endwall, the tip gap flow is driven by the lateral pressure force. The tip gap flow direction is almost perpendicular to the blade chord because the initial momentum of the near wall flow is very low. The skin friction velocity on the endwall as shown in Figure 3.14 reaches its maximum at profile b or c for 1.65% and profile c and s for 3.30%, corresponding to the locations of the maximum  $W$  at  $x/c_a = 0.18$ . The endwall oil flow visualizations confirmed the strong shear region underneath the gap.

The tip leakage vortex is formed and separates from the endwall by the intersection of the gap flow with the primary flow in the passage on the suction side of the blade. The tip leakage vortex affects the endwall pressure distribution as shown in Figure 3.10. In

the separation line coordinate system, Figure 3.52 clearly show that the separation point was not captured with current LDV data but it is close to profile e3 for 1.65% and profile x5 for 3.30%. However, the endwall oil flow visualization displayed the separation region as shown in Figures 3.6. The location of tip leakage vortex separation-line derived from the LDV data is further from the suction side than the separation location from the endwall oil flow visualization.

Figure 3.53 shows  $\vec{Q} = U\vec{i} + W\vec{k}$  plots, independent of the rotation of coordinate system about  $y$ . The direction of  $\vec{Q}$  represents the flow angle. The direction of  $\vec{Q}$  changes at a given  $(x,z)$  location for both 1.65% and 3.30%. The short vectors that are nearly perpendicular to the chord are near the endwall. The longer vectors are more parallel to the blade chord are away from the endwall. The varying range of FA demonstrates the extent of three dimensionality of the flow. Along the normal to chord direction, the flow directions are highly skewed. Figure 3.53 also shows that the origin of the tip leakage vortex occurs at  $x/c_a = 0.16$  for 1.65% tip gap and  $x/c_a = 0.36$  for 3.30% tip gap. Around the origin of the tip leakage vortex, the pressure difference is biggest.

The secondary flow VW vectors in Figure 3.54 show the nearly constant mid gap  $W$  profile and two shear layers bound to the endwall and blade tip for a given profile in the gap. The mean  $W$  profiles from the local gap inflow to the suction side look like a incompletely developed channel entrance flow. The center of the tip separation vortex shifts away from the pressure side as the tip gap flow develops from the leading edge to trailing edge.

In the front part of blade ( $x/c_a < 0.04$ ), the tip gap flow is weak because of the small pressure difference between the pressure side and suction side, as shown in Figure 3.12. Since the primary flow is dominant, the tip gap flow adjusts its flow direction slightly and gradually merges with the primary flow. For the 1.65% tip gap, the mean  $W/U_{ref}$  around

the mid gap increases from 0.24 at  $x/c_a = 0.00$  to 0.36 at  $x/c_a = 0.04$  (Figure 3.55a) as  $\Delta C_p$  changes from 0 at  $x/c_a = 0.00$  to 0.10 at  $x/c_a = 0.04$ . Meanwhile, FA varies about  $10^\circ$  near the endwall.

From the  $x/c_a = 0.04$  to the origin of tip leakage vortex, the tip gap flow becomes stronger. The primary flow and tip gap flow intersect together almost perpendicularly near the endwall. A strong interaction occurs when the two flows impinge. The mass flux of the primary flow is much bigger than that of the tip gap flow, so that the primary flow acts like a virtual wall. The tip gap flow encounters the primary flow, rolls up from the endwall. For 1.65% tip gap, the mean  $W/U_{ref}$  around the mid gap increases from 0.36 at  $x/c_a = 0.04$  to 0.8 at  $x/c_a = 0.18$  (Figure 3.55a) as  $\Delta C_p$  changes from 0.10 at  $x/c_a = 0.04$  to 0.49 at  $x/c_a = 0.18$ . Meanwhile, FA varies about  $30^\circ$  near the endwall.

From the origin of the tip leakage vortex to the  $x/c_a = 0.65$ , the primary flow and tip gap flow encounter together almost perpendicularly near the endwall. The strong shear layer occurs after the tip leakage vortex is detached from the blade tip. From oil flow visualizations, dark regions show strong wall shear. Calculated endwall skin friction coefficients show that the magnitudes reach a peak in the middle between the pressure side and suction sides for both the 1.65% case listed in Table 3.8 and the 3.30% case listed in Table 3.9. For the 1.65% tip gap, the mean  $W/U_{ref}$  around the mid gap increases from 0.8 at  $x/c_a = 0.18$  to 0.7 at  $x/c_a = 0.65$  (Figure 3.55a) as  $\Delta C_p$  changes from 0.49 at  $x/c_a = 0.18$  to 0.25 at  $x/c_a = 0.65$ . Meanwhile, FA varies about  $-5^\circ$  near the endwall.

From  $x/c_a = 0.65$  to the trailing edge, the tip gap flow becomes weaker. For the 1.65% tip gap, the mean  $W/U_{ref}$  around the mid gap increases from 0.7 at  $x/c_a = 0.65$  to 0.24 at  $x/c_a = 1.00$  (Figure 3.55a) as  $\Delta C_p$  changes from 0.25 at  $x/c_a = 0.65$  to 0 at  $x/c_a = 1.00$ . Meanwhile, FA varies about  $-40^\circ$  near the endwall. The tip separation vortices on both the pressure side and the suction side detach from the trailing edge.

The tip leakage vortex straightens the curvature of streamline of the primary flow, based on less turning of the tip leakage vortex trajectory shown in Figure 3.6. The secondary flow induced by the primary flow becomes weaker. The tip leakage vortex improves the corner separation on the suction side of the trailing edge, as discussed by Storer (1989). The tip gap flow mixes with the wake of the blade.

From the vector plots of Figures 3.56 and 3.57 in the local camber coordinate system defined in Section 3.1, the flow at the chord ratios -0.33, 0.00, and 0.04 are not affected compared to the main flow. It is very clear to see that the strong crossflow approaches from the pressure side, almost vertically downward and leaves the gap upward at chord ratios from 0.09 to 0.65. Then at chord ratio 1.00, the flow leaves the blade row. It seems that the crossflow is more perpendicular to the camber line instead of the chord line.

Based on the discussion above, conceptual gap models are shown in Figure 3.58. Before the origin of the tip leakage vortex, the tip gap flow is weak but a tip separation vortex forms. As the flow develops along the blade chord, the location of tip separation vortex shifts slightly from the pressure side to suction side. After the origin of the tip leakage vortex, the location of the tip separation vortex depends on the ratio of the blade thickness-to-gap height. For the smaller tip gap like 1.65%, the tip separation vortex is discrete; for the larger gap like 3.30%, the tip separation vortex does not reattach on the blade tip and may be entrained by the tip leakage vortex.

### 3.7.3 Tip Gap Flow Turbulence

Because of the existence of the mean  $W$ ,  $-\overline{uw}$  and  $-\overline{vw}$  cannot be ignored in the gap in Figure 3.59. Distributions of Reynolds stresses and triple products versus the wall distance  $y$  show that inertial forces dominate in the mid gap flow while viscous effects

are dominant in the two bounded shear flow layers. The turbulent shear-stress direction is generally different from the mean flow direction and the mean-velocity gradient direction because SSA, FA, and FGA are different as demonstrated in Figures 3.60 and 3.61.

Based on the FA, FGA, and SSA for a given profile in the viscous sublayer, the shear stress flow lags the mean flow. Therefore, the effective eddy viscosity not isotropic. In Figure 3.34, the log-log plot of the  $N$  versus  $y^+$  does not collapse well.

For the  $W$  component of the gap flow at a given profile,  $\partial W/\partial y$  is significant near the endwall and the blade tip, where the viscous effect is strong in a very thin layer. But away from the two bounded thin shear layers, the viscous effect becomes weak so that the flow acts like inviscid flow. The flow accelerates perpendicularly to the chord so that  $W$  increases as the flow passes from the pressure side to the suction side. The  $\overline{w^2}$  at the mid gap does not change much in the gap and slightly increases around the exit of the gap at  $x/c_a = 0.18$  for 1.65% tip gap and  $x/c_a = 0.18$  for 1.65% tip gap as shown in Figure 3.62. However, the  $\overline{w^2}$  increases significantly near the endwall and the blade tip from the pressure side to the suction side. In addition, the  $\overline{w^2}$  is large in the center of the tip leakage vortex. On the other hand, the  $\overline{u^2}$  the  $\overline{v^2}$  do not change much in the gap. Thus, the  $\overline{w^2}$  mainly contributes the variation of the TKE as shown in Figure 3.63.

In Figure 3.63, the TKE distribution near the endwall has a distribution like a two-dimensional boundary layer because the TKE increases as  $y^+$  increases and then decreases after  $y^+ > 100$ . On the other hand, the peak value of the TKE near the blade tip is 10 times bigger than that of the TKE near the endwall. From plots of TKE production in Figure 3.64, TKE is barely produced away from the physical boundary of endwall and blade tip. The significant TKE production occurs in the endwall shear layer, tip separation vortex, and tip leakage vortex, where Figure 3.65 shows that the TKE transport vectors vary substantially relative to the secondary flow velocity components  $VW$

vectors. The maximum production of TKE results from the interaction between the tip separation vortex and the surrounding shear flow.

Conceptual gap models for turbulence in Figure 3.66 show the high turbulence zone associated with the endwall shear layer, tip separation vortex, and the tip leakage vortex. Also in the passage, the primary flow and tip gap flow interact because flow angles are different for two flows in the lower endwall region. The lower endwall flow is not compressed by the blades and just interacts with the tip leakage flow in the passage. The vortex flow region grows from the upstream to the downstream. Muthanna (2002) pointed out the high turbulence along the trajectory of the tip leakage vortex is caused by the deficit of the streamwise velocity component.

As the tip gap flow develops from the leading edge to trailing edge of the blade, the turbulence-based quantities change significantly. The correlation coefficient of  $\overline{uw}$  decreases from -0.8 at the leading edge to 0.3 at the trailing edge on the suction side for 3.30% tip gap in the chord coordinate system, as shown in Figure 3.67b. Meanwhile,  $1/S$  decrease from 0.6 at the leading edge to 0.08 at the trailing edge. There appears to be a decorrelation between the shear stress and the normal stress due to the different histories of the near blade tip and endwall flow structures - they come from different upstream directions.

In summary, the tip gap flow is a highly skewed three-dimensional and nonisotropic turbulent flow based on the observation of turbulence-modelling related quantities such as  $N$  and  $1/S$ . The overall unsuccessful collapse of cross-products between mean and turbulence quantities reflect that the rapid distortion theory ideas do not apply to the tip gap flow because the mean and turbulence quantities are not directly coupled. Some turbulence models for two-dimensional flow fail to predict the tip gap flow because anisotropy factor  $N$  is not 1 and  $1/S$  is not 0.6. The LDV data in the gap region can help to validate



new turbulence models of stress transport equations for CFD efforts of the tip gap flow.

$$\frac{D(-\overline{uv})}{Dt} = \overline{v^2} \frac{\partial U}{\partial y} - \overline{\frac{p'}{\rho} \left( \frac{\partial u}{\partial y} + \frac{\partial v}{\partial x} \right)} + \frac{\partial}{\partial y} \left( \frac{\overline{p'u}}{\rho} + \overline{uv^2} \right) - \nu (\overline{v \nabla^2 u} + \overline{u \nabla^2 v}) \quad (3.30)$$

$$\frac{D(-\overline{vw})}{Dt} = \overline{v^2} \frac{\partial W}{\partial y} - \overline{\frac{p'}{\rho} \left( \frac{\partial w}{\partial y} + \frac{\partial v}{\partial z} \right)} + \frac{\partial}{\partial y} \left( \frac{\overline{p'w}}{\rho} + \overline{v^2 w} \right) - \nu (\overline{w \nabla^2 v} + \overline{v \nabla^2 w}) \quad (3.31)$$

$$\frac{1}{2} \frac{D(\overline{v^2})}{Dt} = -\overline{v^2} \frac{\partial V}{\partial y} - \frac{\partial}{\partial y} \left( \frac{\overline{v^3}}{2} \right) - \frac{\overline{v}}{\rho} \frac{\partial p}{\partial y} + \nu (\overline{v \nabla^2 v}) \quad (3.32)$$

### 3.7.4 Tip Gap Size Effects

By comparing the 1.65% case and the 3.30% case, the tip gap size effect on the flow structure can be obviously recognized. Both oil flow visualizations in Figure 3.6 and the endwall pressure distributions in Figure 3.10 show that the starting location of tip leakage vortex moves rearward and the trajectory of the tip leakage vortex shifts closer to the pressure side of the neighboring blade from the starting point to the downstream as the tip gap height increases. The LDV results reveal that the  $W/U_{ref}$  changes from 1.0 to 0.8 when the gap size changes from 1.65% to 3.30% in Figure 3.51. The flow angles near the endwall turn more perpendicular to the camber line as the gap height rises. The tip separation vortex may reattach on the blade tip for the smaller tip gap while it may not reattach for the bigger tip gap because blade thickness-to-gap height ratio determines flow features in the gap. As pointed out by Storer and Cumpsty (1991), the tip separation reattachment occurs only if the ratio of blade thickness-to-gap height is larger than 2.5. The turbulent nature does not change if the gap size changes. The maximum blade thickness is 0.44 inches for GE rotor B blade. The blade thickness-to-gap height ratio is larger than 2.5 for some part of 1.65% tip gap. The size of "potential core" in the mid gap increases if the gap size increases because the two boundary layers

bounded on the endwall and the blade tip are relatively thin.

Table 3.1: Rotation angles of local camber coordinate systems for both 1.65% and 3.30% tip gaps

$x/c_a$	$\theta_y$
0.00	72.4
0.04	68.4
0.09	66.4
0.12	65.3
0.18	63.3
0.27	60.6
0.42	57.1
0.65	51.6
1.00	42.4

Table 3.2: Rotation angles of local wall-shear coordinate systems for both 1.65% and 3.30% tip gaps

<i>Profile</i>	<i>1.65%</i>	<i>3.30%</i>	<i>Profile</i>	<i>1.65%</i>	<i>3.30%</i>
UU	56.9	56.9	6U	127.5	116.3
UB	56.9	56.9	6P	134.5	131.9
UD	56.9	56.9	6B	134.9	125
1U	75.9	71.9	6C	129.3	120.1
1B	81.1	75.8	6S	122.3	126.5
1D	68.5	84.2	7U	125.2	126.4
2U	85.8	145.2	7P	129.5	132.9
2P	88.8	85.5	7B	117.5	109.4
2C	100.7	88	7C	107.6	137.3
2S	102.9	89.3	7S	124.8	138.8
3U	117.2	89	X1	-	142.9
3P	116.1	97	X4	-	143
3B	116.7	57.5	X2	-	141
3C	113	102	X3	-	94.3
3S	105.7	99.9	X5	-	134.5
4U	121.2	98	8U	116.3	110
4P	123.6	105.9	8P	121.3	122.3
4B	124.6	88.9	8B	95.3	122.7
4C	123.3	106.5	8C	115.3	110.9
4S	115.6	102.3	8S	115.3	124
5U	128.8	104.8	9U	53.1	70.1
5P	129.3	111.4	9P	71.4	72.7
5B	125.1	112.9	9B	80.1	76.2
5C	126.8	113	9C	83.2	83.6
5S	116.	106.6	9S	88	91.9
E1	88.6	94.3			
E2	102.7	85.9			
E3	93.8	-			

Table 3.3: Uncertainties for the stationary wall data measured quantities with 21:1 odds

$U/U_{ref}$	$\pm 2.05E - 03$	$\overline{u^2 v}/U_{ref}^3$	$\pm 2.37E - 07$
$V/U_{ref}$	$\pm 4.33E - 03$	$\overline{u^2 w}/U_{ref}^3$	$\pm 4.94E - 07$
$W/U_{ref}$	$\pm 3.29E - 03$	$\overline{v^2 w}/U_{ref}^3$	$\pm 3.77E - 06$
$\overline{u^2}/U_{ref}^2$	$\pm 1.15E - 04$	$\overline{uv^2}/U_{ref}^3$	$\pm 7.84E - 07$
$\overline{v^2}/U_{ref}^2$	$\pm 1.21E - 04$	$\overline{uw^2}/U_{ref}^3$	$\pm 4.25E - 07$
$\overline{w^2}/U_{ref}^2$	$\pm 1.32E - 04$	$\overline{vw^2}/U_{ref}^3$	$\pm 3.18E - 06$
$\overline{uv}/U_{ref}^2$	$\pm 1.70E - 05$	$\overline{uvw}/U_{ref}^3$	$\pm 5.67E - 07$
$\overline{uw}/U_{ref}^2$	$\pm 1.56E - 05$	$\overline{u^3}/U_{ref}^3$	$\pm 9.98E - 06$
$\overline{vw}/U_{ref}^2$	$\pm 1.24E - 04$	$\overline{v^3}/U_{ref}^3$	$\pm 8.66E - 06$
		$\overline{w^3}/U_{ref}^3$	$\pm 7.45E - 06$

Table 3.4: Test matrix with stationary endwall(1.65%)

<i>Profile</i>	<i>X (cm)</i>	<i>Z (cm)</i>	<i>Profile</i>	<i>X (cm)</i>	<i>Z (cm)</i>
UU	-4.572	-11.760	E1	2.474	-19.431
UB	-4.572	-12.573	E2	2.474	-20.168
UD	-4.572	-13.310	E3	2.474	-20.625
1U	0.119	-10.592	6U	3.724	-18.288
1B	0.119	-11.748	6P	3.724	-18.745
1D	0.119	-12.852	6B	3.724	-19.228
2U	0.552	-12.065	6C	3.724	-19.736
2P	0.552	-12.827	6S	3.724	-20.955
2C	0.552	-13.399	7U	5.791	-21.869
2S	0.552	-14.135	7P	5.791	-22.225
3U	1.241	-13.310	7B	5.791	-22.657
3P	1.241	-14.288	7C	5.791	-23.165
3B	1.241	-14.859	7S	5.791	-24.130
3C	1.241	-15.319	8U	8.966	-25.578
3S	1.241	-15.900	8P	8.966	-26.721
4U	1.656	-14.757	8B	8.966	-27.140
4P	1.656	-15.088	8C	8.966	-27.686
4B	1.656	-15.494	8S	8.966	-28.194
4C	1.656	-15.824	9U	13.792	-33.274
4S	1.656	-16.510	9P	13.792	-32.995
5U	2.474	-16.205	9B	13.792	-32.741
5P	2.474	-16.662	9C	13.792	-32.588
5B	2.474	-17.094	9S	13.792	-31.242
5C	2.474	-17.510			
5S	2.474	-18.339			

Table 3.5: Test matrix with stationary endwall(3.30%)

<i>Profile</i>	<i>X (cm)</i>	<i>Z (cm)</i>	<i>Profile</i>	<i>X (cm)</i>	<i>Z (cm)</i>
UU	-4.572	-11.760	6U	3.724	-17.780
UB	-4.572	-12.446	6P	3.724	-18.669
UD	-4.572	-13.310	6B	3.724	-19.228
1U	0.119	-10.541	6C	3.724	-19.736
1B	0.119	-11.748	6S	3.724	-20.955
1D	0.119	-13.322	7U	5.791	-21.133
2U	0.552	-12.027	7P	5.791	-22.327
2P	0.552	-12.827	7B	5.791	-23.114
2C	0.552	-13.399	7C	5.791	-23.673
2S	0.552	-14.135	7S	5.791	-24.130
3U	1.241	-13.310	X1	5.791	-25.705
3P	1.241	-14.288	X4	5.791	-26.441
3B	1.241	-14.859	X2	5.791	-26.924
3C	1.241	-15.319	X3	5.791	-27.559
3S	1.241	-15.900	X5	5.791	-28.283
4U	1.656	-14.326	8U	8.966	-25.578
4P	1.656	-15.189	8P	8.966	-26.721
4B	1.656	-15.596	8B	8.966	-27.305
4C	1.656	-16.078	8C	8.966	-27.889
4S	1.656	-16.866	8S	8.966	-28.702
5U	2.474	-15.900	9U	13.792	-31.242
5P	2.474	-16.942	9P	13.792	-32.588
5B	2.474	-17.422	9B	13.792	-32.741
5C	2.474	-17.978	9C	13.792	-32.995
5S	2.474	-18.669	9S	13.792	-33.274
E1	2.474	-19.431			
E2	2.474	-20.168			

Table 3.6: Pressure and its gradient with stationary endwall(1.65%)

<i>Profile</i>	$C_p$	$\partial C_p / \partial X$	$\partial C_p / \partial Z$	<i>Profile</i>	$C_p$	$\partial C_p / \partial X$	$\partial C_p / \partial Z$
UU	-	-	-	E1	-0.3817	-0.119	-0.050
UB	-	-	-	E2	-0.3253	-0.156	-0.045
UD	-	-	-	E3	-0.2957	-0.175	-0.056
1U	0.1863	0.018	-0.014	6U	0.2779	0.281	0.179
1B	0.1959	0.020	0.026	6P	0.1723	0.420	0.294
1D	0.1376	0.073	0.072	6B	-0.012	0.489	0.328
2U	0.1963	0.020	0.048	6C	-0.1119	0.433	0.212
2P	0.1692	0.067	0.039	6S	-0.3595	0.097	0.085
2C	0.1414	0.096	0.060	7U	0.2657	0.407	0.241
2S	0.053	0.085	0.116	7P	0.1671	0.532	0.366
3U	0.2174	0.077	0.023	7B	-0.0083	0.517	0.339
3P	0.1497	0.142	0.095	7C	-0.2528	0.488	0.160
3B	0.0635	0.171	0.101	7S	-0.3282	-0.006	0.149
3C	0.0164	0.176	0.147	8U	0.4642	0.028	0.000
3S	-0.1032	0.052	0.156	8P	0.3947	0.132	0.210
4U	0.1948	0.160	0.098	8B	0.2151	0.488	0.368
4P	0.1741	0.185	0.154	8C	-0.0161	0.564	0.343
4B	0.1249	0.225	0.223	8S	-0.1343	0.226	0.093
4C	0.0001	0.111	0.292	9U	0.4598	-0.017	0.013
4S	-0.2036	0.047	0.172	9P	0.4332	0.047	0.044
5U	0.1508	0.451	0.197	9B	0.4273	0.051	0.035
5P	0.0893	0.403	0.150	9C	0.4156	0.055	0.039
5B	-0.1007	0.409	0.314	9S	0.3971	0.056	0.021
5C	-0.2734	0.324	0.251				
5S	-0.4225	0.213	0.216				



Table 3.7: Pressure and its gradient with stationary endwall(3.30%)

<i>Profile</i>	$C_p$	$\partial C_p / \partial X$	$\partial C_p / \partial Z$	<i>Profile</i>	$C_p$	$\partial C_p / \partial X$	$\partial C_p / \partial Z$
UU	-	-	-	6U	0.2038	0.142	0.069
UB	-	-	-	6P	0.098	0.262	0.193
UD	-	-	-	6B	-0.0161	0.292	0.241
1U	0.1687	0.004	-0.010	6C	-0.1386	0.273	0.231
1B	0.1547	0.026	0.018	6S	-0.3208	-0.089	0.052
1D	0.1076	0.033	0.041	7U	0.2469	0.222	0.119
2U	0.159	0.022	0.023	7P	-0.007	0.501	0.264
2P	0.1423	0.039	0.020	7B	-0.2615	0.544	0.342
2C	0.1274	0.048	0.032	7C	-0.4309	0.372	0.176
2S	0.0939	0.055	0.055	7S	-0.4727	0.267	0.065
3U	0.1688	0.052	0.019	X1	-0.5053	0.074	-0.036
3P	0.1358	0.074	0.048	X4	-0.4614	-0.005	-0.061
3B	0.0896	0.090	0.059	X2	-0.4156	-0.044	-0.056
3C	0.0568	0.086	0.074	X3	-0.3916	-0.097	-0.056
3S	0.0383	0.066	0.042	X5	-0.3096	-0.196	-0.101
4U	0.1647	0.075	0.033	8U	-0.3218	-0.250	-0.111
4P	0.1247	0.119	0.081	8P	0.3218	0.250	0.111
4B	0.0902	0.094	0.069	8B	0.2568	0.309	0.115
4C	0.0436	0.062	0.079	8C	0.1837	0.243	0.089
4S	0.0032	0.022	0.053	8S	0.0937	0.125	0.054
5U	0.1707	0.153	0.057	9U	-0.4292	-0.024	-0.008
5P	0.0659	0.191	0.138	9P	0.4292	0.024	0.008
5B	0.0115	0.135	0.137	9B	0.429	0.028	0.009
5C	-0.0645	0.084	0.112	9C	0.4253	0.034	0.010
5S	-0.1147	-0.038	0.060	9S	0.4207	0.039	0.011
E1	-0.1453	-0.087	-0.005				
E2	-0.1377	-0.144	-0.029				

Table 3.8:  $U_\tau$  and  $y_{shift}$  for stationary endwall(1.65%)

<i>Profile</i>	$U_\tau$	$y_{shift}$	$U_\tau$	$y_{shift}$	<i>Profile</i>	$U_\tau$	$y_{shift}$	$U_\tau$	$y_{shift}$
	(m/s)	( $\mu m$ )	(m/s)	( $\mu m$ )		(m/s)	( $\mu m$ )	(m/s)	( $\mu m$ )
UU	0.90	25	-	-	E1	0.95	-30	0.90	-29
UB	1.13	17	-	-	E2	0.82	17	0.88	8
UD	1.08	31	-	-	E3	0.96	33	0.94	31
1U	0.90	-11	0.92	-13	6U	1.54	34	1.88	16
1B	1.11	36	1.13	35	6P	1.67	-6	1.79	-8
1D	0.96	9	1.03	4	6B	1.73	-11	1.76	-11
2U	0.90	0	0.99	-9	6C	1.52	-6	1.58	-6
2P	1.23	-20	1.27	-21	6S	1.49	8	1.67	2
2C	1.00	21	1.10	14	7U	1.13	3	1.25	3
2S	1.06	20	1.12	17	7P	2.33	-8	2.75	-13
3U	1.23	-4	1.33	-9	7B	2.36	-27	2.43	-30
3P	1.27	2	1.33	2	7C	1.74	-20	1.94	-22
3B	0.98	11	0.95	24	7S	1.19	6	1.18	10
3C	1.16	-9	1.31	-15	8U	1.07	6	0.96	17
3S	1.25	-1	1.40	-7	8P	1.67	-4	1.73	-5
4U	1.15	-3	1.21	-5	8B	1.70	-33	-1.80	-30
4P	1.51	-4	1.72	-10	8C	1.76	21	2.08	8
4B	1.18	-4	1.25	-4	8S	0.98	18	1.17	5
4C	1.36	-3	1.45	-5	9U	0.87	47	0.89	45
4S	1.27	11	1.46	2	9P	1.04	22	1.14	12
5U	1.00	13	1.30	-2	9B	0.96	38	0.90	49
5P	1.33	-5	1.43	-7	9C	1.20	43	1.41	22
5B	1.84	-20	2.02	-22	9S	1.18	27	1.33	15
5C	1.26	-7	1.33	-6					
5S	1.48	7	1.61	3					

Table 3.9:  $U_\tau$  and  $y_{shift}$  for stationary endwall(3.30%)

<i>Profile</i>	$U_\tau$	$y_{shift}$	$U_\tau$	$y_{shift}$	<i>Profile</i>	$U_\tau$	$y_{shift}$	$U_\tau$	$y_{shift}$
	(m/s)	( $\mu m$ )	(m/s)	( $\mu m$ )		(m/s)	( $\mu m$ )	(m/s)	( $\mu m$ )
UU	1.06	16	-	-	6U	0.94	29	1.02	24
UB	-4.91	-12.51	-	-	6P	1.10	30	1.24	26
UD	0.95	20	-	-	6B	1.35	8	1.57	1
1U	0.88	26	0.95	17	6C	1.16	-2	1.66	6
1B	0.88	86	0.90	85	6S	1.40	14	1.57	2
1D	1.02	-10	1.06	-12	7U	1.08	85	1.35	55
2U	0.91	7	1.00	-1	7P	1.53	32	1.83	20
2P	1.06	-21	1.19	-28	7B	1.56	-35	1.91	-53
2C	1.15	5	1.23	1	7C	1.92	18	2.13	11
2S	1.00	37	1.19	19	7S	1.66	3	1.74	1
3U	0.79	48	0.77	55	X1	1.70	35	1.87	24
3P	0.86	27	0.80	39	X4	1.80	-6	1.62	5
3B	1.05	-51	1.01	-49	X2	1.51	24	1.63	16
3C	1.11	15	1.26	5	X3	1.04	12	0.81	32
3S	1.02	79	1.18	56	X5	0.77	9	0.66	10
4U	0.87	28	0.84	33	8U	1.05	31	0.94	44
4P	0.94	22	1.03	16	8P	0.96	9	1.09	3
4B	1.05	-25	1.06	-25	8B	1.13	25	1.32	13
4C	1.25	40	1.28	41	8C	1.18	-9	1.22	-8
4S	1.04	26	1.07	25	8S	1.15	11	1.26	6
5U	0.97	1	1.02	0	9U	0.61	102	0.59	110
5P	1.04	2	1.21	-6	9P	0.87	47	0.92	16
5B	1.40	20	1.48	17	9B	0.70	30	0.59	53
5C	1.14	18	1.16	19	9C	0.93	6	0.90	7
5S	1.31	15	1.29	18	9S	0.80	14	0.82	11
E1	1.07	19	1.18	9					
E2	1.11	23	1.25	11					

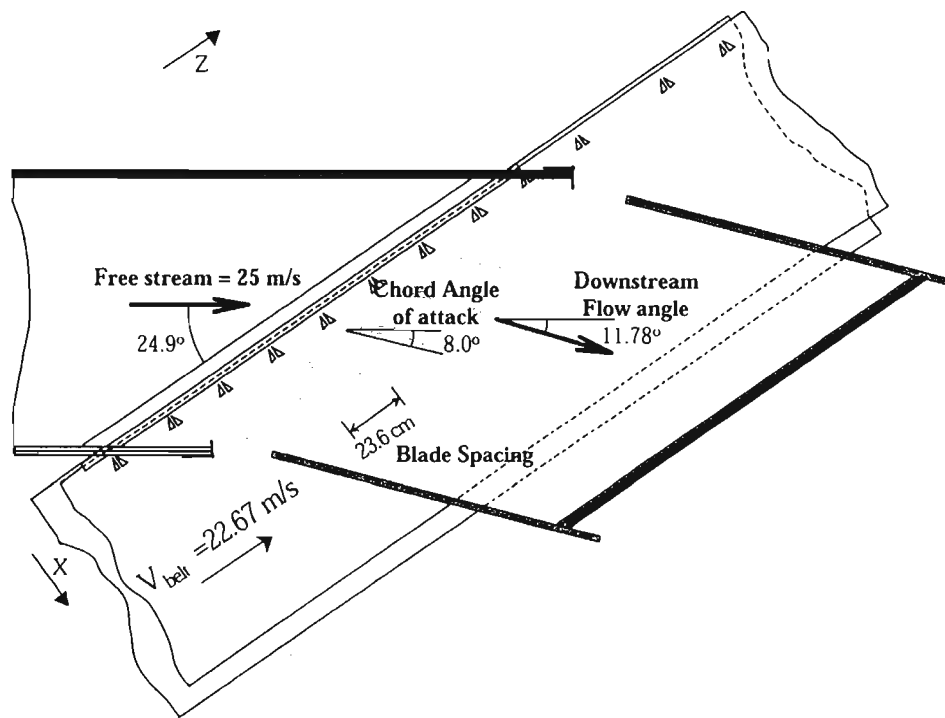


Figure 3.1: Setup of Compressor Cascade Wind Tunnel from Kuhl (2001)

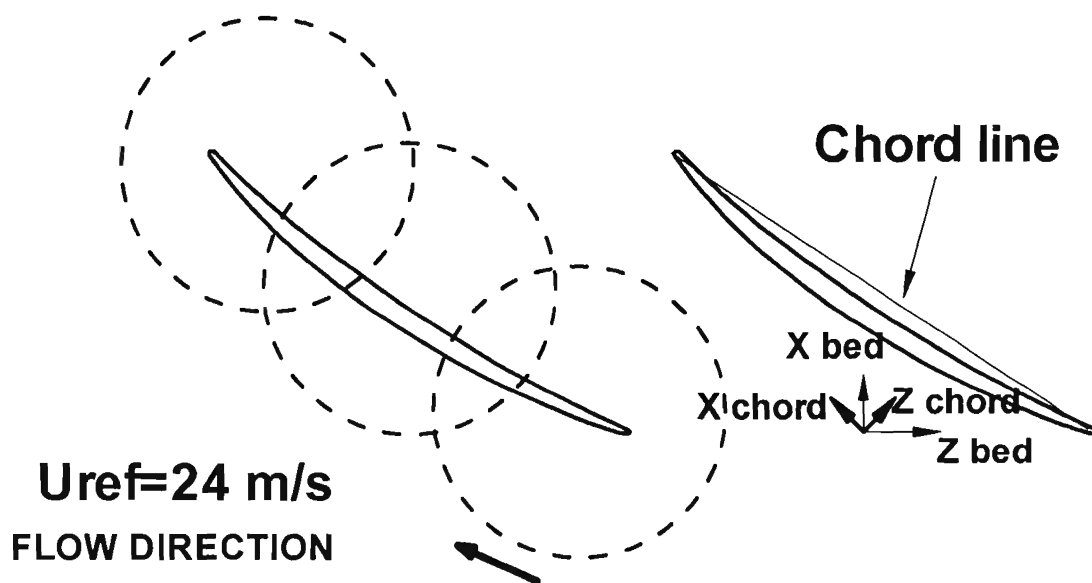


Figure 3.2: Coordinate systems and multiple window locations in the test section

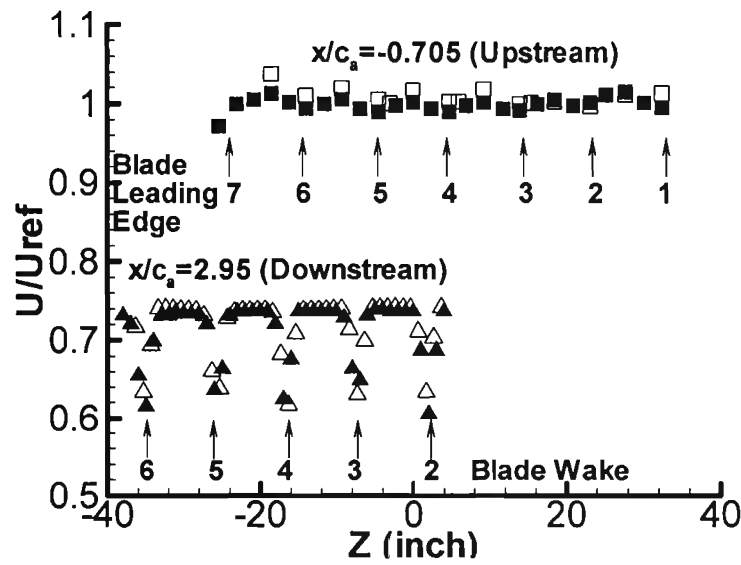
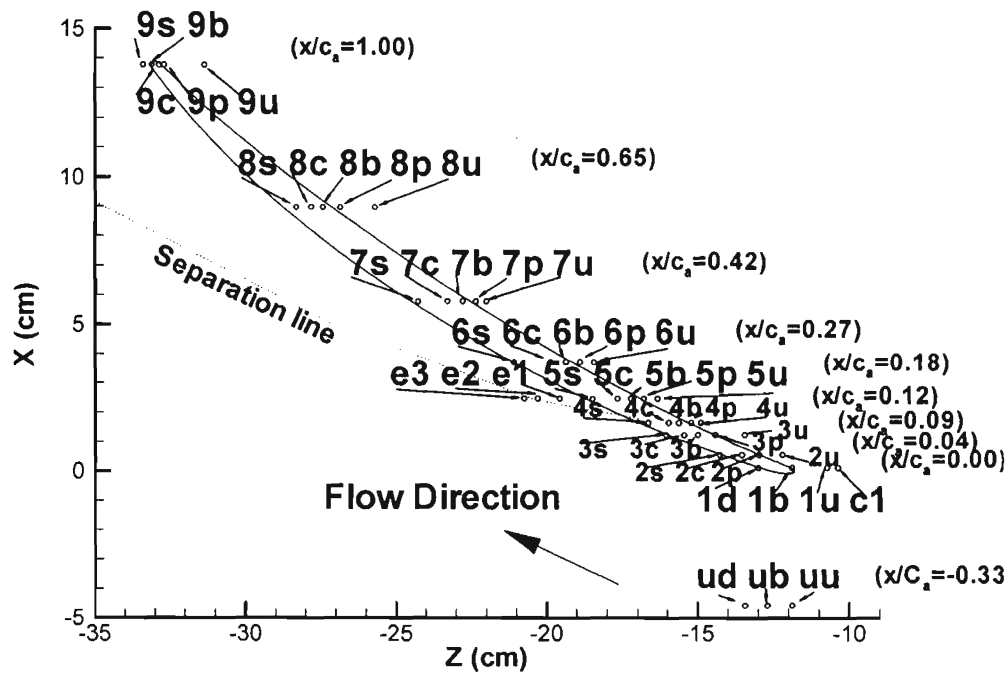
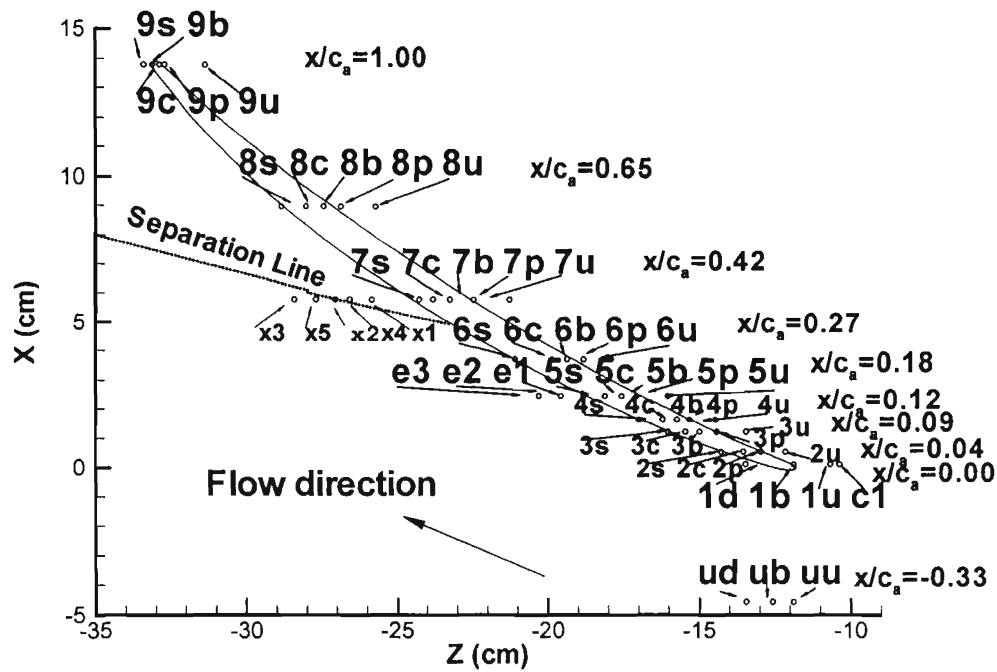


Figure 3.3: Velocities at tunnel half height upstream ( $x/c_a = -0.705$ ) and downstream ( $x/c_a = 2.95$ ) of blade row for stationary wall experiments in bed co-ordinates; arrows show location of given blade number; for this study:  $\square$ ,  $x/c_a = -0.705$ ;  $\triangle$ ,  $x/c_a = 2.95$ ; From Kuhl (2001):  $\blacksquare$ ,  $x/c_a = -0.705$ ;  $\blacktriangle$ ,  $x/c_a = 2.95$ .



(a) 1.65%



(b) 3.30%

Figure 3.4: Test matrices for 1.65% and 3.30%

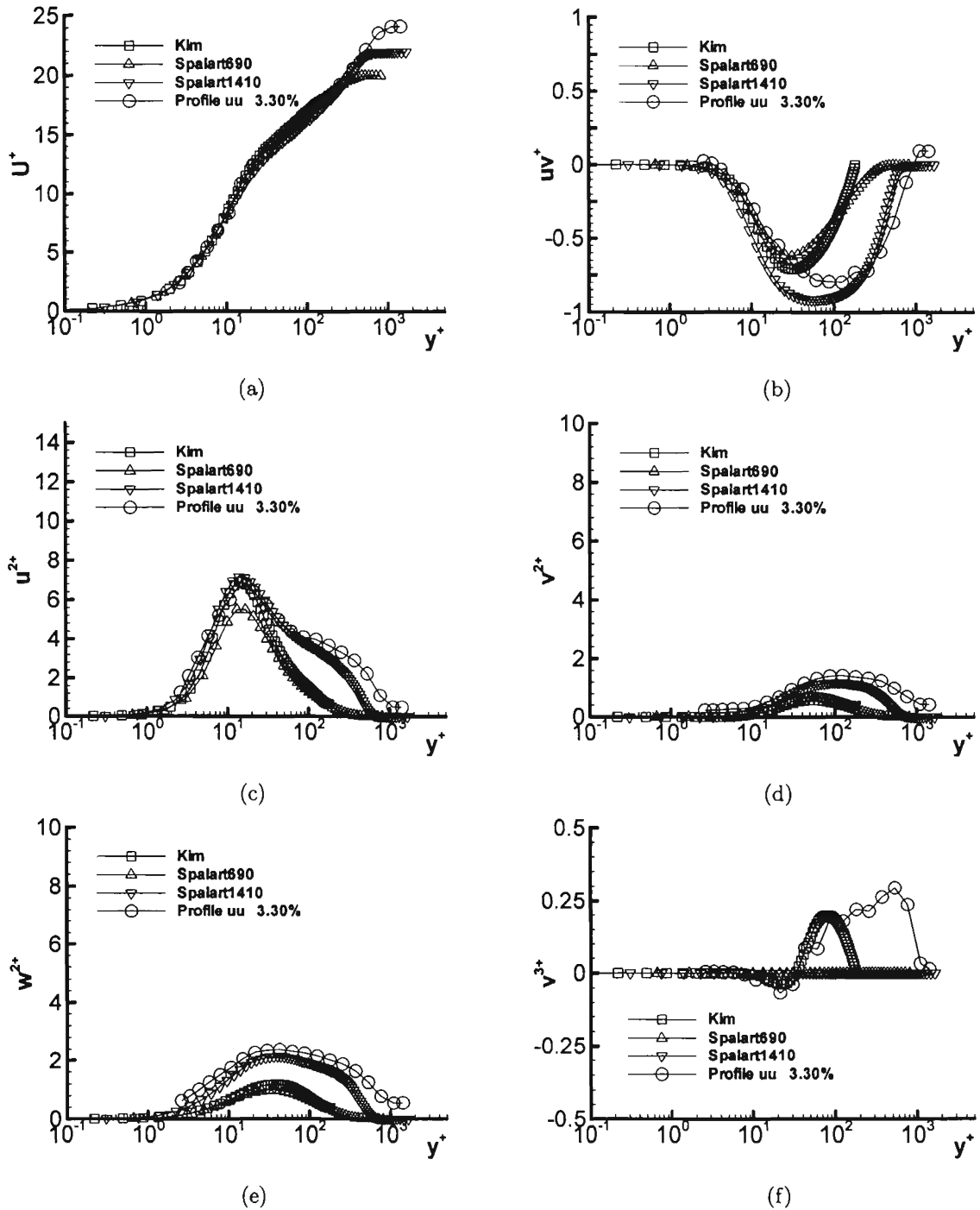
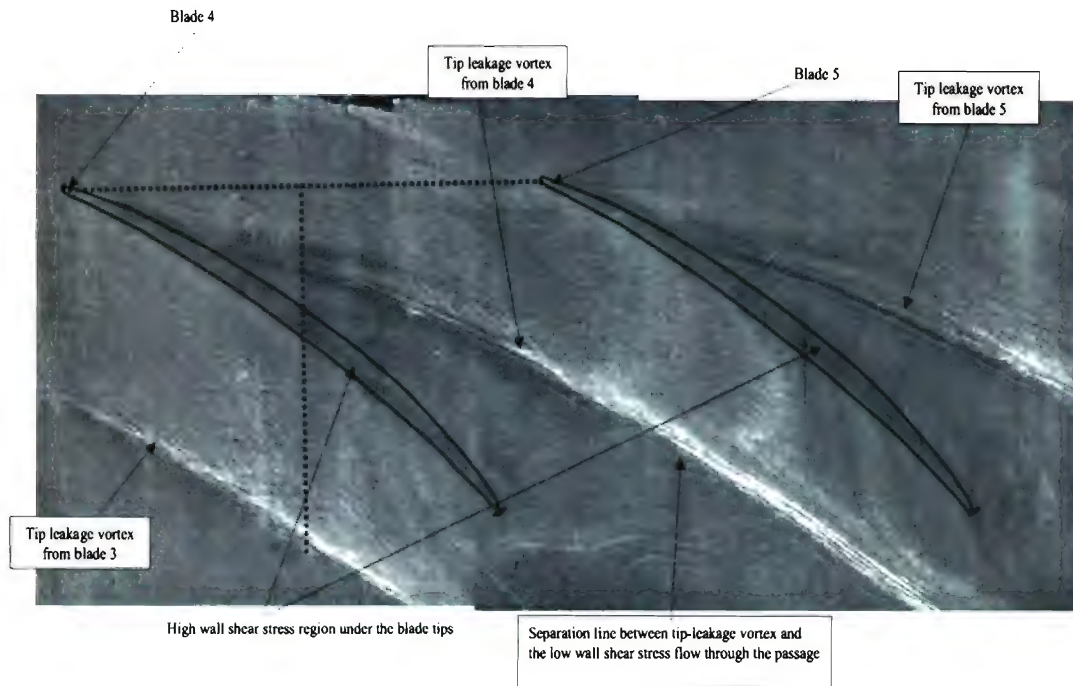
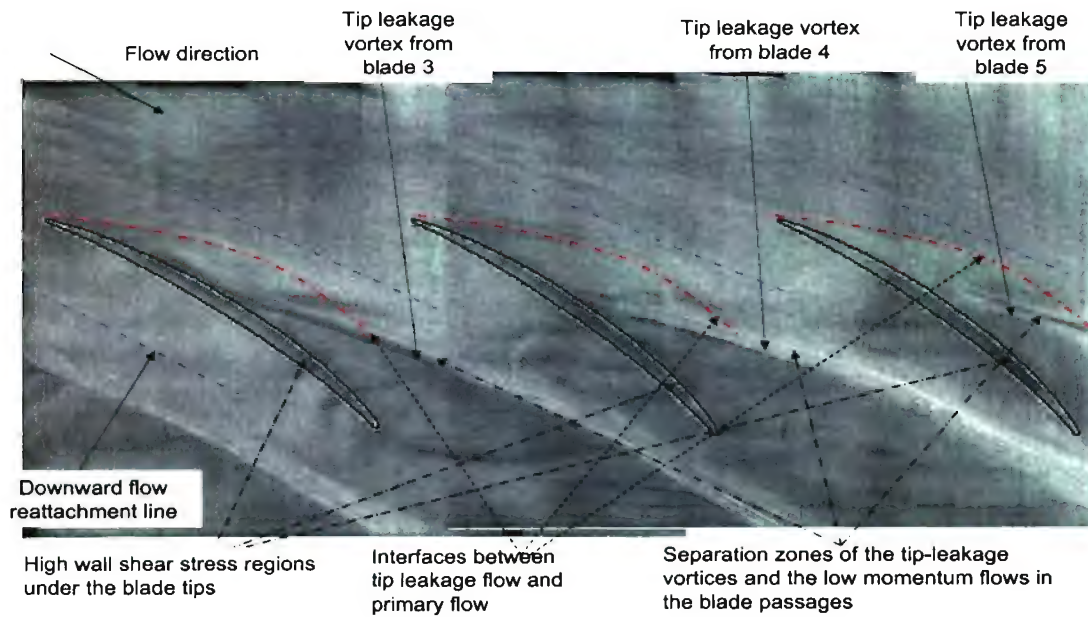


Figure 3.5: Validation with direct numerical simulation for the LDV measurement at profile  $uu$  of 3.30% tip gap in the free-stream coordinate system





(a) 1.65% (Muthanna, 2002)



(b) 3.30%

Figure 3.6: Endwall oil flow visualizations for 1.65% and 3.30%

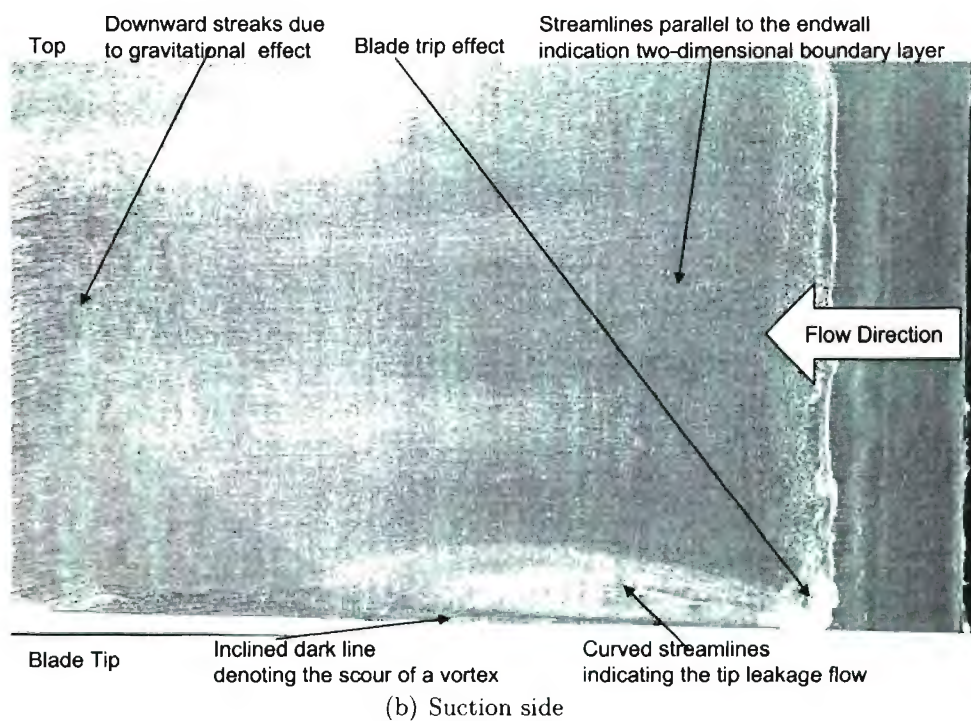
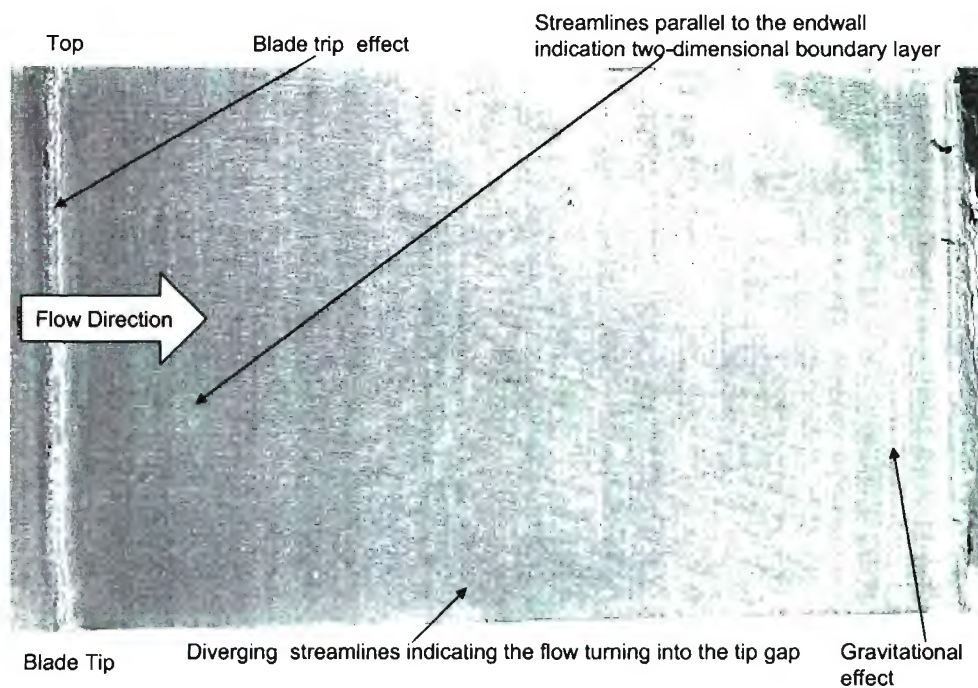


Figure 3.7: Blade surface oil flow visualizations for 1.65%



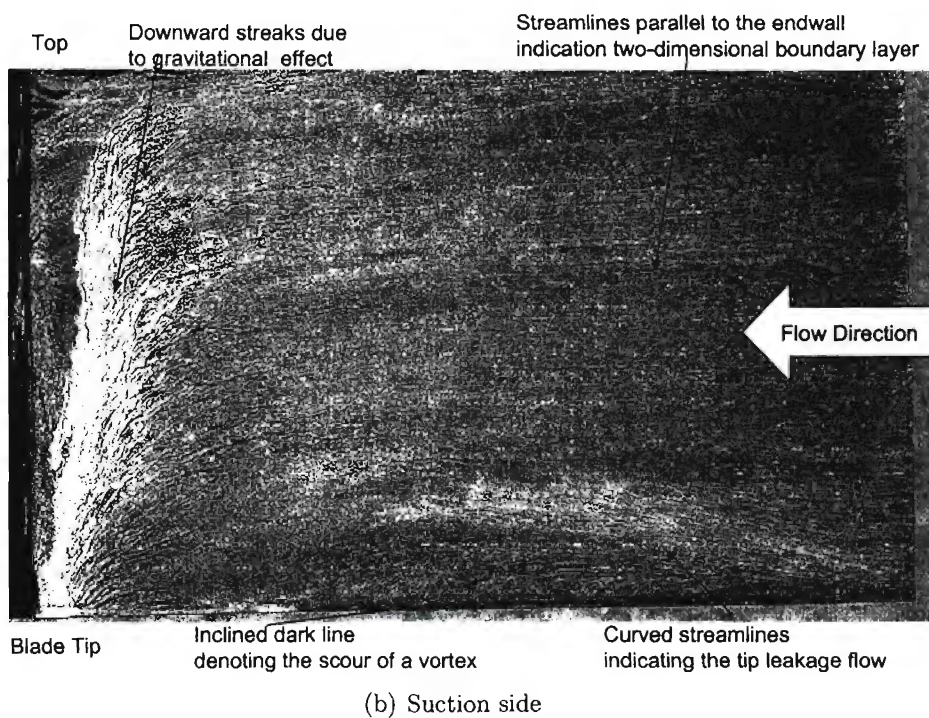
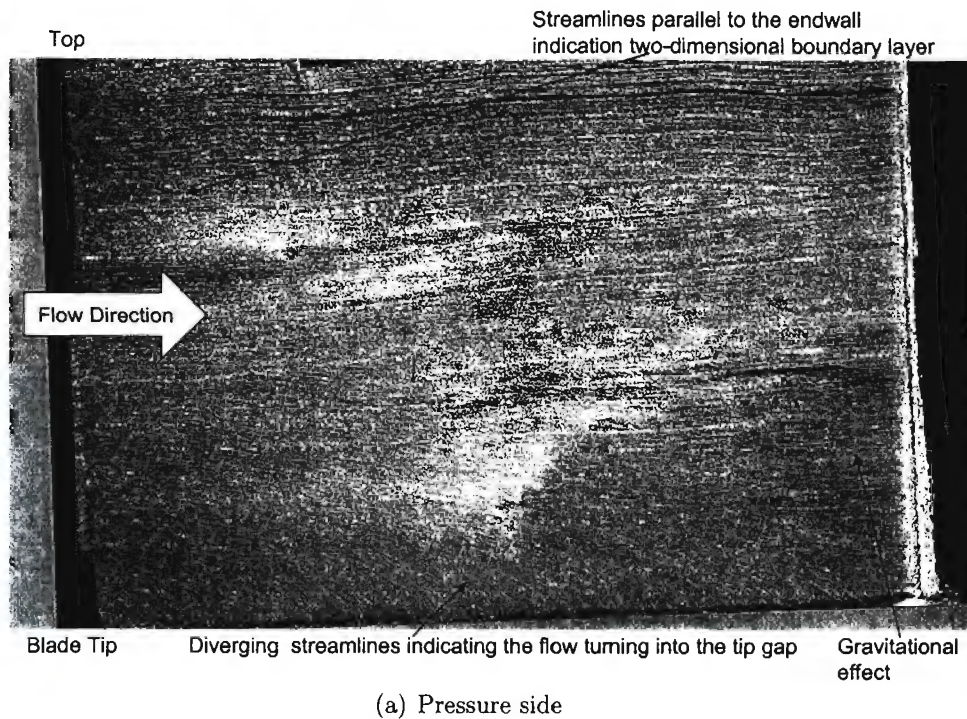


Figure 3.8: Blade surface oil flow visualizations for 3.30%

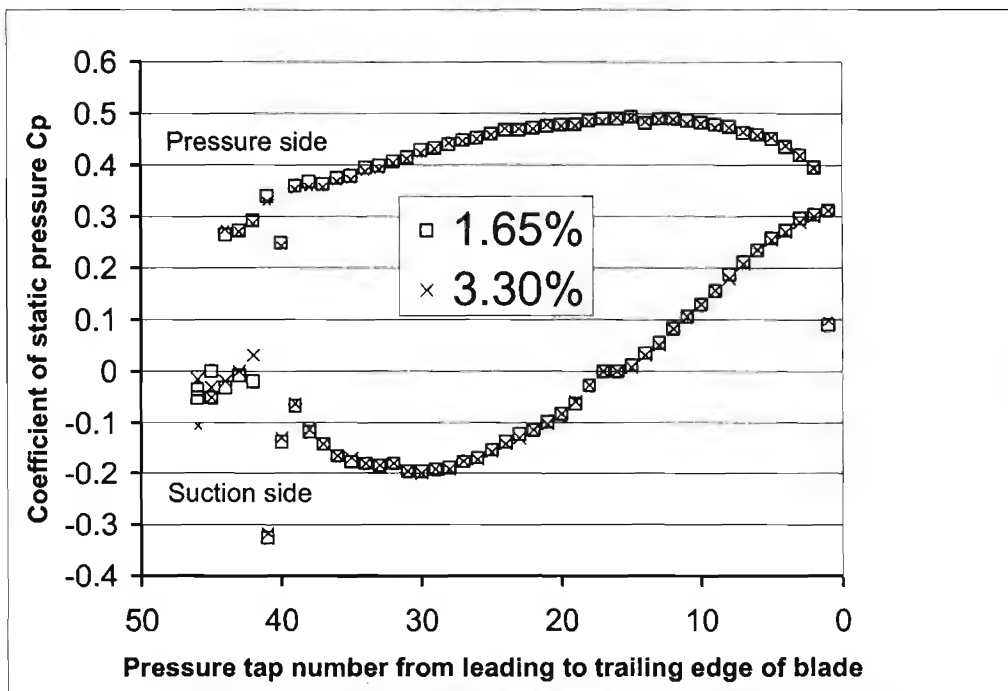
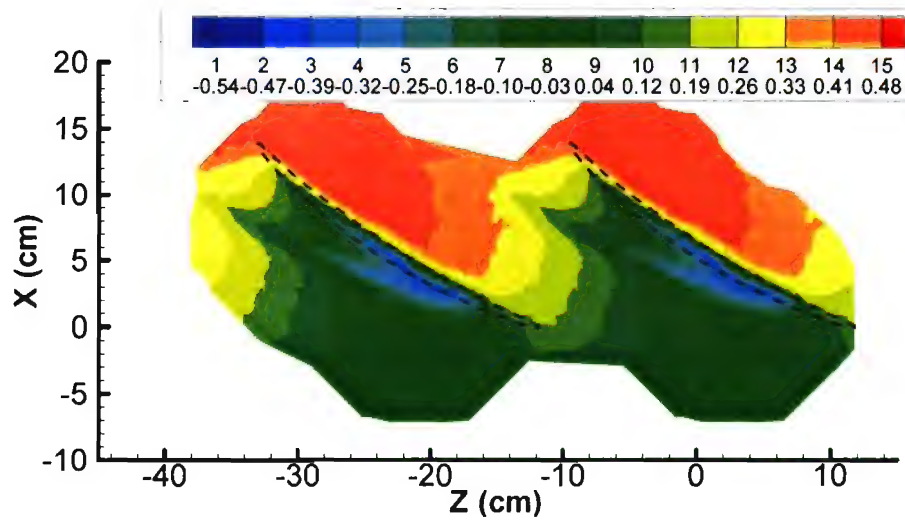
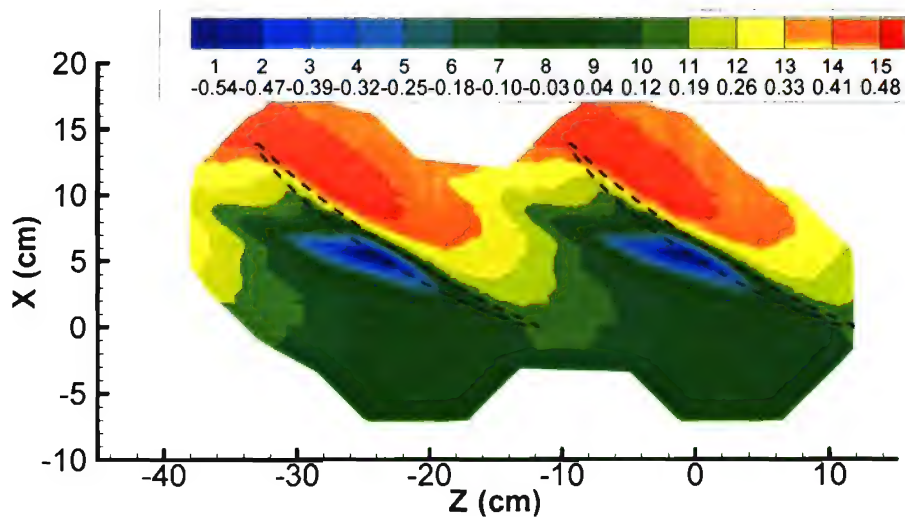


Figure 3.9: Mid-span pressure blade loading for 1.65% and 3.30%



(a) 1.65%



(b) 3.30%

Figure 3.10: Endwall static pressure distributions for 1.65% and 3.30%

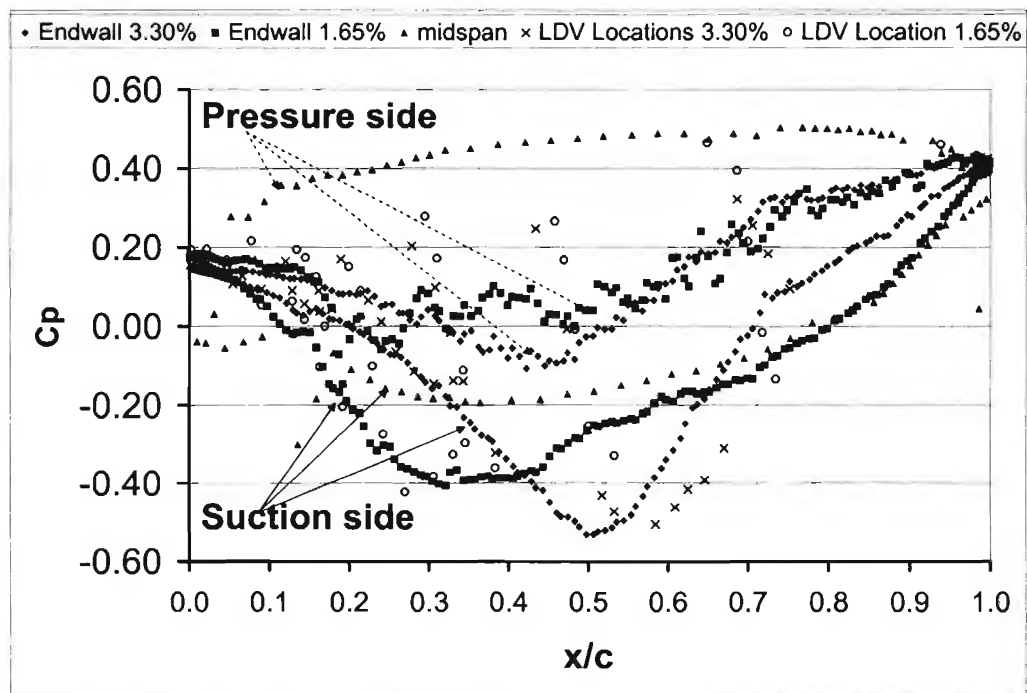


Figure 3.11: Static pressure  $C_p$  distribution of blade projection onto endwall in chord coordinate system

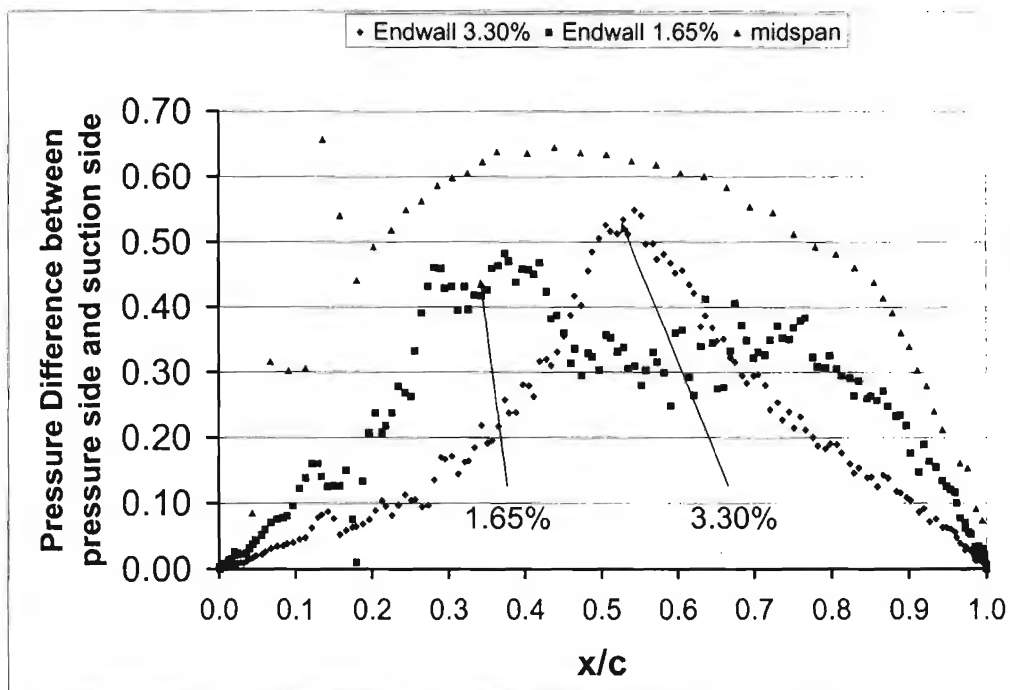


Figure 3.12: Static pressure difference  $\Delta C_p$  of mid-span and projection onto endwall in chord coordinate system

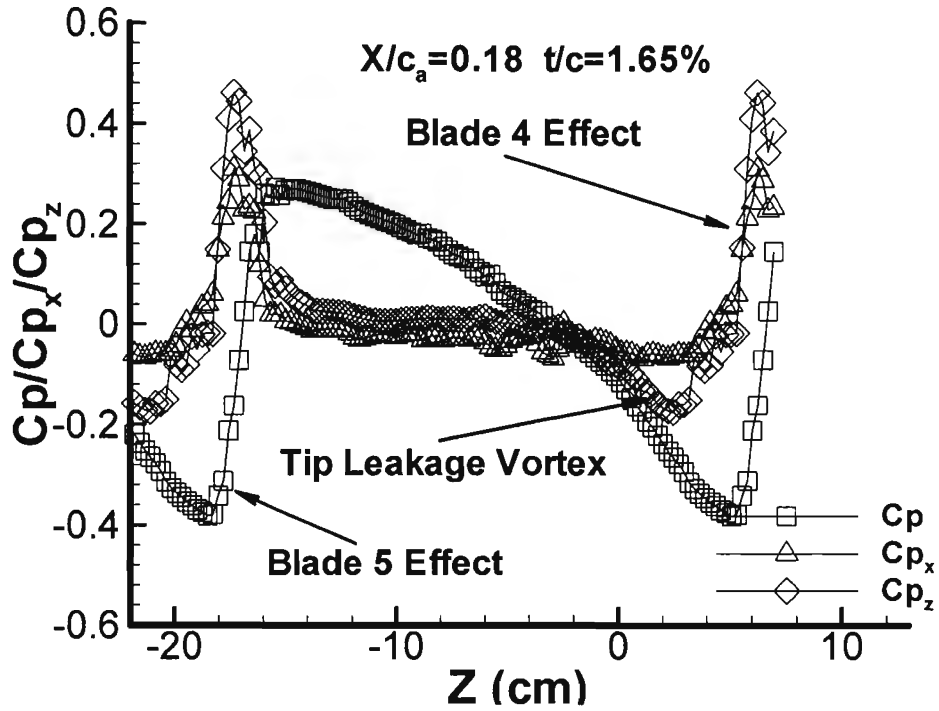
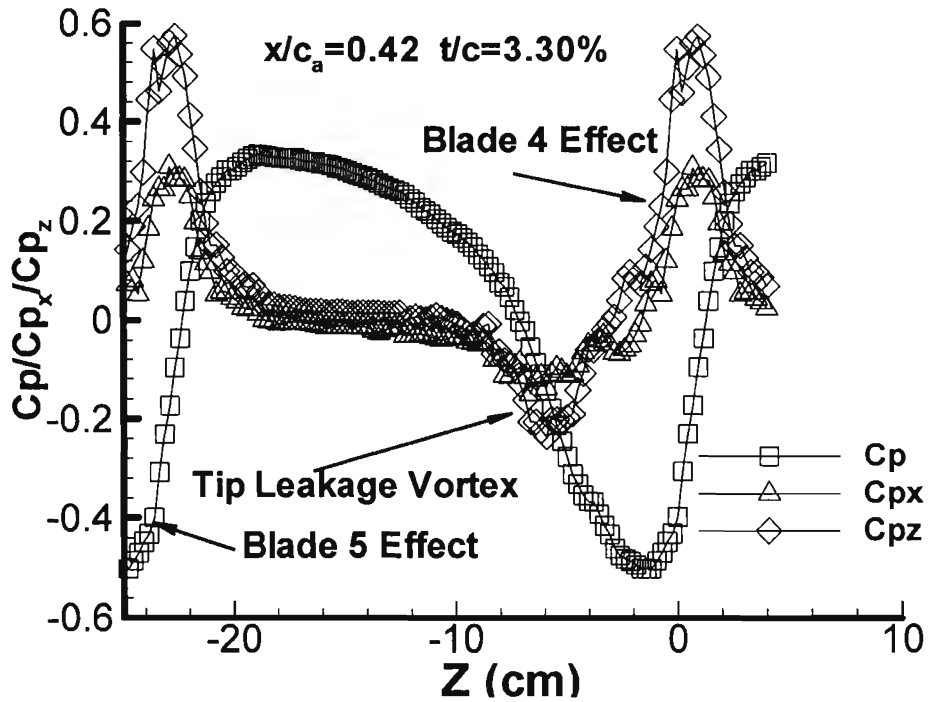
(a)  $x/c_a = 0.18$  1.65%(b)  $x/c_a = 0.42$  3.30%

Figure 3.13: Pressure and pressure gradient along  $x/c_a = 0.18$  for 1.65% and  $x/c_a = 0.42$  for 3.30% in the bed coordinate system



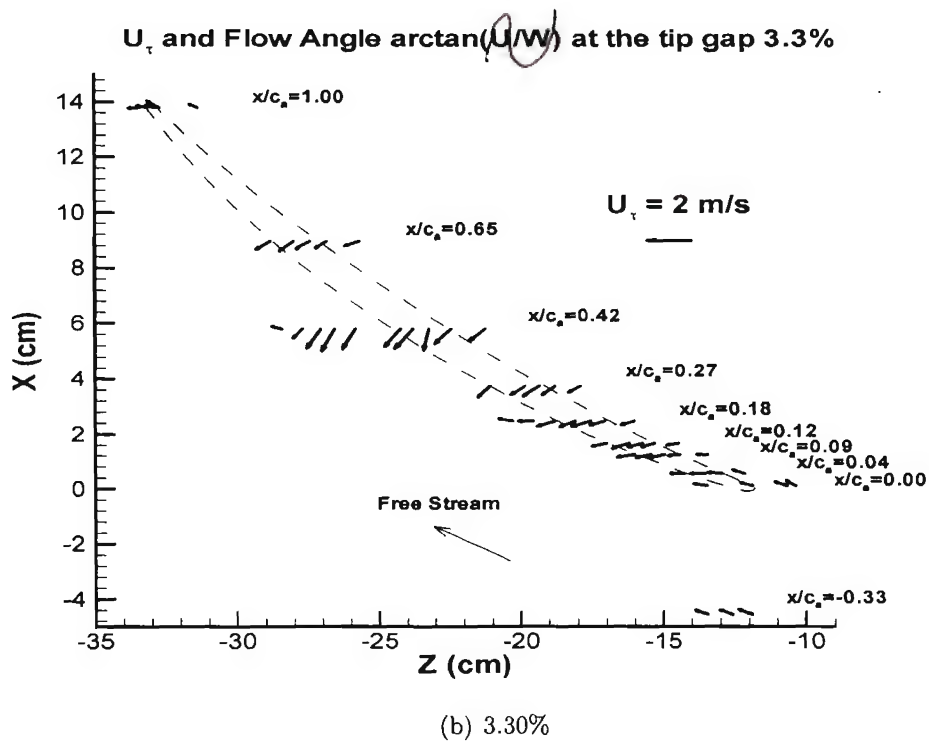
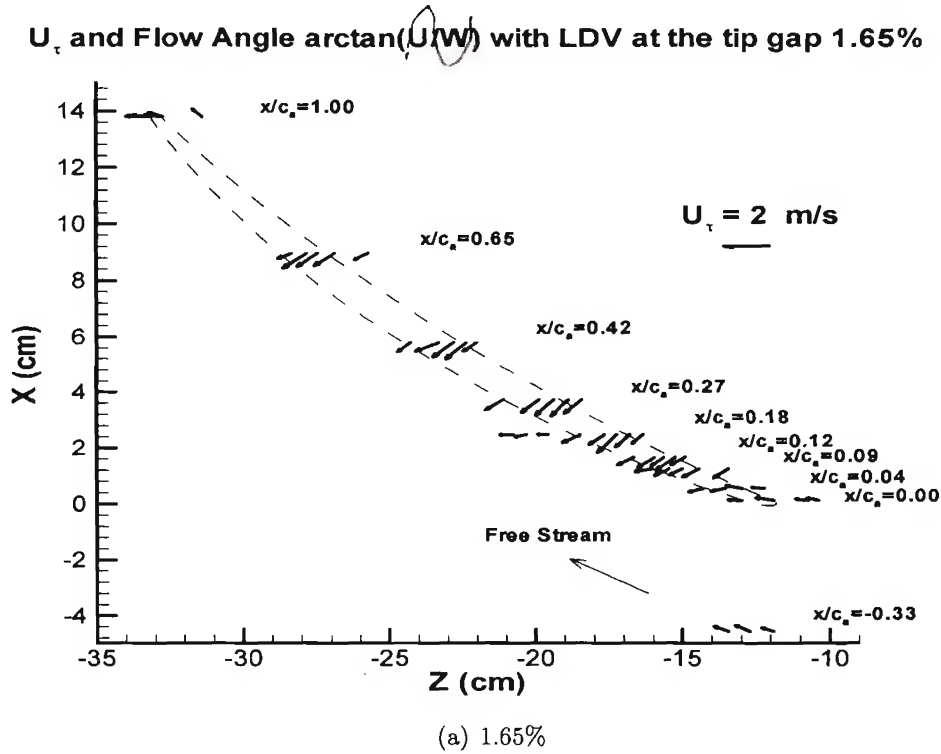


Figure 3.14: Skin friction velocity on endwall for 1.65% and 3.30%

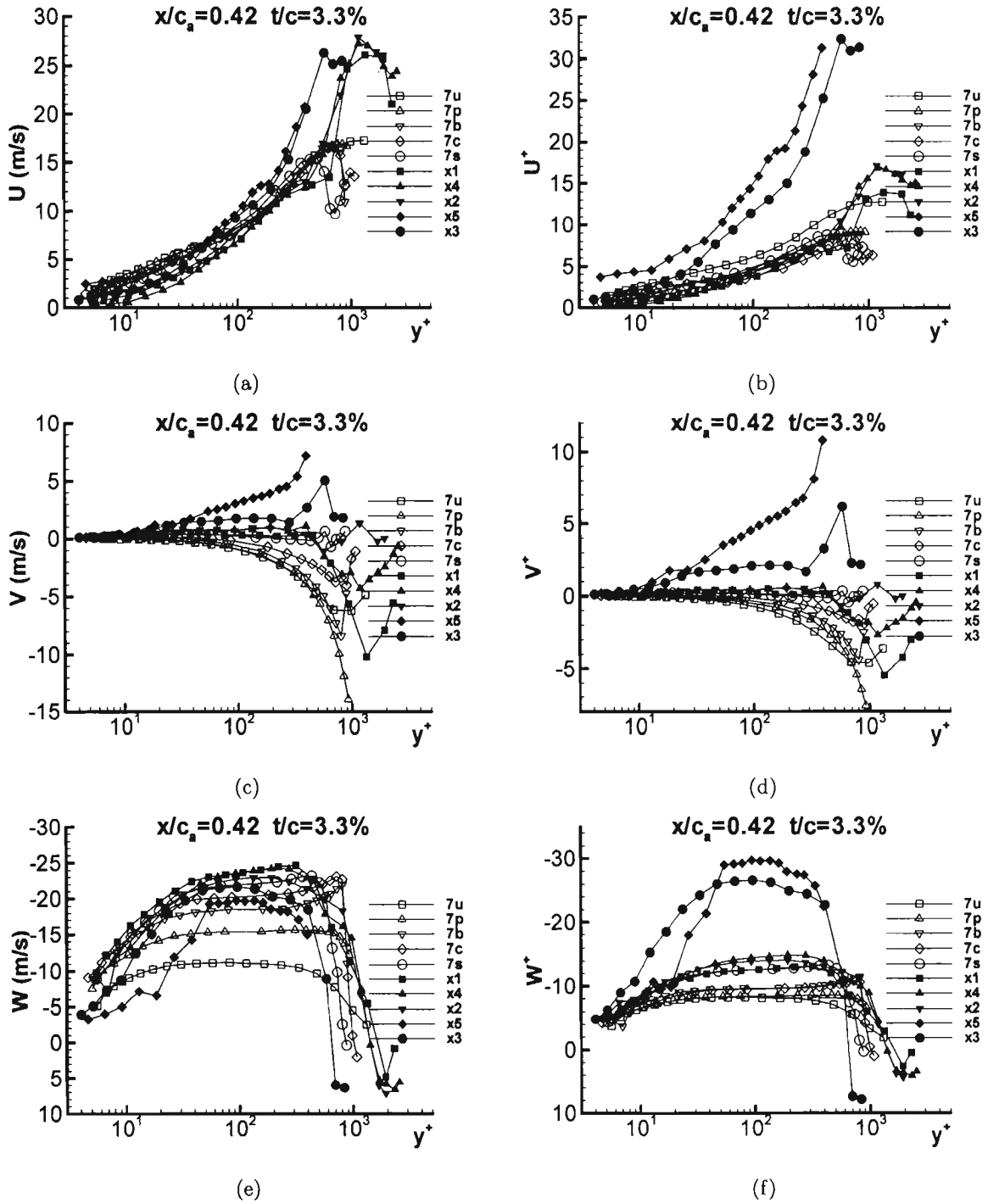
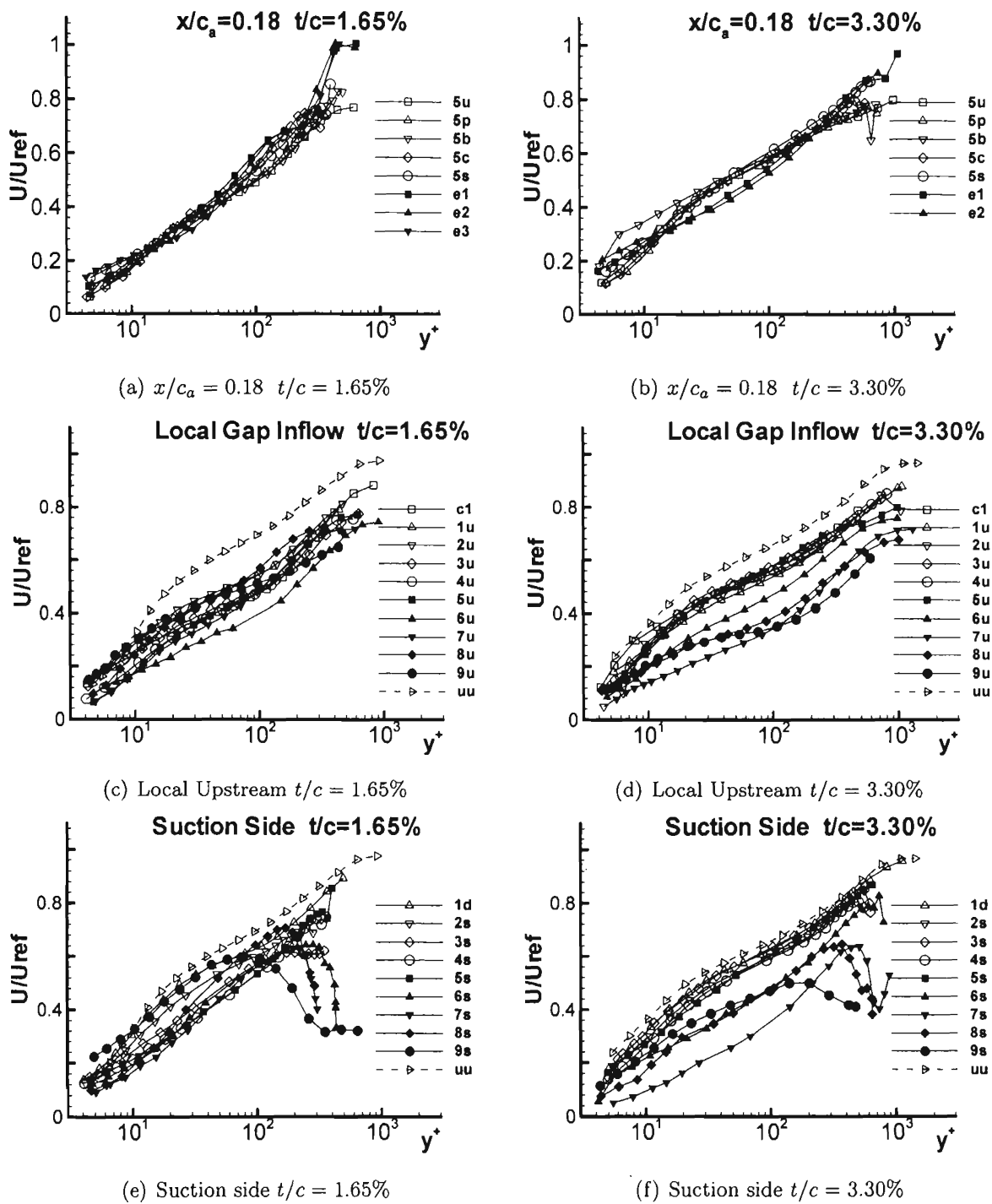
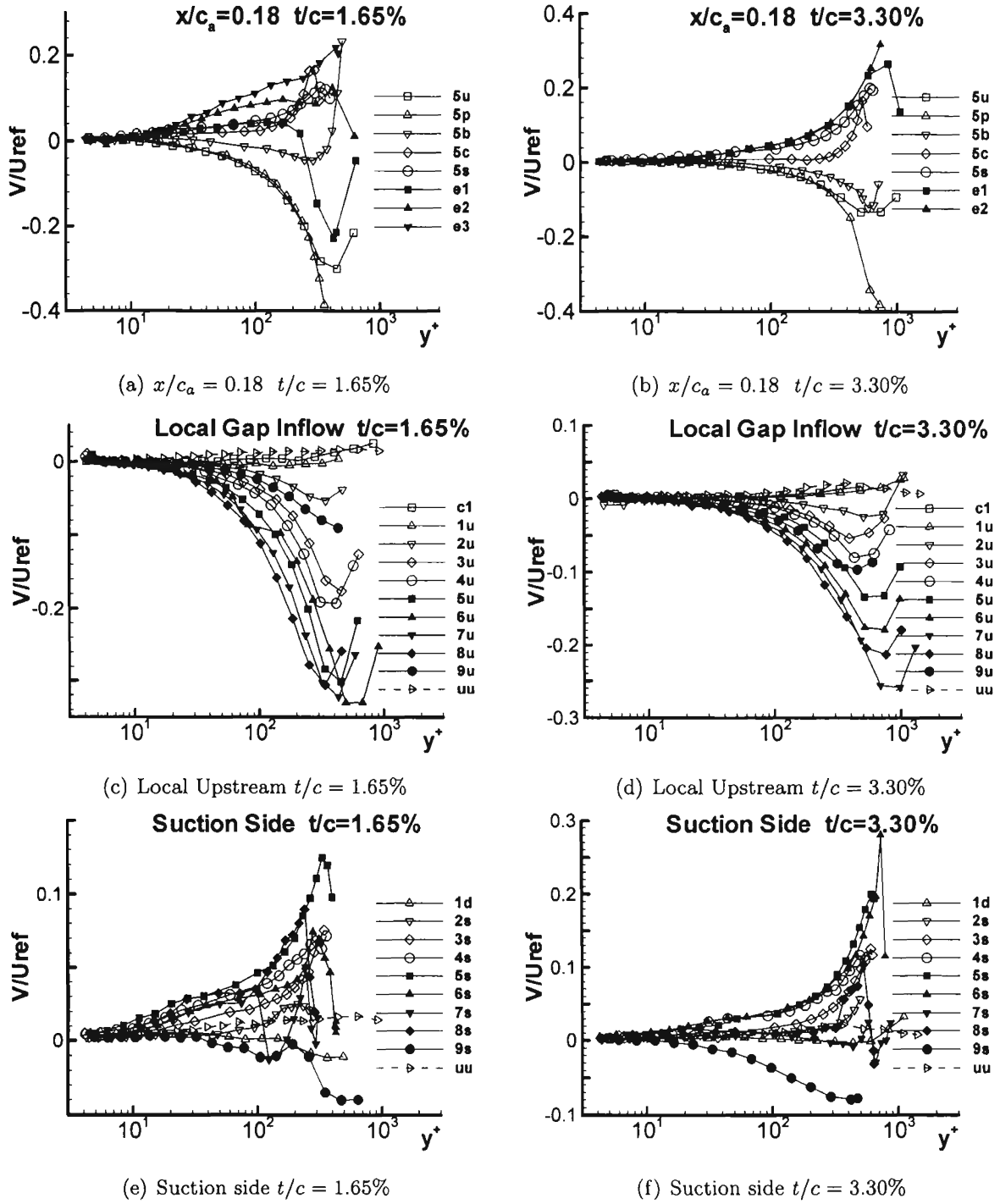
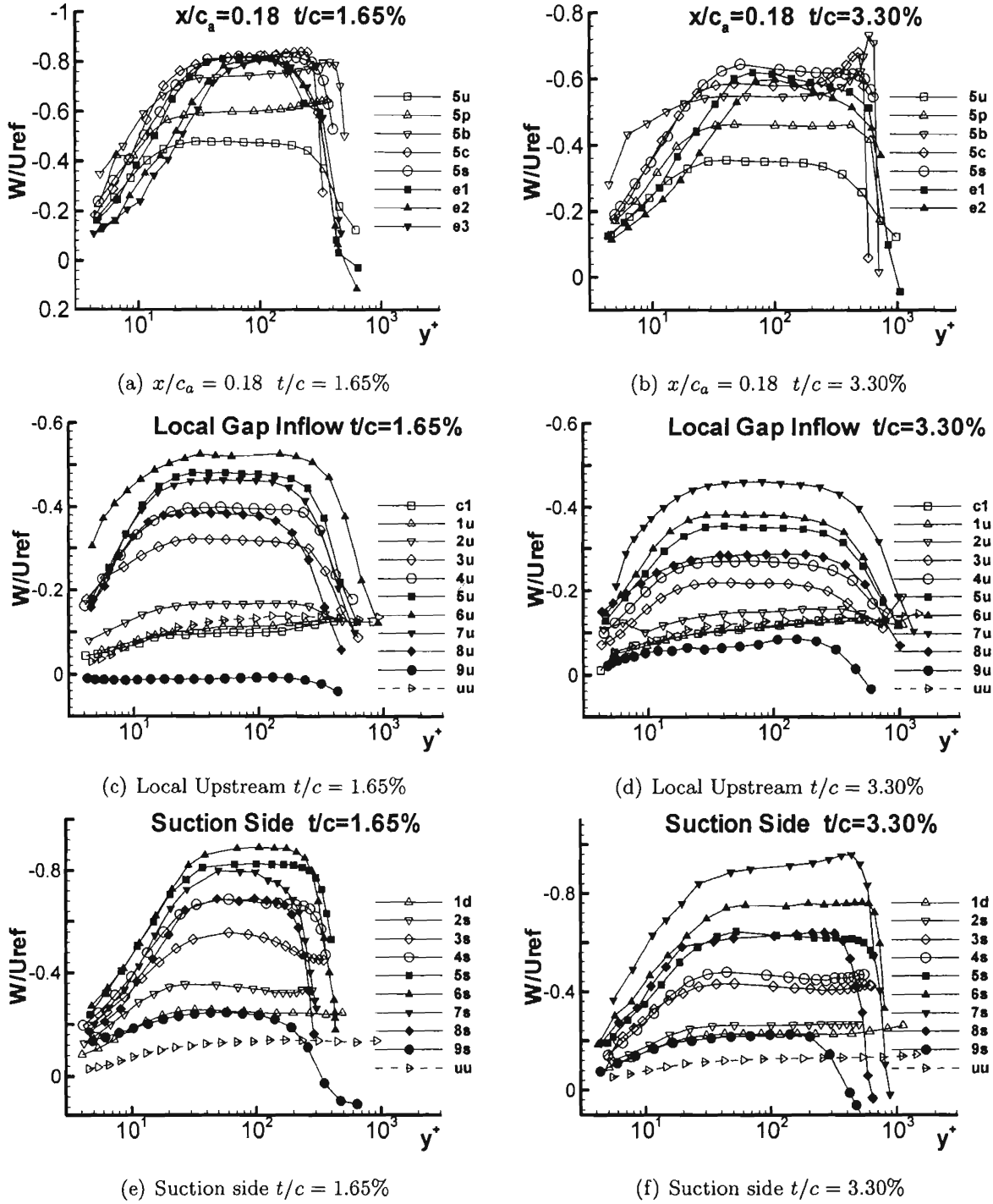
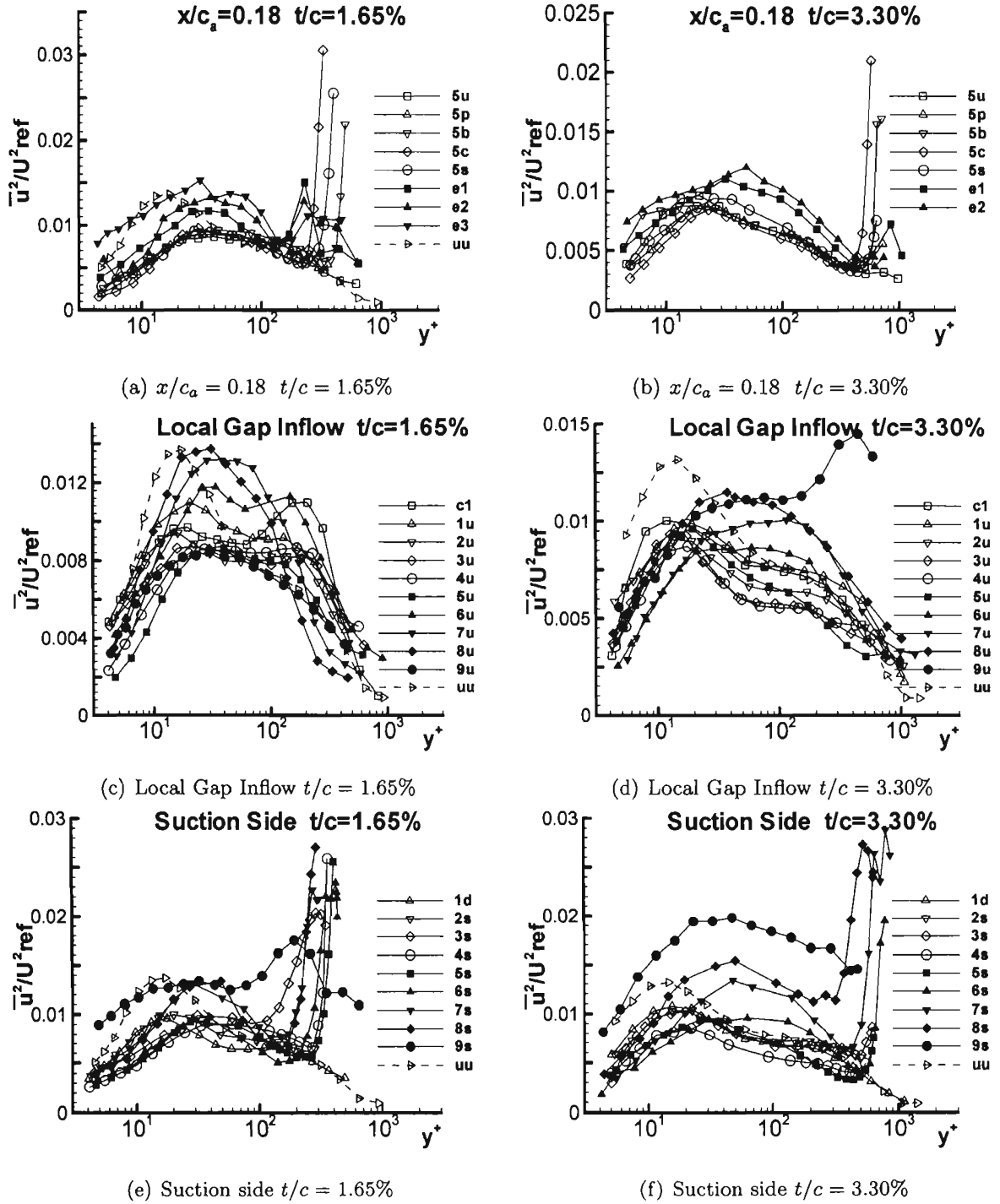


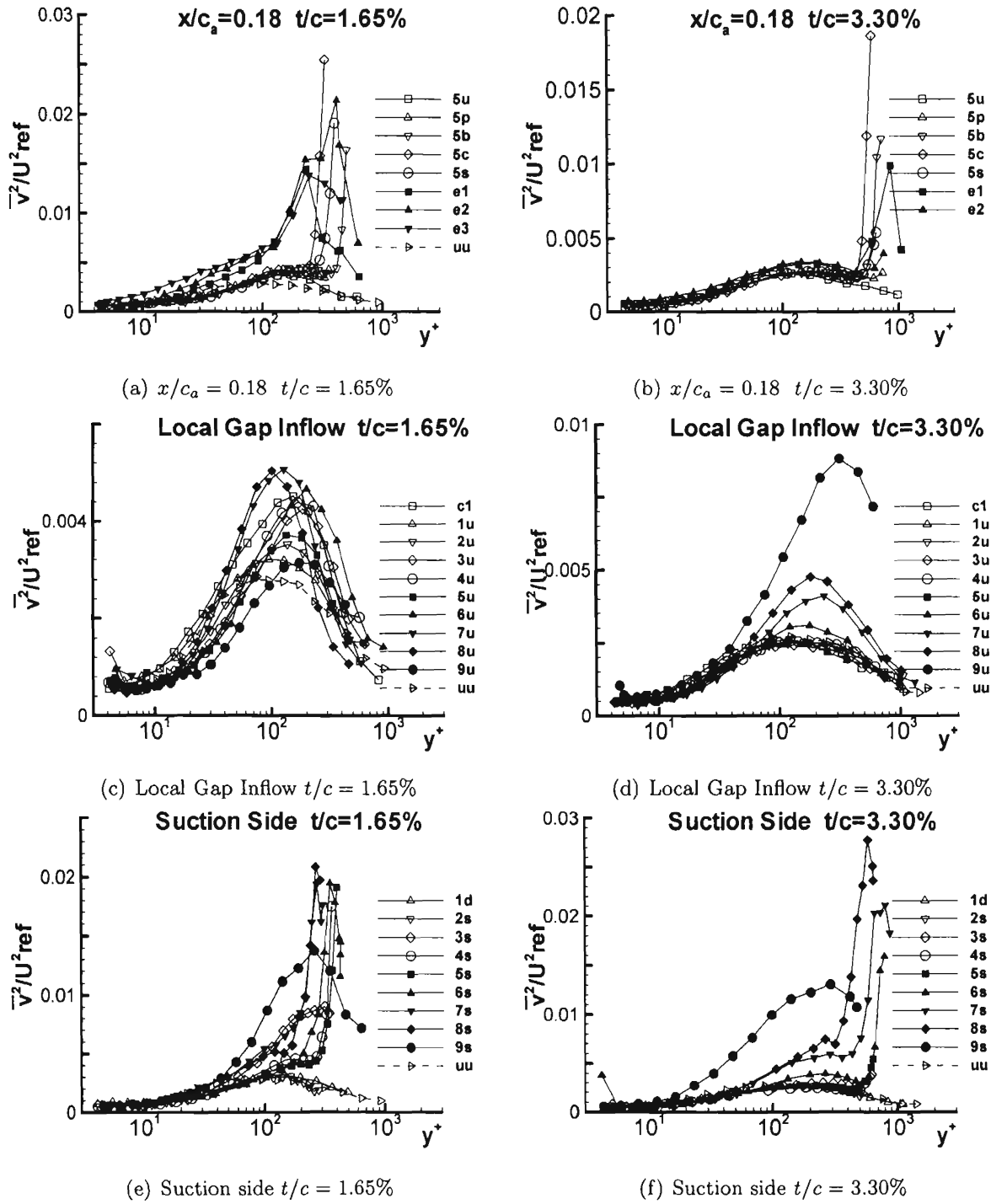
Figure 3.15: Mean  $U$ ,  $V$ ,  $W$  and  $U^+$ ,  $V^+$ ,  $W^+$  at  $x/c_a = 0.42$  for 3.30% in chord coordinate system

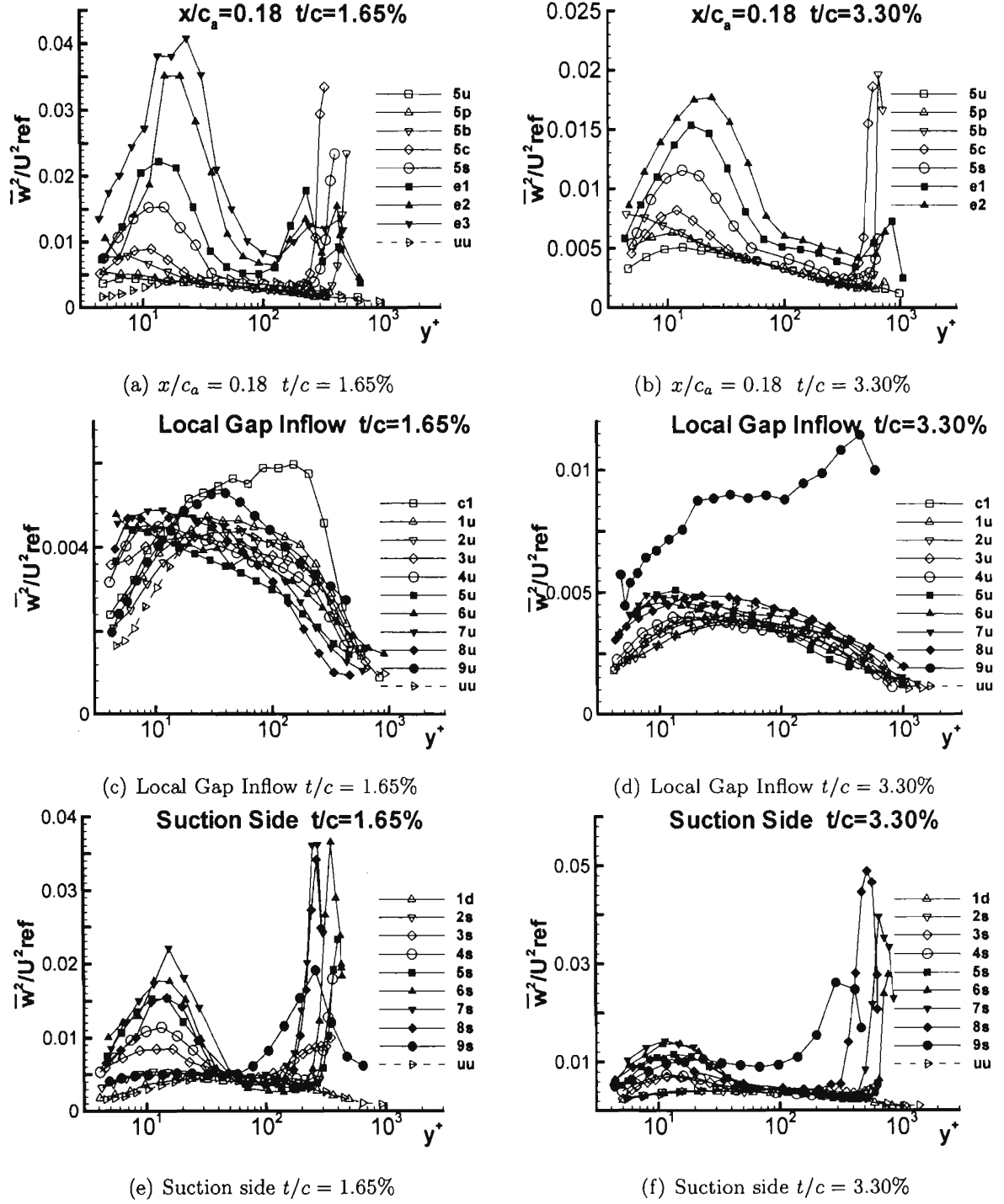
Figure 3.16: Mean  $U/U_{ref}$  for both 1.65% and 3.30% in chord coordinate system

Figure 3.17: Mean  $V/U_{ref}$  for both 1.65% and 3.30% in chord coordinate system

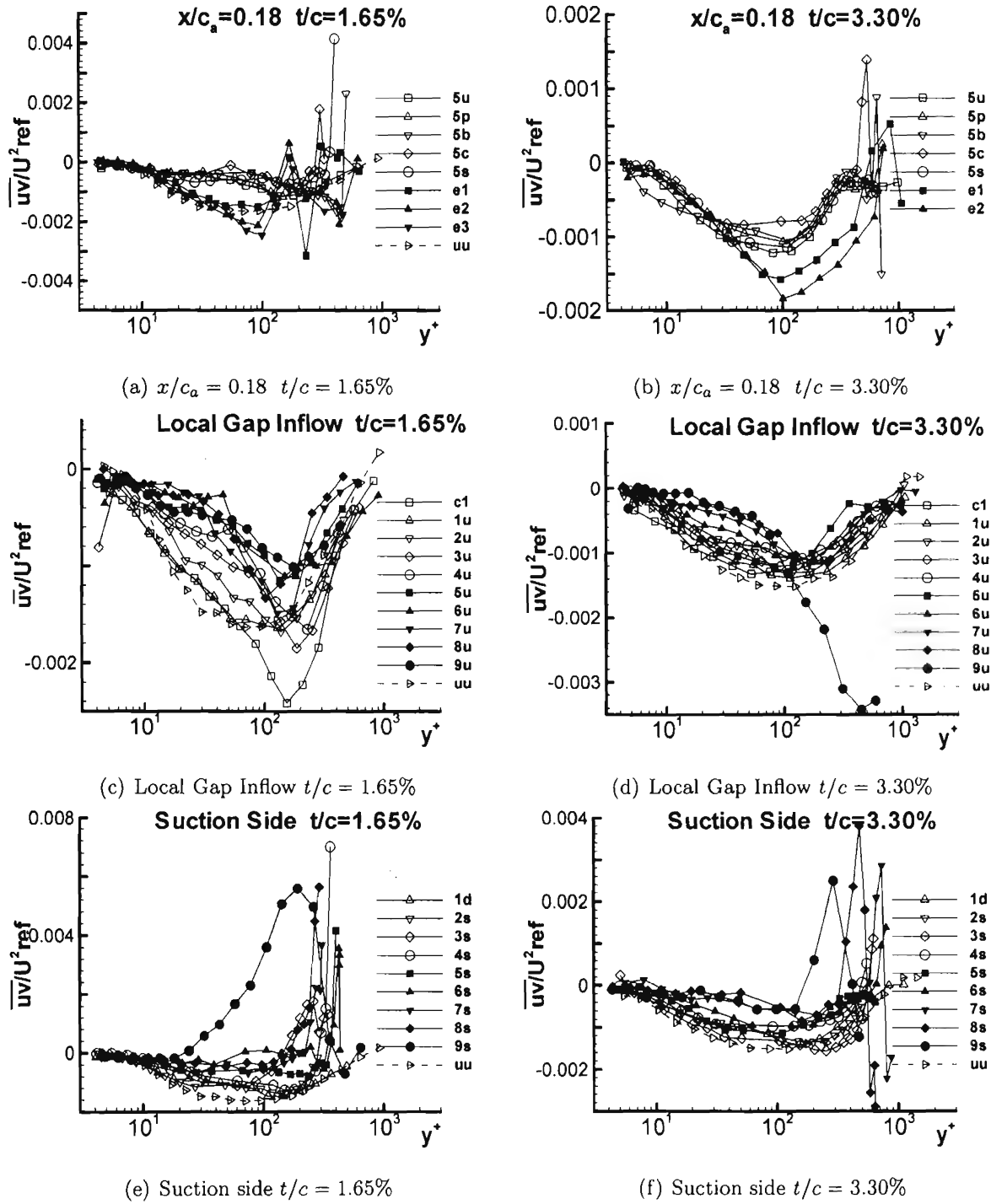
Figure 3.18: Mean  $W/U_{ref}$  for both 1.65% and 3.30% in chord coordinate system

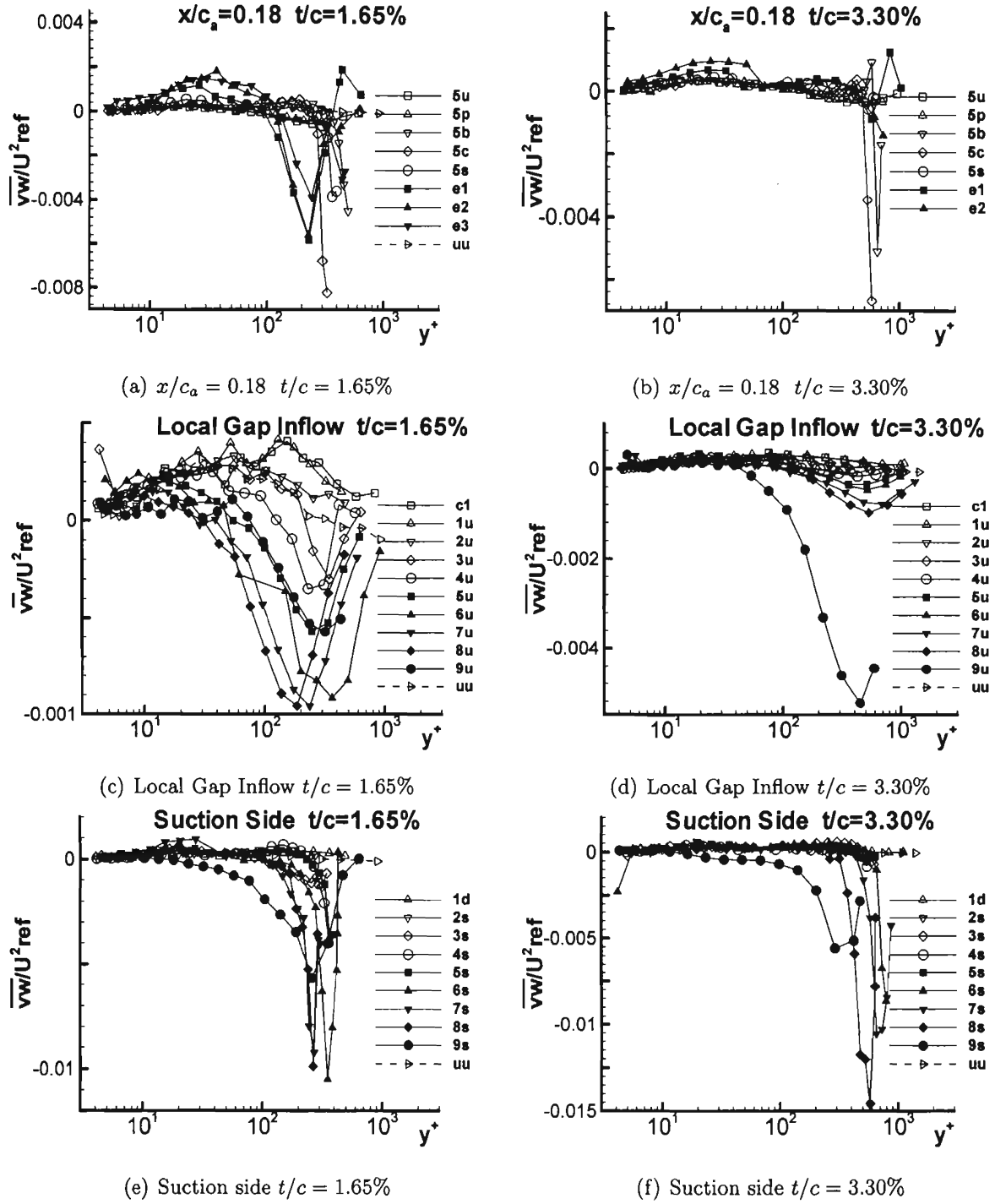
Figure 3.19: Normal stress  $\overline{u^2}/U_{ref}^2$  for both 1.65% and 3.30% in chord coordinate system

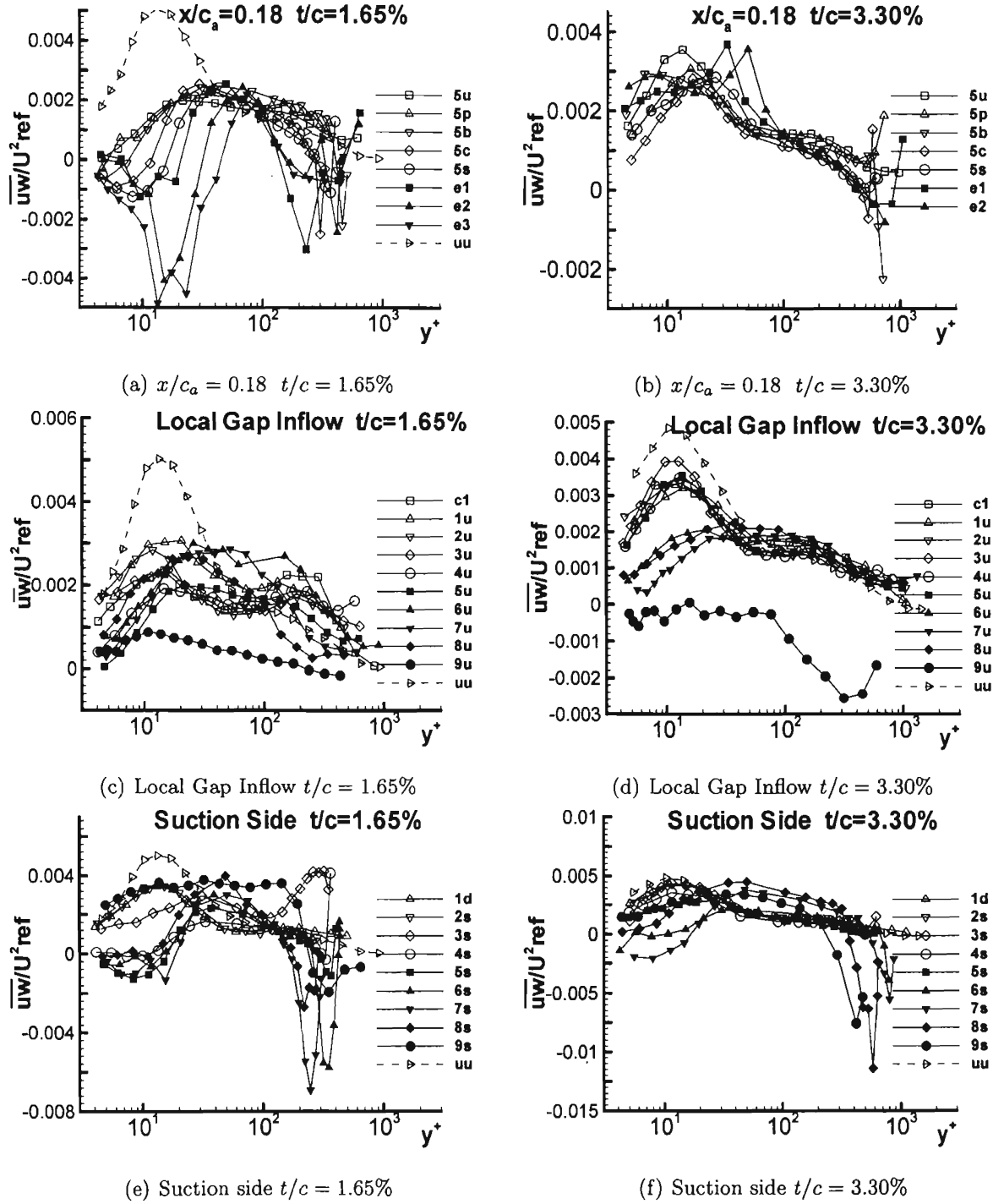
Figure 3.20: Normal stress  $\overline{v^2}/U_{ref}^2$  for both 1.65% and 3.30% in chord coordinate system

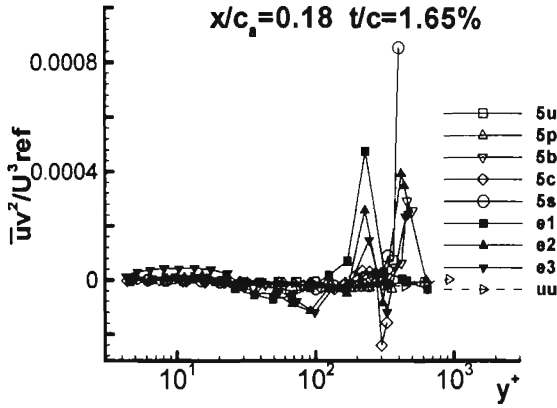
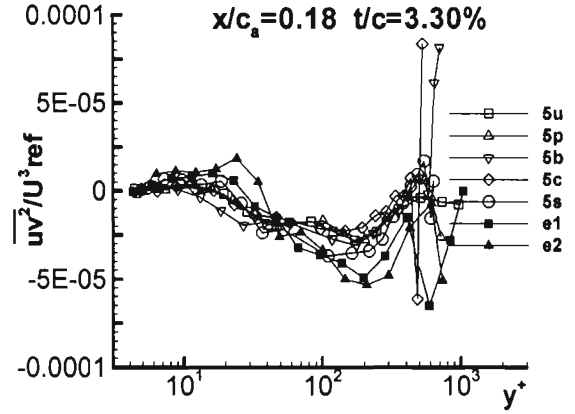
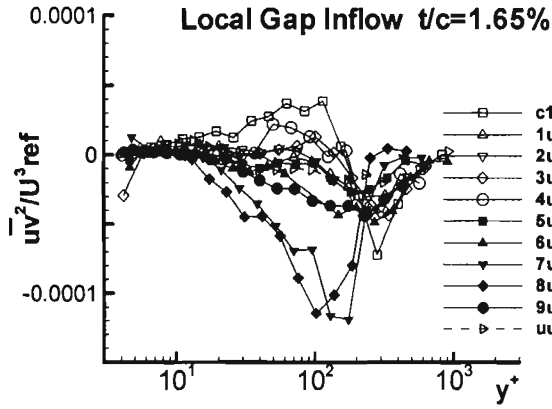
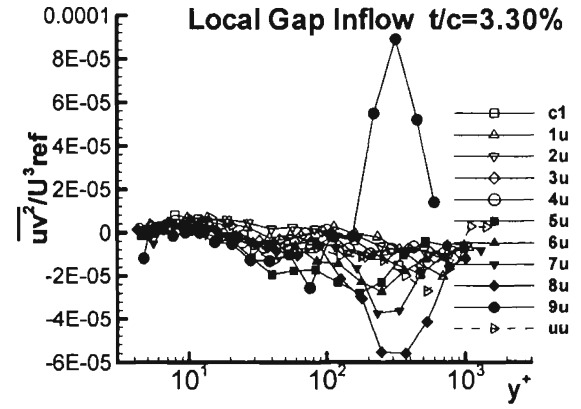
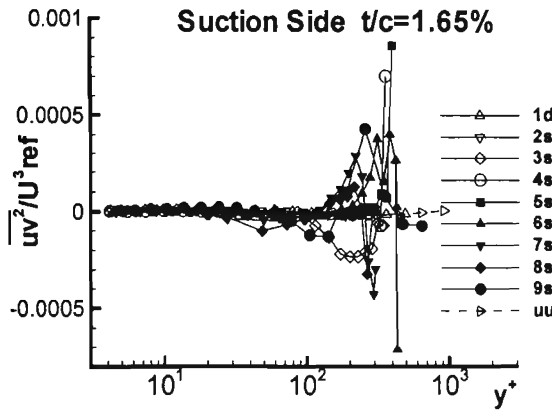
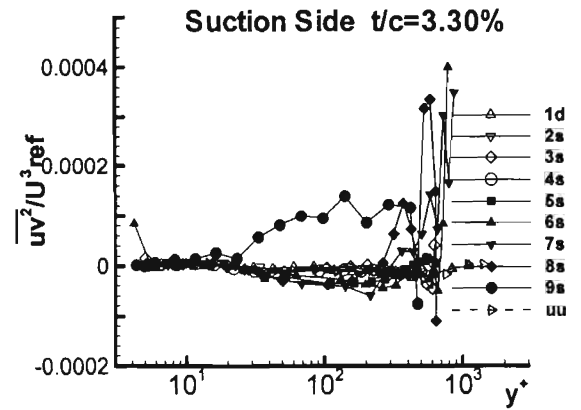
Figure 3.21: Normal stress  $\overline{w^2}/U_{ref}^2$  for both 1.65% and 3.30% in chord coordinate system

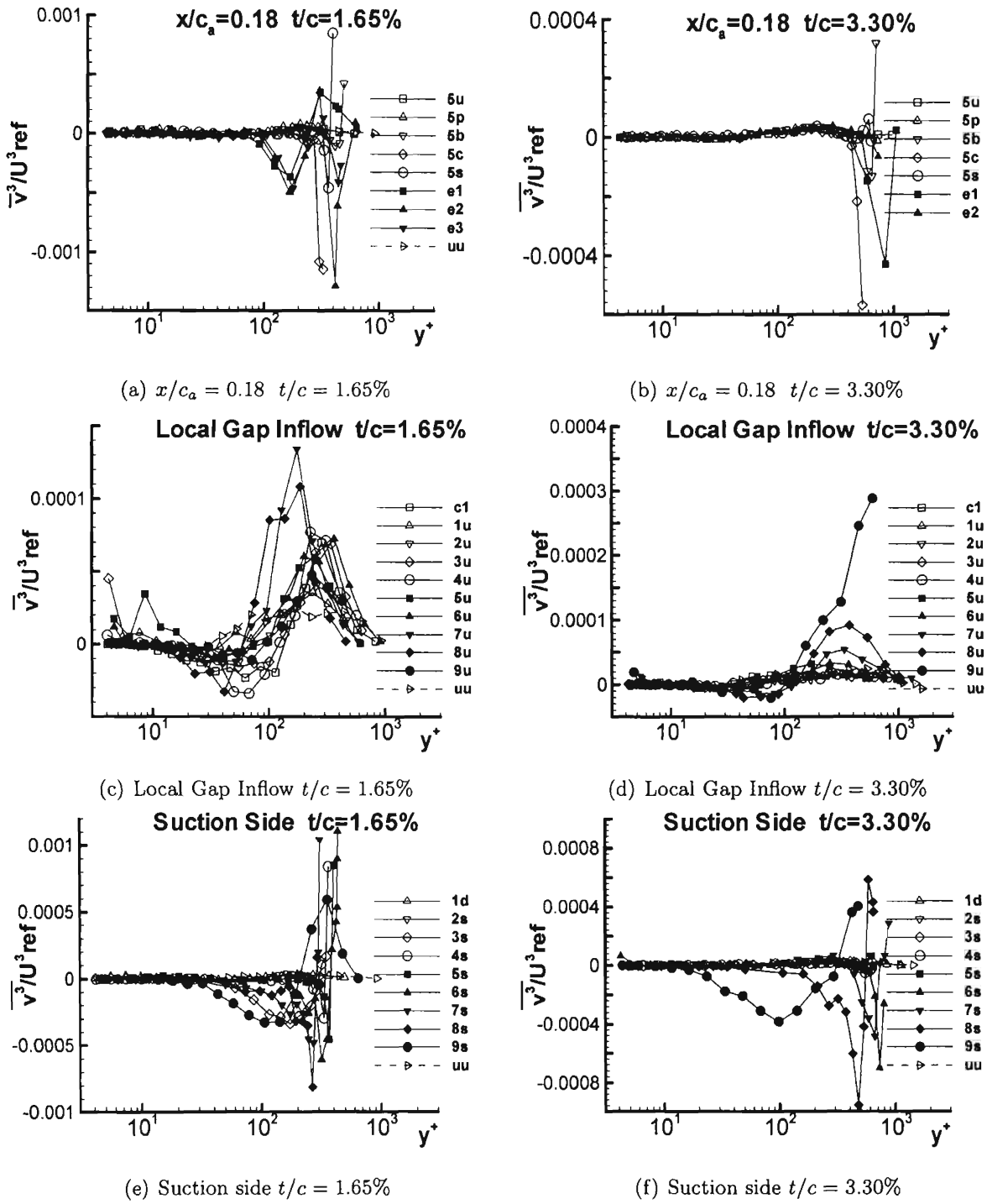


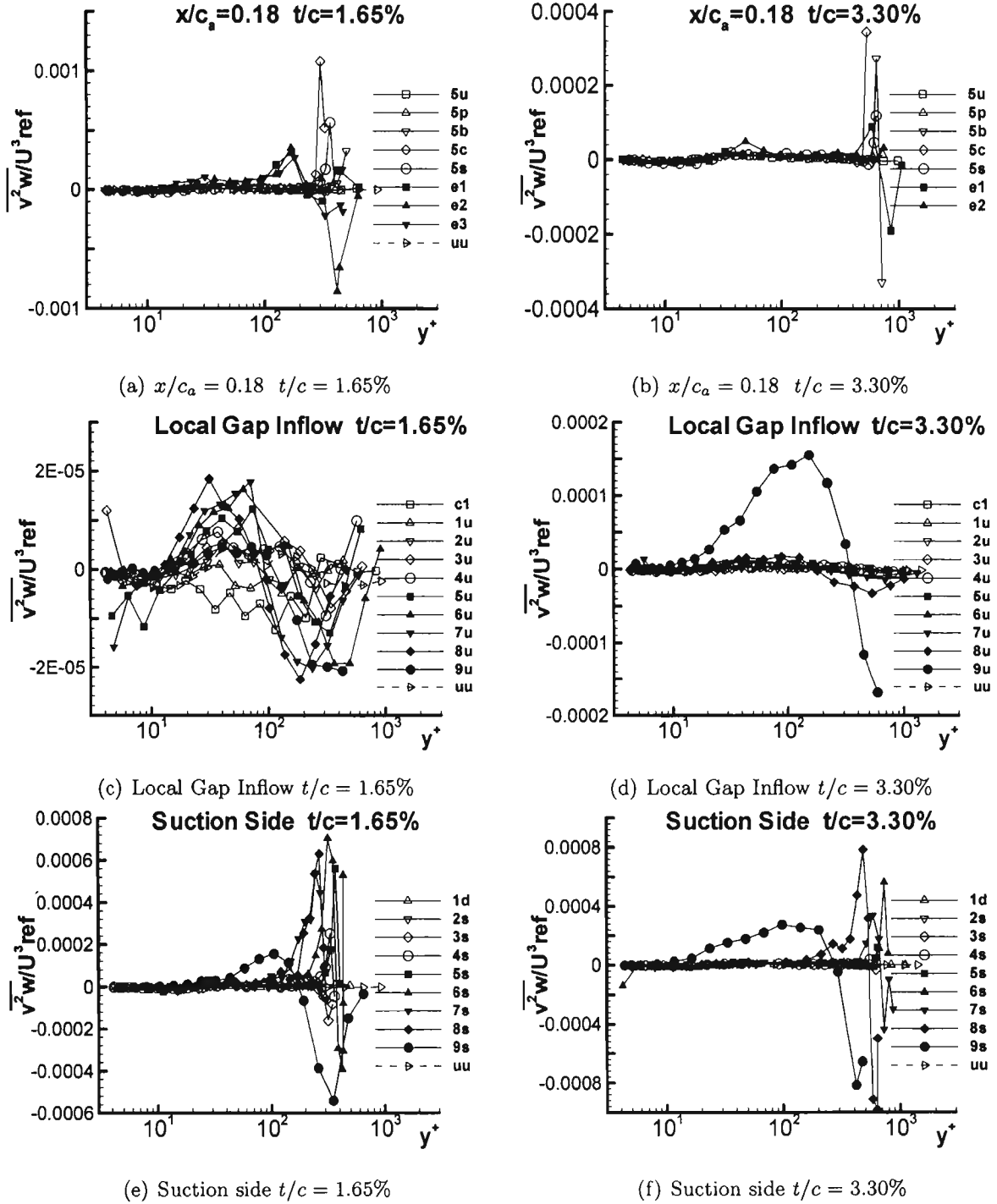
Figure 3.22: Shear stress  $-\overline{uv}/U_{ref}^2$  for both 1.65% and 3.30% in chord coordinate system

Figure 3.23: Shear stress  $-\overline{vw}/U_{ref}^2$  for both 1.65% and 3.30% in chord coordinate system

Figure 3.24: Shear stress  $-\overline{uw}/U_{ref}^2$  for both 1.65% and 3.30% in chord coordinate system

(a)  $x/c_a = 0.18 \quad t/c = 1.65\%$ (b)  $x/c_a = 0.18 \quad t/c = 3.30\%$ (c) Local Gap Inflow  $t/c = 1.65\%$ (d) Local Gap Inflow  $t/c = 3.30\%$ (e) Suction side  $t/c = 1.65\%$ (f) Suction side  $t/c = 3.30\%$ Figure 3.25: Triple product  $\overline{uv^2}/U_{ref}^3$  for both 1.65% and 3.30% in chord coordinate system

Figure 3.26: Triple product  $\overline{v^3}/U^3_{ref}$  for both 1.65% and 3.30% in chord coordinate system

Figure 3.27: Triple product  $\overline{v^2 w} / U^3_{ref}$  for both 1.65% and 3.30% in chord coordinate system

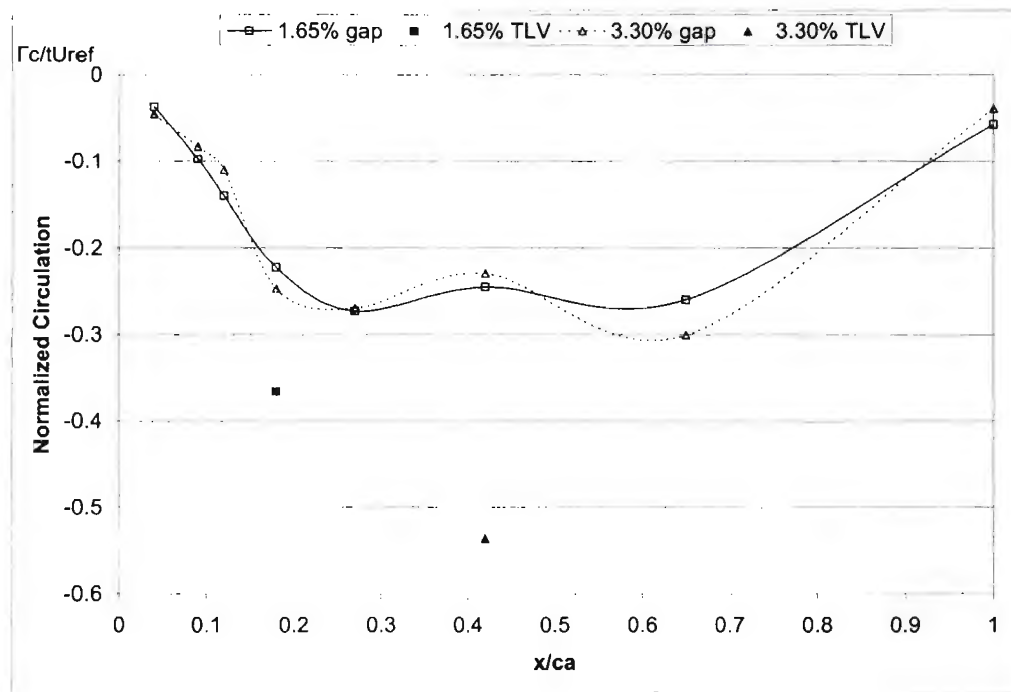
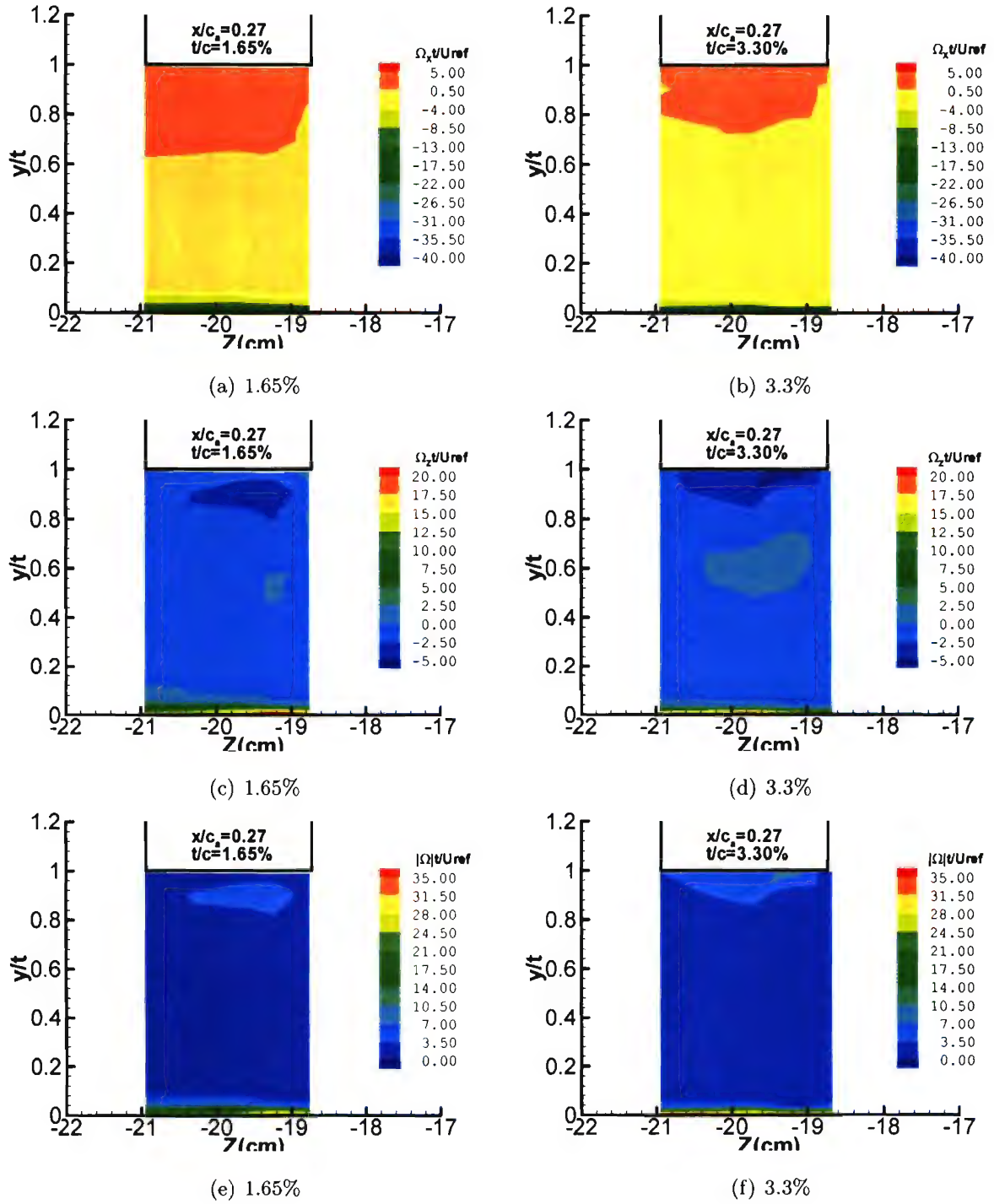
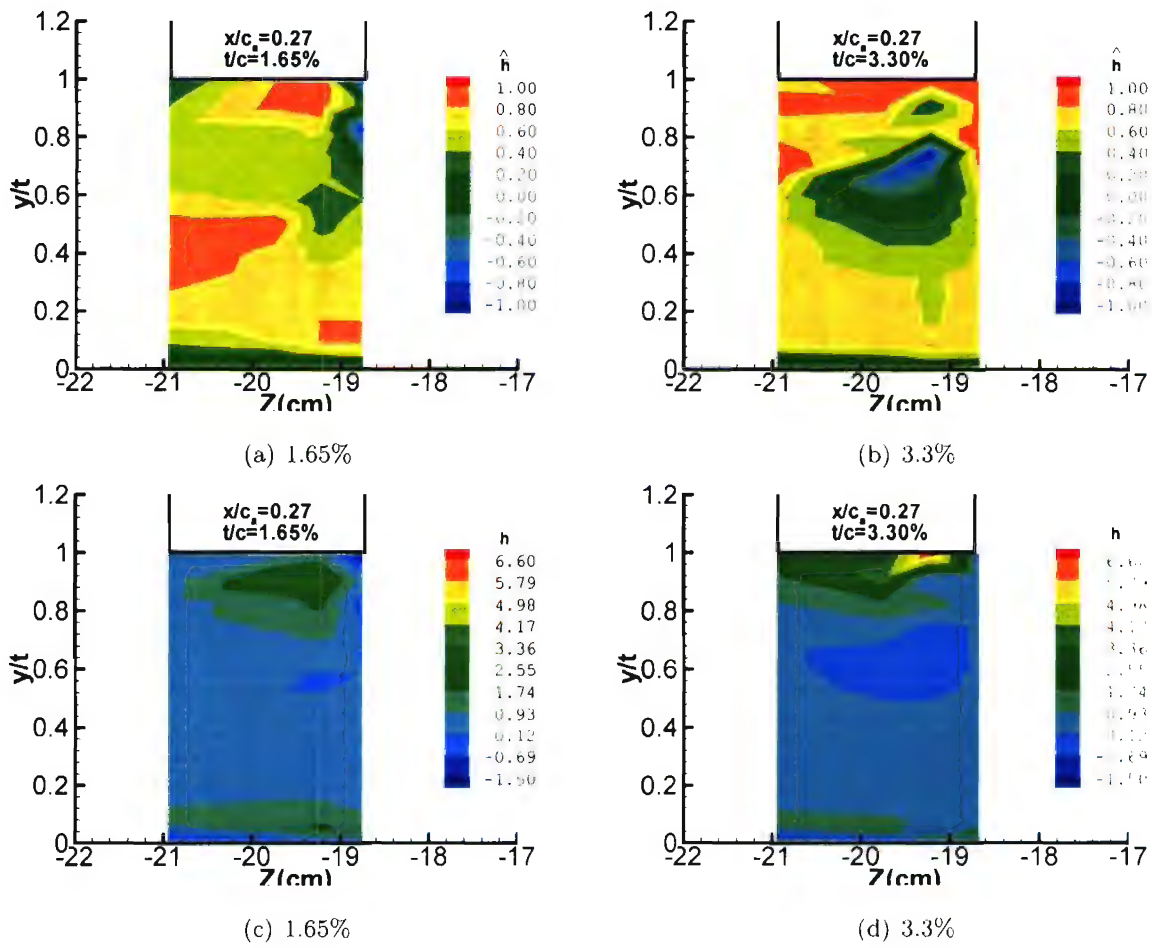


Figure 3.28: Circulation  $\Gamma_x$  for both 1.65% and 3.30% in bed coordinate system;  $\square$ , locations under the 1.65% tip gap;  $\triangle$ , locations under the 3.30% tip gap;  $\blacksquare$ ,  $x/c_a = 0.18$  cross-section of tip leakage vortex with the 1.65% tip gap;  $\blacktriangle$ ,  $x/c_a = 0.42$  cross-section of tip leakage vortex with the 3.30% tip gap.

Figure 3.29: Vorticity at  $x/c_a = 0.27$  for both 1.65% and 3.30% in bed coordinate system



Figure 3.30: Helicity at  $x/c_a = 0.27$  for both 1.65% and 3.30% in bed coordinate system

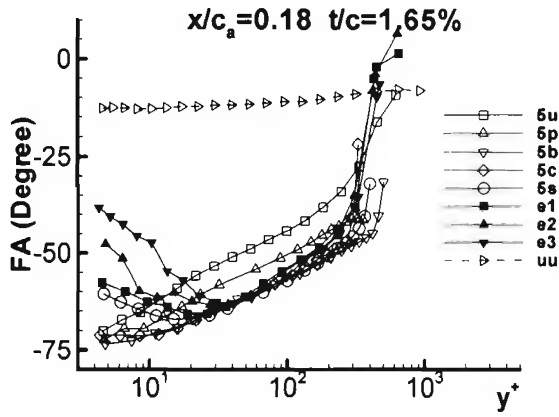
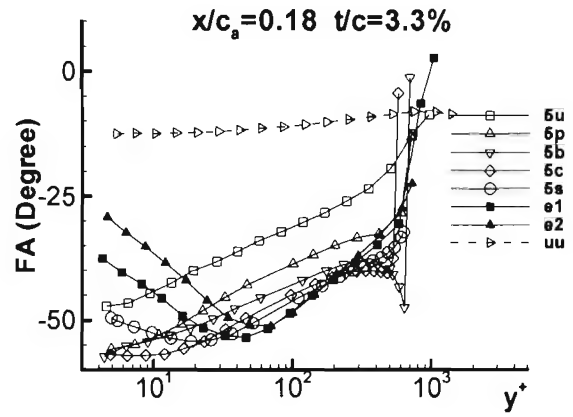
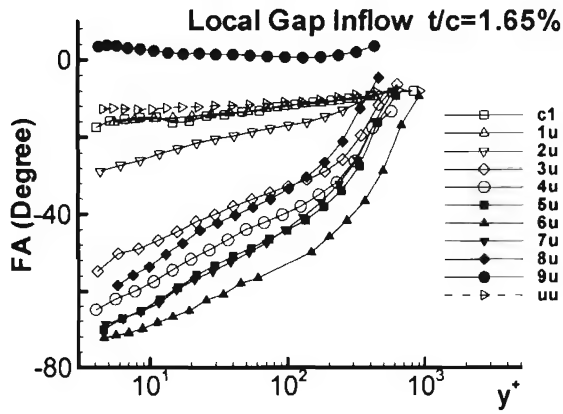
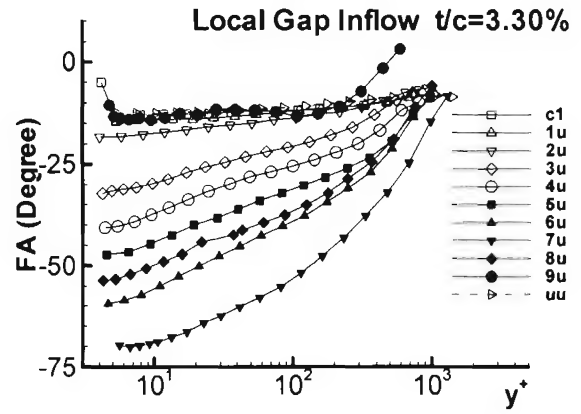
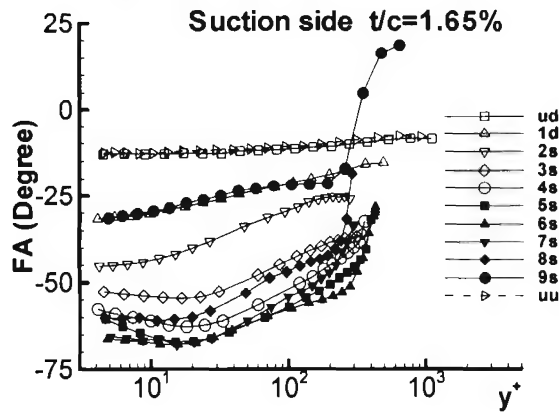
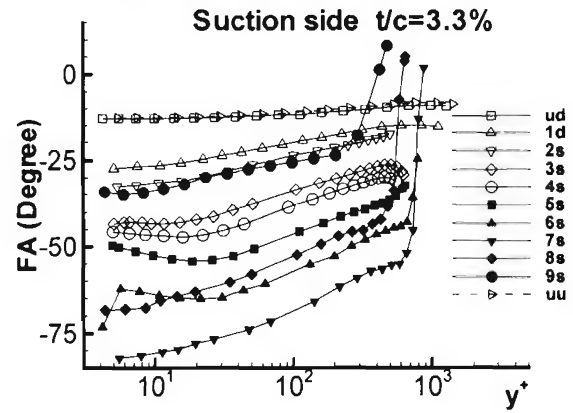
(a)  $x/c_a = 0.18 \quad t/c = 1.65\%$ (b)  $x/c_a = 0.18 \quad t/c = 3.30\%$ (c) Local Gap Inflow  $t/c = 1.65\%$ (d) Local Gap Inflow  $t/c = 3.30\%$ (e) Suction side  $t/c = 1.65\%$ (f) Suction side  $t/c = 3.30\%$ 

Figure 3.31: Flow angle for both 1.65% and 3.30% in chord coordinate system

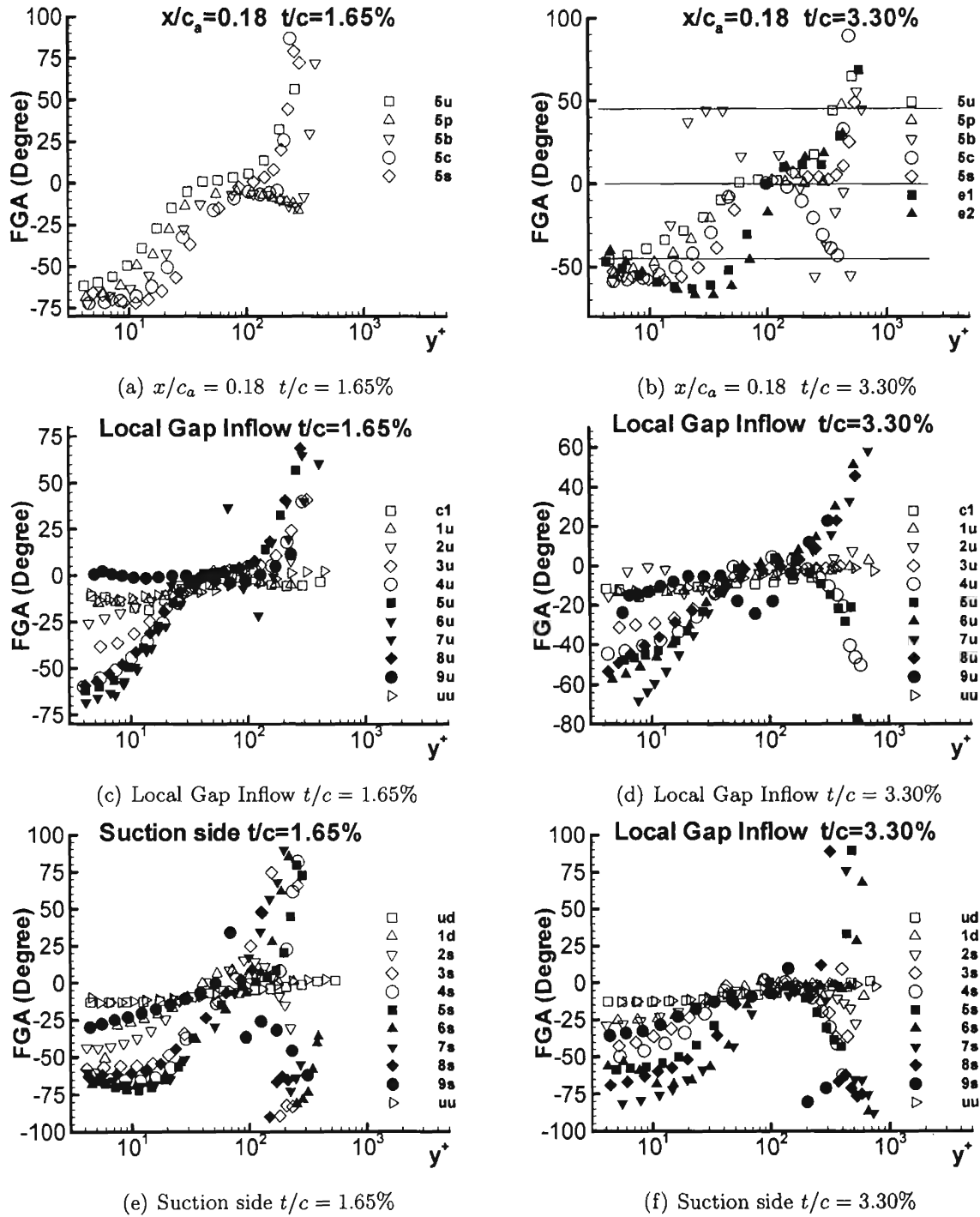


Figure 3.32: Flow gradient angle for both 1.65% and 3.30% in chord coordinate system

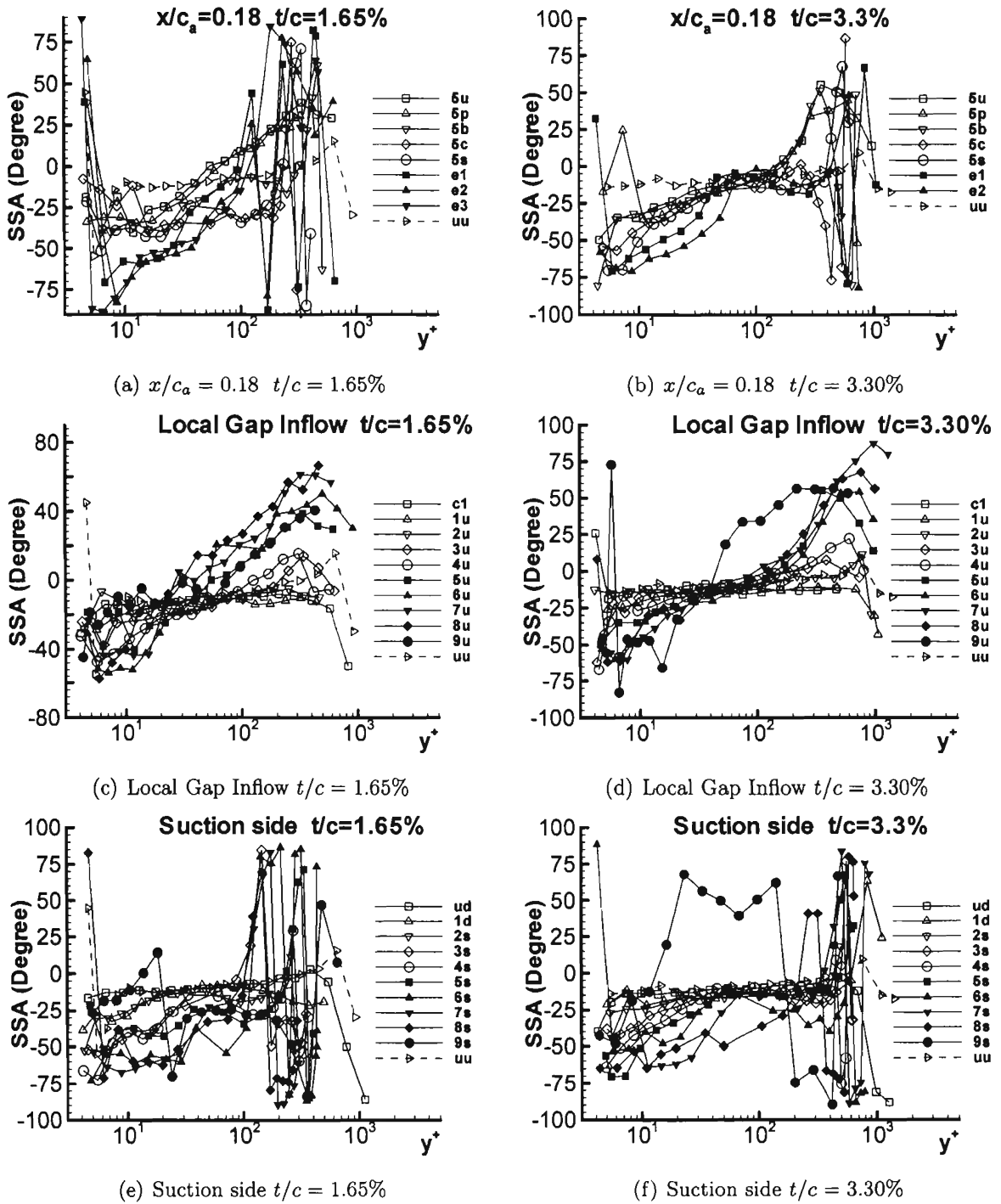
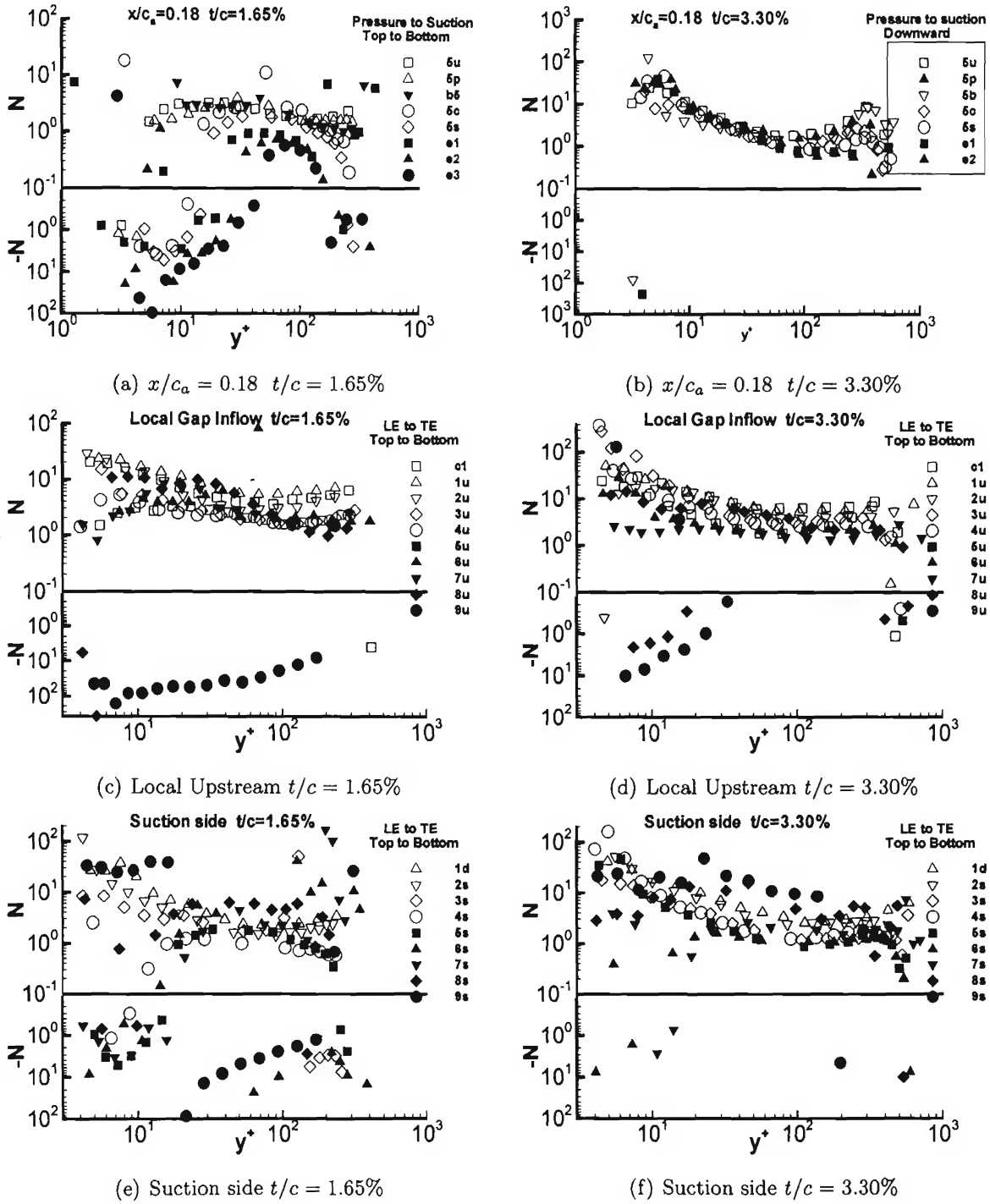
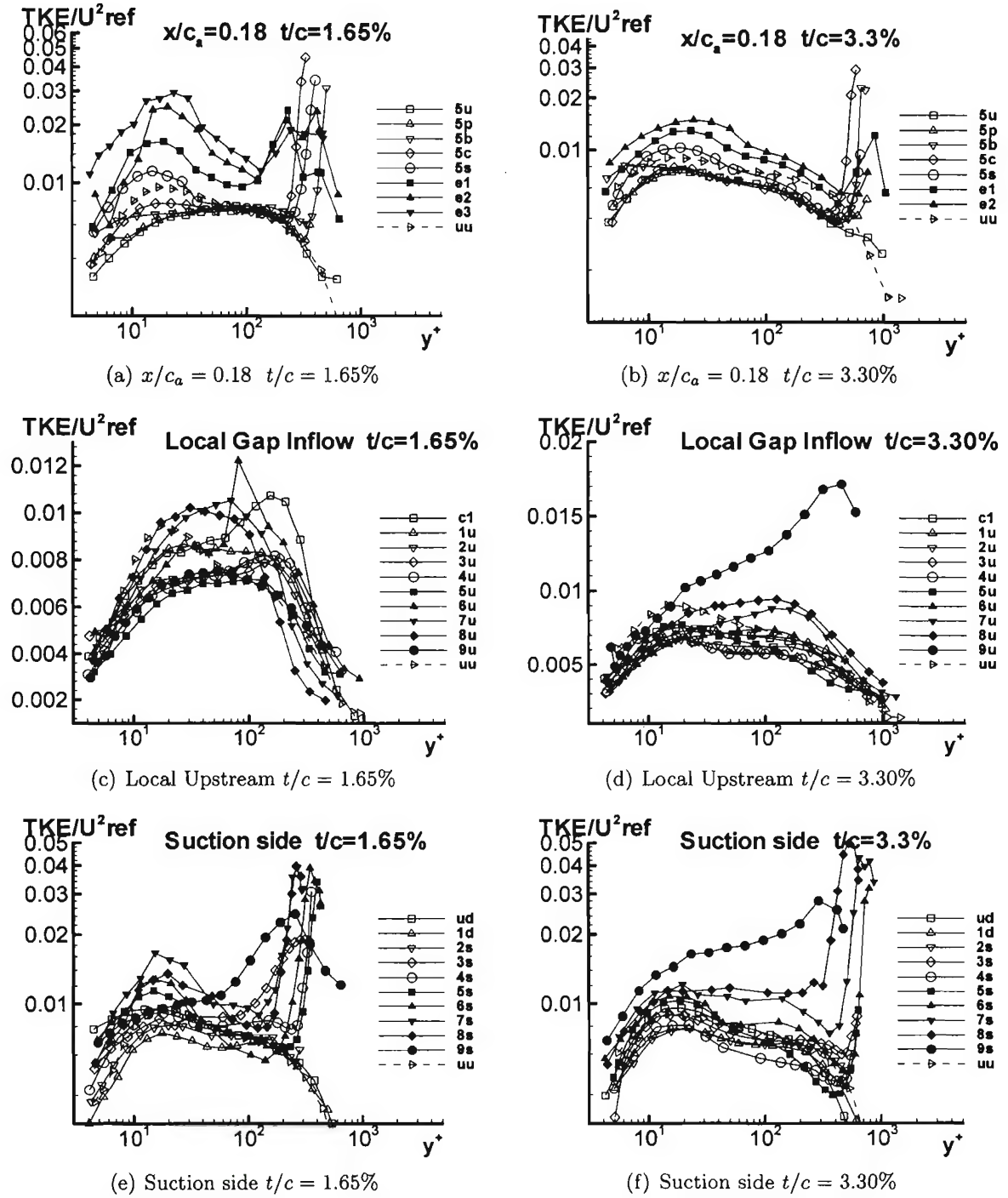
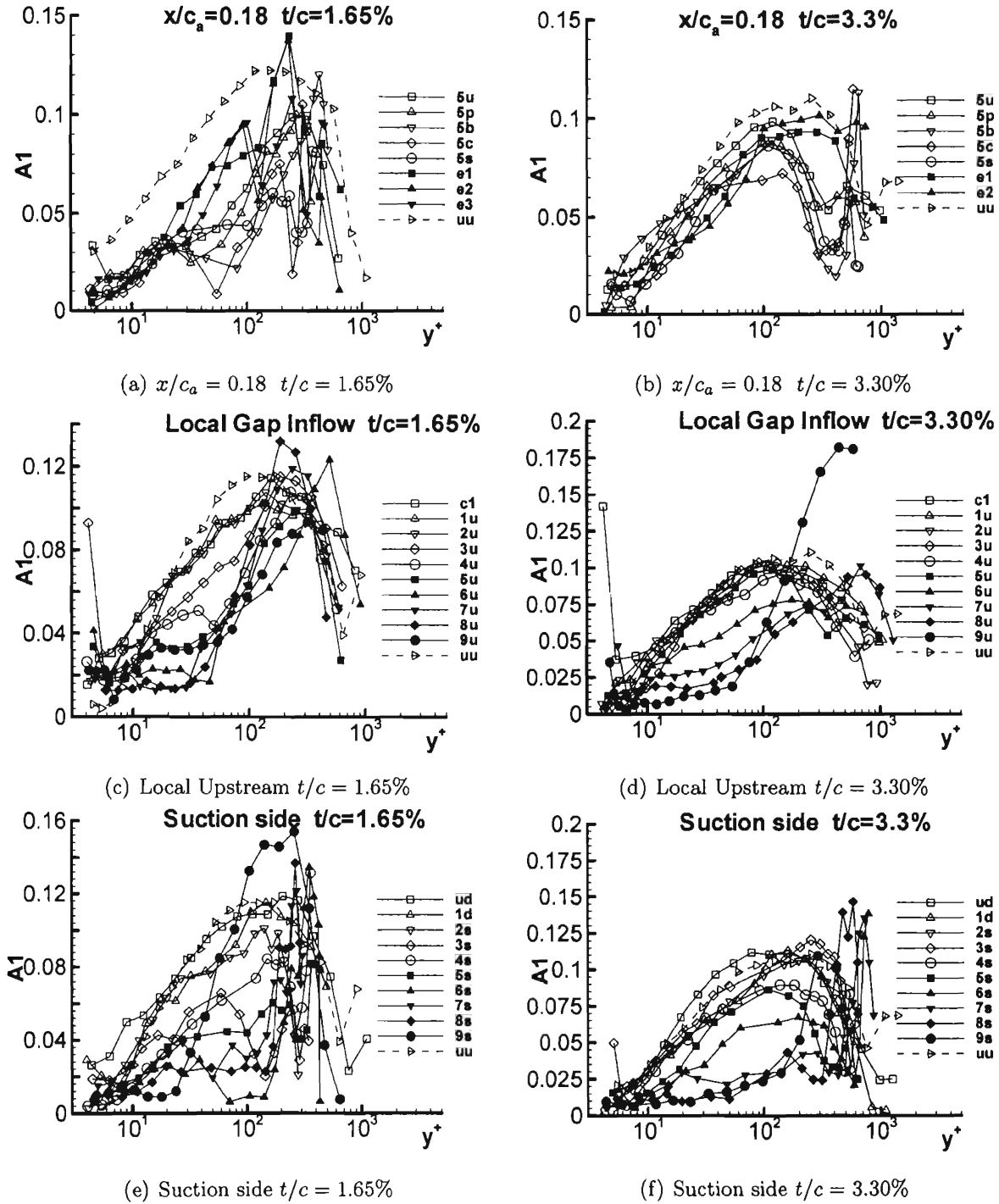
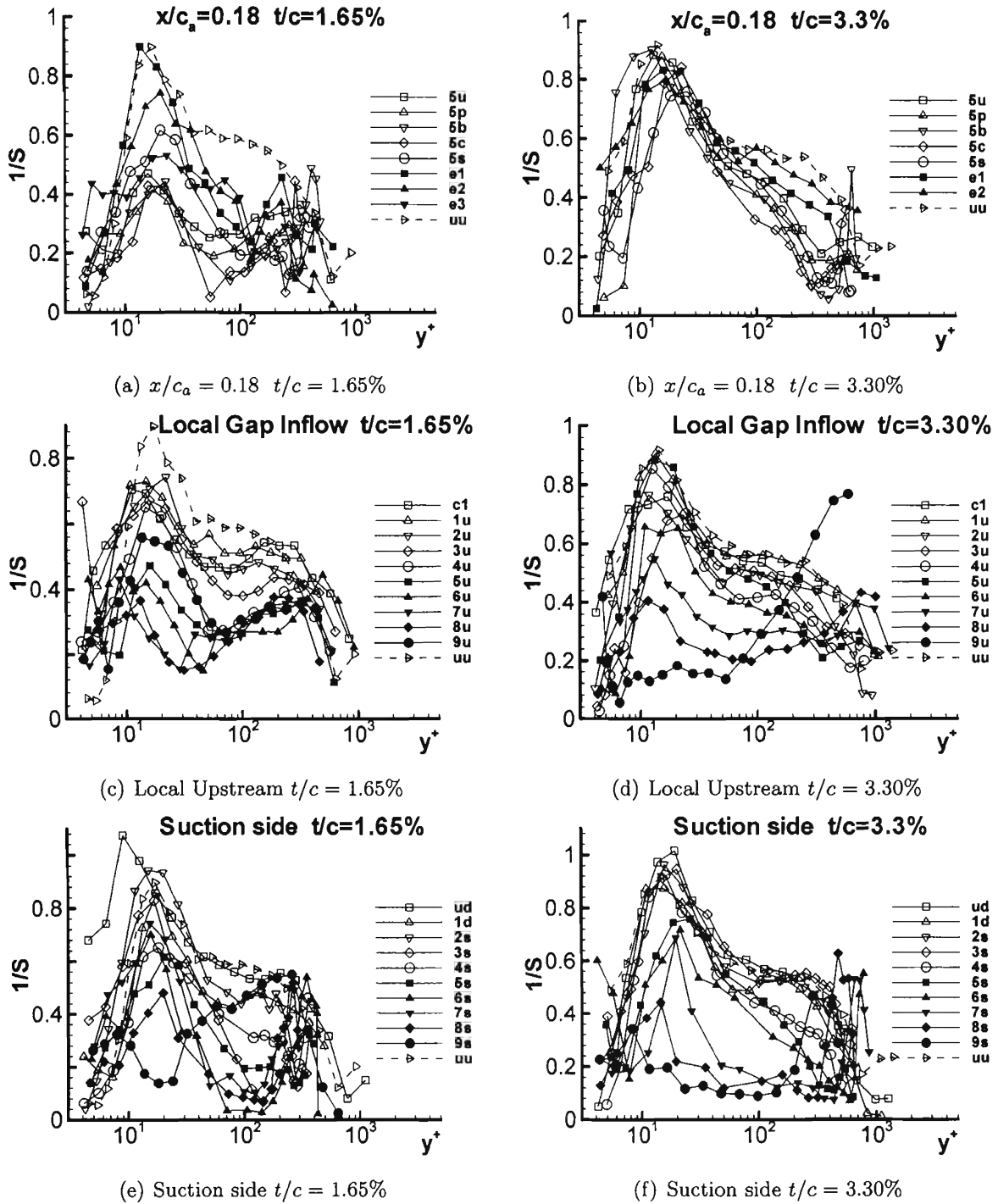


Figure 3.33: Shear stress angle for both 1.65% and 3.30% in chord coordinate system

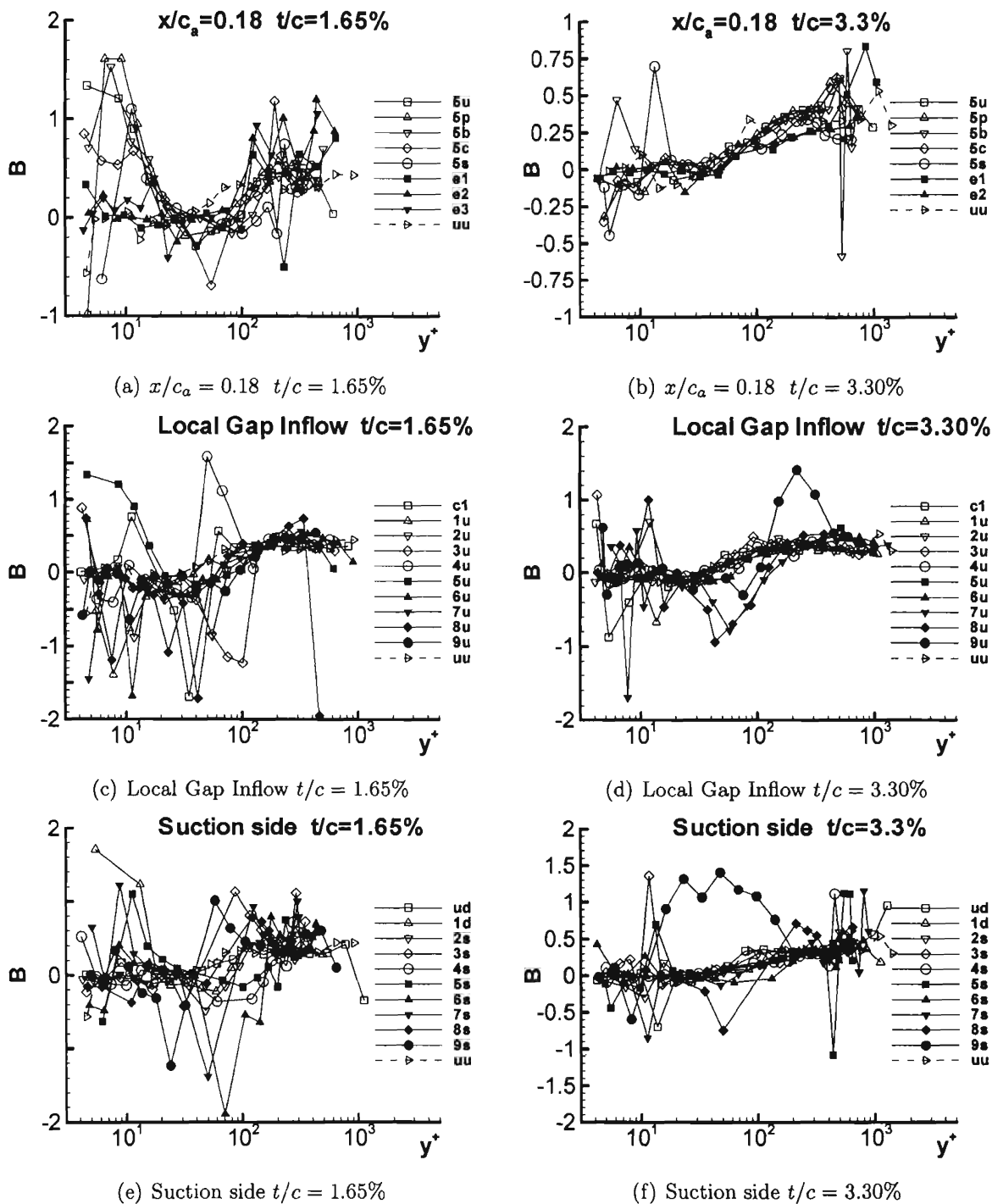
Figure 3.34: Anisotropy factor  $N$  for both 1.65% and 3.30% in chord coordinate system

Figure 3.35: Turbulent kinetic energy  $TKE/U^2_{ref}$  for both 1.65% and 3.30%

Figure 3.36: Townsend structure  $a_1$  for both 1.65% and 3.30% in chord coordinate system

Figure 3.37:  $1/S$  for both 1.65% and 3.30%



Figure 3.38:  $B$  for both 1.65% and 3.30% in chord coordinate system

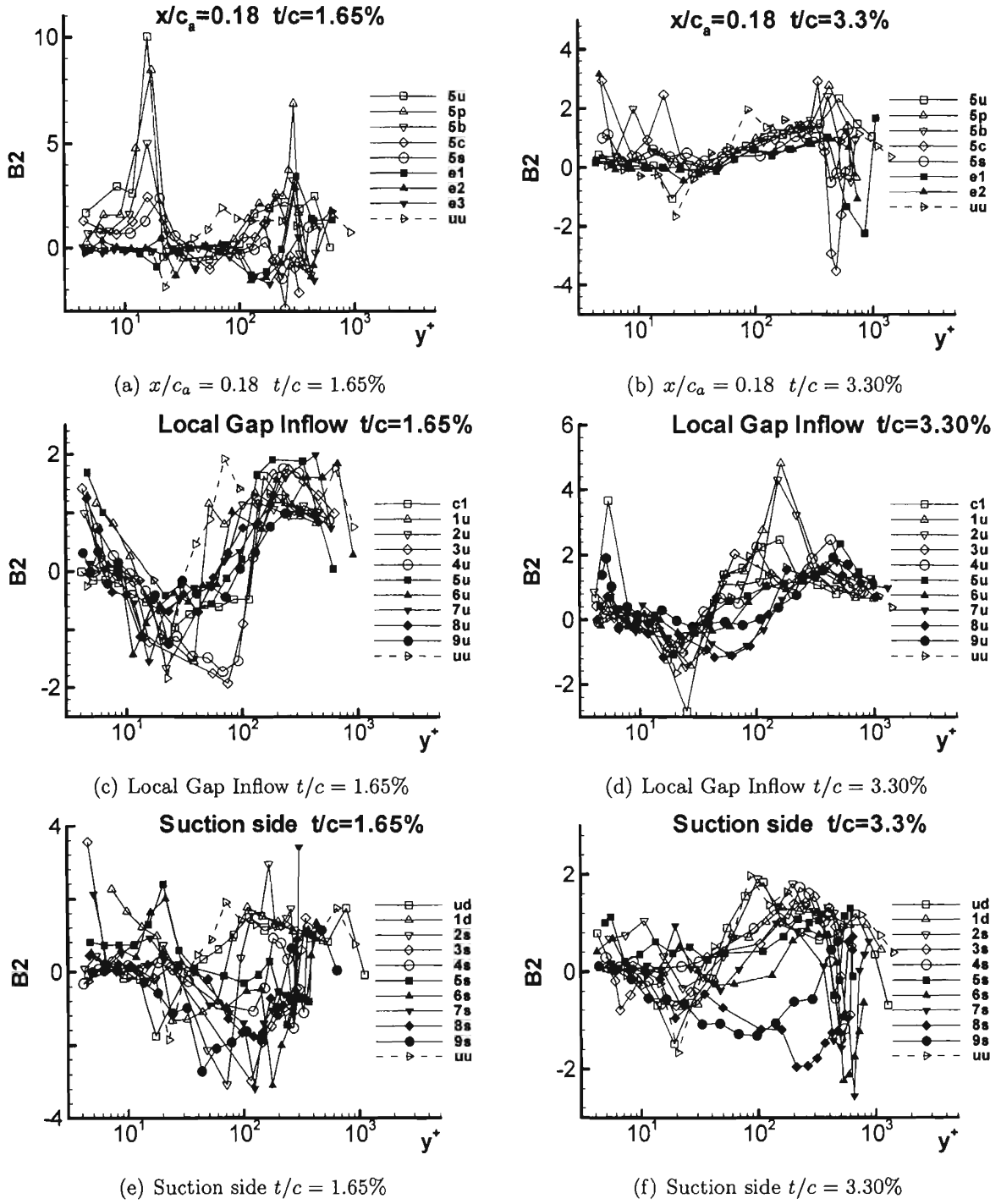


Figure 3.39: B2 for both 1.65% and 3.30% in chord coordinate system

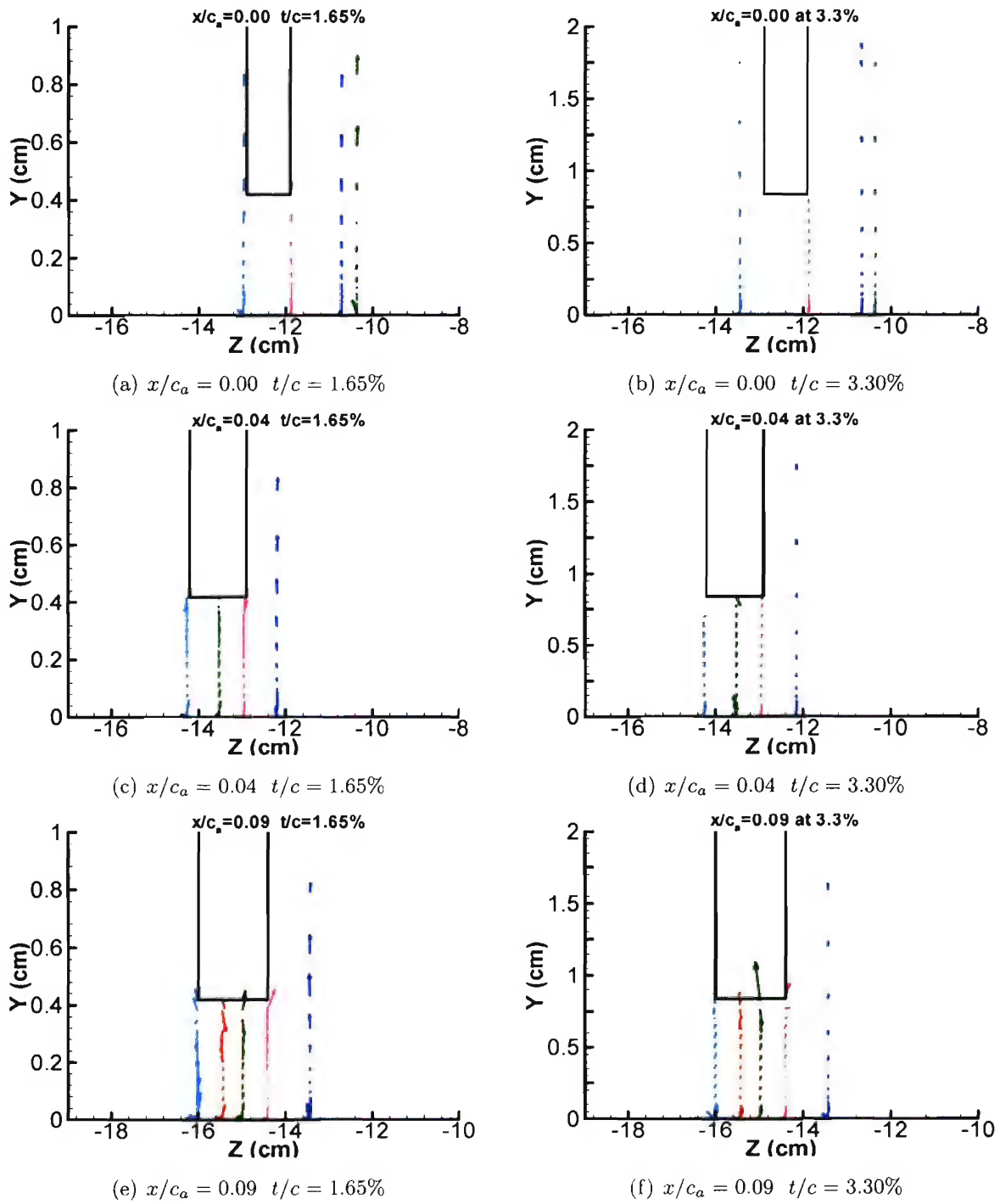


Figure 3.40: TKE Transport vector for 1.65% and 3.30% in chord coordinate system

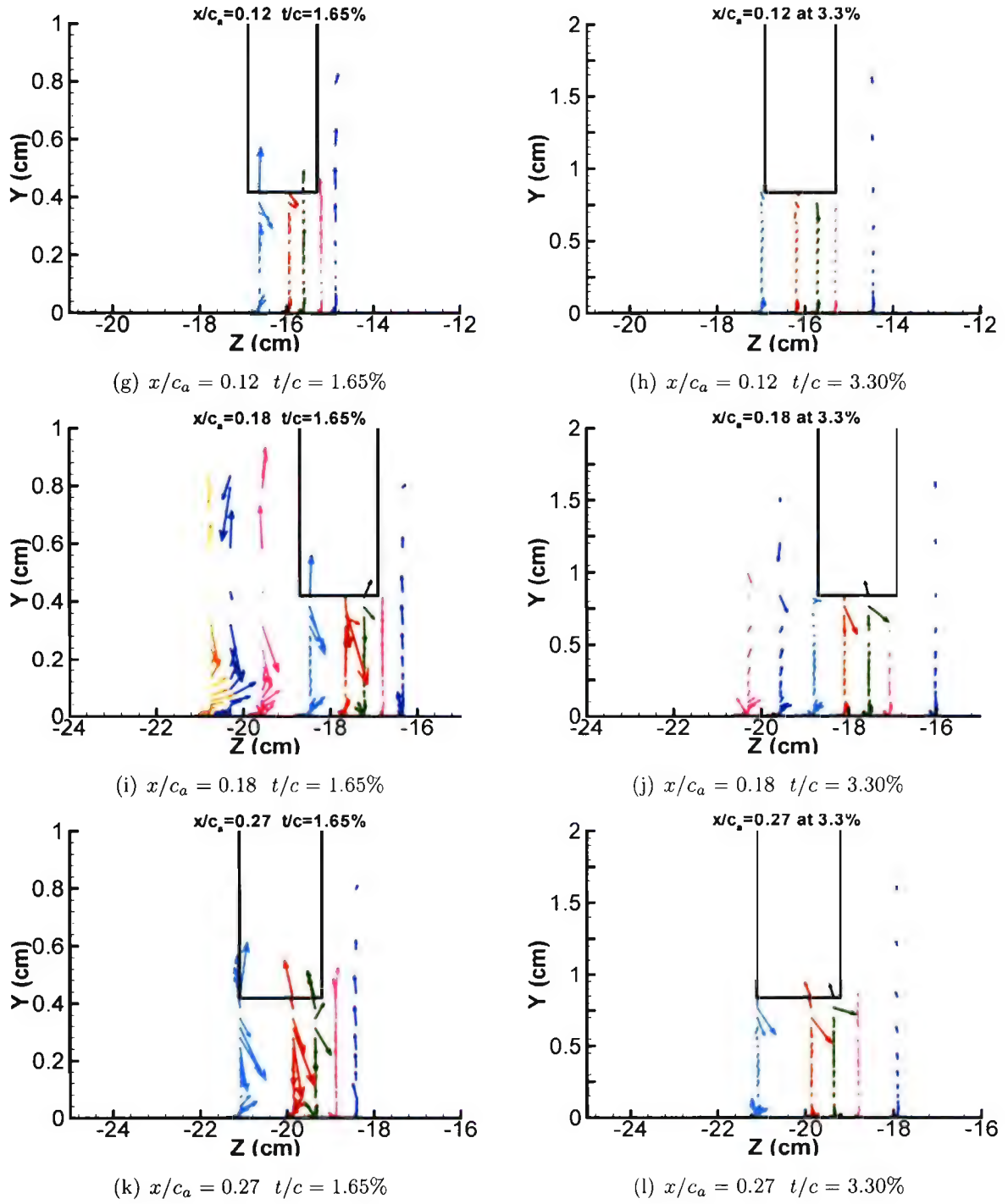


Figure 3.40: TKE Transport vector for 1.65% and 3.30% in chord coordinate system (cont.)

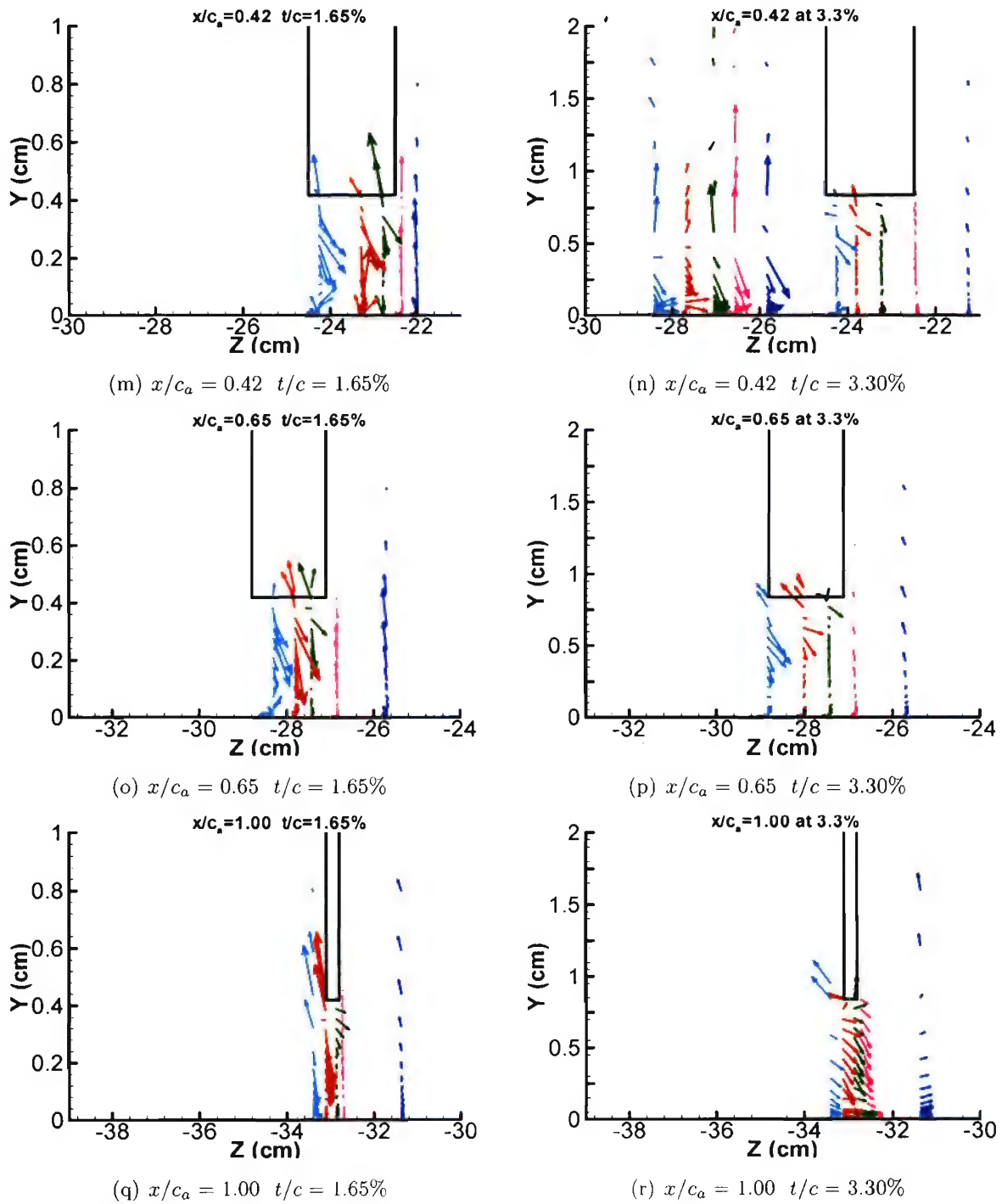


Figure 3.40: TKE Transport vector for 1.65% and 3.30% in chord coordinate system (cont.)

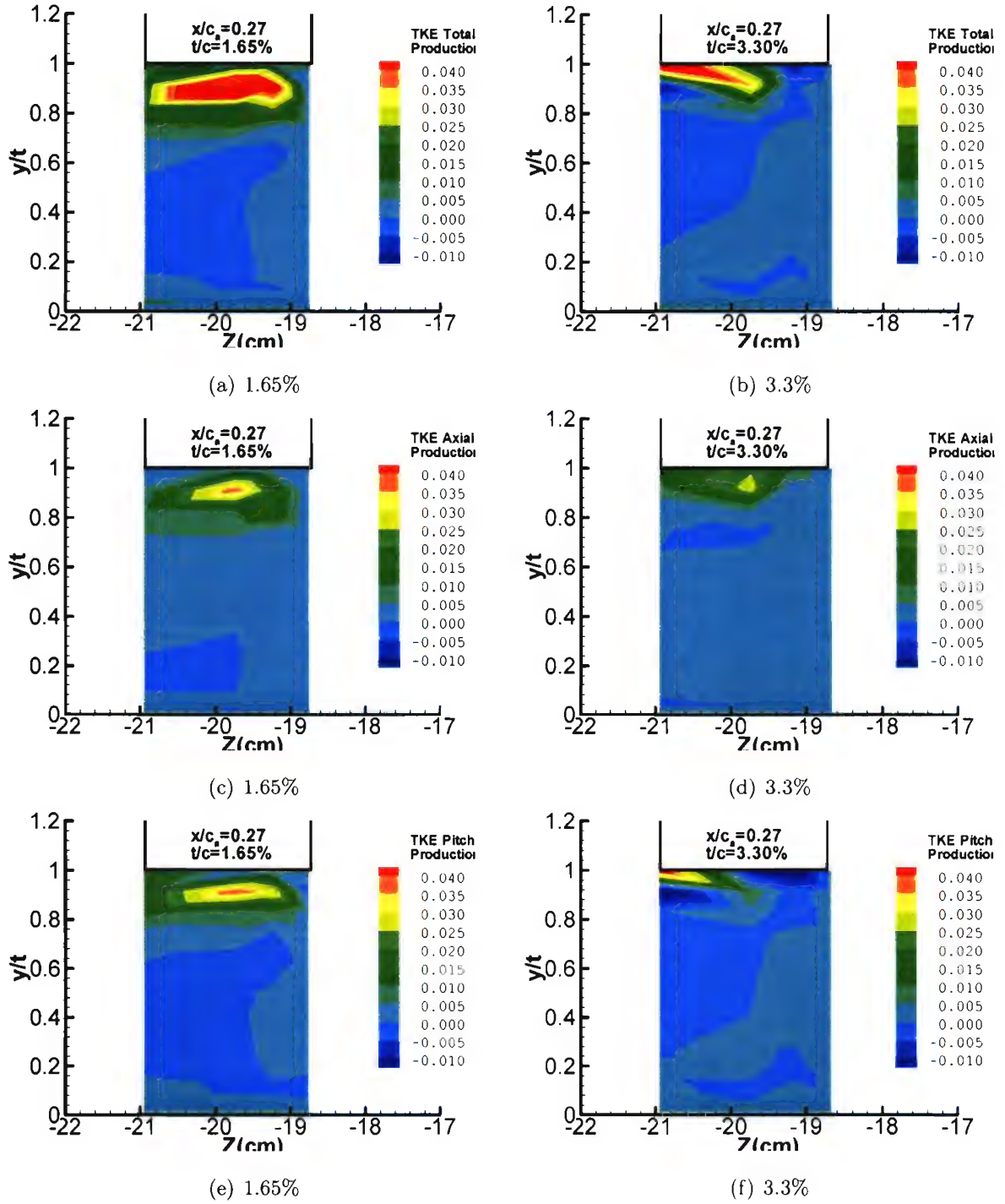


Figure 3.41: TKE production at  $x/c_a = 0.27$  for both 1.65% and 3.30% in bed coordinate system

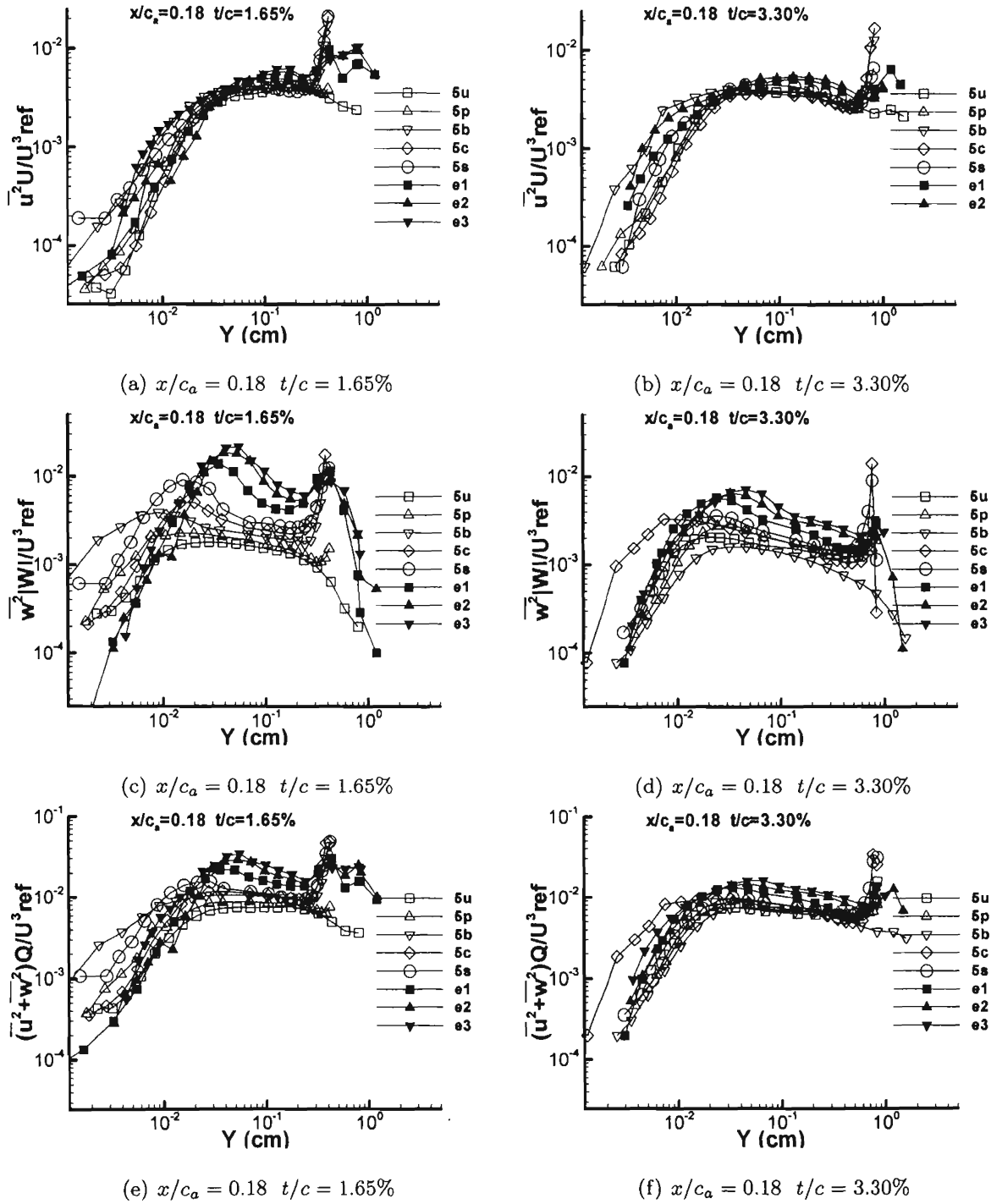


Figure 3.42:  $\overline{u^2}U/U_{ref}^3$ ,  $\overline{w^2}W/U_{ref}^3$ ,  $(\overline{u^2} + \overline{w^2})Q/U_{ref}^3$  at  $x/c_a = 0.18$  for both 1.65% and 3.30% in chord coordinate system

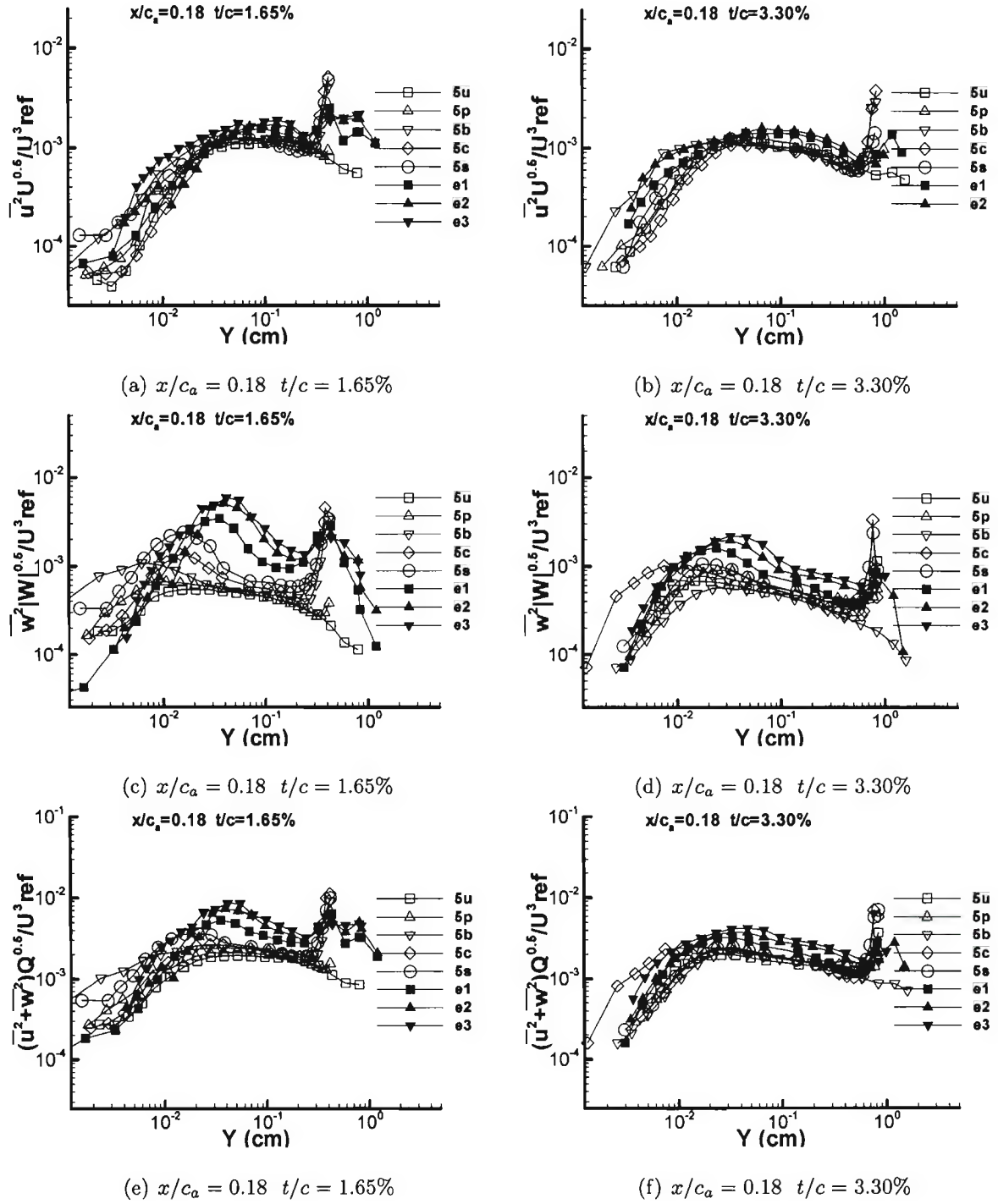


Figure 3.43:  $\overline{u^2}U^{0.5}/U_{ref}^3$ ,  $\overline{w^2}W^{0.5}/U_{ref}^3$ ,  $(\overline{u^2} + \overline{w^2})Q^{0.5}/U_{ref}^3$  at  $x/c_a = 0.18$  for both 1.65% and 3.30% in chord coordinate system



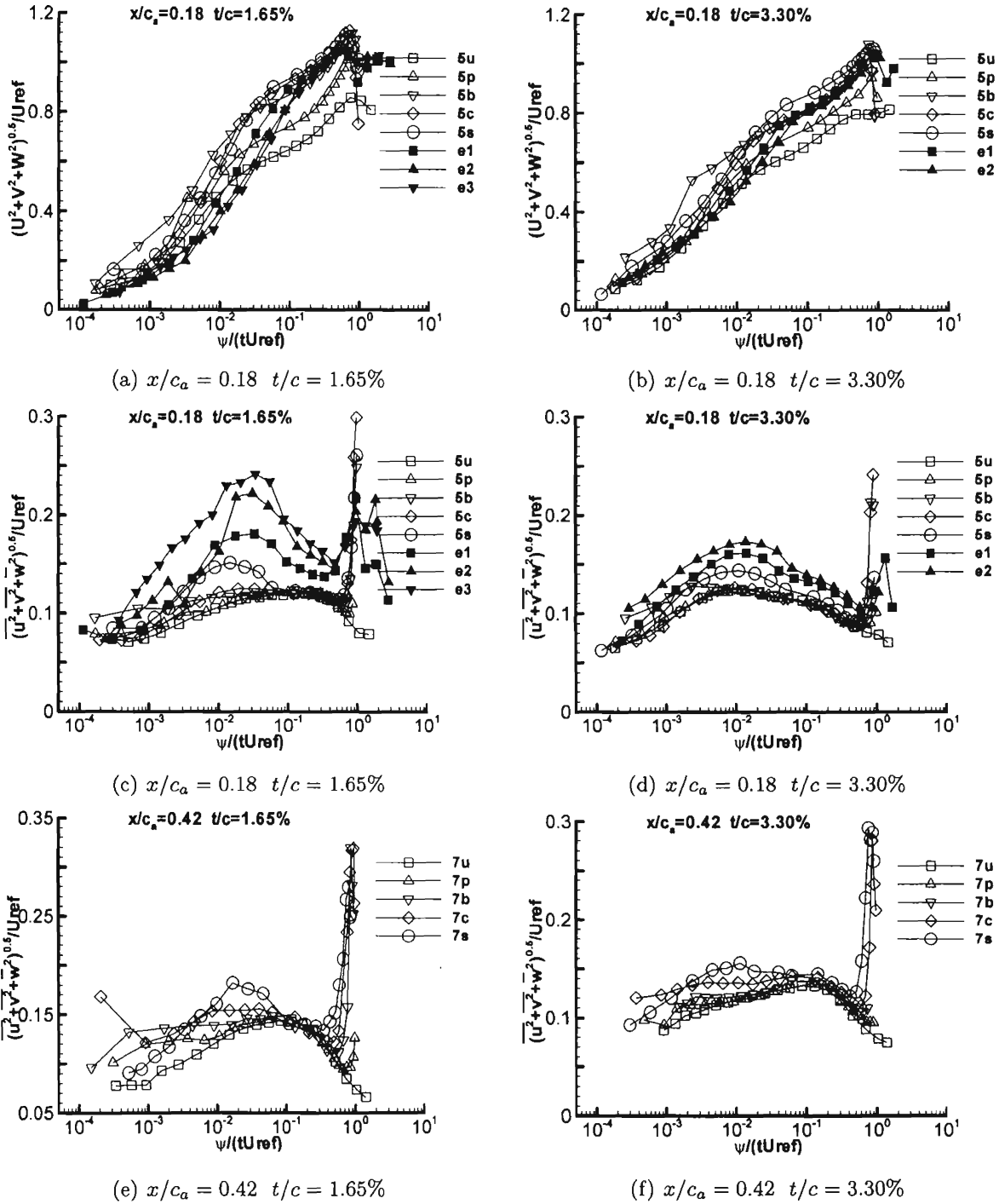


Figure 3.44:  $\sqrt{U^2 + V^2 + W^2} / U_{ref}$ ,  $\sqrt{u^2 + v^2 + w^2} / U_{ref}$  at  $x/c_a = 0.18$  and  $x/c_a = 0.42$  for both 1.65% and 3.30% in chord coordinate system

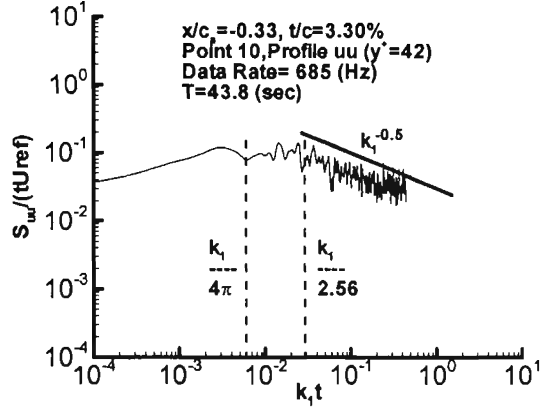
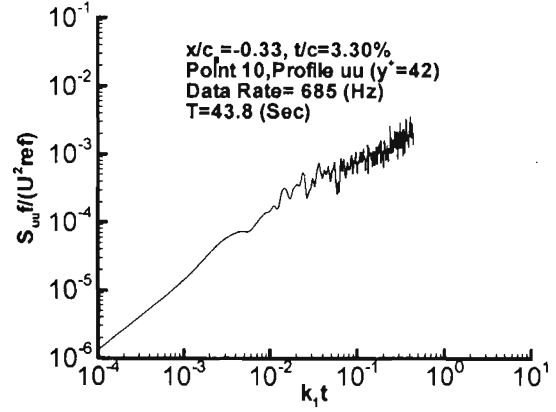
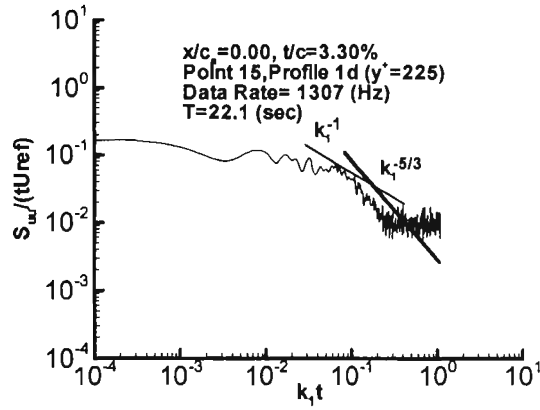
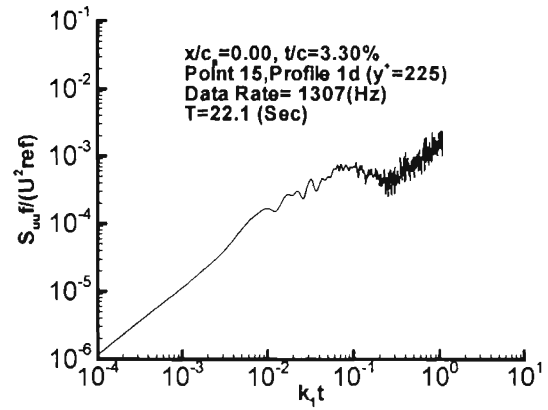
(a) Profile uu  $t/c = 3.30\%$ (b) Profile uu  $t/c = 3.30\%$ (c) Profile 1d  $t/c = 3.30\%$ (d) Profile 1d  $t/c = 3.30\%$ 

Figure 3.45: Spectra estimation of velocity component  $u$  for profile  $uu$  and  $1d$  in free-stream chord coordinate system. Note that  $k_1 = 2\pi f/U_{ref}$ .

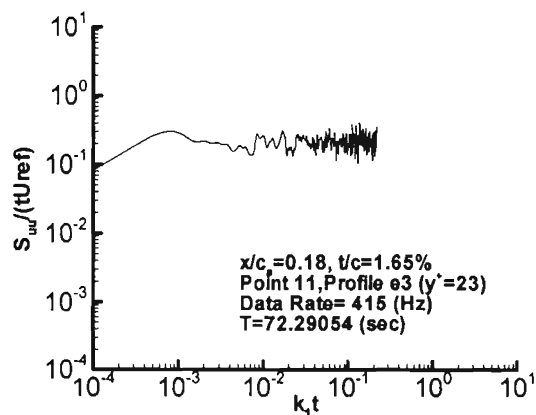
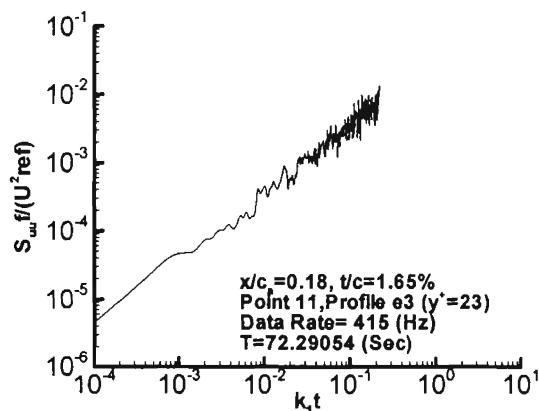
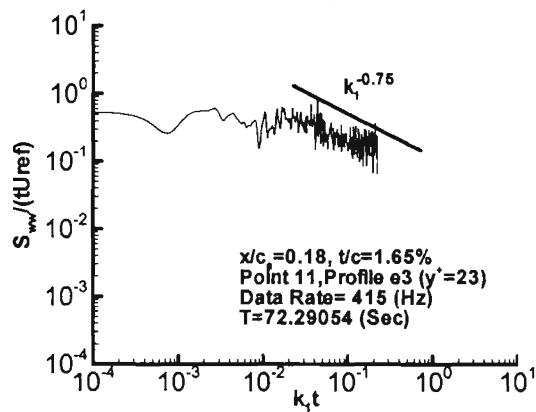
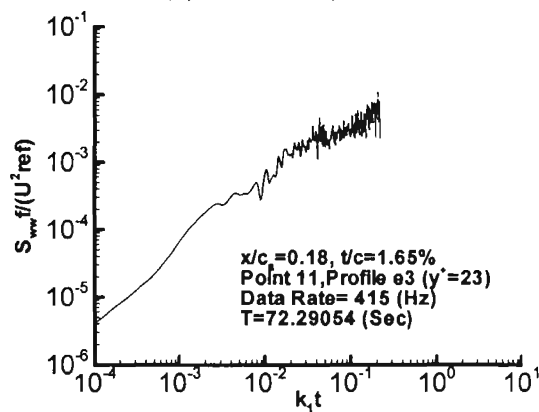
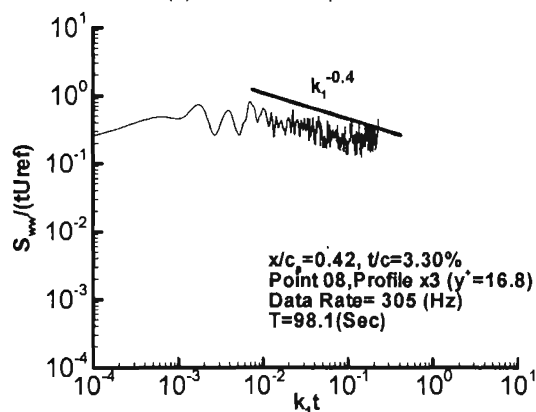
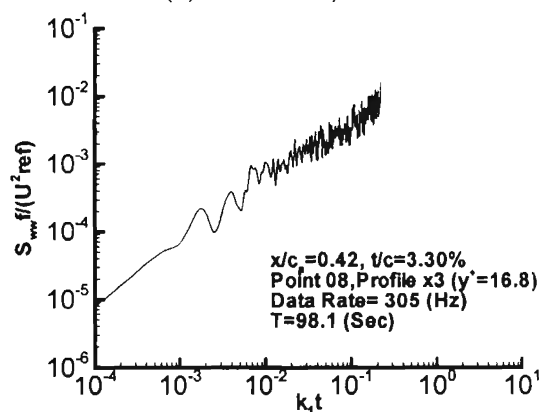
(a) Profile e3  $t/c=1.65\%$ (b) Profile e3  $t/c=1.65\%$ (c) Profile e3  $t/c=1.65\%$ (d) Profile e3  $t/c=1.65\%$ (e) Profile x3  $t/c=3.30\%$ (f) Profile x3  $t/c=3.30\%$ 

Figure 3.46: Spectra estimation of velocities for tip leakage vortex with 1.65% and 3.30% tip gaps. Note that  $k_1 = 2\pi f/U_{ref}$ .

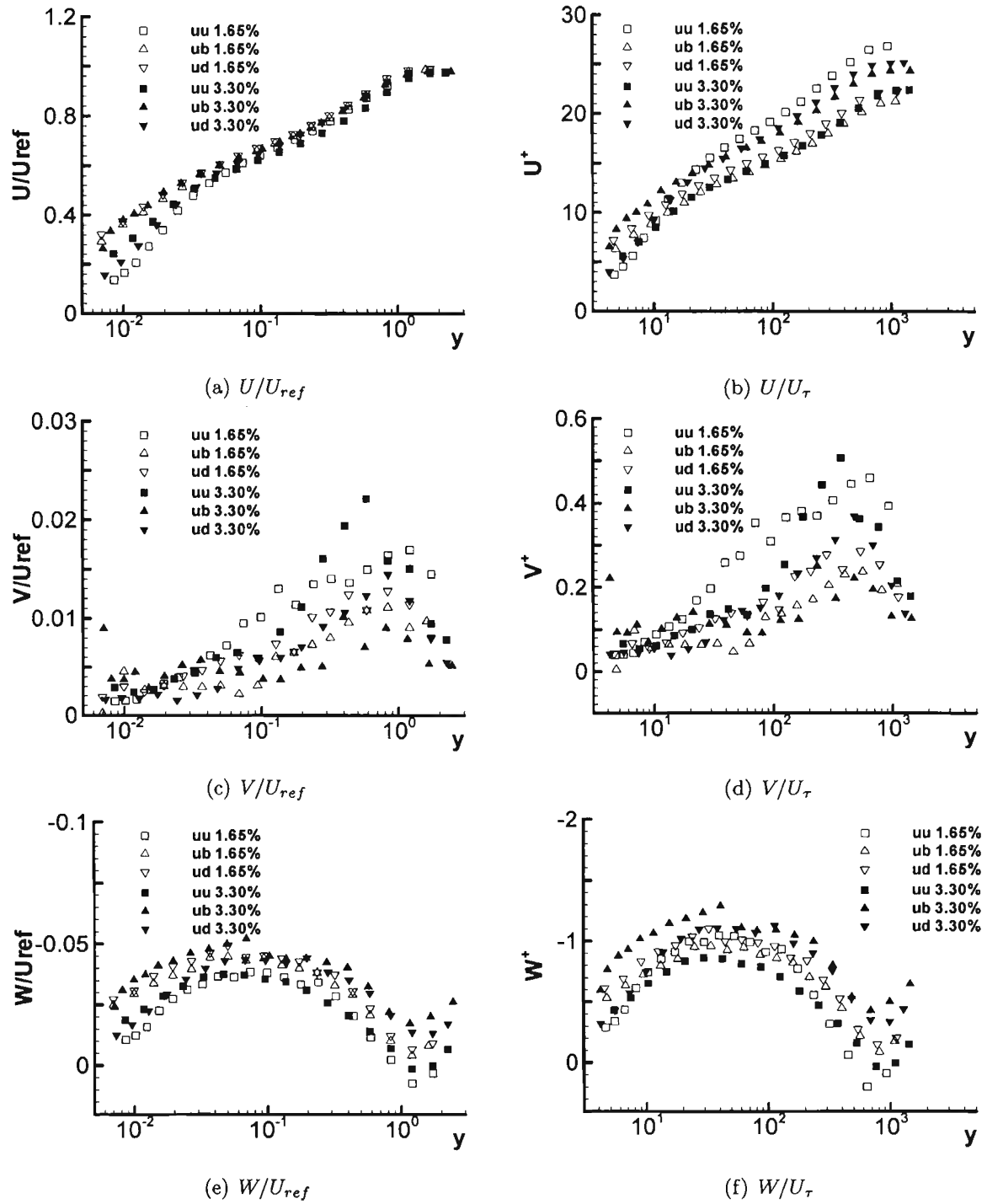


Figure 3.47: Inflow U, V, and W profiles at  $x/c_a$  for both 1.65% and 3.30% in free-stream coordinate system

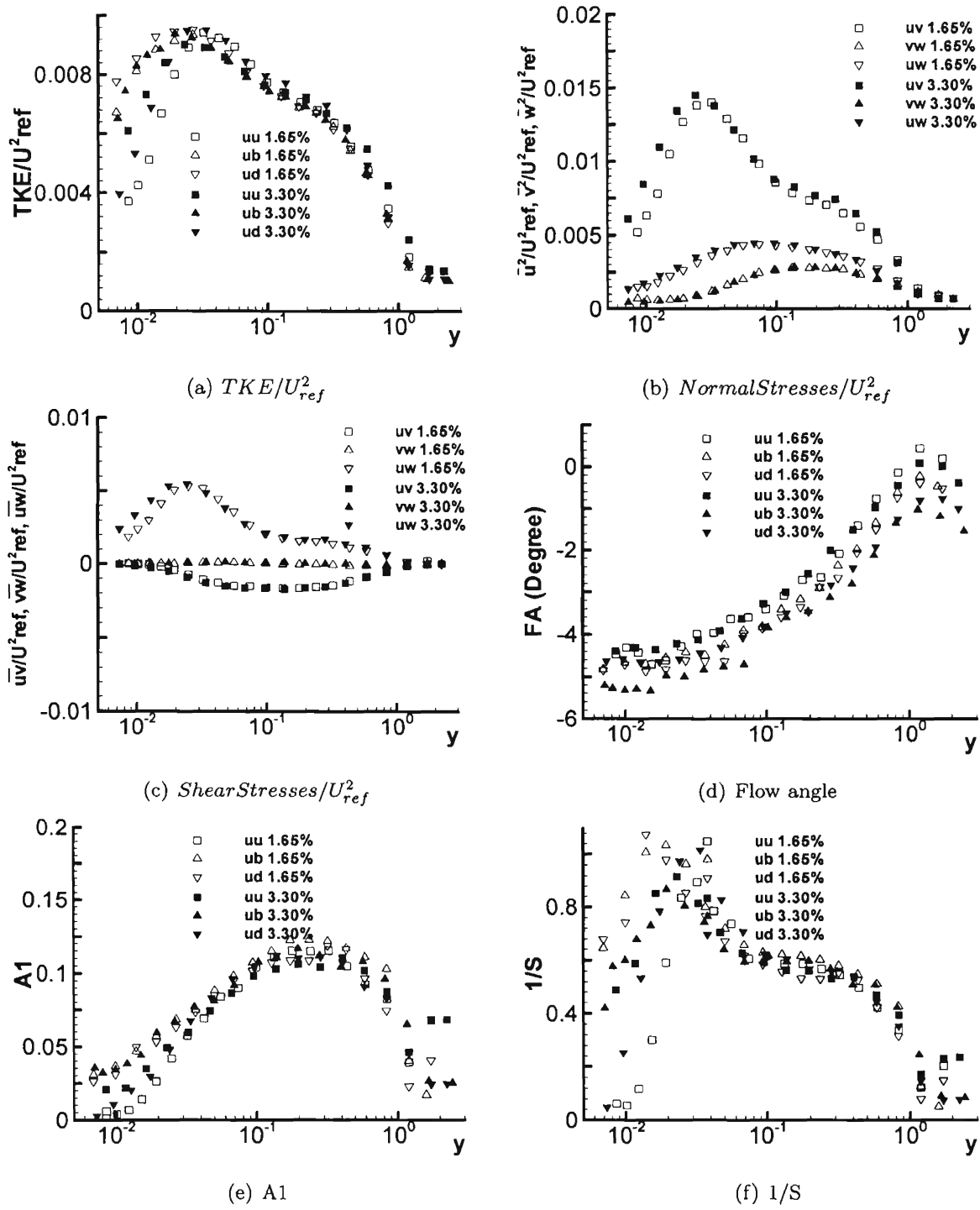


Figure 3.48: Inflow TKE, Reynolds stress, FA, A1, and 1/S for both 1.65% and 3.30% in free-stream coordinate system

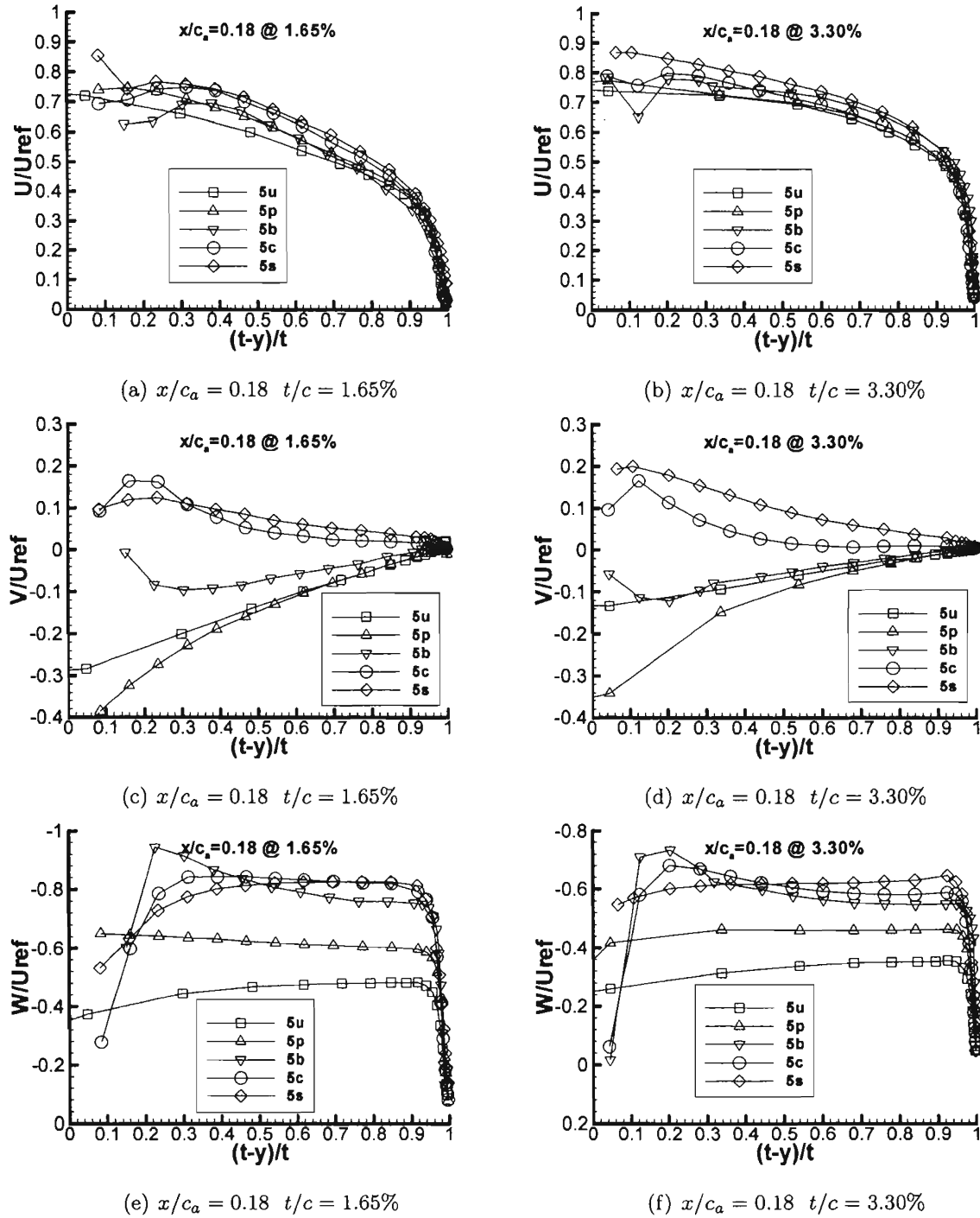
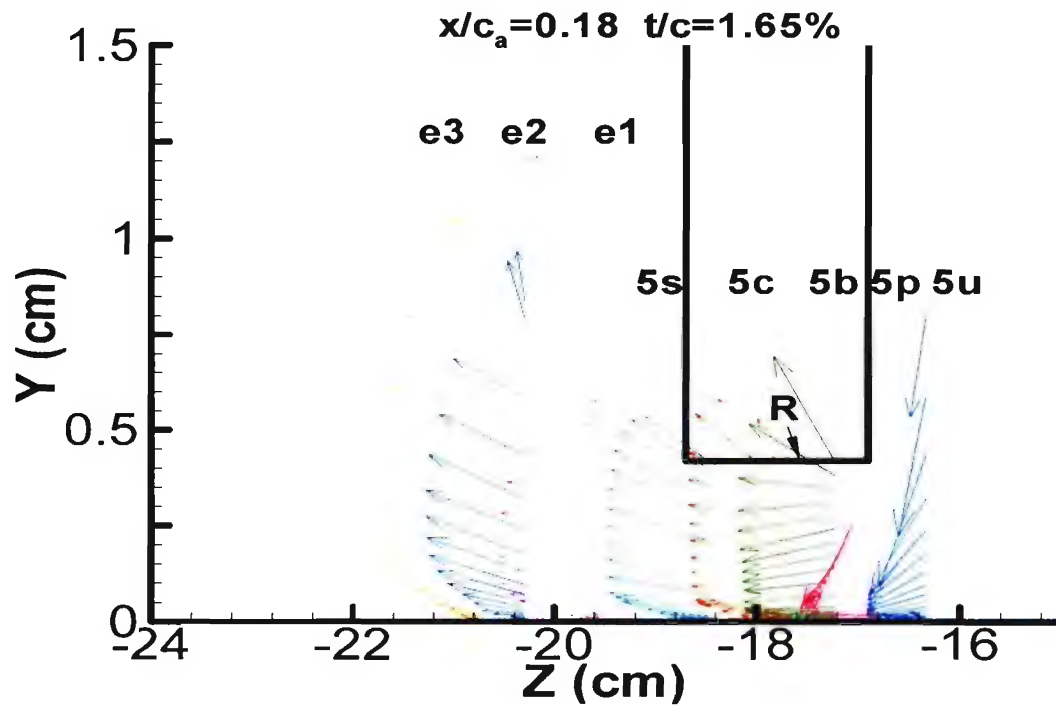
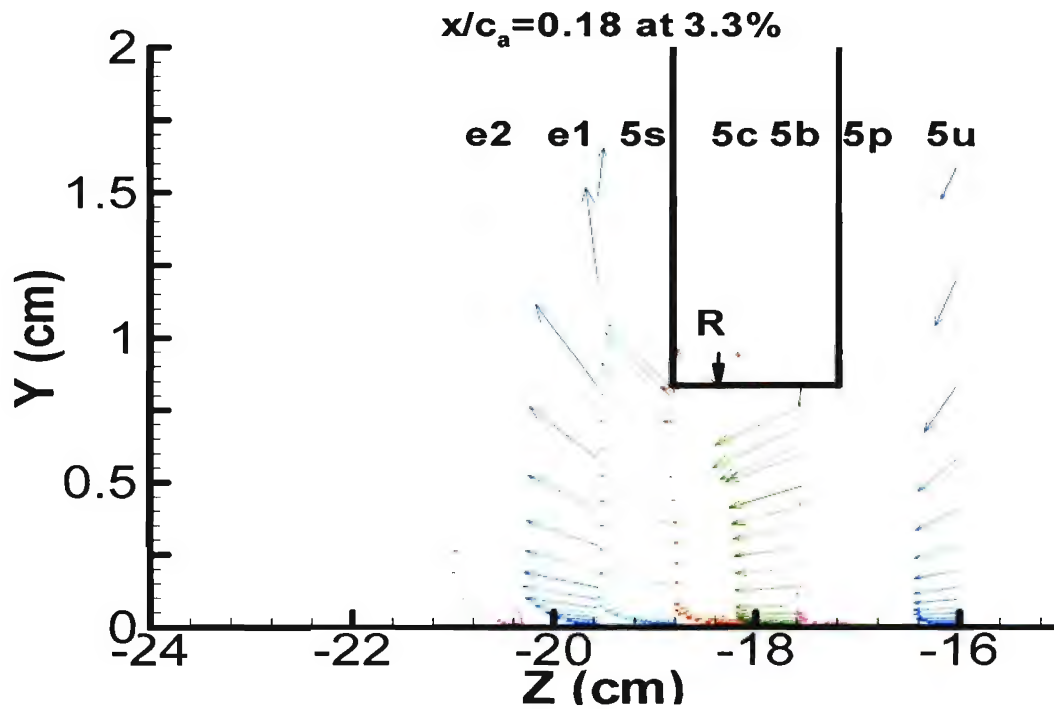
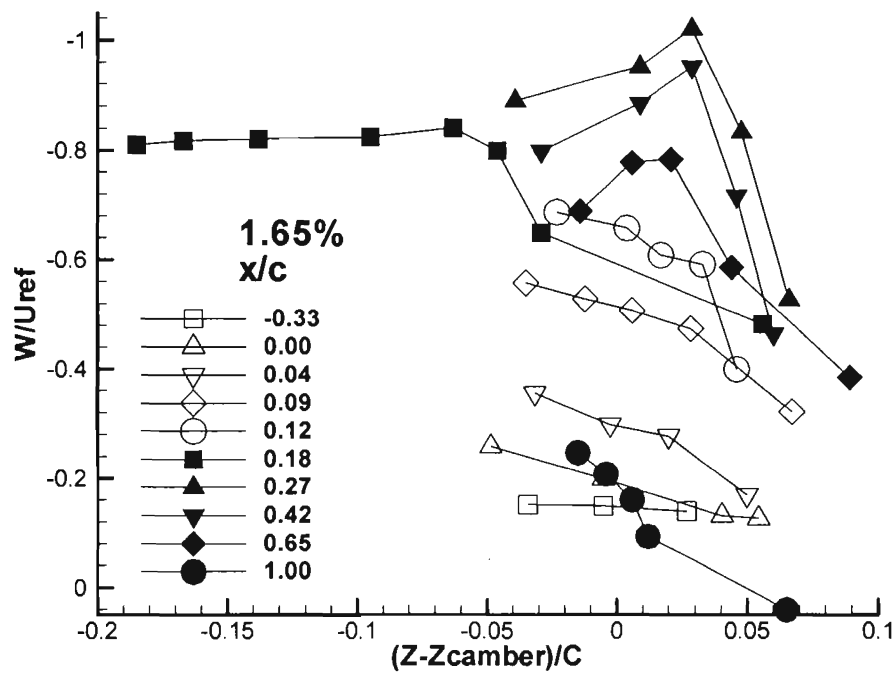
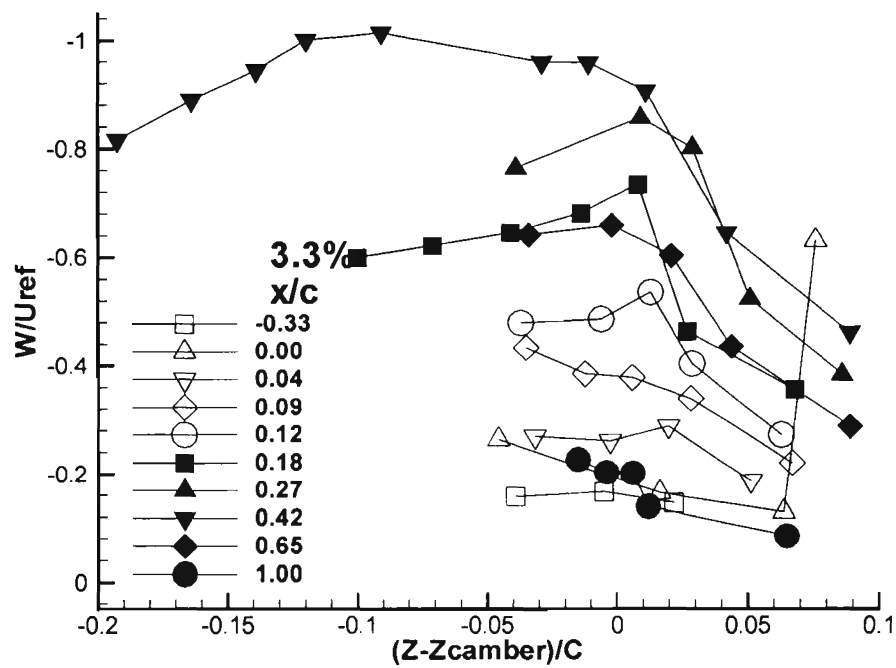


Figure 3.49:  $U/U_{ref}$ ,  $V/U_{ref}$ ,  $W/U_{ref}$  at  $x/c_a = 0.18$  for both 1.65% and 3.30% in chord coordinate system. Note that endwall is at  $(t-y)/t=1.0$ .

(a)  $x/c_a = 0.18 \quad 1.65\%$ (b)  $x/c_a = 0.18 \quad 3.30\%$ Figure 3.50: VW vector plots at  $x/c_a = 0.18$  for both 1.65% and 3.30% in chord coordinate system



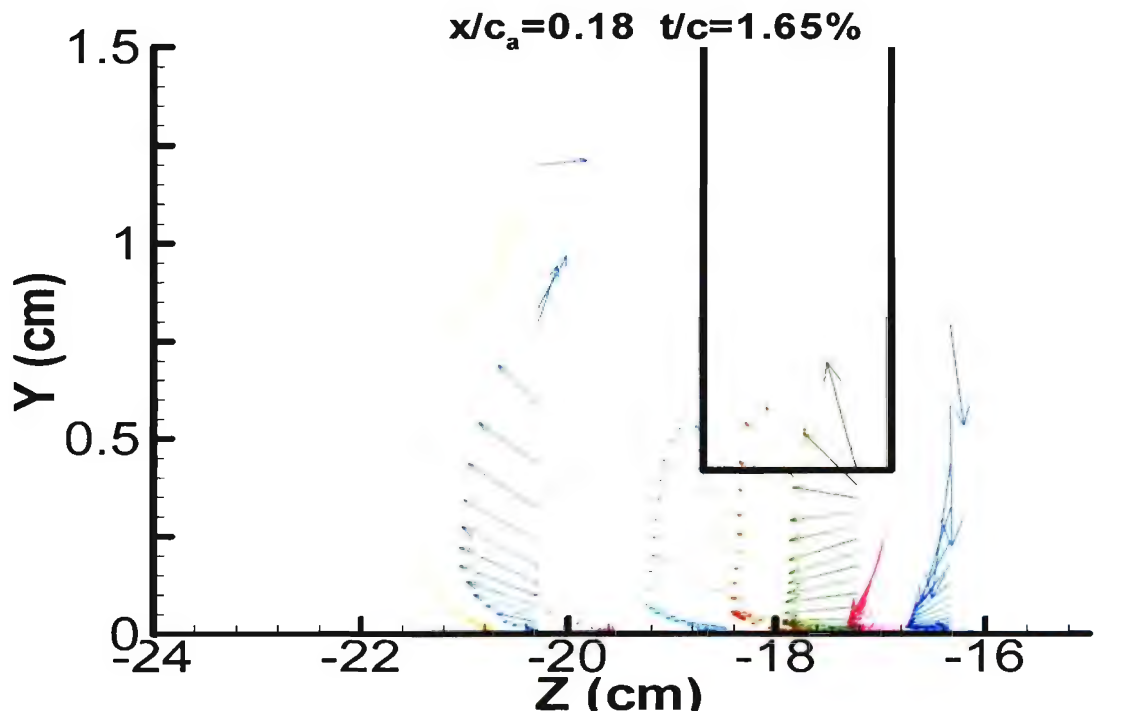
(a) 1.65%



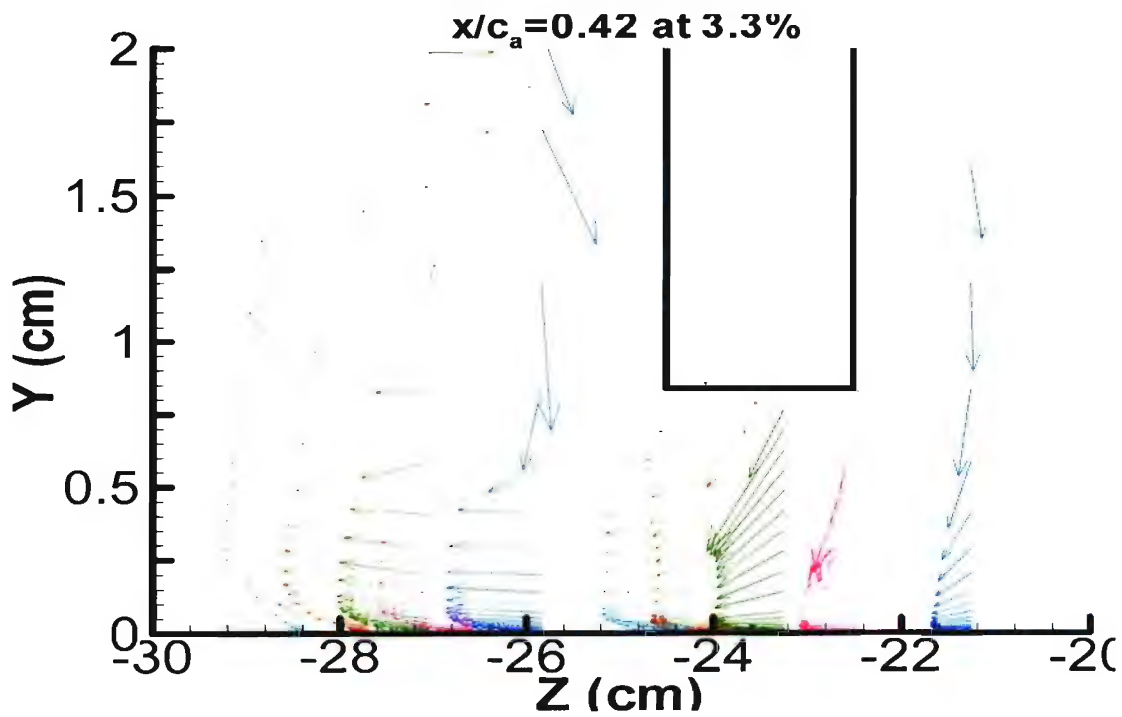
(b) 3.30%

Figure 3.51: Maximum  $W$  for 1.65% and 3.30% in the chord coordinate system



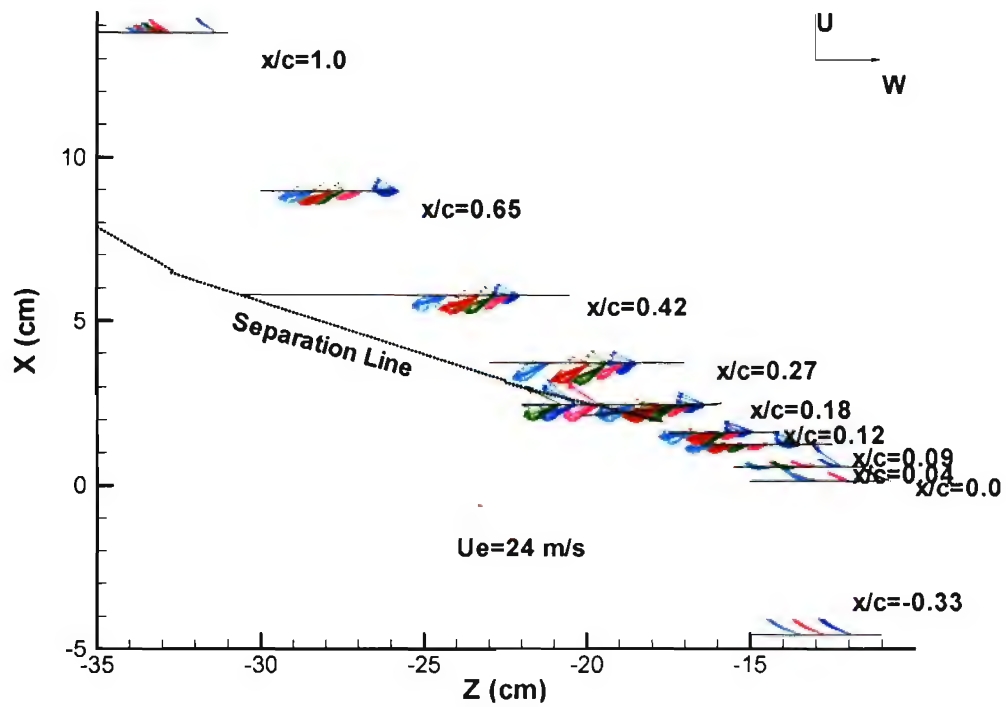


(a)  $x/c_a = 0.18 \quad 1.65\%$

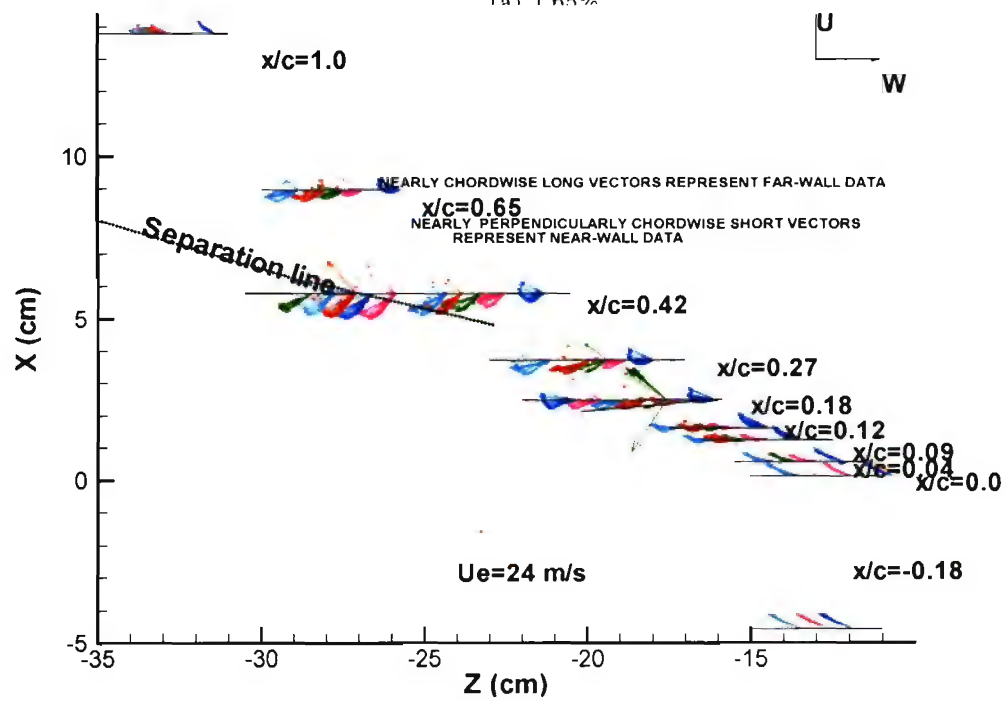


(b)  $x/c_a = 0.42 \quad 3.30\%$

Figure 3.52: VW vector plots at  $x/c_a = 0.18$  with 1.65% and  $x/c_a = 0.42$  with 3.30% in the separation-line coordinate system

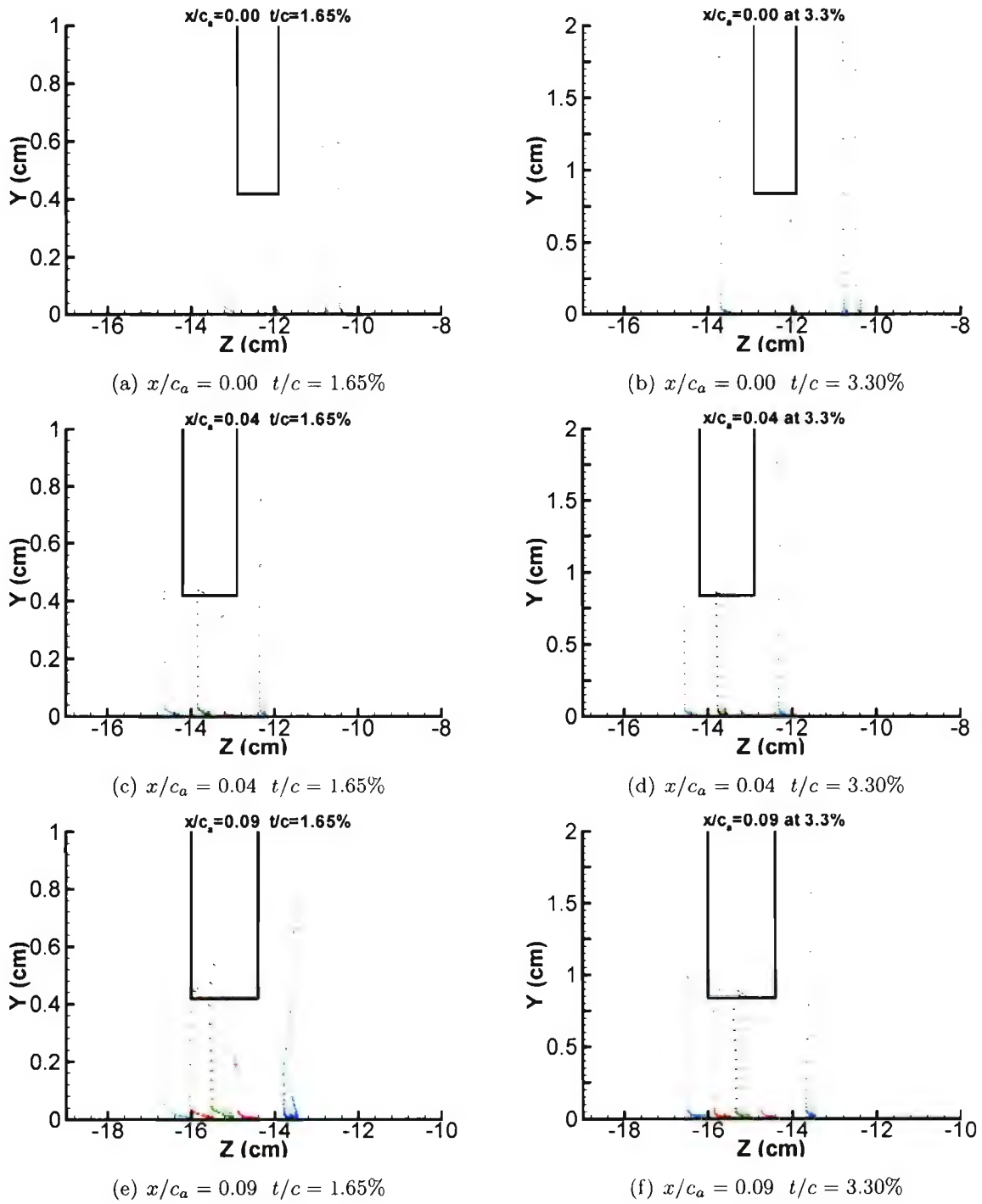


(a) 1.65%



(b) 3.30%

Figure 3.53: Mean Velocity vector  $UW$  for 1.65% and 3.30%

Figure 3.54: Mean velocity vector  $VW$  for 1.65% and 3.30% in chord coordinate system

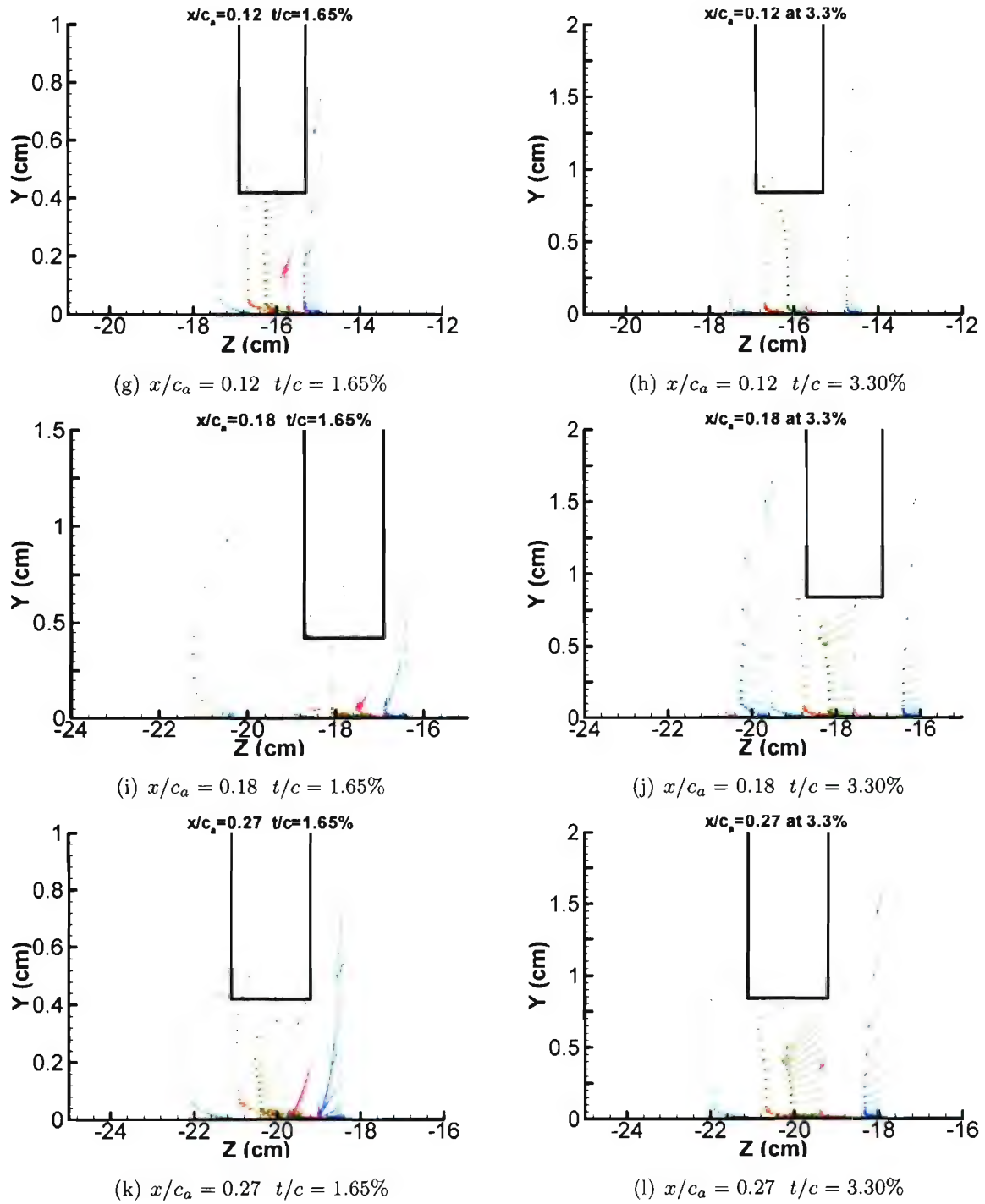


Figure 3.54: Mean velocity vector  $VW$  for 1.65% and 3.30% in chord coordinate system (cont.)

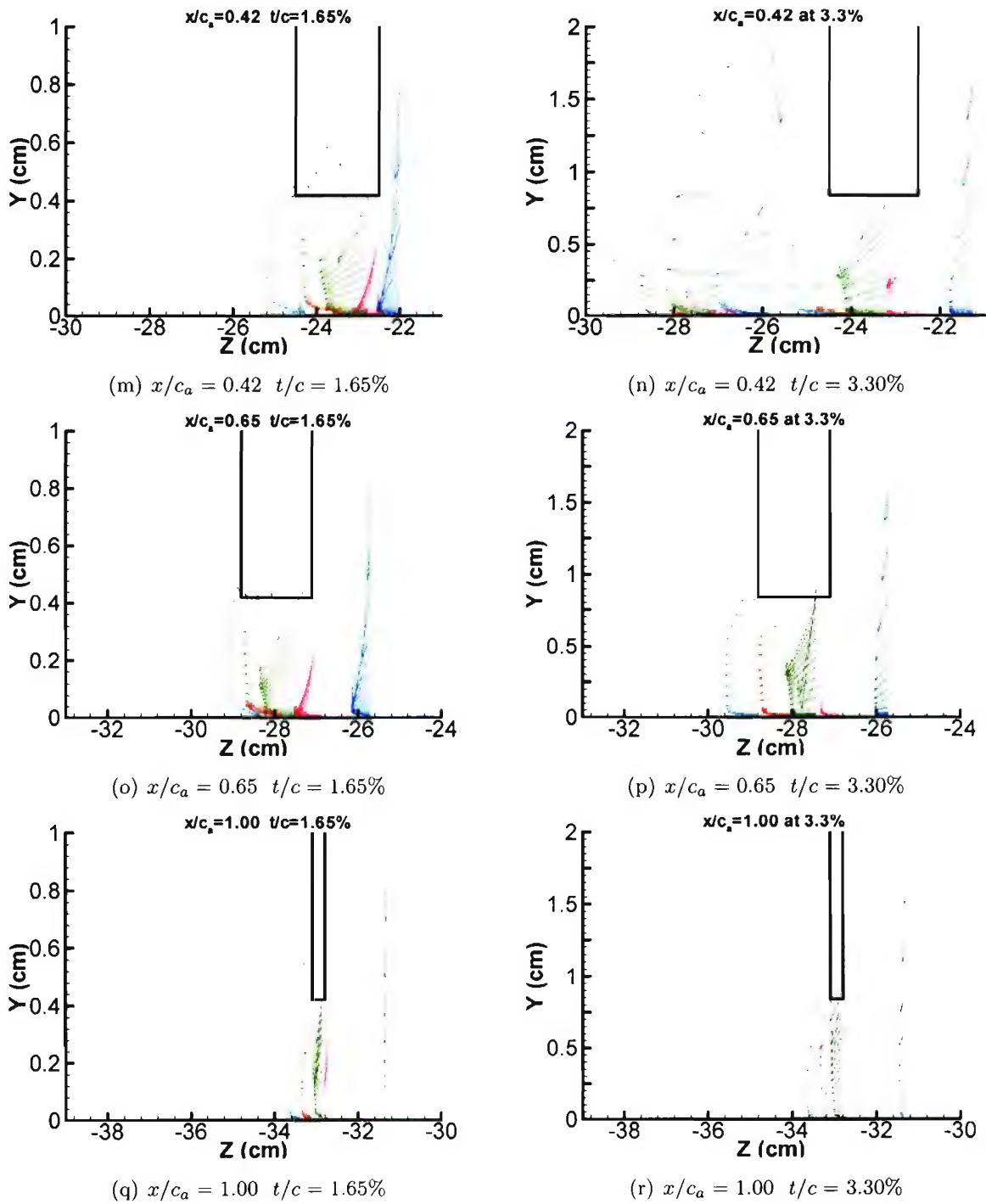
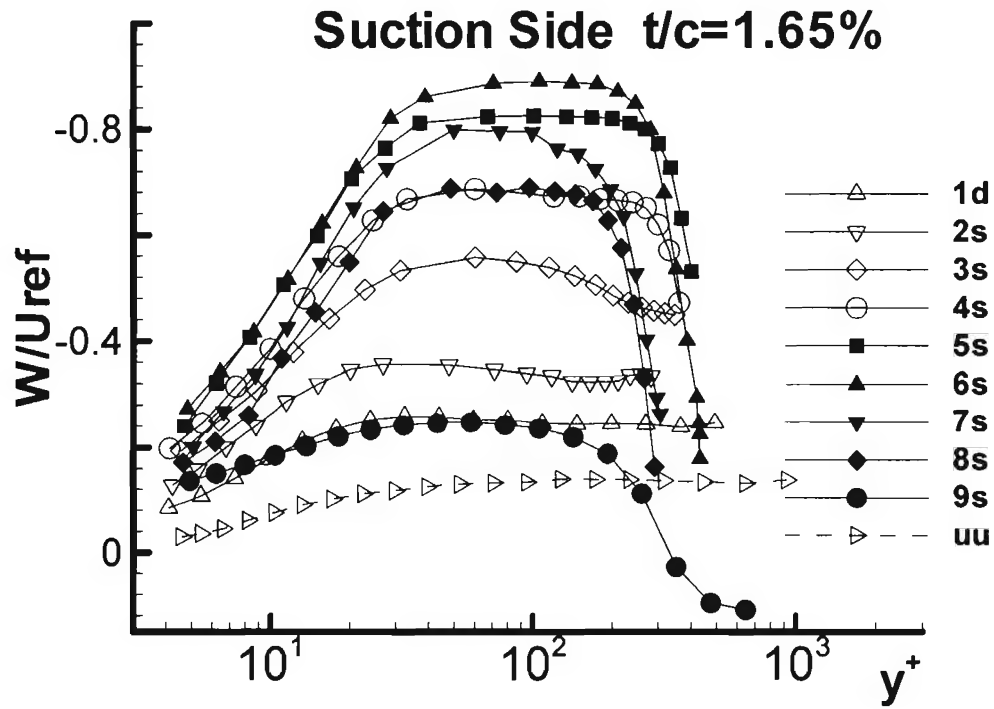
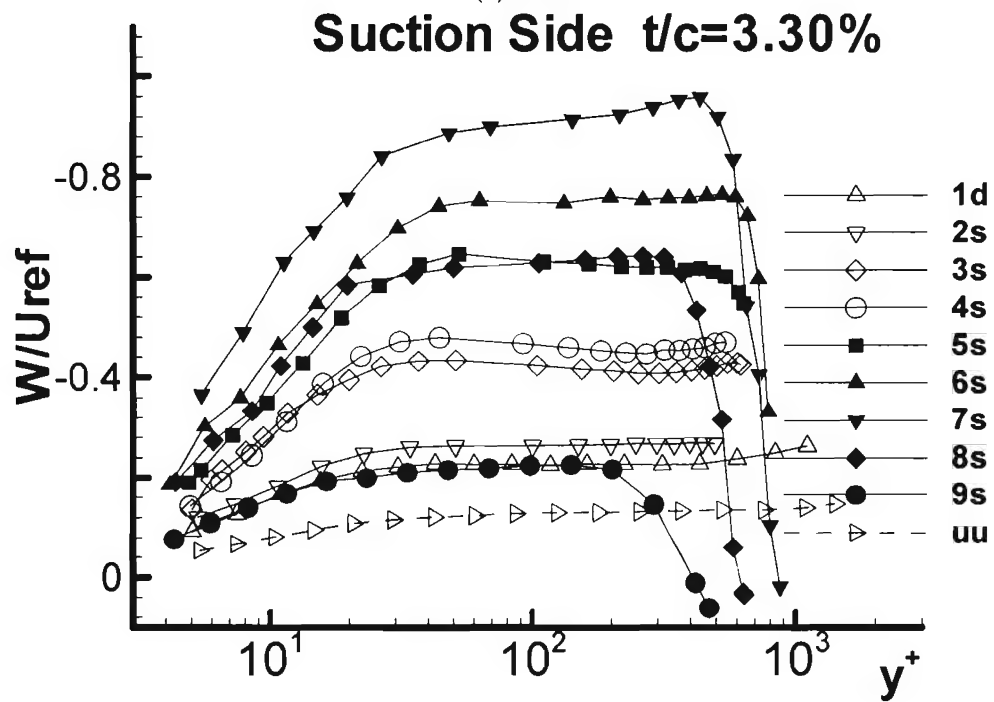


Figure 3.54: Mean Velocity vector  $VW$  for 1.65% and 3.30% in chord coordinate system (cont.)



(a) 1.65%



(b) 3.30%

Figure 3.55:  $W/U_{ref}$  on the suction side for 1.65% and 3.30% in chord coordinate system

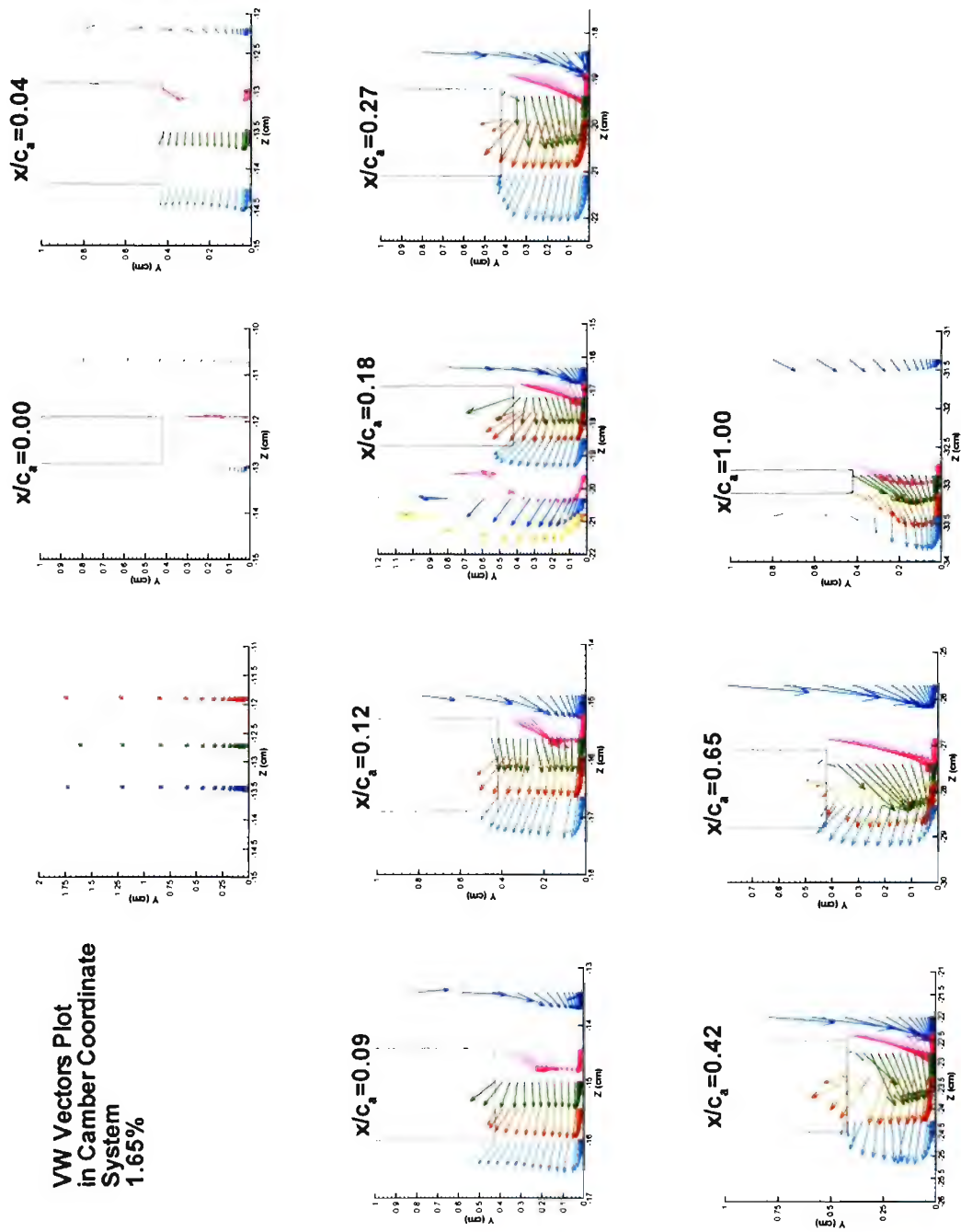


Figure 3.56: VW vector plot in local camber coordinate system for 1.65%

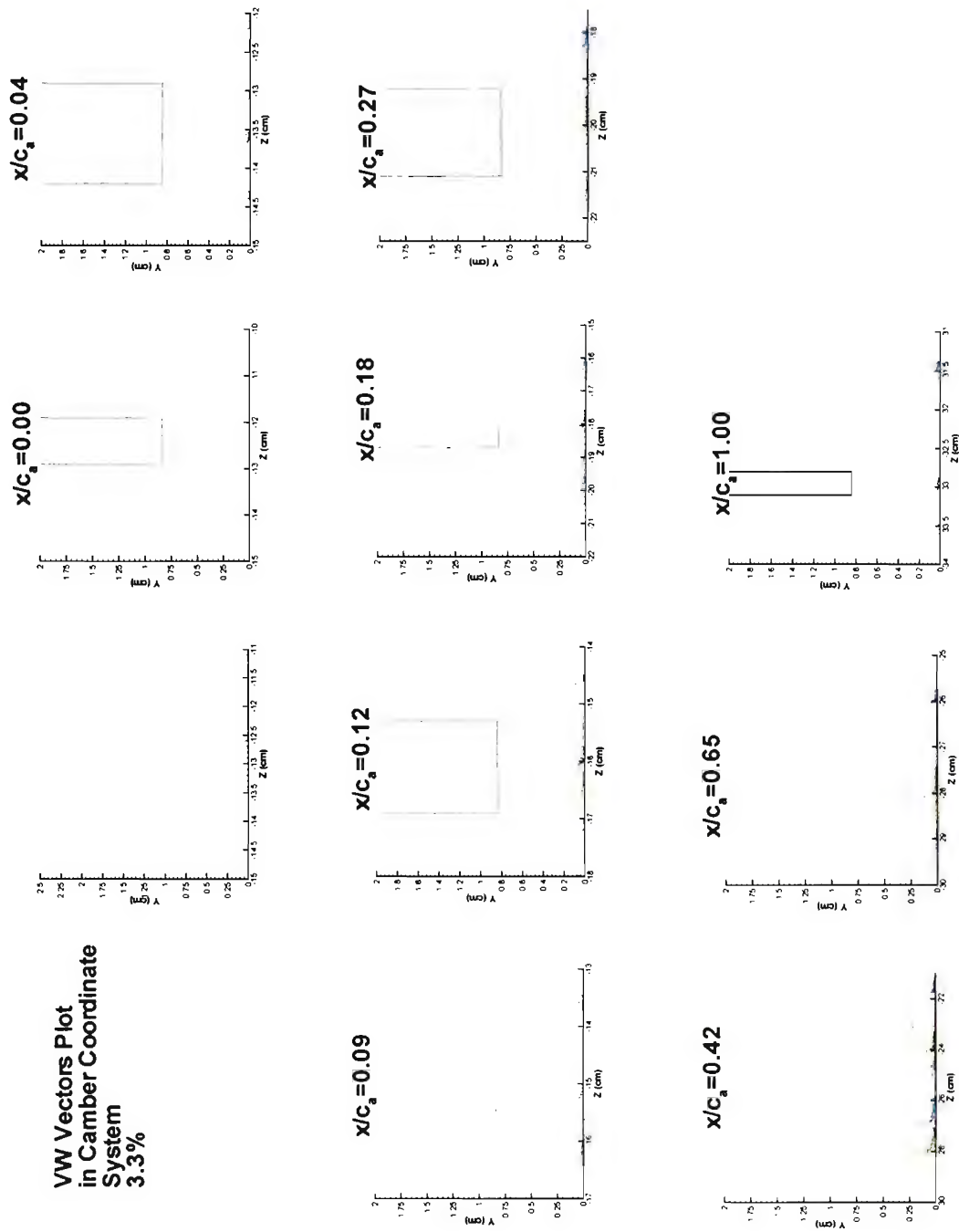


Figure 3.57: VW vector plot in local camber coordinate system for 3.30%



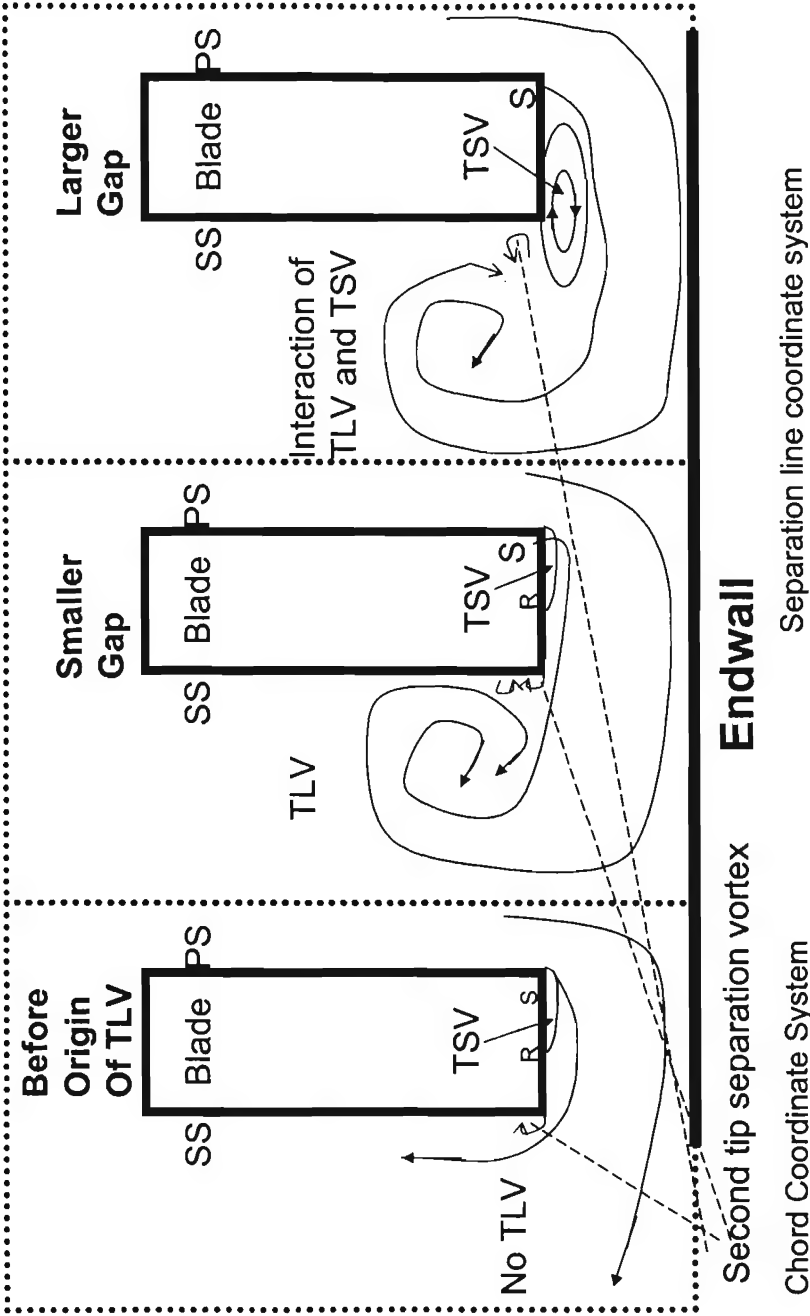


Figure 3.58: Gap Model - Mean Flow

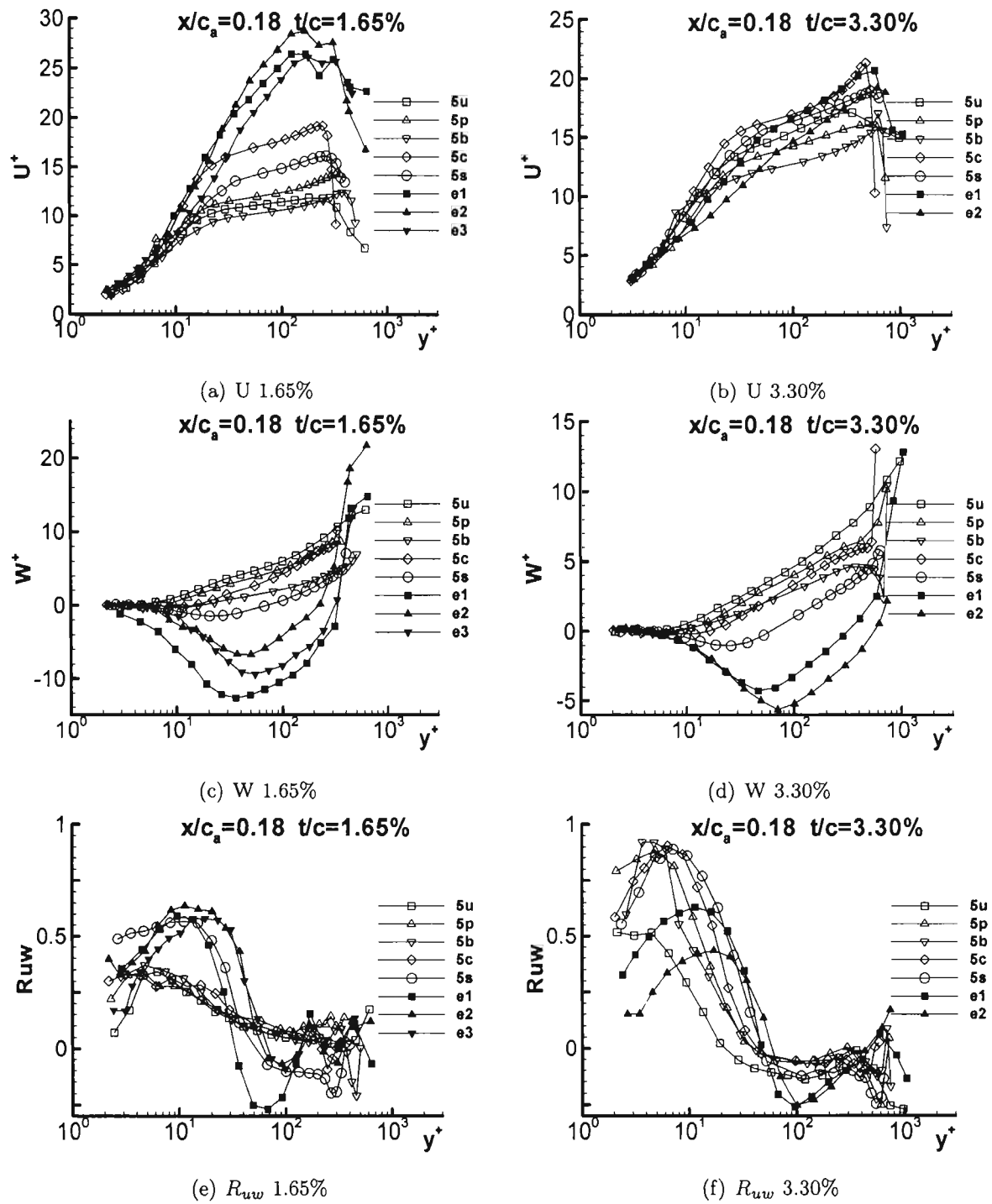


Figure 3.59:  $U/U_\tau$ ,  $W/U_\tau$ , and  $R_{uw}$  at  $x/c_a = 0.18$  for both 1.65% and 3.30% in wall shear coordinate system

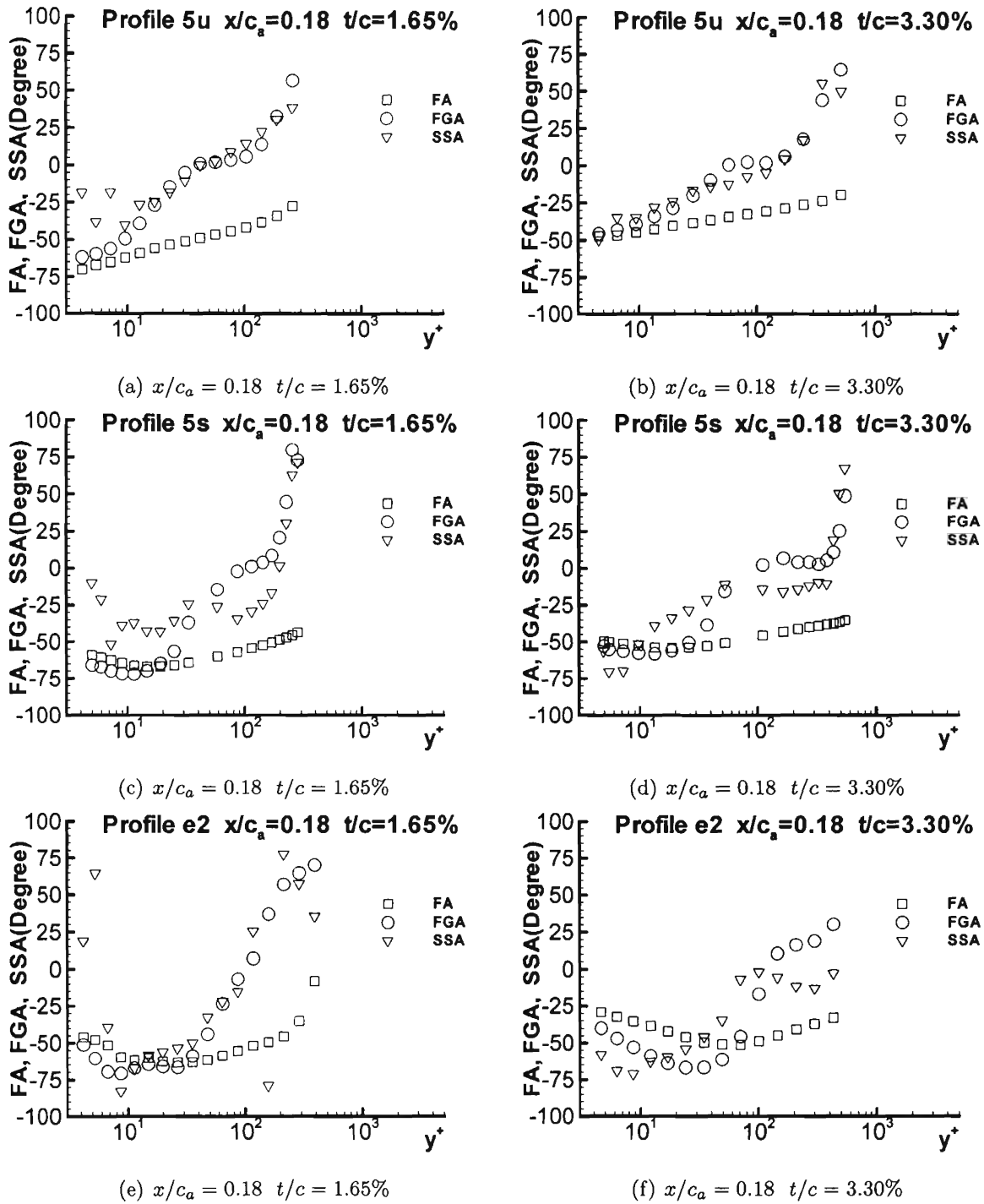


Figure 3.60: FA, FGA, and SSA at  $x/c_a = 0.18$  for both 1.65% and 3.30% in chord coordinate system

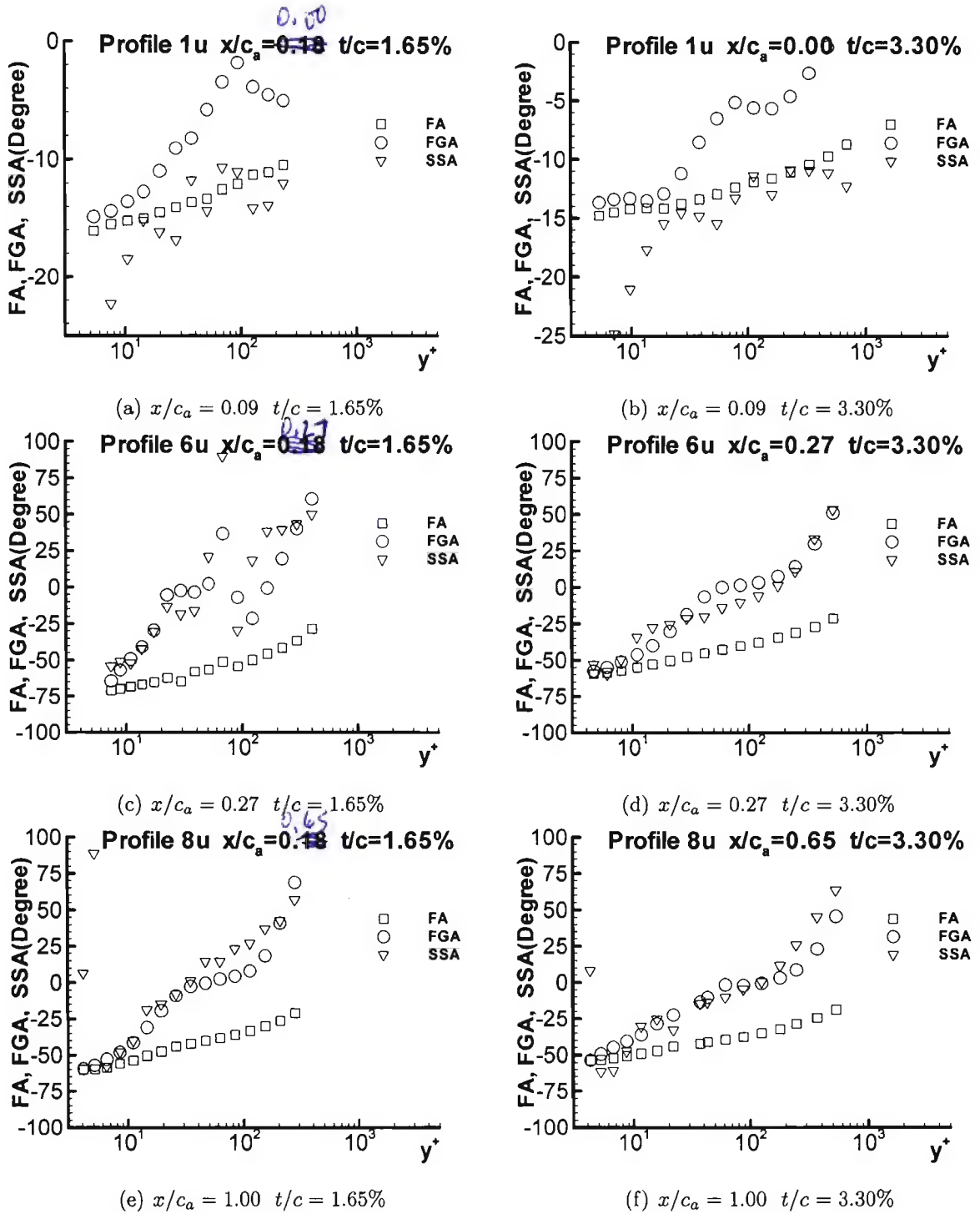


Figure 3.61: FA, FGA, and SSA at local upstream for both 1.65% and 3.30% in chord coordinate system

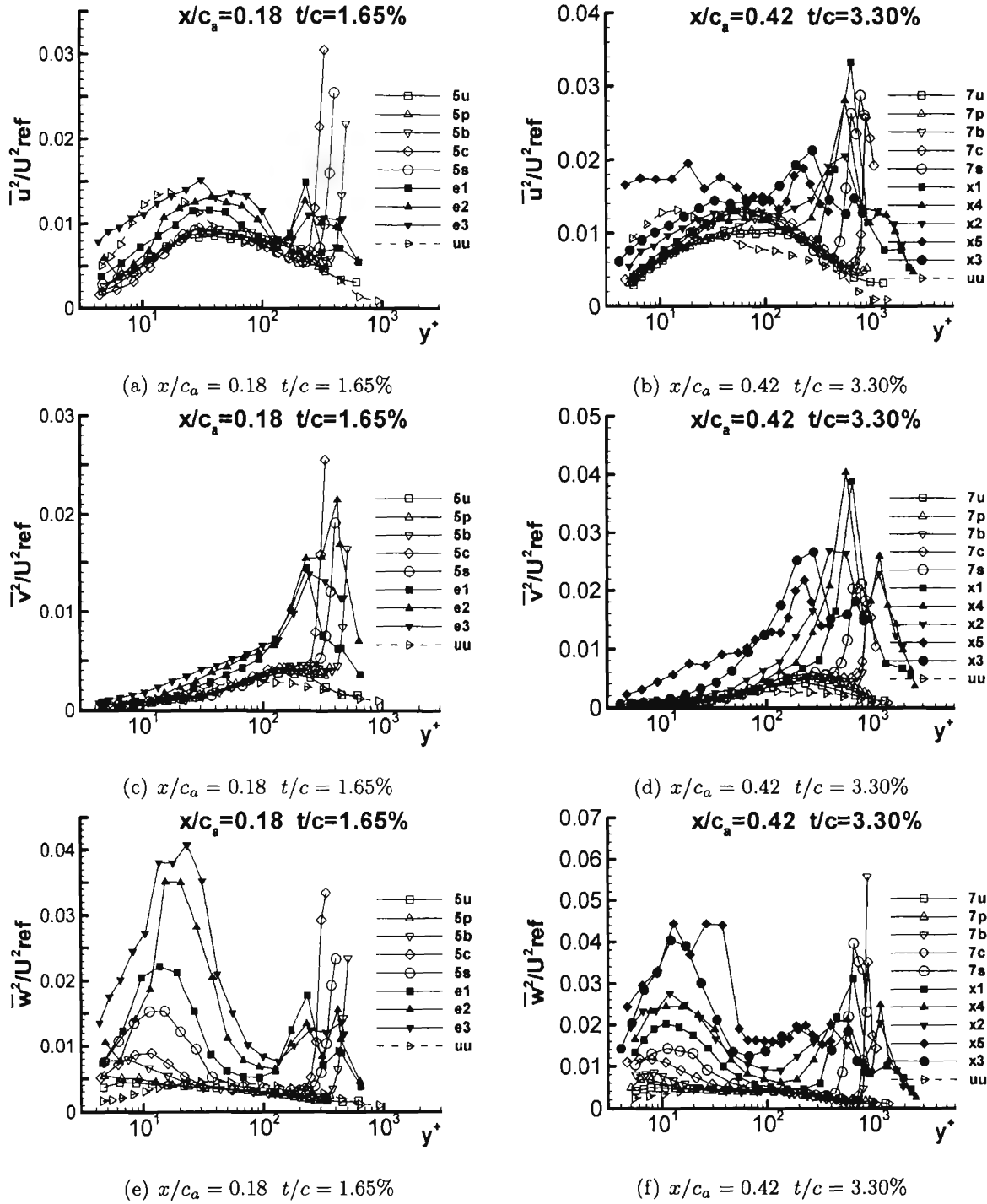
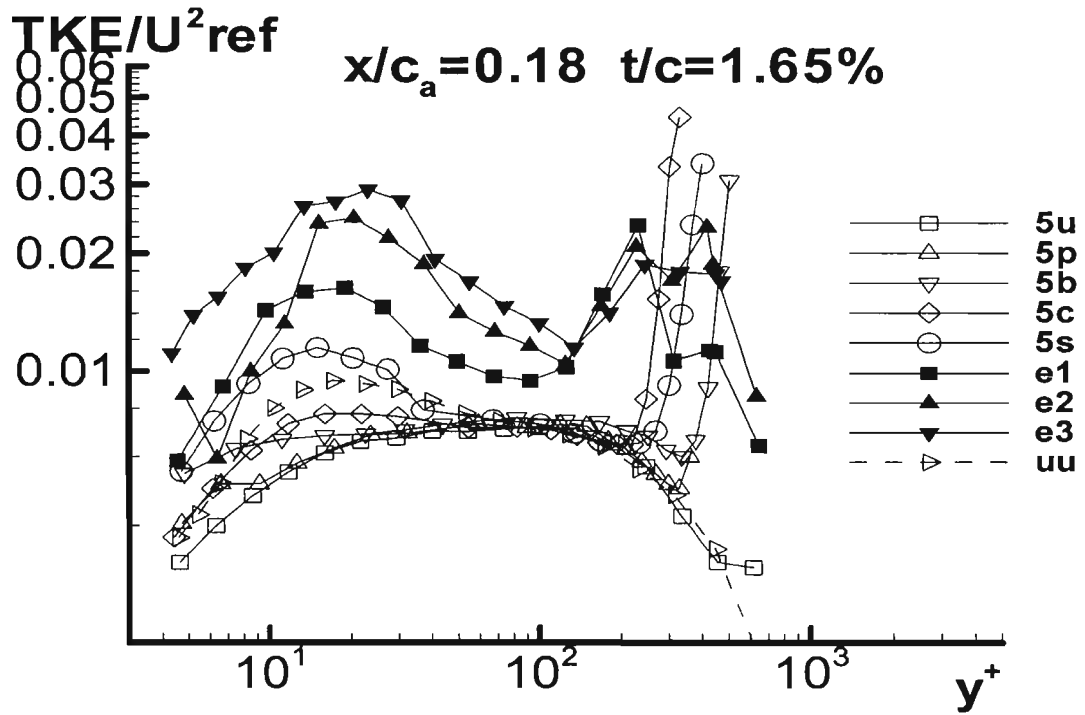
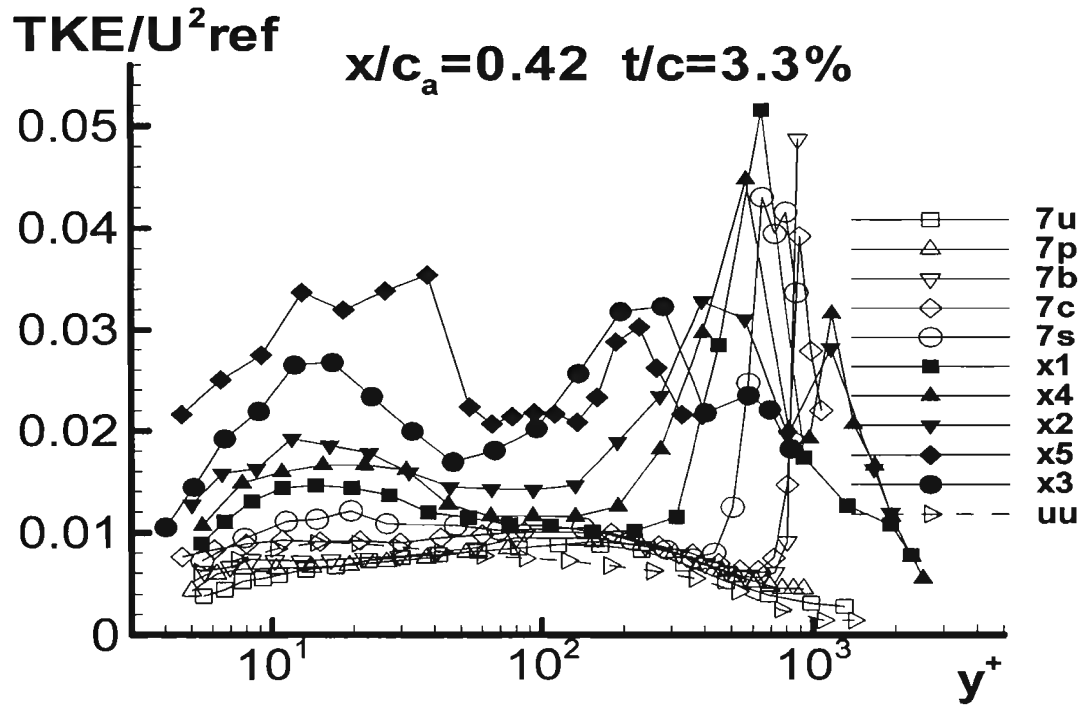


Figure 3.62:  $\overline{u^2}/U_{ref}^2$ ,  $\overline{v^2}/U_{ref}^2$ , and  $\overline{w^2}/U_{ref}^2$  at  $x/c_a = 0.18$  for 1.65% and at  $x/c_a = 0.42$  for 3.30% in chord coordinate system



(a) 1.65%



(b) 3.30%

Figure 3.63:  $TKE/U_{ref}^2$  at the origin of tip leakage vortex for both 1.65% and 3.30%

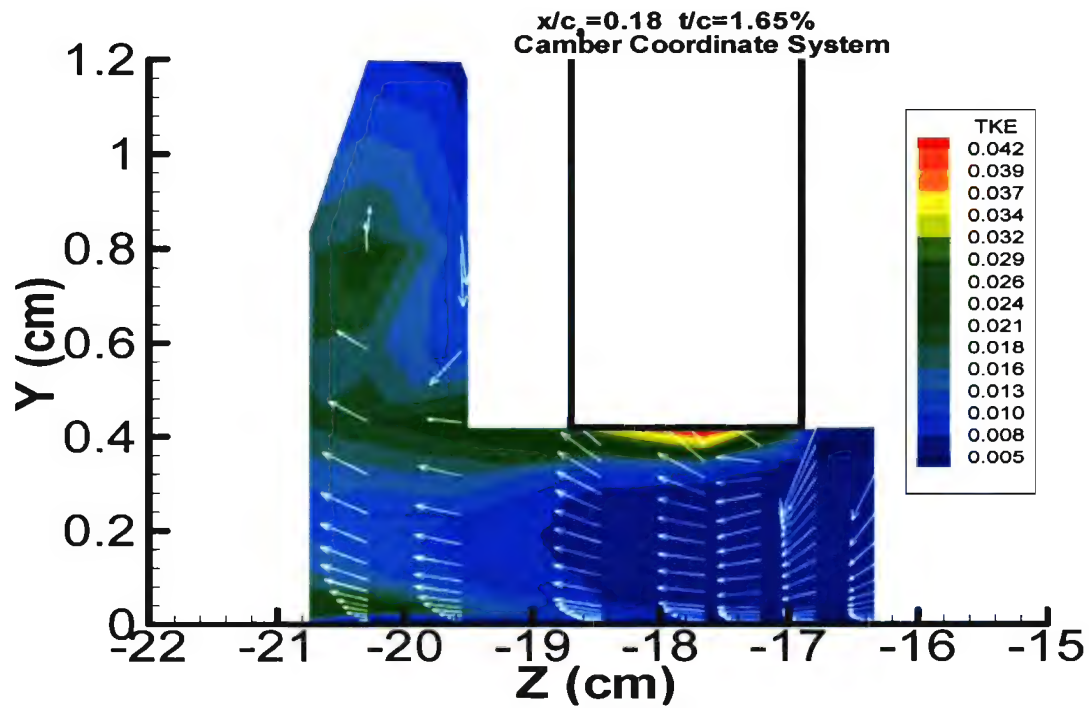
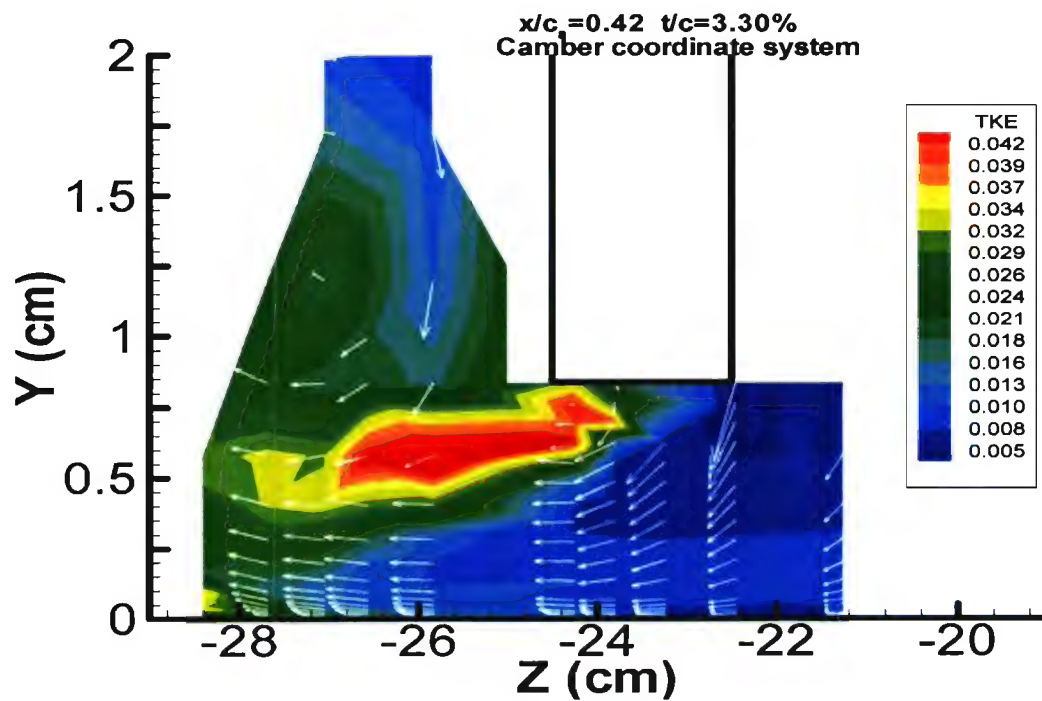
(a)  $x/c_a = 0.18$  1.65%(b)  $x/c_a = 0.42$  3.30%

Figure 3.64: VW vector and TKE contour plots at  $x/c_a = 0.18$  with 1.65% and  $x/c_a = 0.42$  with 3.30% in the chord coordinate system

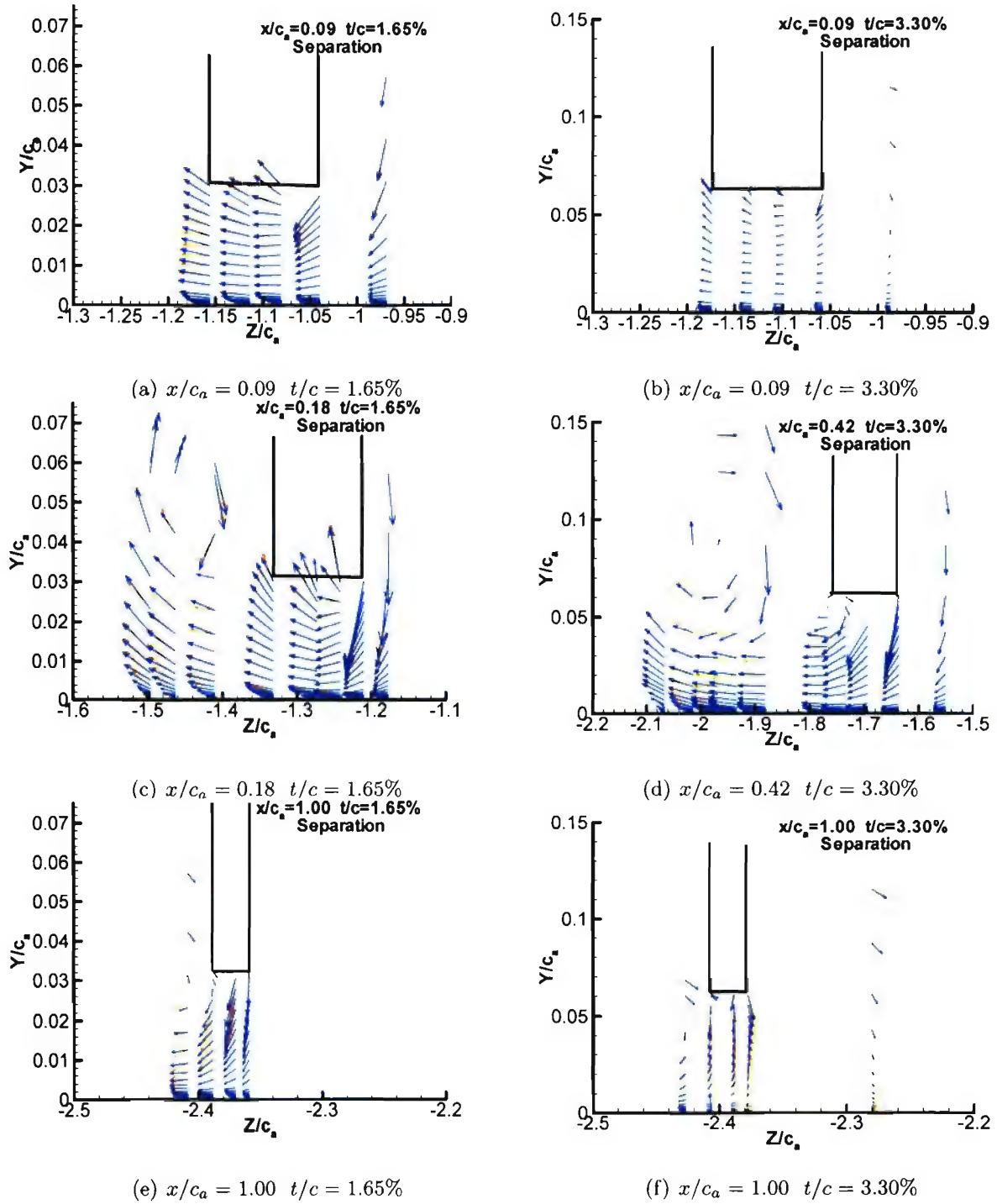


Figure 3.65: Comparison between  $V\vec{W}$  and  $V\vec{W} + \vec{V}_q$  for 1.65% and 3.30% in separation-line coordinate system. Note that blue vectors represent  $V\vec{W}$  vectors and red vectors represent the summation of  $V\vec{W}$  and  $\vec{V}_q$ .  $\rightarrow$  denotes  $0.5U_{ref}$ .



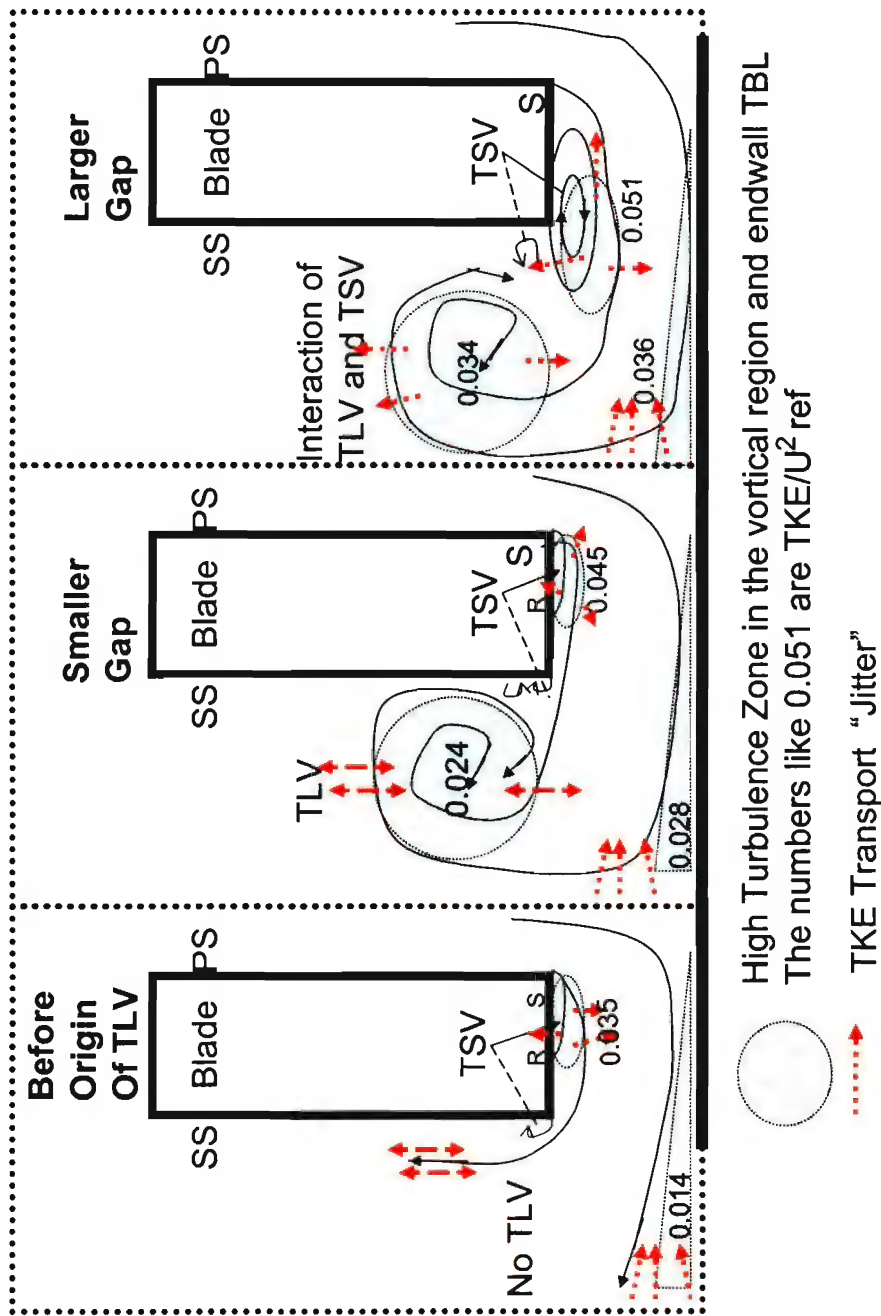
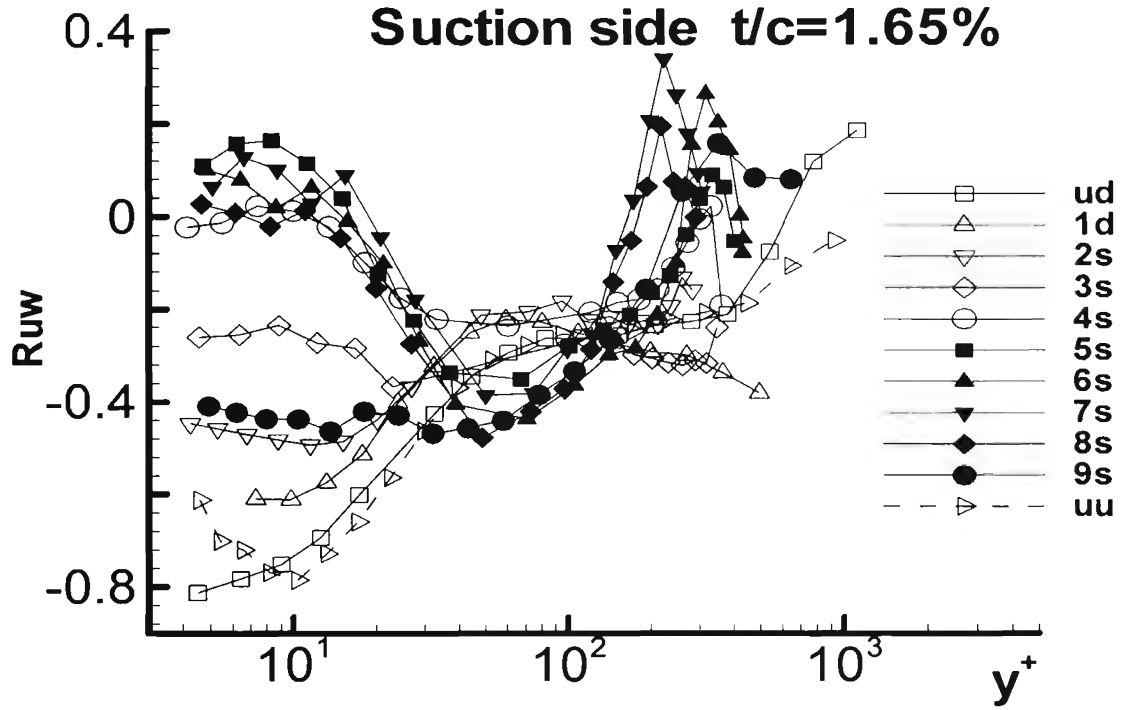
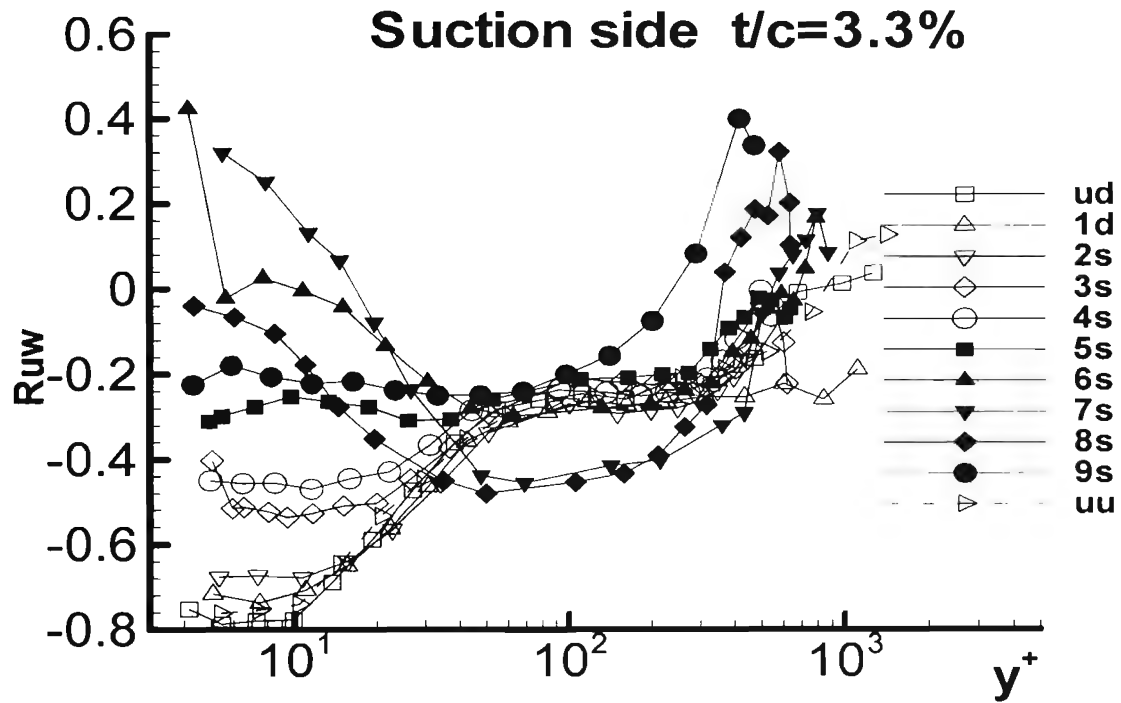


Figure 3.66: Gap Model - Turbulence



(a) 1.65%



(b) 3.30%

Figure 3.67: Correlation coefficients of  $\overline{uw}$  at suction side for both 1.65% and 3.30% in chord coordinate system

# Chapter 4

## Measurements on a Moving Wall

Relative motion is a very important factor for the compressor rotor and its casing. To investigate the effect of relative motion on flow structures of a tip gap flow, a moving belt system was built to simulate the relative motion between the blade row and the endwall in the linear compressor cascade wind tunnel, which was described in Section 2.2.

Due to the difficulty of LDV measurements for the moving wall and the restriction of time, just one profile upstream of the blade with 3.30% tip gap plus a few points in the tip gap region with 1.65% tip gap were taken to examine the critical effect of the relative motion. Their physical locations are shown in Figure 4.1.

In this chapter, the first section describes the calibration and uncertainty of the flow and measurement. Oil flow visualizations and LDV measurements are presented in Section 4.2 and Section 4.3, respectively. The final section discusses the flow structure for the moving wall cases.

## 4.1 Calibration and Uncertainty

To obtain the reliable data for the moving wall experiments, the same procedure was adopted to calibrate the tunnel and instrumentation as in the stationary wall case, described in Section 3.2. An uncertainty analysis of the LDV measurements was also done for the moving wall experiments.

### 4.1.1 Tunnel and LDV Calibration

After the final setup for the moving wall experiments, the velocity distributions upstream and downstream of the blade row are plotted in Figure 4.2. The pressure loading was not measured for the moving wall experiments, but Ma (2003) confirmed that the difference between the stationary wall and moving wall experiments was negligible.

The LDV for the moving wall experiments was re-calibrated because the laser beams also passed through the thin Mylar film that was used. This way the beam crossing changed so that a fine alignment was necessary. Since the running belt speed was known, the LDV calibration of the measurement volume used the known speed of the moving belt rather than the known linear speed of a spinning calibration wheel. The rotation angles of the co-ordinate transformation between the LDV probe and tunnel co-ordinates were  $0.491^\circ$ ,  $2.503^\circ$ , and  $-1.121^\circ$  in pitch, yaw, and roll, respectively.

### 4.1.2 LDV Uncertainty

To evaluate the uncertainty of LDV measurements, two sets of data had to be obtained for one profile. The 21:1 odds method in Appendix B was applied to the tests with the moving wall. For the flow with the moving wall, only two different sets of data were

available to estimate the uncertainty presented in Table 4.1.

## 4.2 Blade Surface Oil Flow Visualization

The mixture of oil for the surface flow visualizations was the same as the mixture for the blade surfaces in the stationary wall experiments. To reduce the effect of the starting process of the moving belt, the mixtures were applied only after reaching full speed. Then the belt ran about 5 minutes till the oil dried on the blade surface. Only the suction surface oil flow visualizations were done for the moving wall cases.

Figure 4.3 shows a dark streak with an inclined angle of  $2 \sim 4^\circ$  above the blade tip edge, which is the tip leakage vortex on the blade surface of the suction side. By comparison, the tip leakage vortex starting point for the 1.65% case is upstream of that of 3.30%. Comparison with Figure 3.7 for stationary wall cases shows that the reattachment line on the blade with a moving wall is upstream of its stationary wall case. What's more, the limiting streamlines on the suction surface are more horizontal than the stationary wall results, which suggests that there is less separation on the rear part of the blade because the gravitational effect is not as severe as that of the stationary wall. Herzig et al. (1954) found similar results from his suction side smoke flow visualizations for both stationary and moving walls.

## 4.3 LDV Measurements

To portray the flow structures, the free-stream coordinate system, the bed coordinate system, and the chord coordinate system addressed in Section 3.1, as well as a moving wall frame ( $W_m = W_s - V_{belt}$ ), were used to describe the moving wall experiments. Table 4.2

displays all the profiles taken in the study in the bed coordinate system. Profile uu was a full profile across the boundary layer of the upstream flow at  $x/c_a = -0.33$  with a 3.30% tip gap. The data reflected the relative motion effect on the boundary layer of the inflow. Around the 1.65% tip gap, just a few points were taken at locations 5p and 5s with one point each and at location e3 with four points. Hence the tip gap data above were not enough to fully understand the flow structures caused by the relative motion of the endwall. The available data are used to tentatively explain the flow in the following sections.

### 4.3.1 Mean Velocity

The upstream flow at  $x/c_a = -0.33$  for a stationary endwall with 3.30% tip gap in the cascade wind tunnel was nearly a two-dimensional flow as discussed in Section 3.7.1. Figure 4.4 for profile uu in the free-stream coordinate system clearly shows that for the stationary wall. The mean velocity U plot is the typical distribution of a two-dimensional boundary layer profile with clearly identified inner, semi-log, and wake regions along the normal distance to the endwall. The V and W components of velocity approach zero. However, for the moving wall case, the flow at the same profile uu is not a two-dimensional flow after the belt motion is applied. The U does not approach zero as y decreases from the outer layer to the endwall. However, the U is almost a constant  $0.82U_{ref}$  from near the wall to  $y = 5mm$ . The W component of velocity is not zero from  $y = 5mm$  to the endwall. The comparison of the U and W for both stationary wall data and the moving wall data in the same location indicates that the inflow with wall motion was not a two-dimensional boundary layer flow in the free-stream coordinate system.

Furthermore, from Figure 4.5a for the same profile uu in the stationary bed coordinate

system, the  $U/U_{ref}$  and  $V/U_{ref}$  are almost the same for both stationary wall and moving wall cases, so they change slightly due to the relative motion. However, the  $W/U_{ref}$  profiles are greatly different between the stationary wall case and the moving wall case. The  $W$  distribution for the stationary wall is like a two-dimensional boundary layer profile. The mean  $W$  for the moving wall case is almost invariant, close to, but less than the belt speed  $V_{belt} = U_{ref} \cos(24.9^\circ) = 0.907U_{ref}$  except very near the wall and its local free-stream. The flow angles for the stationary wall case and the moving wall case are in Figure 4.5b. The flow angle changes slightly from the wall to the local free-stream in the stationary wall case. For the moving wall, the flow angle varies dramatically about  $22^\circ$  from  $-90^\circ$  to  $-68^\circ$ . The flow was skewed from the beginning of the moving belt edge and changed the two-dimensional boundary layer for the stationary endwall to a three-dimensional boundary flow in the moving endwall case.

The belt motion was in the negative  $z$  direction in the stationary bed coordinate system. The  $W$  distribution in Figure 4.5a is determined by the combination of a tangential component in the outer layer of the inflow boundary layer and the relative motion of the endwall in the inner layer. The belt velocity was designed to equal the tangential velocity of the inflow freestream in the bed coordinate system. The tangential velocity  $W$  of the inflow changed gradually in the boundary layer from the endwall to the outer layer. The  $W/U_{ref}$  in Figure 4.5a is a combination of the moving wall and no-slip condition for the inner region and the outer region of the inflow boundary layer. Hence, the  $\partial W/\partial y$  near the wall was greatly reduced at profile  $uu$  by the moving wall.

Also from the point of view of the moving frame, in Figure 4.6a, the  $U$  has a semi-log region in the boundary layer that Kannepalli and Piomelli (2000) found in the LES of a moving plate flow as well. The small  $W$  implies that the axial shear layer existed only if the endwall motion was imposed, because the tangential shear layer was cancelled by

adding the endwall motion at the same speed of the tangential free-stream flow. The flow angle in Figure 4.6b changes across the boundary layer of the inflow, so that the inflow was not a collateral flow in the moving wall frame.

The UW vector plots in the stationary bed co-ordinate system in Figure 4.7a show that the flow angles closely follow the tangential direction of the blade leading edge, so that the angle of attack is about zero. From Figure 4.7b in the moving wall co-ordinate system, the flow angles tend to be axially toward the blade.

Figure 4.8 presents the mean velocity component  $U$ ,  $V$ , and  $W$  for profiles 5p, 5s, and e3 with 1.65% tip gap in the bed and chord coordinate systems. In this figure, the data for the stationary wall are plotted for comparison. The stationary bed coordinate system was used to compare the tangential velocity  $W$  and  $V_{belt}$ . From Figures 4.8c and 4.8e, the magnitude of  $W$  is bigger than  $V_{belt}$  in the upper layer, unlike profile uu in Figure 4.4. Accordingly, the flow structures with pressure gradient in and around the gap were different than the upstream flow with zero pressure gradient. The chord coordinate system was used to compare the moving wall case with the stationary wall case. In Figure 4.8b for profile 5p, the mean velocity components  $U$  and  $V$  do not change much, but the magnitude of  $W$  drops almost in half. For profile 5s in Figure 4.8d and profile e3 in Figure 4.8f, the mean velocity components  $U$ ,  $V$ , and  $W$  vary significantly. The influence of the moving endwall is significant on the tip gap flow structures discussed in Chapter 3.

Figure 4.9a shows the mean velocity UW vectors of profile 5p on the pressure side, profile 5s on the suction side, and profile e3 in the tip leakage vortex region at  $x/c_a = 0.18$  with the 1.65% tip gap in the bed coordinate system. In the same plots, the mean velocity vector for the stationary wall is plotted for comparison. Obviously, the flow angles in Figure 4.10 change from the stationary wall to the moving wall. In particular, the near



wall UW vectors point in the belt moving direction (negative  $z$ ), but the UW vectors for the stationary wall case turn more forward from the negative axis  $z$  direction. The flow angles of profile e3 demonstrate that the near wall flow closely followed the belt moving direction and the outer flow appeared to be in a similar direction as the stationary wall case. The flow speed,  $Q = \sqrt{U^2 + W^2}$ , decreased at  $y = 4mm$  in profile 5p and increased at  $y = 2.4mm$  in profile 5s.

Figure 4.9b shows VW vectors in profiles 5p, 5s, and e3 at  $x/c_a = 0.18$  with the 1.65% tip gap in the stationary bed coordinate system. For profile e3, the lower two points and the upper two points have opposite  $V$ , which is similar to profile e1 for the stationary wall case, which is located on the right side of the vortex center as seen in Figure 3.58a. If this feature of opposite  $V$  is an indicator of vortex locations, this suggests that the tip leakage vortex was spiral and its trajectory displaced further away from the suction side of that blade when the endwall was moving.

In the moving wall frame, Figure 4.11a shows the scraping effect or upper movement on the pressure side because the UW vector is the opposite of the flow direction. Figure 4.11b at profile e3, the tip leakage vortex is also probable on the suction side because the  $V$  of the two lower and the upper two points are opposite.

### 4.3.2 Turbulence

Turbulence data were also measured for the moving wall case. For Profile uu at  $x/c_a = -0.33$  with both stationary wall and moving wall cases in the free-stream co-ordinate system, Figures 4.12a shows the normal stresses  $\overline{u^2}$ ,  $\overline{v^2}$ , and  $\overline{w^2}$ , Figure 4.12c shows the shear stresses  $-\overline{uv}$ ,  $-\overline{vw}$ , and  $-\overline{uw}$ , and Figure 4.12e shows the coefficients of correlation  $R_{uv}$ ,  $R_{vw}$ , and  $R_{uw}$ . The flow at profile uu was nearly a two-dimensional boundary layer

as discussed in Section 3.7.1. After the relative motion of the endwall was imposed, the magnitudes of Reynolds stresses decreased in the boundary layer region except the  $\overline{w^2}$  from  $y = 0.17mm$  to  $y = 0.45mm$ . The exception might be caused by the effect of relative motion as a cross shear flow to increase the fluctuation of the W component. Also from Figures 4.12e,  $R_{uw}$  decreases from 0.85 for the stationary wall case to 0.40 for the moving wall case, suggesting a flow decorrelation so that the skewed flow by the moving endwall was less coupled with the primary flow.

For the same profile  $uu$  in the stationary bed coordinate system, Figures 4.12b, 4.12d, and 4.12f show that the magnitude of Reynolds stresses with the moving wall were less than those with the stationary wall, similar to the observation in the free-stream coordinate system, except  $\overline{u^2}$  for the moving wall case is bigger than for the stationary wall case. The  $\overline{w^2}$  was much less in the moving wall case than with the stationary wall, indicating that the production decreased because  $\partial w / \partial y$  decreased significantly near the wall. The low correlation coefficient,  $R_{uw}$ , indicated that the skewed flow by the moving endwall was decorrelated from the primary inflow.

TKE and  $1/S$  in Figures 4.13 are independent of the  $y$  rotation of the coordinate system, as described in Section 3.6.7. For inflow of profile  $uu$ , the TKE for the moving wall case was much smaller than for the stationary wall case. The  $1/S$  of the moving wall was less than that of the stationary wall case, indicating the flow decorrelation between the inflow and the endwall shear flow by skewing. The absence of a plateau with 0.6 for  $1/S$  was evidenced by the upstream flow turning from a two-dimensional flow to the three-dimensional flow.

For profiles 5p, 5s, and e3 around the gap, in Figure 4.14, Reynolds stresses are plotted at  $x/c_a = 0.18$  in the blade tip gap region of tip gap 1.65%. The normal stresses do not change much at  $y = 4mm$  of profile 5p (see Figure 4.14a), but they increase

significantly at  $y = 2.4\text{mm}$  of profile 5s (see Figure 4.14c). The normal stresses at profile e3 in Figure 4.14e are different between the moving wall case and the stationary wall at the same normal distance to the wall. The normal stresses at profile e3 appeared to have a local peak between  $y = 2.5\text{mm}$  and  $y = 4\text{mm}$ . In general, the  $\overline{v^2}$  varied substantially from the stationary wall to the moving wall, implying the entrainment of fluid on blade suction surface boundary layer into the tip leakage flow. It appears that the moving wall changed the turbulence structure off the wall because the moving wall altered the interaction pattern between the tip leakage flow and the primary flow.

Looking at shear stresses of profiles 5p, 5s, and e3 in Figures 4.14b, 4.14d, and 4.14f, a similar difference in the stationary bed co-ordinate system is observed between the moving wall and stationary wall. Basically, the shear stresses appear to be influenced much more in profiles 5s and e3 of the suction side than in profile 5p of the pressure side.

TKE and  $1/S$  in Figure 4.15 also reveal that the TKE and  $1/S$  of the moving wall case were less than those of the stationary wall case, probably reflecting the flow structure changes. However, for better understanding of relative motion needs more data for the moving wall case.

## 4.4 Flow Structure Discussion

From Figure 4.4, the belt motion creates streamwise (x) vorticity at the belt leading edge in the stationary bed co-ordinate system that influences the flow up to a height up to 4 mm at the measurement location upstream of the blade row. The influence height increases as the flow passes from upstream to the downstream. Since the gap size of the 1.65% case was 4.2mm, the effect of wall motion probably extended through the whole gap. However, the mid-span pressure loading was not affected by the moving

endwall according to the measurements of Ma (2003). It signified that the influence of the relative motion of the endwall did not extend to the mid-span of the blade passage. From the comparison between Figure 4.3 and Figure 3.6, the influence of the moving endwall propagated up to some spanwise distance above the blade tip in the mid-chord of the blade and produced a weaker separated flow than with a stationary wall. Wang and Devenport (2004) found the influence height roughly varied from 14 mm to 28 mm when the downstream flow travelled from  $x/c_a = 1.51$  to  $x/c_a = 2.35$  in the same facility and condition. The influence height was less than ten times of the initial influence height, which was predicted by Kannepalli and Piomelli (2000) in the LES of a moving plate flow as an asymptotic state in the far downstream. It probably suggested that the blade obstacle suppressed the outward propagation of streamwise vorticity that was induced by the moving endwall.

For the upstream profile  $uu$  at  $x/c_a = -0.33$ , the blade row disturbance exists but was less important compared to the relative motion. It could be treated as flow without a pressure gradient. The mean flow results stated above have revealed the effect of the moving endwall. The tangential shear boundary layer was cancelled so that streamwise vorticity was not imposed by the moving wall shear.

Unlike a spinning cylinder flow investigated experimentally by Lohmann (1976) and Bissonnette and Mellor (1974), as well as a moving plate flow simulated by Kannepalli and Piomelli (2000) with LES, the endwall motion creates streamwise vorticity at the leading edge which is opposite to the streamwise vorticity created in the tip gap by the pressure difference across the blade. This is similar to the behavior in a real compressor.

The belt motion turns a more two-dimensional boundary layer flow into a three-dimensional boundary layer. In the moving wall frame, the  $U$  had a semi-log layer as stated in Kannepalli and Piomelli (2000) in the LES results of a moving plate flow and the

outer layer was a collateral flow as observed experimentally in the spinning cylinders flow of Lohmann (1976) and Bissonnette and Mellor (1974). The TKE increases substantially in the inner region because its production drops. The  $1/S$  became less and lost the characteristics of a two-dimensional boundary layer in the stationary wall case, indicating that the flow was decorrelated between the inflow and the wall shear flow. The Reynolds shear stresses went down in the moving wall case, similar to the observation by Driver and Johnston (1990) that the stresses for the three-dimensional boundary layer is smaller than for two-dimensional turbulent boundary layer.

The wall shear imposed by the motion propagated outwardly so that the influence of the endwall motion would apply some distance above the blade tip, as confirmed by the oil flow visualization of the blade suction surface. Since there was less effect of stall for the moving, the moving endwall improved the tip blade loading as suggested by Herzig et al. (1954). From the data of this study, the smaller  $W$  on the pressure side and the bigger  $W$  on the suction side fairly supported this observation. The improved tip loading and the removal of the endwall shear layer probably increased the tip leakage flow rate as measured by Sjolander and Cao (1995). The wall shear dragged the tip leakage vortex away from the suction side. The vectors plots of profile e3 explained this inward and pitchwise shift of the center of the tip leakage vortex. Wang (2000) found that the similar movement of the tip leakage vortex in the downstream of the blade row changed its shape from round in the stationary wall to elliptic in the moving wall.

In the gap region, comparison with the data at the same location of a stationary wall, profile 5p shows the scraping effect or upward movement on the pressure side because the tip loading improved so that the mean  $W$  decreased. It seems that the flow turning around the pressure side corner was even sharper. The scraping effect was seen by Herzig et al. (1954), which means the blade pressure surface scrapes up fluid entrained on the

moving wall and thus imparts a rolling motion to the air in the vicinity of the pressure surface. Turbulence did not change much, as shown in Figure 4.15a.

Profile 5s shows the  $W$  magnitude increased which means that the tip leakage flow rate increased because of the endwall motion. It seems that the endwall motion removes the low momentum fluid so that the flow near endwall increases. Herzig et al. (1954) concluded that the relative motion improved flow characteristics on the blade suction surface even at some spanwise distance from the tip by reducing the blade boundary layer that existed when the endwall was stationary. Turbulence changed significantly, as shown in Figure 4.15c.

Profile e3 shows the shift of the tip leakage vortex away from the suction side and inward to the endwall. The velocity vectors demonstrated the tip leakage vortex was a spiral vortex. From UW vectors, the height influenced by the moving endwall was 3mm. The direction kept the same after this point. Turbulence changed as well, as shown in Figure 4.15e.

The belt motion creates a tangential shear-driven flow which changed the flow structure all the way from the inflow to the far downstream. But the inflow was less coupled with the belt driven shear flow, which was also observed in the spinning cylinder flow of Bissonnette and Mellor (1974). The flow became more coupled based on the flow with pressure gradient that Driver and Johnston (1990) investigated, the adverse pressure gradient in the downstream of a spinning cylinder. Herzig et al. (1954) observed using flow visualization that the scraping effect or upward movement existed on the pressure side and the entrainment occurred on the suction side. Wang and Devenport (2004) pointed out the endwall motion substantially changes the mean flow structures but did not change the turbulence structures much in the downstream of the blade. However, their hot-wire data were not close to the physical boundaries since no data were avail-

able when  $y < 5.8mm$  normal to the endwall. The upstream profile  $uu$  showed that the turbulence changed in the inner region. The limited tip gap data showed that the flow turbulence changed substantially next to the corner of the suction side and the tip leakage vortex in the passage. The complete understanding of the relative motion effect on the near wall of the gap flow needs more experiments.

Table 4.1: Uncertainties for the moving wall data measured quantities with 21:1 odds

$U/U_{ref}$	$\pm 4.56E - 03$	$\overline{u^2 v}/U_{ref}^3$	$\pm 2.92E - 07$
$V/U_{ref}$	$\pm 6.06E - 03$	$\overline{u^2 w}/U_{ref}^3$	$\pm 5.01E - 07$
$W/U_{ref}$	$\pm 1.29E - 02$	$\overline{v^2 w}/U_{ref}^3$	$\pm 3.43E - 06$
$\overline{u^2}/U_{ref}^2$	$\pm 1.30E - 04$	$\overline{uv^2}/U_{ref}^3$	$\pm 8.84E - 07$
$\overline{v^2}/U_{ref}^2$	$\pm 1.60E - 04$	$\overline{uw^2}/U_{ref}^3$	$\pm 4.86E - 07$
$\overline{w^2}/U_{ref}^2$	$\pm 1.56E - 04$	$\overline{vw^2}/U_{ref}^3$	$\pm 3.39E - 06$
$\overline{uv}/U_{ref}^2$	$\pm 1.10E - 05$	$\overline{uvw}/U_{ref}^3$	$\pm 6.21E - 07$
$\overline{uw}/U_{ref}^2$	$\pm 1.14E - 05$	$\overline{u^3}/U_{ref}^3$	$\pm 1.18E - 06$
$\overline{vw}/U_{ref}^2$	$\pm 1.13E - 04$	$\overline{v^3}/U_{ref}^3$	$\pm 3.03E - 06$
		$\overline{w^3}/U_{ref}^3$	$\pm 4.15E - 06$

Table 4.2: Test matrix for moving endwall

Moving End-Wall (3.30%)		
Profile	$X$ (cm)	$Z$ (cm)
uu	-4.572	-11.760

Moving End-Wall (1.65%)			
Profile	$X$ (cm)	$y$ (cm)	$Z$ (cm)
5p	2.474	0.413	-16.662
5s	2.474	0.231	-18.339
e3	2.474	0.128	-20.625
e3	2.474	0.247	-20.625
e3	2.474	0.318	-20.625
e3	2.474	0.496	-20.625



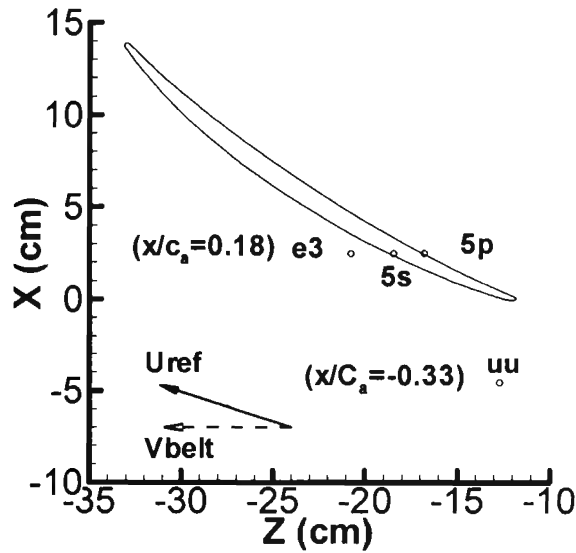


Figure 4.1: Location of data taken for moving wall; for 1.65% tip gap: 5p, 5s, e3; for 3.30% tip gap: uu

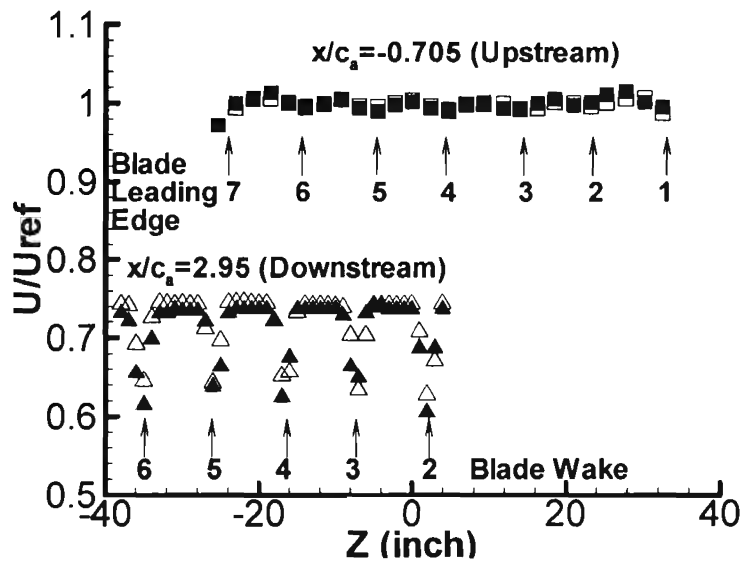
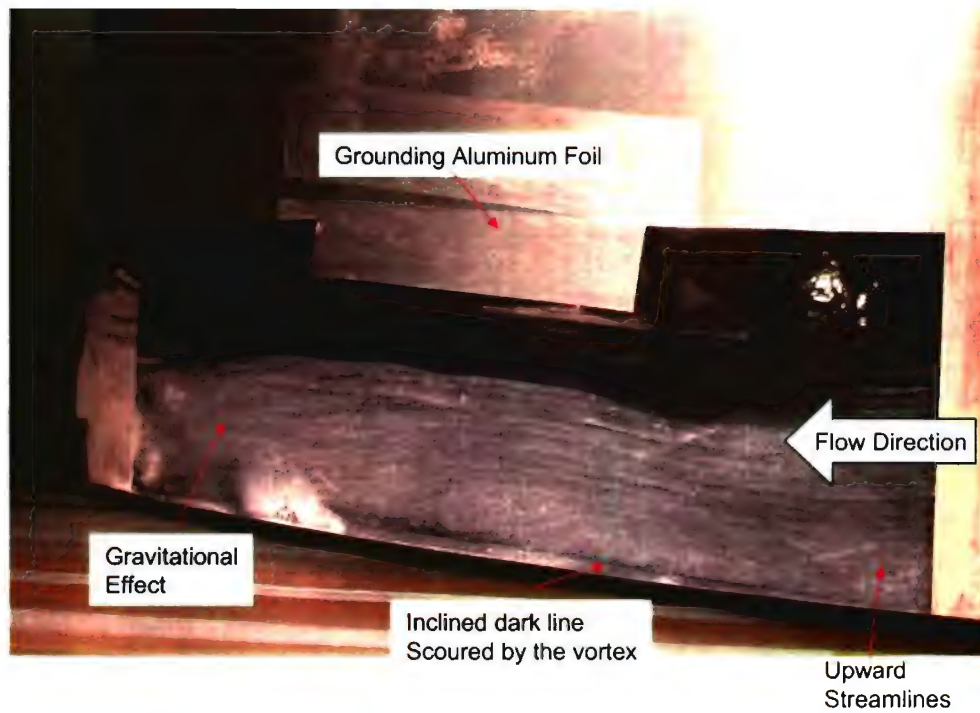
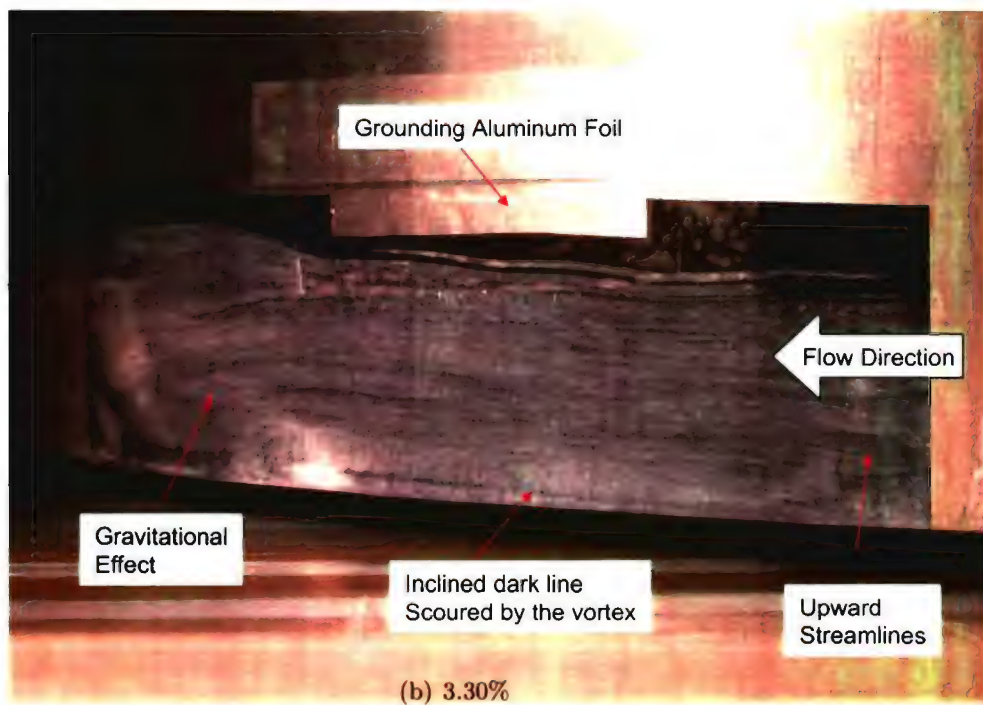


Figure 4.2: Velocities at tunnel half height upstream ( $x/c_a = -0.705$ ) and downstream ( $x/c_a = 2.95$ ) of blade row in bed co-ordinates; for moving wall:  $\square$ ,  $x/c_a = -0.705$ ;  $\triangle$ ,  $x/c_a = 2.95$ ; for stationary wall:  $\blacksquare$ ,  $x/c_a = -0.705$ ;  $\blacktriangle$ ,  $x/c_a = 2.95$ .



(a) 1.65%



(b) 3.30%

Figure 4.3: Blade suction surface oil flow visualizations for 1.65% and 3.30% with moving wall

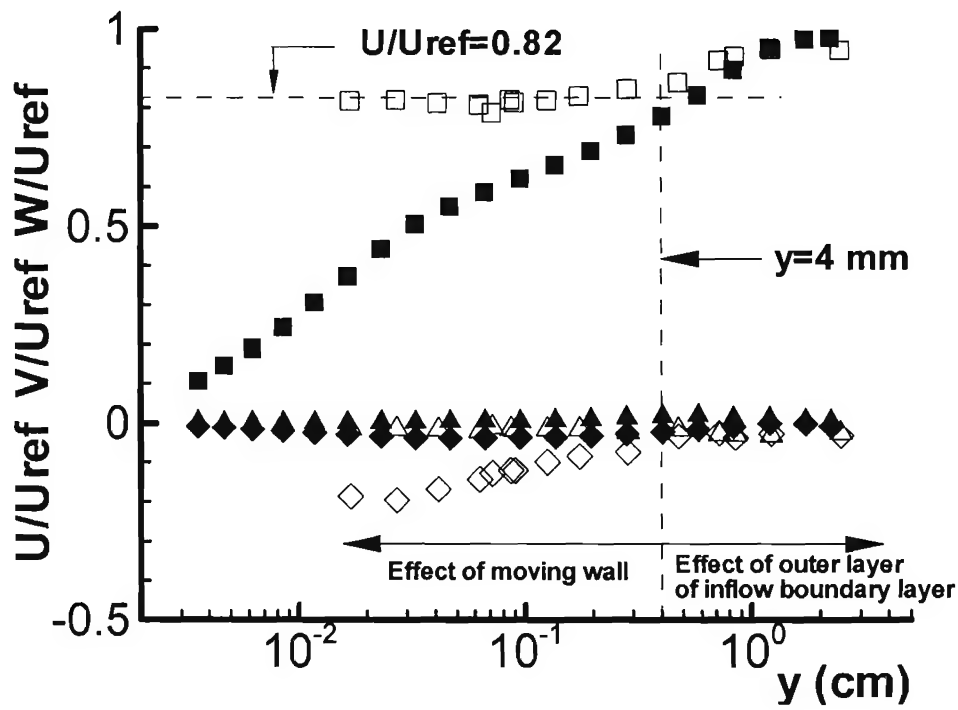
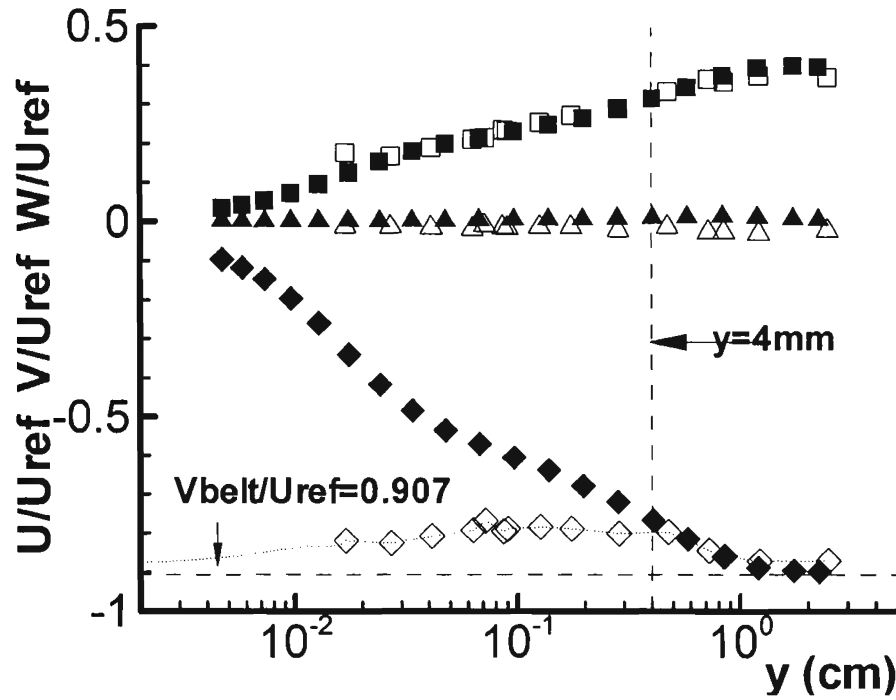
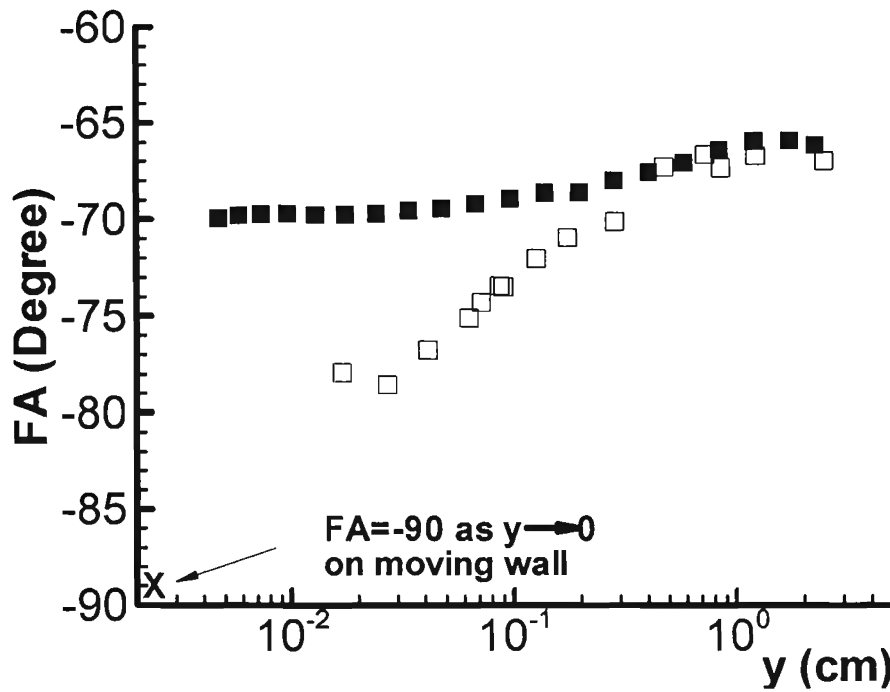


Figure 4.4: Mean velocity  $U$ ,  $V$ ,  $W$  at  $x/c_a = -0.33$  with 3.30% tip gap in the free stream coordinate system; for moving wall:  $\square$ ,  $U$ ;  $\triangle$ ,  $V$ ;  $\diamond$ ,  $W$ ; for stationary wall:  $\blacksquare$ ,  $U$ ;  $\blacktriangle$ ,  $V$ ;  $\blacklozenge$ ,  $W$ .

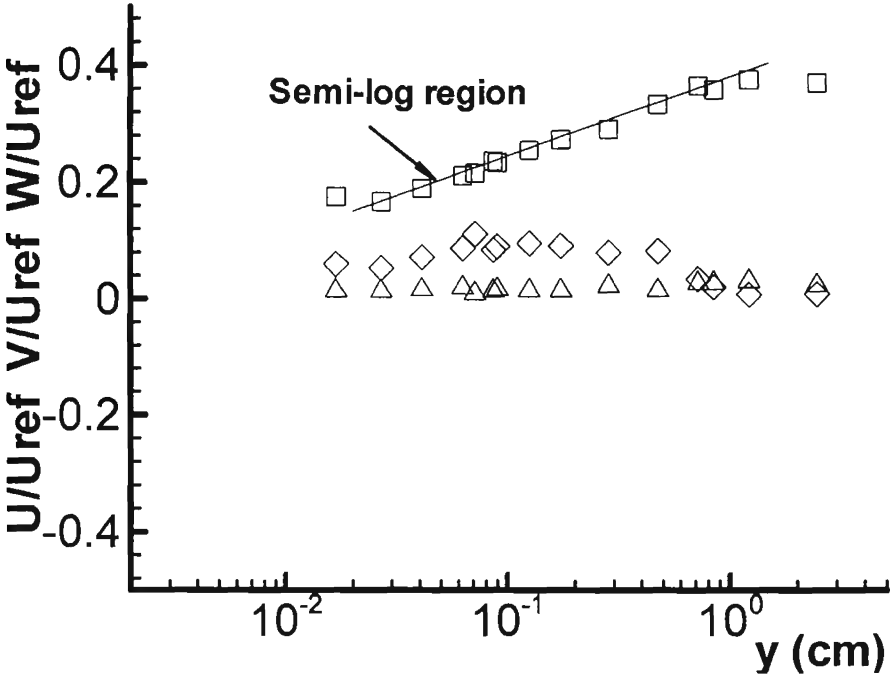


(a) Mean velocity

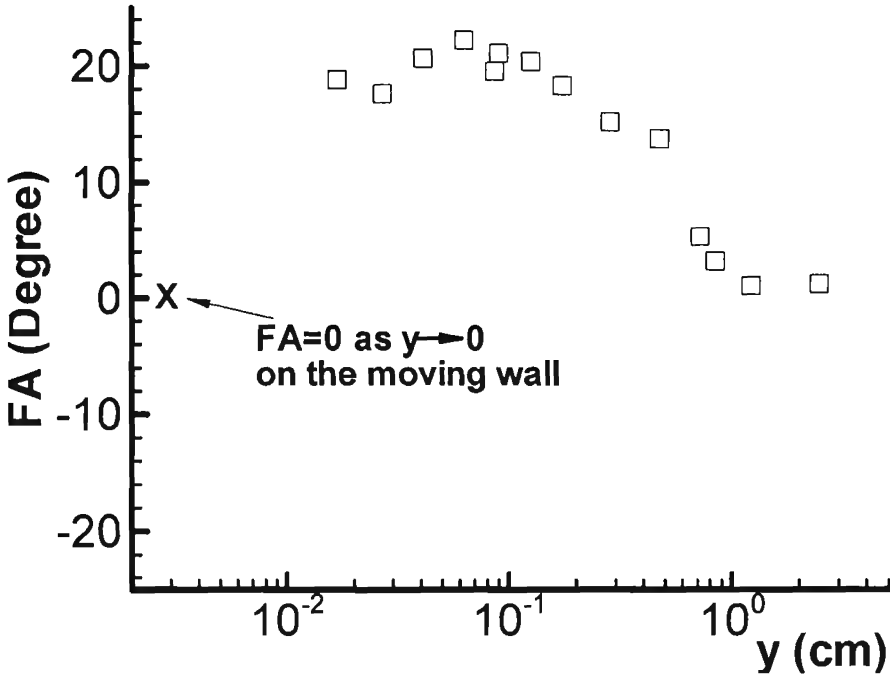


(b) Flow angle

Figure 4.5: Mean velocity  $U$ ,  $V$ ,  $W$  at  $x/c_a = -0.33$  with 3.30% tip gap in the bed coordinate system; for moving wall:  $\square$ ,  $U$  and  $FA$ ;  $\triangle$ ,  $V$ ;  $\diamond$ ,  $W$ ; for stationary wall:  $\blacksquare$ ,  $U$  and  $FA$ ;  $\blacktriangle$ ,  $V$ ;  $\blacklozenge$ ,  $W$ .

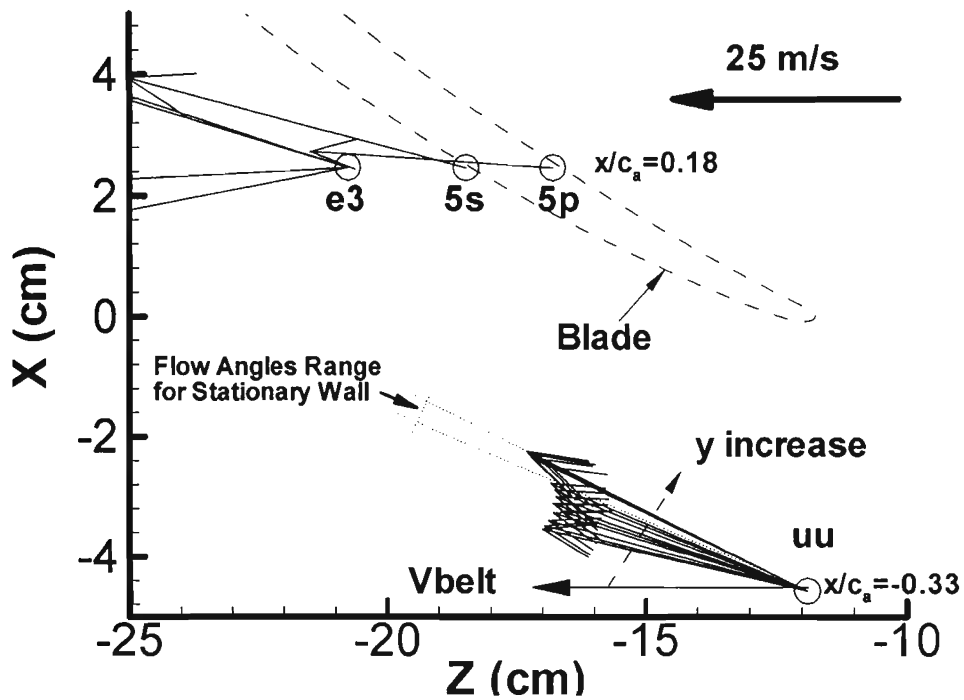


(a) Mean velocity

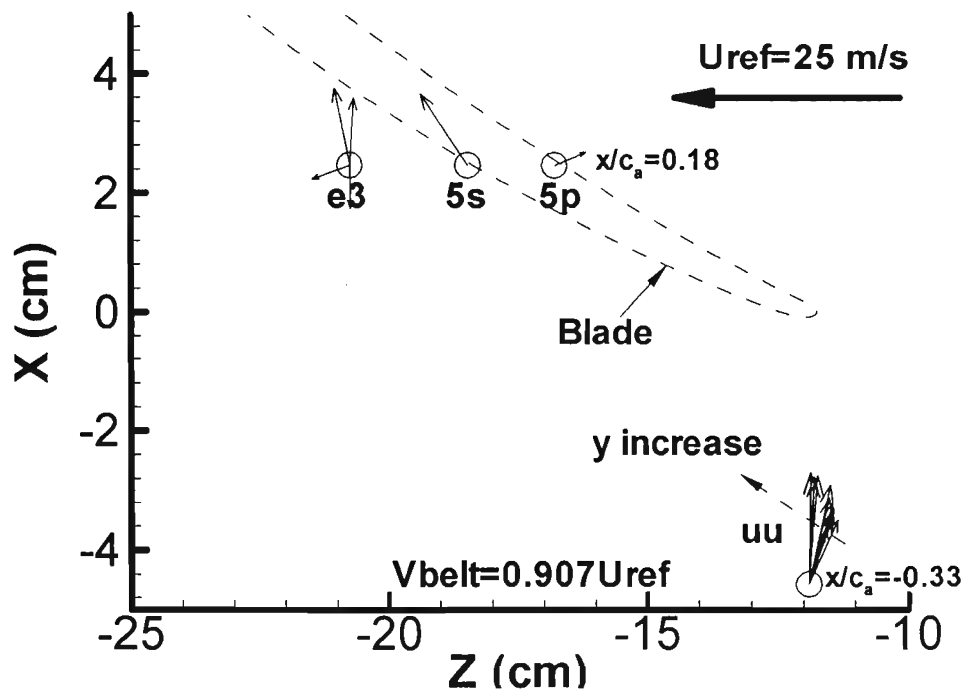


(b) Flow angle

Figure 4.6: Flow angles at  $x/c_a = -0.33$  with 3.30% tip gap in the moving coordinate system;  $\square$ ,  $U$  and  $FA$ ;  $\triangle$ ,  $V$ ;  $\diamond$ ,  $W$ .



(a) Bed Coordinate System



(b) Moving Coordinate System

Figure 4.7: UW Vector plots of profile  $uu$  at  $x/c_a = -0.33$  with 3.30% tip gap in stationary bed and moving wall coordinate systems

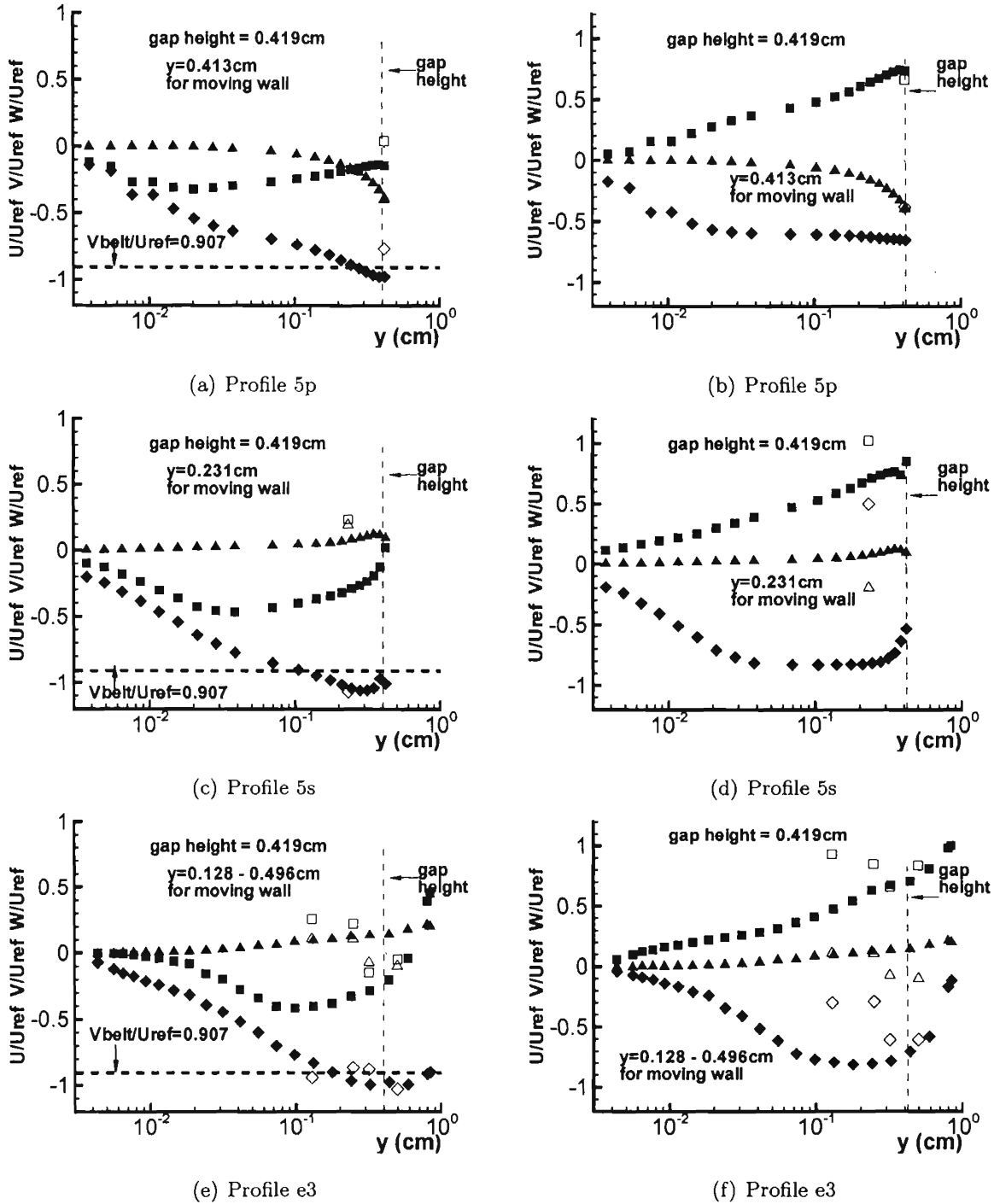
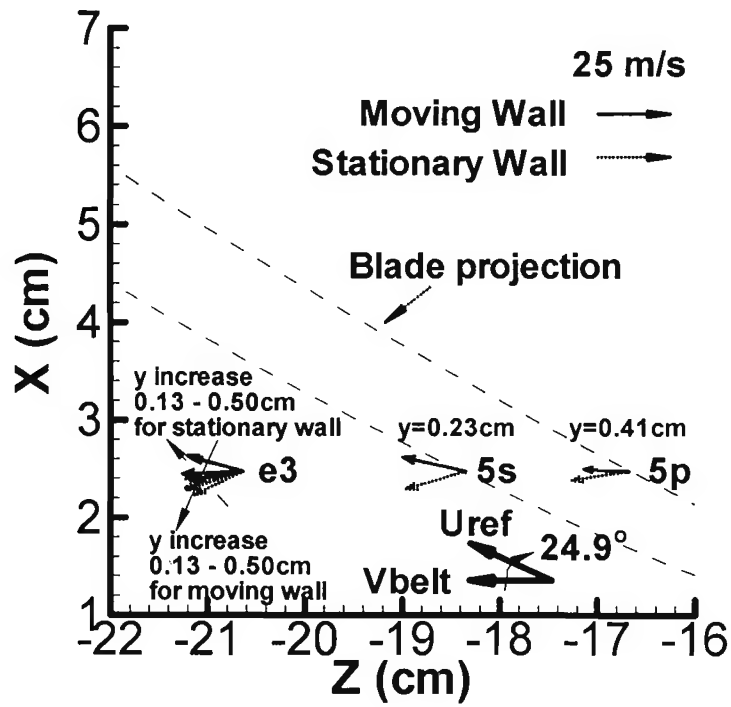
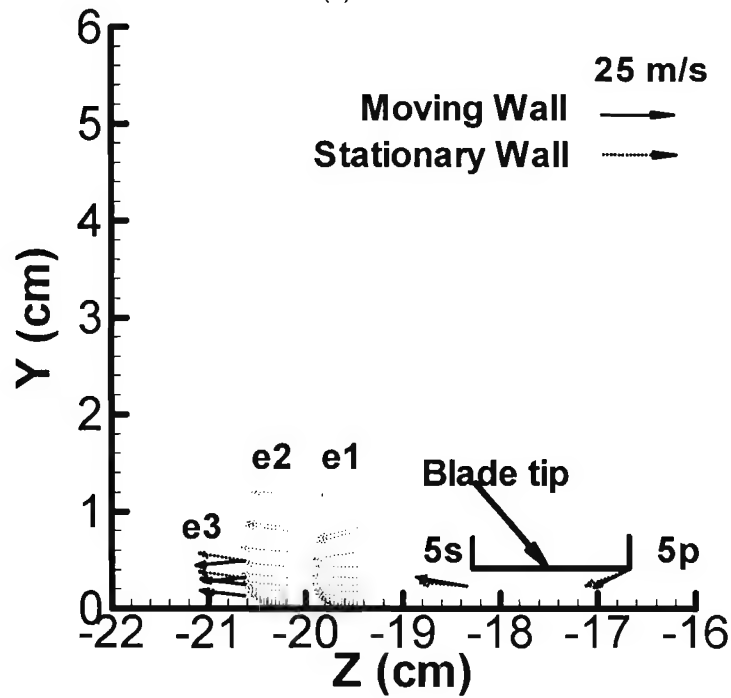


Figure 4.8: Mean velocity  $U$ ,  $V$ , and  $W$  of profiles 5p, 5s, and e3 at  $x/c_a = 0.18$  with 1.65% tip gap in the bed and chord coordinate systems: (a), (c), and (e) in the bed coordinate system; (b), (d), and (f) in the chord coordinate system; For moving wall:  $\square$ ,  $U$ ;  $\triangle$ ,  $V$ ;  $\diamond$ ,  $W$ . For stationary wall:  $\blacksquare$ ,  $U$ ;  $\blacktriangle$ ,  $V$ ;  $\blacklozenge$ ,  $W$ .



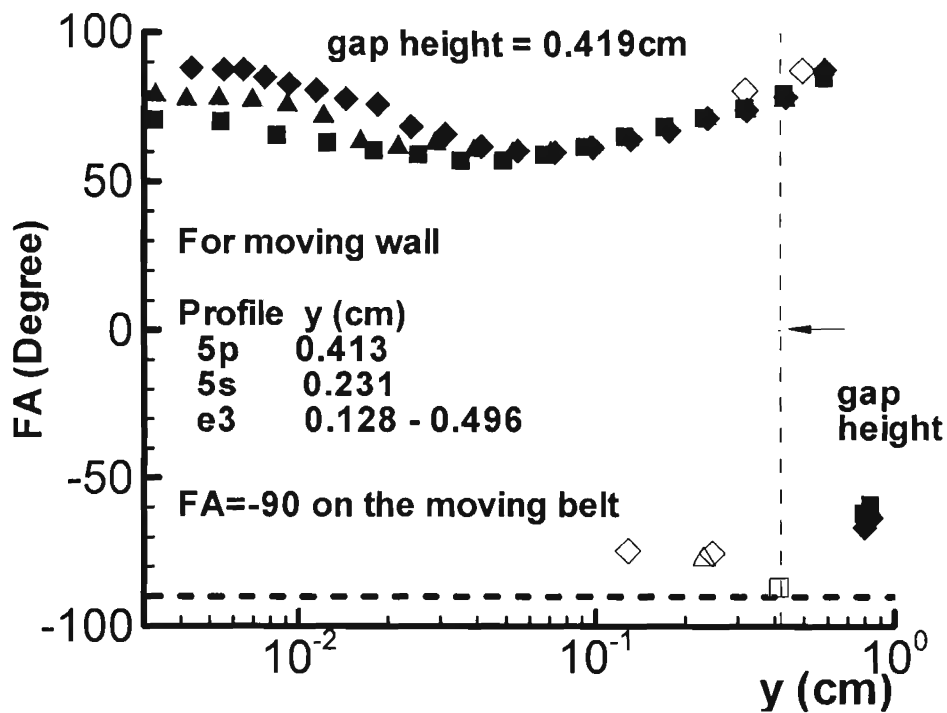
(a) UW Vector



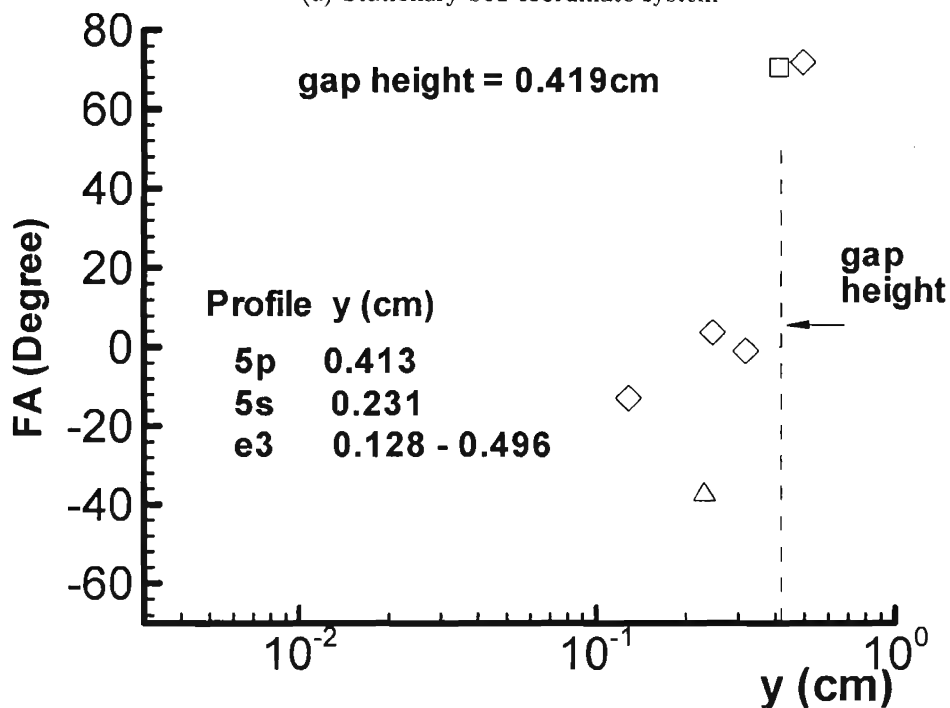
(b) VW Vector

Figure 4.9: Velocity vector plots of profiles 5p, 5s, and e3 at  $x/c_a = 0.18$  with 1.65% tip gap in the stationary bed coordinate system



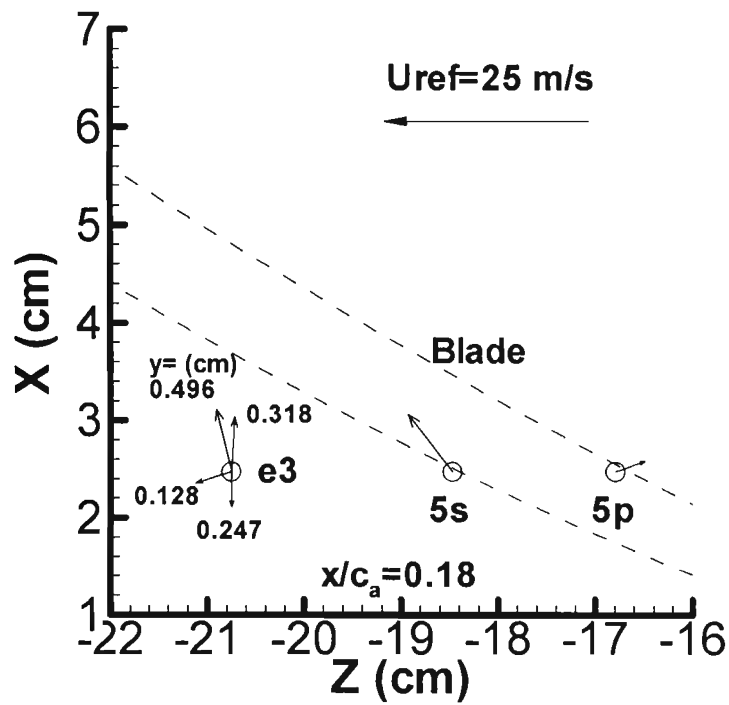


(a) Stationary bed coordinate system

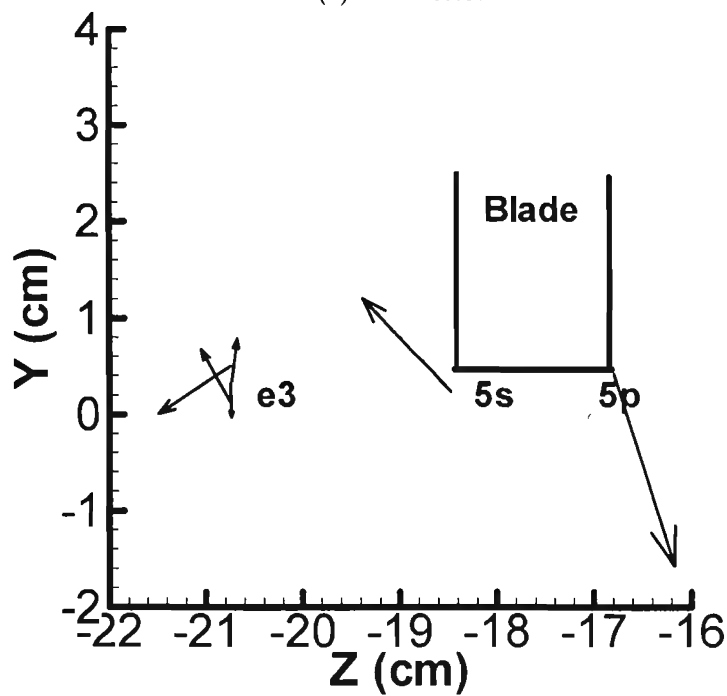


(b) Moving wall coordinate system

Figure 4.10: Flow angles of profiles 5p, 5s, and e3 at  $x/c_a = 0.18$  with 1.65% tip gap in the stationary bed and moving wall coordinate systems; for moving wall:  $\square$ , 5p;  $\triangle$ , 5s;  $\diamond$ , e3; for stationary wall:  $\blacksquare$ , 5p;  $\blacktriangle$ , 5s;  $\blacklozenge$ , e3.



(a) UW Vector



(b) VW Vector

Figure 4.11: Velocity vector plots of profiles 5p, 5s, and e3 at  $x/c_a = 0.18$  with 1.65% tip gap in the moving coordinate systems

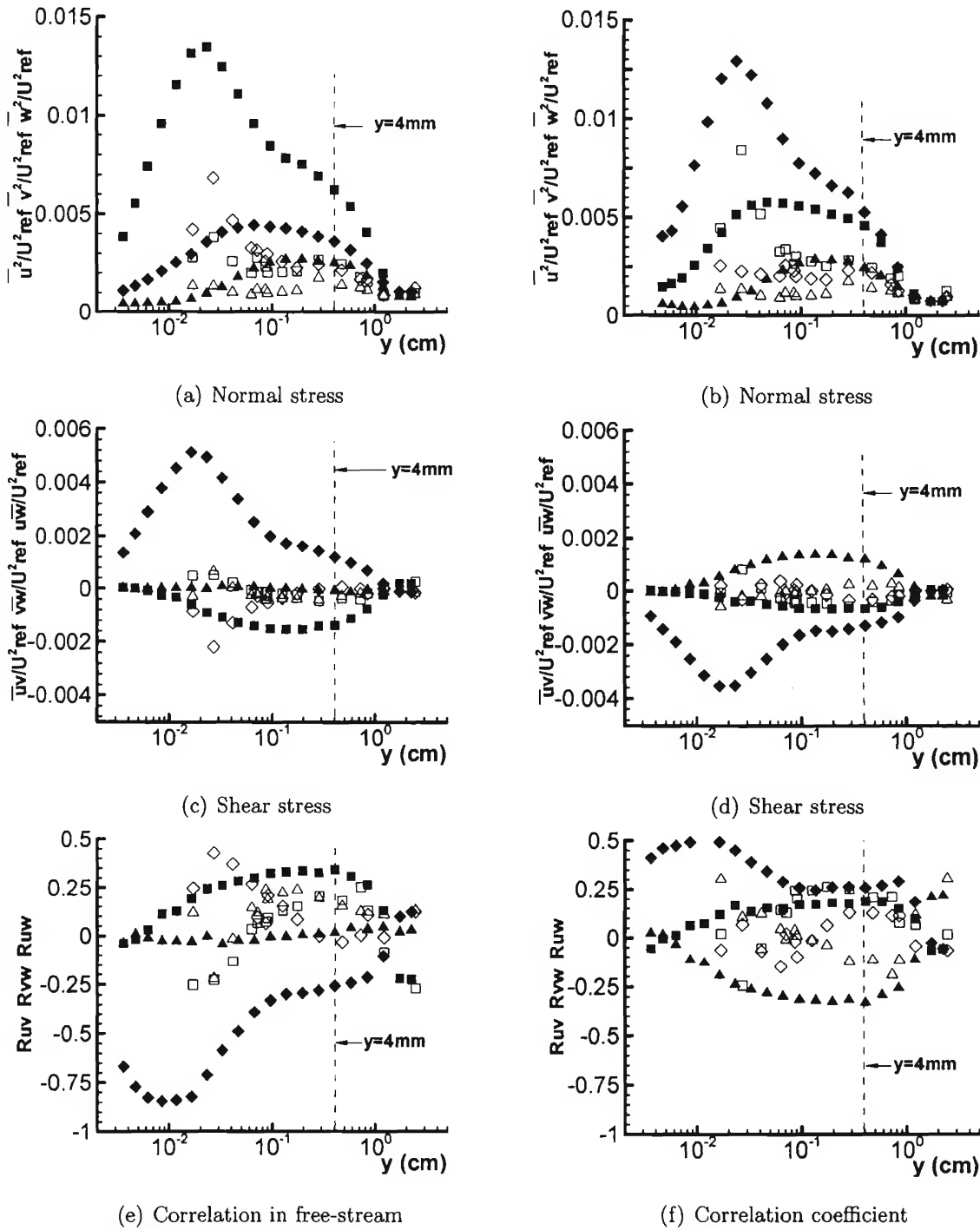
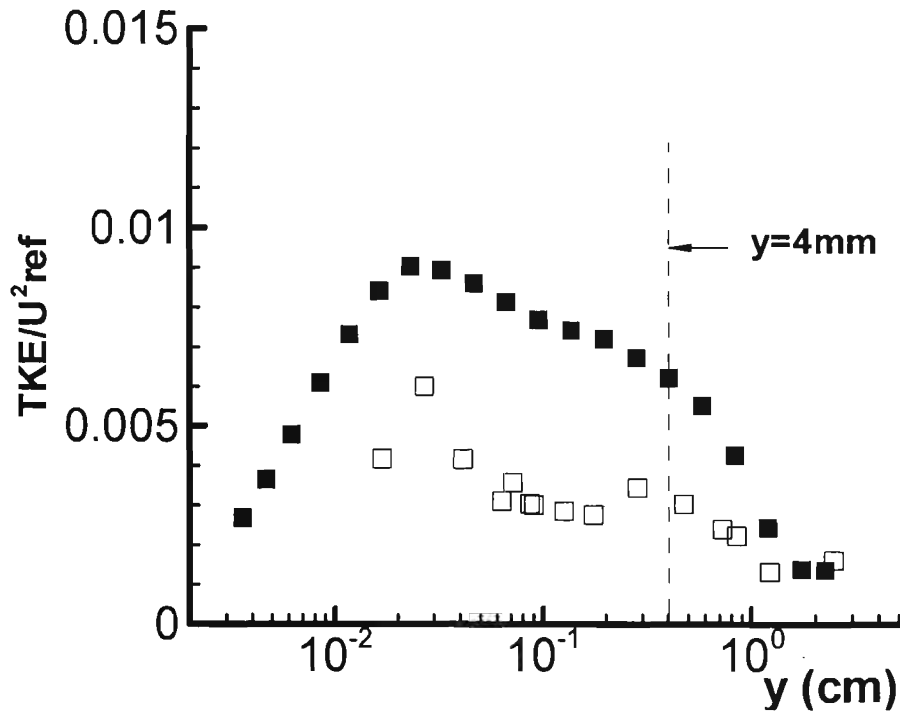
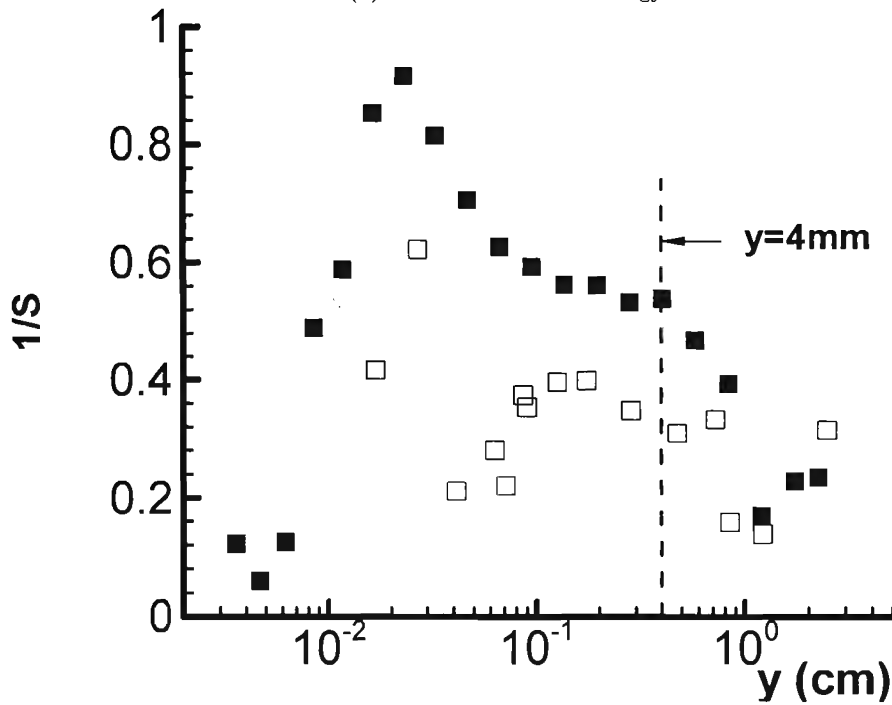


Figure 4.12: Reynolds stress profile  $uu$  at  $x/c_a = -0.33$  with 3.30% tip gap for both free-stream and bed coordinate systems: (a), (c), and (e) in the free-stream coordinate system; (b), (d), and (f) in the bed coordinate system. For moving wall: □,  $\overline{u^2}$ ,  $\overline{uv}$ , and  $R_{uv}$ ; △,  $\overline{v^2}$ ,  $\overline{vw}$ , and  $R_{vw}$ ; ◇,  $\overline{w^2}$ ,  $\overline{uw}$ , and  $R_{uw}$ . For stationary wall: ■,  $\overline{u^2}$ ,  $\overline{uv}$ , and  $R_{uv}$ ; ▲,  $\overline{v^2}$ ,  $\overline{vw}$ , and  $R_{vw}$ ; ◆,  $\overline{w^2}$ ,  $\overline{uw}$ , and  $R_{uw}$ .



(a) Turbulent kinetic energy



(b) Ratio of shear stress over normal stress

Figure 4.13: Normalized TKE and  $1/S$  of profile  $uu$  at  $x/c_a = -0.33$  with 3.30% tip gap; for moving wall:  $\square$ ; for stationary wall:  $\blacksquare$ .

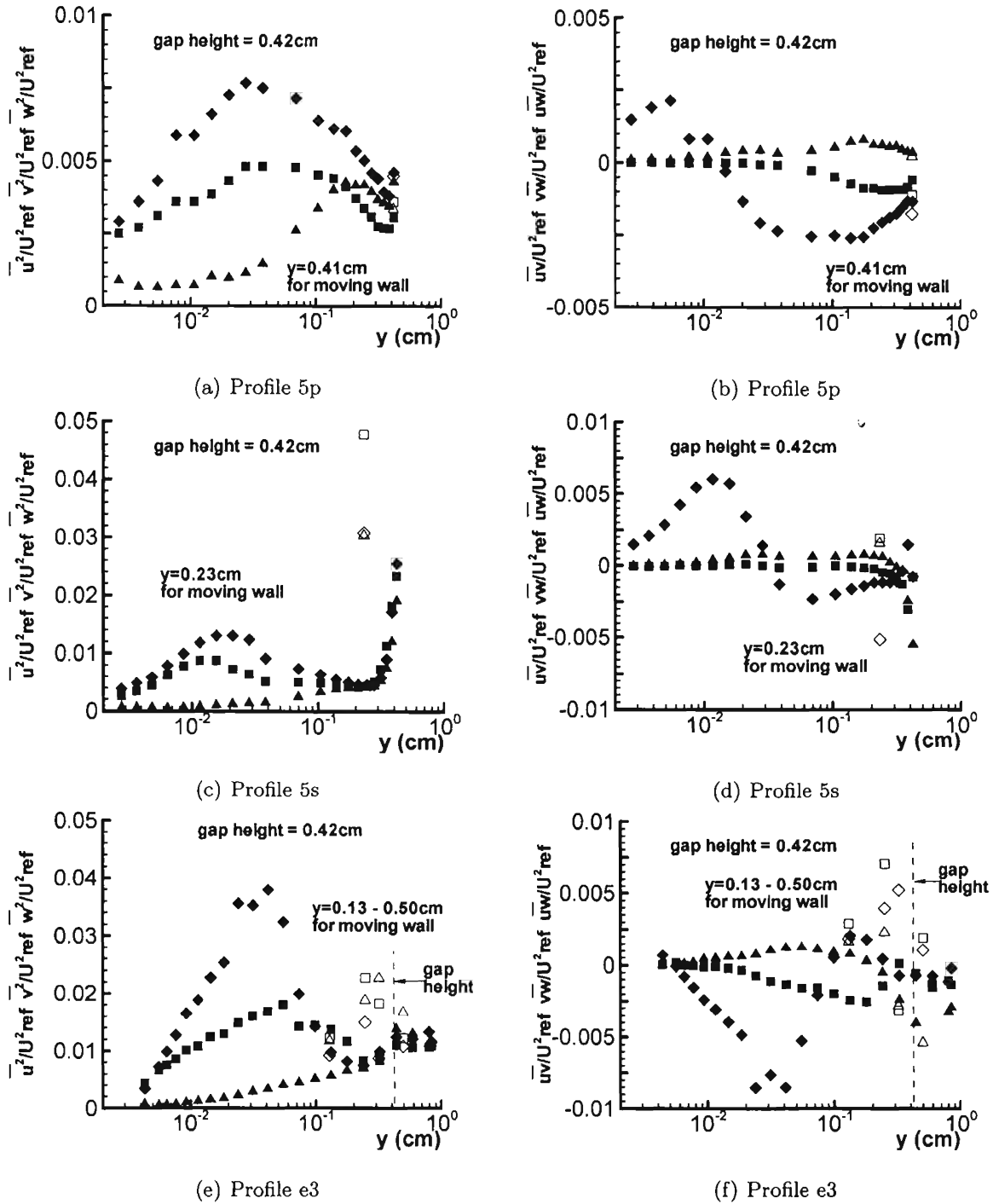
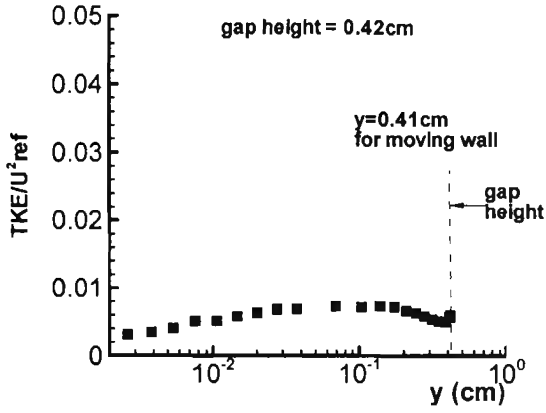
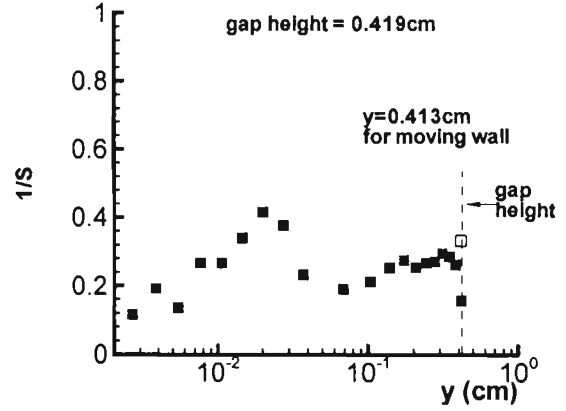


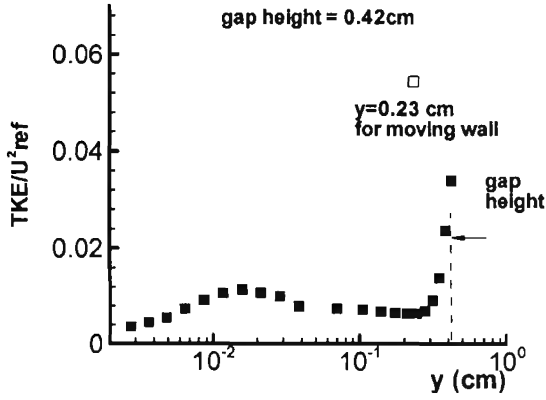
Figure 4.14: Reynolds stress of profiles 5p, 5s, and e3 at  $x/c_a = 0.18$  with 1.65% tip gap in bed coordinate system; for moving wall:  $\square$ ,  $\overline{u^2}$  and  $\overline{uv}$ ;  $\triangle$ ,  $\overline{v^2}$  and  $\overline{vw}$ ;  $\diamond$ ,  $\overline{u^2}$  and  $\overline{uv}$ ; for stationary wall:  $\blacksquare$ ,  $\overline{u^2}$  and  $\overline{uv}$ ;  $\blacktriangle$ ,  $\overline{v^2}$  and  $\overline{vw}$ ;  $\blacklozenge$ ,  $\overline{u^2}$  and  $\overline{uv}$ .



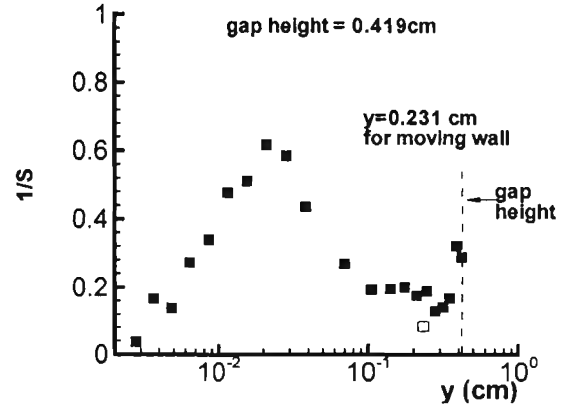
(a) Profile 5p



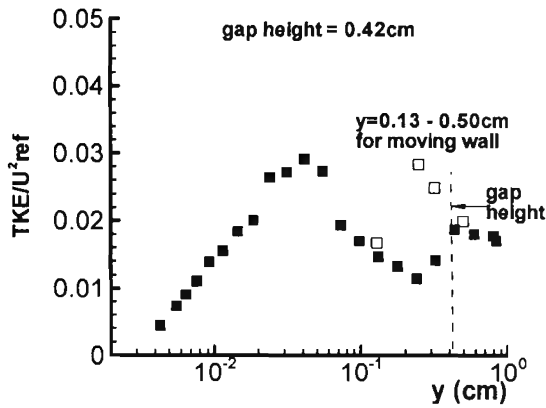
(b) Profile 5p



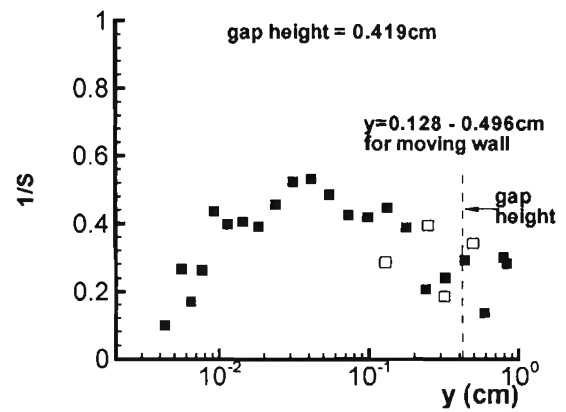
(c) Profile 5s



(d) Profile 5s



(e) Profile e3



(f) Profile e3

Figure 4.15: Normalized TKE and  $1/S$  of profiles 5p, 5s, and e3 at  $x/c_a = 0.18$  with 1.65% tip gap; for moving wall:  $\square$ ; for stationary wall:  $\blacksquare$ .

# Chapter 5

## Conclusions

The literature review in Chapter 1 introduced the results from previous studies for the tip gap flow in a compressor cascade. The present study has investigated the tip gap turbulent flow with and without wall motion. The measurement and discussion in Chapters 3 and 4 have characterized the tip gap turbulent flow structure. The first two sections will highlight the key conclusions for a stationary wall and a moving wall, separately, from the present study. The final section will suggest future work.

### 5.1 Stationary End-Wall

A thorough study was done for tip gap flows including surface oil flow visualizations, surface pressure measurements, and LDV measurements. The most complete data sets were acquired for 1.65% and 3.30% tip gap/chord ratios in a low-speed linear compressor cascade. The oil flow visualizations of an endwall and blade surfaces were made to depict the flow structures near the physical boundaries. The mid-span blade pressure loading and the endwall pressure distribution were measured. The fine spatial resolution three-

velocity-component LDV was applied for the first time to take measurements within the gap. Non-intrusive measurements provided reliable and precise data to validate any CFD efforts. High data rates up to 1700 samples/second at some LDV profiles permitted an estimate of low frequency turbulence spectra to examine the tip gap flow.

The endwall oil flow visualizations show the good periodicity of flow structures. The limiting surface streamlines on the endwall illustrate the unsteady flow separation of the tip leakage vortex and the passage vortex next to the suction side in the blade passage as well as the reattachment of downward flow on the endwall close to the pressure side. Dark regions represent the strong wall shear layer underneath the tip gap due to the strong pressure driven cross flow. Around the separation region from the starting point to the far downstream, accumulated white powder on the endwall characterizes low momentum fluid in the separation region. Fine limiting surface streamlines were digitized by Tian (2003) from the oil flow to find flow angles on the endwall which are consistent with the averaged flow angles in the viscous sublayer from the LDV measurements in the same profile locations, except for the separating flow region.

The limiting streamlines on blade surfaces indicate that the pressure and suction side boundary layers are two-dimensional, except some spanwise distance away from the blade tip and up to a few times of tip gap height on the pressure surface. The flow turns into the gap at an asymptotically right angle to the blade square tip edge. However, flow structures are very complicated in the lower 20% of the blade span around the blade tip corner of the suction side, including the upward primary flow, the second tip separation vortex, and the reattachment of the tip leakage vortex.

The endwall static pressure distributions portray similar flow structures to those observed from the endwall oil flow visualizations, such as the repeatability and periodicity of the test flow, strong cross flow driven by the lateral pressure gradient below the blade



tip, the starting and development of a tip leakage vortex on the suction side, and the trajectory of the tip leakage vortex in the passage. The endwall high lateral pressure gradient changed  $U_\tau$  up to 20% after the correction of the pressure gradient.

The mid-span blade loading is independent of gap sizes and relative motion of the endwall. Previous studies of Chen et al. (1991) predicted the tip leakage flow field based on the mid-span blade loading. Actually, the crossflow velocity across the gap relies on local tip pressure loading that is different from the mid-span pressure loading because of tip leakage vortex influence.

The mean flow velocity was only measured at the exit of the compressor gap using Pitot tubes by Storer and Cumpsty (1991) and Kang and Kirsh (1994), but no velocity profiles inside the gap. Storer and Barton (1991) took turbulence intensity data within the gap. In this study, the LDV was used to measure four profiles inside the gap at nine different chord ratios and normal to the endwall from the viscous sublayer ( $y^+ < 4$ ) to the blade tip end. The LDV data were used to examine the flow structures for the first time including mean velocities and turbulence inside the gap. Thus, the LDV data in this study is unprecedented for tip gap flow. The crossflow velocity to the blade chord is nearly uniform in the mid tip-gap, but increases from the pressure to suction side at a specific chord ratio. The chordwise velocity does not change much so that the tip gap flow acts like a jet flow.

Spectral analysis at several profiles of LDV data also shows that the low frequency turbulence energy changes from upstream to downstream of the blade row. Due to the limitation of data rates, only low frequency spectra were estimated. The streamwise velocity spectra at the leading edge roughly agree with the universal law of a two dimensional flow, such as the power of -1 in the inner region and the power of -5/3 in the log region.

The tip leakage vortex is unsteady because the interaction of primary flow and the crossflow out of the gap. Its meandering may exist tangentially and vertically from the observation of the TKE transport vector and the endwall oil flow visualization. Spectral analysis of LDV measurements did not reveal the flow meandering of tip leakage vortex because the LDV data rate was not high enough in the separation region of the tip leakage vortex.

This study with several different experimental techniques characterized the pressure-driven tip gap flows that are very complex unsteady three-dimensional turbulent flows. From the conceptual gap models, the first tip separation vortex forms at the blade tip corner on the pressure side and the second tip separation vortex is produced at the blade tip corner on the suction side because of the sharp flow turning around the square blade tip. The tip leakage vortex separated from the passage on the suction side. Other than the nearest endwall and blade tip regions, the TKE does not vary much in tip gap. The tip leakage vortex produces high turbulence intensities. Although the primary inflow approaching the blade row is nearly a two-dimensional flow, the flow becomes three-dimensional mainly because of the cross flow perpendicular to the camber line. The pressure driven tip leakage flow is dominant in the gap in the lower endwall region. The tip gap flow is highly skewed because the flow angle in a full gap changes about  $90^\circ$  from the endwall to the blade tip. The tip gap flow correlation of shear stresses and normal stresses decreases significantly from the leading edge to the trailing edge of the blade due to flow skewing through the gap.

Viscosity plays an important role in the two distinct viscous layers bounded on endwall and blade tip, respectively. Between the two layers is generally treated as a potential core because the TKE does not change much. The size of the potential core is approximately proportional to the gap size. For a smaller gap (less than 1% of the chord length), the

viscous effects are dominant as pointed out by Rains (1954). However, for a larger gap, viscosity still imposed some effect on the flow from the turbulence measurement in the 1.65% and 3.30% tip gap. The tip gap flow is a strongly anisotropic turbulent flow. Rapid distortion ideas can not apply to it. A turbulence model based on the experimental data is necessary to reflect the tip gap flow physics.

The gap size determines the starting point of the tip leakage vortex if the camber and stagger angle are fixed. As the gap size increased from 1.65% to 3.30%, the starting point shifts rearward of the blade from 16% of the chord to 36% of the chord. Normalized circulation in the tip gap is independent of the gap size, but it varies along the chord with the change of pressure loading. Tip gap flow features like tip separation and reattachment strongly depend on the blade thickness-to-gap height ratio after the origin of tip leakage vortex but is weakly related to it before the origin of tip leakage vortex for a moderate tip gap.

## 5.2 Moving End-Wall

Relative motion of the endwall significantly affects the tip gap flow structures. The end-wall motion in this study skewed the near wall flow and the corresponding flow angles changed substantially. The upstream LDV profile in this study and the downstream hot-wire data measured by Wang (2000) reflected the flow structure changes from the stationary wall to the moving wall, suggesting that the influence of relative motion developed from the moving endwall leading edge to the downstream of the blade row. In the gap region, Herzig et al. (1954) found that the scraping effect increased the blade tip pressure loading to reduce the separation on the suction side, the boundary layer flow next to the square blade tip tended to move upward on the pressure side, and the tip

leakage vortex in the passage shifted further away from the suction side. The limited LDV data around the gap region in this study appeared to agree with the observation of Herzig et al. (1954) from the smoke visualization of the tip gap flow with the moving wall. Due to the combination effect of the endwall shear induced by the endwall motion and the improvement of the blade tip pressure loading, the shape of the tip leakage vortex probably changes from the round for the stationary endwall to the elliptic for the moving endwall. Wang (2000) confirmed that the tip leakage vortex shape with the moving wall was different from the stationary wall. For the moving endwall, this study discovered that the relative motion skewed the inner region flow to decorrelate with the outer layer flow. Hence, the TKE and the  $1/S$  decreased in the upstream of the blade.

### 5.3 Future Work

The LDV measurement technique is a powerful tool with which to measure the three-dimensionality of complex flow in a non-intrusive manner. The  $30\ \mu m$  diameter measurement volume of the LDV probe in this study permitted measurements of the near endwall flow and very close to the tip surface in tip gap of the compressor cascade. A greater understanding of the tip gap flow has been gained through the LDV data set acquired for the stationary endwall in this study, which also can be used to validate turbulence models in CFD efforts. Due to the difficulty to avoid the beam flaring on the physical boundaries, the LDV experiments for a moving wall were not measured at the same profiles as those for stationary wall. A new LDV is under construction to permit laser beams from the side wall instead of the endwall to avoid the problems in this study caused by the moving belt such as particle blocking, blade flare, and belt flare.

Flow structures near the square tip corner of the blade suction side is unclear. More

---

data are necessary to clarify the complex region for the stationary wall case. Tip gap data with a moving wall are highly valuable to discover the effect of relative motion on the flow structures. The new LDV will be capable to complete the measurement of the tip gap flow.

# References

- Ahn, S. 1986 *“Some Unsteady Features Turbulent Boundary Layers,”* MS Thesis, AOE Dept, Virginia Tech.
- AGARD, Advisory Group for Aerospace Research and Development 1996 *“Turbulent Boundary Layers in Subsonic and Supersonic Flow,”* AGARD-AG-335, North Atlantic Treaty Organization, pp. 25-28.
- Batchelor, G.K. 1953 *“The Theory of Homogeneous Turbulence,”* Cambridge Univ. Press, pp. 68-75.
- Bissonnette, L.R. and Mellor, G.L. 1974 *“Experiments on the behavior of an axisymmetric turbulent boundary layer with a sudden circumferential strain,”* Journal of Fluid Mechanics, Vol 63, Apr., pp. 369-413.
- Boutier, A. 2002 *“POST-PROCESSING OF EXPERIMENTAL AND NUMERICAL DATA: VELOCITY MEASUREMENT ACCURACY IN LDV,”* Lectures Series 2002-04, von Karman Institute for Fluid Dynamics, April 22-26.
- Brown, J.L. 1989 *“Geometric bias and time coincidence in 3-dimensional laser Doppler velocimeter system,”* Experimental Fluids, Vol. 7, pp. 25-32.
- Chen, C.-Y., Kim, P.J., and Walker, D.T. 1996 *“Angular Bias Errors in Three-*

- Component Laser Velocimeter Measurements*," J. Fluids Engineering, Vol. 118, pp.555-561.
- Chen, G.T., Greitzer, E.M., Tan, C.S., and Marble, F.E. 1990 "*Similarity Analysis of Compressor Tip Clearance Flow Structure*," Transactions of the ASME Journal of Turbomachinery, Vol 113, April, pp. 260-271.
- Chesnakas, C.J. and Simpson, R.L. 1994 "*Full three-dimensional measurements of the cross-flow separation region of a 6 : 1 prolate spheroid*," Experiments in Fluids, Vol. 17, pp. 68-74.
- Chesnakas, C.J. 1995 "*The Miniature, 3-D, Fiber-Optic, Laser Doppler Velocimeter*," Internal Report, Aerospace and Ocean Engineering Department, Virginia Polytechnic Institute and State University, November.
- Chesnakas, C.J. and Simpson R.L. 1996 "*Measurements of the Turbulence Structure in the Vicinity of a 3-D Separation*," Transactions of the ASME Journal of Fluids Engineering, Vol. 118, June, pp. 268-275.
- Ciochetto, D.S. 1997 "*Analysis of Three-Dimensional Turbulent Shear-Flow Experiments with Respect to Algebraic Modeling Parameters*," M.S. Thesis, Virginia Tech, Blacksburg, VA.
- de la Riva, D. H. 2001 "*Turbulence Interaction in a Highly Staggered Cascade-Propulsor Configuration*," MS Thesis, AOE Dept, Virginia Tech.
- Denton, J.D. 1993 "*Loss Mechanisms in Turbomachines*," Transactions of the ASME Journal of Turbomachinery, Vol 115, April, pp. 621-656.
- Driver, D.M. and Johnston, J.P. 1990 "*Experimental Study of a Three-Dimensional*

- Shear-Driven Turbulent Boundary Layer with Streamwise Adverse Pressure Gradient,*" NASA TM 102211.
- Durst, F., Melling, A., and Whitelaw, J.H. 1981 "*Principles and Practice of Laser-Doppler Anemometry,*" Second ed., Acad. Press, p. 32 and p. 207.
- Durst, F., Martinuzzi, R., Sender, J., and Thevenin, D. 1992 "*LDV-Measurements of Mean Velocity, RMS-Values and Higher Order Moments of Turbulence Intensity Fluctuations in Flow Fields with Strong Velocity Gradients,*" Proceedings of the 6th International Symposium on Applications of Laser Techniques to Fluid Mechanics, Lisbon, Portugal, paper 5.1.1.
- Durst, F., Jovanovic, J., and Sender, J. 1995 "*LDA measurements in the near-wall region of a turbulent pipe flow,*" Journal of Fluid Mechanics, Vol. 295, pp. 305-335.
- Echols, W.H. and Young, J.A. 1963 "*Studies of portable air-operated aerosol generator,*" NRL Report, 5929.
- Fuchs, W., Albrecht, H., Nobach, H., Tropea, C. and Graham, L.J.W. 1992 "*Simulation and experimental verification of statistical bias in laser Doppler anemometry including non-homogenous particle density,*" Proceedings of the 6th International Symposium on Applications of Laser Techniques to Fluid Mechanics, Lisbon, Portugal, paper 8.2.1.
- Herzig, H.Z., Hansen, A.G., and Costello., G.R. 1954 "*A VISUALIZATION STUDY OF SECONDARY FLOWS IN CASCADES,*" NACA Eeport 1163.
- Hobson, G.V. and Dober, D.M. 1997 "*Three-Dimensional Laser-Doppler Velocimetry Measurements in the End-Wall Region of a Linear Cascade,*" International Journal of Turbo and Jet Engines, 14, 1-15(1997).



- Hussain, A.K.M.F. 1986 "Coherent structures and turbulence," J. Fluid Mech. (1986), Vol. 173, pp. 303-356.
- Inoue M. and Kuroumaru M. 1988 "Structure of a Tip Clearance Flow in an Isolated Axial Compressor Rotor," ASME paper 88-GT-251.
- Kang, S. and Kirsh, C. 1993 "Experimental Study of Three-Dimensional Flow within a Compressor Cascade with Tip Clearance: Part I - Velocity and Pressure Fields", Journal of Turbomachonery, Vol. 115, pp. 435-443.
- Kang, S. and Kirsh, C. 1994 "Tip Leakage Flow in Linear Compressor Cascade", Journal of Turbomachonery, Vol. 116, pp. 657-664.
- Kannepalli, C. and Piomelli, U. 2000 "Large-eddy simulation of a three-dimensional shear-driven turbulent boundary layer," Journal of Fluid Mechanics, Vol 423, Sept., pp. 175-203.
- Kim, J., Moin, P. and Moser, R. 1987 "Turbulence statistics in fully developed channel flow at low Reynolds number", Journal of Fluid Mechanics, Vol. 177, pp. 133.
- Kuhl, D. 2001 "NEAR WALL INVESTIGATION OF THREE DIMENSIONAL TURBULENT BOUNDARY LAYERS," MS Thesis, AOE Dept, Virginia Tech.
- Lakshminarayana, B. and Horlock, J.H. 1967 "Leakage and Secondary Flows in Compressor Cascades," ARC R&M No.3483.
- Lakshminarayana, B. and Murthy, K.N.S. 1988 "Laser-Doppler Velocimeter Measurement of Annulus Wall Boundary Layer in a Compressor Rotor," Transactions of the ASME Journal of Turbomachinery, Vol 110, July, pp. 377-385.

- Lakshminarayana, B., Zaccaria, M., and Marathe, B. 1995 *"The Structure of Tip Clearance Flow in Axial Flow Compressors,"* Transactions of the ASME Journal of Turbomachinery, Vol 117, July, pp. 336-347.
- Lee, Y.T., Feng, J., Merkle, C., and Tse, M. 1997 *"Effects of Tip-Clearance Flows,"* Twenty-First Symposium on Naval Hydrodynamics (1997), pp. 959-972.
- Lohmann, R. 1976 *"The Response of a Developed Turbulent Boundary Layer of Local Transverse Surface Motion,"* Transactions of ASME, Journal of Fluids Engineering, Vol 98, Sept., pp. 354-363.
- Ma, R., Saha, N., Devenport, W.J., and Wang, Y. 2000 *"Unsteady Behavior of a Tip Leakage Vortex Produced by Simulated Stator/Rotor interaction,"* AIAA paper 2000-2217, Fluids 2000, Denver, CO, June 19-20.
- Ma, R., 2003 *"Unsteady Turbulence Interaction in a Tip Leakage Flow Downstream of a Simulated Axial Compressor Rotor,"* Ph.D. Dissertation, Virginia Tech, Blacksburg, VA.
- Macrodyne 1992 *"Laser Doppler Velocimetry (LDV) Electronics Frequency Domain Processor Model 3100 Users Manual,"* Rev. 060192A, Macrodyne Inc., 4 Chelsea Place, PO box 376, Clifton Park, NY 12065.
- Madden, M.M., and Simpson, R.L. 1997 *"Octant Analysis of the Reynolds Stresses in the Three-Dimensional Turbulent Boundary Layer of a Prolate Spheroid,"* Report Number VPI-AOE-252, Aerospace and Ocean Engineering Dept, VPI&SU.
- Meyers, J.F., Kjølgaard, S.O., and Hepner, T.E. 1992 *"Investigation of Particle sampling Bias in the Shear Flow Field Downstream of a Backward Facing Step"* Proceedings

- of the 6th International Symposium on Applications of Laser Techniques to Fluid Mechanics, Lisbon, Portugal, paper 29.1.
- Mish, P.F. 2003 *"An Experimental Investigation of Unsteady Surface Pressure on Single and Multiple Airfoils in Turbulence,"* Ph.D. Dissertation, Virginia Tech, Blacksburg, VA.
- Morphis, G. and Bindon, J.P. 1988 *"The Effects of Relative Motion, Blade Edge Rains and Gap Size on the Blade Tip Pressure Distribution in an Annular Turbine Cascade with Clearance,"* ASME Paper 88-GT-256, 1988.
- Murthy, K.N.S. 1985 *"An Experimental Investigation of End-wall Flowfield of a Compressor Rotor"* Ph.D. Thesis, Pennsylvania State University, State College, PA.
- Murthy, K.N.S. and Lakshminarayana, B. 1986 *"Laser Doppler Velocimeter Measurement in the Tip Region of A Compressor Rotor,"* AIAA Journal, Vol.24, No.5, pp. 807-814.
- Muthanna, C., 1998 *"Flowfield Downstream of a Compressor Cascade with Tip Leakage,"* M.S. Thesis, Virginia Tech, Blacksburg, VA.
- Muthanna, C., 2002 *"The Effects of Free Stream Turbulence on the Flow Field through a Compressor Cascade,"* Ph.D. Dissertation, Virginia Tech, Blacksburg, VA.
- Muthanna, C. and Devenport, W.J. 2004 *"THE WAKE OF A COMPRESSOR CASCADE WITH TIP GAP: PART 1. MEAN FLOW AND TURBULENCE STRUCTURE,"* AIAA Journal (submitted).
- Ölçmen, S.M., and Simpson, R.L. 1995a *"A five-velocity -component laser-Doppler velocimeter for measurements of a three-dimensional turbulent boundary layer,"* Measurement Science and Technology, Vol. 6, pp. 702-716.

- Ölçmen, S.M., and Simpson, R.L. 1995b "An experimental study of a three-dimensional pressure-driven turbulent boundary layer," J. Fluid Mech. (1995), vol.290, pp. 225-262.
- Ölçmen, S.M., Simpson, R.L., and Goody, M. 1998 "An Experimental Investigation of Two-Point Correlations in Two- and Three Dimensional Turbulent Boundary Layers," AIAA paper 98-0427, 36th Aerospace Sciences Meeting and Exhibit, Reno, NV, January 12-15.
- Perry, A.E., Henbest, S.M., and Chong, M.S. 1986 "A theoretical and experimental study of wall turbulence," Journal of Fluid Mechanics, Vol. 165, pp. 163-199.
- Rains D.A. 1954 "Tip Clearance Flows in Axial Flow Compressors and Pumps," California Institute of Technology, Hydrodynamics and Mechanical Engineering Laboratories, Report No.5, June, 1954.
- Robert J.B. 1986 "Spectral analysis of randomly sampled signals using a correlation-based slotting technique," IEE PROCEEDINGS. Vol 133. Pt. E. APRIL. 1986.
- Robinson, E.A. 1981 "Least squares regression analysis in terms of linear algebra," Goose Pond Press, Houston, Tex.
- Saha, N., Ma, R., and Devenport, W.J. 2001 "Characterizing Unsteady Periodic Disturbances in the Tip Leakage Vortex of an Idealized Axial Compressor Rotor Blade," 39th Aerospace Sciences Meeting and Exhibit, Reno, NV, January 8-11.
- Shin, S., 2001 "Reynolds-Averaged Navier-Stokes Computation of Tip Clearance Flow in a Compressor Cascade Using an Unstructured Grid," Ph.D. Dissertation, Virginia Tech, Blacksburg, VA.
- Simpson, R.L., Agarwal, N.K., Nagabushshanan, K.A., and Ölçmen, S. 1990 "Spectral

- Measurements and Other Features of Separating Turbulent Flows*," AIAA Journal. Vol. 28, No.3 pp. 446-452.
- Simpson, R.L. 1996 "ASPECTS OF TURBULENT BOUNDARY-LAYER SEPARATION," Prog. Aerospace Sci. Vol. 32. pp. 457-521.
- Simpson, R.L., and Ölçmen, S.M. 1998 "Some Structural Features of Pressure-Driven Three-Dimensional Turbulent Boundary Layers from Experiments for  $500 \leq Re_\theta \leq 23000$ ," 22nd ONR Symposium on Naval Hydrodynamics, Washington, D.C., August 9-14.
- Sjolander, S.A. and Cao, D. 1995 "Measurements of the Flow in an Idealized Turbine Tip Gap," Transactions of the ASME Journal of Turbomachinery, Vol 117, October, pp. 578-584.
- Sjolander, S.A. 1997 "Secondary and Tip-Clearance Flows in Axial Turbines," Lectures Series 1997-01, von Karman Institute for Fluid Dynamics.
- Spalart, P.R. 1988 "Direct simulation of a turbulent boundary layer up to  $R=1410$ ," Journal of Fluid Mechanics, Vol.187, p. 61.
- Stauter, R.C. 1993 "Measurement of the Three-Dimensional Tip Region Flow Field in an Axial Compressor," Transactions of the ASME Journal of Turbomachinery, Vol 115, July, pp. 468-476.
- Storer, J.A. 1989 "The Interaction between Tip Clearance Flow and the Passage Flowfield in an Axial Compressor Cascade," ISABE 89-7024.
- Storer, J.A. and Cumpsty, N.A. 1990 "Tip Leakage Flow in Axial Compressors," Transactions of the ASME Journal of Turbomachinery, Vol 113, April, pp. 252-259.

- Storer, J.A. and Barton, J.P. 1991 "AN INVESTIGATION OF THE FLOW WITHIN THE CLEARANCE SPACE OF A COMPRESSOR BLADE TIP," ISABE 91-7013.
- Tian, Q., 2003 "Some Features of Tip Gap Flow Fields of a Linear Compressor Cascade," MS Thesis, AOE Dept, Virginia Tech.
- Wang, Y., Muthanna, C., and Devenport, W. J. 1999 "The Design and Operation of a Moving End-Wall System for a Compressor Cascade Wind Tunnel," AIAA paper 99-0741, 37th Aerospace Sciences Meeting and Exhibit, Reno, NV, January 11-14.
- Wang, Y., 2000 "Tip Leakage Flow Downstream a Compressor Cascade with Moving End Wall," MS Thesis, AOE Dept, Virginia Tech.
- Wang, Y. and Devenport, W.J. 2004 "THE WAKE OF A COMPRESSOR CASCADE WITH TIP GAP: PART 2. EFFECTS OF ENDWALL MOTION," AIAA Journal (submitted).
- Wenger, C.W., 1999 "Analysis of Two-point Turbulence Measurements for aeroacoustics," MS Thesis, AOE Dept, Virginia Tech.
- Wernet, M.P., Zante, D.V., Strazisar, T.J., John, W.T., and Prahst, P.S. 2002 "3-D Digital PIV Measurements of the Tip Clearance Flow in an Axial Compressor," GT-2002-30643, Proceedings of ASME Turbo\_EXPO 2002, June 3-6, 2002, Amsterdam the Netherlands.
- Wetzel, T.G. 1996 "Unsteady Flow Over a 6:1 Prolate Spheroid," Ph.D. Dissertation, Virginia Tech, Blacksburg, VA.
- Whiffen, M.C., Lau, J.C., and Smith, D.M. 1979 "Design of LV Experiments for Turbulence Measurements," Laser Velocimetry and Particle Sizing, Thompson, H.D. and Stevenson, W.H., eds. Hemisphere, pp. 197-207.

- Yaras, M.I., Zhu, Y., and Sjolander S.A. 1989 “*Flow Field in the Tip Gap of a Planar Cascade of Turbine Blades,*” Transactions of the ASME Journal of Turbomachinery, Vol 111, July, pp. 276-283.
- Yaras, M.I. and Sjolander S.A. 1992 “*Effects of Simulated Rotation on Tip Leakage in a Planar Cascade of Turbine Blades: Part I - Tip Gap Flow,*” Transactions of the ASME Journal of Turbomachinery, Vol 114, July, pp. 660-667.
- Yaras, M.I., Sjolander S.A., and Kind, R.J. 1992 “*Effects of Simulated Rotation on Tip Leakage in a Planar Cascade of Turbine Blades: Part II - Downstream Flow Field and Blade Loading,*” Transactions of the ASME Journal of Turbomachinery, Vol 114, July, pp. 652-659.
- You, D., Wang, M., Mittal, R., and Moin P. 2003 “*Study of Rotor Tip-clearance Flow Using Large-Eddy Simulation,*” AIAA 2003-0838.

# Appendix A

## Operation and Maintenance of a High quality LDV

High quality data at a high data rate requires the reliable setup of an LDV system and a test flow of interest. LDV is a complex optical technique from which to acquire optical signals with many factors that influence its success, such as laser beam quality, alignment of measurement volumes, signal processing, data transfer, and so on. Major factors are discussed below.

### A.1 Beam Intensity

When a proper laser power is chosen as beam sources of LDV, maximizing the beam intensity of each beam is fundamental step to obtain the highest data rate. For example, arranging the optical parts effectively to produce two colors in five beams; launching laser beams into the fiber with minimum loss; balancing beam power. The contrast of a fringe pattern is usually defined by Boutier (2002) as  $C = 2\sqrt{I_1 I_2} / (I_1 + I_2)$  for two



coherent laser beams with intensities of  $I_1$  and  $I_2$ . Assuming  $I_1 + I_2$  is fixed, C reaches its maximum when  $I_1 = I_2$ . A power meter is used to measure each beam intensity for balancing the equality of two blues beams or three green beams.

## A.2 Beam Polarization

The data rate is proportion to the  $\cos^2(\beta)$  from Ölçmen and Simpson (1995b), where  $\beta$  is the angle between the two linear polarization vectors of a beam pair. The stability of polarization is very important so that when a beam launches into the optical fiber, the polarization has to match with the fast and slow axis of the fiber beam propagation within  $\pm 1^\circ$  tolerance. Otherwise, the polarization orientation is not stable and its orientation can oscillate or rotate. The beams polarization from the LDV probe was determined to be stable when shaking of the fibers connected with the probe did not produce fluctuations of the polarization line.

## A.3 Beam Frequency

A beam frequency has to be as accurate as possible because a Doppler frequency is a physical signal to represent a measured velocity. The reference beam should be the single frequency without broadening. For one laser, an etalon can purify the reference frequency of an unshifted beam. The shift frequency of Bragg cell has to be accurate as well. The drift of Bragg cell frequency occurs over time so that it should be calibrated frequently. The Bragg cell frequencies must be apart different enough to avoid any cross talk between two pairs of fringe pattern for the same color. The Bragg cell frequency should be high enough to capture the highest flow velocity and any flow reversal.

## A.4 Beam Path

Beam path equality is important for the Doppler signal. the etalon reduces the sensitivity to the beam path difference within two inches described by Chesnakas (1995). The beam paths accommodate this tolerance by manual arrangement of optical parts.

## A.5 Beam Mode

A beam with  $TEM_{00}$  mode has a Gaussian distribution intensity that reduces the energy loss after the beam launch into the fiber core. To get the  $TEM_{00}$  mode beams, the pinhole of the laser output is adjusted while looking at the beam cross-section pattern on a piece of white paper.

## A.6 Alignment of Measurement Volume

Misalignment of the measurement volume reduces the size of a measurement volume so that the data rate drops and fringe pattern could be distorted. Meanwhile, it can result in LDV biases discussed later in Appendix B.1.2. The alignment procedure was described in Section 2.3.1.

## A.7 Receiving Adjustment

After good alignment of the measurement volume, the LDV works at high coincidence data rate. By adjusting the focal point of receiving lens, the data rate can increase about 150 samples/sec more or less.

## A.8 Photomultiplier Tube

The photomultiplier tube face is sensitive to the wavelength of the laser beams. After choosing the photomultiplier for a specific color of blue or green, the high input voltage has to be optimized for the specific photomultiplier tube to get high data rate with high validation ratio.

## A.9 Signal conditioning and Processing

Since the outputs from the PMTs are small and broadband electrical signals, signal conditioning is necessary to satisfy the requirement of signal processors, filter out unwanted noise while keeping the signal frequency, and maintain high signal-to-noise ratio. High performance and fast frequency domain signal processors like the Macrodyne 3100 are a plus to obtain high quality LDV data at a high data rate.

## A.10 Radio Frequency

An adjustable radio frequency is used to downshift the signal frequency. It removes the carrier frequency generated by the Bragg cell from the measured signal. The regular adjustment of the radio frequency keeps the peak of histogram in the center of the display panel of Macrodyne.

## A.11 Data Transfer

For the current system, digital data from the Macrodyne signal processors transfer into the data acquisition computer. A high data transfer rate was required to reduce the loss of data for a high efficient measurements of LDV.

## A.12 Seeding

The seeding is critical for high data rate and high quality of LDV data. The adequate particle density of the uniform size improves the LDV measurement accuracy. Maintenance of the DOP at a certain level in the pressure cooker containing the Laskin nozzles, emptying the impactor can often, and optimizing the pressure setting were required for a good data rate with high validation ratio.

## A.13 Test Flow

A test flow of interest has to be calibrated before the LDV measurements and needs to be monitored during the daily operation of LDV measurements. This can ensure the repeatable flow quality for a long period of experiments using a LDV system.

## A.14 Daily Maintenance

To obtain high quality LDV data at a high data rate, daily operation is necessary, such as maximizing the beam intensity, checking the DOP level, monitoring the tunnel velocity.

## A.15 Troubleshooting

The statement above reflects the factors to affect the proper function of LDV. After the setup of the LDV system, things can go wrong for the daily operation of LDV. Troubleshooting is the key to isolate the cause of LDV disfunction.

# Appendix B

## Uncertainty Analysis of LDV

Even though the operation of the LDV was maintained at high quality with high data rates as described in Appendix A, the LDV still produces signals with uncertainties like any instrument does. All uncertainty sources for the LDV are identified first. An uncertainty estimation procedure is provided to obtain the uncertainty of velocity and turbulence.

### B.1 Uncertainty Sources

The LDV is a complicated system integrated with optical signal and electrical signals so that the identification of related uncertainty sources is critical to improve the LDV accuracy. The uncertainty factors can be classified in different categories: beam quality, fringe pattern, signal and data processing, and seeding.

### B.1.1 Beam Quality

The laser beam quality is essential to ensure high data rate with high quality. As mentioned in Appendix A, the laser beam wave with amplitude, wavelength, phase, and polarization. The failure of any parameter definitely degrades the signal and produces noise. The thermal stability is very important during the LDV measurements.

### B.1.2 Fringe Pattern

The measurement volume properties are major contributions to the uncertainty of LDV, which consists of three fringe patterns for a three-dimensional LDV. To make physically meaningful measurements, three pairs of laser beams have to cross at their beam waists and coincide with three centers of beam waists at a point. After the LDV probe is set up in the flow, beam angles are measured in a tunnel coordinate system. The alignment and measurement can not be perfect, which results in uncertainties, such as fringe bias described by Whiffen et al. (1979), geometric bias proposed by Brown (1989), angular bias Chen et al. (1996), velocity bias, and velocity gradient bias. The fringe bias, geometric bias, angular, and velocity gradient bias are not important because the measurement volume of the LDV used in this study is small and nearly spherical.

The velocity bias corrections of LDV measurements might be necessary as discussed in Fuchs et al. (1992). To assess whether or not there were velocity bias effects in our data, a method similar to that of Meyers et al. (1992) was used. A standard correlation coefficient (CC) between velocity magnitude fluctuation and data rate fluctuation was calculated for each profile in the two setups. As all the correlation coefficients in Chapter 3 are on the order of  $10^{-2}$ , there is no correlation between the velocity magnitude fluctuation and data rate fluctuation for either case, and thus no velocity bias. The correlation coefficient

was defined by Kuhl (2001) as follows.

$$CC = \frac{(\sum_{i=1}^n (|V| - |v_i|)(R - r_i)/n)}{\sigma_v \sigma_r} \quad (\text{B.1})$$

Here  $n$  is the sample number for a given point of the LDV profile,  $|v_i|$  is the  $i^{th}$  instantaneous velocity magnitude,  $|V|$  is the mean velocity magnitude  $\sum_{i=1}^n |v_i|/n$ ,  $r_i$  is the  $i^{th}$  instantaneous data rate  $1/(t_i - t_{i-1})$ ,  $R$  is the mean data rate  $\sum_{i=1}^n |r_i|/n$ ,  $\sigma_v$  is the standard deviation of velocity magnitude  $\sum_{i=1}^n v_i^2/n$ , and  $\sigma_r$  is the standard deviation of data rate  $\sum_{i=1}^n r_i^2/n$ .

Velocity gradient bias occurs because the LDV system receives signals over the measurement volume in a flow with velocity gradients. Especially near the wall, velocity gradient is large. Velocity gradient bias can be greatly reduced by using a small enough measurement volume. Using the following equations suggested by Durst et al. (1992), this effect can be calculated.

$$U_{measured} = U_{true} + \frac{d^2}{32} \frac{d^2 U}{dy^2} + \dots \quad (\text{B.2})$$

$$\overline{u^2}_{measured} = \overline{u^2}_{true} + \frac{d^2}{16} \left( \frac{dU}{dy} \right)^2 + \dots \quad (\text{B.3})$$

$$\overline{u^3}_{measured} = \overline{u^3}_{true} + \frac{3d^2}{16} \left( \frac{dU}{dy} \right) \left( \frac{d\overline{u^2}}{dy} \right) + \frac{d^2}{32} \frac{d^2 \overline{u^3}}{dy^2} + \dots \quad (\text{B.4})$$

The velocity gradient bias effect was less than the uncertainty in the data.

### B.1.3 Signal and Data Processing

Finite transit time broadening and instrument broadening effects may exist for an LDV system. The transit time broadening is due to a small number of cycles of a Doppler



signal being processed (Durst et al., 1981). A smaller number of cycles produces a greater variance for the turbulence intensity. The transit time broadening  $\overline{u^2}_{transit-time}/U_{ref}^2$  was negligible for the worst case, the nearly two-dimensional inflow, which was estimated by the following equation

$$\frac{\overline{u^2}_{transit-time}}{U_{ref}^2} = \frac{\overline{u^2}_{measured} - \overline{u^2}_{hot-wire}}{U_{ref}^2} \quad (B.5)$$

Here  $U_{ref}$  is the free-stream velocity,  $\overline{u^2}_{measured}/U_{ref}^2$  is 0.0010 from the LDV, and  $\overline{u^2}_{hot-wire}/U_{ref}^2$  is 0.0011 from the hot-wire (Muthanna, 2002), indicating that the  $\overline{u^2}_{measured}/U_{ref}^2$  from LDV was smaller than  $\overline{u^2}_{hot-wire}/U_{ref}^2$ . Therefore, the effect of transit time broadening on the data was negligible. Ölçmen et al. (1998) studied the instrument broadening effects by setting different bandwidth of Macrodyne signal processors used in this LDV system and proved that the bandwidth broadening of the Macrodyne signal processors were negligible.

### B.1.4 Seeding Particles

LDV measures the velocity of seeding particles injected into the flow instead of the fluid velocity itself. Generally speaking, the  $0.5\mu m$  to  $2\mu m$  DOP particles used here follow the low-speed flow correctly if the flow does not have strong velocity variations, such as in the present work.

## B.2 Uncertainty Estimation

Many factors determine the measurement uncertainty of LDV so it is complex to evaluate the uncertainty by the square root of the sum of the mean square of the component of

each factor. A simple but effective way is to consider the LDV data wholly and use Chauvenet's method, the same as Ölçmen and Simpson (1995a) and Kuhl (2001).

The procedure is to measure a profile in the flow on two consecutive days, two sets of good data are used to analyze its uncertainty. Generally 21:1 odds is a good number to represent the uncertainty of the LDV measurements. Equation B.6,

$$\frac{d_{max}}{\sigma} = 1.15 \quad (\text{B.6})$$

is used, where  $d_{max}$  is the average of the half of the differences between two data values and  $\sigma$  is the standard derivation. The value of 1.15 is chosen to give us 21 to 1 odds uncertainties calculated as  $\pm 2\sigma$ .

### B.3 Skin-friction Velocity Uncertainty

For a few profiles, two sets of LDV data in the viscous sublayer were measured at the same location on two consecutive days. The skin friction velocity  $U_\tau$  was evaluated twice. The difference between the two skin friction velocities was within 5% for all repeatedly-taken profiles. Thus, the uncertainty of skin friction velocity was about  $\pm 5\%$ .

### B.4 Wall Location Uncertainty

Since the center of the LDV measurement volume can not be visualized exactly, a wall location procedure was developed to detect the location of the real wall relative to the probe volume. The wall location uncertainty depends on the probe size, the wall finding procedure, and the resolution of the vertical traverse for the LDV. The uncertainty of

the wall location is the order of diameter of measurement volume,  $\pm 50\mu m$ . This value is determined from the iterative procedure provided in Appendix C.2 for a specific profile.

# Appendix C

## Skin Friction Velocity and Wall Location Refinement

This appendix contains a derivation of the skin friction equation and a description of the method used to determine the real wall position.

### C.1 Skin Friction Velocity

In any three-dimensional flow, the skin friction can be estimated by analogy to a two-dimensional boundary flow if the viscous sublayer flow is in a single direction or is a collateral flow. In general, if the collateral flow direction is  $\vec{t}$  in a three-dimensional flow, a momentum equation along this direction can be written

$$Q \frac{\partial Q}{\partial t} + V \frac{\partial Q}{\partial y} = -\frac{1}{\rho} \vec{\nabla} P \cdot \vec{t} + \frac{\partial}{\partial y} (-\overline{qv} + \nu \frac{\partial Q}{\partial y}) - \frac{\partial(\overline{u^2} - \overline{v^2})}{\partial t} \quad (\text{C.1})$$

where  $Q$  is the mean velocity in the  $\vec{t}$  direction,

Assume  $\partial/\partial t \ll \partial/\partial y$  and  $V \approx 0$ , the equation can be reduced to

$$0 = -\frac{1}{\rho} \vec{\nabla} P \cdot \vec{t} + \frac{\partial}{\partial y} (-\overline{qv} + \nu \frac{\partial Q}{\partial y}) \quad (\text{C.2})$$

Furthermore  $q \sim y^2$  and  $v \sim y$  next to the walls to satisfy the velocity fluctuation continuity equation of the flow. Thus  $\overline{qv} \sim y^3$ . After integrating the reduced equation, one obtains

$$Q = \frac{\tau_w}{\mu} y + \frac{\vec{\nabla} P \cdot \vec{t}}{2\mu} y^2 + Cy^4 \quad (\text{C.3})$$

where  $y = y_{\text{measured}} + y_{\text{shift}}$ , so  $\tau_w$ ,  $C$ , and  $y_{\text{shift}}$  are unknowns. The surface pressure gradient from pressure measurements is used and  $y_{\text{shift}}$  is a wall position refinement used to produce a higher correlation of the data to the fit of equation C.3. To solve for these three unknowns, at least five points in the viscous sublayer ( $y^+ < 9$ ) are used to fit equation C.3 above. For simplicity, the curve fit equation becomes

$$Q = C_1 y + \frac{\vec{\nabla} P \cdot \vec{t}}{2\mu} y^2 + C_2 y^4 \quad (\text{C.4})$$

where  $C_1 = \tau_w/\mu$  and  $C_2$  are determined by the data. Thus, the skin friction velocity

$$U_\tau = \sqrt{\frac{C_1}{\nu}} \quad (\text{C.5})$$

## C.2 Wall Location Refinement

Since a measurement volume of the LDV has finite size, its center can not be determined precisely. The LDV probe is mounted in a traverse with high precision. A wall location procedure is used to approximately locate the real wall. However, the signal to noise ratio is low near the wall. This manual procedure can not determine the wall exactly.

However, the boundary condition is known for a solid wall bounded flow. More than five points can be acquired from the viscous sublayer. Accordingly, these data points are used to determine the skin friction velocity and  $y_{shift}$  relative to the measured distance normal to the wall from equation C.4 above. However, both  $Q$  and  $y$  are measured with some uncertainty. An iterative optimization procedure is necessary to finalize the data profile with an accurate normal to wall distance,  $y$ .

$$E(C_1, C_2, y_{shift}) = \sum_{i=1}^N (Q_i - C_1 y_i - \frac{\bar{\nabla} P \cdot \vec{t}}{2\mu} y_i^2 - C_2 y_i^4)^2 \quad (C.6)$$

Since  $y_{shift}$  is implicit in  $y_i = y_{measured} + y_{shift}$ , values of  $y_{shift}$  can be guessed in an iterative procedure. For a specific  $y_{shift}$ ,  $C_1$  and  $C_2$  can be determined by a least square fit of the equation above to minimize  $E$ . Then the correlation coefficient is calculated

$$R^2(y_{shift}) = 1 - \frac{\sum_{i=1}^N (Q_i - C_1 y_i - \frac{\bar{\nabla} P \cdot \vec{t}}{2\mu} y_i^2 - C_2 y_i^4)^2}{\sum_{i=1}^N (Q_i - \frac{\sum_{i=1}^N Q_i}{N})^2} \quad (C.7)$$

A search procedure of  $y_{shift}$  values is used to maximize  $R^2$ .

# Appendix D

## Least Square Fitting of Experimental Data

Suppose that a set of data points is collected from experimental measurements with some errors. To calculate the gradient of parameters at measurement stations, a specific curve fit is used. In this study, parabolic and quadric fits, as described by Robinson (1981), are applied to extract the velocity gradient and pressure gradient, respectively.

### D.1 Parabolic Fit

A parabolic fit is used to calculate the y derivative in a profile and cut off the outlier of samples in LDV experiments. Equation D.1 is a model equation,

$$y = ax^2 + bx + c \tag{D.1}$$

Given a set of data  $(x_i, y_i, i = 1, 2, \dots, N)$ , then a set of linear equations can be

written:

$$\begin{cases} ax_1^2 + bx_1 + c = y_1 \\ ax_2^2 + bx_2 + c = y_2 \\ \vdots \\ ax_N^2 + bx_N + c = y_N \end{cases}$$

It can be written in a matrix form:

$$AX = B \quad (\text{D.2})$$

Where

$$A = \begin{bmatrix} x_1^2 & x_1 & 1 \\ x_2^2 & x_2 & 1 \\ \vdots & \vdots & \vdots \\ x_N^2 & x_N & 1 \end{bmatrix}; X = \begin{bmatrix} a \\ b \\ c \end{bmatrix}; B = \begin{bmatrix} y_1 \\ y_2 \\ \vdots \\ y_N \end{bmatrix};$$

## D.2 Quadric Fit

A quadric fit is used to calculate pressure gradients with irregularly spaced data in x and y. Equation D.3 is a model equation,

$$z = ax^2 + bxy + cy^2 + dx + ey + f \quad (\text{D.3})$$

Given a set of data  $(x_i, y_i, z_i, i = 1, 2, \dots, N)$ , then a set of linear equations can be



written:

$$\begin{cases} ax_1^2 + bx_1y_1 + cy_1^2 + dx_1 + ey_1 + f = z_1 \\ ax_2^2 + bx_2y_2 + cy_2^2 + dx_2 + ey_2 + f = z_2 \\ \vdots \\ ax_N^2 + bx_Ny_N + cy_N^2 + dx_N + ey_N + f = z_N \end{cases}$$

It can be written in a matrix form:

$$AX = B \quad (\text{D.4})$$

Where

$$A = \begin{bmatrix} x_1^2 & x_1y_1 & y_1^2 & x_1 & y_1 & 1 \\ x_2^2 & x_2y_2 & y_2^2 & x_2 & y_2 & 1 \\ \vdots & \vdots & \vdots & \vdots & \vdots & \vdots \\ x_N^2 & x_Ny_N & y_N^2 & x_N & y_N & 1 \end{bmatrix}; X = \begin{bmatrix} a \\ b \\ c \\ d \\ e \\ f \end{bmatrix}; B = \begin{bmatrix} z_1 \\ z_2 \\ \vdots \\ z_N \end{bmatrix};$$

## D.3 Least Square Error

To determine the coefficients of data fitting, the number of data points must be greater than the number of coefficients. Use least square fitting to minimize the total error between the actual data and the fitted data.

The error equations are

$$e = AX - B \quad (\text{D.5})$$

The summation square of errors for all data points is

$$E = (AX - B)^T(AX - B) \quad (\text{D.6})$$

The minimum E occurs when the gradient of E is the zero vector,

$$\nabla E = A^T(AX - B) = 0$$

## D.4 Pseudo-Inverse

Then X can be solved

$$X = A^\dagger B$$

Where  $A^\dagger = (A^T A)^{-1} A^T$  is defined pseudo-inverse of matrix A. Even though A is not a square matrix but  $A^T A$  reduces to a square matrix.

## Appendix E

### Mean Velocities for a Stationary Endwall

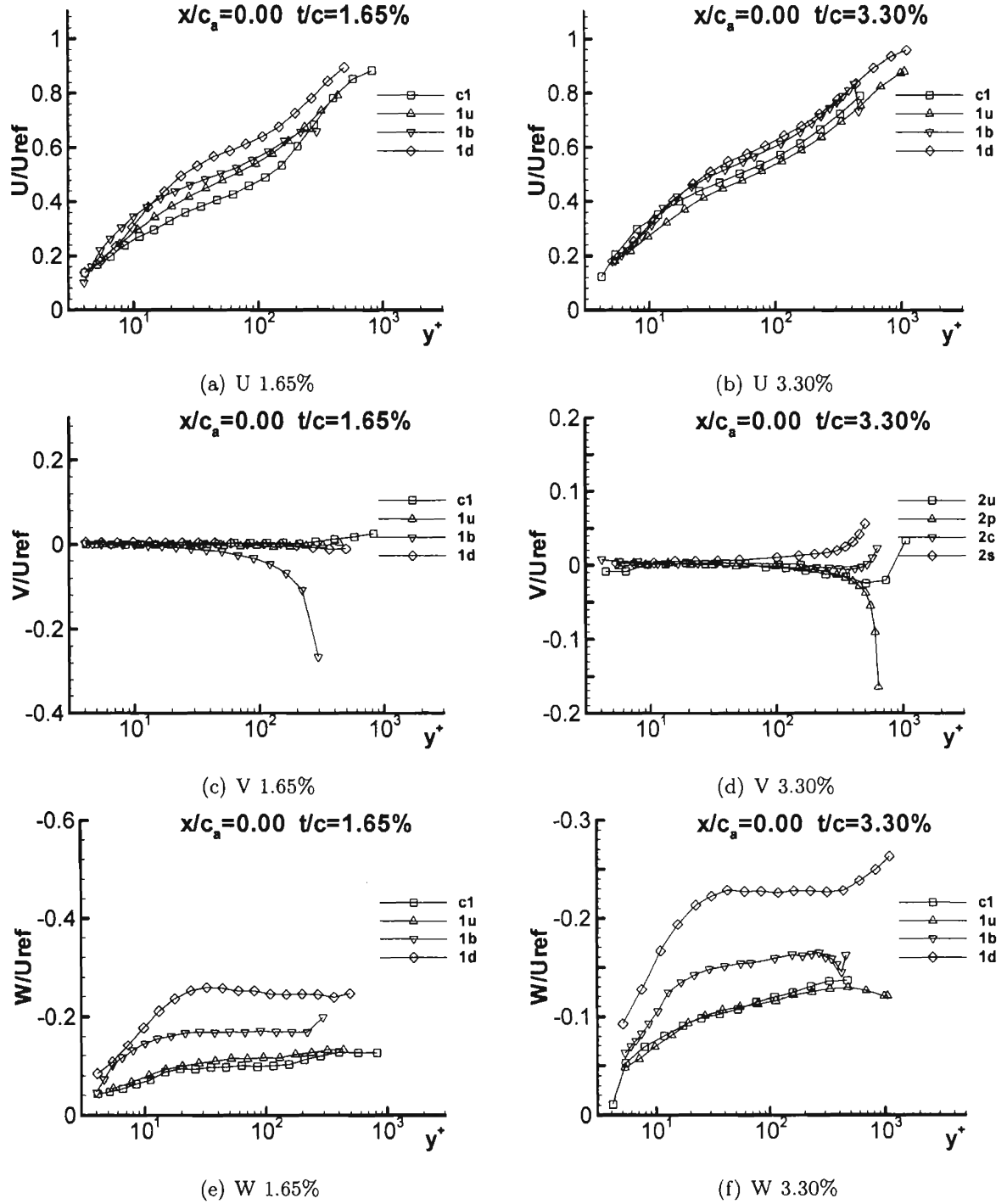


Figure E.1: Mean  $U/U_{ref}$ ,  $V/U_{ref}$ , and  $W/U_{ref}$  at  $x/c_a = 0.00$  for both 1.65% and 3.30% in chord coordinate system

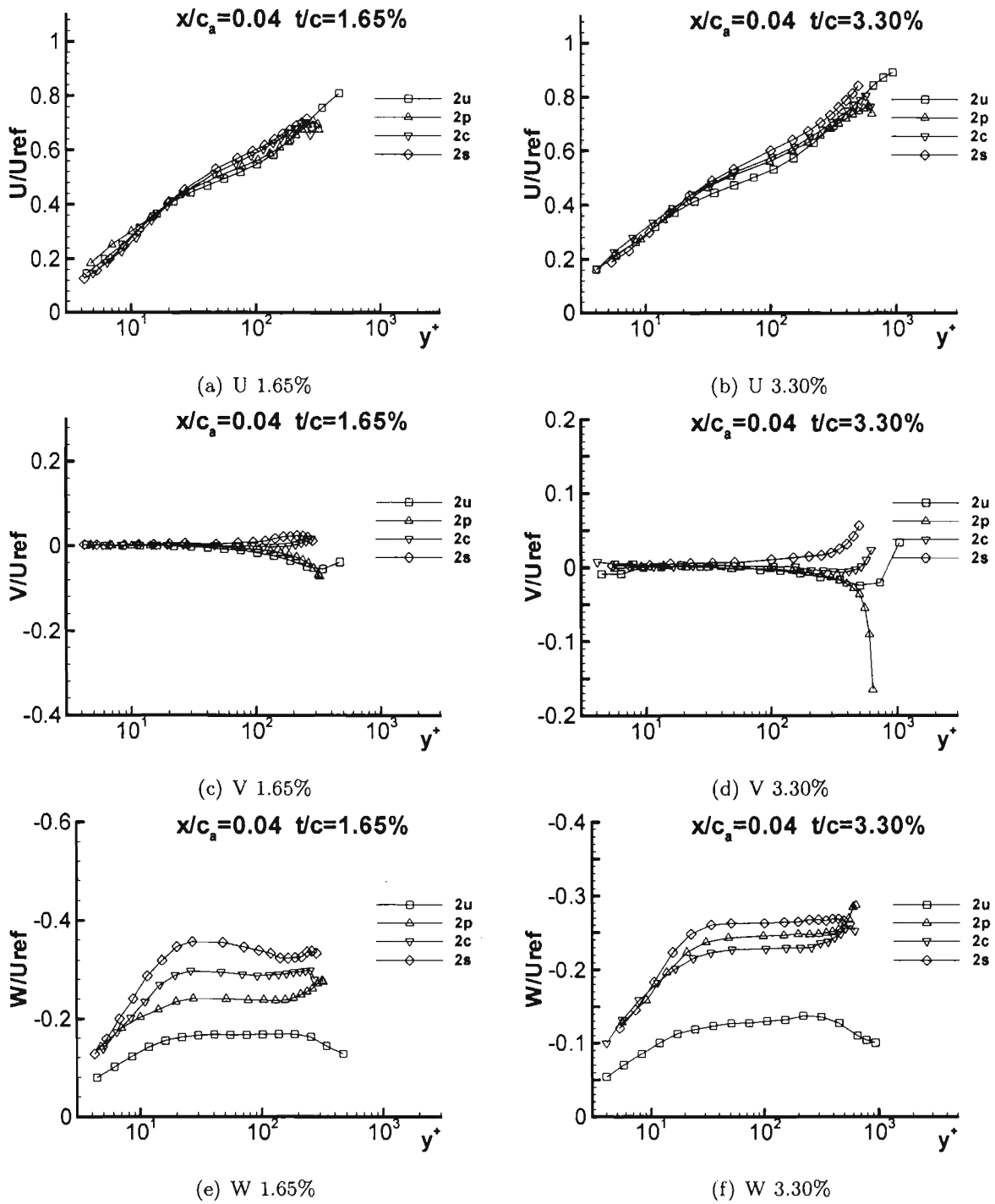


Figure E.2: Mean  $U/U_{ref}$ ,  $V/U_{ref}$ , and  $W/U_{ref}$  at  $x/c_a = 0.04$  for both 1.65% and 3.30% in chord coordinate system

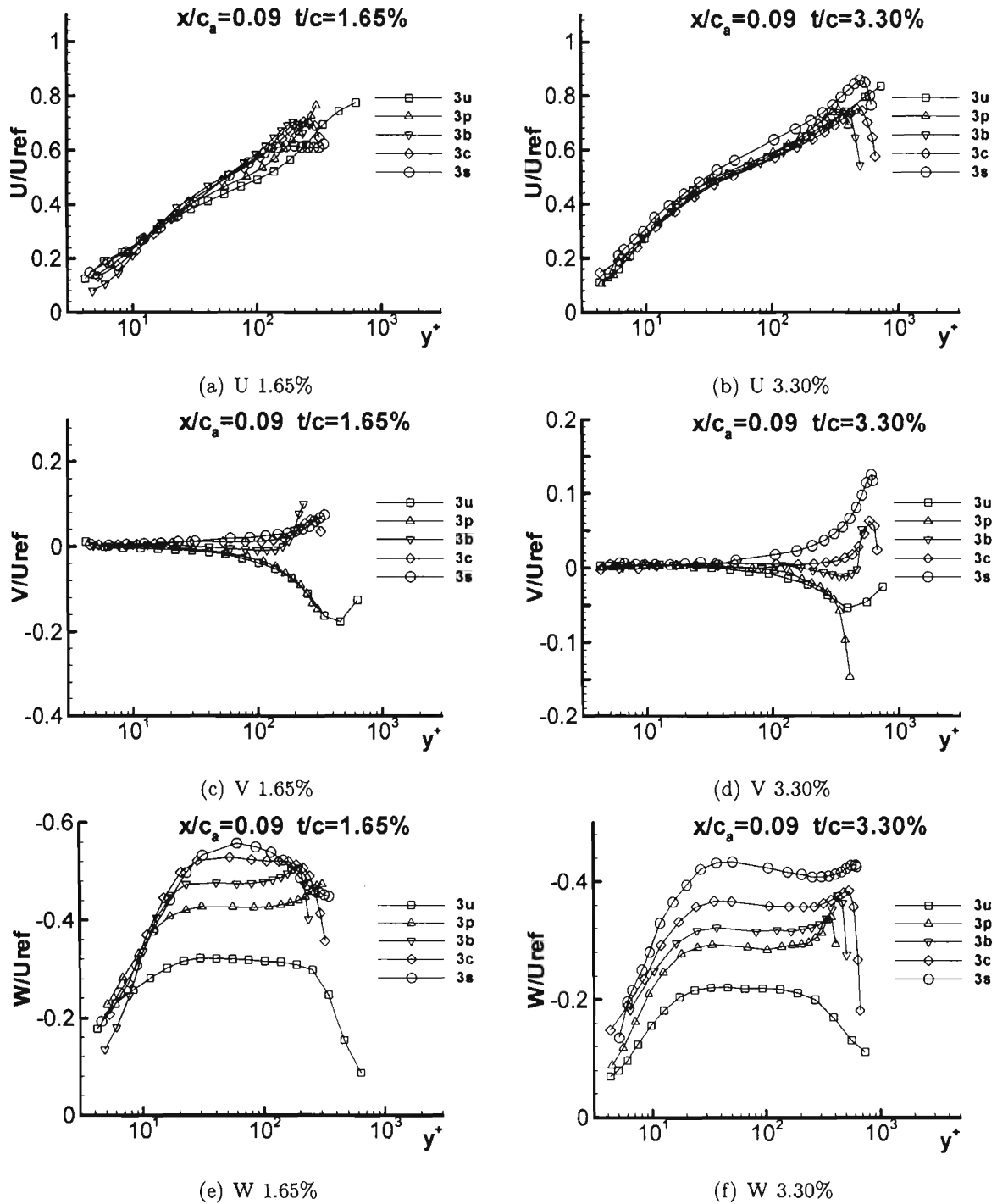


Figure E.3: Mean  $U/U_{ref}$ ,  $V/U_{ref}$ , and  $W/U_{ref}$  at  $x/c_a = 0.09$  for both 1.65% and 3.30% in chord coordinate system

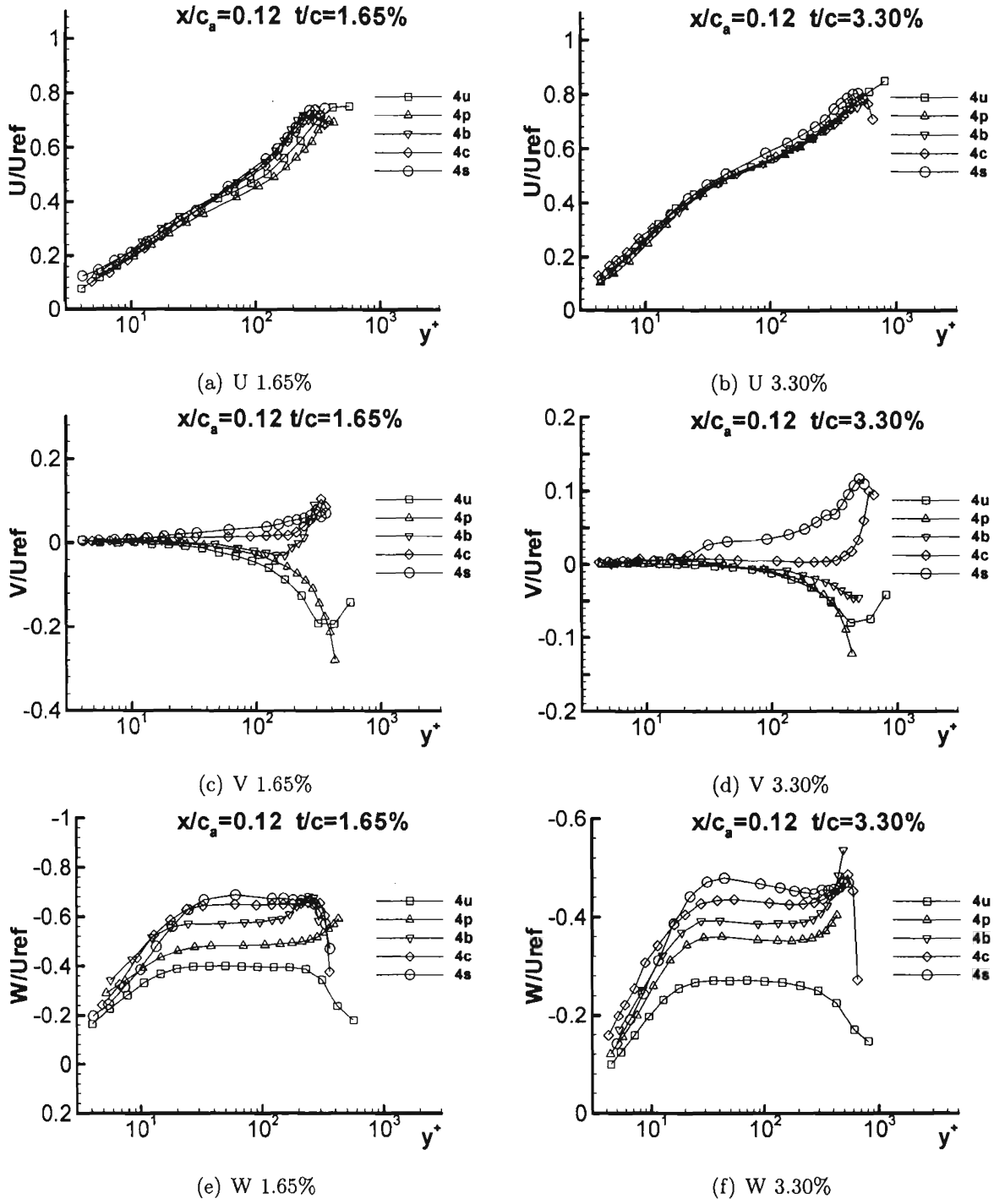


Figure E.4: Mean  $U/U_{ref}$ ,  $V/U_{ref}$ , and  $W/U_{ref}$  at  $x/c_a = 0.12$  for both 1.65% and 3.30% in chord coordinate system

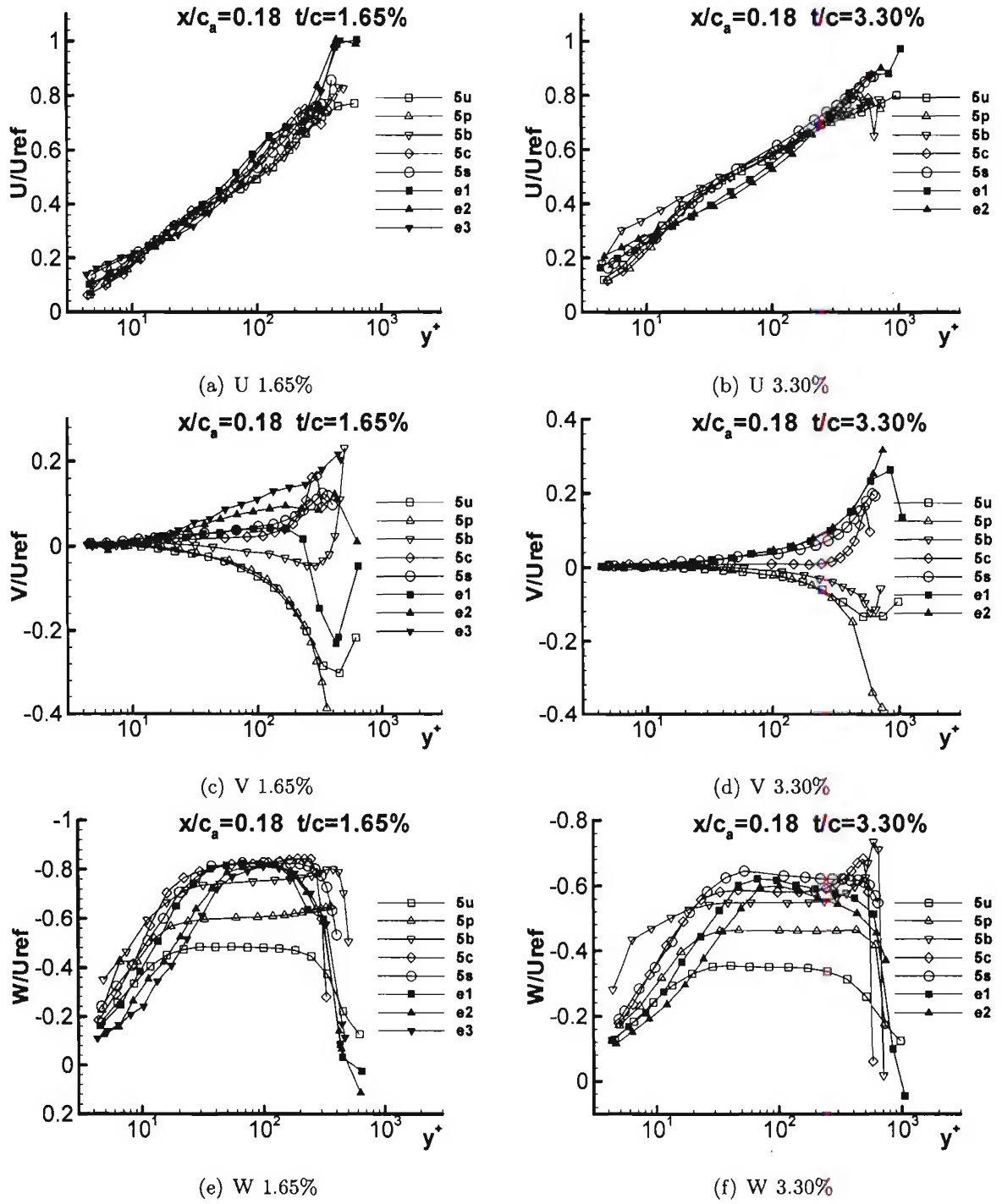


Figure E.5: Mean  $U/U_{ref}$ ,  $V/U_{ref}$ , and  $W/U_{ref}$  at  $x/c_a = 0.18$  for both 1.65% and 3.30% in chord coordinate system



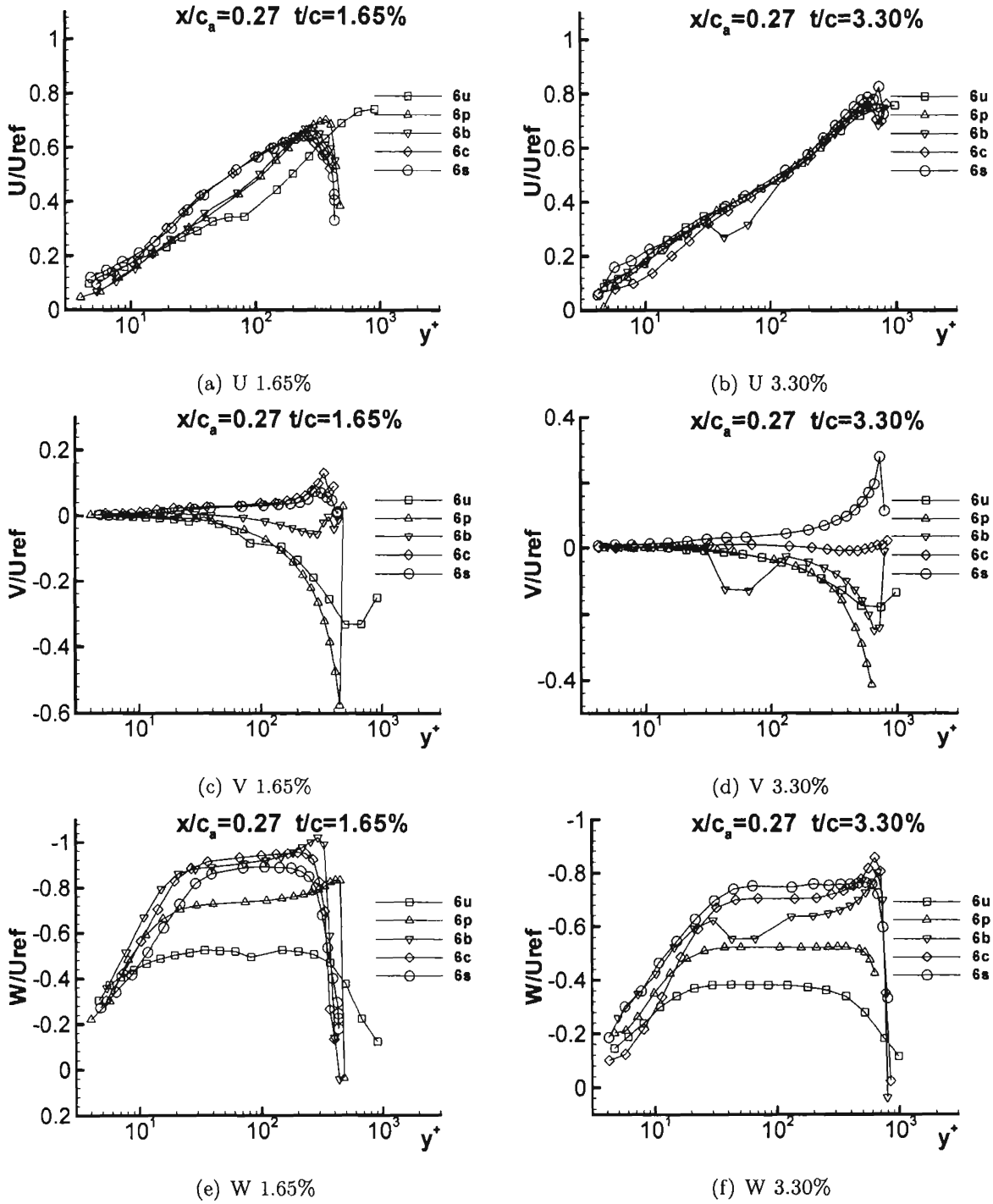


Figure E.6: Mean  $U/U_{ref}$ ,  $V/U_{ref}$ , and  $W/U_{ref}$  at  $x/c_a = 0.27$  for both 1.65% and 3.30% in chord coordinate system

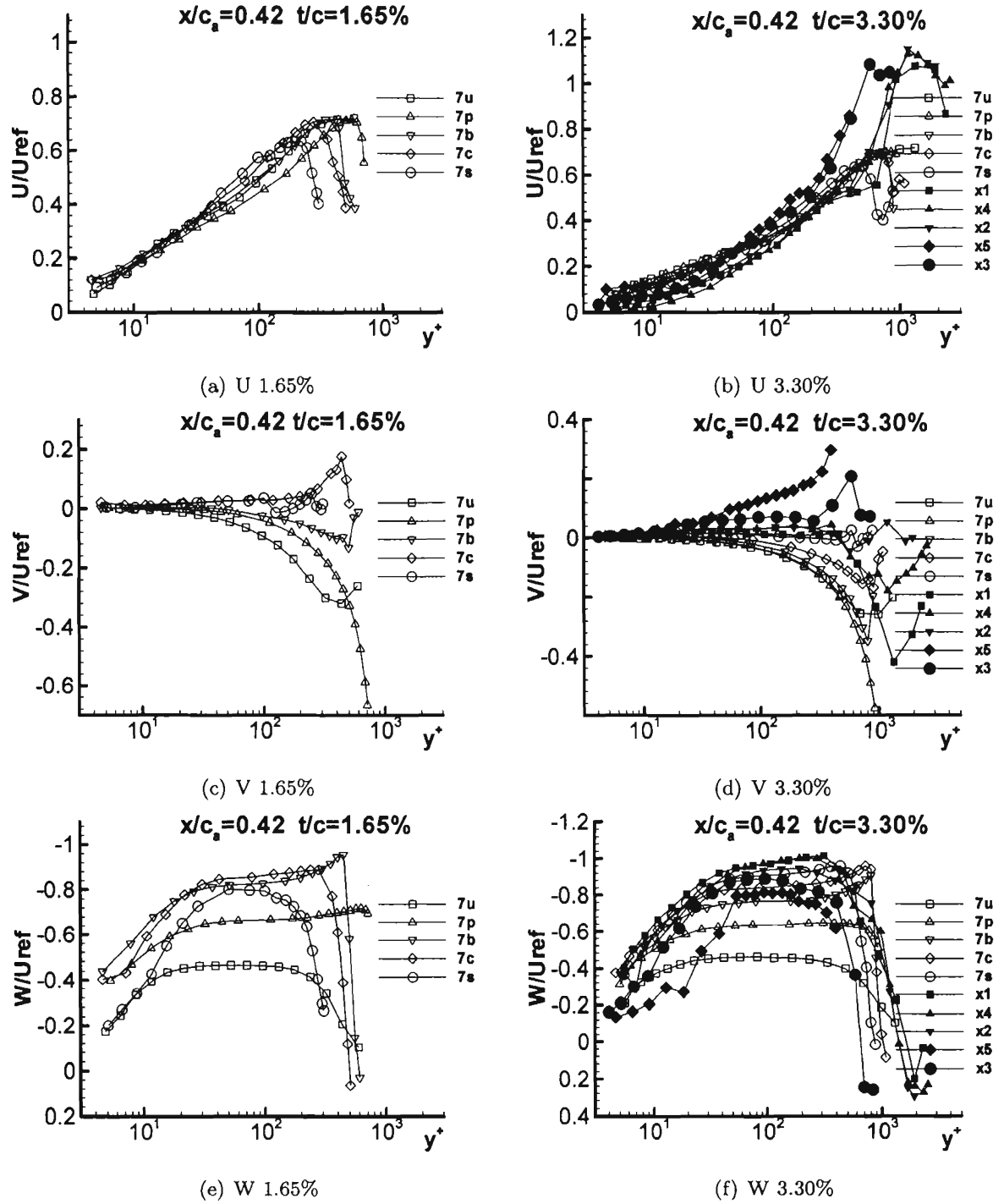


Figure E.7: Mean  $U/U_{ref}$ ,  $V/U_{ref}$ , and  $W/U_{ref}$  at  $x/c_a = 0.42$  for both 1.65% and 3.30% in chord coordinate system

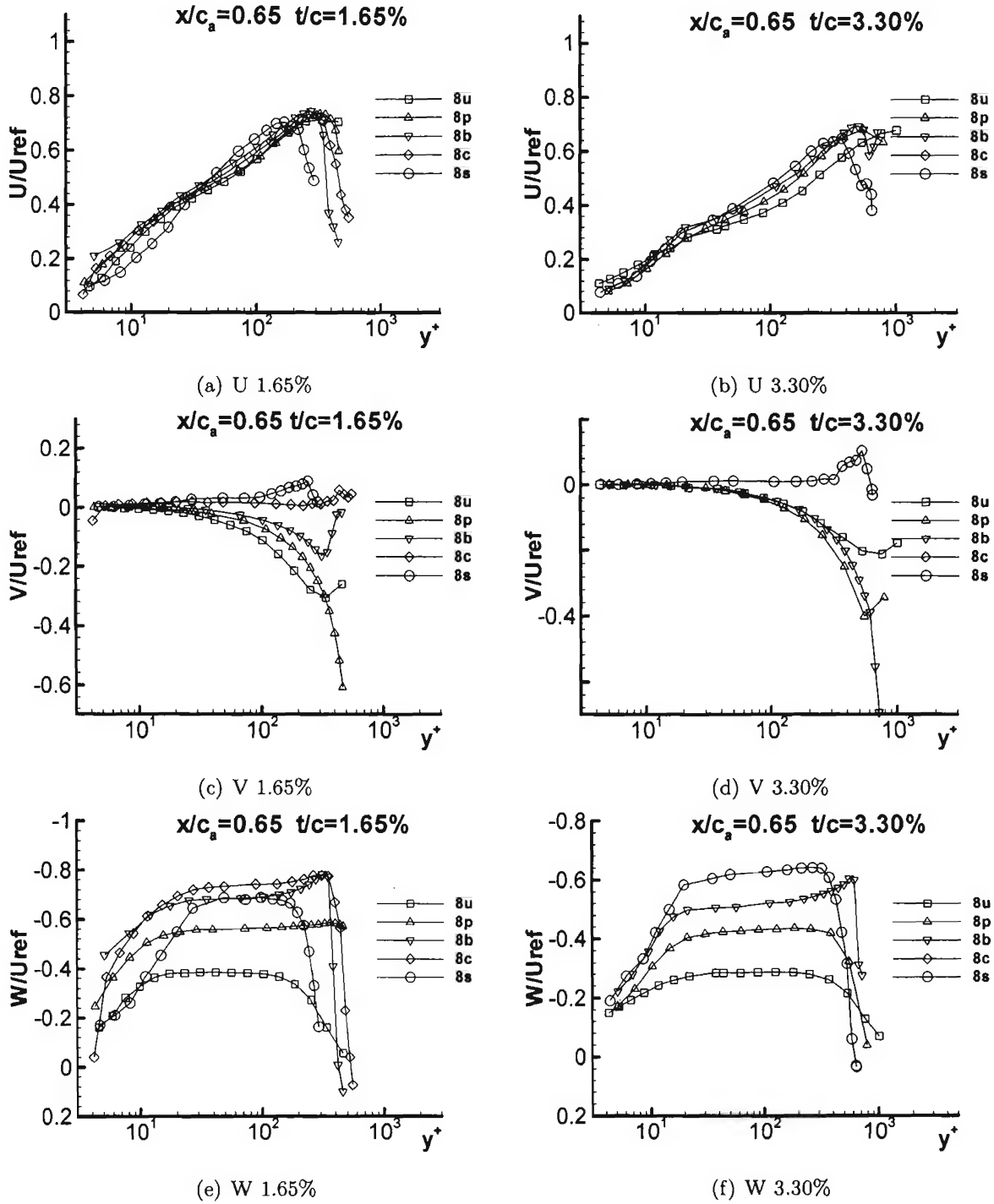


Figure E.8: Mean  $U/U_{ref}$ ,  $V/U_{ref}$ , and  $W/U_{ref}$  at  $x/c_a = 0.65$  for both 1.65% and 3.30% in chord coordinate system

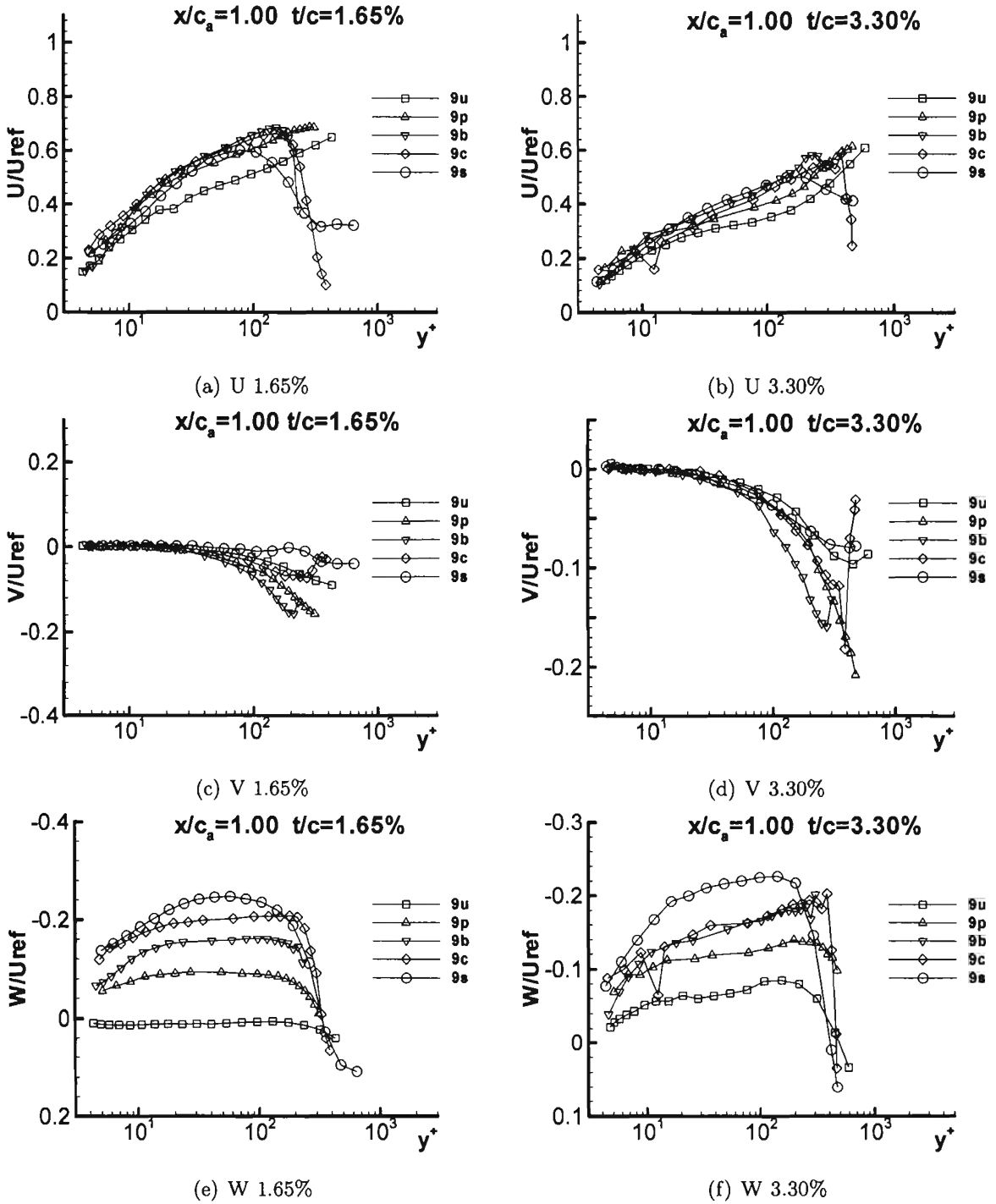


Figure E.9: Mean  $U/U_{ref}$ ,  $V/U_{ref}$ , and  $W/U_{ref}$  at  $x/c_a = 1.00$  for both 1.65% and 3.30% in chord coordinate system

## Appendix F

### Reynolds Stresses for a Stationary Endwall

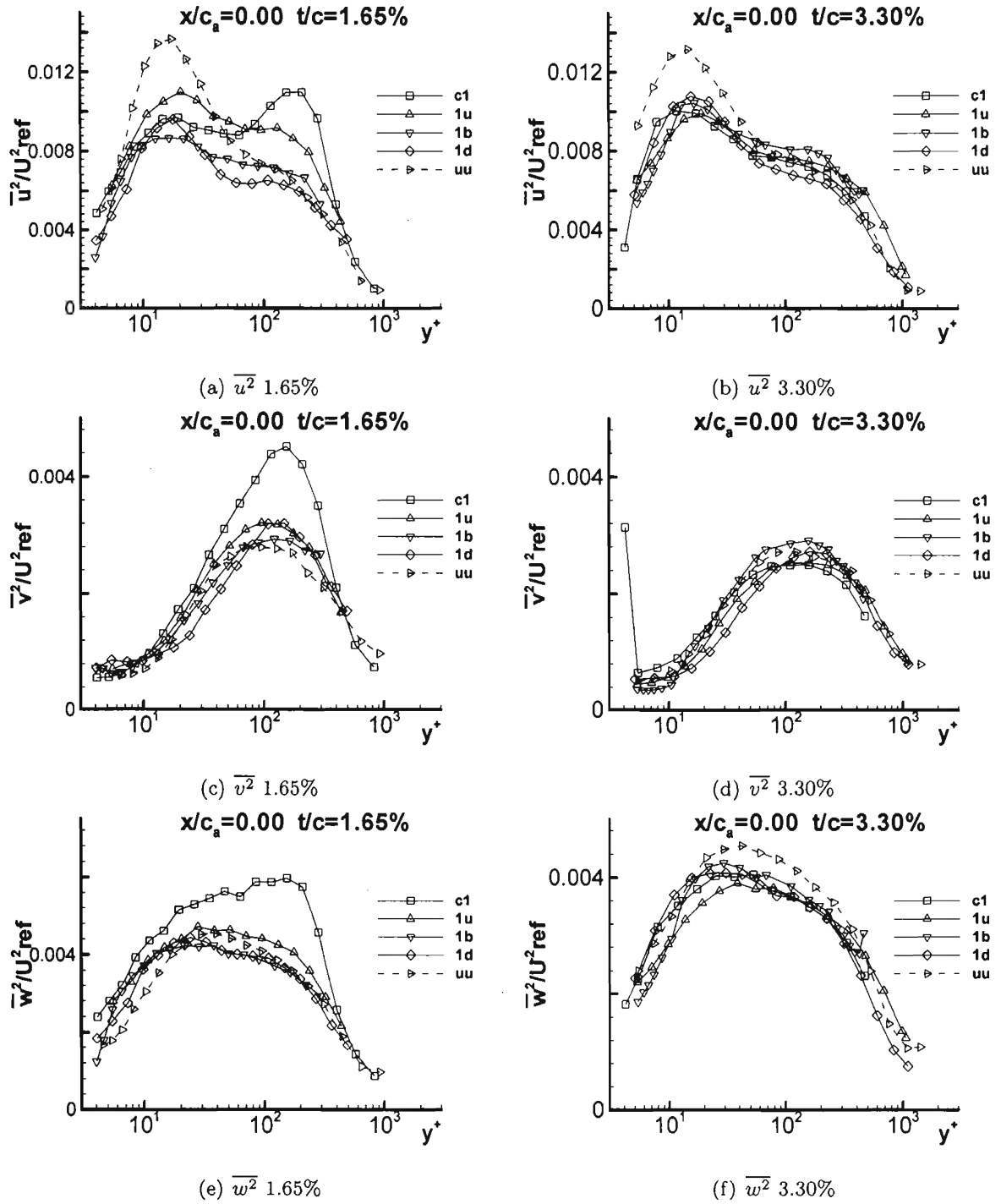


Figure F.1: Reynolds normal stresses  $\overline{u^2}/U_{ref}^2$ ,  $\overline{v^2}/U_{ref}^2$ , and  $\overline{w^2}/U_{ref}^2$  at  $x/c_a = 0.00$  for both 1.65% and 3.30% in chord coordinate system

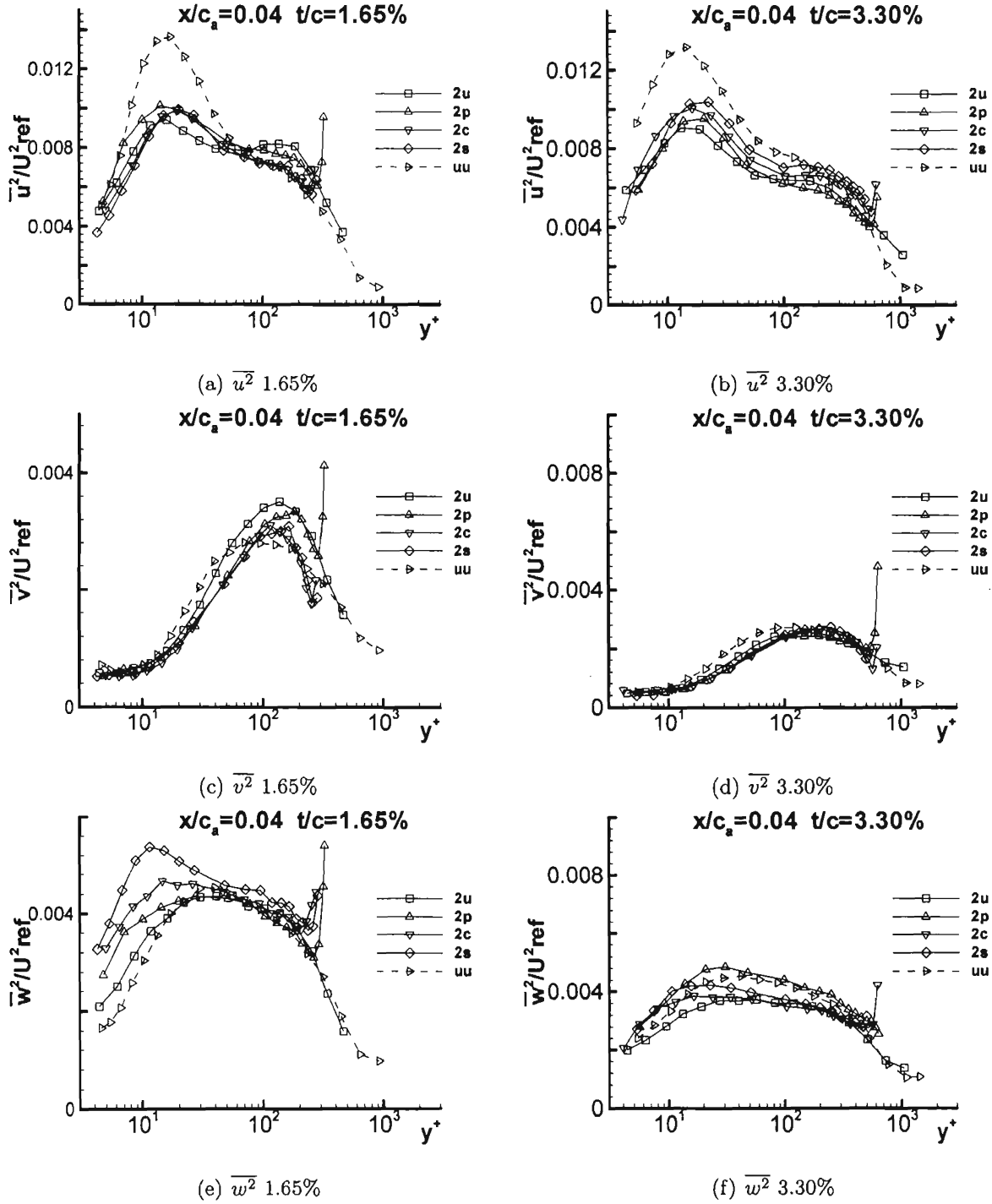


Figure F.2: Reynolds normal stresses  $\overline{u^2}/U_{ref}^2$ ,  $\overline{v^2}/U_{ref}^2$ , and  $\overline{w^2}/U_{ref}^2$  at  $x/c_a = 0.04$  for both 1.65% and 3.30% in chord coordinate system

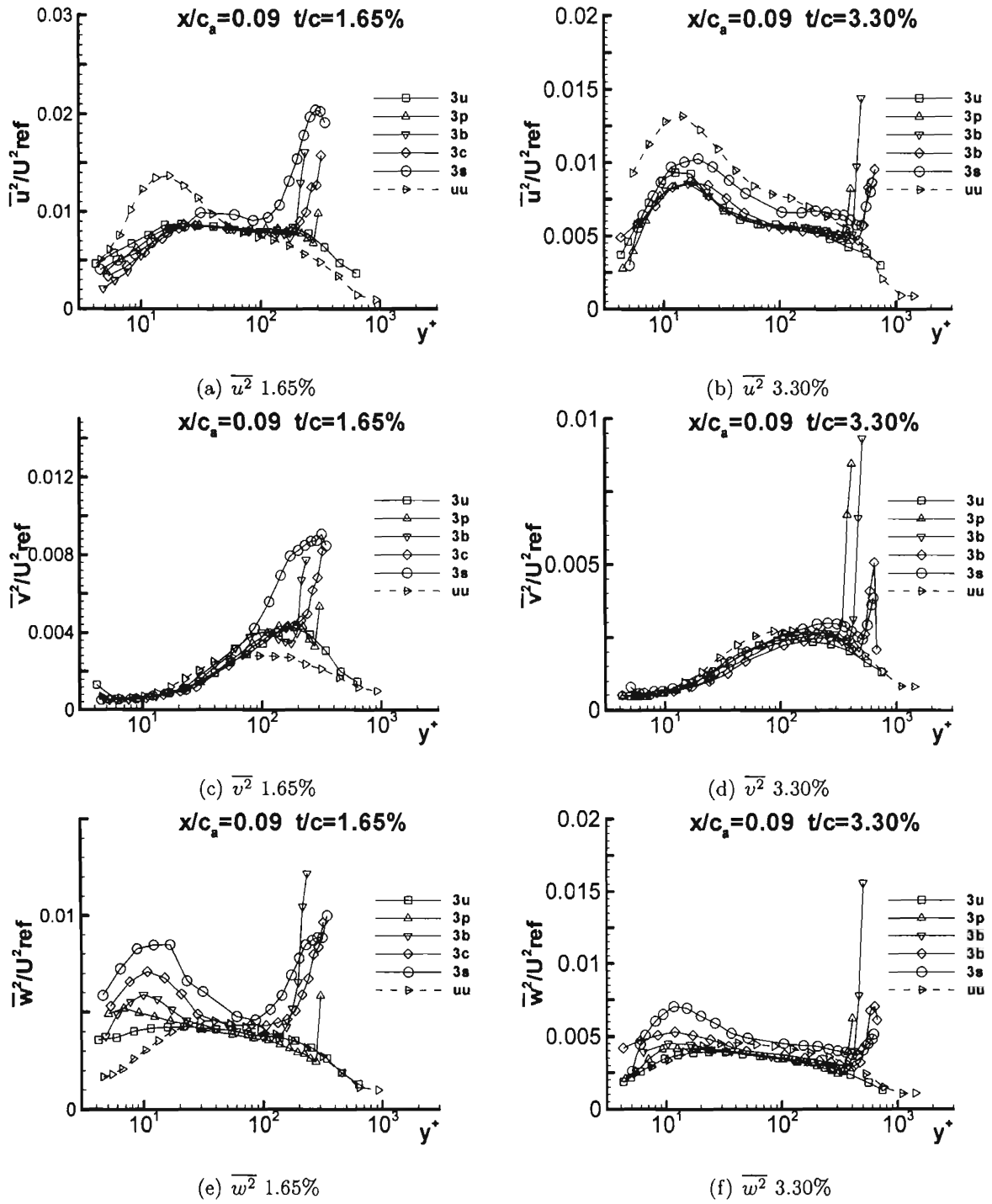


Figure F.3: Reynolds normal stresses  $\overline{u^2}/U^2_{ref}$ ,  $\overline{v^2}/U^2_{ref}$ , and  $\overline{w^2}/U^2_{ref}$  at  $x/c_a = 0.09$  for both 1.65% and 3.30% in chord coordinate system



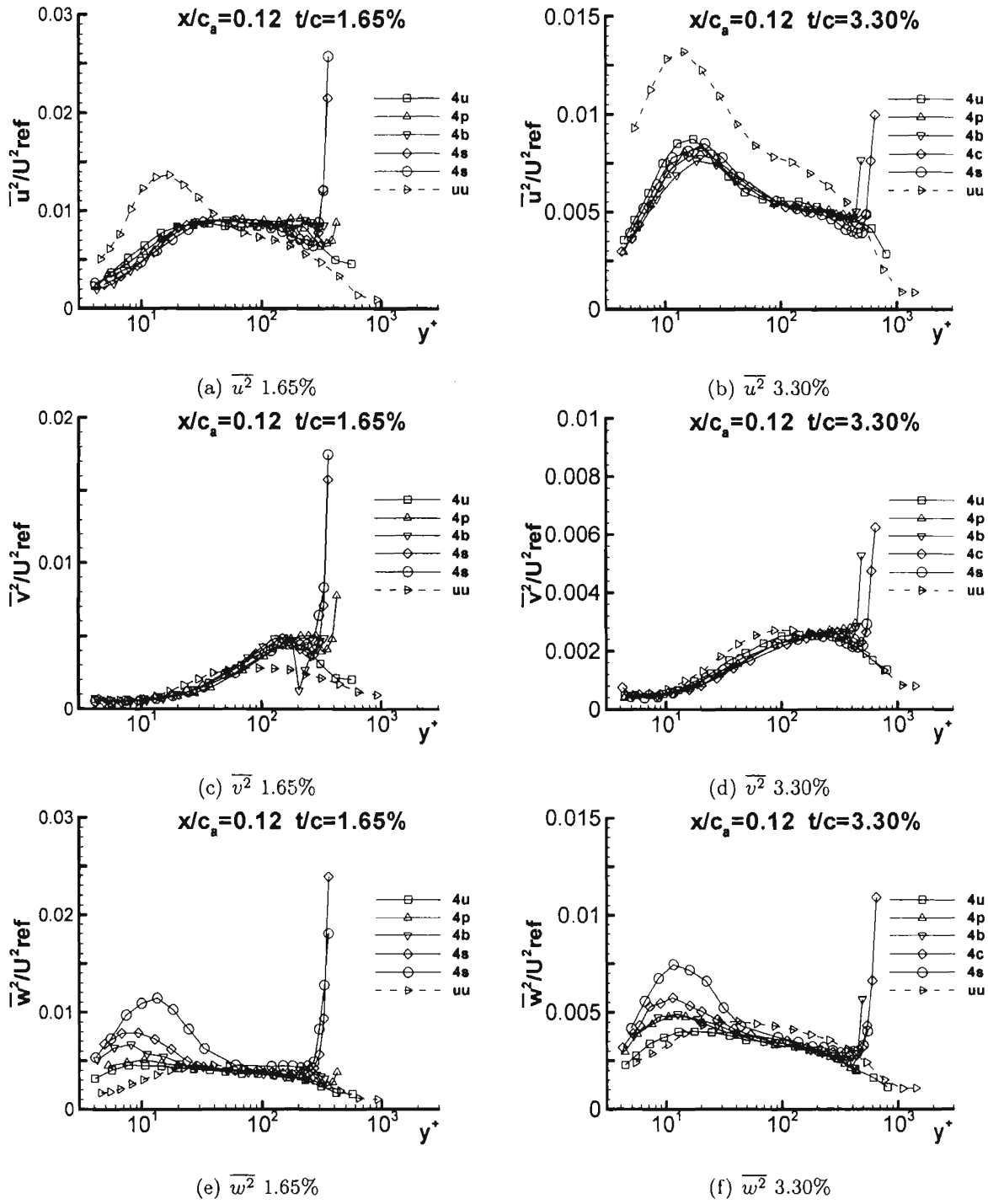


Figure F.4: Reynolds normal stresses  $\overline{u^2}/U_{ref}^2$ ,  $\overline{v^2}/U_{ref}^2$ , and  $\overline{w^2}/U_{ref}^2$  at  $x/c_a = 0.12$  for both 1.65% and 3.30% in chord coordinate system

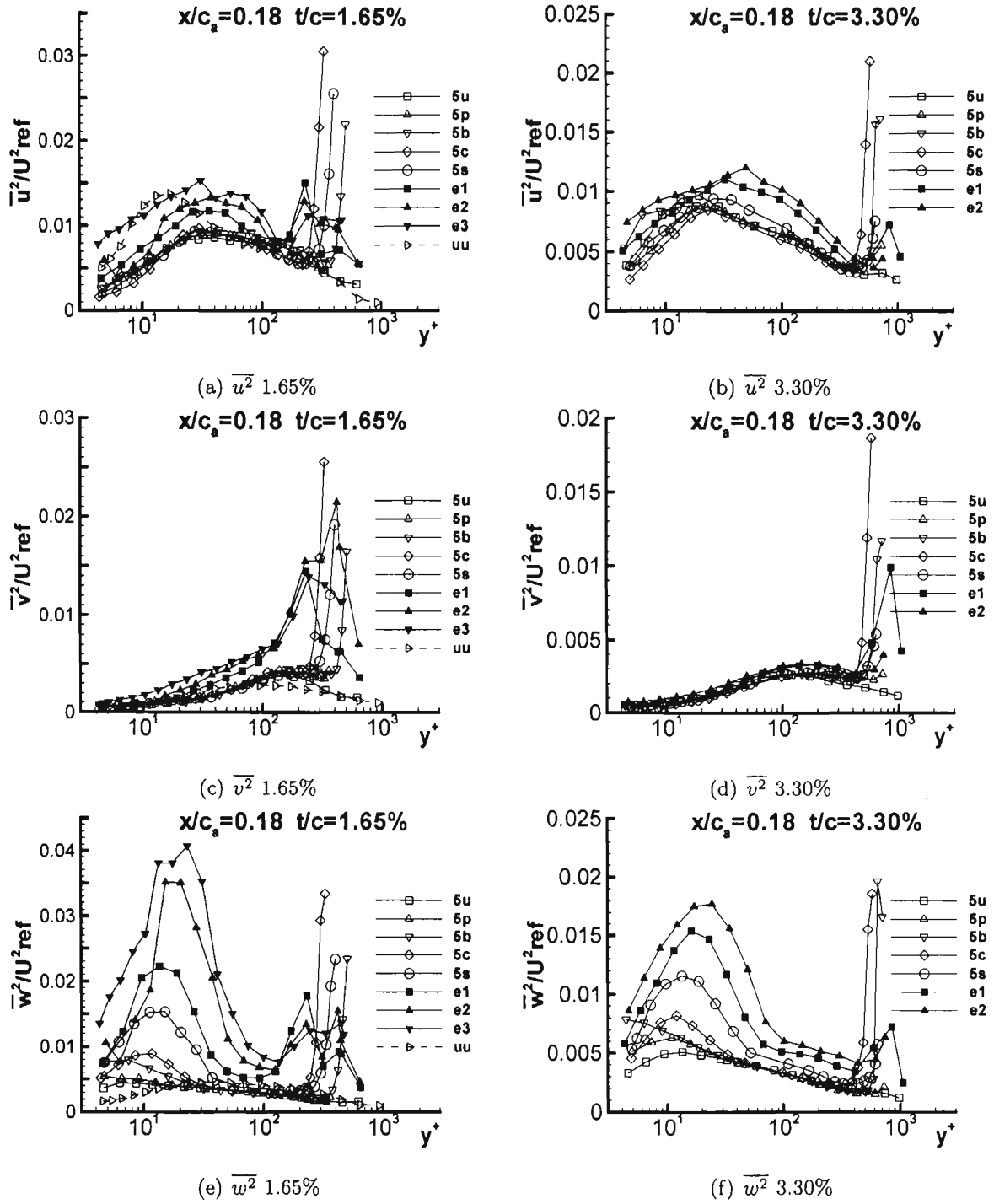


Figure F.5: Reynolds normal stresses  $\overline{u^2}/U_{ref}^2$ ,  $\overline{v^2}/U_{ref}^2$ , and  $\overline{w^2}/U_{ref}^2$  at  $x/c_a = 0.18$  for both 1.65% and 3.30% in chord coordinate system

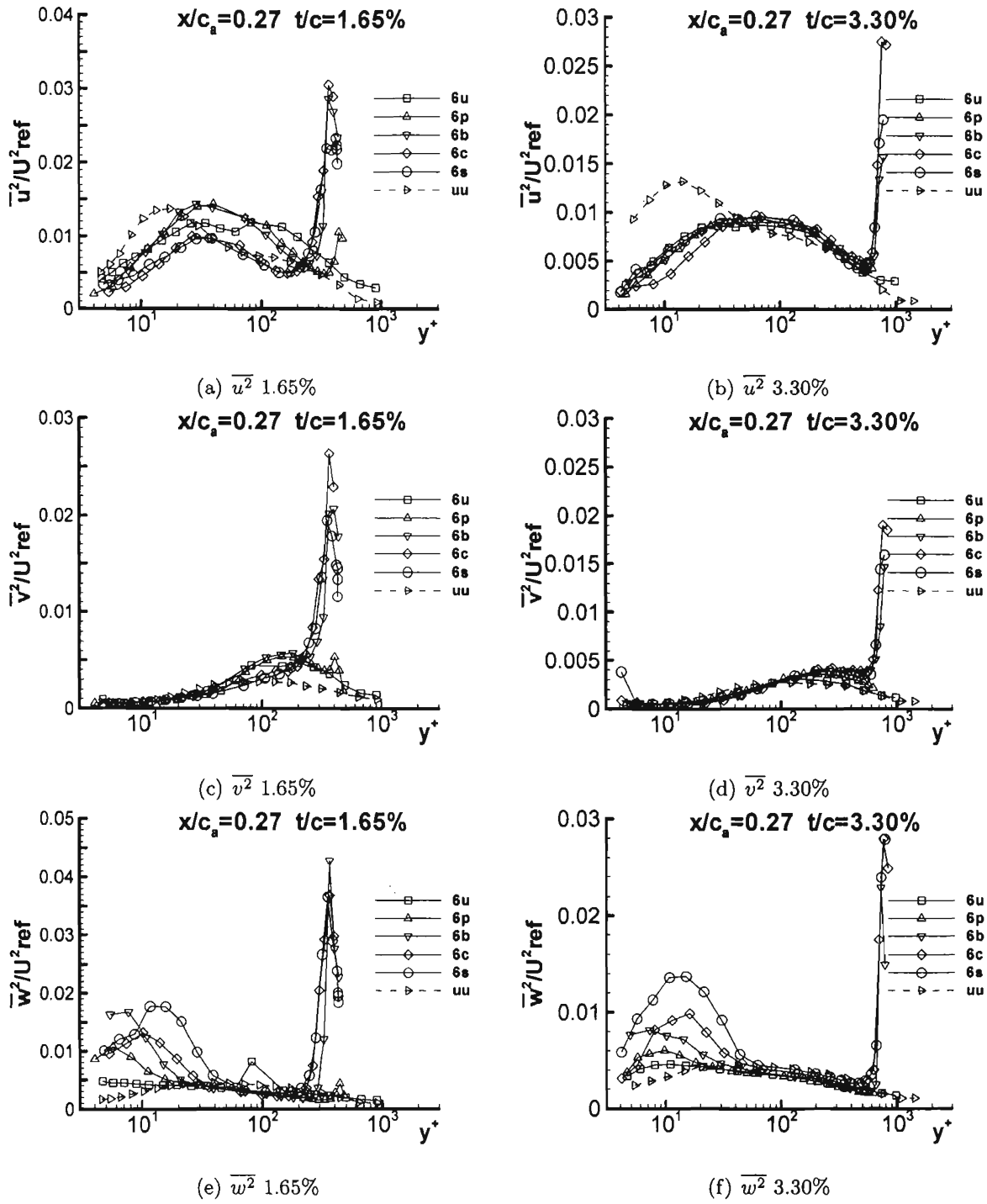


Figure F.6: Reynolds normal stresses  $\overline{u^2}/U_{ref}^2$ ,  $\overline{v^2}/U_{ref}^2$ , and  $\overline{w^2}/U_{ref}^2$  at  $x/c_a = 0.27$  for both 1.65% and 3.30% in chord coordinate system

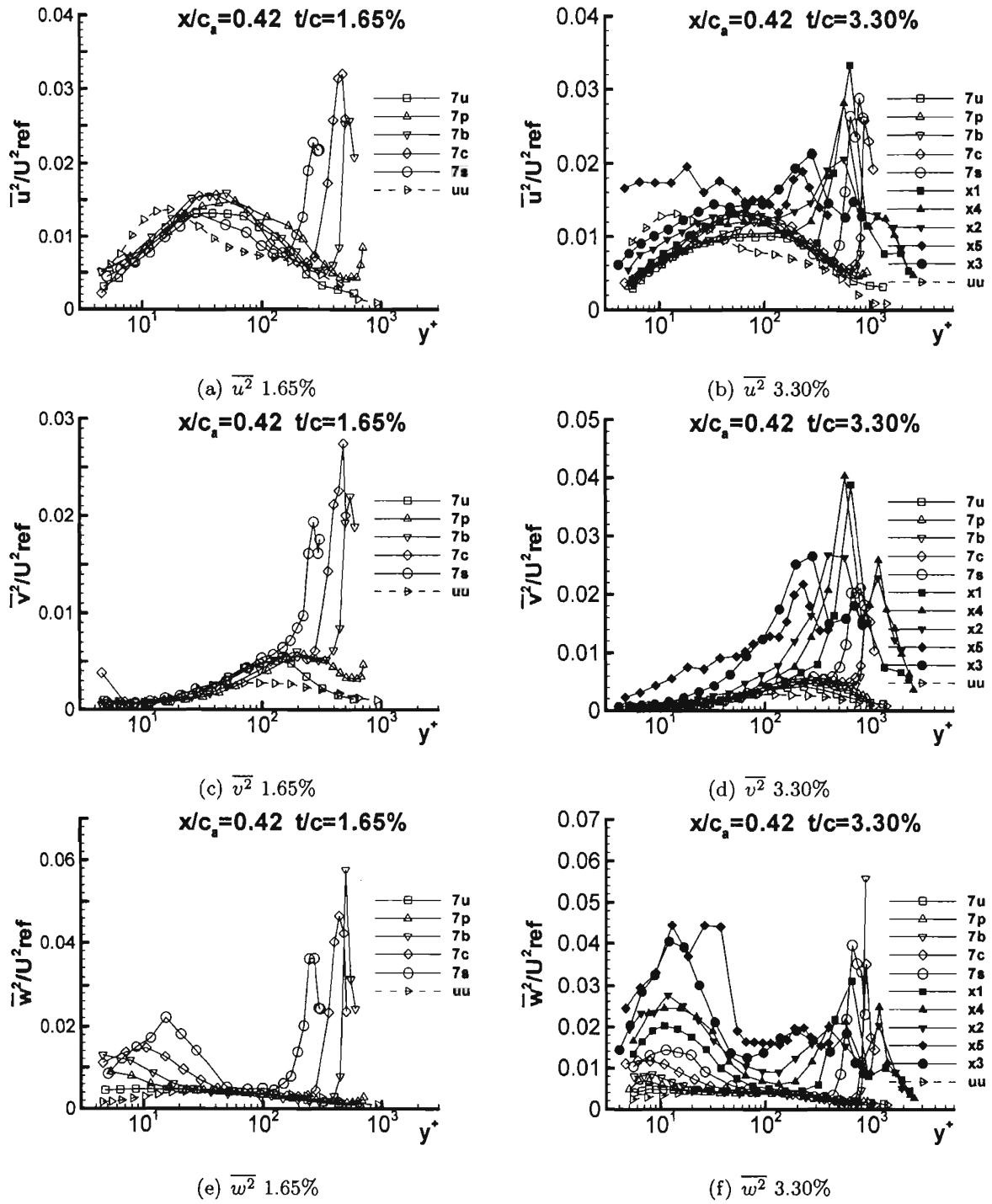


Figure F.7: Reynolds normal stresses  $\overline{u^2}/U_{ref}^2$ ,  $\overline{v^2}/U_{ref}^2$ , and  $\overline{w^2}/U_{ref}^2$  at  $x/c_a = 0.42$  for both 1.65% and 3.30% in chord coordinate system

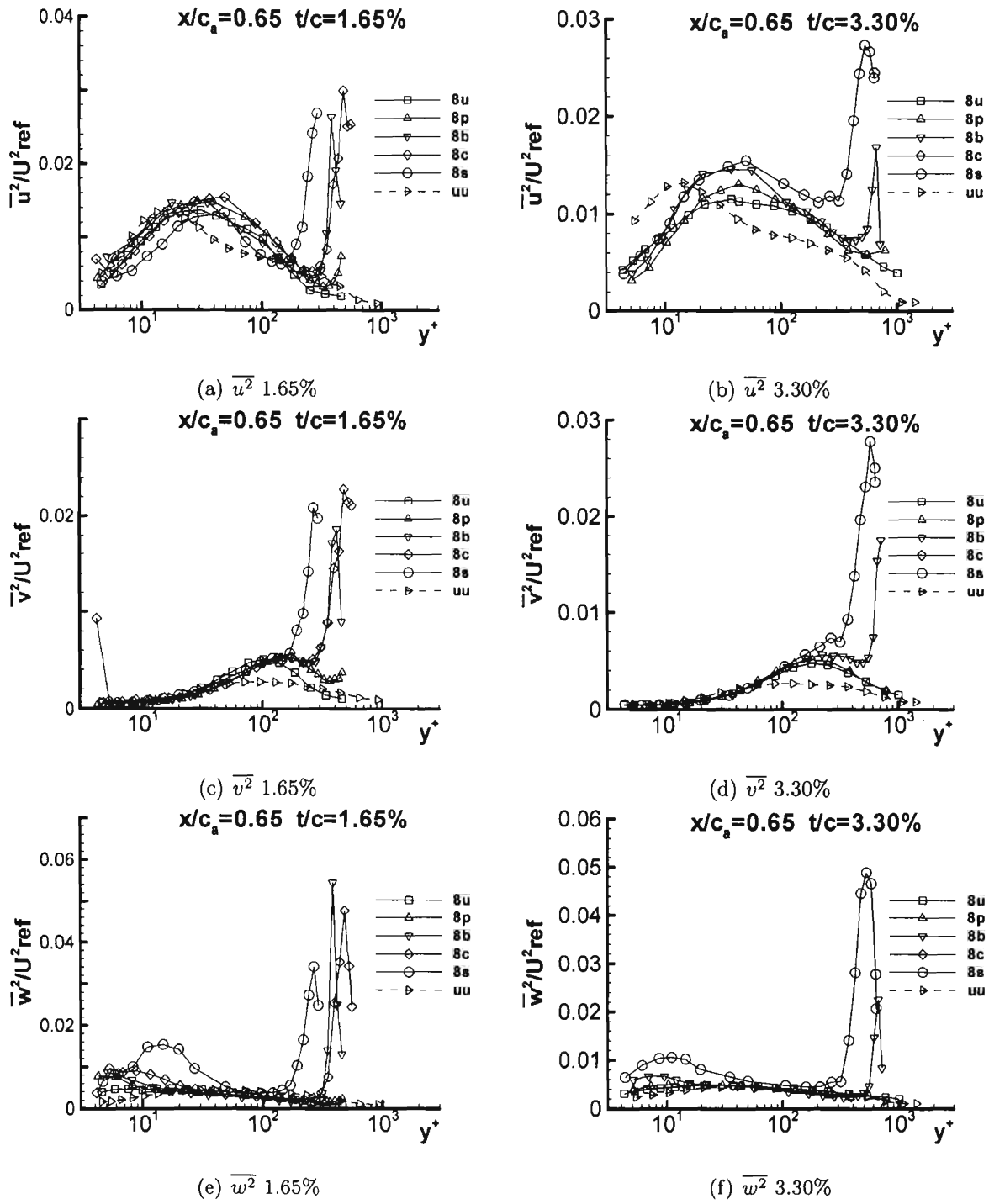


Figure F.8: Reynolds normal stresses  $\overline{u^2}/U_{ref}^2$ ,  $\overline{v^2}/U_{ref}^2$ , and  $\overline{w^2}/U_{ref}^2$  at  $x/c_a = 0.65$  for both 1.65% and 3.30% in chord coordinate system

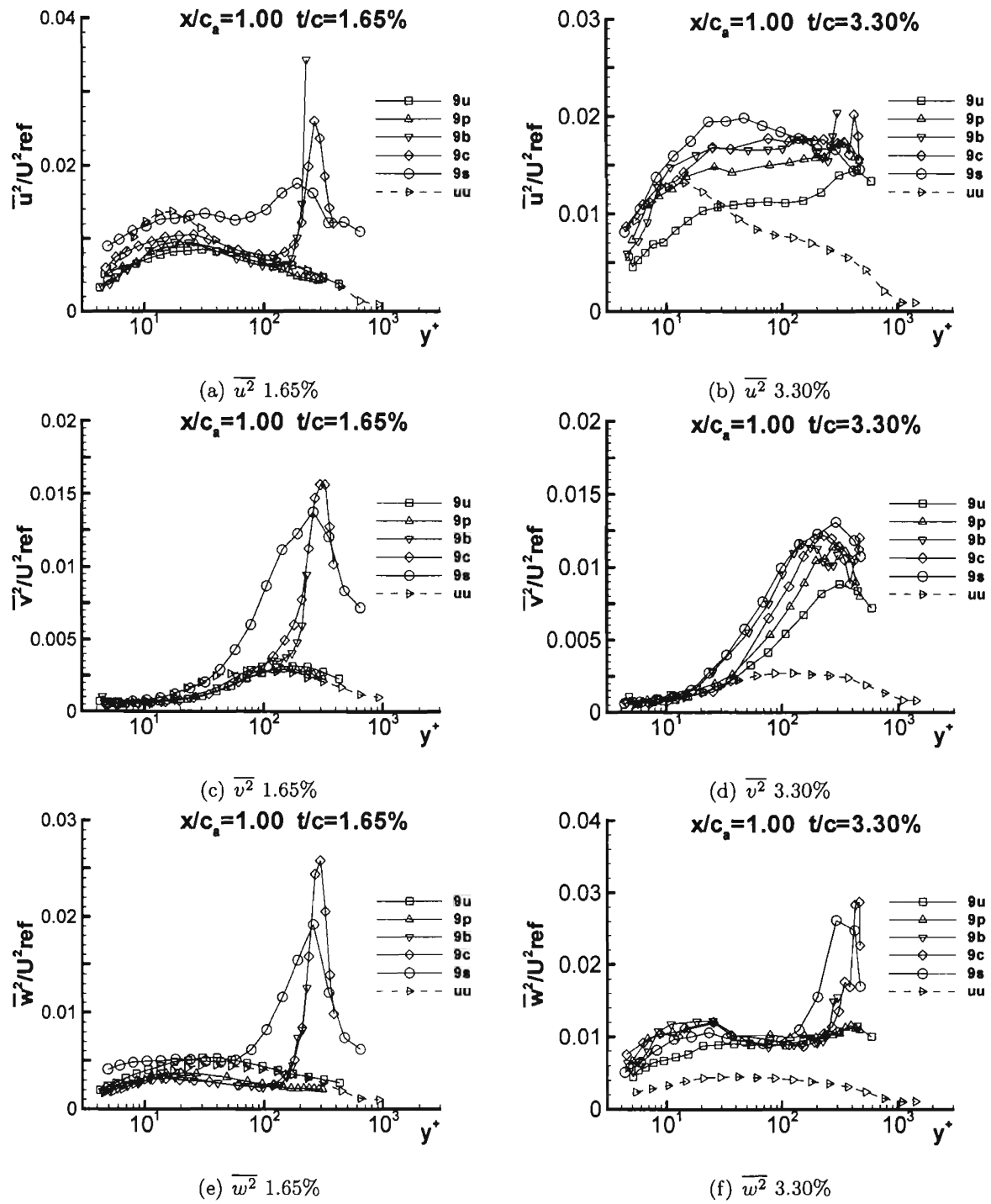


Figure F.9: Reynolds normal stresses  $\overline{u^2}/U^2_{ref}$ ,  $\overline{v^2}/U^2_{ref}$ , and  $\overline{w^2}/U^2_{ref}$  at  $x/c_a = 1.00$  for both 1.65% and 3.30% in chord coordinate system

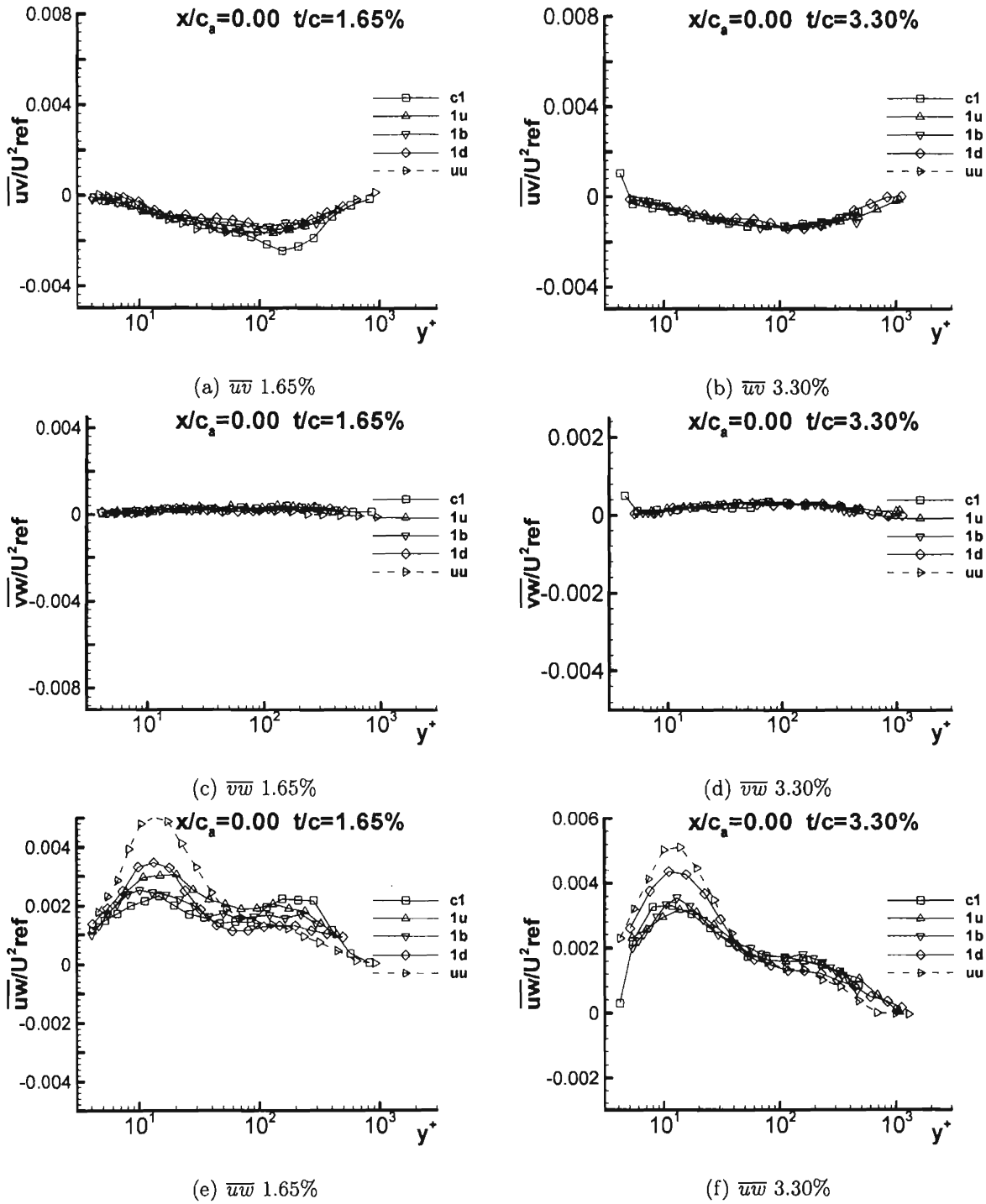


Figure F.10: Reynolds shear stresses  $-\overline{uv}/U_{ref}^2$ ,  $-\overline{vw}/U_{ref}^2$ , and  $-\overline{uw}/U_{ref}^2$  at  $x/c_a = 0.00$  for both 1.65% and 3.30% in chord coordinate system

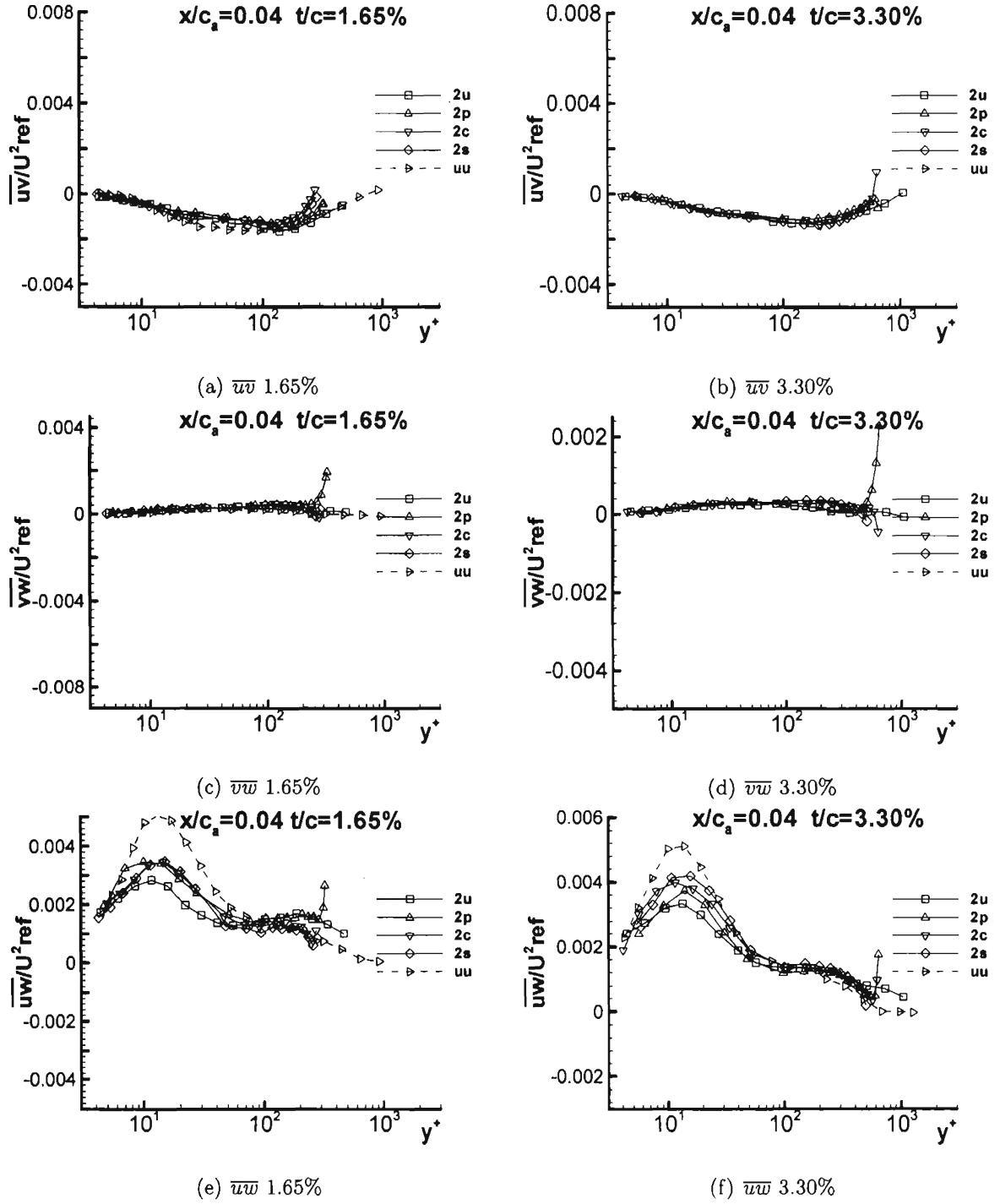


Figure F.11: Reynolds shear stresses  $-\overline{uv}/U_{ref}^2$ ,  $-\overline{vw}/U_{ref}^2$ , and  $-\overline{uw}/U_{ref}^2$  at  $x/c_a = 0.04$  for both 1.65% and 3.30% in chord coordinate system



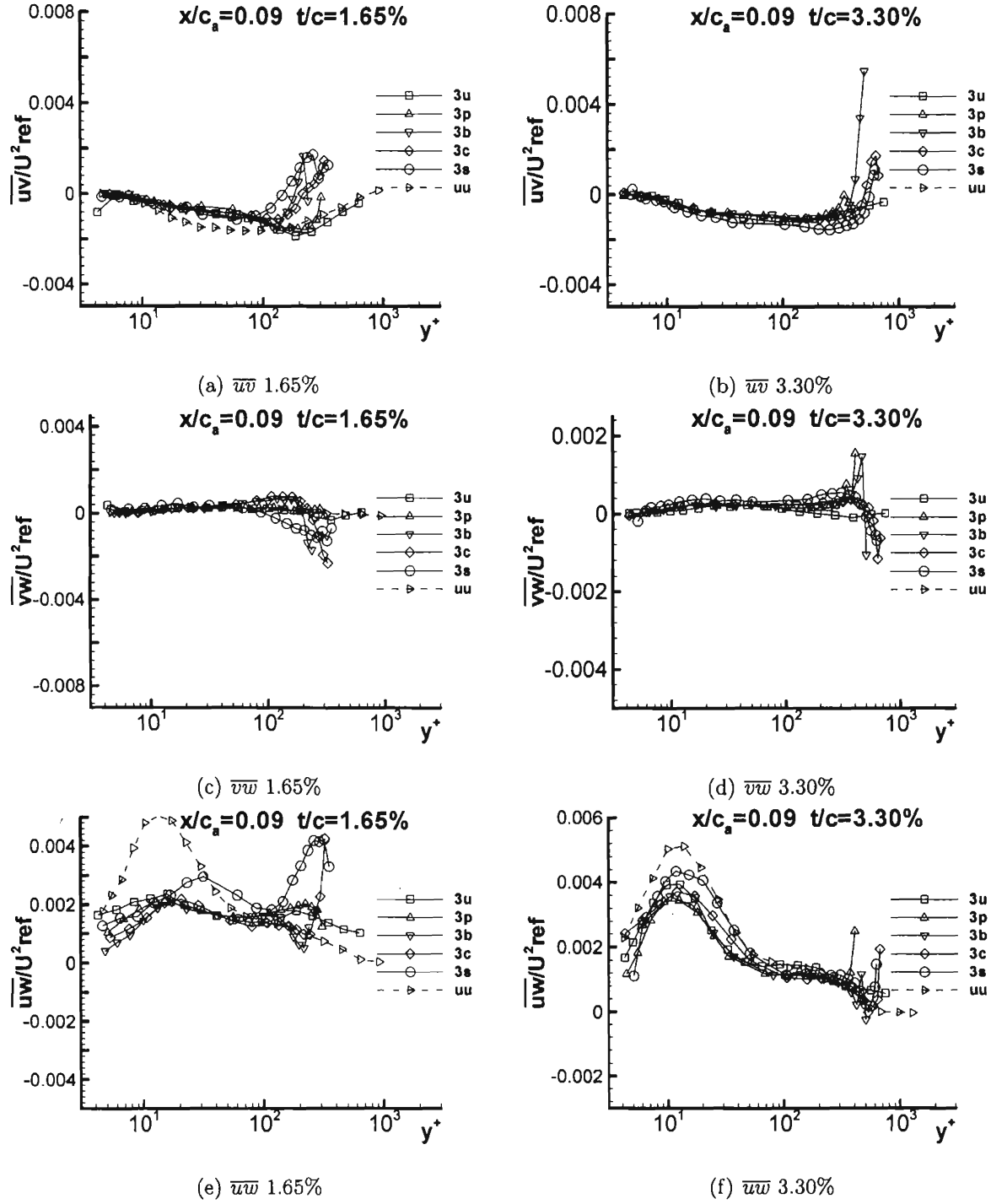


Figure F.12: Reynolds shear stresses  $-\overline{uv}/U_{ref}^2$ ,  $-\overline{vw}/U_{ref}^2$ , and  $-\overline{uw}/U_{ref}^2$  at  $x/c_a = 0.09$  for both 1.65% and 3.30% in chord coordinate system

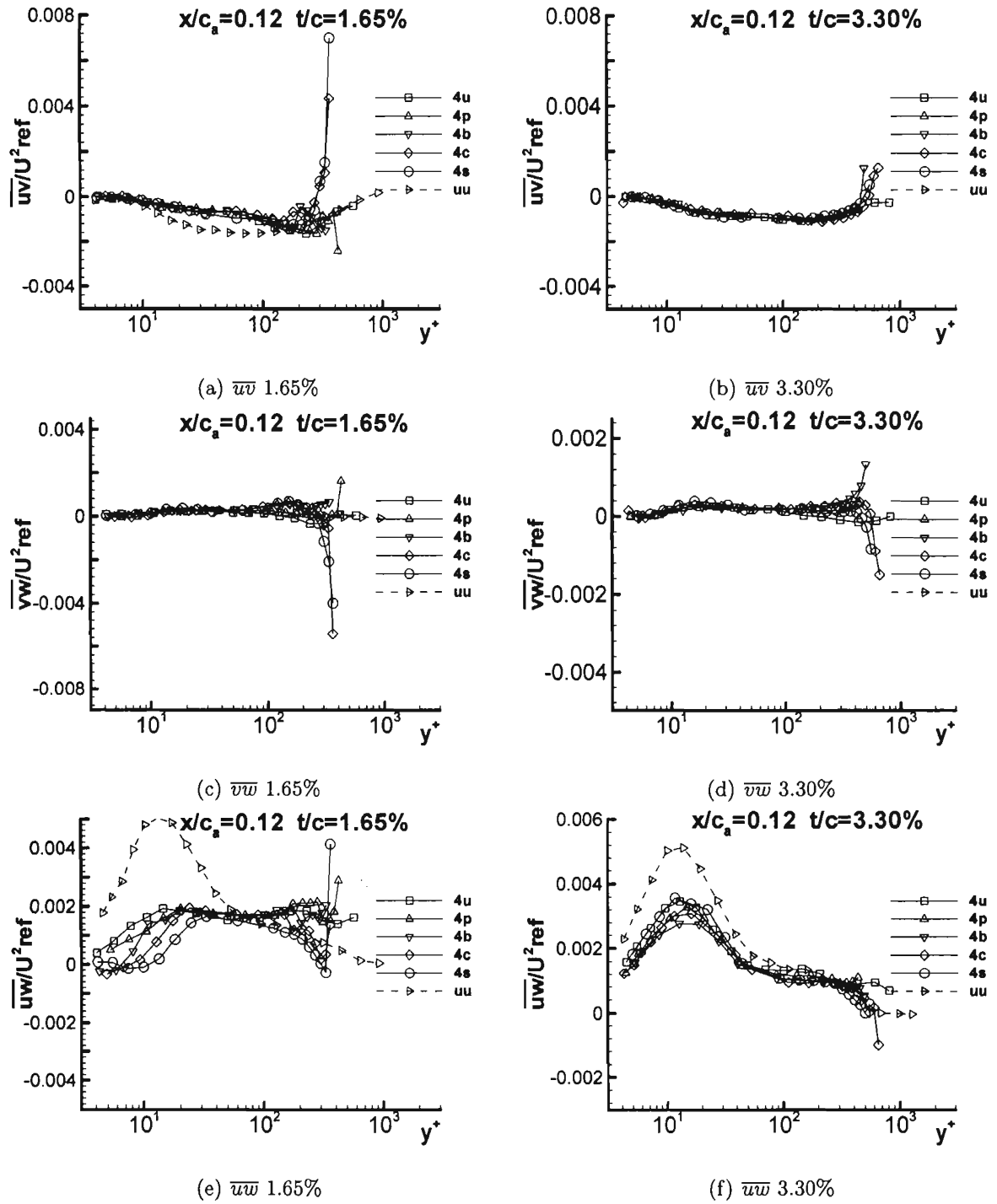


Figure F.13: Reynolds shear stresses  $-\overline{uv}/U_{ref}^2$ ,  $-\overline{vw}/U_{ref}^2$ , and  $-\overline{uw}/U_{ref}^2$  at  $x/c_a = 0.12$  for both 1.65% and 3.30% in chord coordinate system

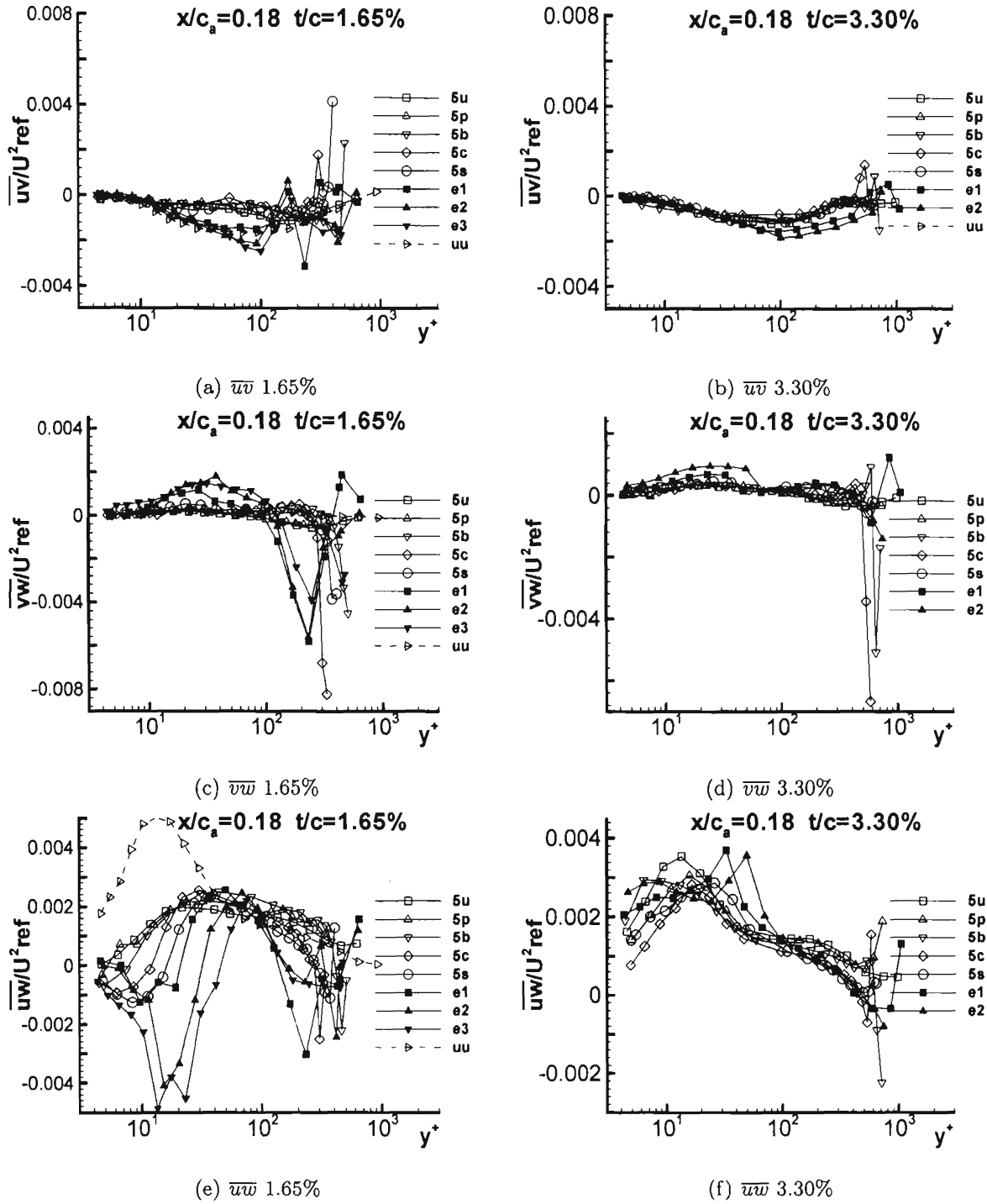


Figure F.14: Reynolds shear stresses  $-\overline{uv}/U_{ref}^2$ ,  $-\overline{vw}/U_{ref}^2$ , and  $-\overline{uw}/U_{ref}^2$  at  $x/c_a = 0.18$  for both 1.65% and 3.30% in chord coordinate system

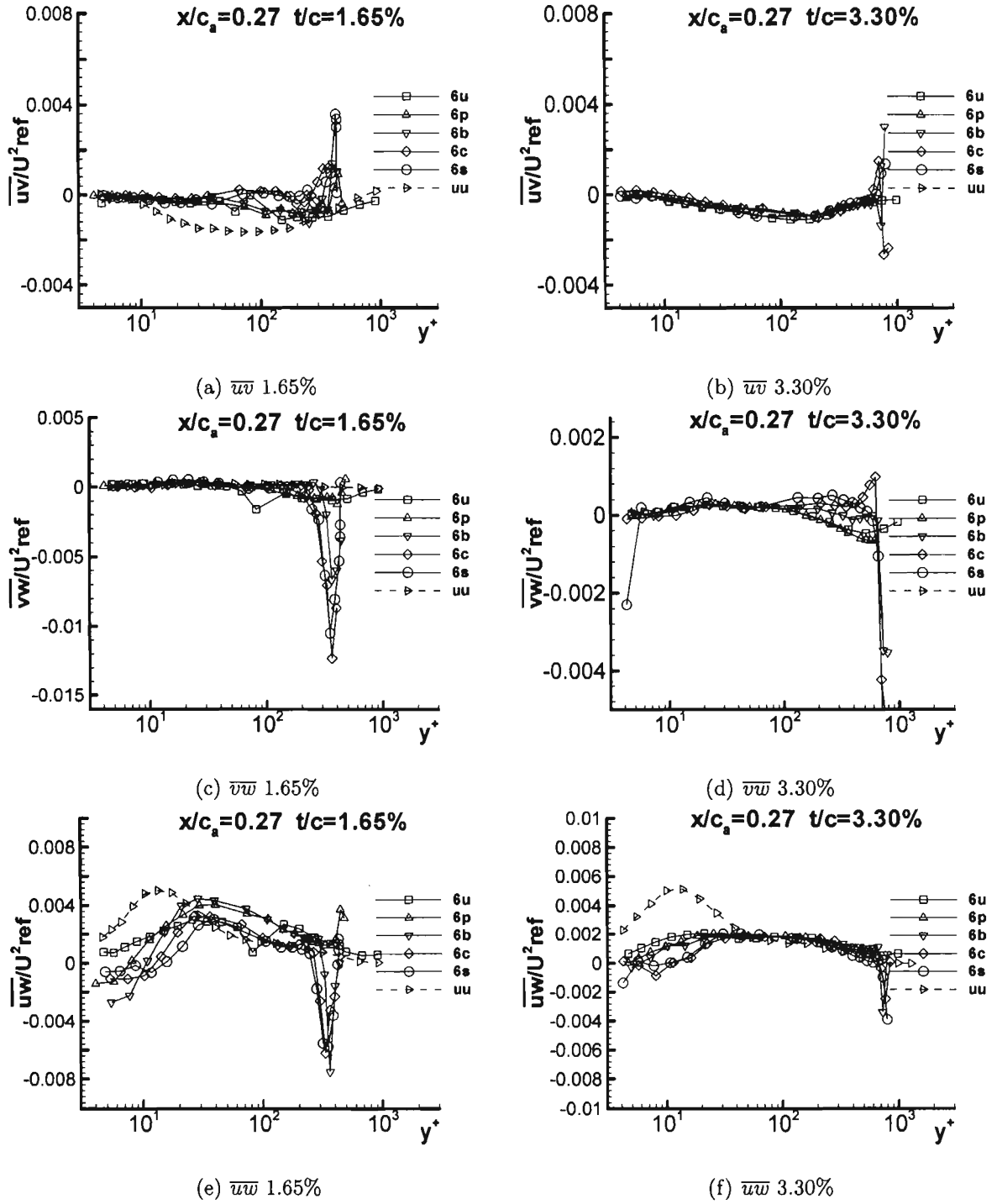


Figure F.15: Reynolds shear stresses  $-\overline{uv}/U_{ref}^2$ ,  $-\overline{vw}/U_{ref}^2$ , and  $-\overline{uw}/U_{ref}^2$  at  $x/c_a = 0.27$  for both 1.65% and 3.30% in chord coordinate system

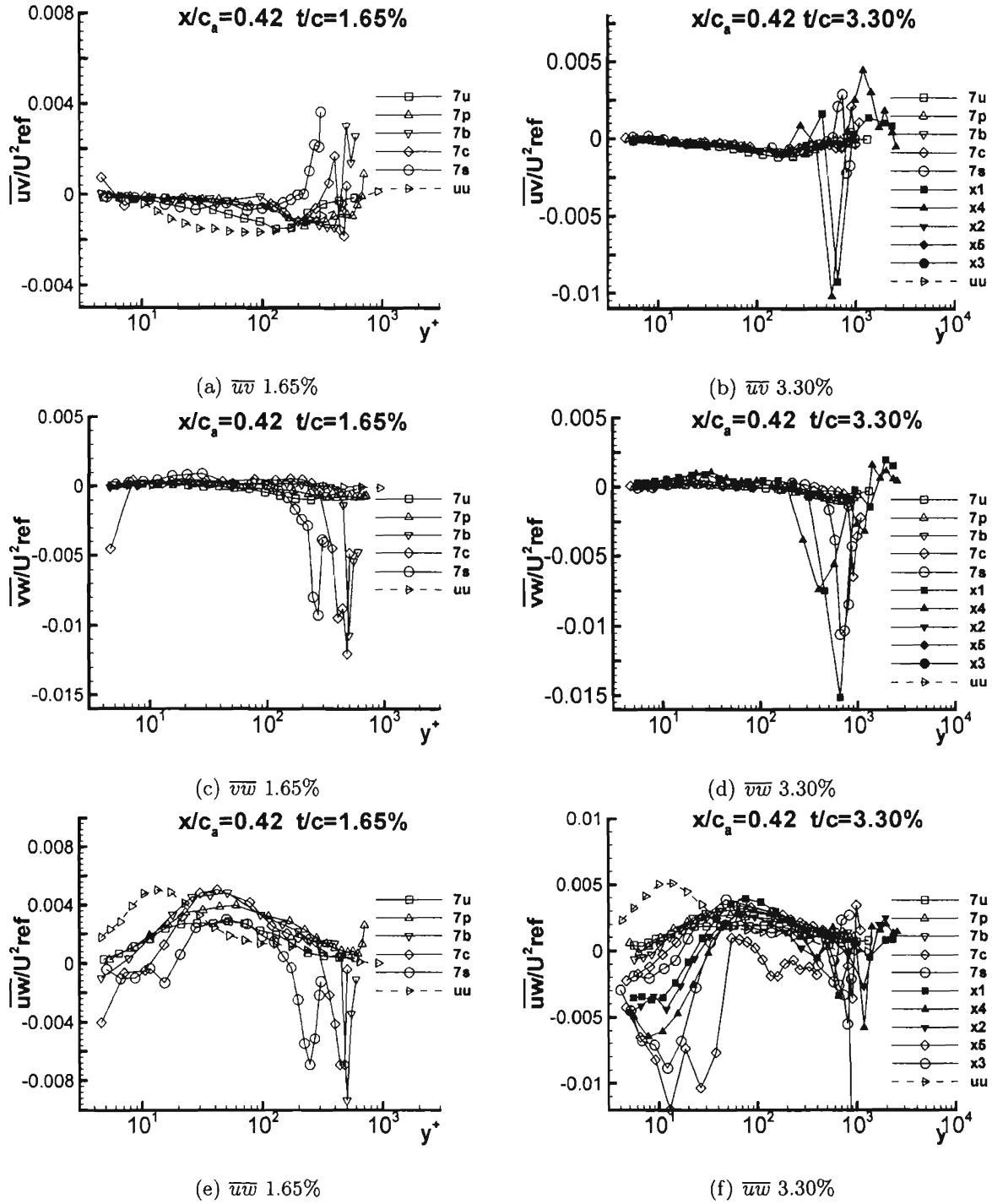


Figure F.16: Reynolds shear stresses  $-\overline{uv}/U_{ref}^2$ ,  $-\overline{vw}/U_{ref}^2$ , and  $-\overline{uw}/U_{ref}^2$  at  $x/c_a = 0.42$  for both 1.65% and 3.30% in chord coordinate system

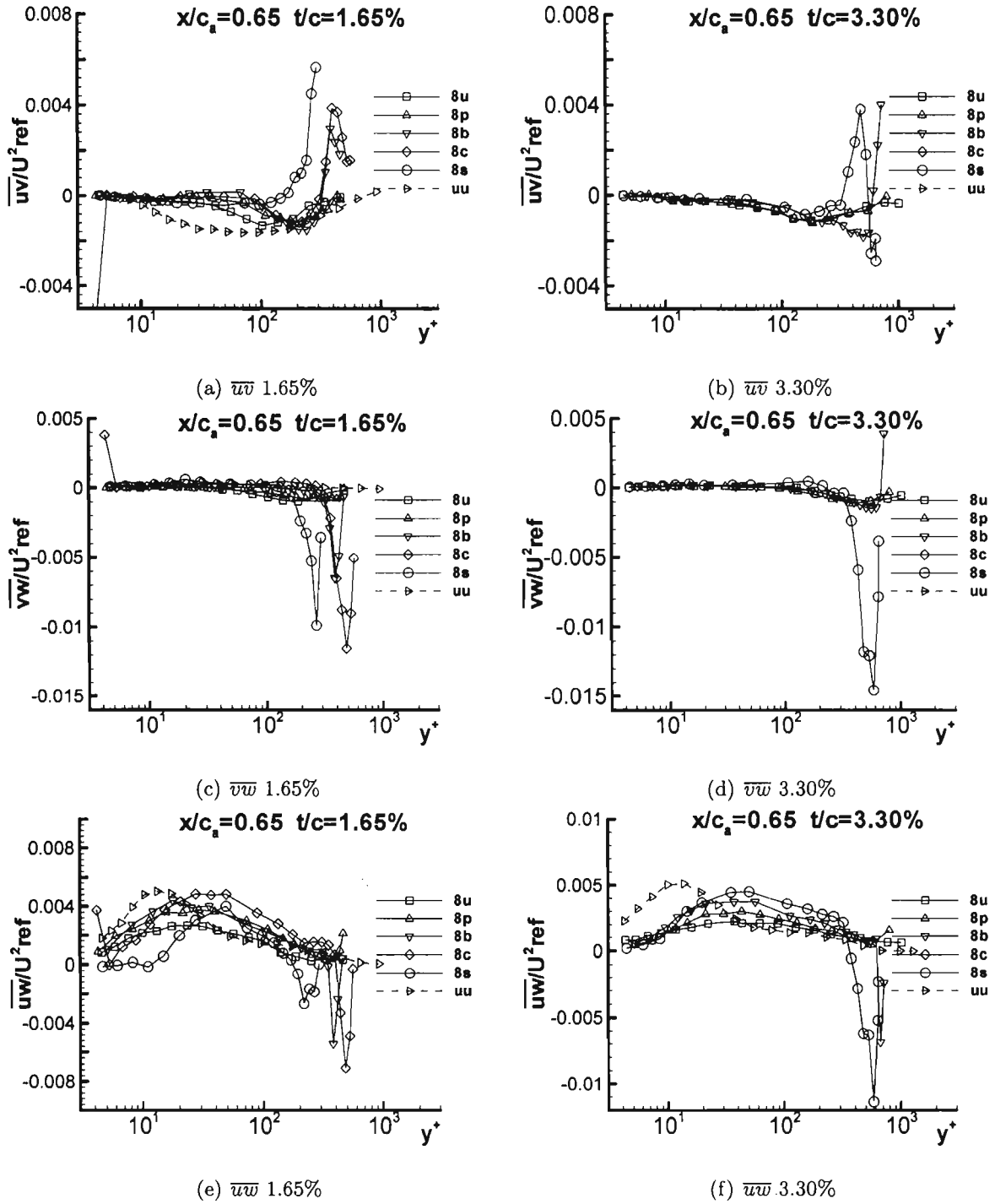


Figure F.17: Reynolds shear stresses  $-\overline{uv}/U_{ref}^2$ ,  $-\overline{vw}/U_{ref}^2$ , and  $-\overline{uw}/U_{ref}^2$  at  $x/c_a = 0.65$  for both 1.65% and 3.30% in chord coordinate system

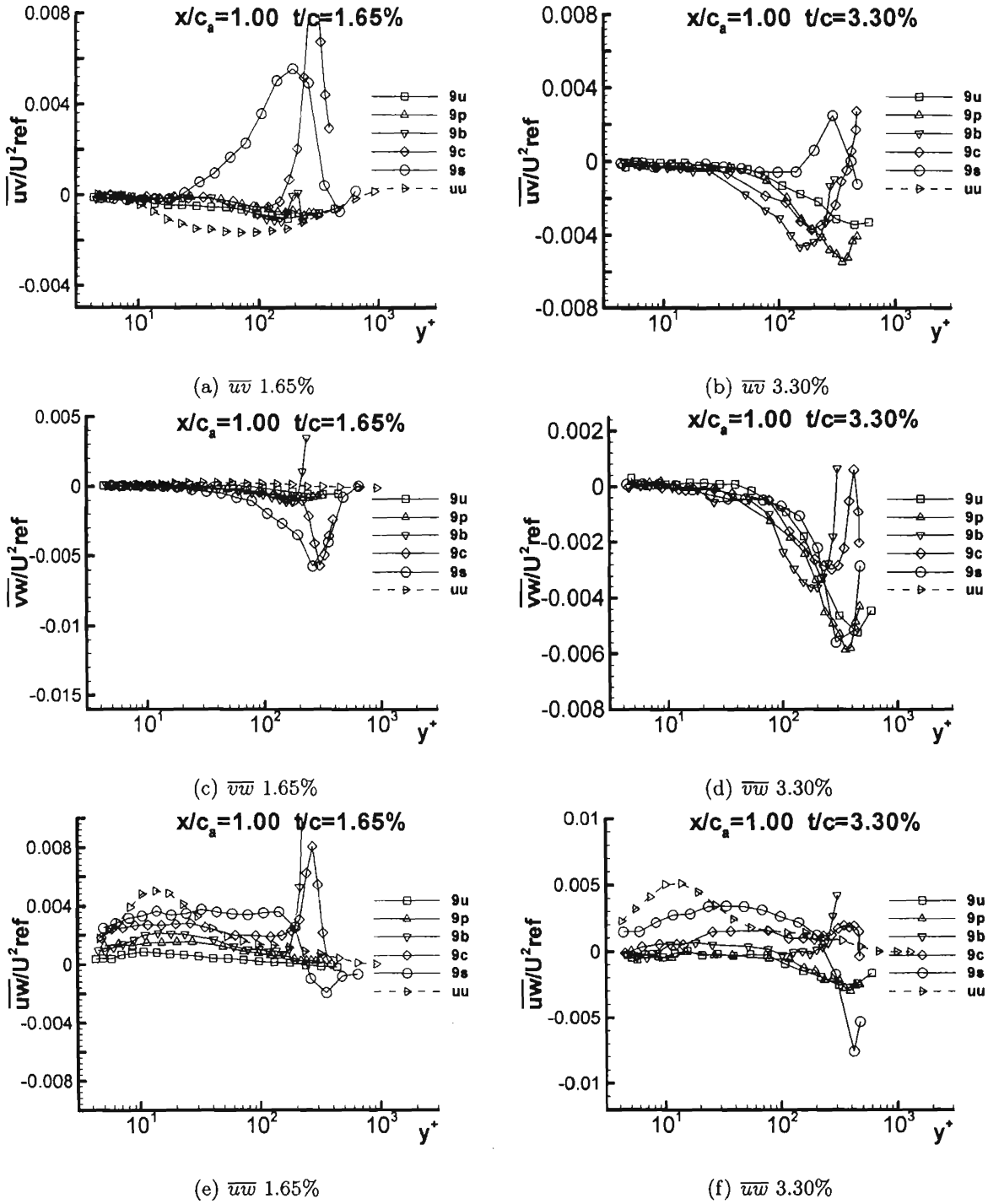


Figure F.18: Reynolds shear stresses  $-\overline{uv}/U_{ref}^2$ ,  $-\overline{vw}/U_{ref}^2$ , and  $-\overline{uw}/U_{ref}^2$  at  $x/c_a = 1.00$  for both 1.65% and 3.30% in chord coordinate system

## Appendix G

### Triple Products for a Stationary Endwall



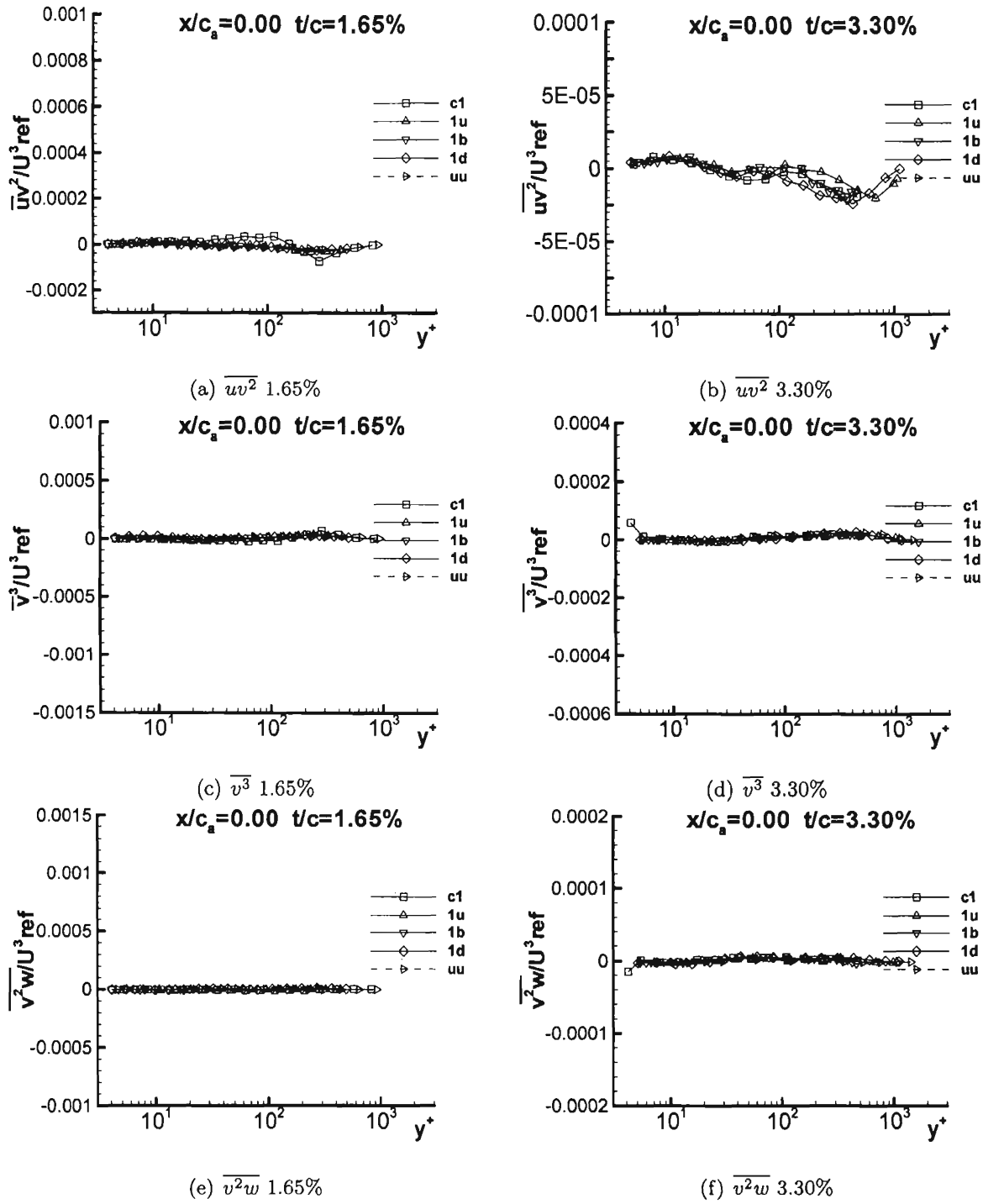


Figure G.1: Triple products  $\overline{uv^2}/U^3_{ref}$ ,  $\overline{v^3}/U^3_{ref}$ , and  $\overline{v^2w}/U^3_{ref}$  at  $x/c_a = 0.00$  for both 1.65% and 3.30% in chord coordinate system

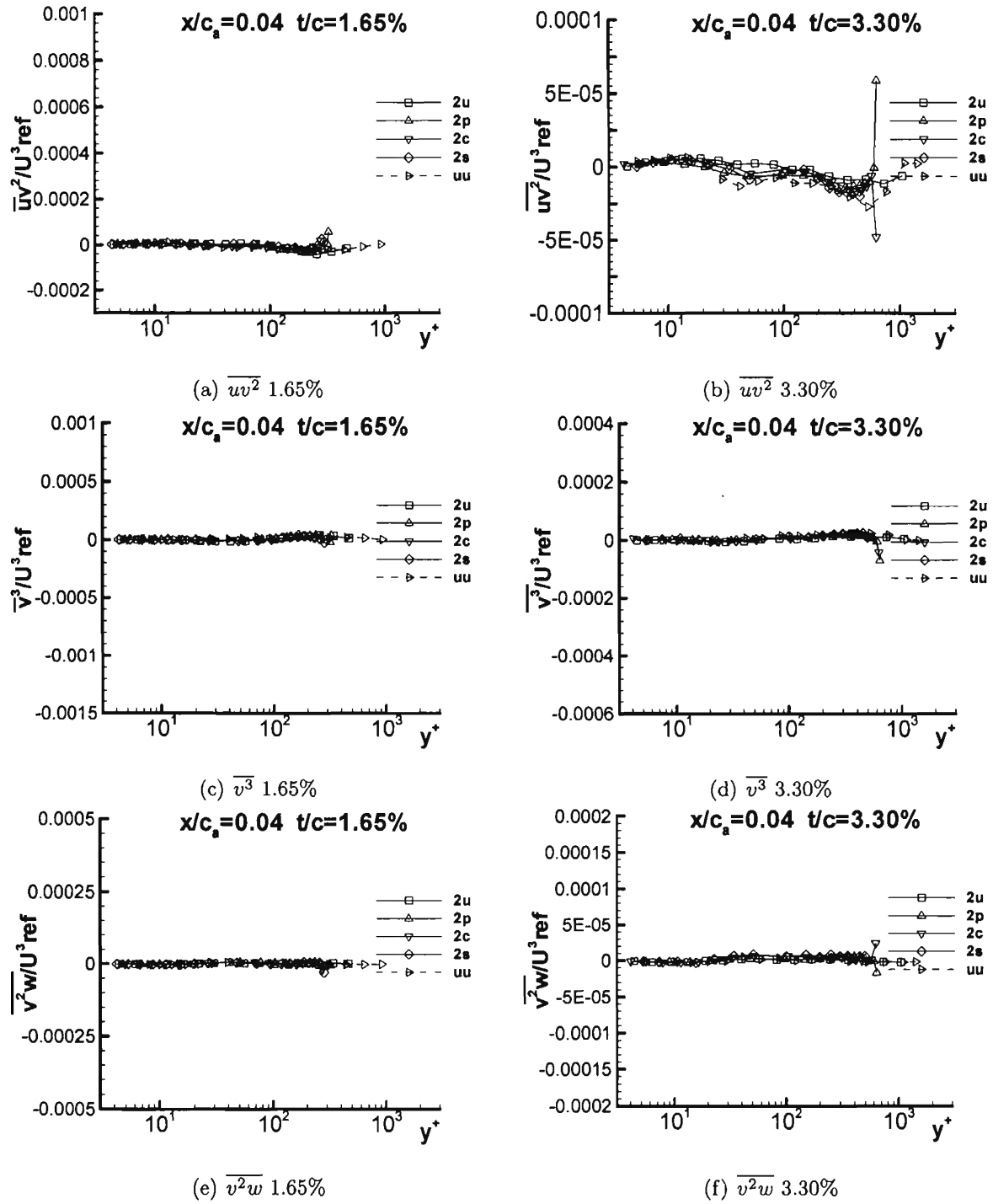


Figure G.2: Triple products  $\overline{uv^2}/U^3_{ref}$ ,  $\overline{v^3}/U^3_{ref}$ , and  $\overline{v^2w}/U^3_{ref}$  at  $x/c_a = 0.04$  for both 1.65% and 3.30% in chord coordinate system

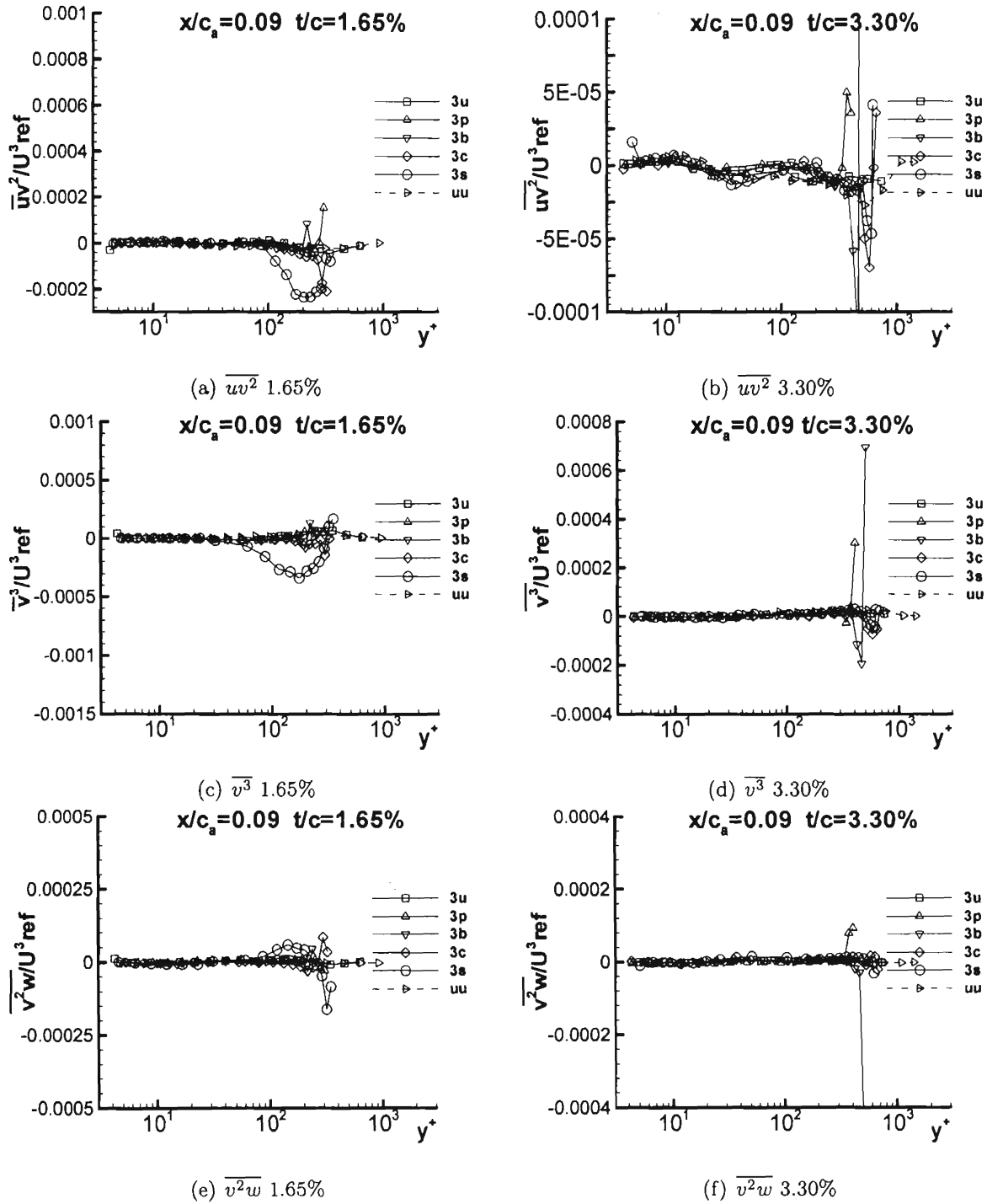


Figure G.3: Triple products  $\overline{uv^2}/U^3_{ref}$ ,  $\overline{v^3}/U^3_{ref}$ , and  $\overline{v^2w}/U^3_{ref}$  at  $x/c_a = 0.09$  for both 1.65% and 3.30% in chord coordinate system

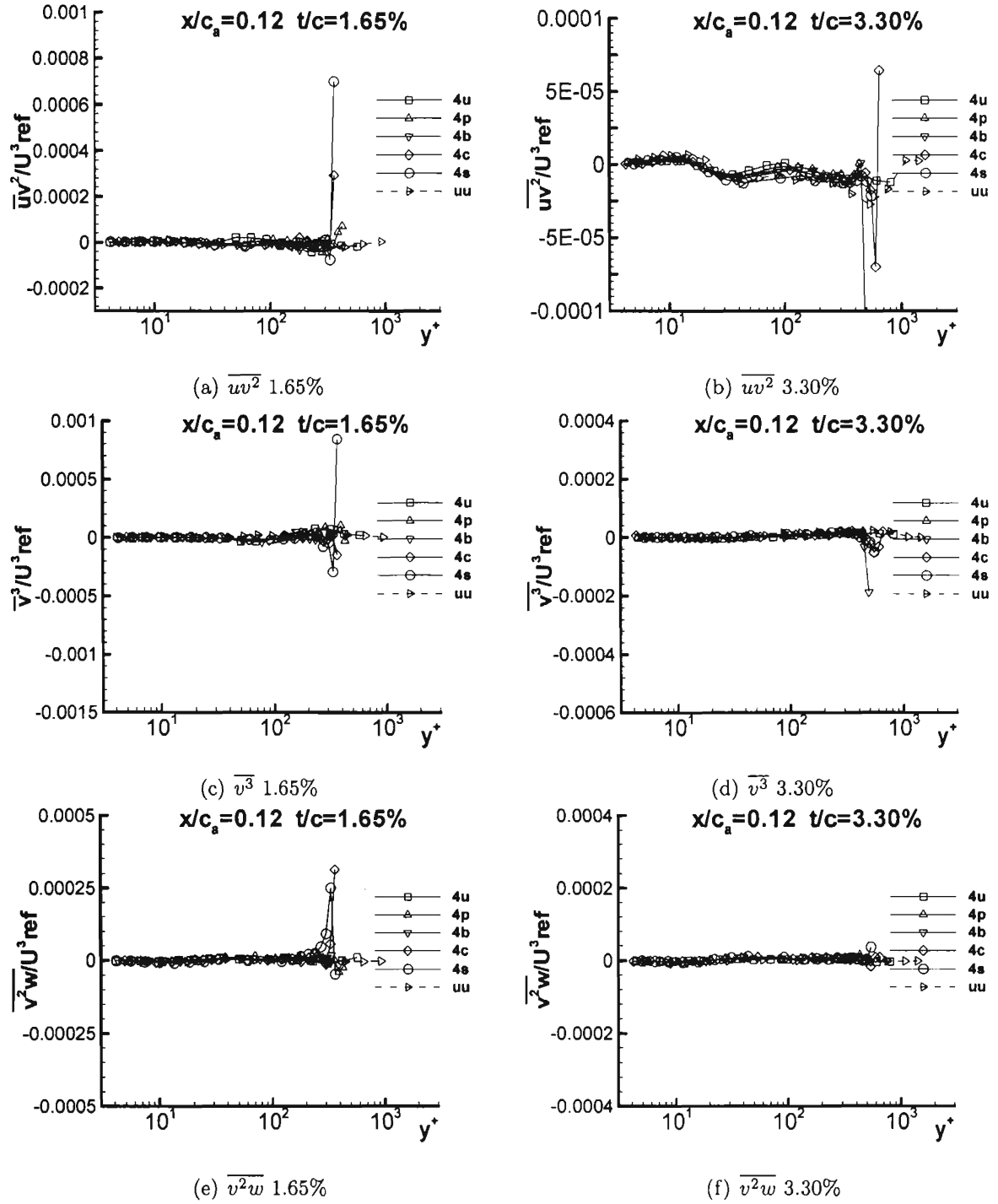


Figure G.4: Triple products  $\overline{uv^2}/U^3_{ref}$ ,  $\overline{v^3}/U^3_{ref}$ , and  $\overline{v^2w}/U^3_{ref}$  at  $x/c_a = 0.12$  for both 1.65% and 3.30% in chord coordinate system

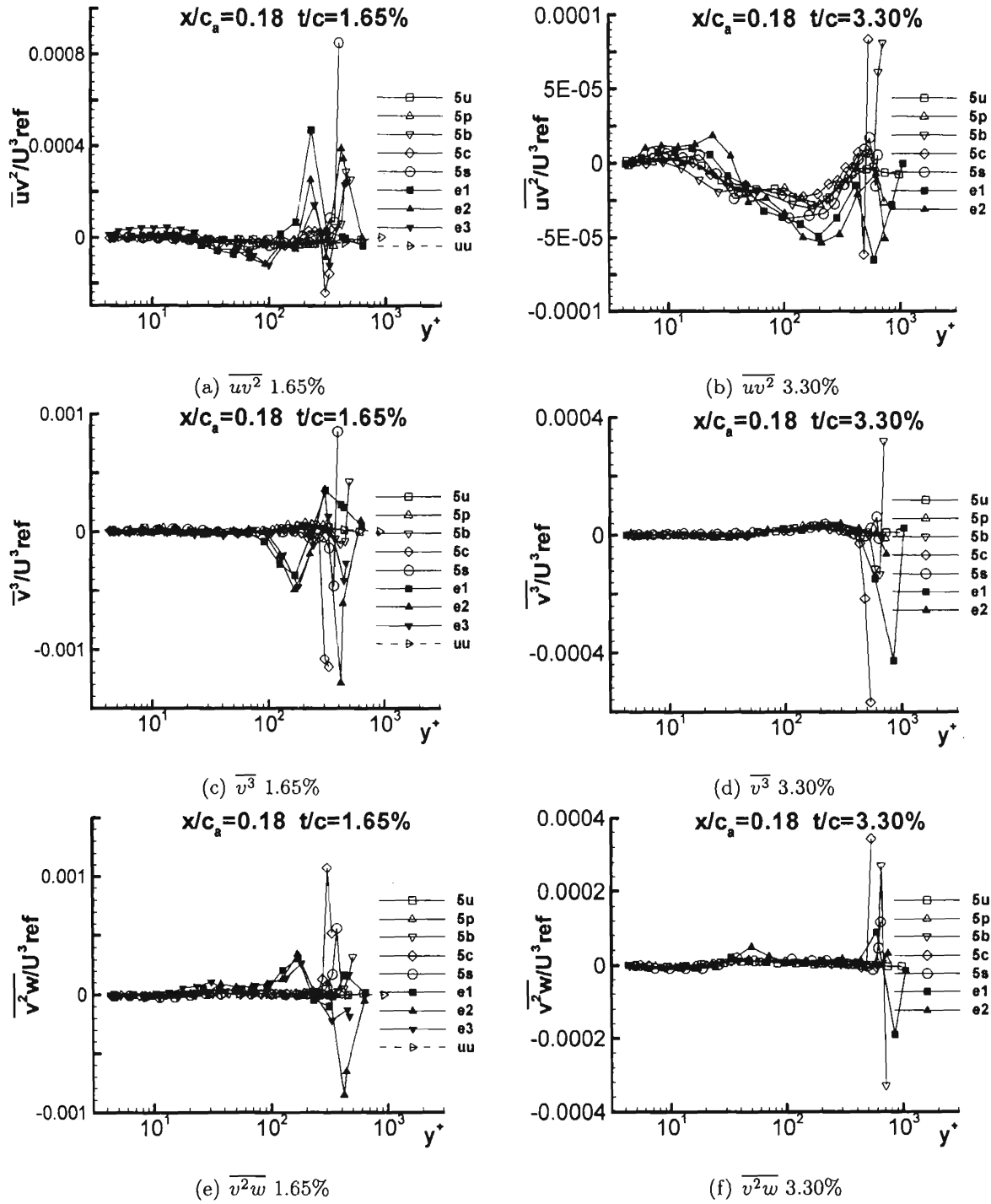


Figure G.5: Triple products  $\overline{uv^2}/U^3_{ref}$ ,  $\overline{v^3}/U^3_{ref}$ , and  $\overline{v^2w}/U^3_{ref}$  at  $x/c_a = 0.18$  for both 1.65% and 3.30% in chord coordinate system

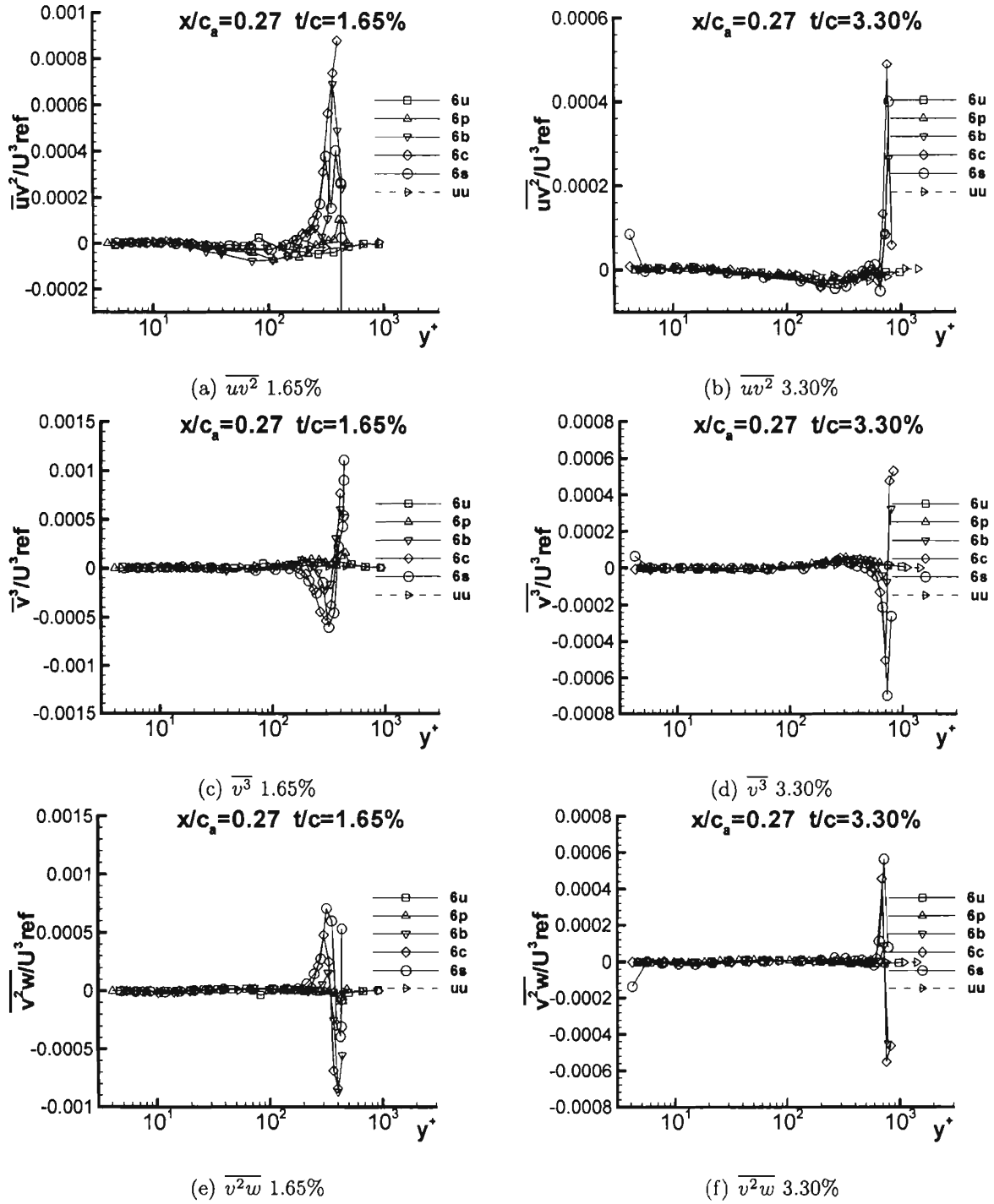


Figure G.6: Triple products  $\overline{uv^2}/U^3_{ref}$ ,  $\overline{v^3}/U^3_{ref}$ , and  $\overline{v^2w}/U^3_{ref}$  at  $x/c_a = 0.27$  for both 1.65% and 3.30% in chord coordinate system

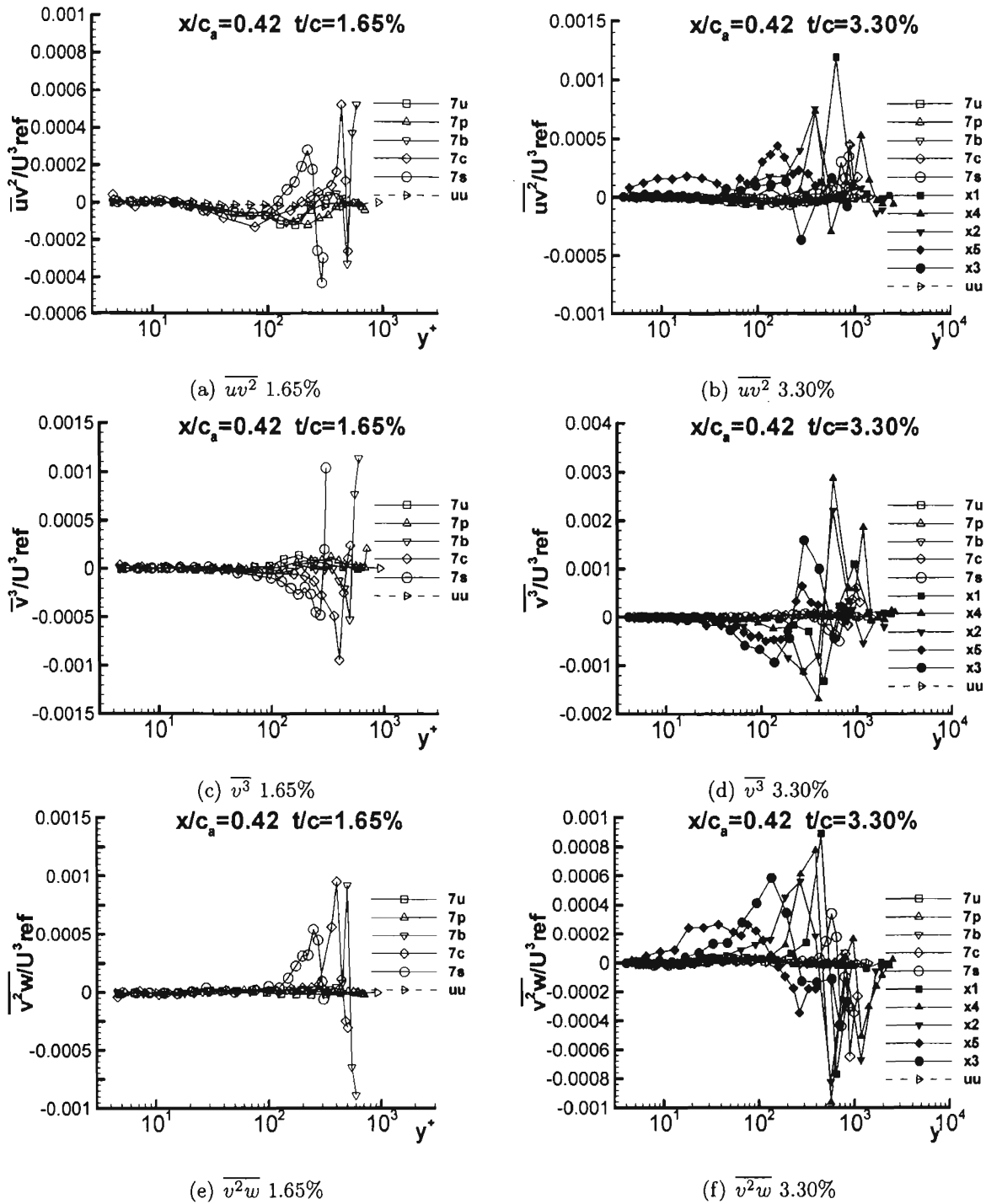


Figure G.7: Triple products  $\overline{uv^2}/U_{ref}^3$ ,  $\overline{v^3}/U_{ref}^3$ , and  $\overline{v^2w}/U_{ref}^3$  at  $x/c_a = 0.42$  for both 1.65% and 3.30% in chord coordinate system

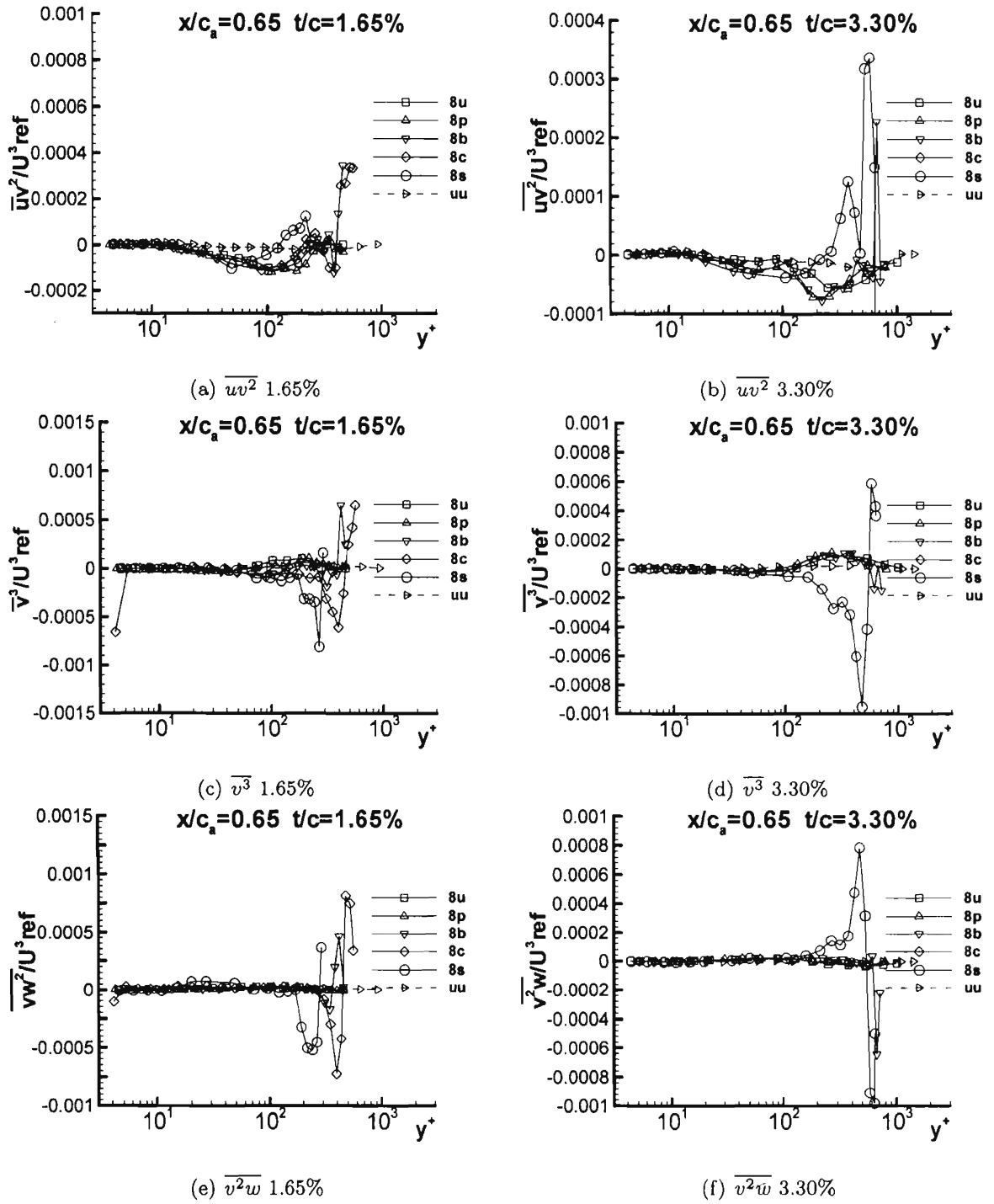


Figure G.8: Triple products  $\overline{uv^2}/U^3_{ref}$ ,  $\overline{v^3}/U^3_{ref}$ , and  $\overline{v^2w}/U^3_{ref}$  at  $x/c_a = 0.65$  for both 1.65% and 3.30% in chord coordinate system



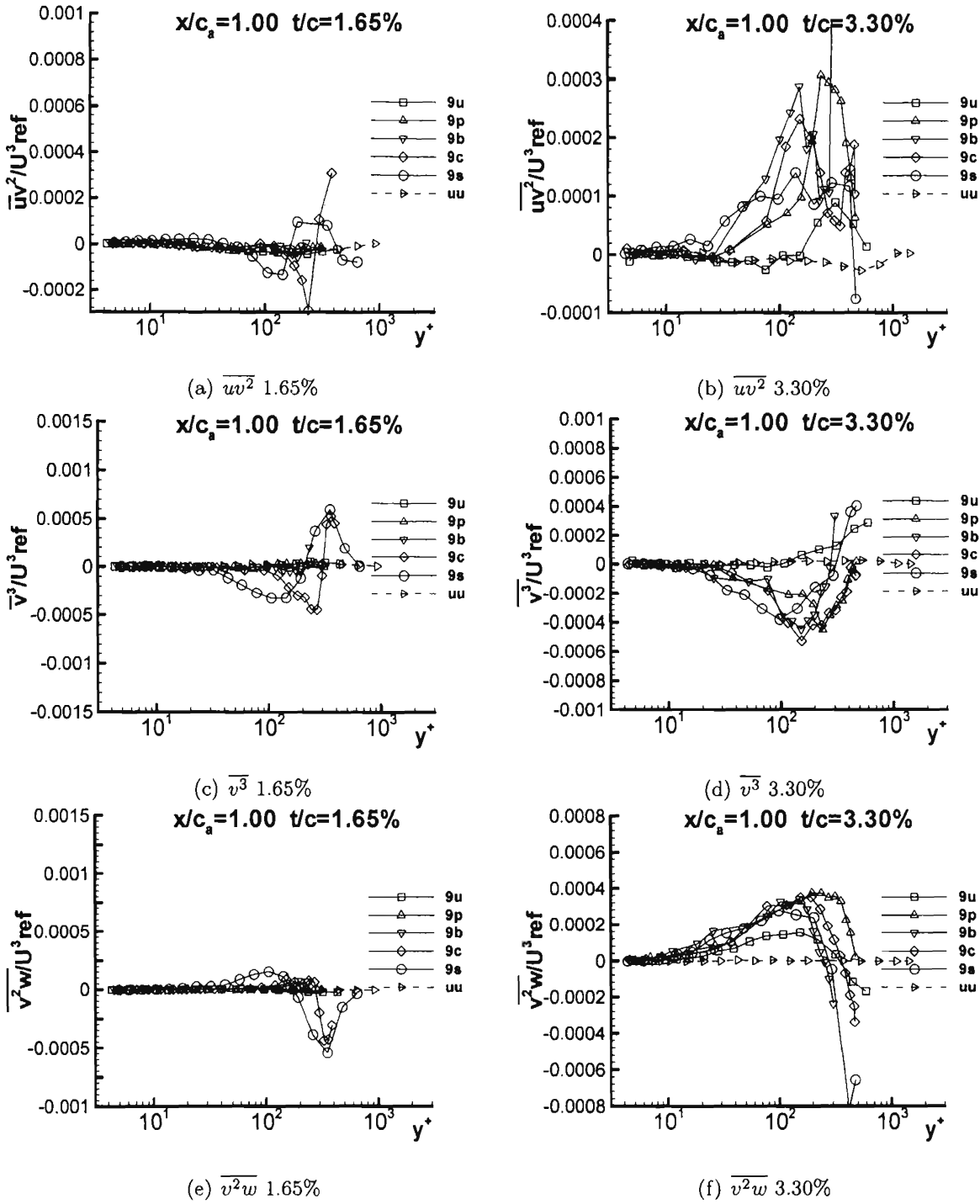


Figure G.9: Triple products  $\overline{uv^2}/U_{ref}^3$ ,  $\overline{v^3}/U_{ref}^3$ , and  $\overline{v^2w}/U_{ref}^3$  at  $x/c_a = 1.00$  for both 1.65% and 3.30% in chord coordinate system

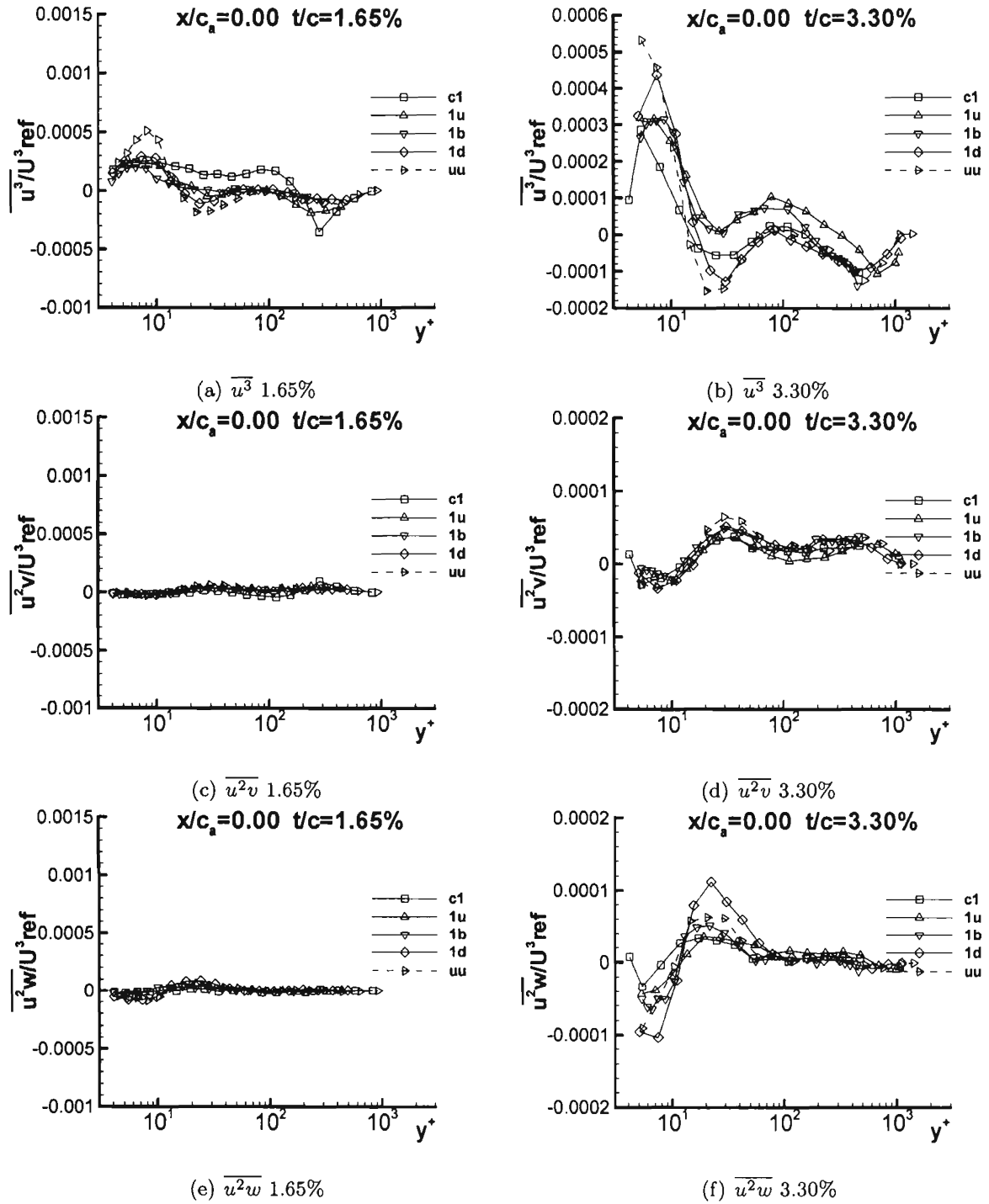


Figure G.10: Triple products  $\overline{u^3}/U_{ref}^3$ ,  $\overline{u^2v}/U_{ref}^3$ , and  $\overline{u^2w}/U_{ref}^3$  at  $x/c_a = 0.00$  for both 1.65% and 3.30% in chord coordinate system

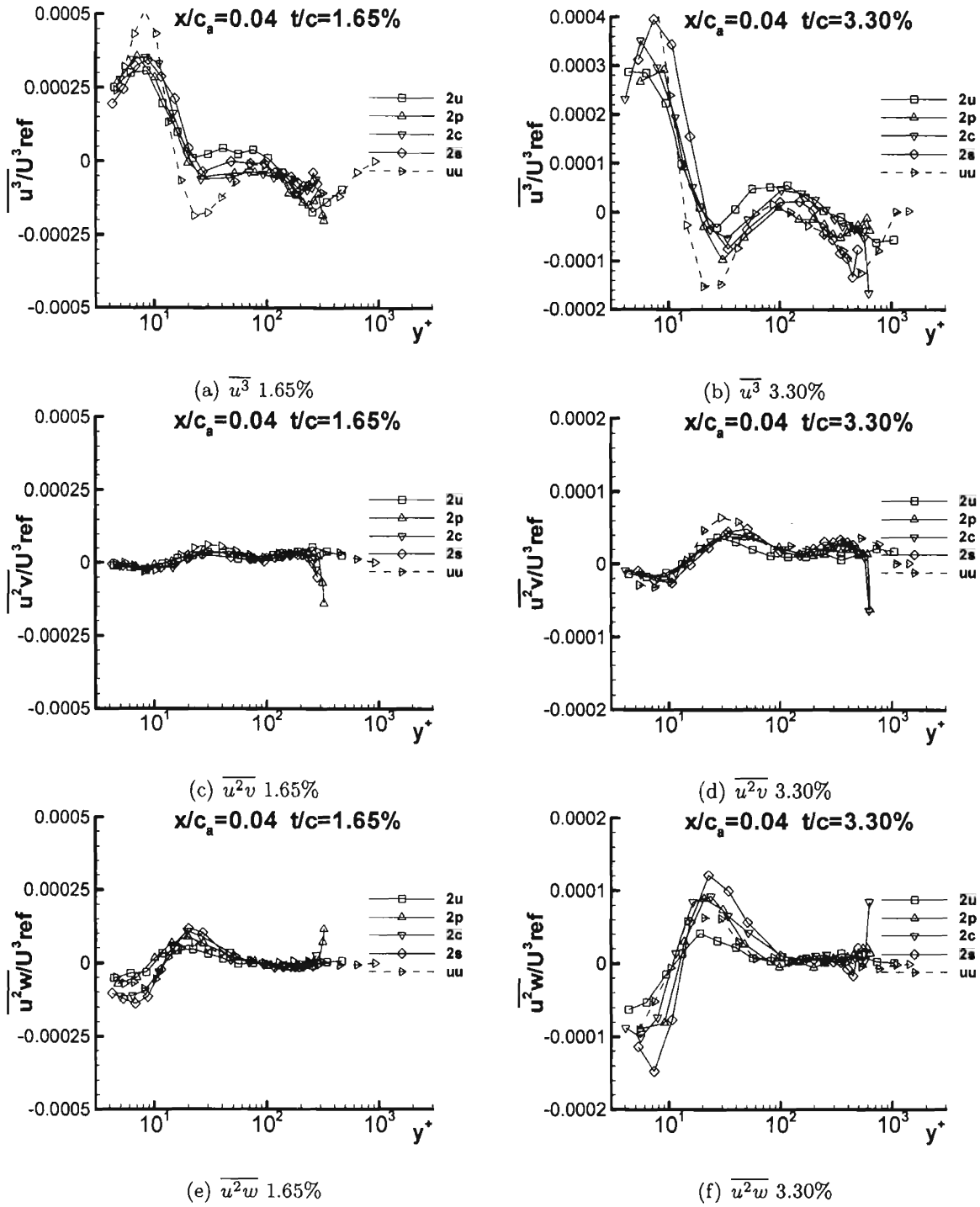


Figure G.11: Triple products  $\overline{u^3}/U_{ref}^3$ ,  $\overline{u^2v}/U_{ref}^3$ , and  $\overline{u^2w}/U_{ref}^3$  at  $x/c_a = 0.04$  for both 1.65% and 3.30% in chord coordinate system

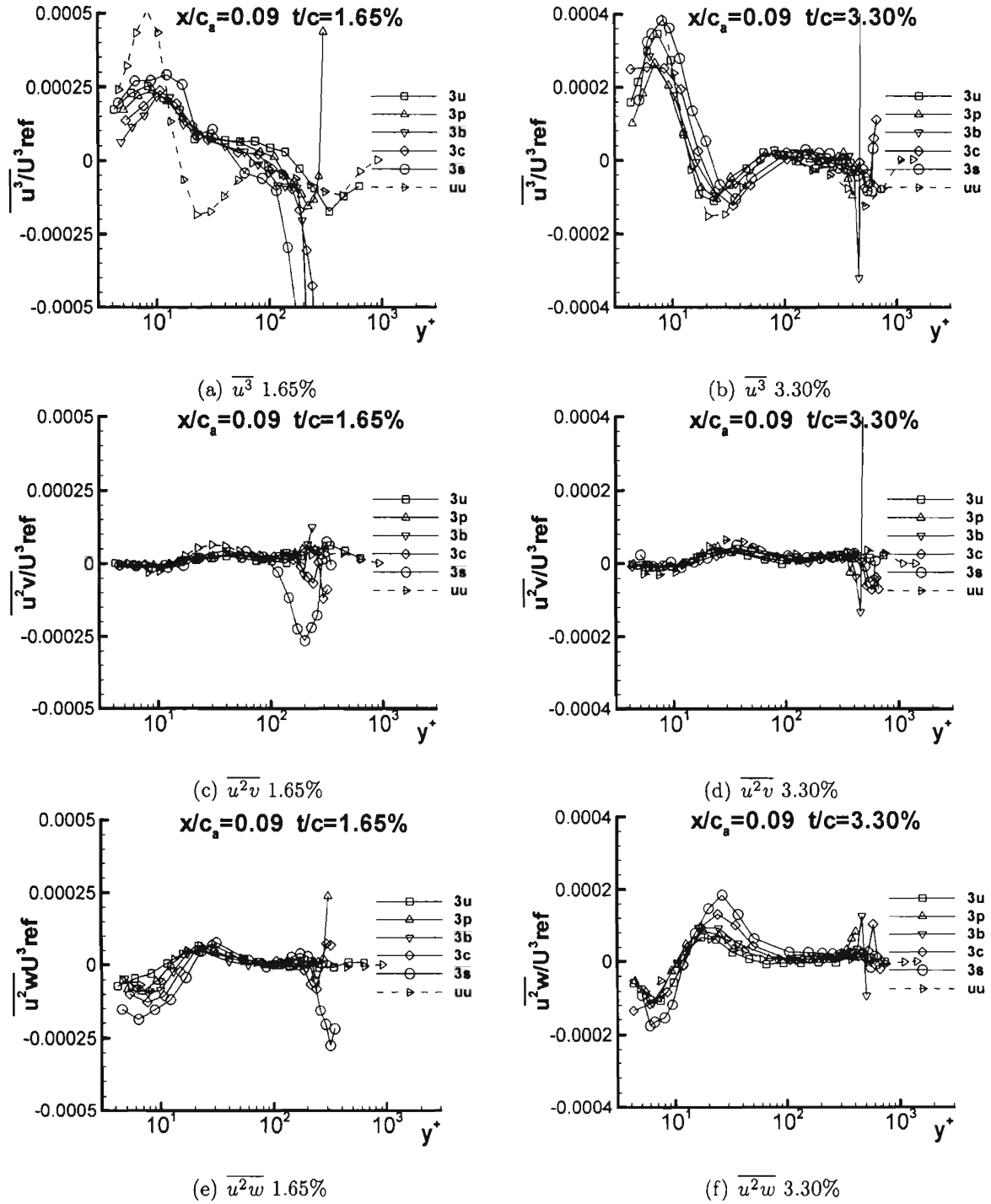


Figure G.12: Triple products  $\overline{u^3}/U_{ref}^3$ ,  $\overline{u^2v}/U_{ref}^3$ , and  $\overline{u^2w}/U_{ref}^3$  at  $x/c_a = 0.09$  for both 1.65% and 3.30% in chord coordinate system

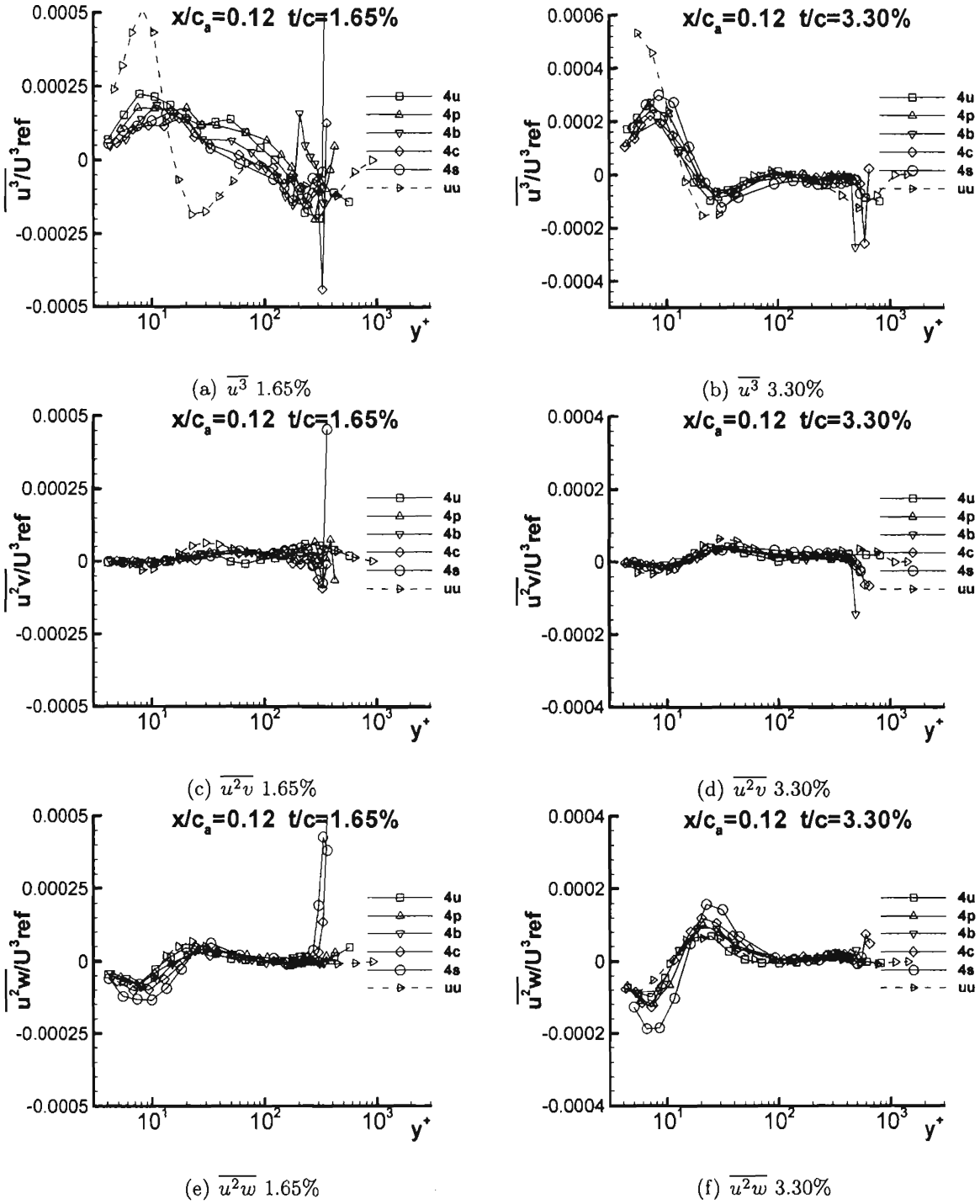


Figure G.13: Triple products  $\overline{u^3}/U_{ref}^3$ ,  $\overline{u^2v}/U_{ref}^3$ , and  $\overline{u^2w}/U_{ref}^3$  at  $x/c_a = 0.12$  for both 1.65% and 3.30% in chord coordinate system

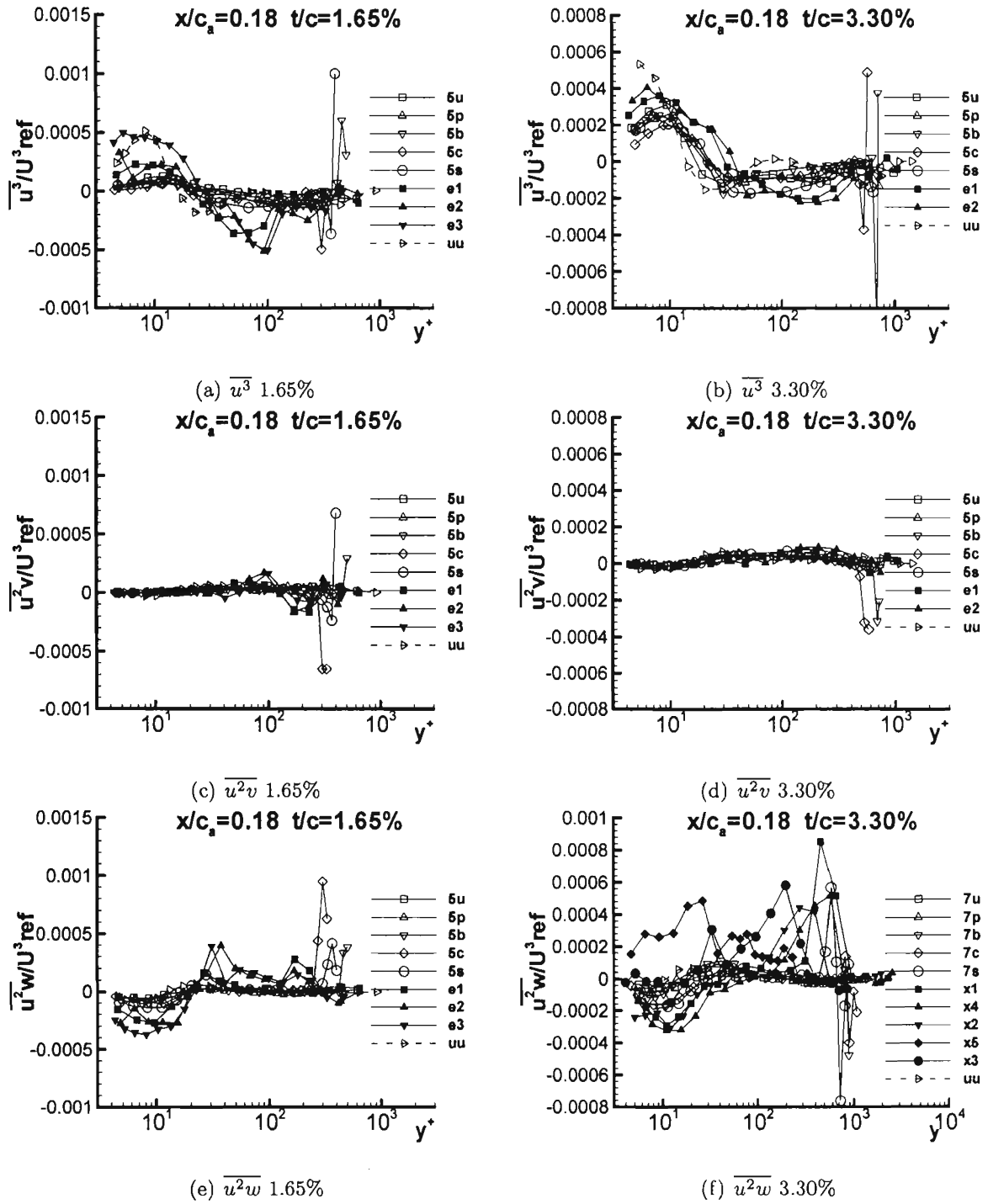


Figure G.14: Triple products  $\overline{u^3}/U^3_{ref}$ ,  $\overline{u^2v}/U^3_{ref}$ , and  $\overline{u^2w}/U^3_{ref}$  at  $x/c_a = 0.18$  for both 1.65% and 3.30% in chord coordinate system

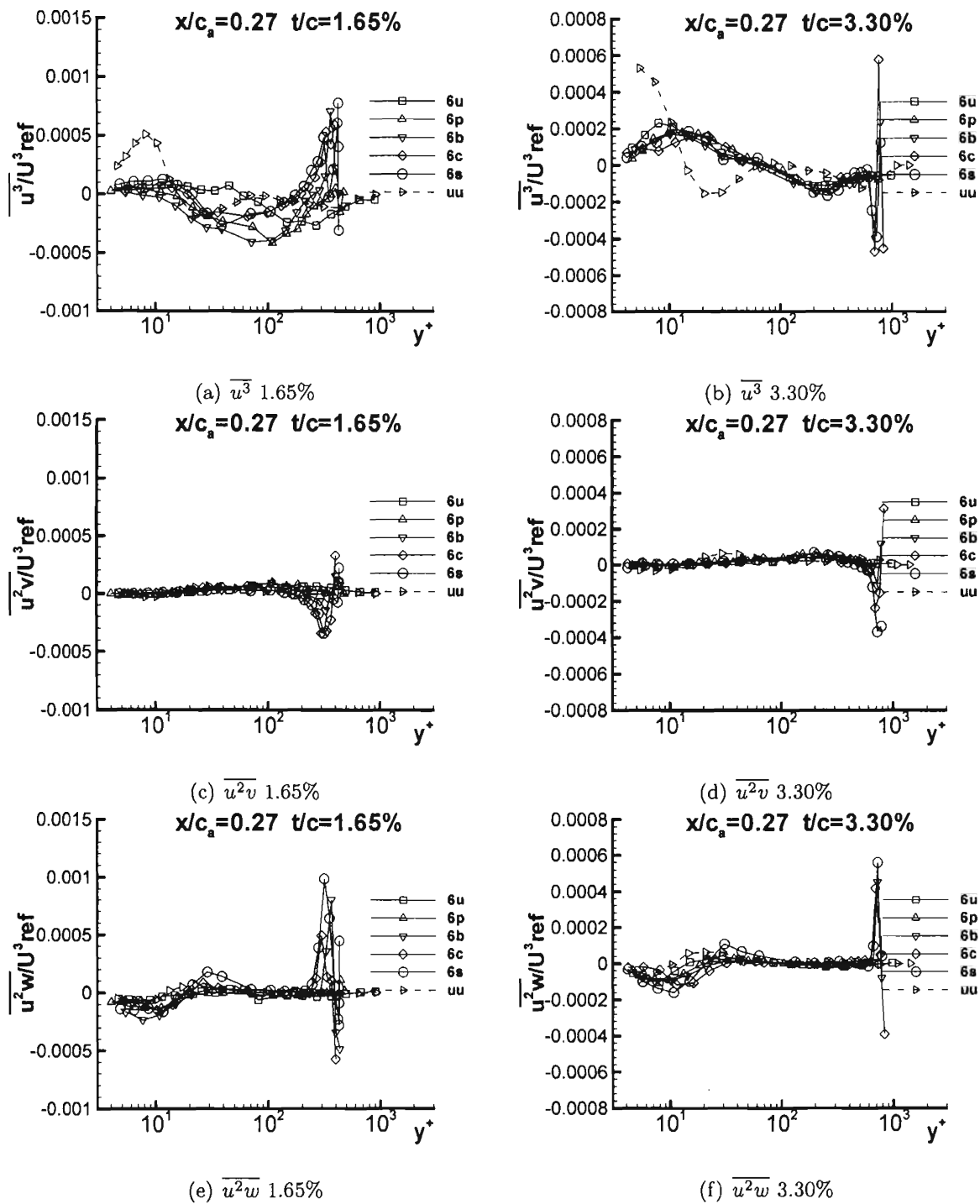


Figure G.15: Triple products  $\overline{u^3}/U_{ref}^3$ ,  $\overline{u^2v}/U_{ref}^3$ , and  $\overline{u^2w}/U_{ref}^3$  at  $x/c_a = 0.27$  for both 1.65% and 3.30% in chord coordinate system

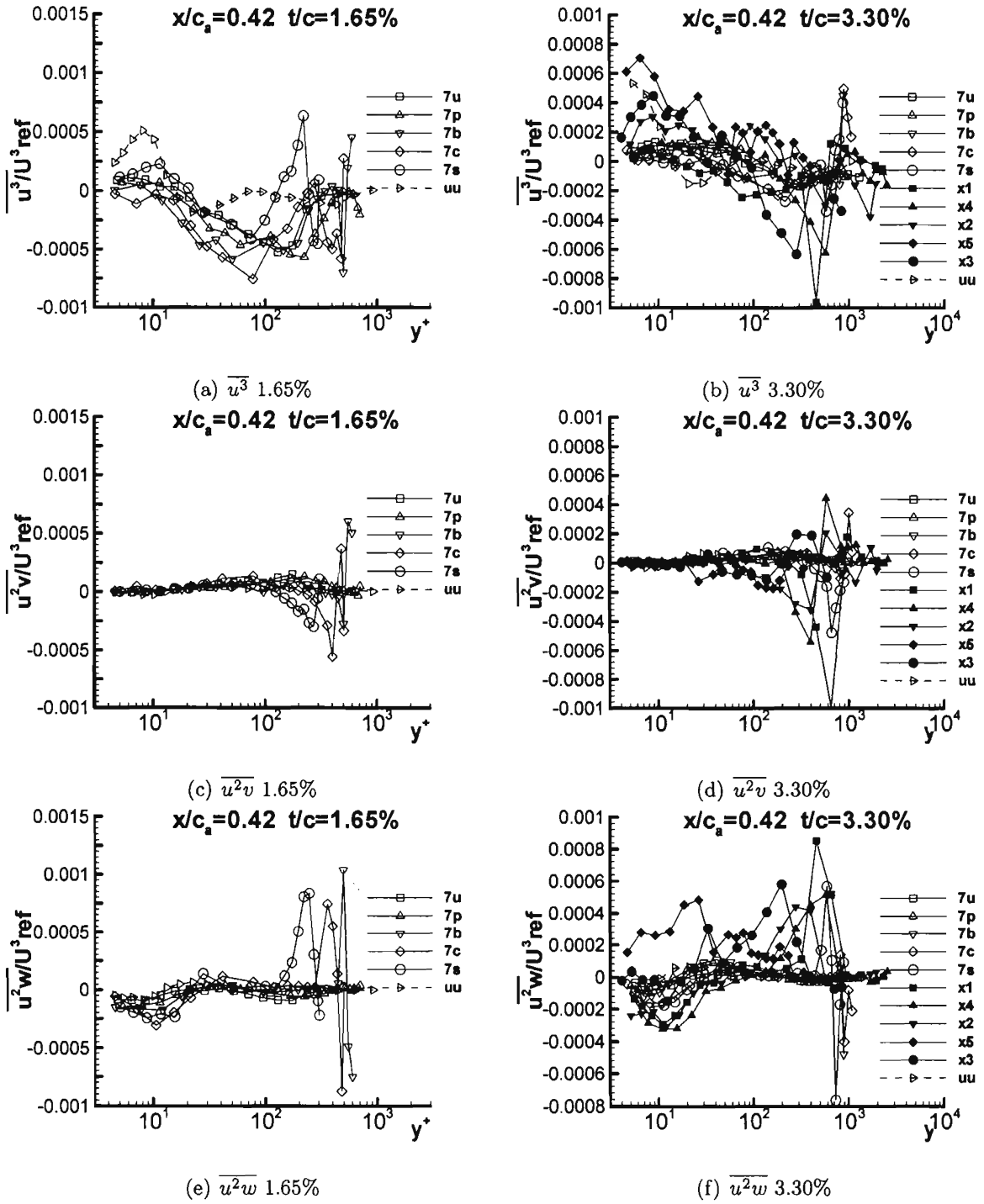


Figure G.16: Triple products  $\overline{u^3}/U_{ref}^3$ ,  $\overline{u^2v}/U_{ref}^3$ , and  $\overline{u^2w}/U_{ref}^3$  at  $x/c_a = 0.42$  for both 1.65% and 3.30% in chord coordinate system



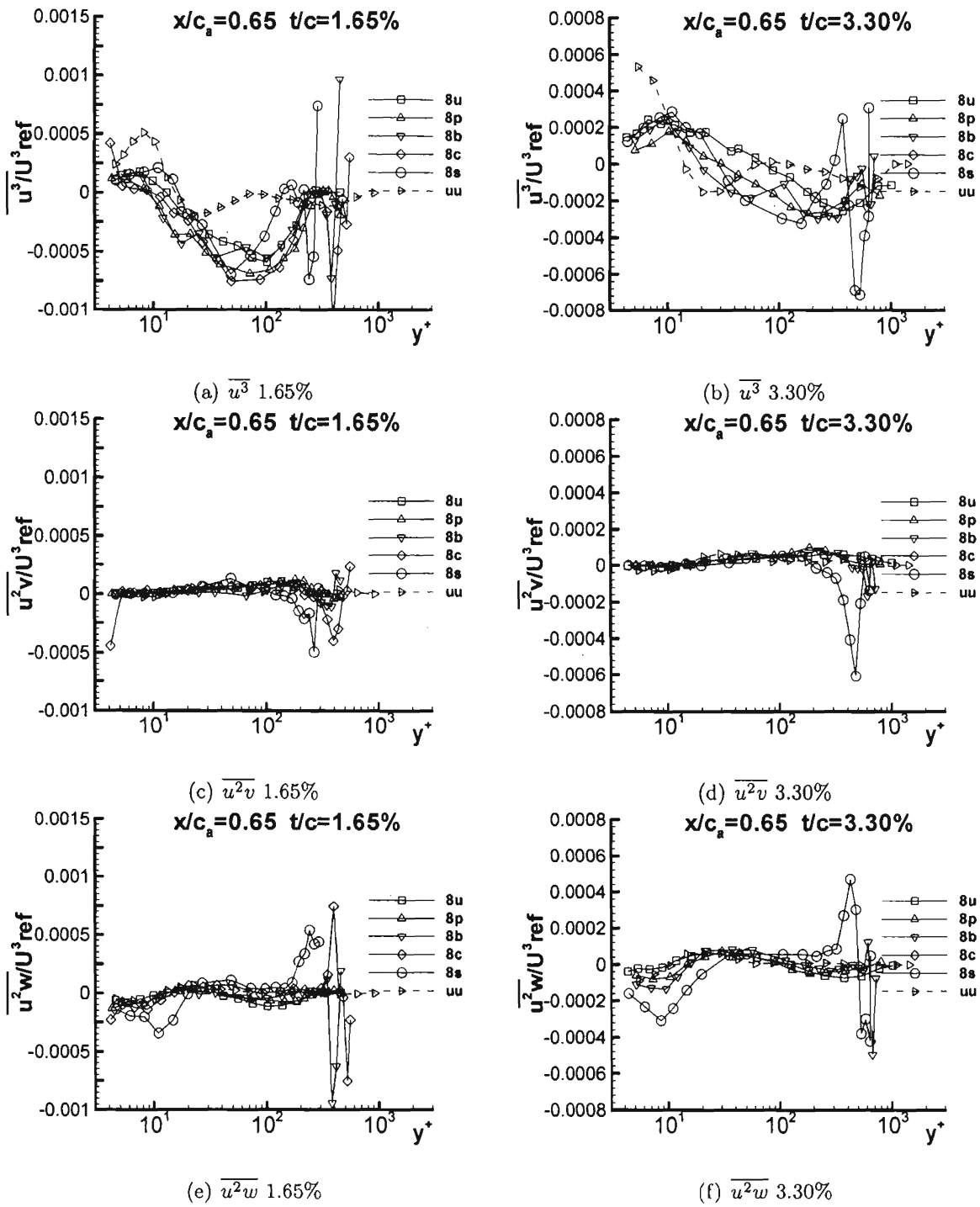


Figure G.17: Triple products  $\overline{u^3}/U_{ref}^3$ ,  $\overline{u^2v}/U_{ref}^3$ , and  $\overline{u^2w}/U_{ref}^3$  at  $x/c_a = 0.65$  for both 1.65% and 3.30% in chord coordinate system

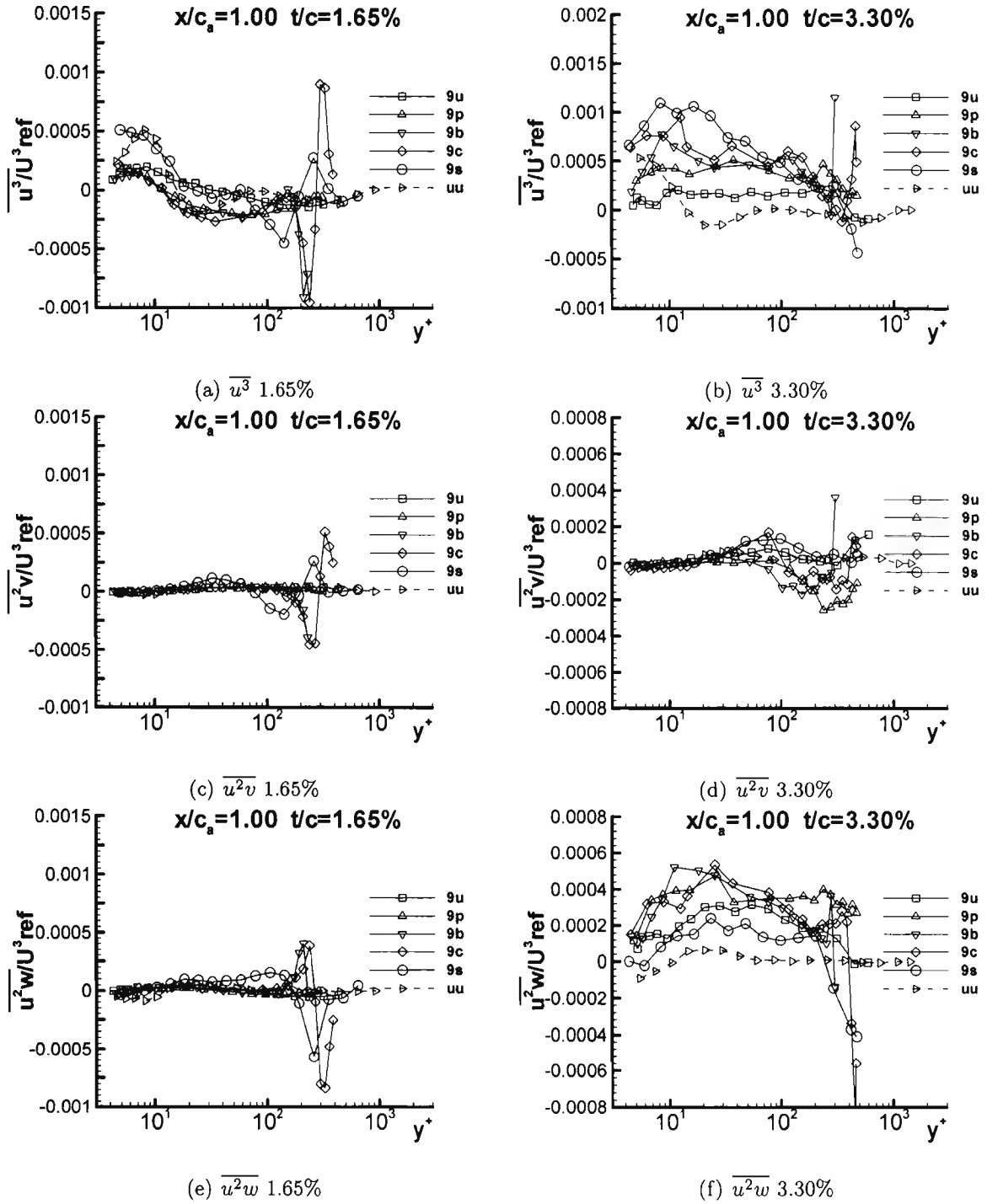


Figure G.18: Triple products  $\overline{u^3}/U^3_{ref}$ ,  $\overline{u^2v}/U^3_{ref}$ , and  $\overline{u^2w}/U^3_{ref}$  at  $x/c_a = 1.00$  for both 1.65% and 3.30% in chord coordinate system

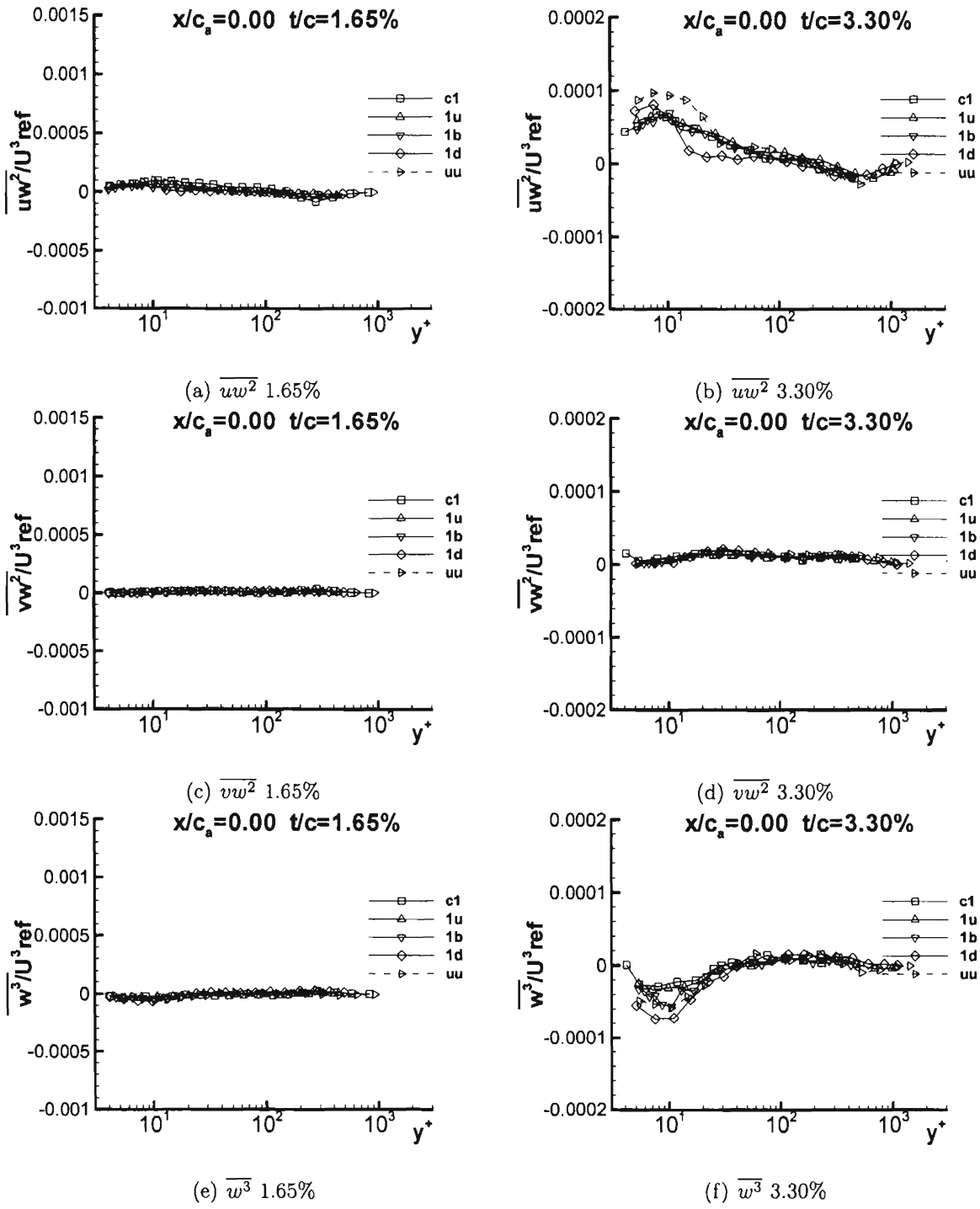


Figure G.19: Triple products  $\overline{uw^2}/U_{ref}^3$ ,  $\overline{vw^2}/U_{ref}^3$ , and  $\overline{w^3}/U_{ref}^3$  at  $x/c_a = 0.00$  for both 1.65% and 3.30% in chord coordinate system

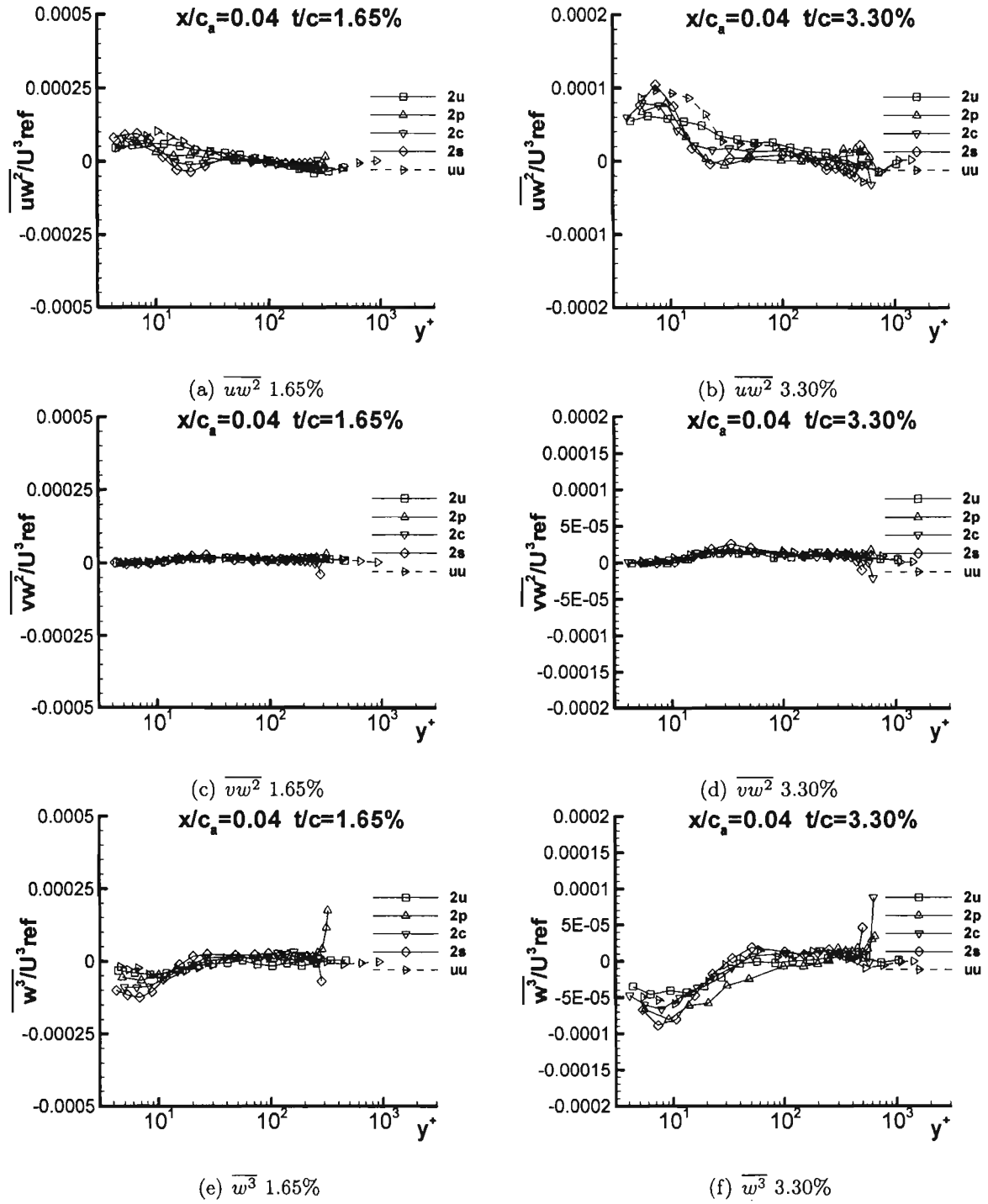


Figure G.20: Triple products  $\overline{uw^2}/U_{ref}^3$ ,  $\overline{vw^2}/U_{ref}^3$ , and  $\overline{w^3}/U_{ref}^3$  at  $x/c_a = 0.04$  for both 1.65% and 3.30% in chord coordinate system

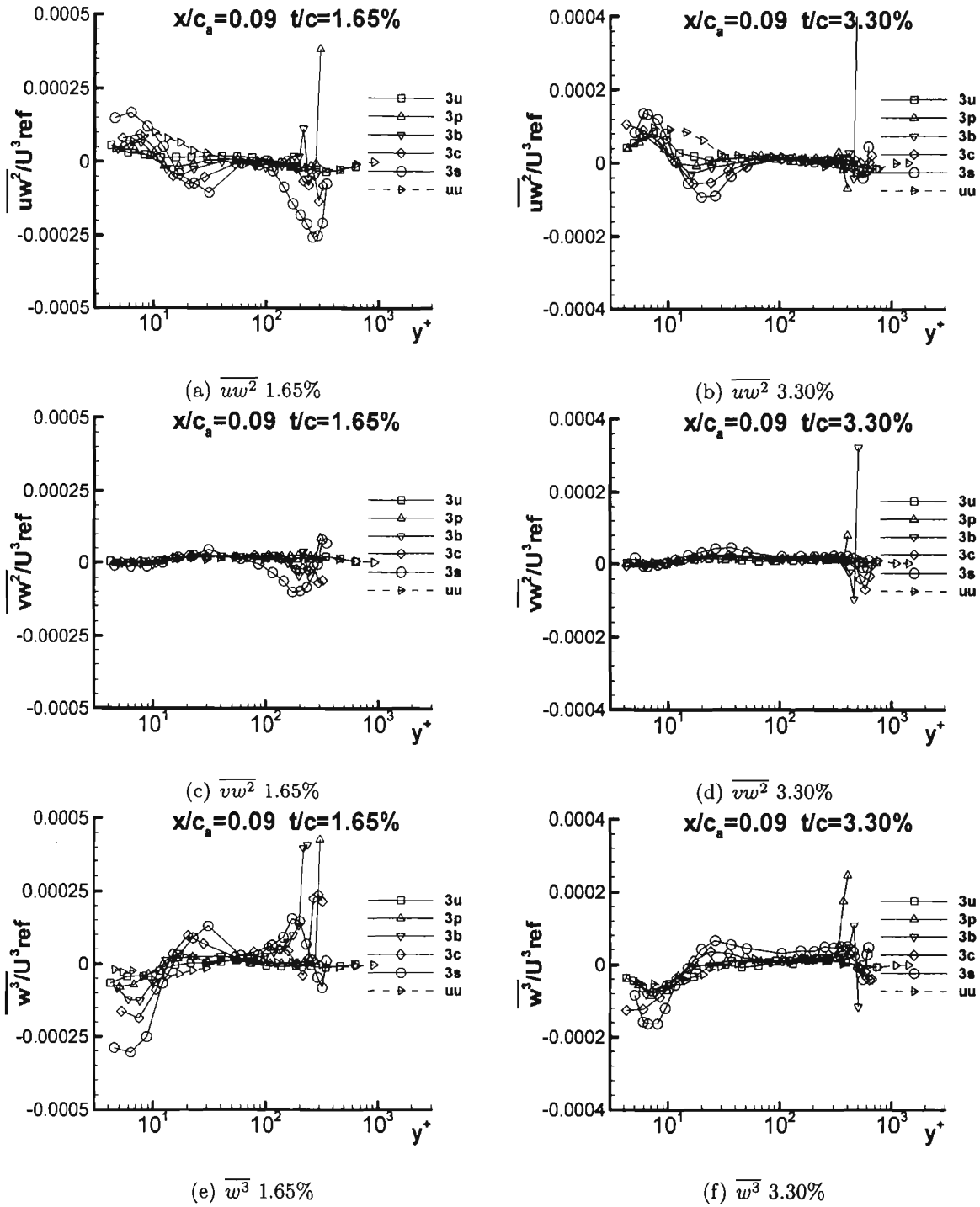


Figure G.21: Triple products  $\overline{uw^2}/U_{ref}^3$ ,  $\overline{vw^2}/U_{ref}^3$ , and  $\overline{w^3}/U_{ref}^3$  at  $x/c_a = 0.09$  for both 1.65% and 3.30% in chord coordinate system

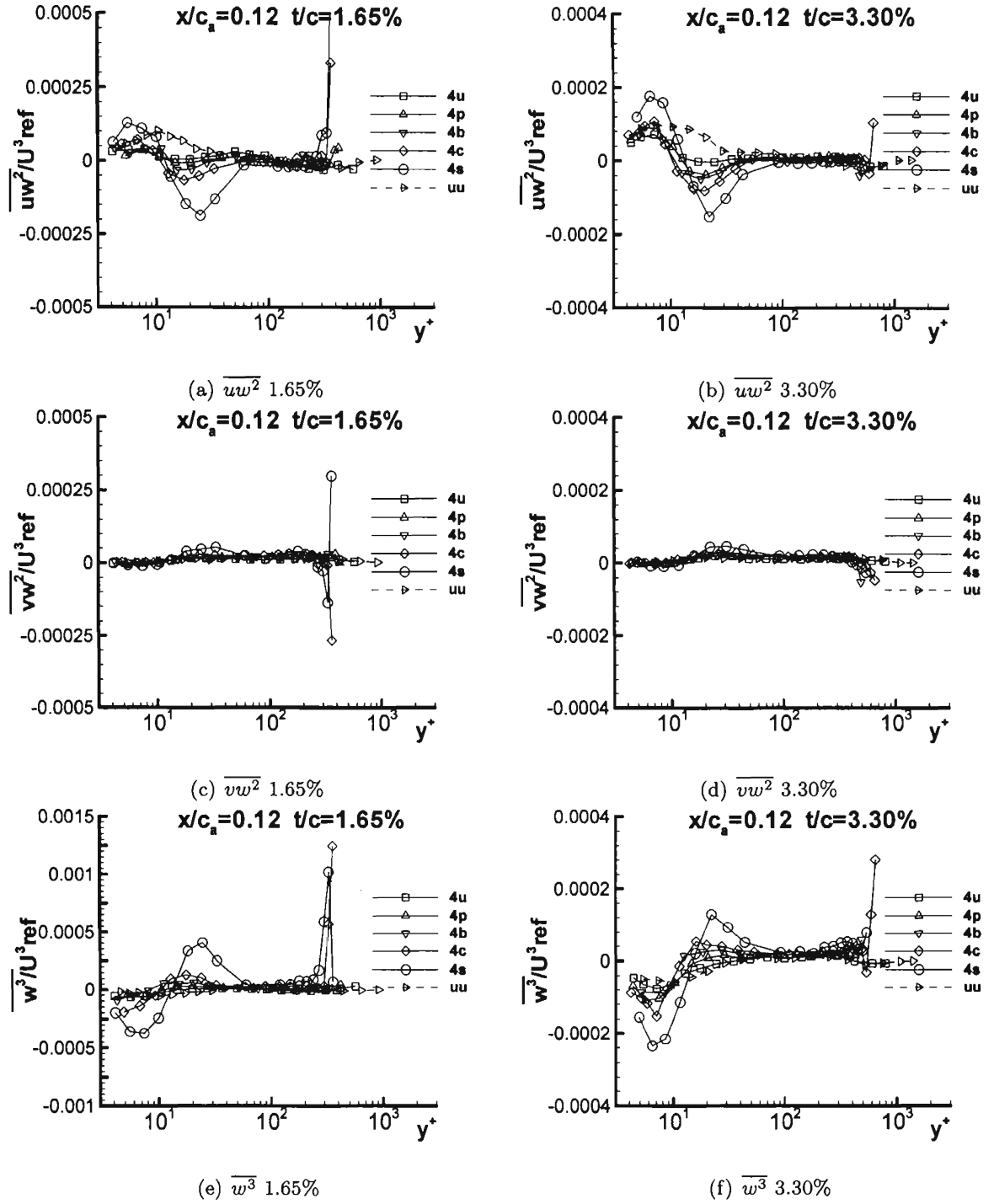


Figure G.22: Triple products  $\overline{uw^2}/U^3_{ref}$ ,  $\overline{vw^2}/U^3_{ref}$ , and  $\overline{w^3}/U^3_{ref}$  at  $x/c_a = 0.12$  for both 1.65% and 3.30% in chord coordinate system

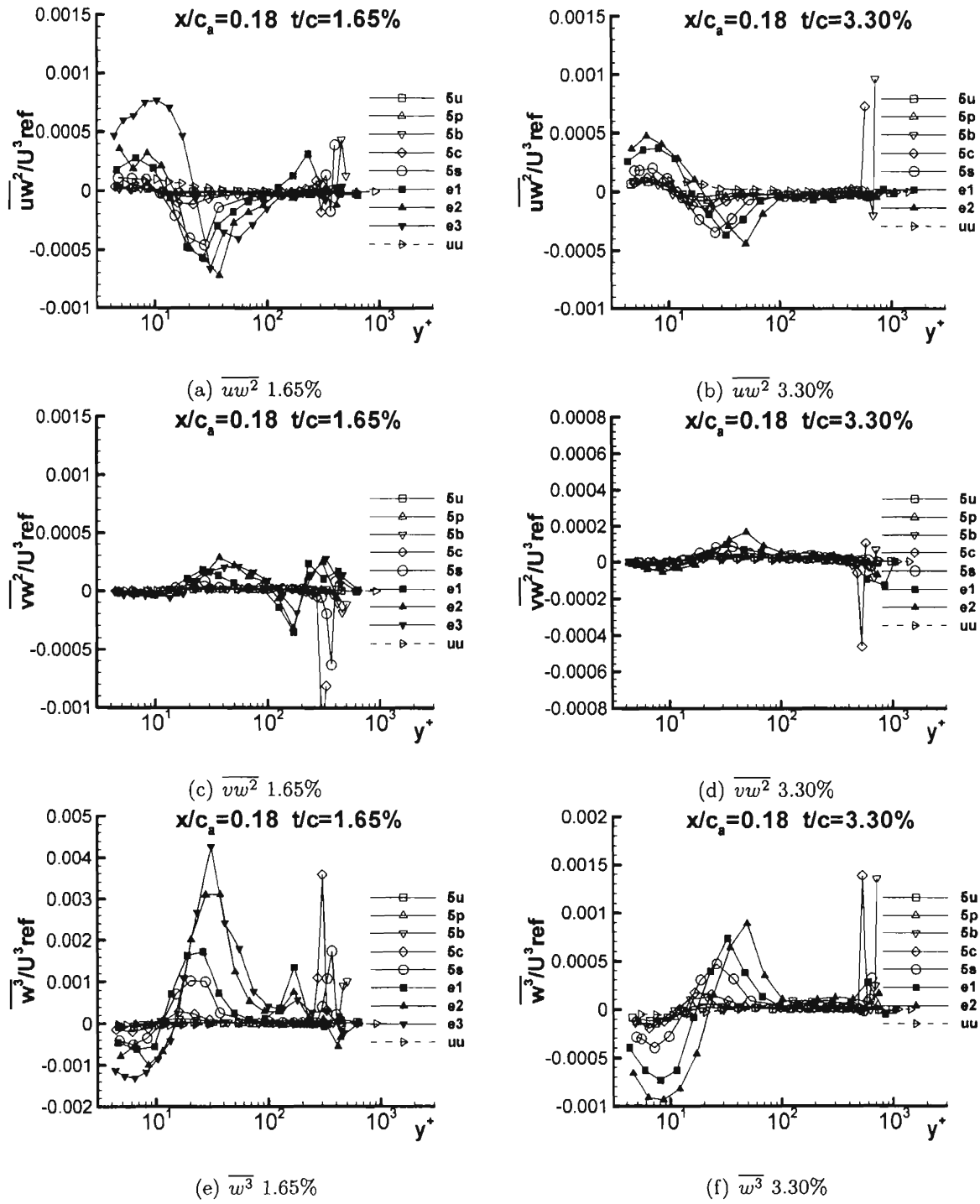


Figure G.23: Triple products  $\overline{uw^2}/U_{ref}^3$ ,  $\overline{vw^2}/U_{ref}^3$ , and  $\overline{w^3}/U_{ref}^3$  at  $x/c_a = 0.18$  for both 1.65% and 3.30% in chord coordinate system

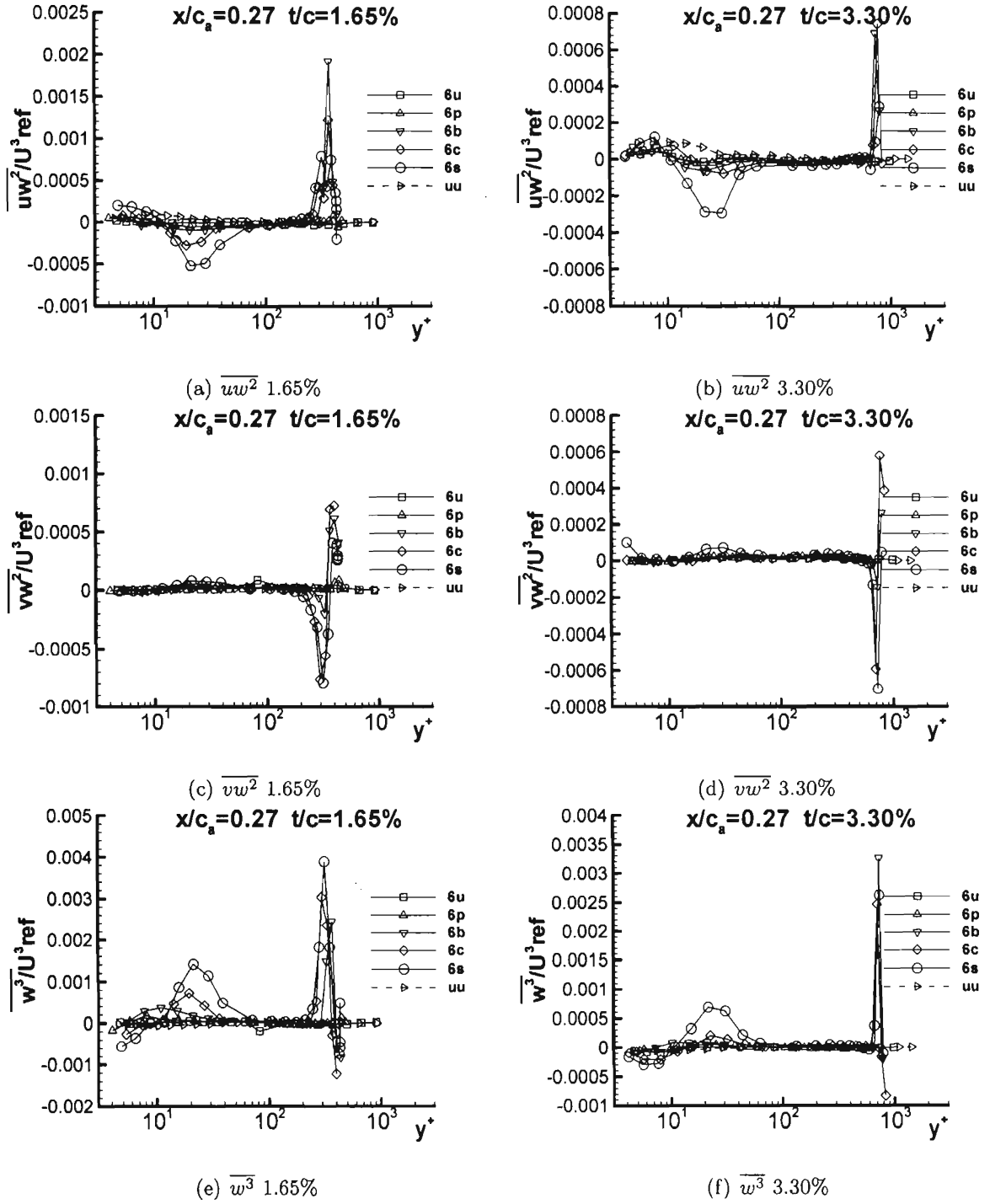


Figure G.24: Triple products  $\overline{uw^2}/U^3_{ref}$ ,  $\overline{vw^2}/U^3_{ref}$ , and  $\overline{w^3}/U^3_{ref}$  at  $x/c_a = 0.27$  for both 1.65% and 3.30% in chord coordinate system



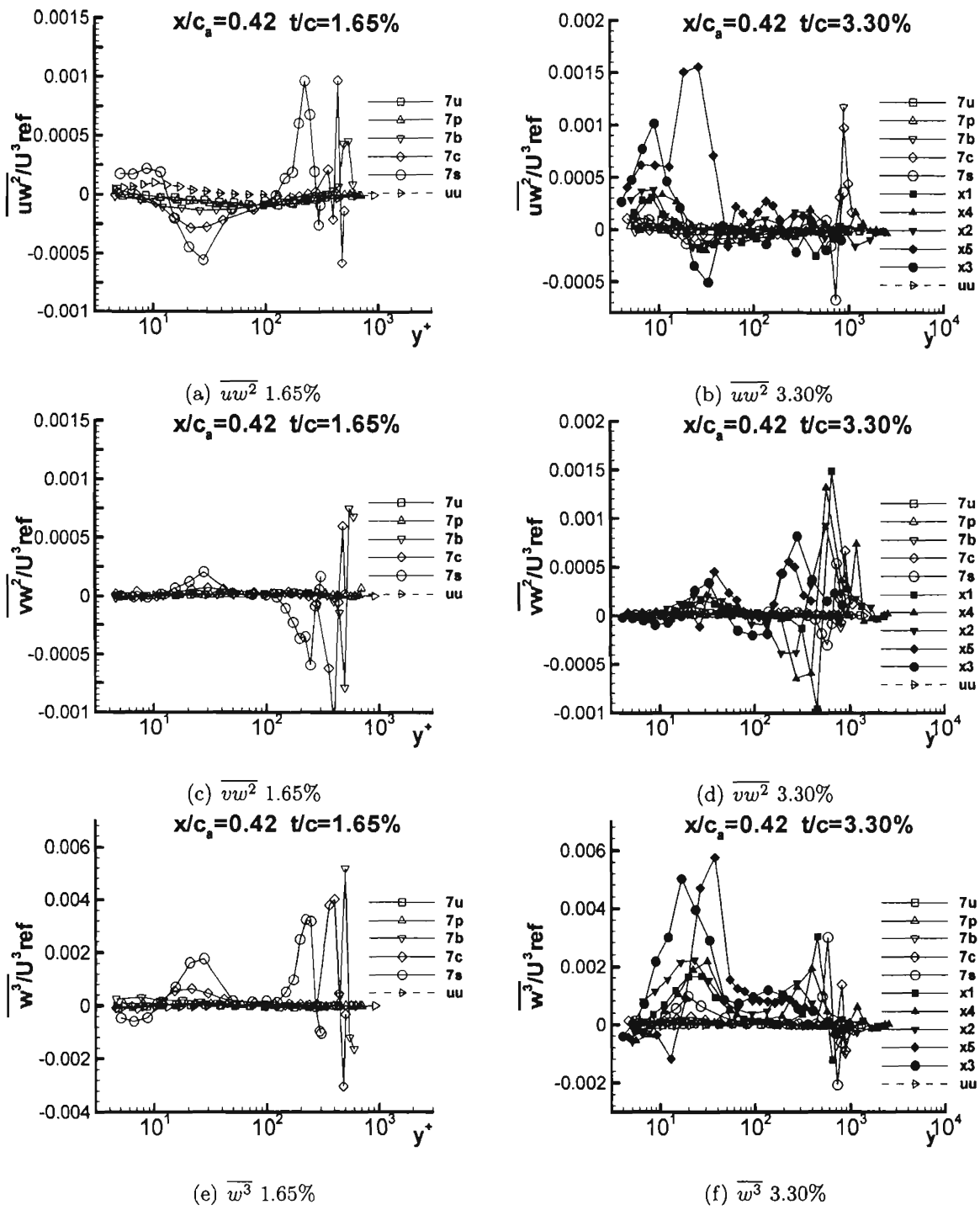


Figure G.25: Triple products  $\overline{uw^2}/U_{ref}^3$ ,  $\overline{vw^2}/U_{ref}^3$ , and  $\overline{w^3}/U_{ref}^3$  at  $x/c_a = 0.42$  for both 1.65% and 3.30% in chord coordinate system

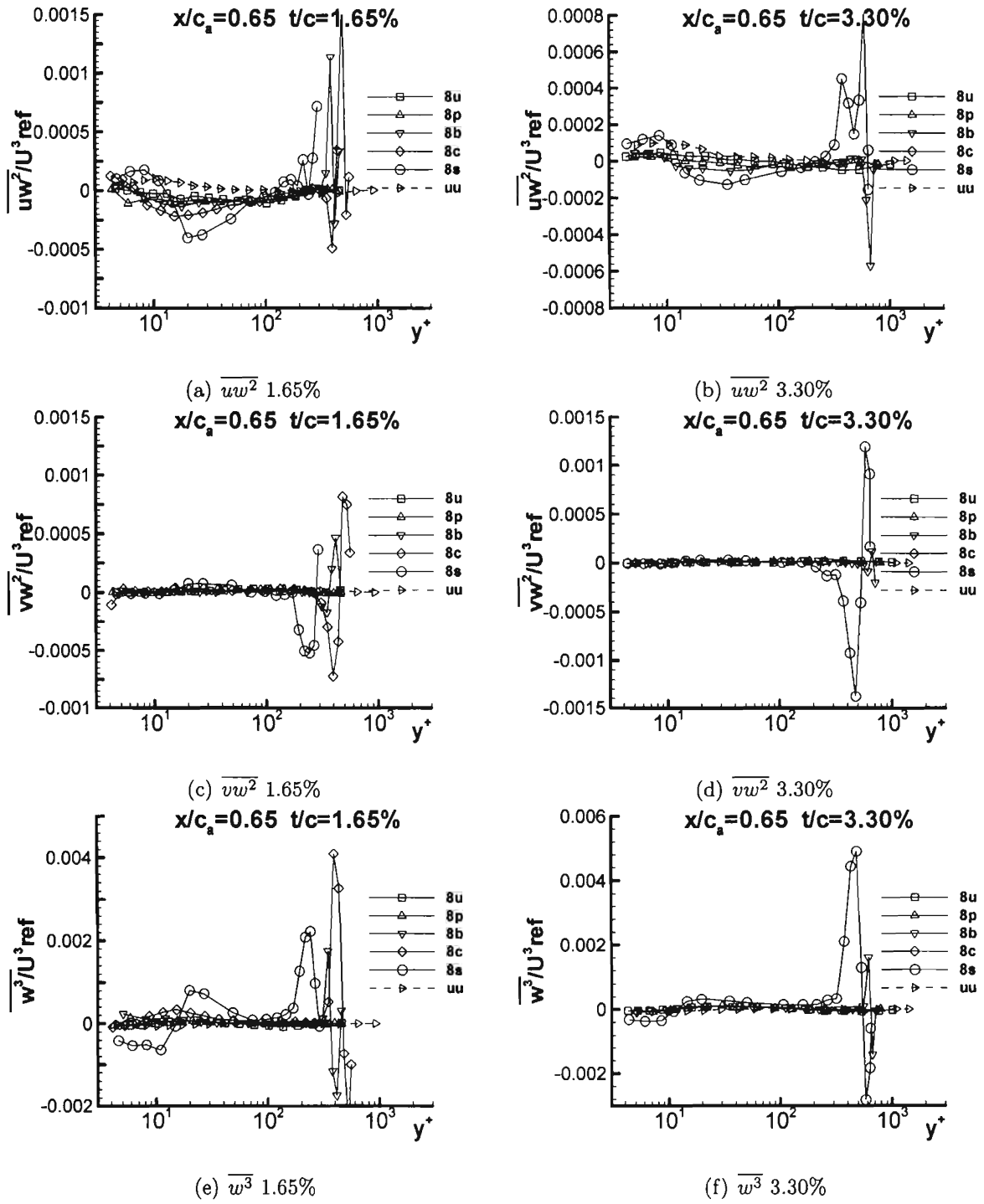


Figure G.26: Triple products  $\overline{uw^2}/U^3_{ref}$ ,  $\overline{vw^2}/U^3_{ref}$ , and  $\overline{w^3}/U^3_{ref}$  at  $x/c_a = 0.65$  for both 1.65% and 3.30% in chord coordinate system

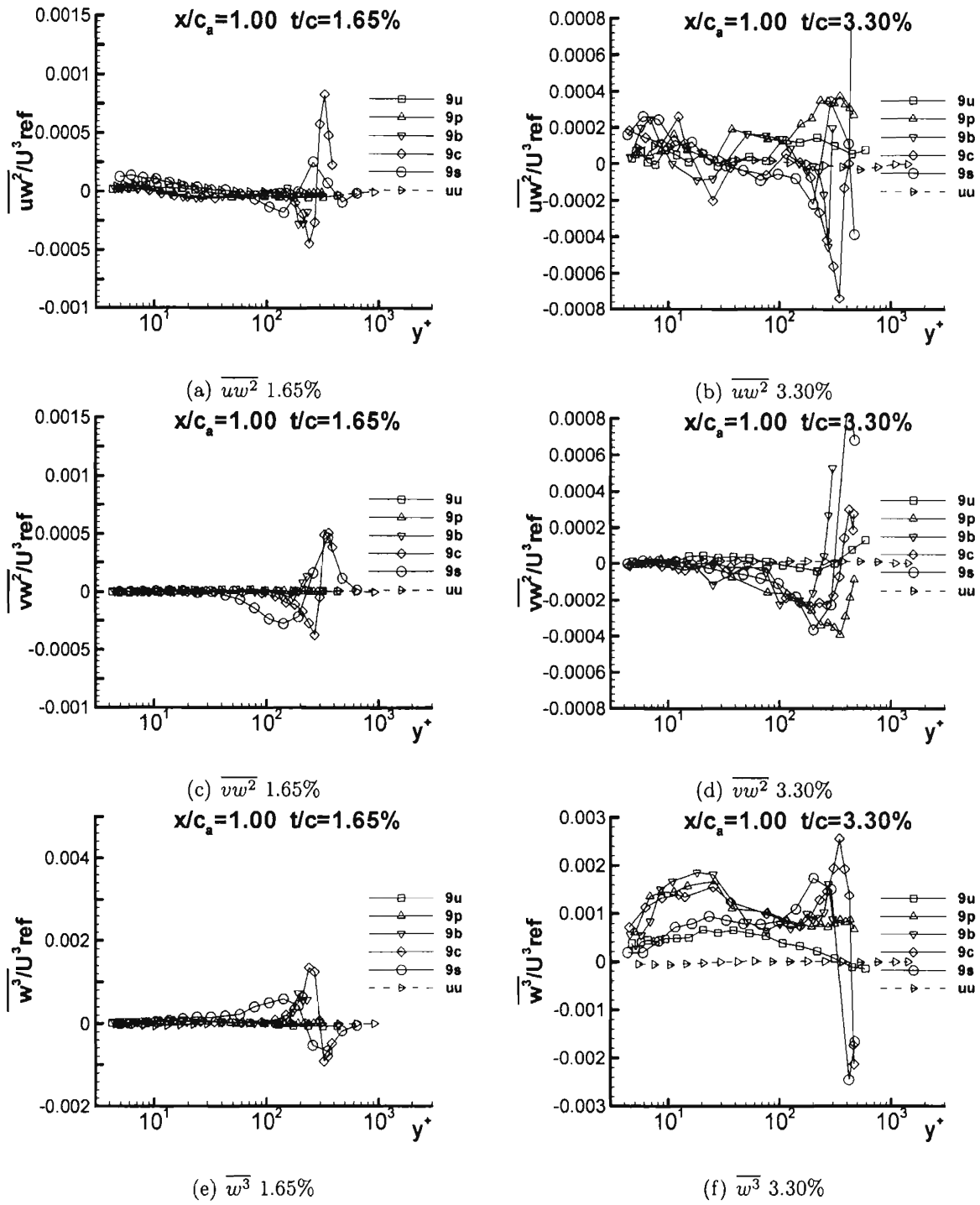
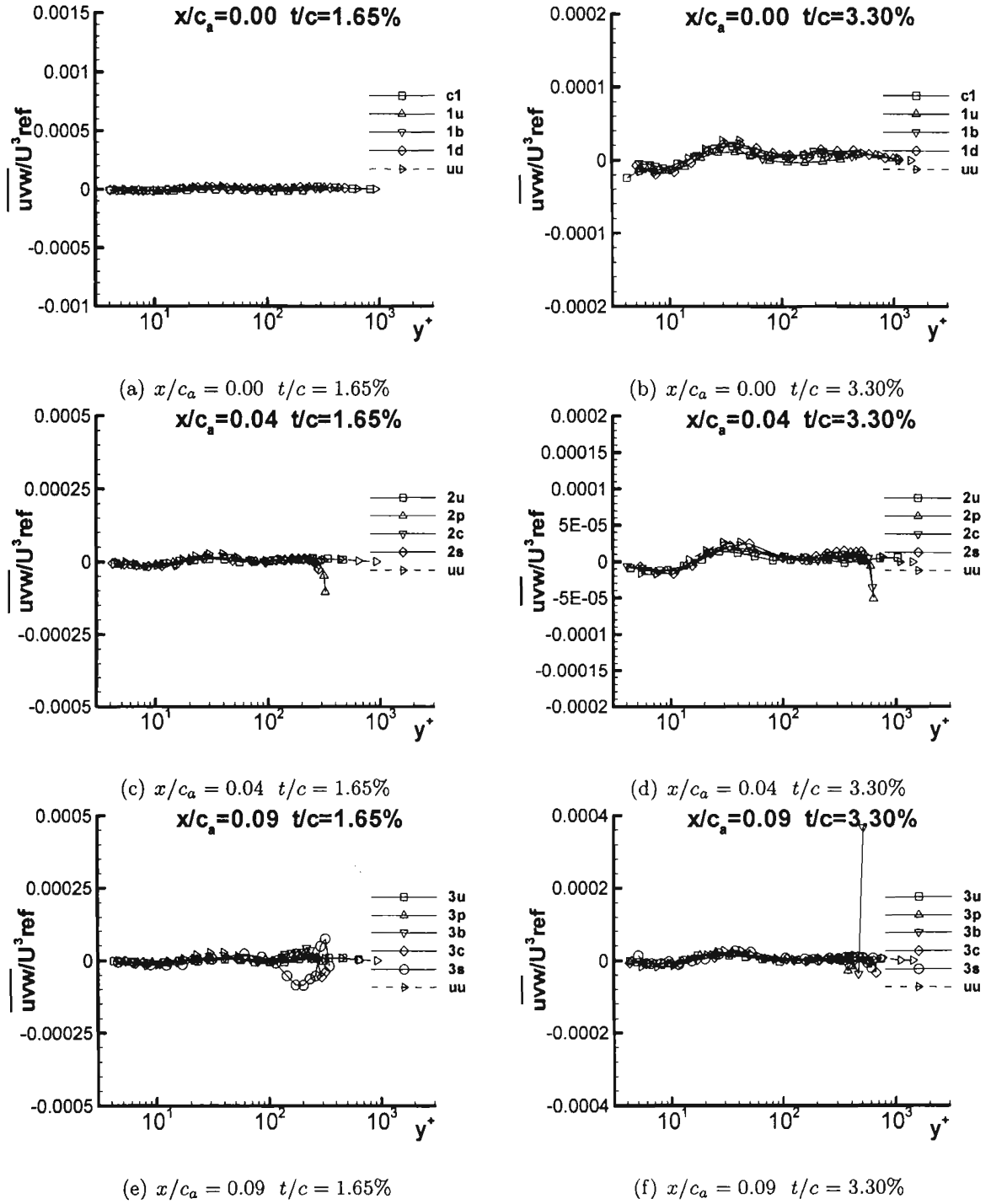
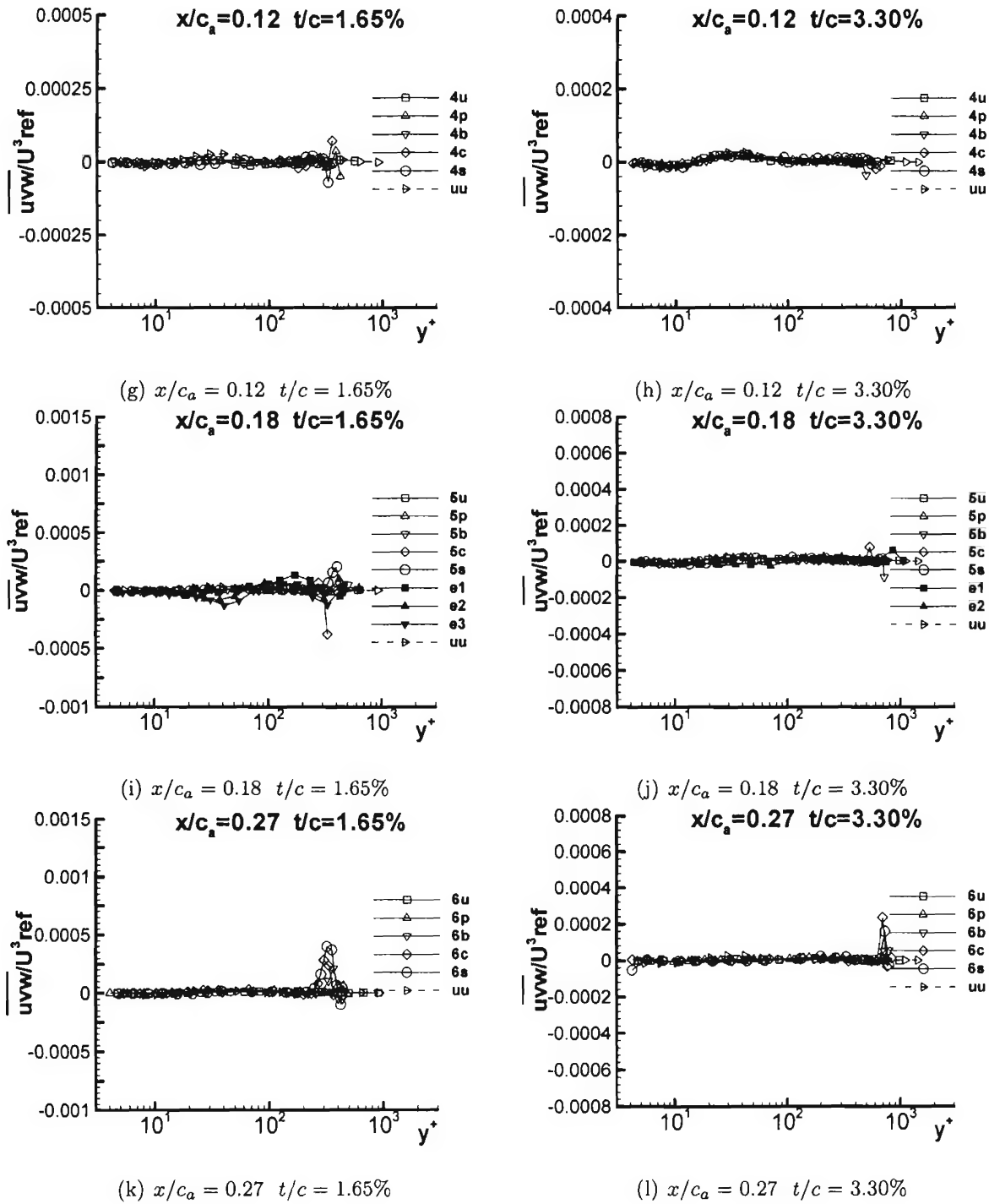
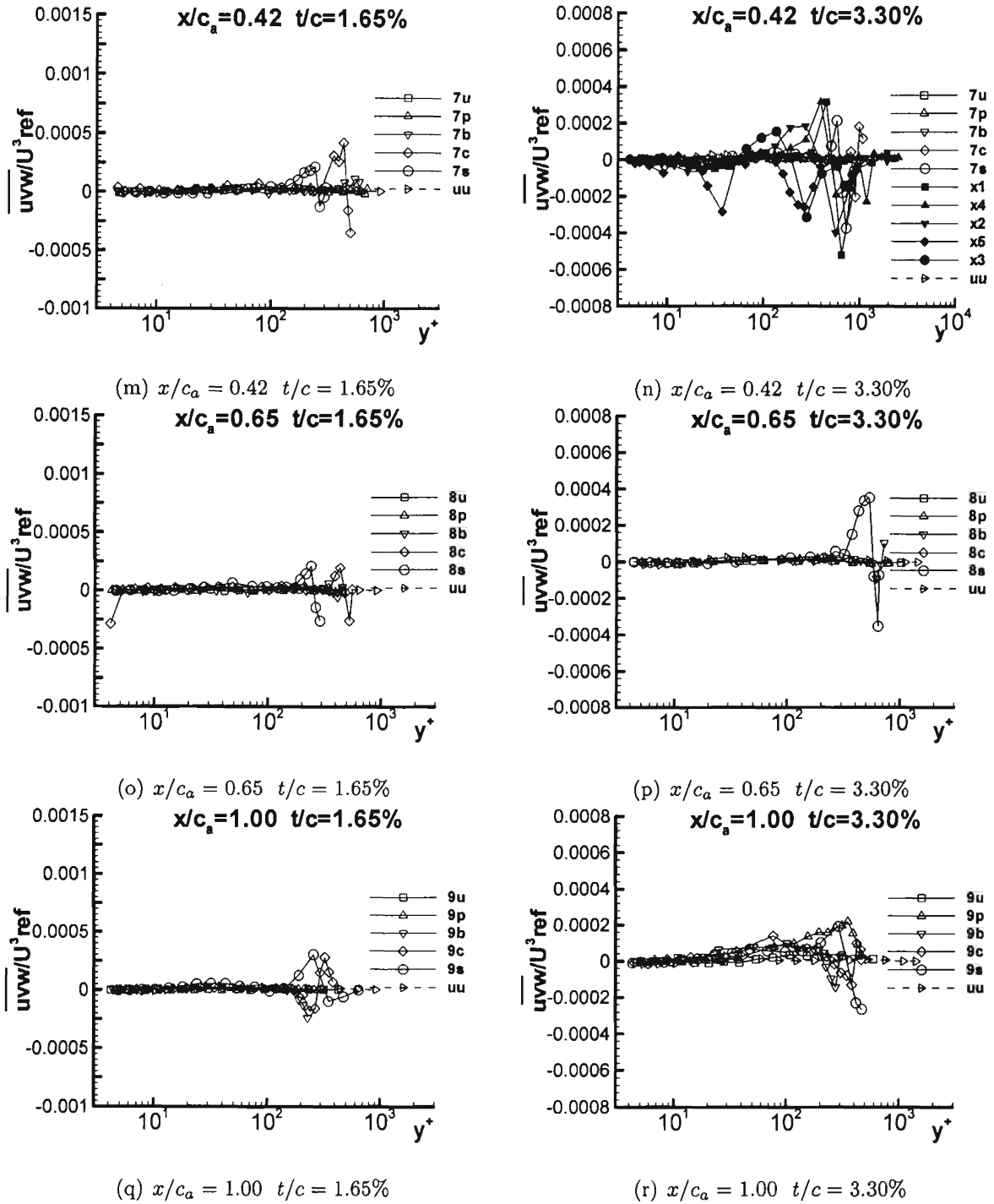


Figure G.27: Triple products  $\overline{uw^2}/U_{ref}^3$ ,  $\overline{vw^2}/U_{ref}^3$ , and  $\overline{w^3}/U_{ref}^3$  at  $x/c_a = 1.00$  for both 1.65% and 3.30% in chord coordinate system

Figure G.28:  $\overline{uvw}/U_{ref}^3$  for both 1.65% and 3.30% in chord coordinate system

Figure G.28:  $\overline{uvw}/U_{ref}^3$  for both 1.65% and 3.30% in chord coordinate system (cont.)

Figure G.28:  $\overline{uvw}/U_{ref}^3$  for both 1.65% and 3.30% in chord coordinate system (cont.)

## Appendix H

### Comprehensive Parameters for a Stationary Endwall

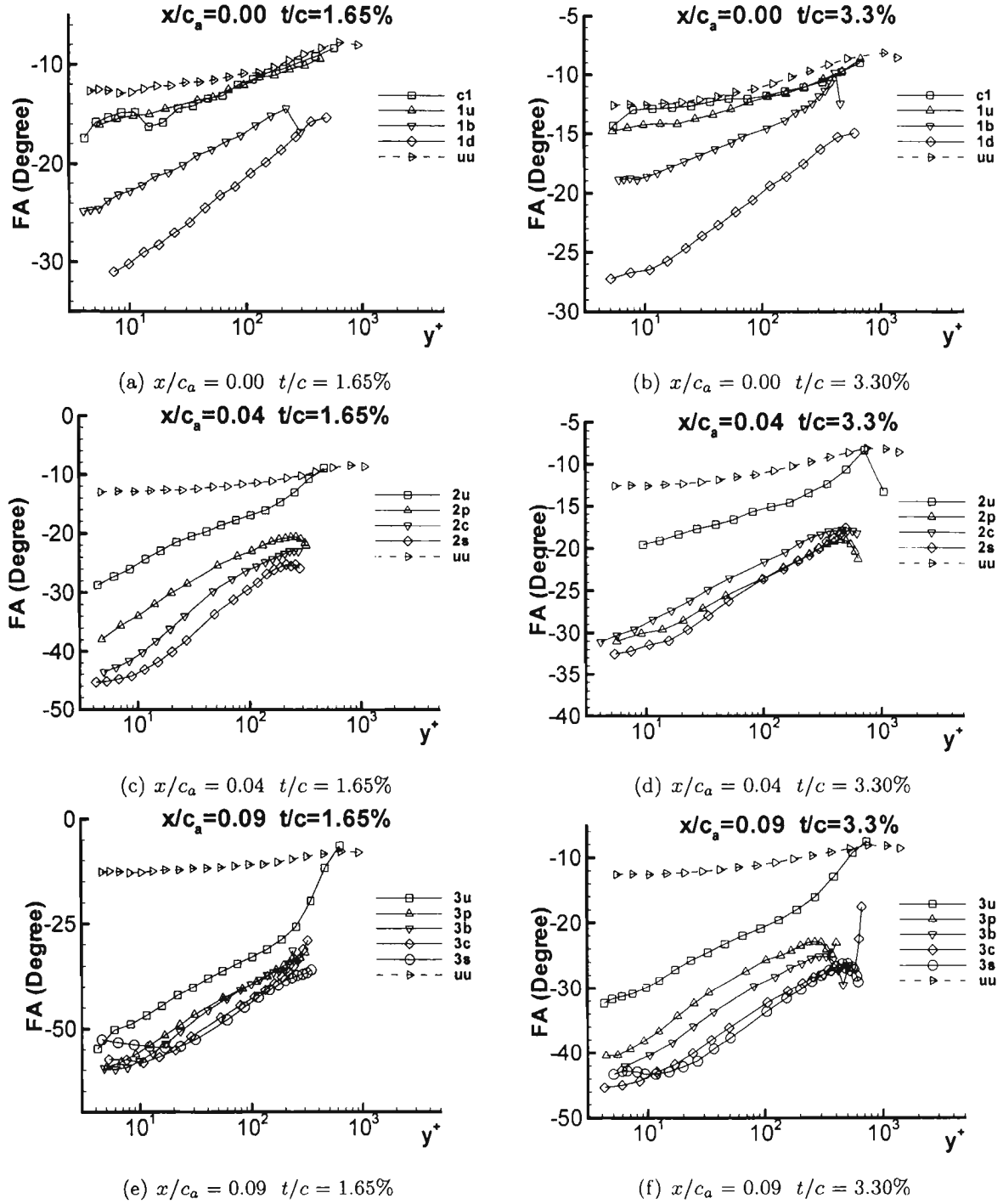


Figure H.1: Flow angle (FA) for both 1.65% and 3.30% in chord coordinate system



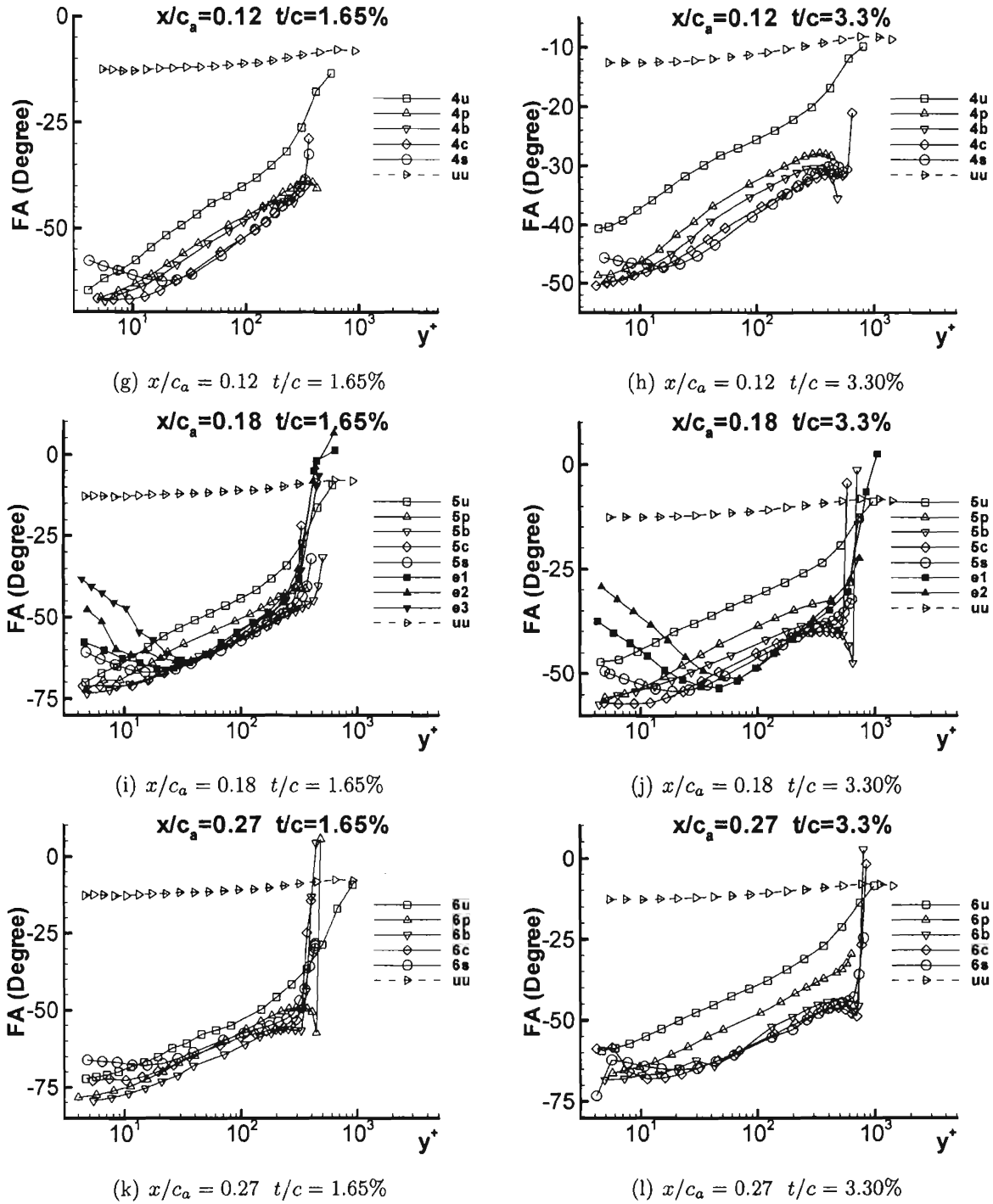


Figure H.1: Flow angle (FA) for both 1.65% and 3.30% in chord coordinate system (cont.)

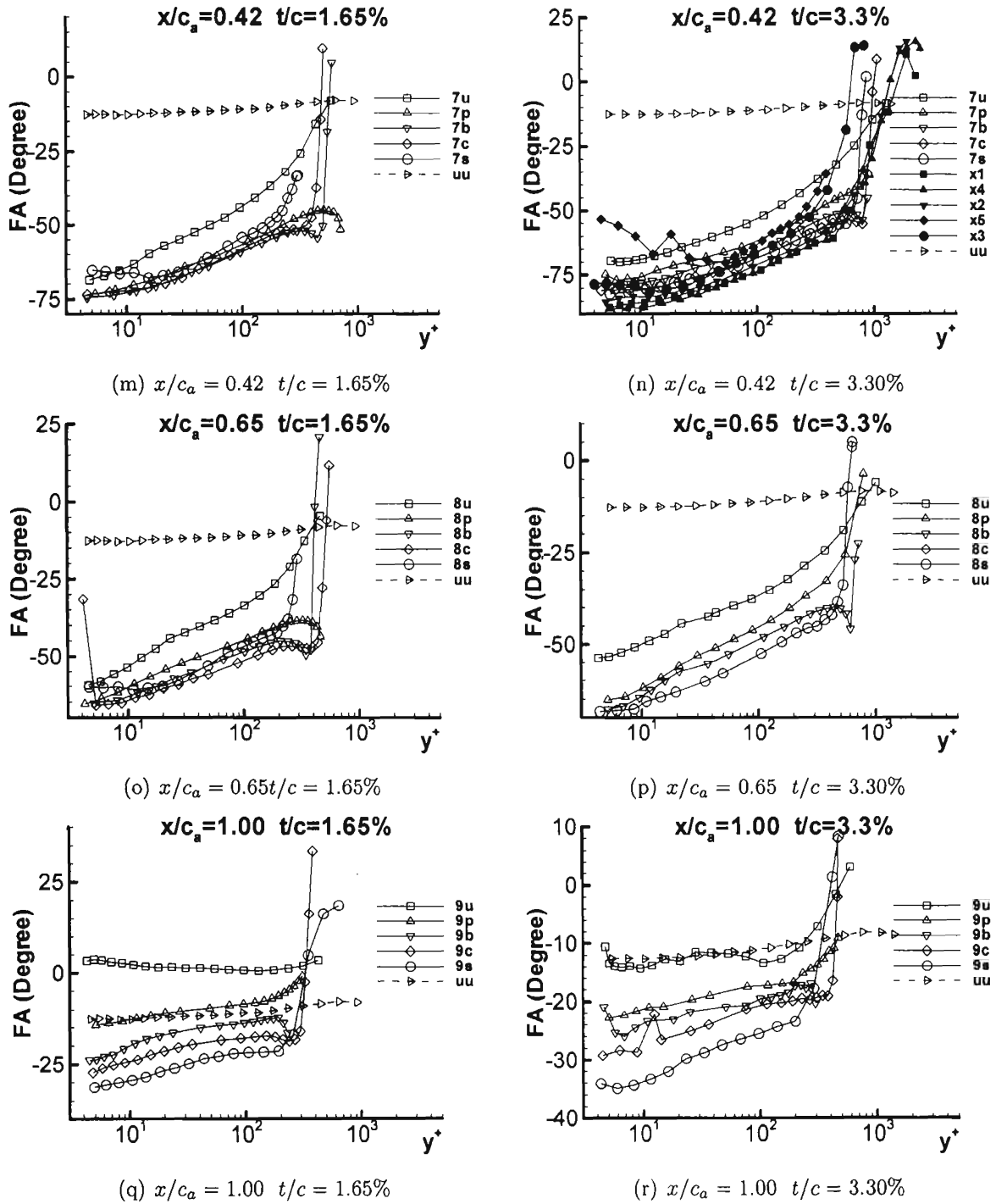


Figure H.1: Flow angle (FA) for both 1.65% and 3.30% in chord coordinate system (cont.)

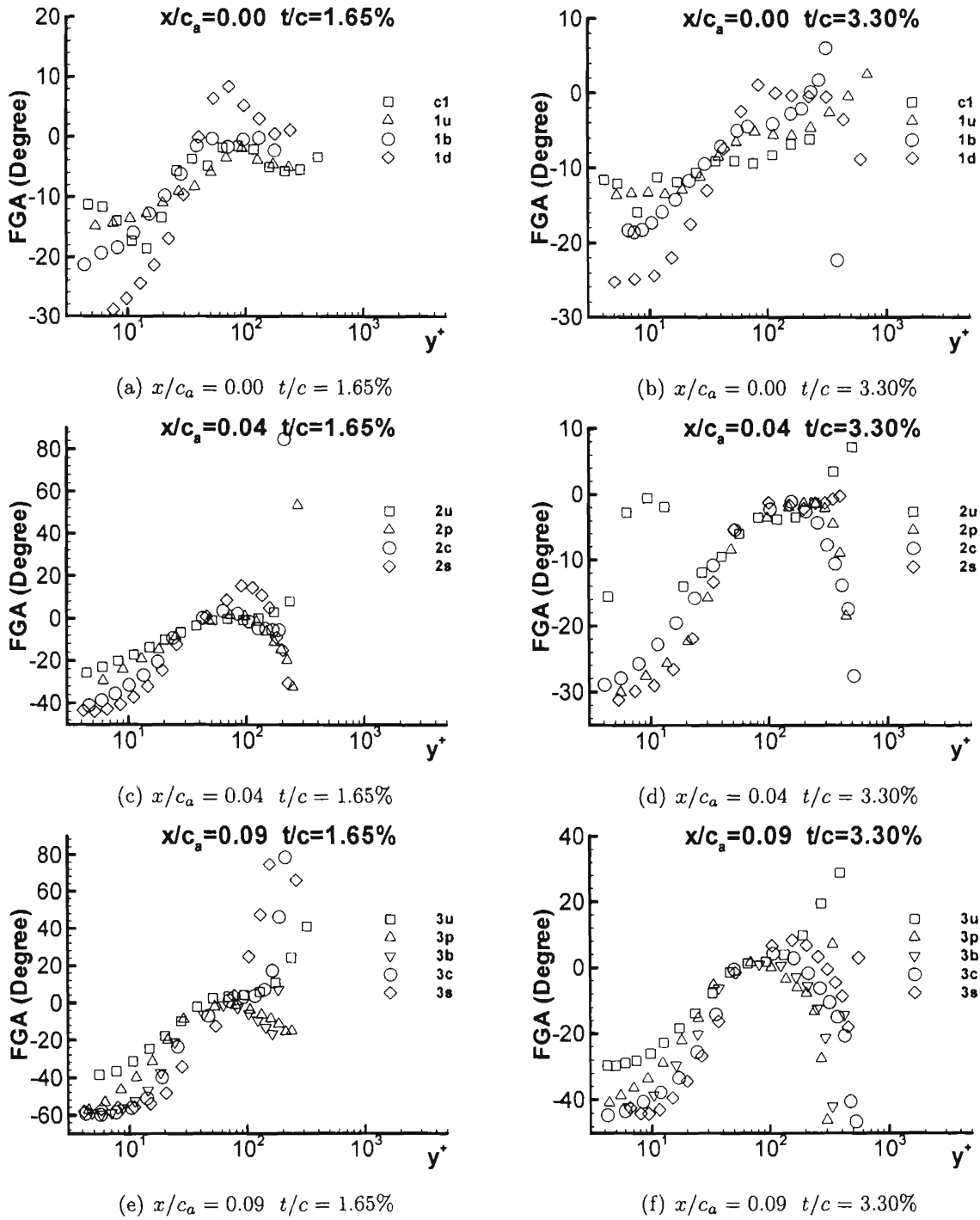


Figure H.2: Flow gradient angle (FGA) for both 1.65% and 3.30% in chord coordinate system

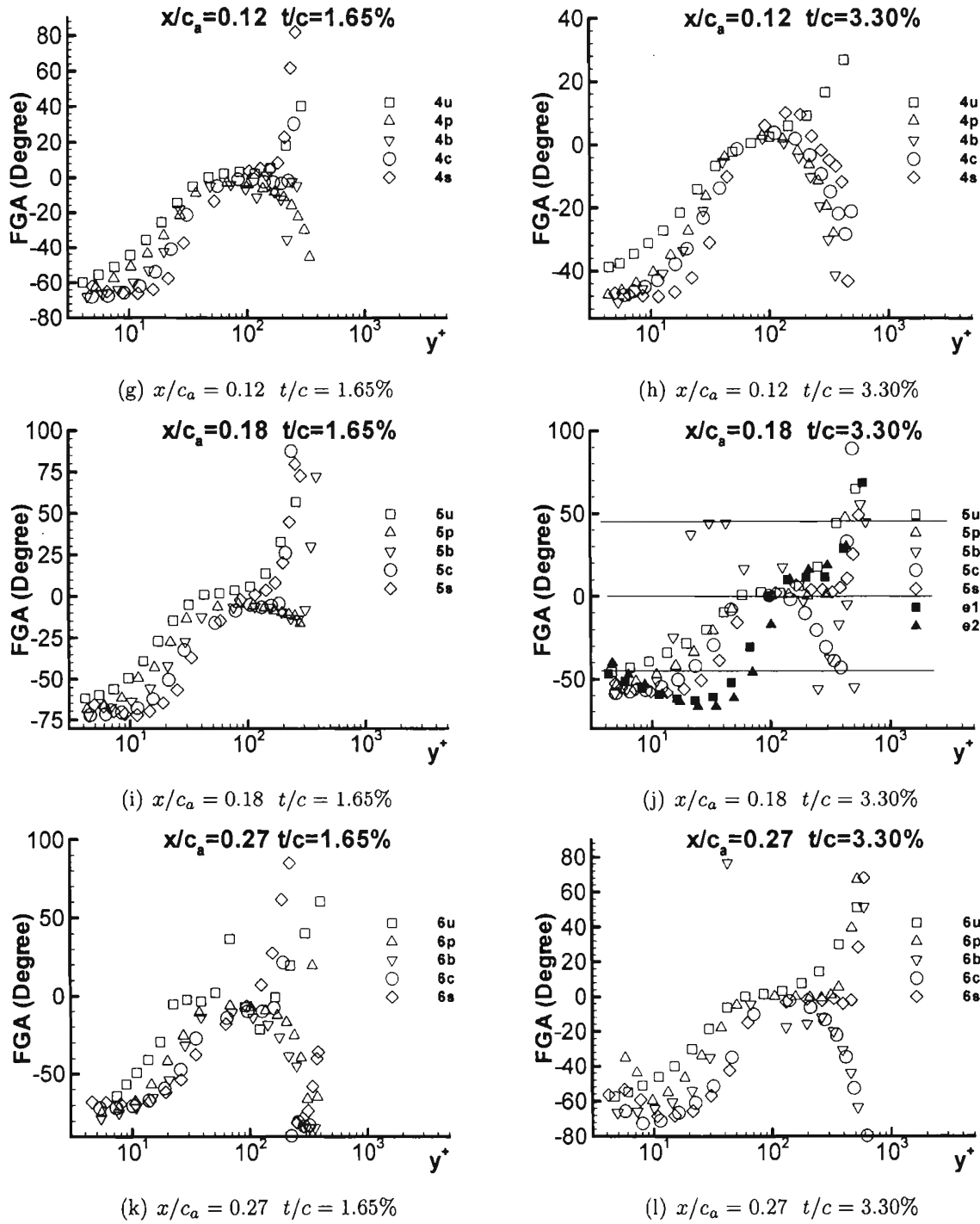


Figure H.2: Flow gradient angle (FGA) for both 1.65% and 3.30% in chord coordinate system (cont.)

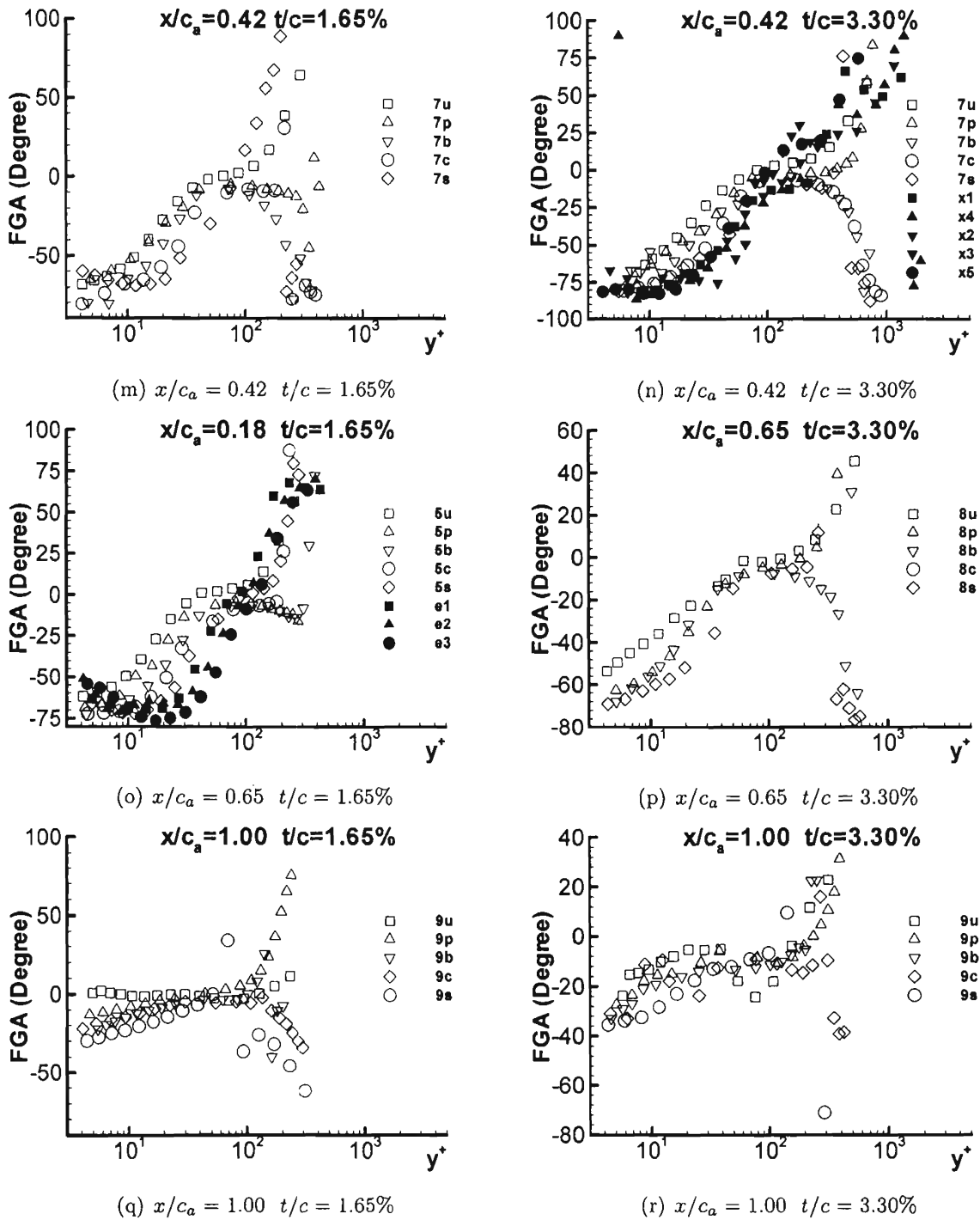


Figure H.2: Flow gradient angle (FGA) for both 1.65% and 3.30% in chord coordinate system (cont.)

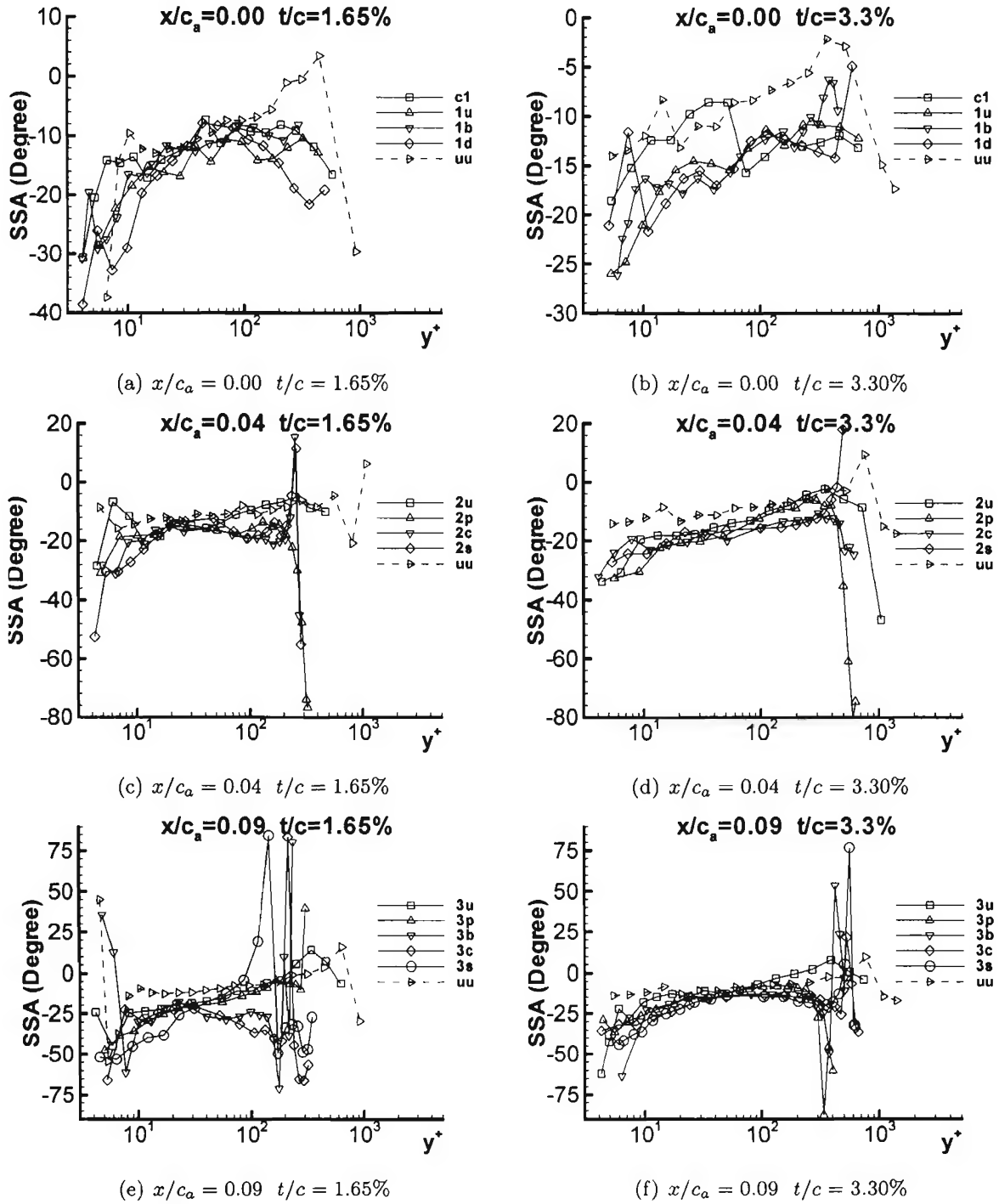


Figure H.3: Shear stress angle (SSA) for both 1.65% and 3.30% in chord coordinate system

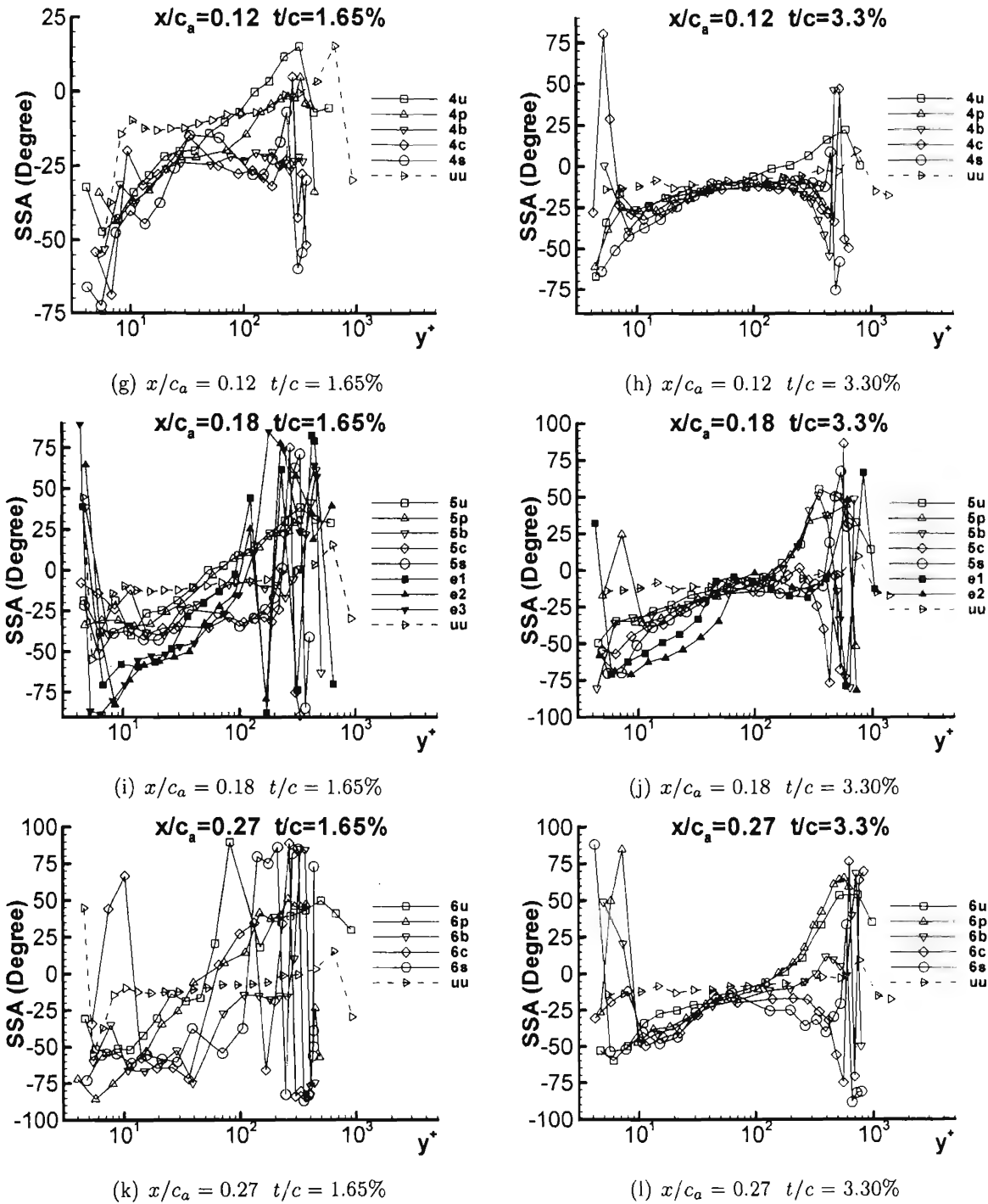


Figure H.3: Shear stress angle (SSA) for both 1.65% and 3.30% in chord coordinate system (cont.)

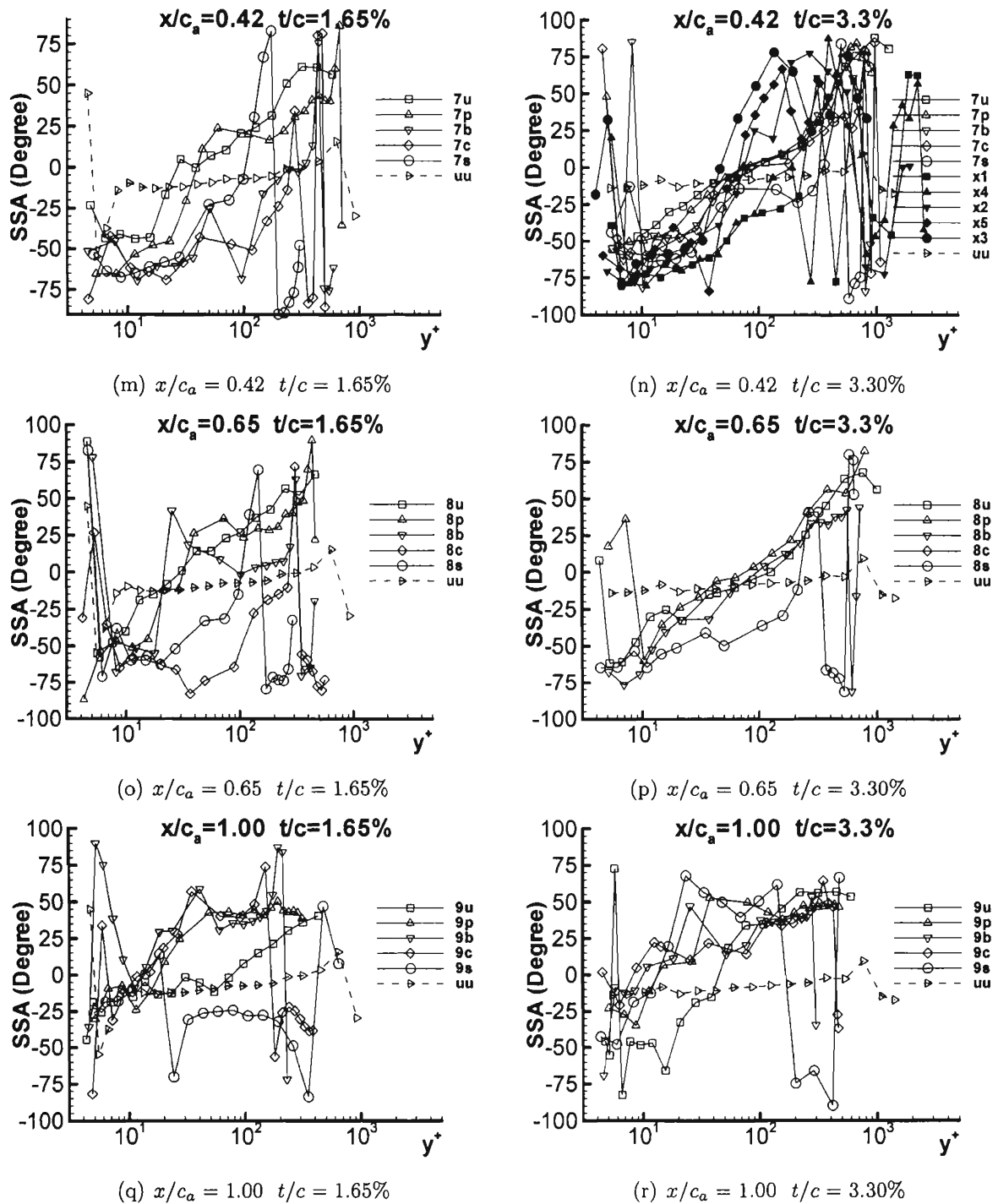


Figure H.3: Shear stress angle (SSA) for both 1.65% and 3.30% in chord coordinate system (cont.)



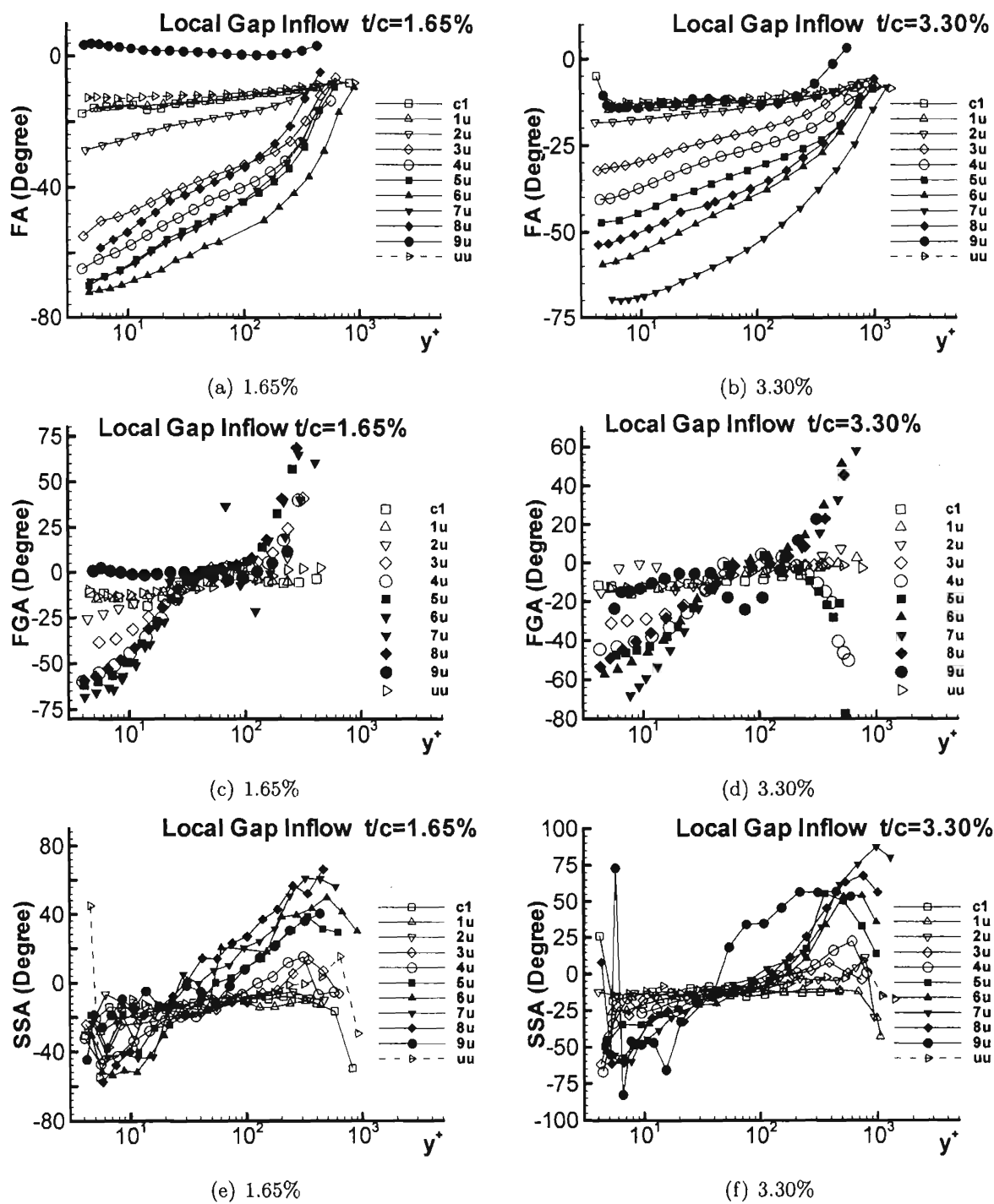


Figure H.4: FA, FGA, and SSA away from pressure side for both 1.65% and 3.30% in chord coordinate system

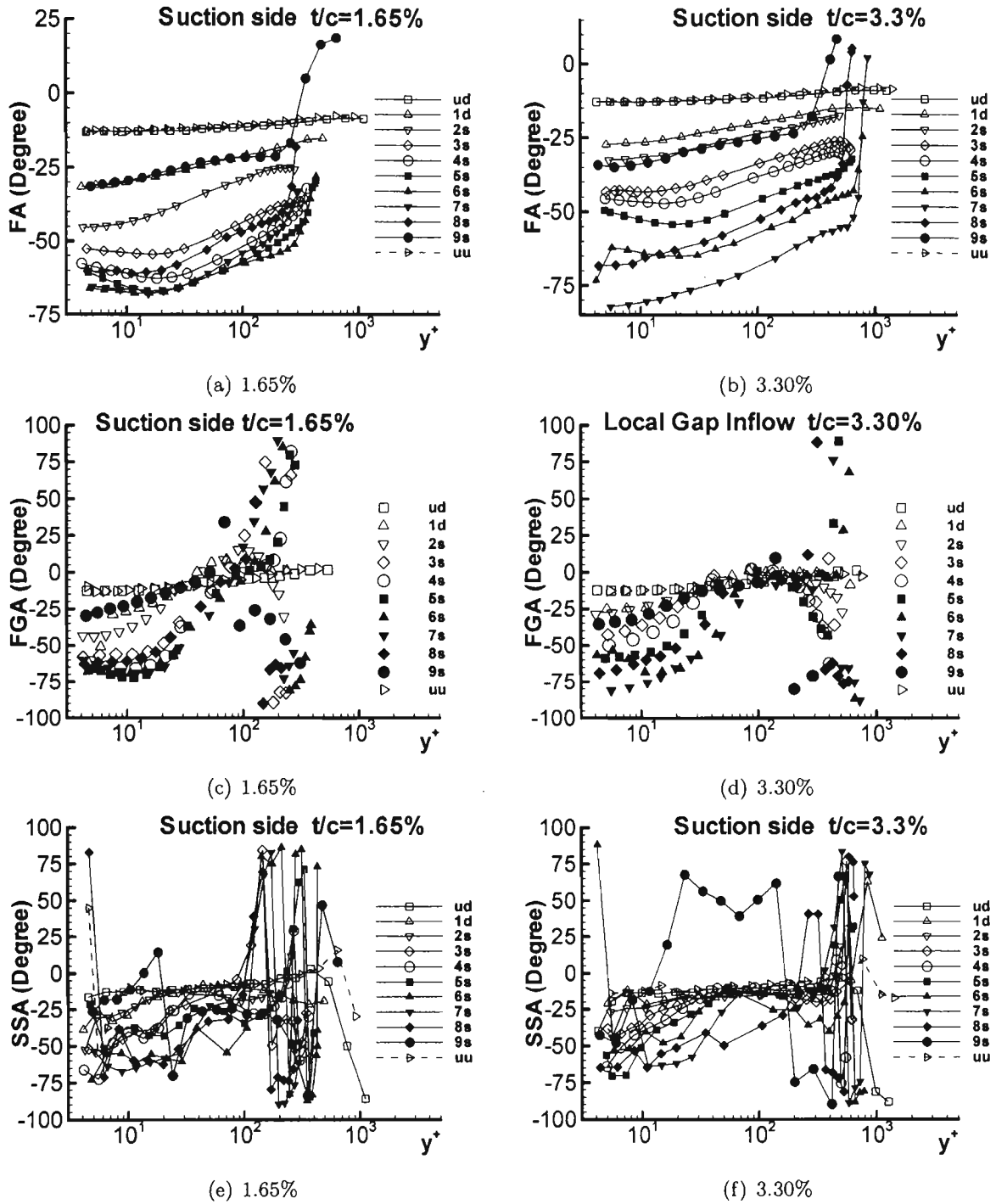
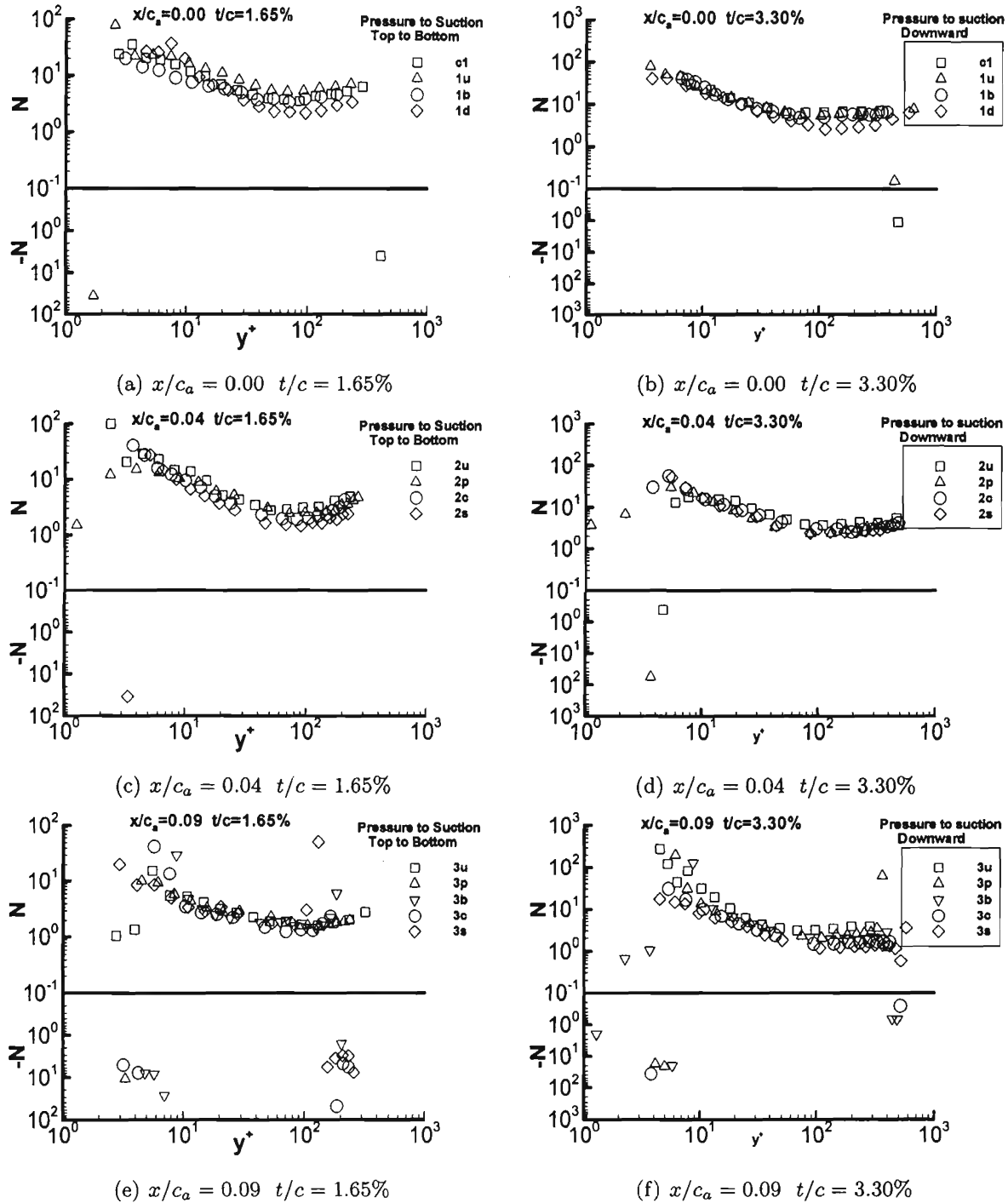
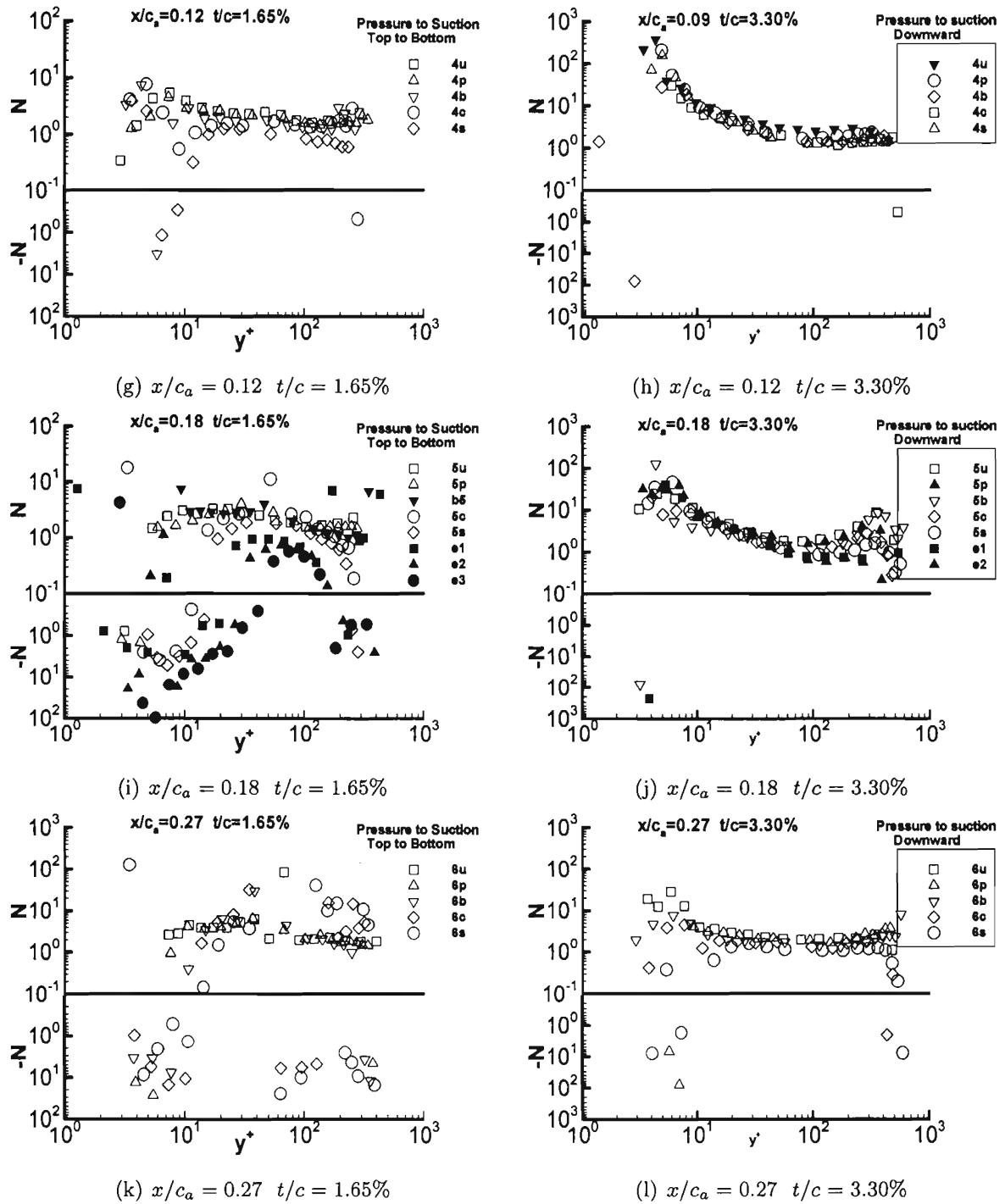
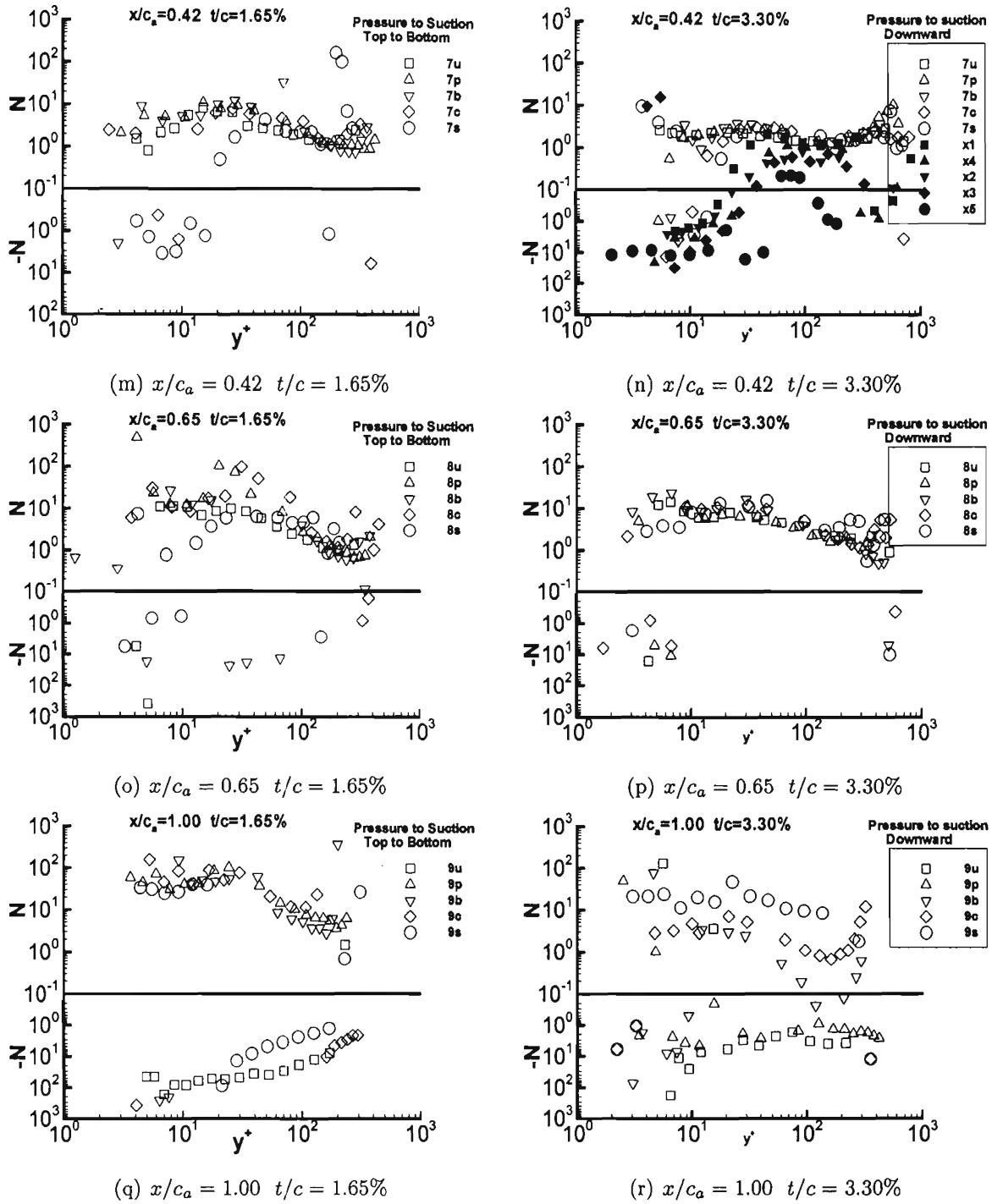
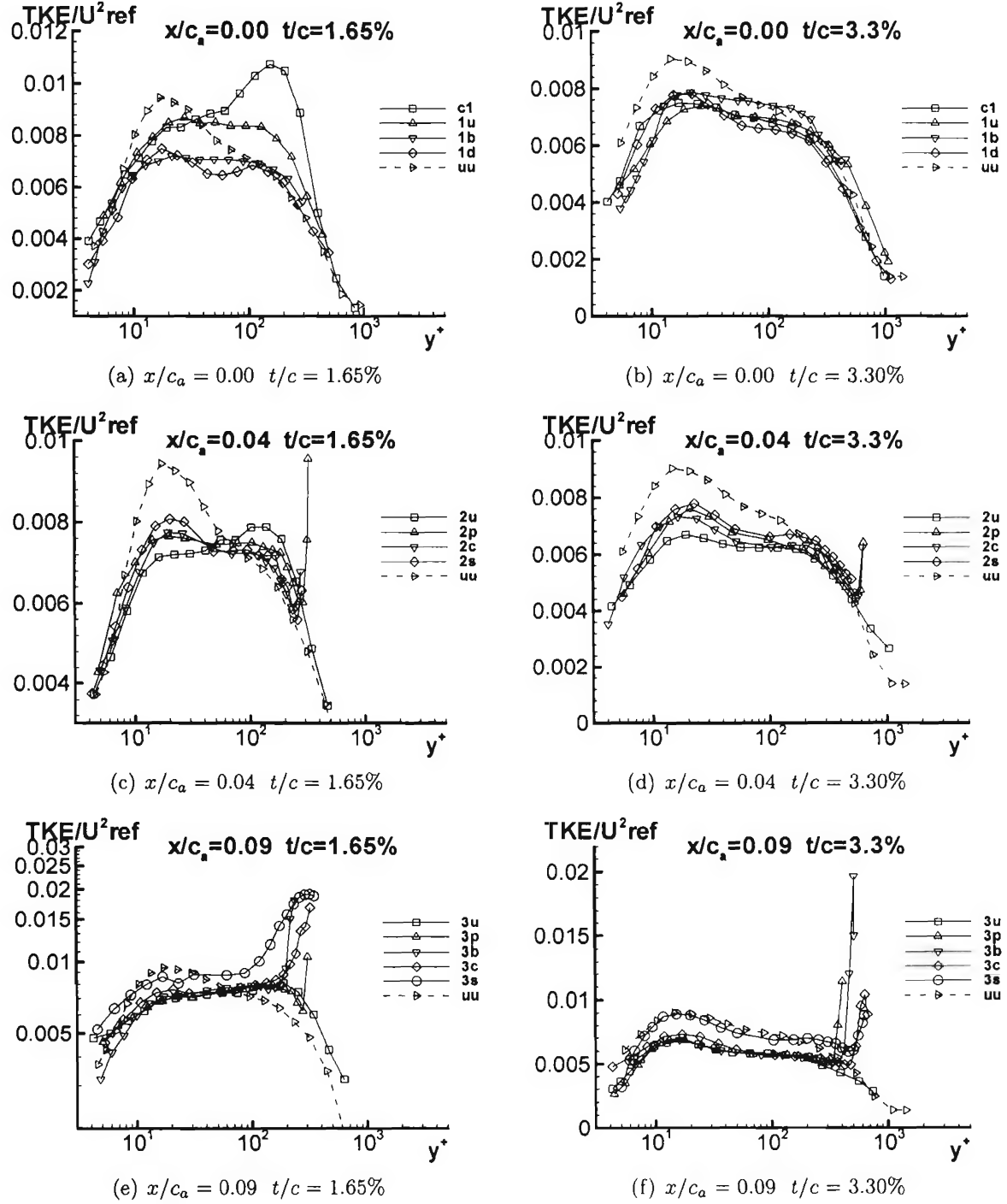


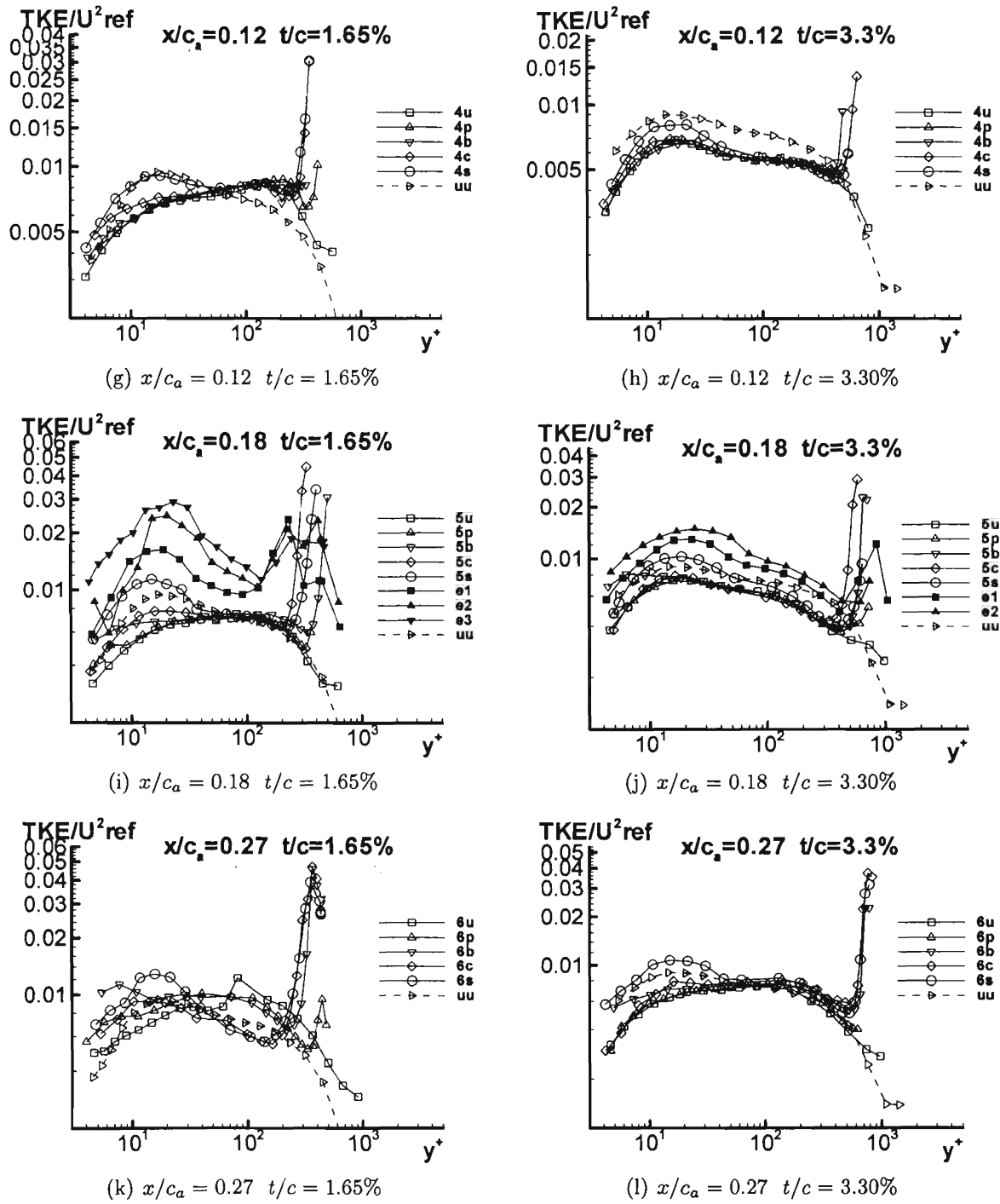
Figure H.5: FA, FGA, and SSA on suction side for both 1.65% and 3.30% in chord coordinate system

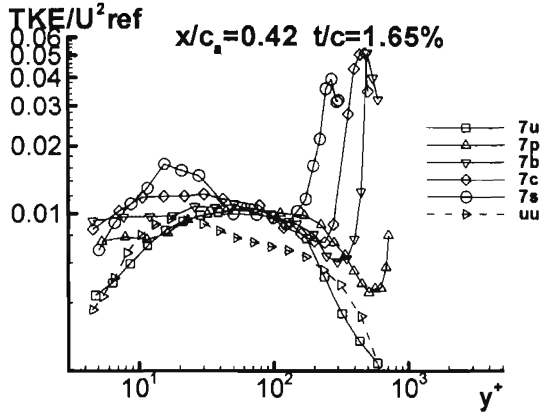
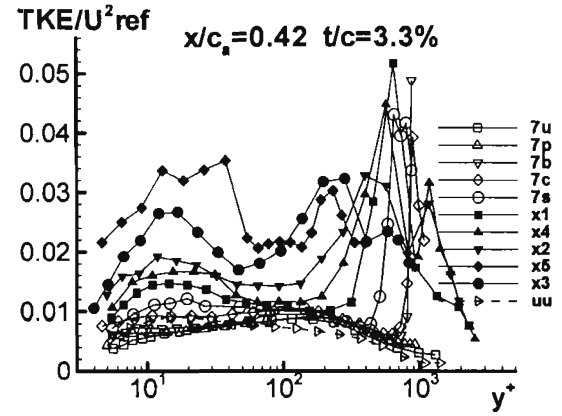
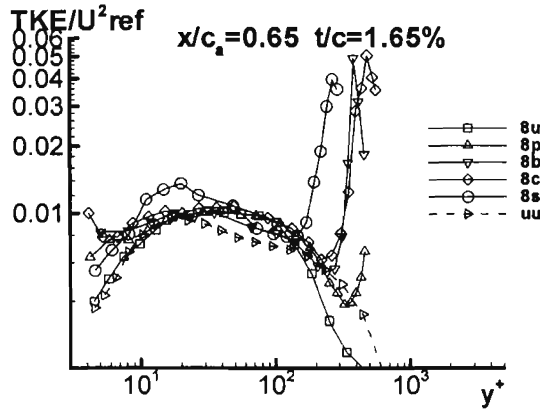
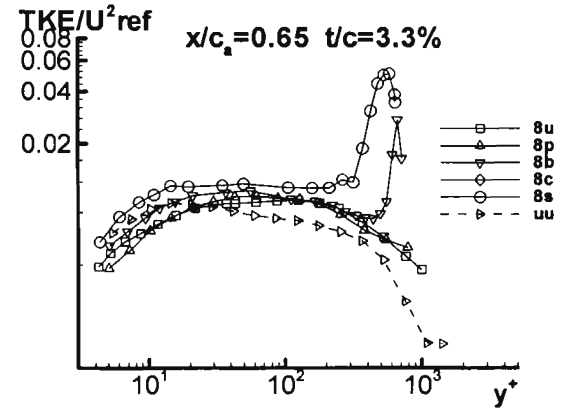
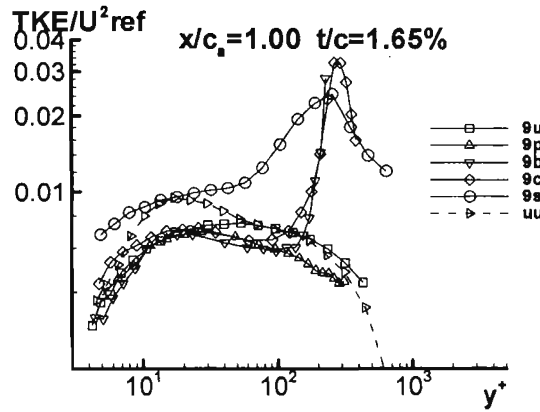
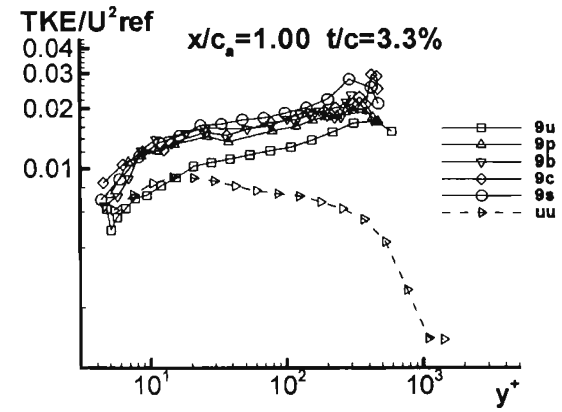
Figure H.6: Anisotropy factor  $N$  for both 1.65% and 3.30% in chord coordinate system

Figure H.6: Anisotropy factor  $N$  for both 1.65% and 3.30% in chord coordinate system (cont.)

Figure H.6: Anisotropy factor  $N$  for both 1.65% and 3.30% in chord coordinate system (cont.)

Figure H.7:  $TKE/U_{ref}^2$  for both 1.65% and 3.30%

Figure H.7:  $TKE/U_{ref}^2$  for both 1.65% and 3.30% (cont.)

(m)  $x/c_a = 0.42$   $t/c = 1.65\%$ (n)  $x/c_a = 0.42$   $t/c = 3.30\%$ (o)  $x/c_a = 0.65$   $t/c = 1.65\%$ (p)  $x/c_a = 0.65$   $t/c = 3.30\%$ (q)  $x/c_a = 1.00$   $t/c = 1.65\%$ (r)  $x/c_a = 1.00$   $t/c = 3.30\%$ Figure H.7:  $TKE/U^2_{ref}$  for both 1.65% and 3.30% (cont.)



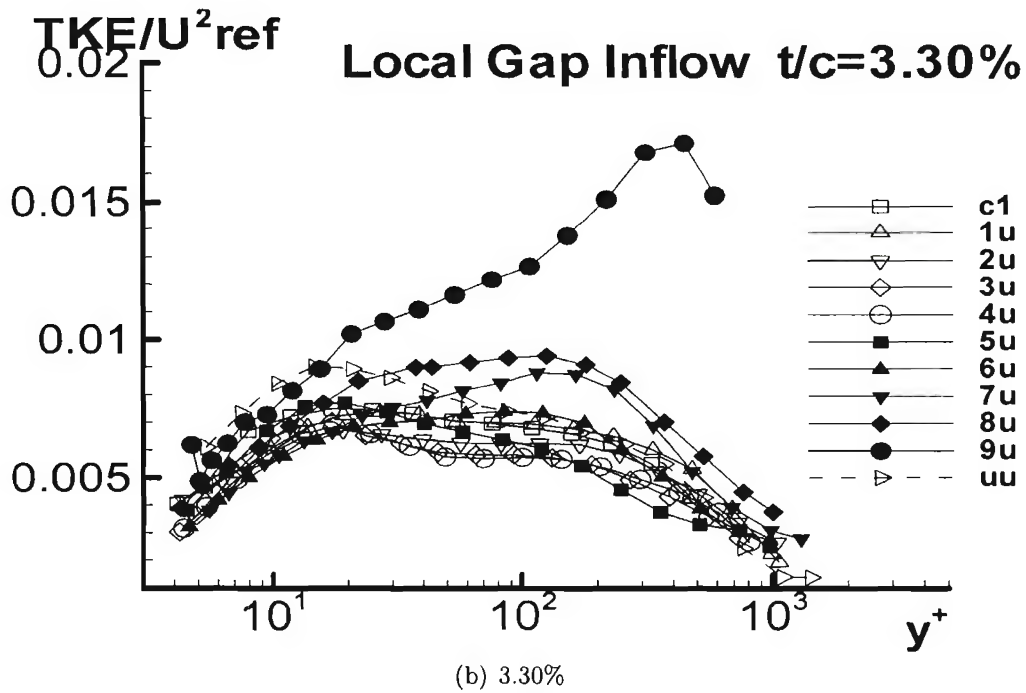
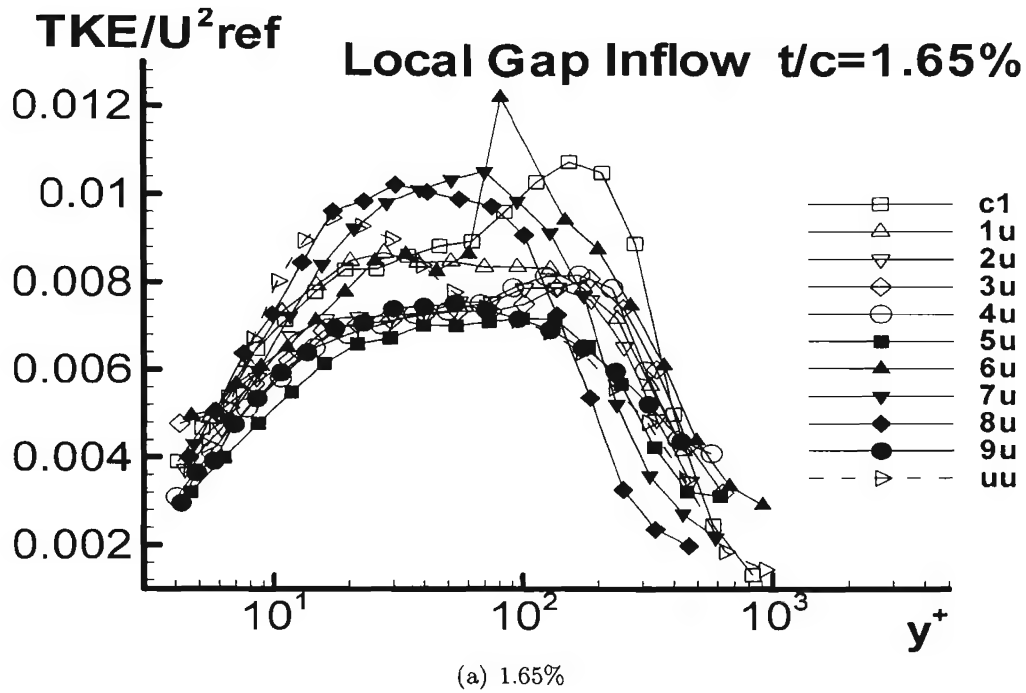


Figure H.8:  $TKE/U_{ref}^2$  of local gap inflow for both 1.65% and 3.30%

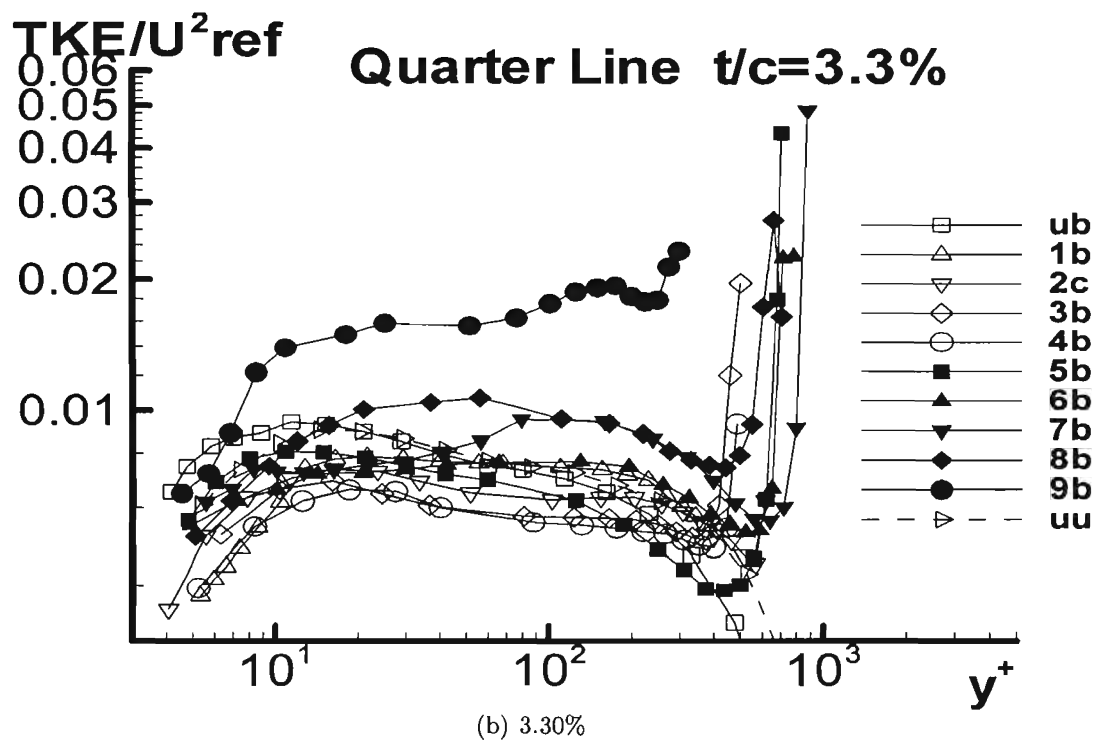
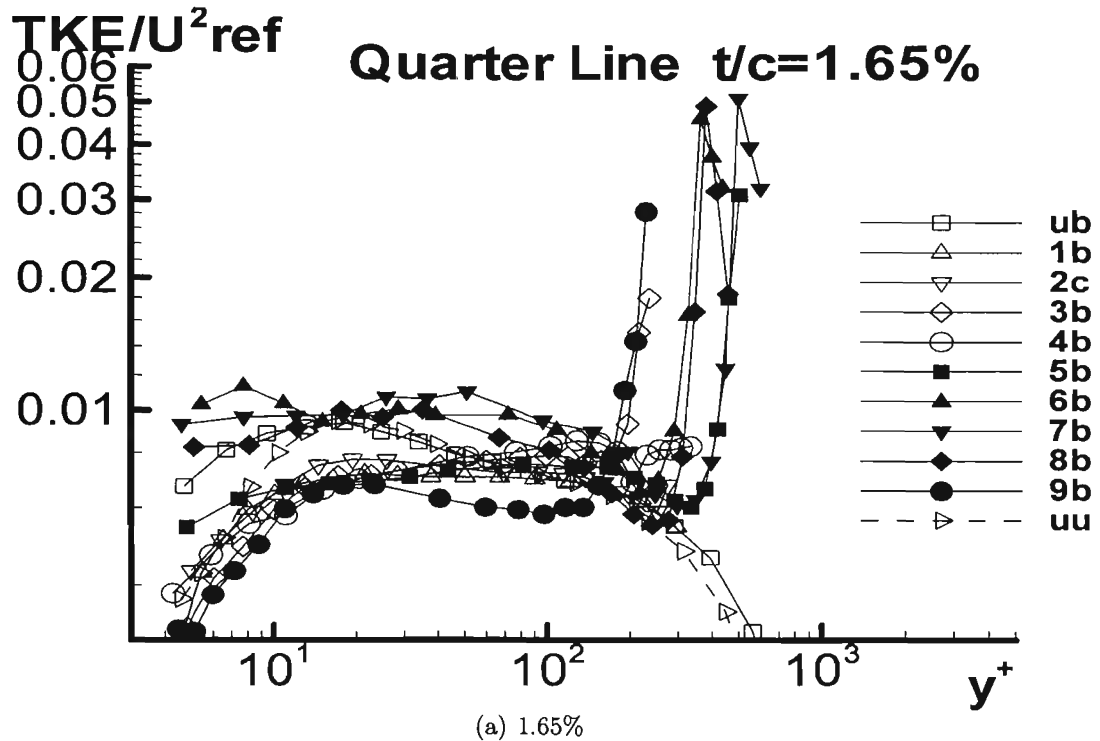
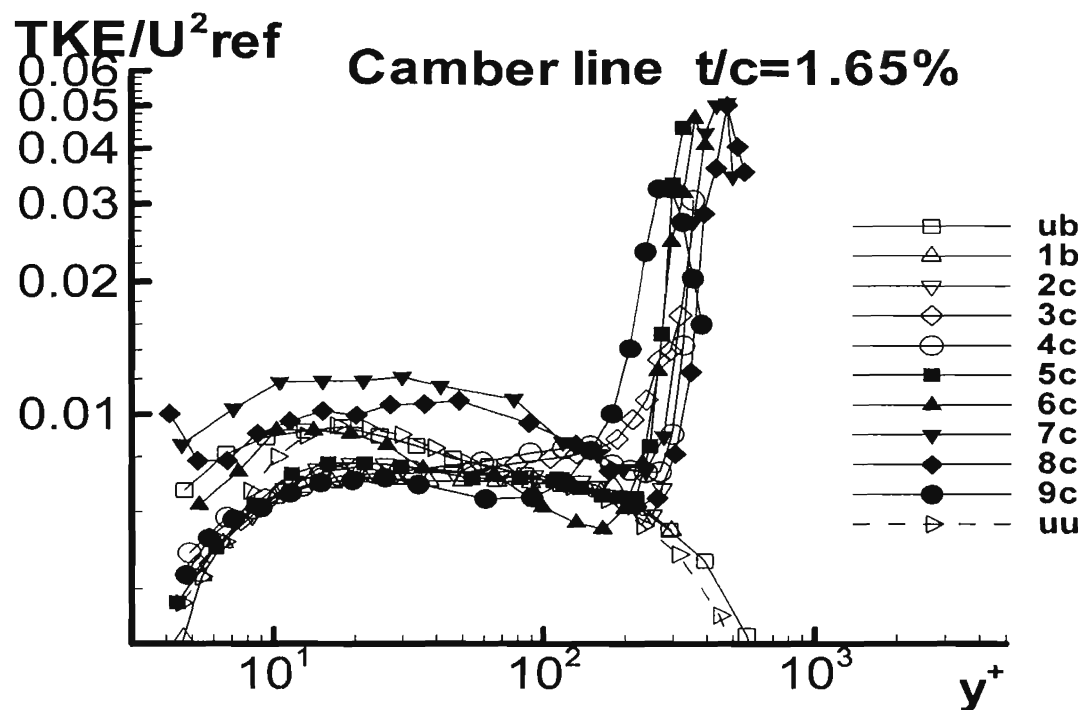
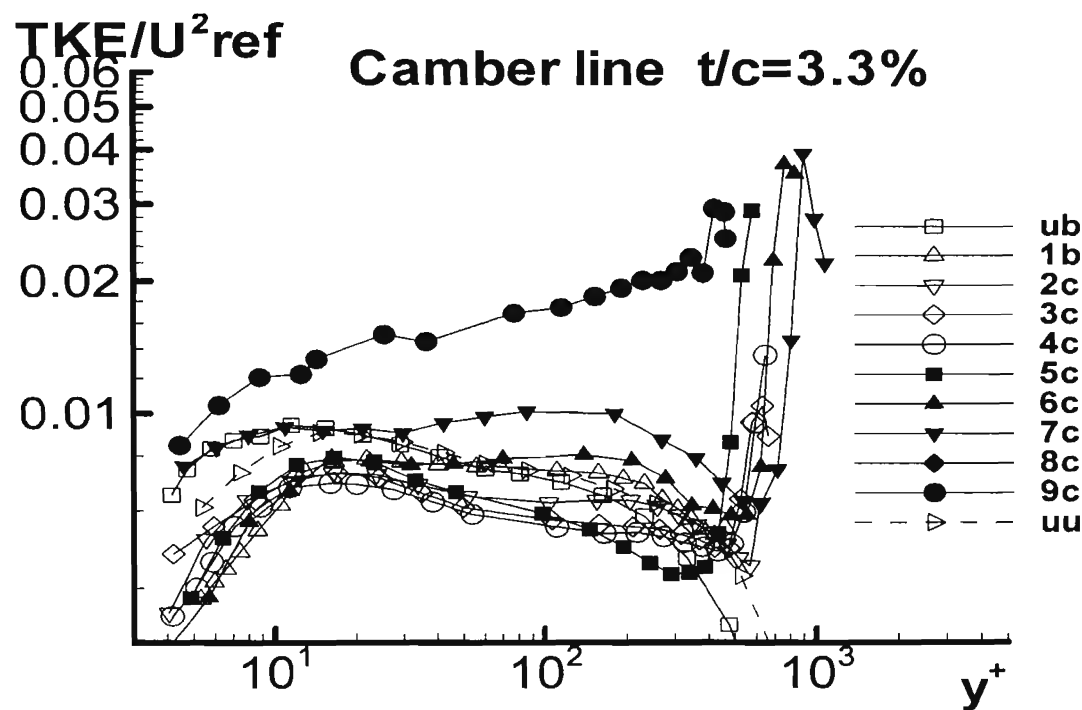


Figure H.9:  $TKE/U^2_{ref}$  underneath quarter line of the blade from the pressure side for both 1.65% and 3.30%

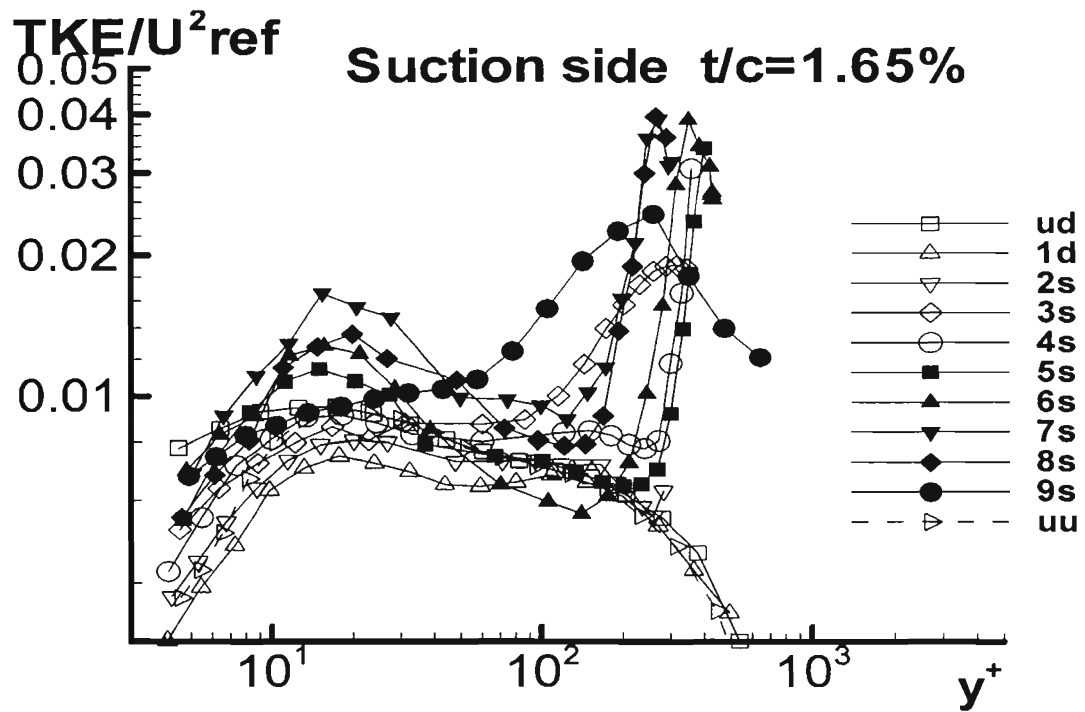


(a) 1.65%

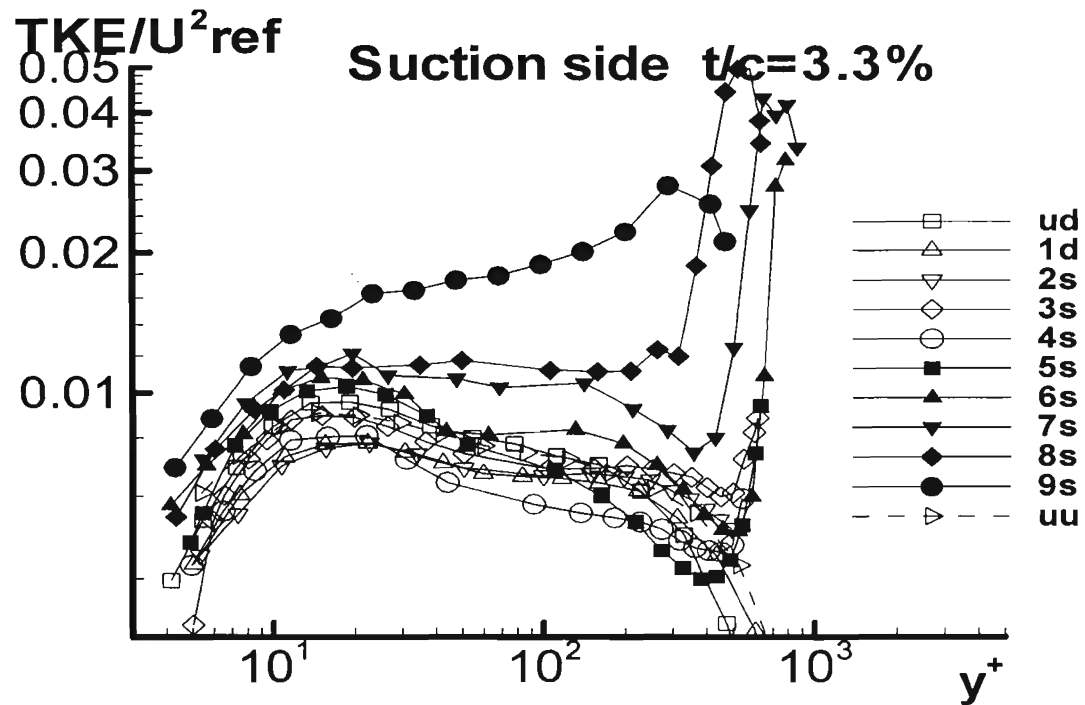


(b) 3.30%

Figure H.10:  $TKE/U_{ref}^2$  underneath the camber line for both 1.65% and 3.30%



(a) 1.65%



(b) 3.30%

Figure H.11:  $TKE/U_{ref}^2$  on the suction side for both 1.65% and 3.30%

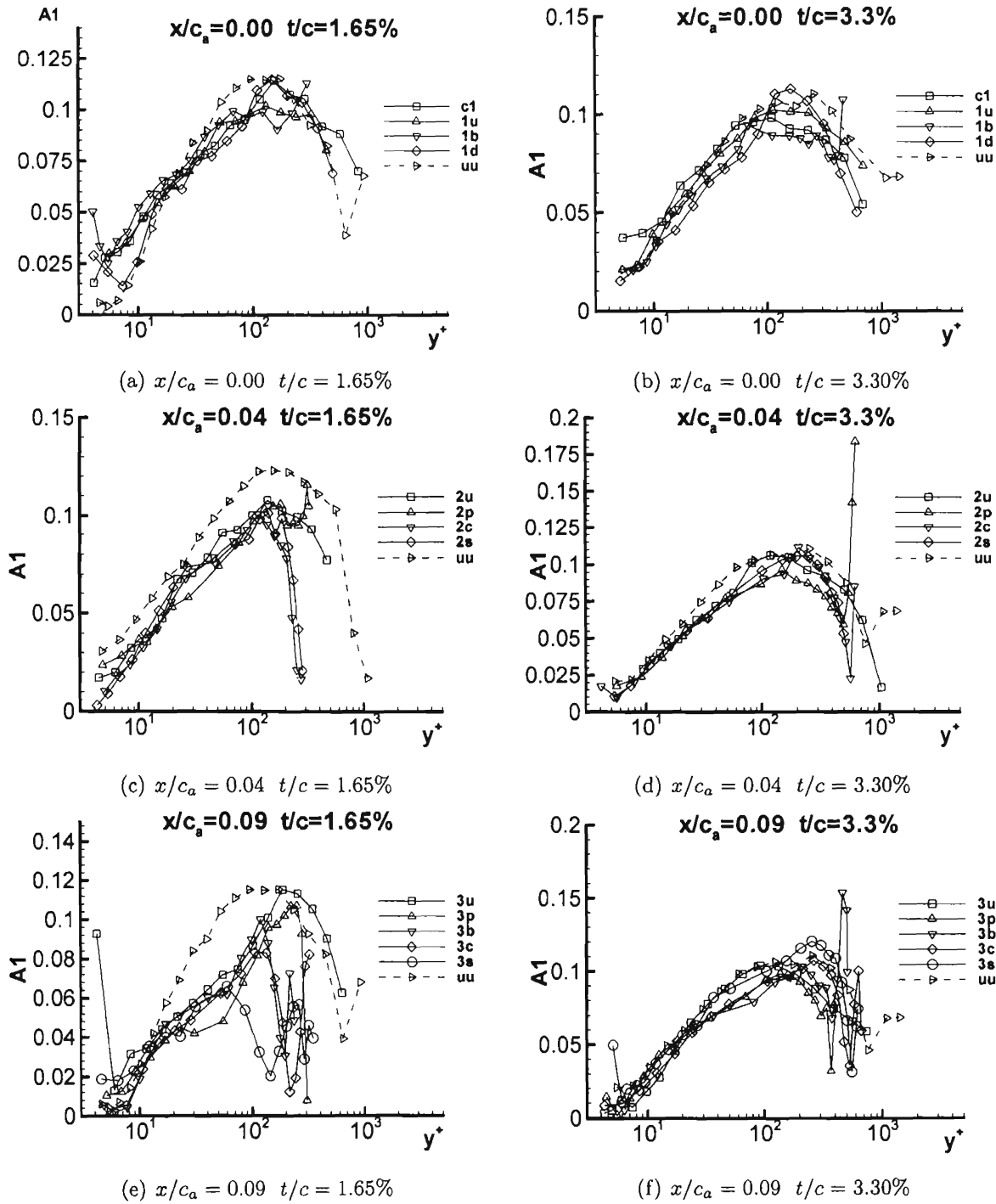


Figure H.12: A1 for both 1.65% and 3.30% in chord coordinate system

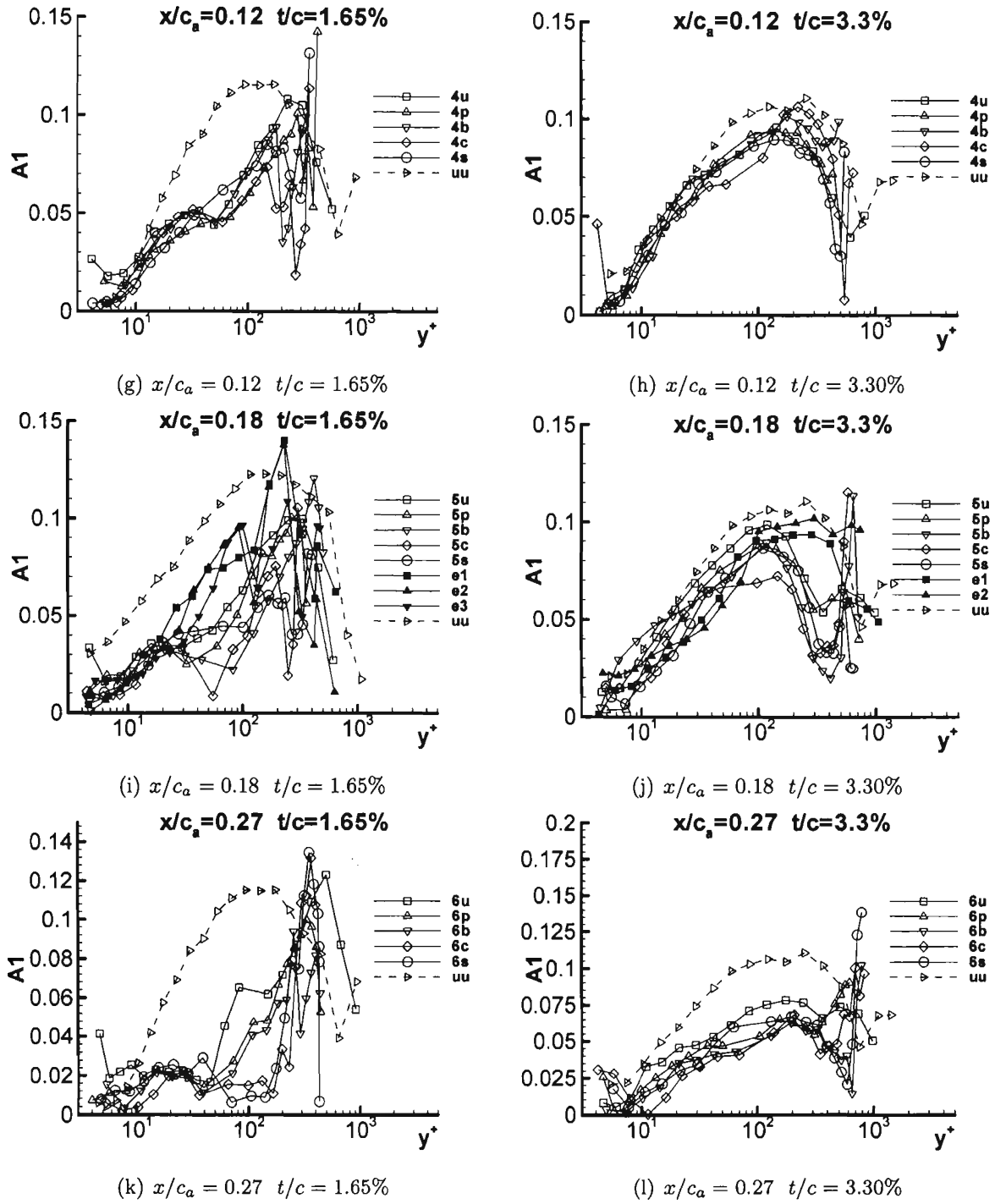
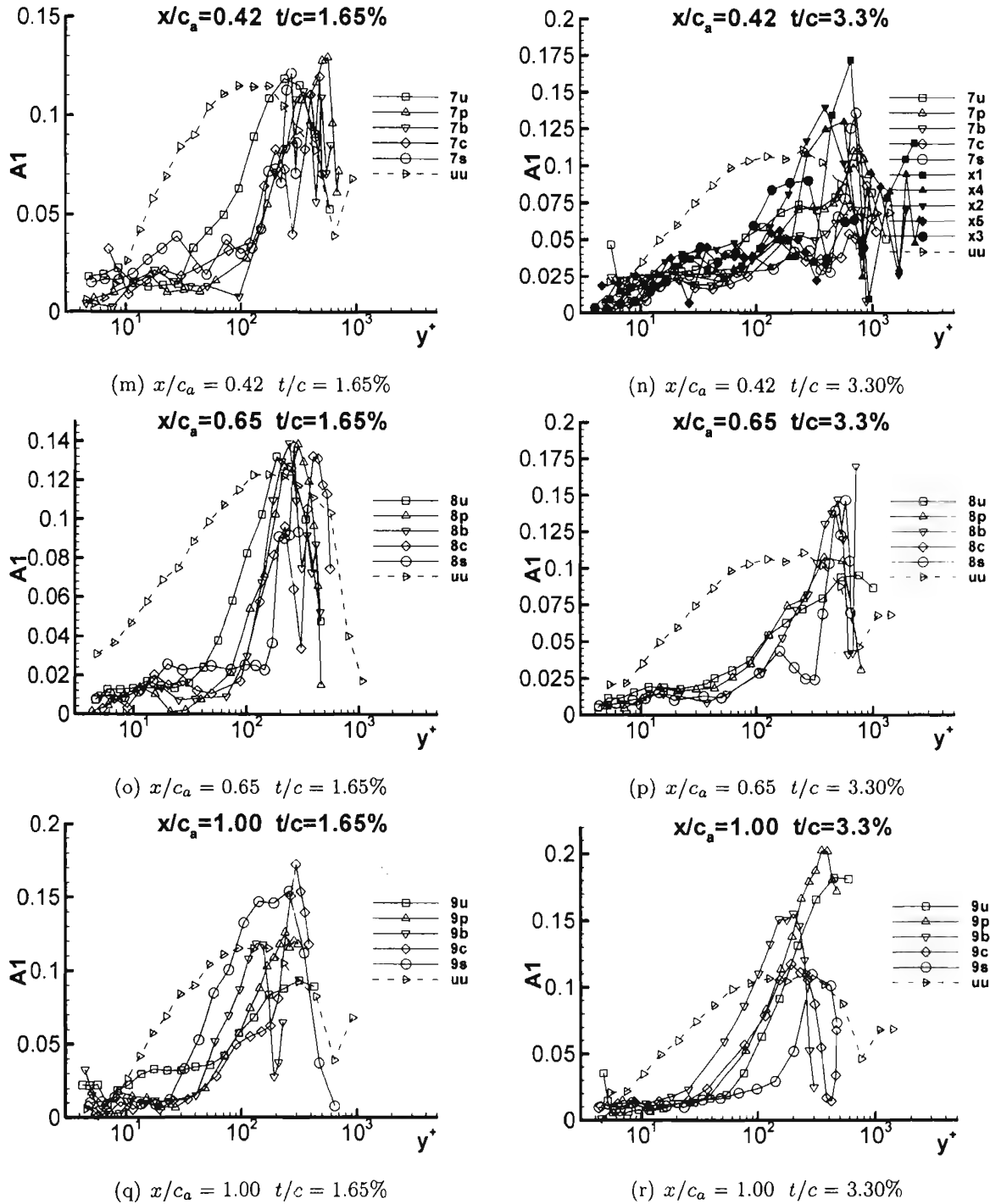
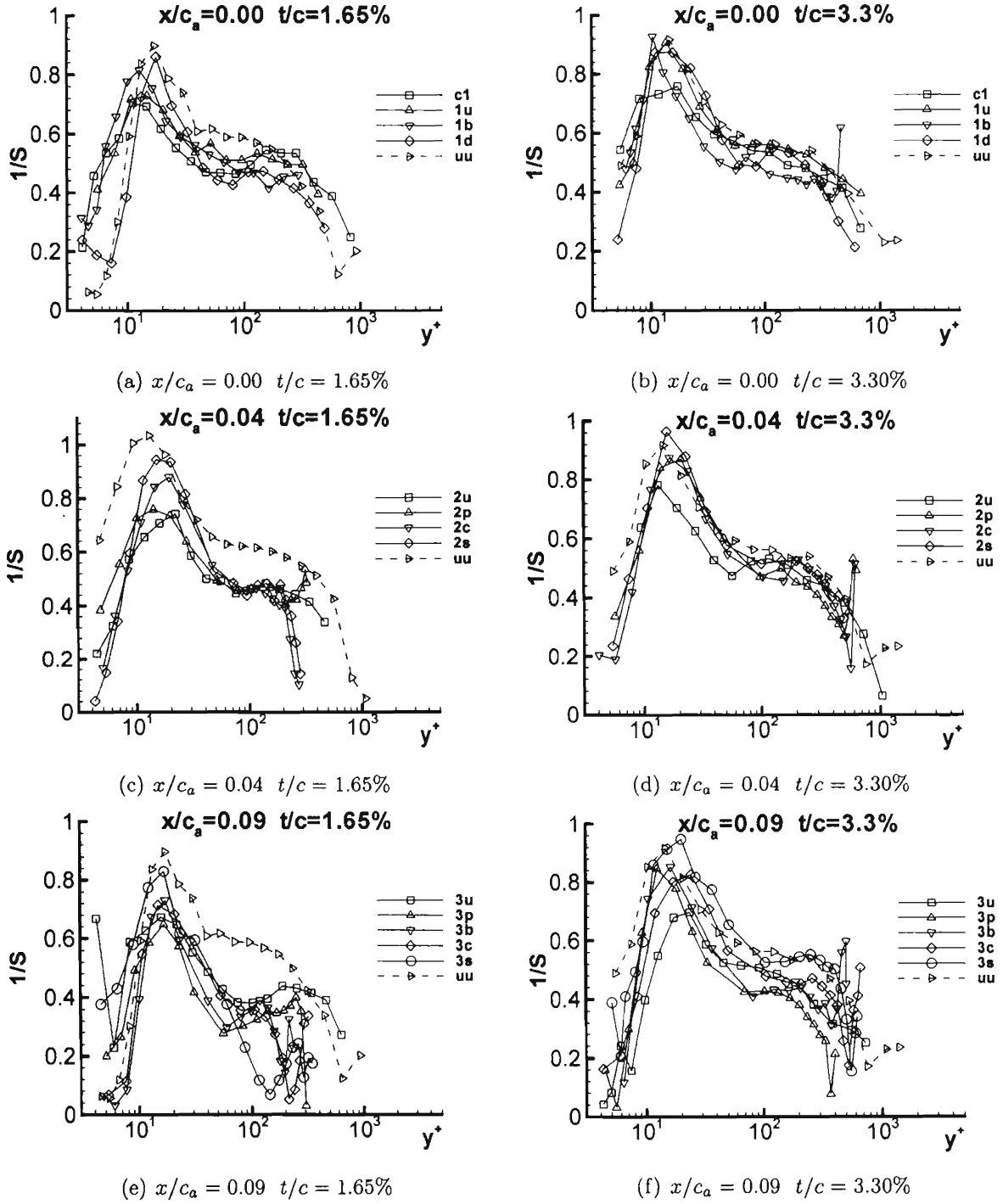
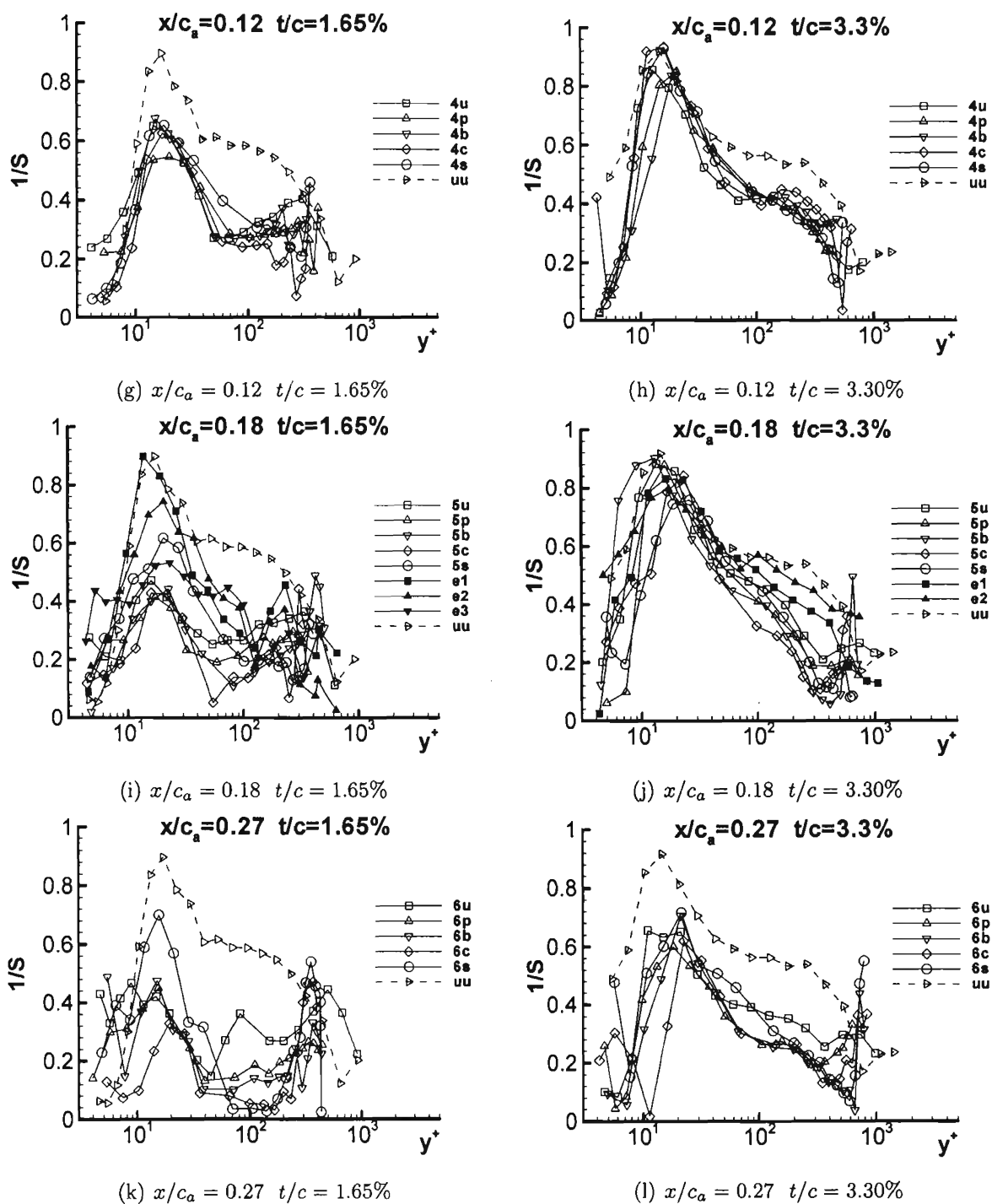


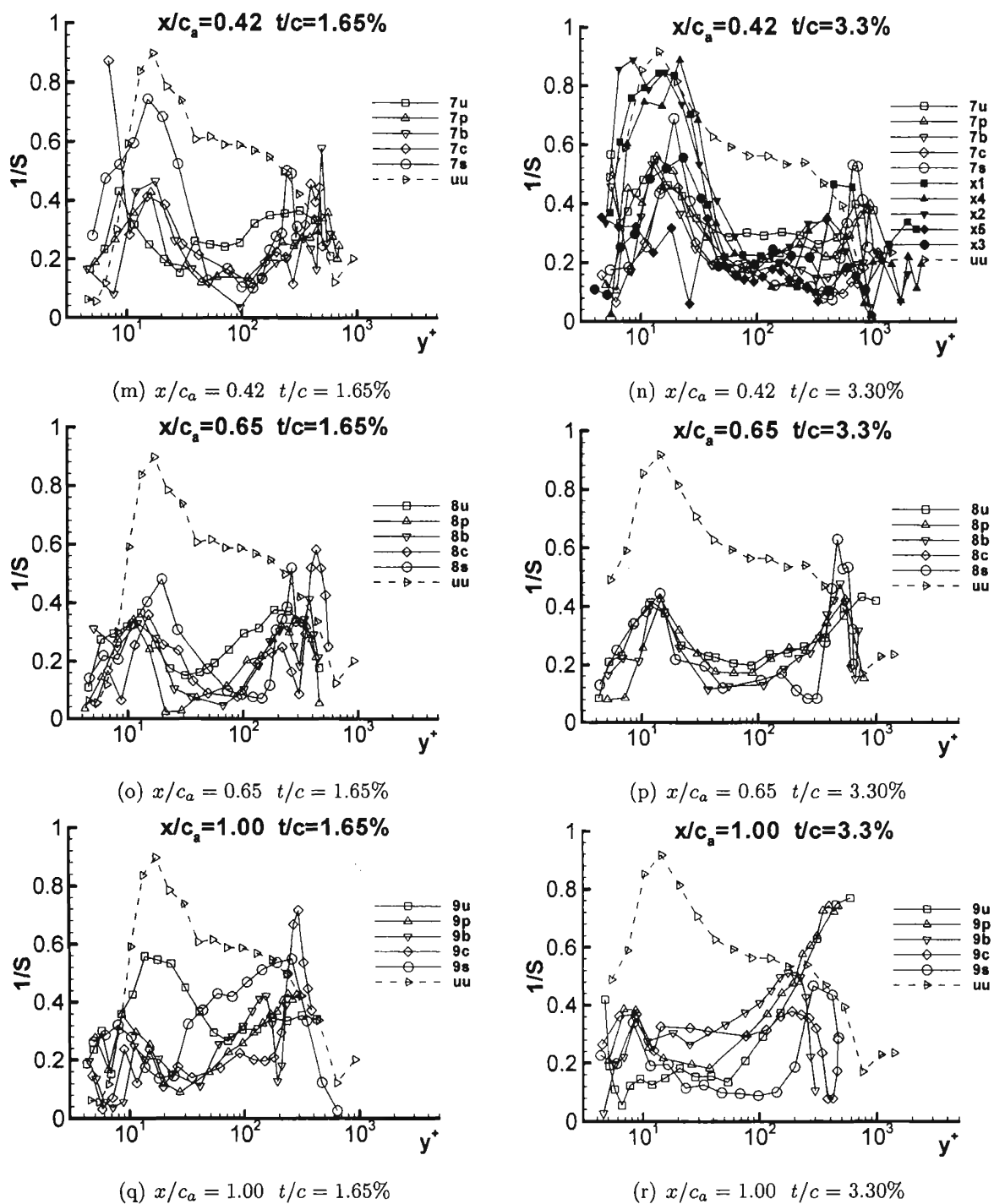
Figure H.12: A1 for both 1.65% and 3.30% in chord coordinate system (cont.)

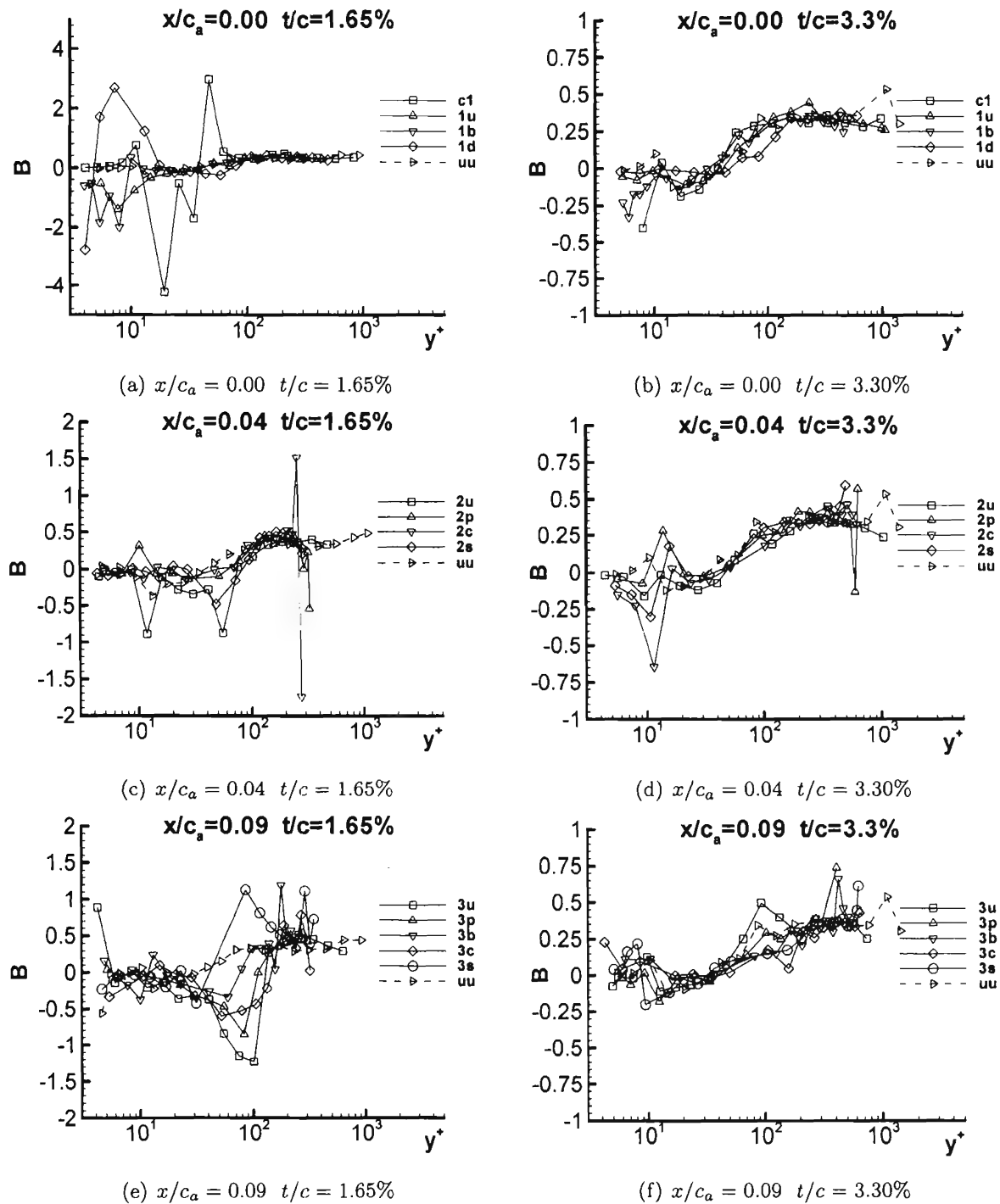
Figure H.12:  $A1$  for both 1.65% and 3.30% in chord coordinate system (cont.)

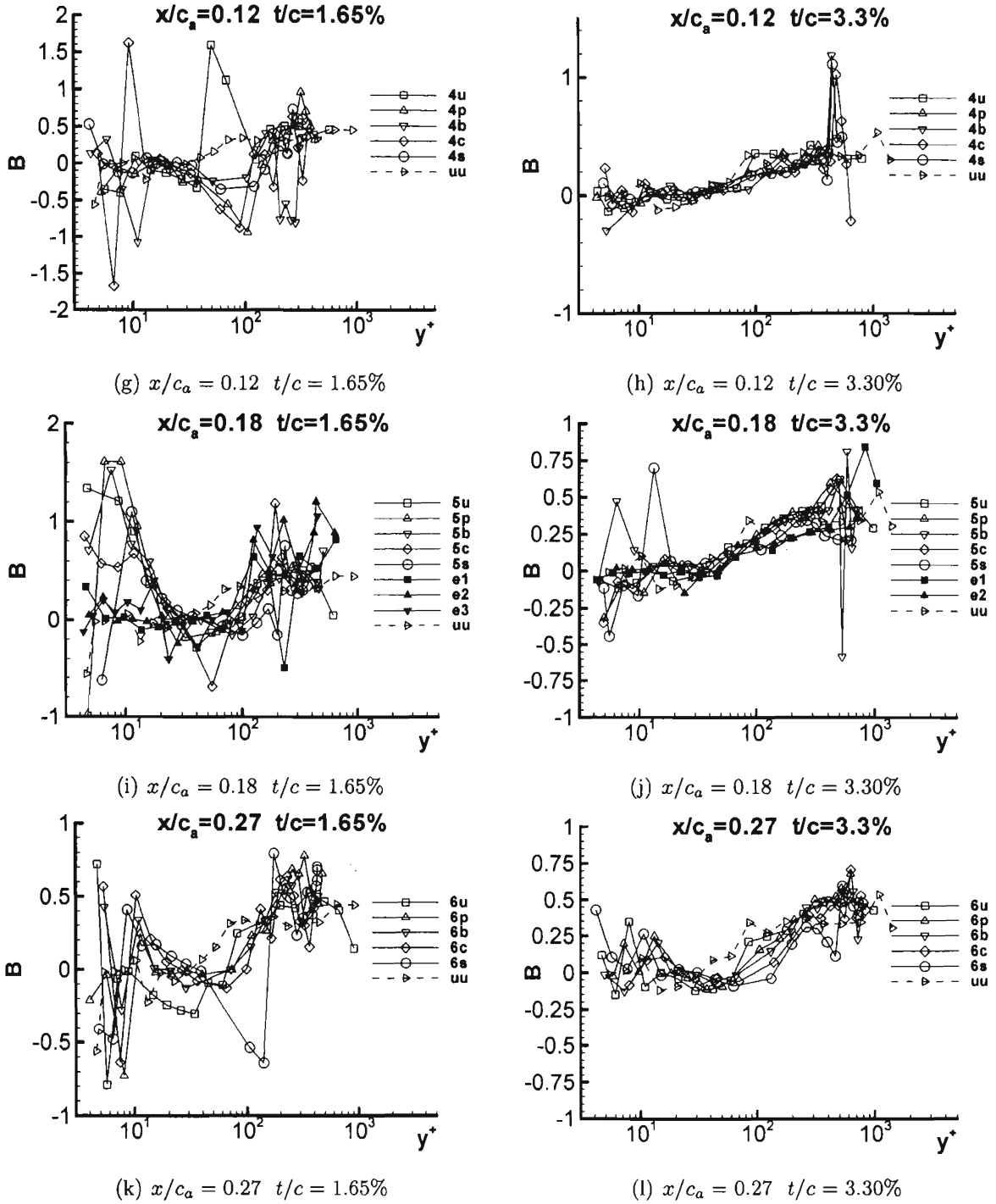
Figure H.13:  $1/S$  for both 1.65% and 3.30%

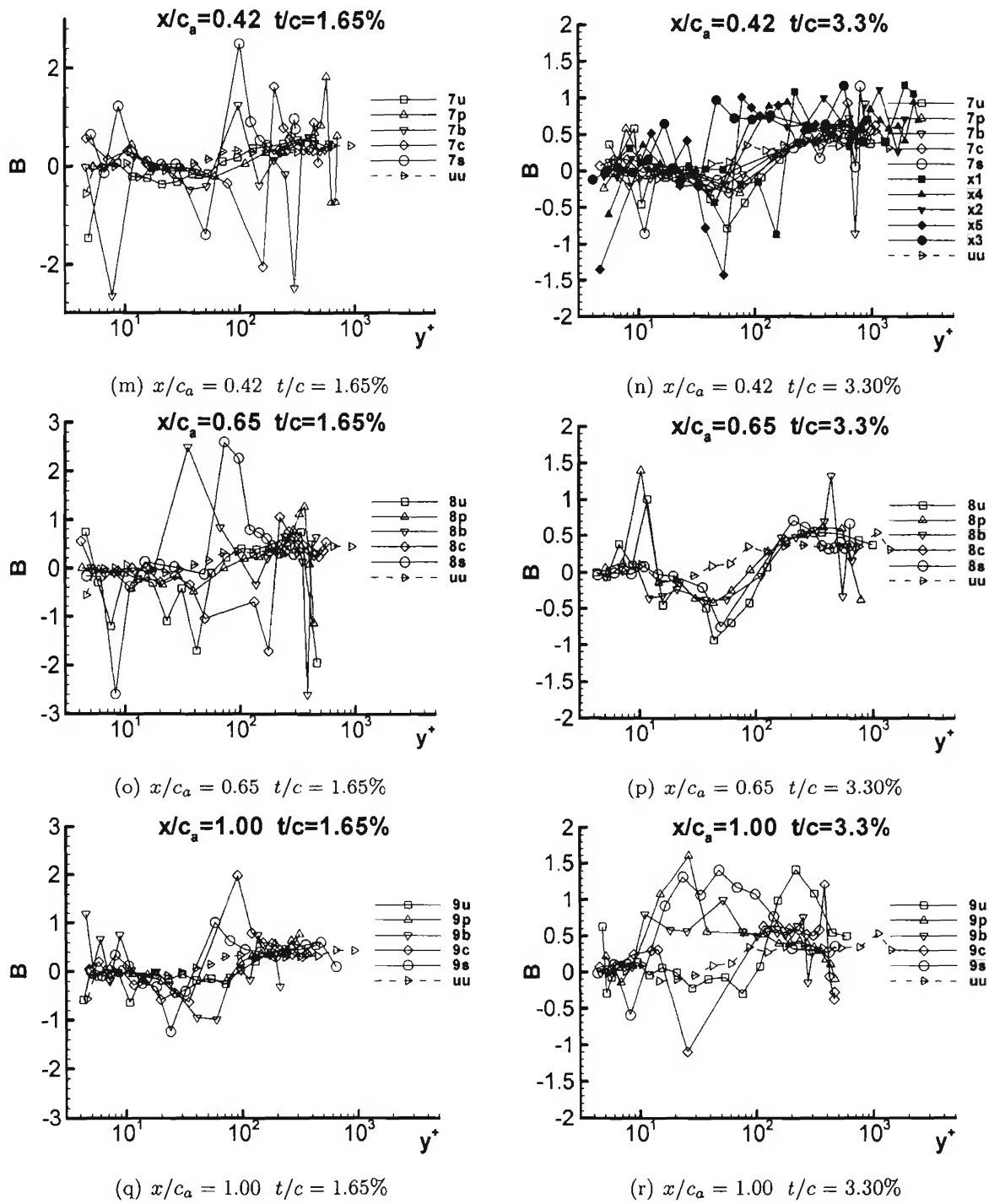


Figure H.13:  $1/S$  for both 1.65% and 3.30% (cont.)

Figure H.13:  $1/S$  for both 1.65% and 3.30% (cont.)

Figure H.14:  $B$  for both 1.65% and 3.30% in chord coordinate system

Figure H.14:  $B$  for both 1.65% and 3.30% in chord coordinate system (cont.)

Figure H.14:  $B$  for both 1.65% and 3.30% in chord coordinate system (cont.)

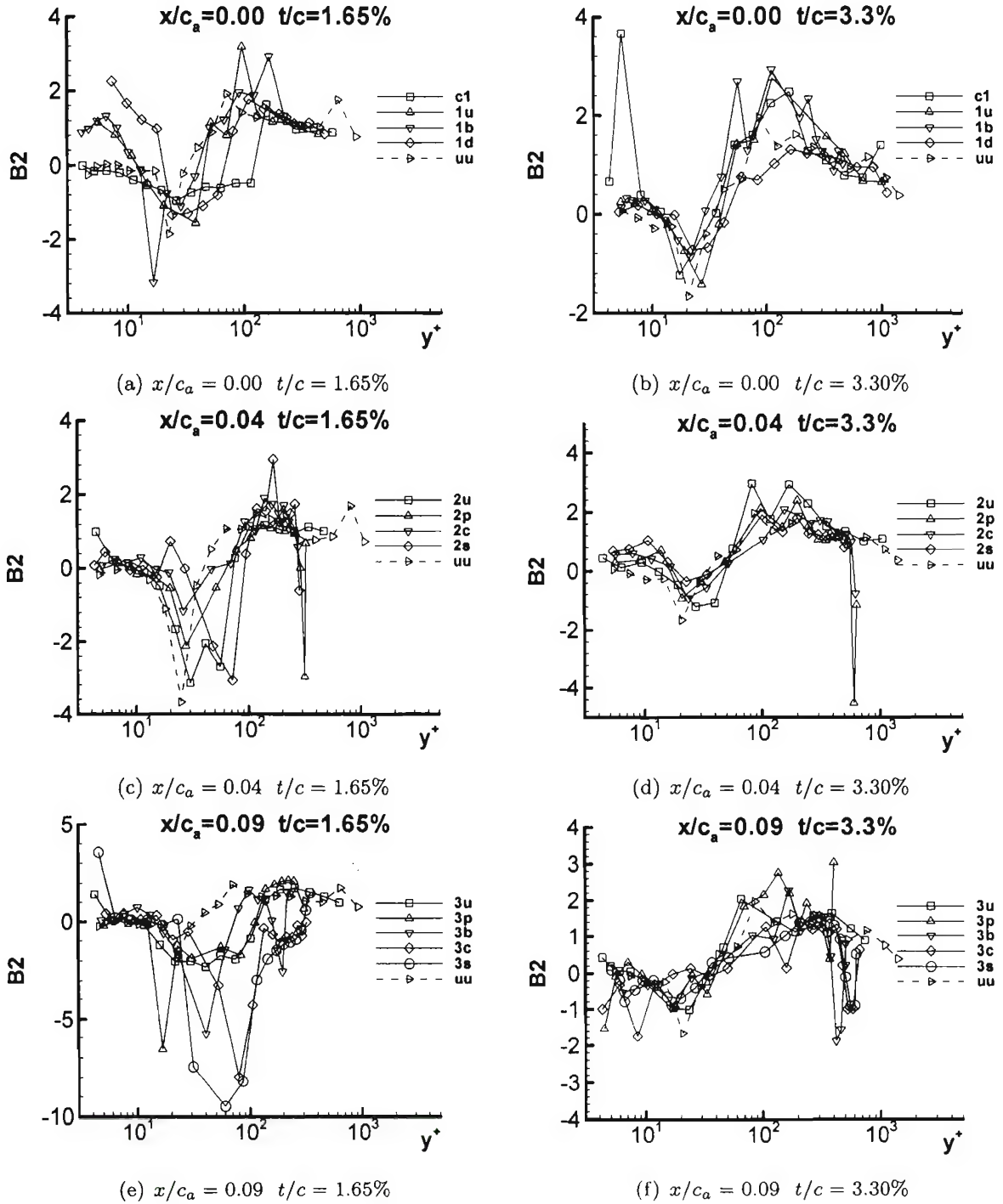
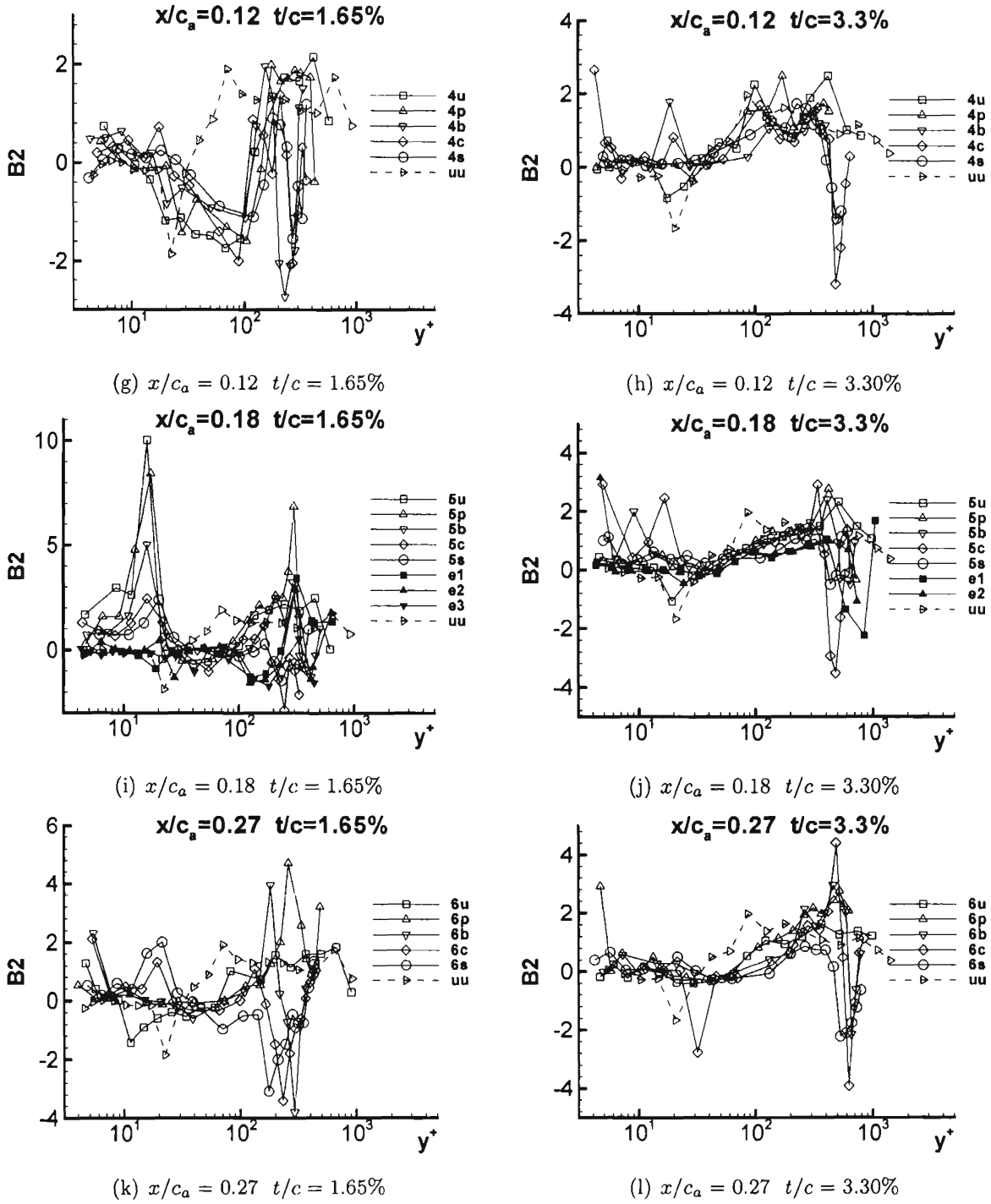
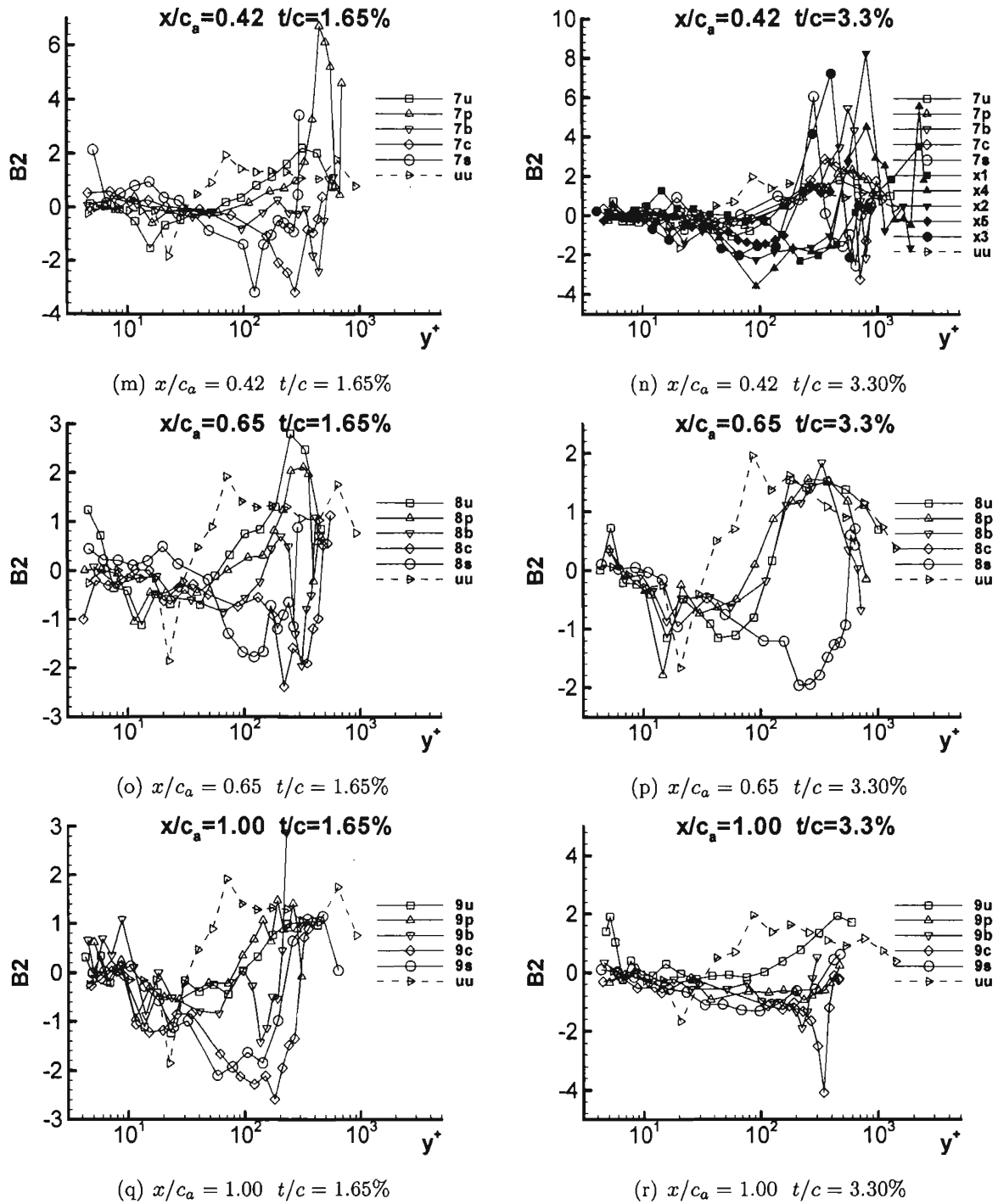


Figure H.15: B2 for both 1.65% and 3.30% in chord coordinate system

Figure H.15:  $B2$  for both 1.65% and 3.30% in chord coordinate system (cont.)

Figure H.15:  $B2$  for both 1.65% and 3.30% in chord coordinate system (cont.)



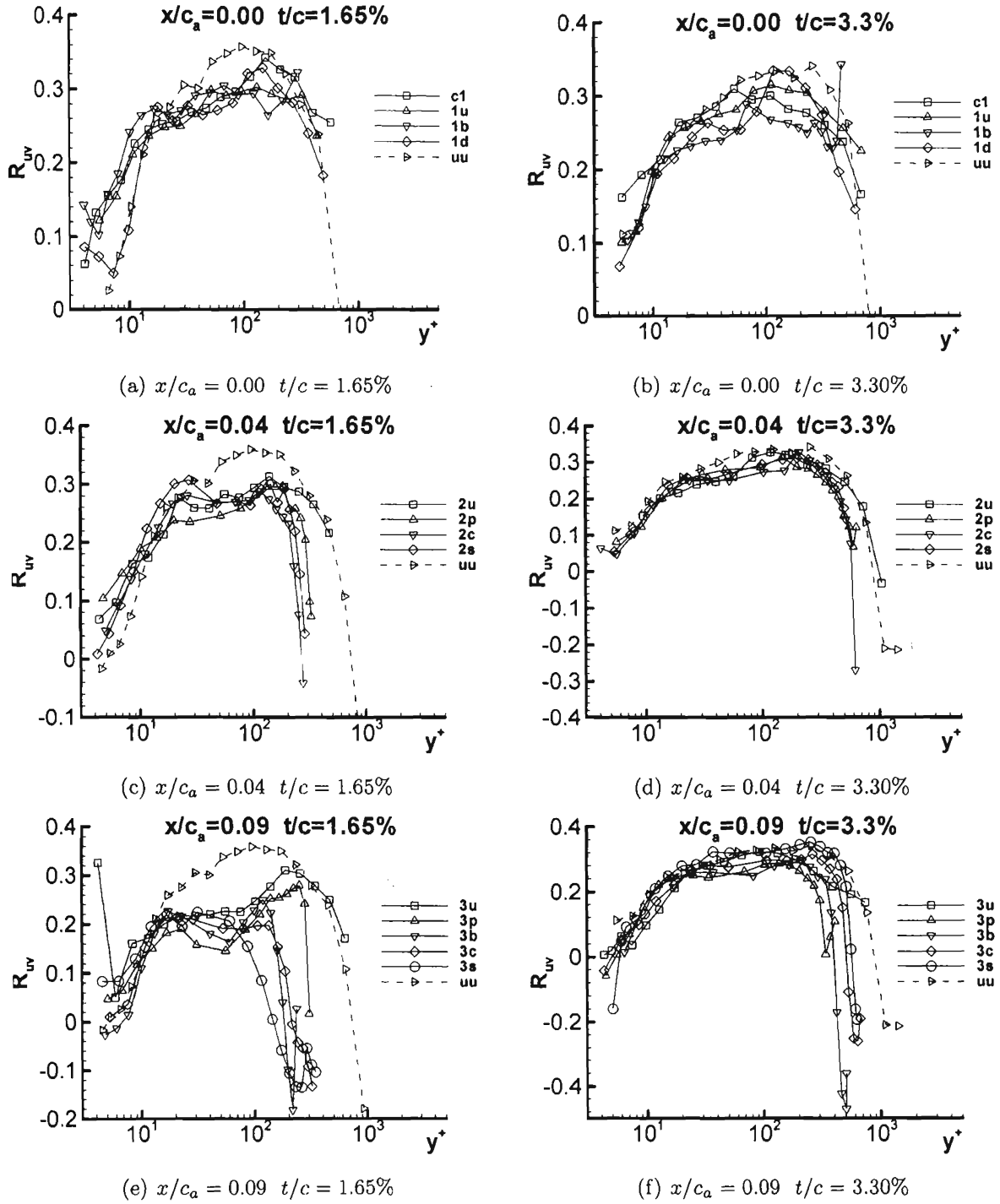


Figure H.16: Correlation coefficients of  $\overline{uv}$  for both 1.65% and 3.30% in chord coordinate system

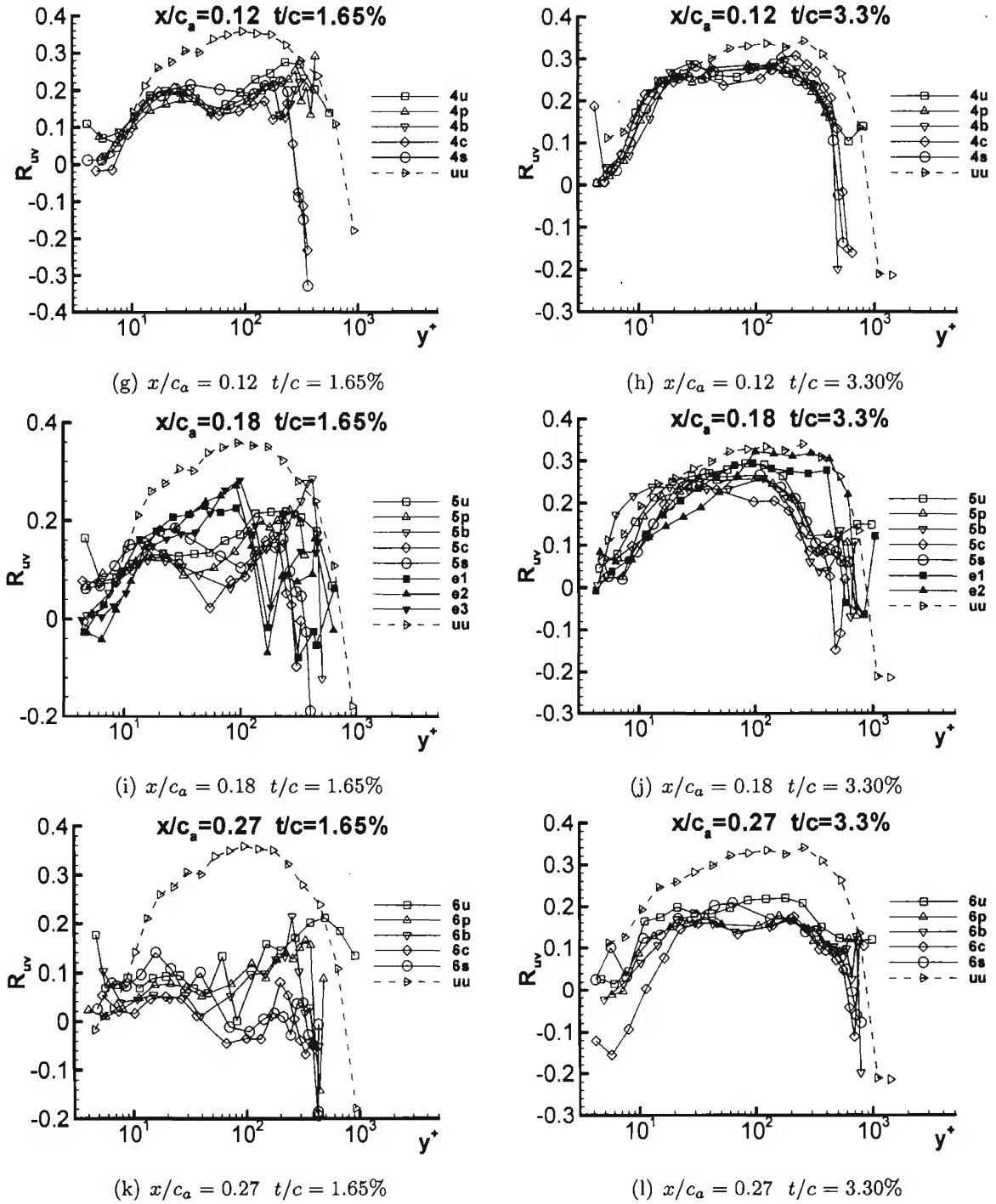


Figure H.16: Correlation coefficients of  $\overline{uv}$  for both 1.65% and 3.30% in chord coordinate system (cont.)

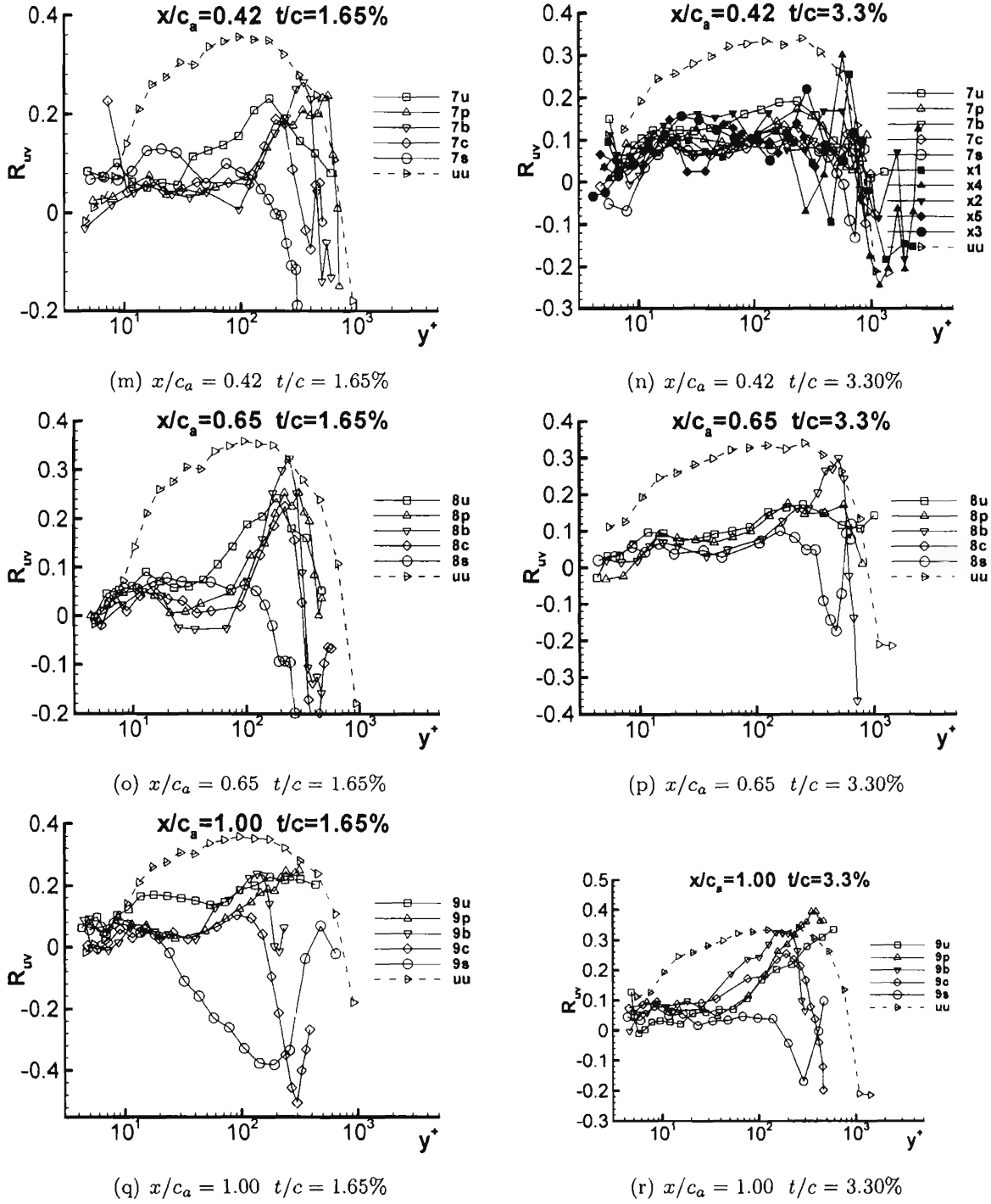


Figure H.16: Correlation coefficients of  $\overline{uv}$  for both 1.65% and 3.30% in chord coordinate system (cont.)

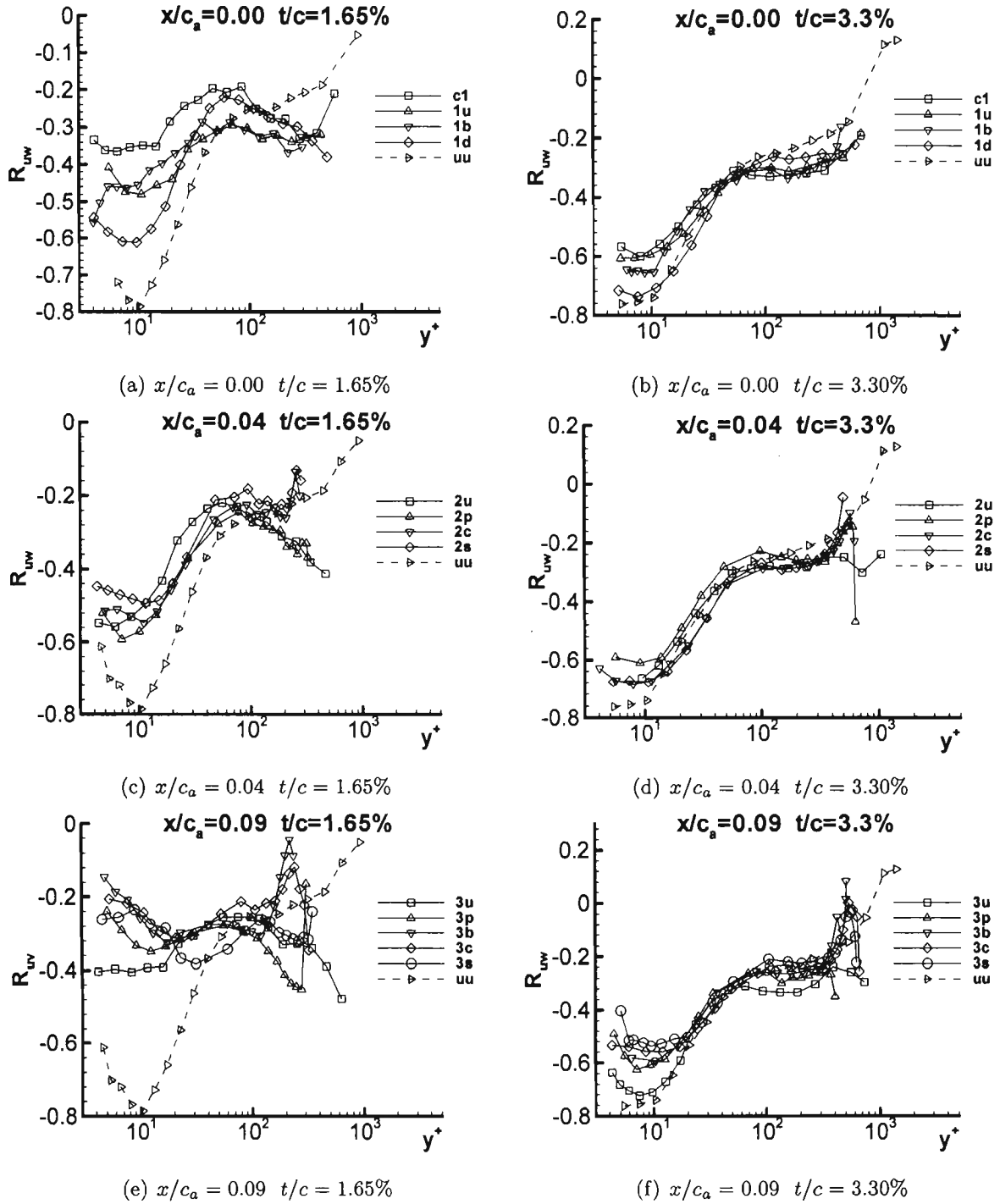


Figure H.17: Correlation coefficients of  $\overline{uw}$  for both 1.65% and 3.30% in chord coordinate system

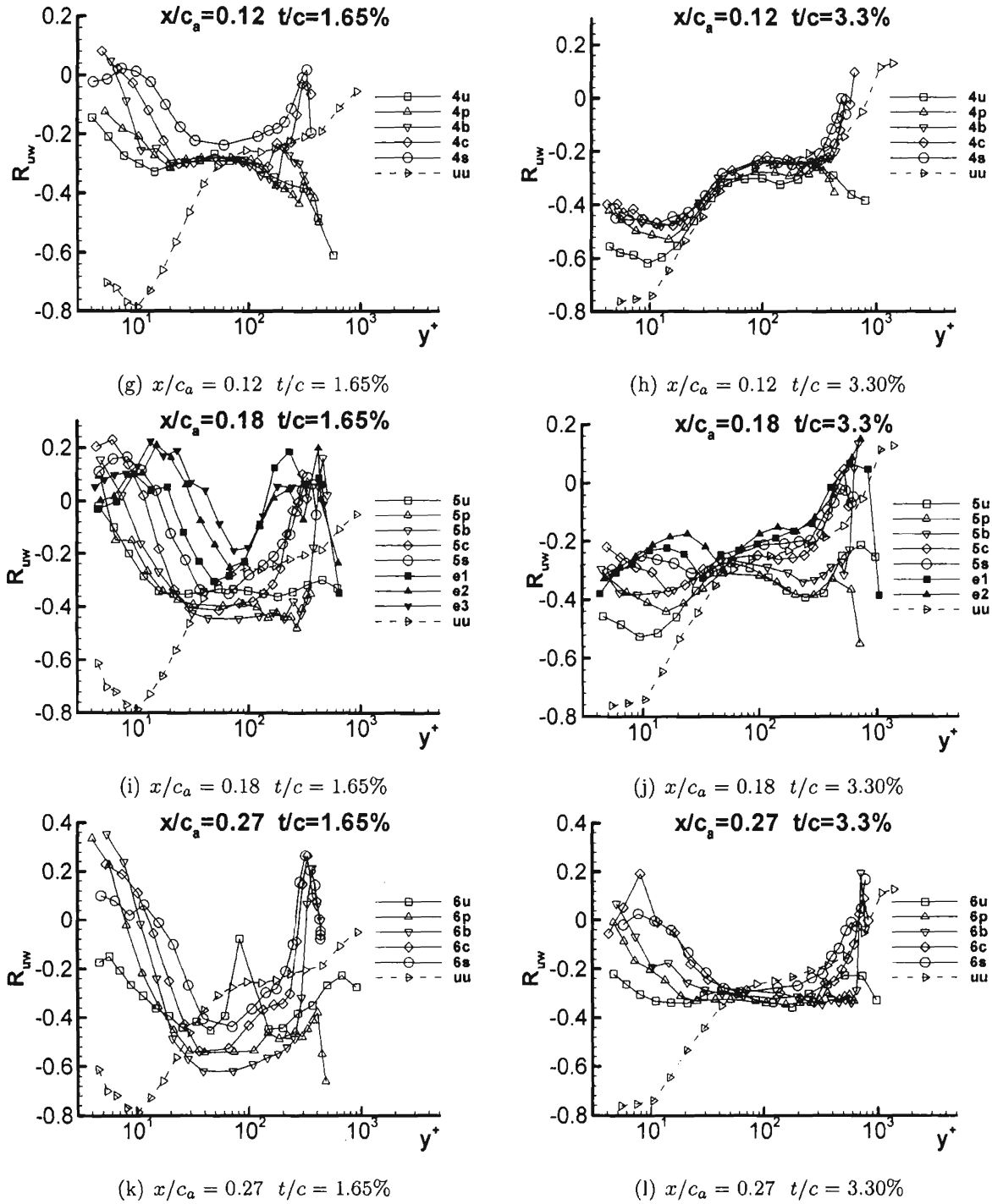


Figure H.17: Correlation coefficients of  $\overline{uw}$  for both 1.65% and 3.30% in chord coordinate system (cont.)

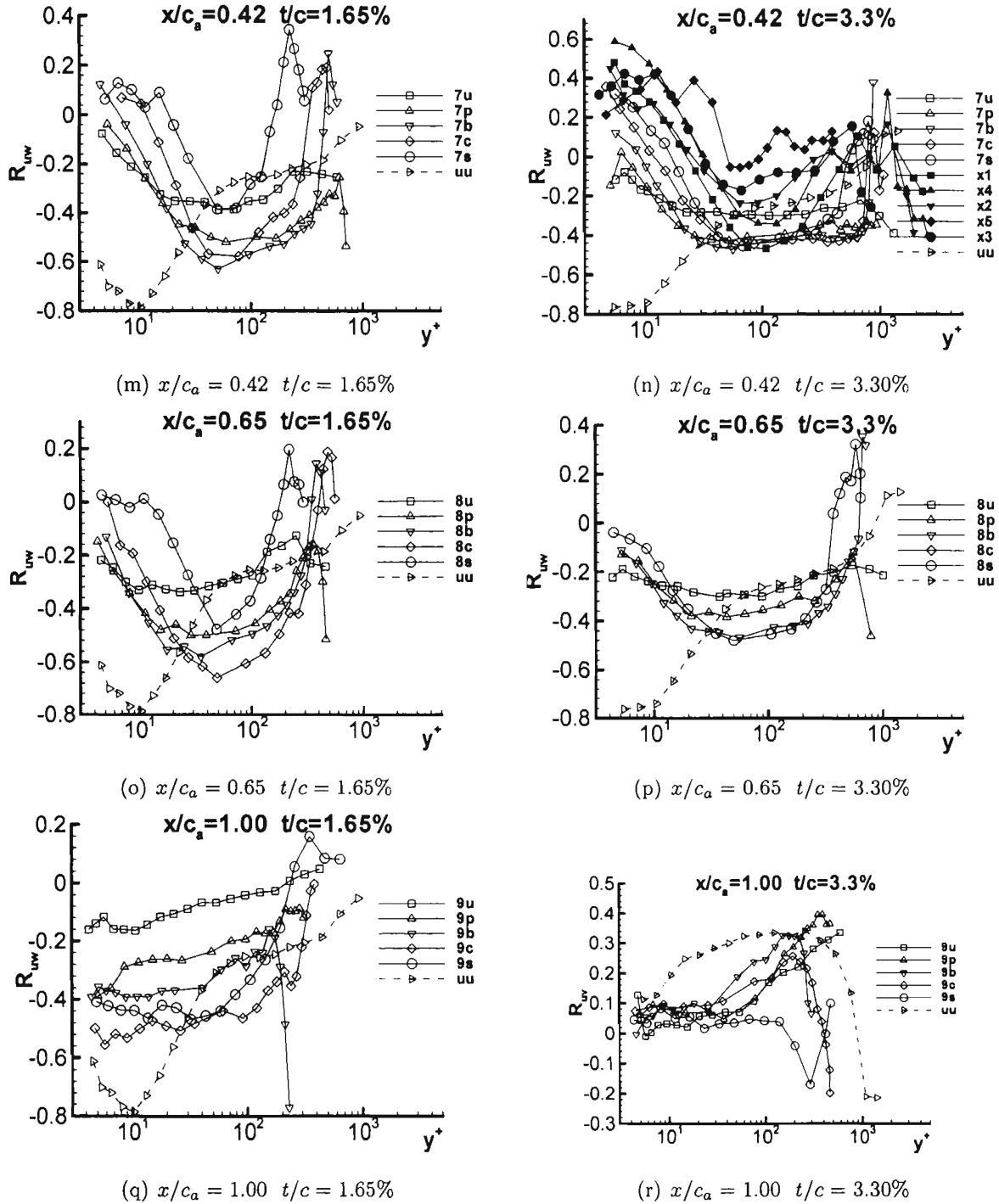


Figure H.17: Correlation coefficients of  $\overline{uv}$  for both 1.65% and 3.30% in chord coordinate system (cont.)

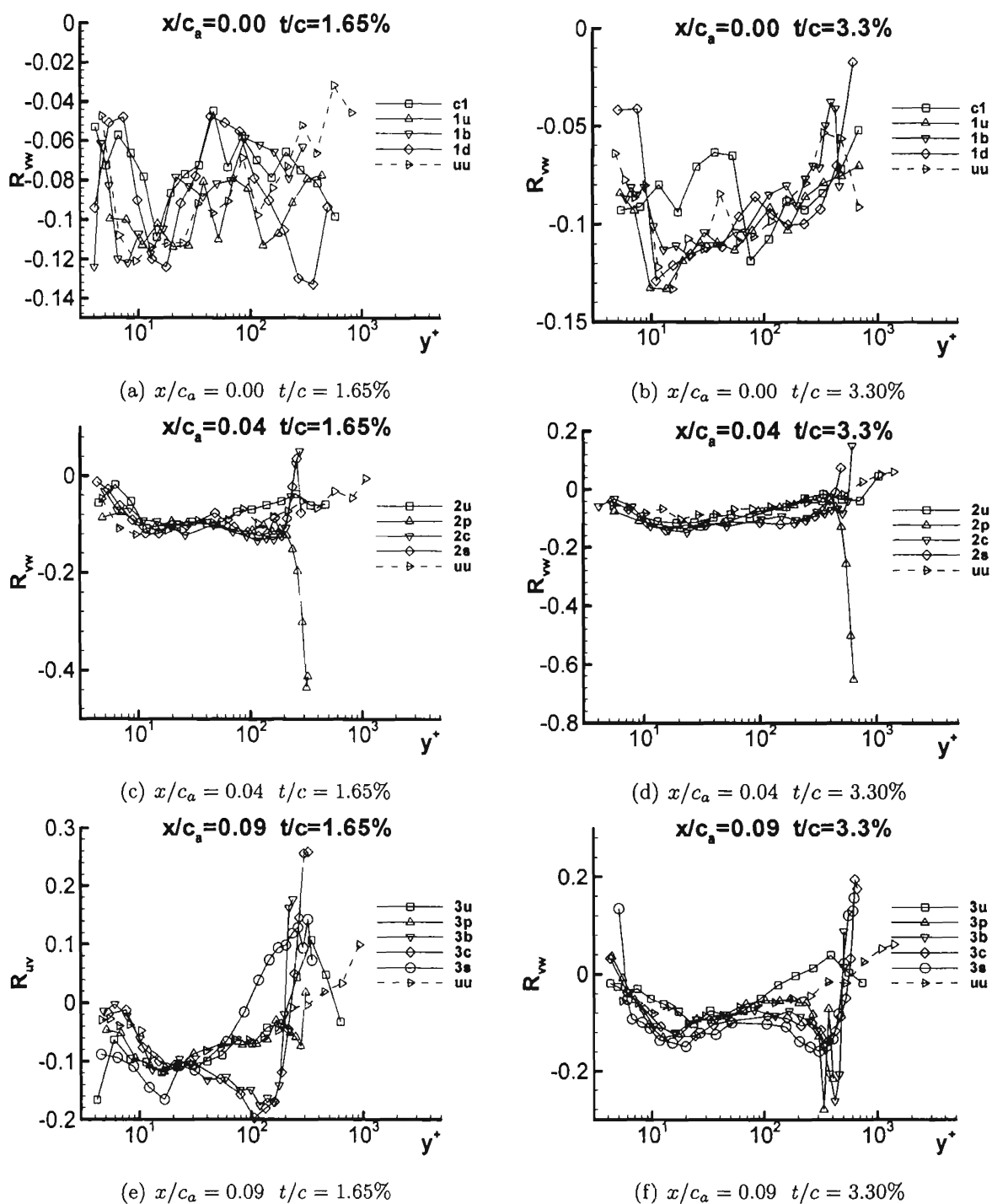


Figure H.18: Correlation coefficients of  $\overline{vw}$  for both 1.65% and 3.30% in chord coordinate system

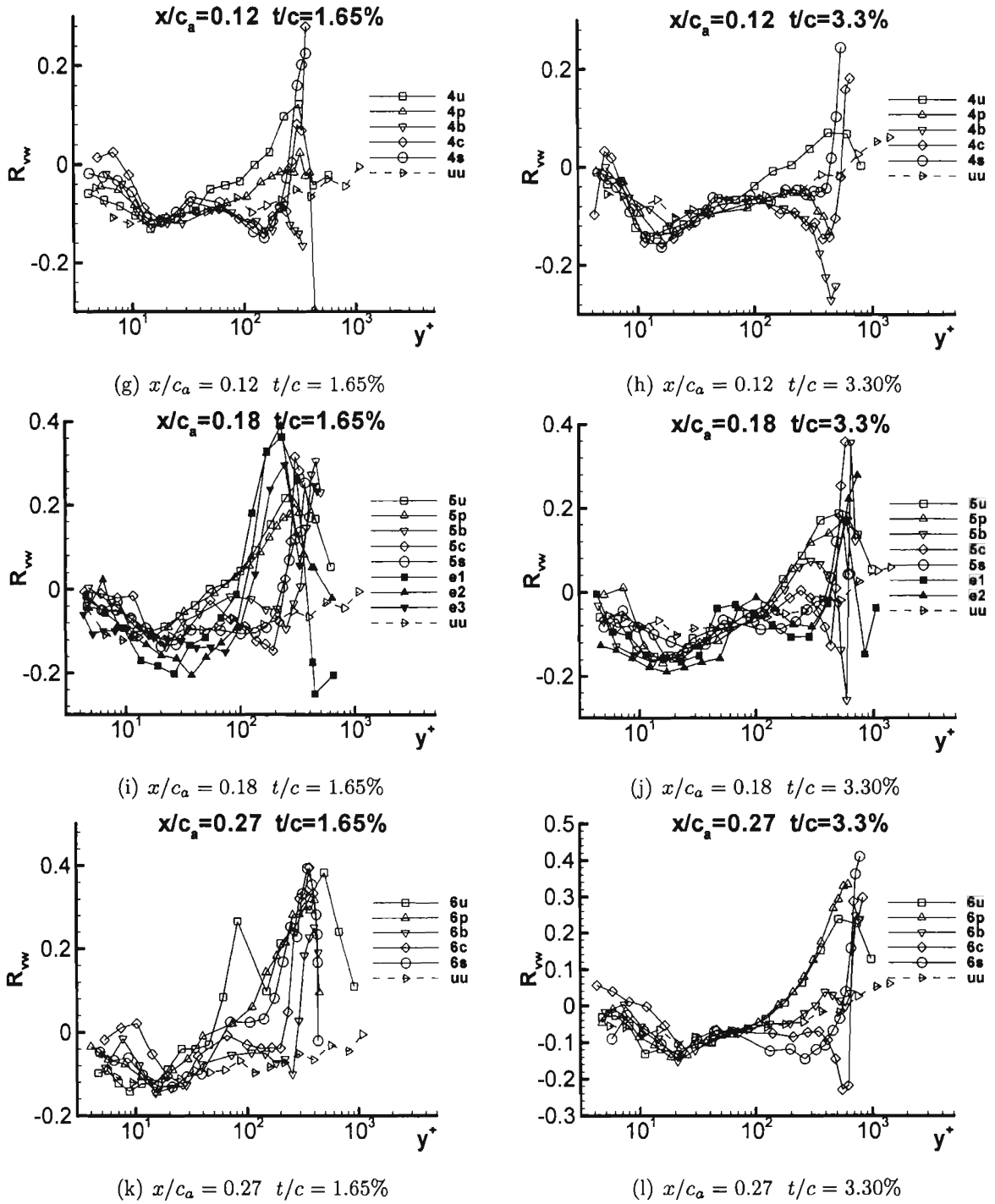


Figure H.18: Correlation coefficients of  $\overline{vw}$  for both 1.65% and 3.30% in chord coordinate system (cont.)



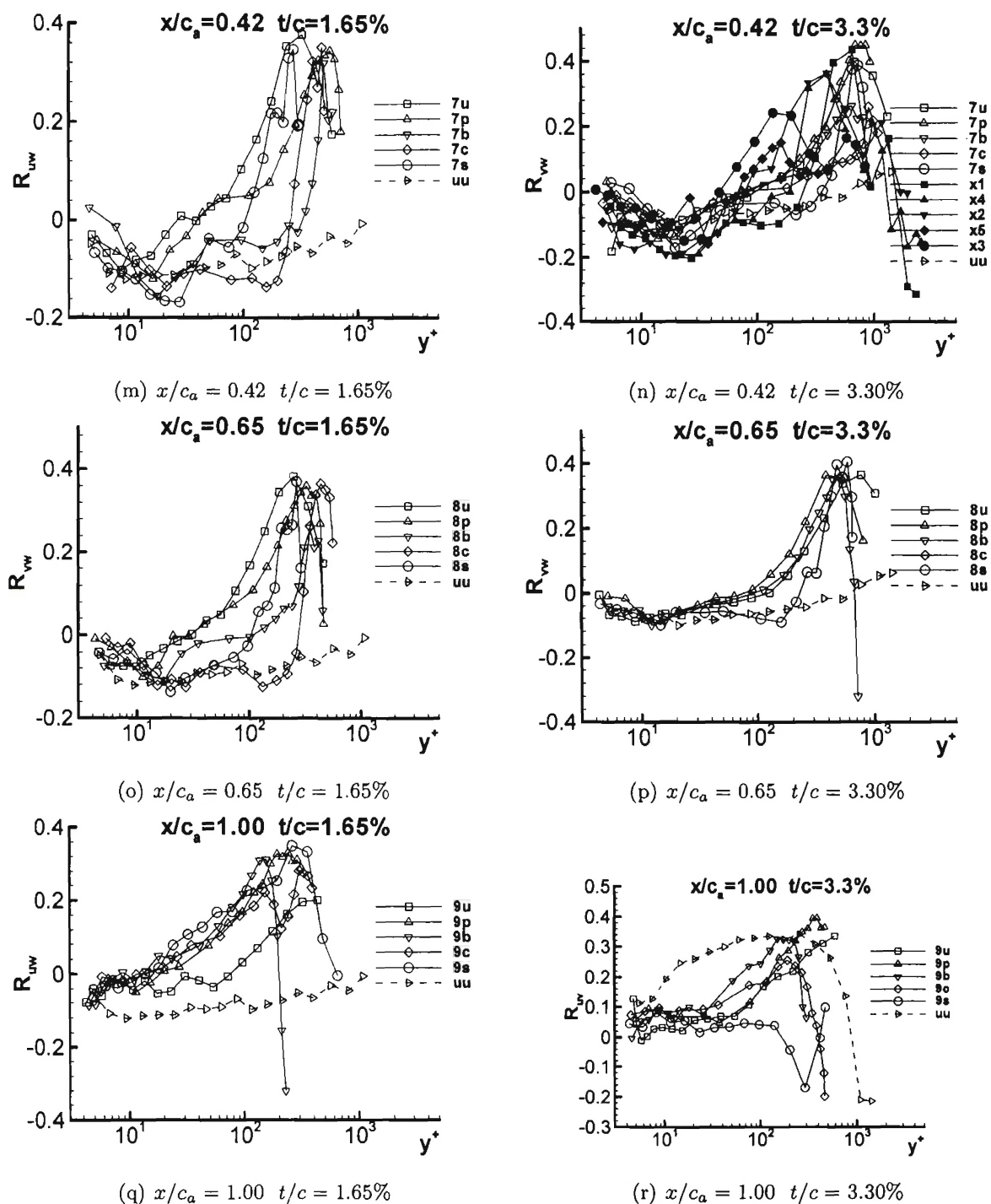


Figure H.18: Correlation coefficients of  $\overline{vw}$  for both 1.65% and 3.30% in chord coordinate system (cont.)

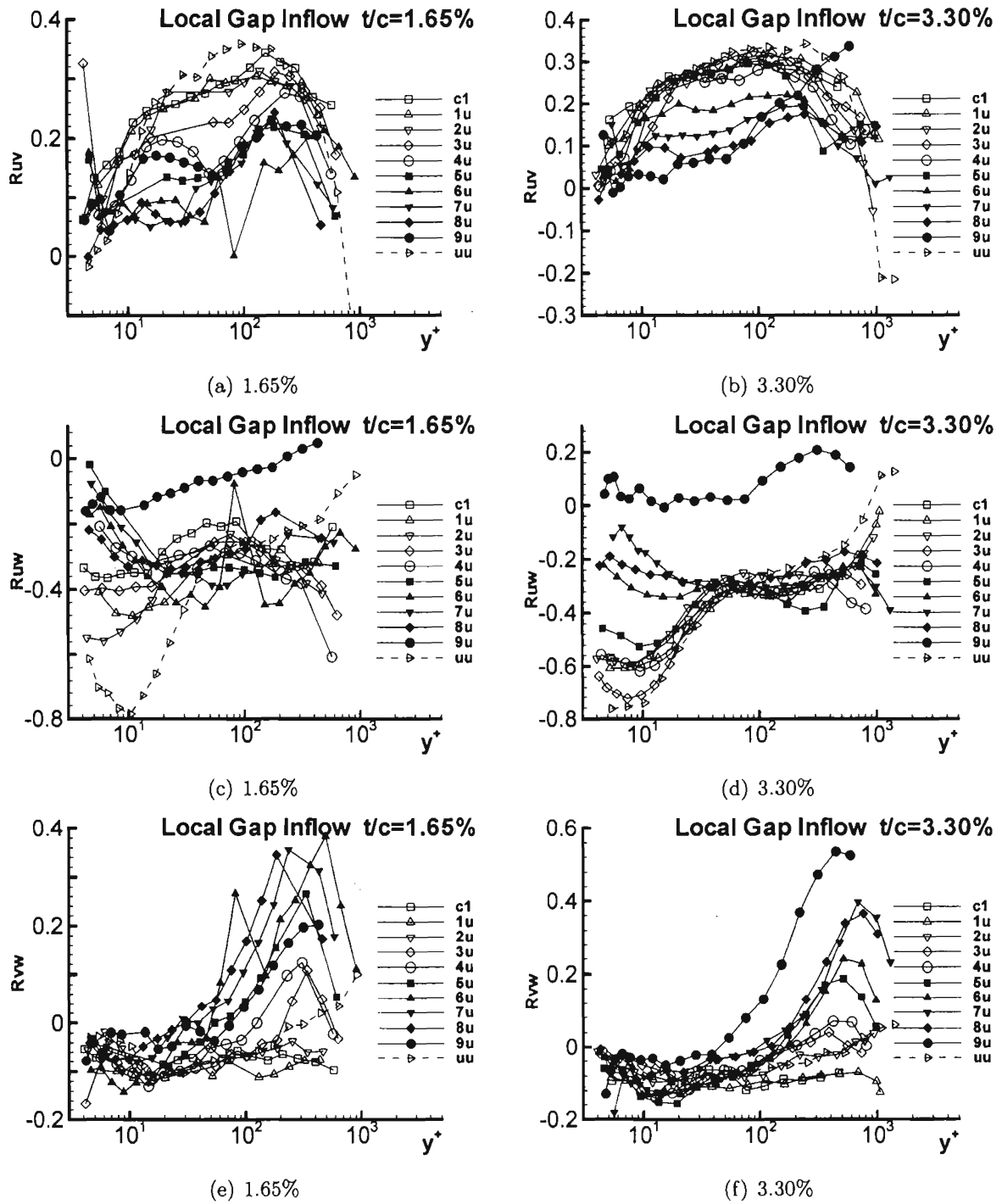


Figure H.19: Correlation coefficients of  $\overline{uv}$ ,  $\overline{uw}$ ,  $\overline{vw}$  on pressure side for both 1.65% and 3.30% in chord coordinate system

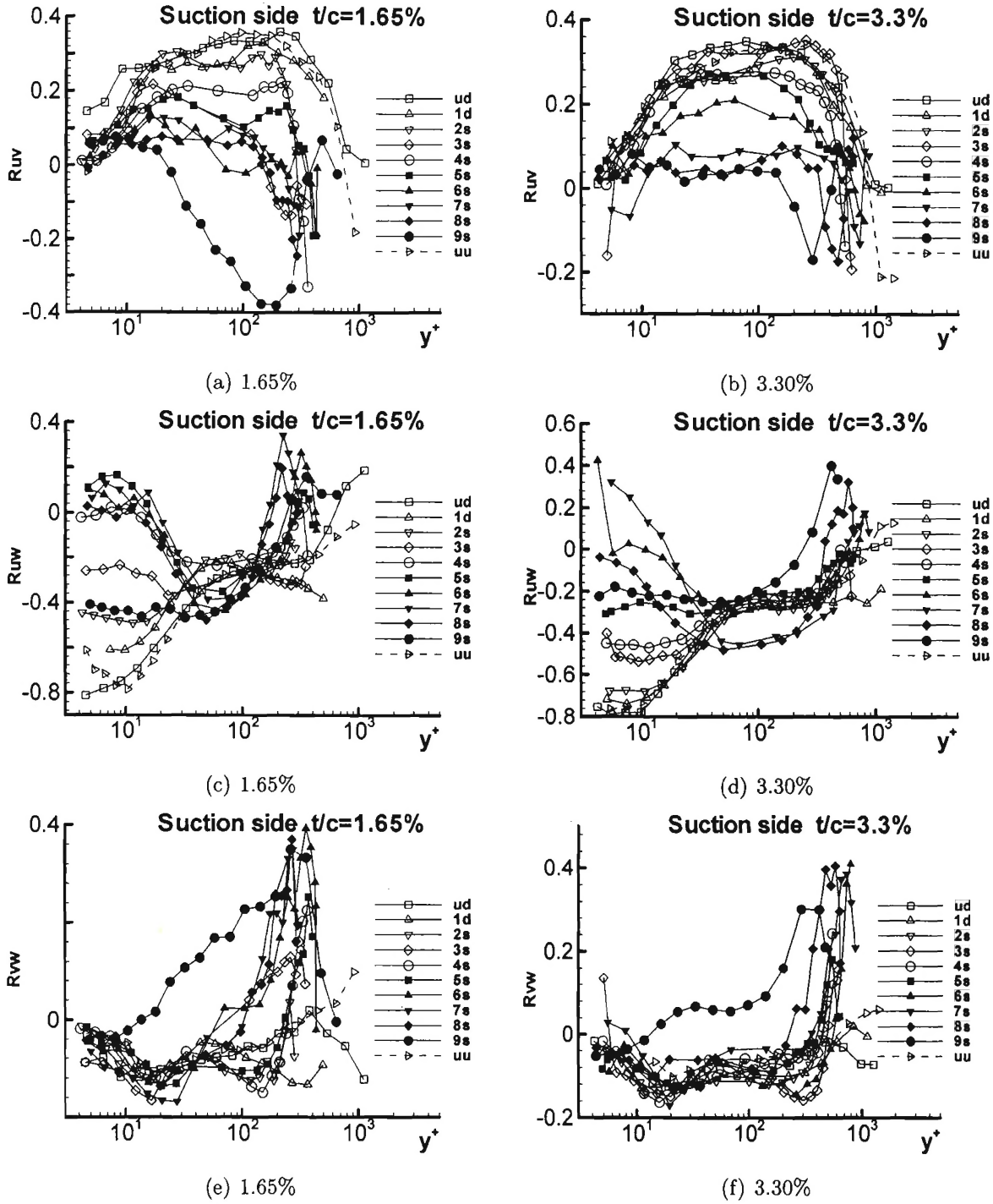


Figure H.20: Correlation coefficients of  $\overline{uv}$ ,  $\overline{uw}$ ,  $\overline{vw}$  on suction side for both 1.65% and 3.30% in chord coordinate system

# Vita

Genglin Tang obtained his Bachelor's and Master's Degrees in mechanical engineering from Beijing University of Aeronautics and Astronautics (BUAA) in July 1987 and March 1990, respectively. After he had worked over seven years as a full-time faculty member in the Department of Jet Propulsion at BUAA, he came to the United States to pursue his Ph.D. degree in aerospace engineering at Virginia Tech in August 1997. He finished his Ph.D. program in May 2004. His experience covered aerodynamics, turbomachinery, optical measurement, and vehicle diagnostics.